Experimental and Computational Analysis of Oil Flow in Cooling Galleries of Diesel Engine Pistons

Jens Lahr

Birmingham City University
Faculty of Computing, Engineering and the Built Environment

A thesis submitted in partial fulfilment of the requirement of
Birmingham City University for the degree of

DOCTOR OF PHILOSOPHY

January 2016

For my loving parents and my brother. And me.

A fool thinks himself to be wise, but a wise man knows himself to be a fool.

William Shakespeare

DECLARATION

I hereby declare that except where specific reference is made to the work of others, the contents of this dissertation are original and have not been submitted in whole or in part for consideration for any other degree or qualification in this, or any other university. This dissertation is my own work and contains nothing which is the outcome of work done in collaboration with others, except as specified in the text and Acknowledgements. This dissertation contains fewer than 65,000 words excluding appendices, bibliography, footnotes, tables and equations and has fewer than 150 figures.

Jens Lahr

January 2016

ACKNOWLEDGEMENTS

My grateful thank goes to my supervisor Dr. David Ashman for his advice, guidance, taking the time for long discussion and encouragement during hard times.

I also like to thank Dr. Manjit S. Srai for his alternative directions of thought and constructive discussions.

Particular thank goes to Tricia and Ray LeGallais for the encouragement and advise outside my field of study and for looking after my well-being.

Thanks also to the staff at the School of Computing, Engineering and Built Environment, in particular to Prof. Adrian Cole and the workshop lads.

ABSTRACT

This thesis describes in details the experimental and numerical investigations conducted to determine the filling and flow behaviour inside dynamic operating piston cooling galleries.

An experimental test rig was built to replicate the reciprocating motion of internal combustion engine pistons to allow for varying engine speed, stroke length, oil flow rate and piston size. Two transparent models were produced, representing cooling galleries for small sized engine pistons found in passenger vehicles and large sized engine pistons found in heavy goods vehicles and earth moving equipment. High speed image processing was undertake to capture the flow behaviour inside the galleries during the piston cycle. An oil mixture was used to replicate the properties of engine oil at engine operating conditions. The flow inside the gallery was recorded from various view positions to capture the flow throughout the gallery. The flow domains representing the investigated gallery shapes were generated and computational fluid dynamic (*CFD*) studies of the two-phase flow behaviour were performed. The studies of gallery filling and in-gallery flow behaviour were undertaken for the same parametric conditions as defined in the experiments. The flow behaviour and filling of both studies, experimental and numerical, are compared and discussed.

The results of the experimental and numerical studies compared well in terms of the identified directions of the main bulk oil flow within the small and large gallery and for the investigated crank speed and flow rate conditions. Both galleries showed that the flow in the gallery from inlet to outlet was mainly driven by the oil jet entering the gallery. The continuous entering jet forced a flow of the oil into the gallery branches. Strong turbulence in the direct vicinity of the inlet occurred as air and oil mixing was significant. It was found that the size of the turbulence region depended on the flow rate and engine speed, as well as the direction of movement of the gallery. It also sustained the presence of a large amount of medium-sized air bubbles due to mixing effects. Although the *CFD* did not predict the fine detail of the turbulent mixing, it did capture the underlying main flow characteristics,

including short circuiting at the inlet. In the mid-gallery section the formation of large air bubbles took place, which could span across the gallery height. The flow behaviour was still driven by the inflow, but also controlled by the gallery cross-sectional shape. At the gallery outlet the flow was predominantly inertia driven as a result of the gallery movement with the oil exiting mainly during the upward stroke, allowing formation of large air bubbles.

Distinctly different flows were encountered within the large and small gallery. The large gallery volume showed more unstructured or chaotic flow behaviour, especially in the mid-gallery section, as a result of the complex cross-sectional shape. In the small gallery volume the bulk flow was more controlled and wall-guided due to the limited space and regular cross-sectional shape. It was also found that the overall gallery filling for both galleries varied only by approximately 2% during the crank cycle. In contrast the variation of gallery section fillings of up to 30% and 50% for the large and small gallery respectively were determined, highlighting the effects of air movement within the galleries.

The experimental results showed that an increase in flow rate, reflected by an increase in jet exit velocity, led to strong air entrainment of micro-scale bubbles into the oil clearly visible inside the gallery, while an increase in engine speed led to significantly lower formation of micro-scale air bubbles in the gallery. In contrast the *CFD* struggled to capture such fine details, unless the mesh density reached a very fine level, resulting in unsustainably long simulation times.

TABLE OF CONTENTS

LIST OF FIGURES

LIST OF TABLES

NOMENCLATURE

Acronyms / Abbreviations

AC	Alternating Current
ADAMS	Multi-body dynamic analysis software
ALE	Arbitrary Lagrangian Eulerian (method)
ASMM	Algebraic Slip Mixture Model
aBDC	after Bottom Dead Centre
bBDC	before Bottom Dead Centre
BDC	Bottom Dead Centre
BL	Boundary Layer
CA	Crank angle
CAD	Computer Aided Design
CATIA	Computer aided design software
CFD	Computational Fluid Dynamic
CI	Compression Ignition
CPU	Central Processing Unit
CSF	Continuum Surface Force
CSS	Continuum Surface Stress
DC	Direct Current
DNS	Direct Numerical Simulation
FEA	Finite Element Analysis
GCI	Grid Convergence Index
GCR	Gallery Catch Ratio
GPU	Graphics Processing Unit
HGV	Heavy Goods Vehicle
HP	Horse Power

HTC	Heat Transfer Coefficient
ICE	Internal Combustion Engine
ICR	Inlet Catch Ratio
LES	Large Eddy Simulation
LGM	Large Gallery Model
LSM	Level–Set Model
LVD	Light Duty Vehicle
MAS	Micro-Alloyed Steel
NOx	Nitrous Oxides
OFR	Oil Fill Ratio
PISO	Pressure Implicit with Splitting of Operators
PIV	Particle Image Velocimetry
rpm	Revolutions per minute
RSM	Reynolds Stress Model
SBD	Solid Body Dynamics
SGM	Small Gallery Model
SI	Spark Ignition
SIMPLE	Semi Implicit Method for Pressure Linking Equations
aTDC	after Top Dead Centre
bTDC	before Top Dead Centre
TDC	Top Dead Centre
VOF	Volume of Fluid
WNN	Wavelet Neural Network

Roman Symbols

A_0, A_s	Constant in the calculation of the turbulent energy dissipation
A_i	Face normal vector, where i indicates x, y or z-direction
a_p	Piston acceleration
a, b, c	Position indicator
B	Constant for calculation of velocity in wall boundary layer
C_μ	Adjustable constant for calculation of turbulent energy dissipation
C_f	Wall friction factor
c_i	Neighbouring cell centre vector, where i indicates x, y or z-direction

d_n	Nozzle exit diameter
d	Diameter
E	Energy
F_{CSF}	Continuum surface force for phase interface modelling
F_{CSS}	Continuum surface stress for phase interface modelling
$f_{i\,LGM}$	Indicator frequency for large gallery model flow rate
$f_{i\,SGM}$	Indicator frequency for small gallery model flow rate
f_i	Cell centre to face edge vector, where i indicates x, y or z-direction
f	Friction factor
fps	Frames per second
$h_{gallery}$	Height of gallery
h_{oil}	Height of oil fill level in gallery
I_{ox}, I_{oy}, I_{oz}	Inertia vectors relative to part origin and in direction indicated
I	Turbulent intensity
K	Oil fill ratio after gallery filling period
k	Turbulent kinetic energy
L_{BL}	Boundary Layer thickness
L_{CR}	Conrod length
l_t	Turbulent length scale
l	Characteristic length
$\dot{m}_o$	Mass flow rate of oil
$\dot{m}_{pq}, \dot{m}_{qp}$	Mass transfer between q^{th} and p^{th} phase
m_e	Mass of empty container
m_f	Mass of filled container
M	Momentum
n_0	Exponent for turbulent profile description
n_{em}	Electric motor rotational speed
n, q, p	Counter
$\overline{OFR}$	Average oil fill ratio
OFR^*_{cas}	Oil fill ratio for every 5^{th} crank angle
OFR_h	Oil fill ratio height based
OFR_V	Oil fill ratio volume based

p	Pressure
Q_o	Orthogonal element quality
R_n	Nozzle radius
R	Convergence ratio of mesh independence assessment
R	Radius
r	Radial coordinate
s_p	Piston position relative to TDC
S	Source term
t_f	Time to fill container
T	Torque
t	Time
$\bar{u}, \bar{v}, \bar{w}$	Mean velocities in x, y, z–direction
u	Combined direction description refering to x, y, z–direction
U^+	Dimensionless mean velocity near wall
u', v', w'	Velocity fluctuations in x, y, z–direction
$U^\star$	Constant in the calculation of the turbulent energy dissipation
u_τ	Velocity in wall boundary layer
u_i, v_i, w_i	Velocity with coordinate direction index
u_m	Velocity of mixture
U	Free stream velocity outside wall boundary layer
u, v, w	Velocity in x, y, z–direction
$\dot{V}_{in}$	Volumetric flow rate entering through the gallery inlet
$\dot{V}_n$	Volumetric flow rate from the nozzle exit
$\dot{V}_{out}$	Volumetric flow rate exiting from the gallery outlet
$\dot{V}_o$	Volumetric flow rate of oil
v_{avg}	Average velocity in flow cross-section
v_e	Exit velocity of jet from nozzle
$V_{gallery}$	Volume of gallery
$v_{max\,l}$	Maximum velocity for laminar velocity profile description
$v_{max\,t}$	Maximum velocity for turbulent velocity profile description
V_{oil}	Volume of oil inside gallery
$v_{p\,l}$	Velocity for laminar velocity profile description

$v_{p\,t}$	Velocity for turbulent velocity profile description
v_p	Piston velocity
x, y, z	Coordinate system directions
y^+	Dimensionless wall boundary layer thickness

Greek Symbols

α_p	Phase volume fraction of p^{th} phase
α_q	Phase volume fraction of q^{th} phase
ε	Turbulent kinetic energy dissipation
ε_s	Surface roughness
κ_{vK}	von Karman constant (dimensionless)
λ	Second viscosity coefficient
μ	Dynamic viscosity
ω	Angular crank speed
π	Constant (3.14159)
ρ	Density of medium
ρ	Density
ρ_m	Density of mixture
ρ_o	Density of oil
ρ_p	Density of $p^t h$ phase
$\overline{\sigma}_{OFR}$	Average standard deviation of oil fill ratio
$\sigma_{\overline{OFR}}$	Standard deviation of average oil fill ratio
σ_{OFR}	Standard deviation of oil fill ratio
σ_s	Surface tension
τ	Time constant
τ_w	Wall shear stress in wall boundary layer
$\tau_{xy}, \tau_{yx}, \tau_{xz}, \tau_{zx}, \tau_{yz}, \tau_{zy}$	Shear stresses in direction normal to plane

Dimensionless Numbers

CFL	Courant–Fridrichs–Lewy number
Oh	Ohnesorge number
Re_x	Reynolds number in wall boundary layer
Re	Reynolds number
We	Weber number

CHAPTER 1 INTRODUCTION

1.1 Background and scope of the project

The main power source for the majority of current transportation vehicles is still the internal combustion engine (*ICE*), despite the engine still reflecting the design mainly developed a century ago. While electric vehicles are emerging, energy storage is still one of the major obstacles for this technology to be a replacement for new vehicles in the mass market. Hybrid vehicles are seen as an alternative in the meantime and have recently seen increasing popularity. These, however, are still employing the same internal combustion engines as power source, as found in conventional vehicles.

Much research has been conducted on internal combustion engines and together with advances in manufacturing, materials and control this has led to significant performance improvements and reductions of emissions and energy consumption. Although the main driver may be found in legislation, via introduction of tighter emission laws and energy consumption taxing, customers also have a strong input by demanding vehicles with reduced fuel consumption in times of increasing energy prices.

Internal combustion engines may be classified in many ways. In terms of combustion initiation and progression two fundamentally different types can be identified. The spark ignition (*SI*) engines, also referred to as petrol engines, use a controlled spark to initiate combustion of a pre-mixed mixture of air and fuel. On the contrary, compression ignition (*CI*) engines, also referred to as diesel engines, use a high compression pressure and temperature inside the engine cylinder to trigger combustion of a fuel injected into air. While both types share the majority of the principal internal components, the design of these does differ quite significantly. This is especially so with regards to the piston.

The perception of customers with regards to diesel engine powered vehicles has shifted over the last 30 years. New car registrations in the European Union in the last decade show

that the majority of cars were equipped with a diesel engine (ACEA, 2015), as shown in Figure 1.1. One reason can be found in the higher specific torque output, in comparison to the

Fig. 1.1 Share of diesel in new car registrations in Western Europe 1990 - 2014

(ACEA, 2015)

petrol engines (*SI*). A closer inspection also reveals that diesel engines are preferred for high annual mileage. Although the litre price of diesel in the UK is almost on par with the price of petrol, the lower fuel consumption together with financial considerations (tax) can provide lower overall annual costs for diesel engine power vehicles.

Many tests and experiments were conducted to further improve engines performance. This can be achieved through the increase in cylinder pressure and applies for *CI* as well as *SI* engines. The pressure can be raised in many ways, but always leads to an increase in the gas temperature inside the engine cylinder. The increase in pressure and temperature also increases component stresses, especially on the internal dynamic components of the engine, such as crankshafts, connecting rods and pistons. The latter is one of the most stressed components of the engine, being exposed to thermal, dynamic and inertia loads, all occurring at the same time.

The steady increase in engine performance has led to the requirement of active piston cooling to guarantee the reliability of the engine over its lifetime. This is achieved through the introduction of an internal open cooling gallery into the piston top and a fixed oil nozzle in the crank case. A constant free stream of oil from the nozzle is delivered to the piston

cooling gallery. Heat is removed from the critical and hottest zones at the piston top generally by transfer to the oil inside the piston gallery, but also by so-called shaker cooling, where the heat passes through the piston by transferring it from the piston top to the bottom via the oil inside the gallery. Whatever the cooling techniques, the underlying aim is always to keep temperatures below the critical material strength limiting temperature.

Internal piston cooling is predominantly found on diesel engines, as the majority of these are turbocharged for high specific power outputs, while the application to petrol engines is limited to few applications, but very comparable.

While the piston temperature is an issue, there are also implications for the overall engine performance. Pumping oil through the piston cooling gallery increases indirectly the fuel consumption, as higher oil pump flow rates mean more power taken off the crankshaft output, reducing overall performance. A compromise needs to be found to deliver the correct amount of oil to the gallery to obtain optimum filling, but at lowest oil pump flow rates. The term 'optimum filling' should be taken very broadly, as detailed information about the actual filling of cooling galleries is hardly available.

Nowadays simulation tools play a vital role in the development and optimisation of engines. Mechanical and thermal system behaviour, processes of combustion, emissions formation and reduction, and the control of these processes can be analysed before any physical component is built. While alterations to designs and processes can be investigated fast with simulations, the limitations are always found in the reliability of the outcomes. Validation of simulation results is always necessary, but is also expensive and difficult to obtain, especially for highly dynamic engine components.

Analytical and numerical investigations are conducted on pistons to assess thermal engine performance and include the processes at the boundary of the cooling gallery. Thereby the conditions inside the gallery are either estimated or guessed, but strongly influence the boundary conditions. Although simulation tools are well capable of dealing with the complex three-dimensional multi-physical problems of the piston, the time, user and hardware demand is very high. In order to reduce development cost a de-coupling of performance, thermal and structural analysis may occur. The interaction between different analysis types may be implemented by simplified static boundary conditions or by semi-empirical models, such as found for heat transfer between combustion gas and cylinder walls. When assessing simulation results of cooling channel heat transfer, a comparison to measured temperatures from pistons

is made. The shortcoming of this method is partially found in the many unknowns affecting the outcomes. One might describe the process as an iteration process, where the heat transfer coefficients are adjusted, until the temperatures of experiment and simulation from specified locations match closely enough. The unknown or non-validated filling of the cooling gallery imposes high uncertainty, as the mass of oil inside the gallery acts as a heat sink and conductor. Over- or under-estimation of the filling changes these coefficients and local overheating of the piston material and oil may result in failure of engine components. Therefore heat transfer simulations should not be separated from the oil filling simulations to establish reliable conditions. More detailed knowledge of the conditions and behaviour of cooling oil inside the cooling gallery can help improve simulations with respect to reduced complexity and time demand.

1.2 Problem definition and aim

Piston cooling is a crucial requirement for modern diesel engines for safe and continuous operation. Despite this being acknowledged by engine manufacturers, a quick analysis of current data available on the subject shows very little information. Although experiments and numerical simulations are performed for heat transfer analysis, both are completely detached from each other and direct comparison is mainly performed on little information. This means that significant estimation work has to be implemented in the investigations of heat transfer, raising questions about the consistency and accuracy of the results.

While experiments can provide reliable data in terms of piston temperature through measurement, the behaviour of cooling oil inside the cooling gallery can only be assumed, but is actually not known. In contrast the simulations are used to optimise heat transfer, but lacking knowledge of the conditions and behaviour inside the cooling gallery. The validation of simulation results is hardly found. Correlation between experiment and simulation can only be performed at best and mainly implemented by “tuning” of boundary conditions, such as heat transfer coefficients, until a close enough match between experimental and numerical results exist.

Due to the limitations stated above the aims of this investigation are to determine and assess the behaviour of cooling oil inside an actual cooling gallery under dynamic conditions,

and to compare and evaluate the quality of numerical simulations with regards to the actual behaviour.

The focus of the study will be primarily on cooling galleries for diesel engines pistons. Internal cooling of petrol engine pistons is limited to few applications only, but the findings from *CI* engine cooling galleries can be transferred to *SI* engines, as the underlying principles are identical.

CHAPTER 2 STATE OF TECHNOLOGY AND KNOWLEDGE

This chapter identifies and assesses work publicised related to the field of piston cooling. Firstly the processes in engines are explained highlighting the path of heat transfer inside the engine, particular on the piston to set the context. This is followed by an overview of how piston cooling is implemented and how it can be determined. Parameters are identified and evaluated with regards to strength of influence. As environmental considerations play an ever increasing role, the effects of piston cooling and arising issues are evaluated.

2.1 Internal combustion engines

Internal combustion engines are the power source in the majority of all transportation vehicles, from small two wheeled scooters to large container ships. As mentioned previously, these can be separated into two specific types with regards to their initiation of combustion, namely spark ignition (*SI*) engine and compression ignition (*CI*) engines. While showing differences in the combustion process, both engines share the same internal components to generate torque and power output. The main components are crankshaft, connecting rod (conrod), piston pin and piston, whereby specific designs apply.

Spark ignition engines use a spark plug to generate a localized high temperature zone to ignite a trapped pre-mixed air and fuel mixture inside the cylinder. Once combustion is initiated, the burning process is based on the progression of the flame through the unburned zone. The combustion releases heat, which in turn raises temperature and subsequent pressure inside the cylinder. The force generated on the piston is transferred via the conrod to the crankshaft, creating the torque and power output.

The combustion process inside the compression ignition engine varies in the way that only pure air is compressed to high temperature and pressure. Liquid fuel is injected into the air and after a vaporisation and mixing process the combustion is initiated due to self-ignition of

the newly formed partial mixture. The progression of the combustion is controlled through the injection of more fuel. Beside the different combustion process, the remaining energy transfer to heat, pressure and torque is identical to the *SI* engine.

The understanding of the specific requirements of both engines has led to dedicated engine component designs to achieve optimum performance output. Besides the different fuelling systems the most significant differences in *SI* and *CI* engine designs are found on the cylinder head and piston.

The piston is the main part inside the engine that seals the cylinder and converts the combustion pressure into a force. The combustion process in *SI* engines allows for pistons with nearly flat tops. This also allows for a low total height of the piston, making it light in mass. The *CI* engine requires a combustion bowl in the top of the piston, accumulating a large mass at the top and therefore leading to a larger total height of the piston. A direct comparison of *SI* and *CI* piston is shown in Figure 2.1. The diesel engine combustion bowl

Fig. 2.1 Example of pistons for 500 cm^3 cylinder size; *SI* engine (left) and *CI* engine (right) at same size scale

shape has a very strong effect on the optimum operation in terms of low emissions and low fuel consumption. The effect of the shape based on the 13 mode Japanese emission cycle was investigated by Kajiwara et al. (2003) and is shown in Figure 2.2. An analysis of the bowl shapes revealed that an increase of the recess of the bowl occurred, meaning that the top open diameter of bowl was smaller than the diameter below the top surface. This is a location where potential material failure due to load and temperature can occur, which can lead to piston failure, as highlighted by Morgan et al. (2013). Figure 2.3 shows a cross-section view of a typical modern diesel piston, identifying key regions, features and significant dimensions.

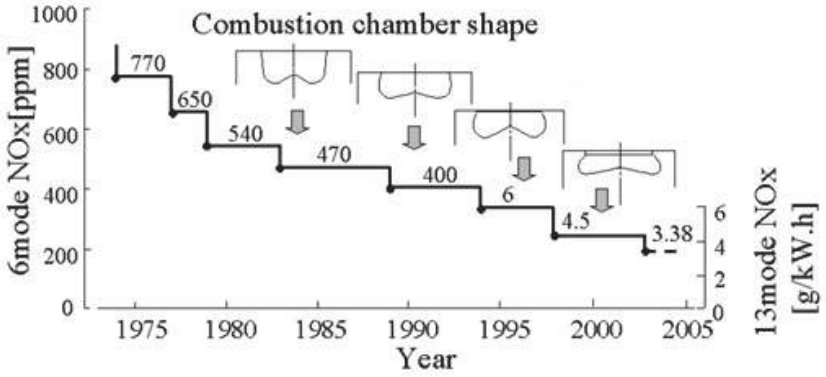

Fig. 2.2 Influence of combustion bowl on emissions over time

(Kajiwara et al., 2003)

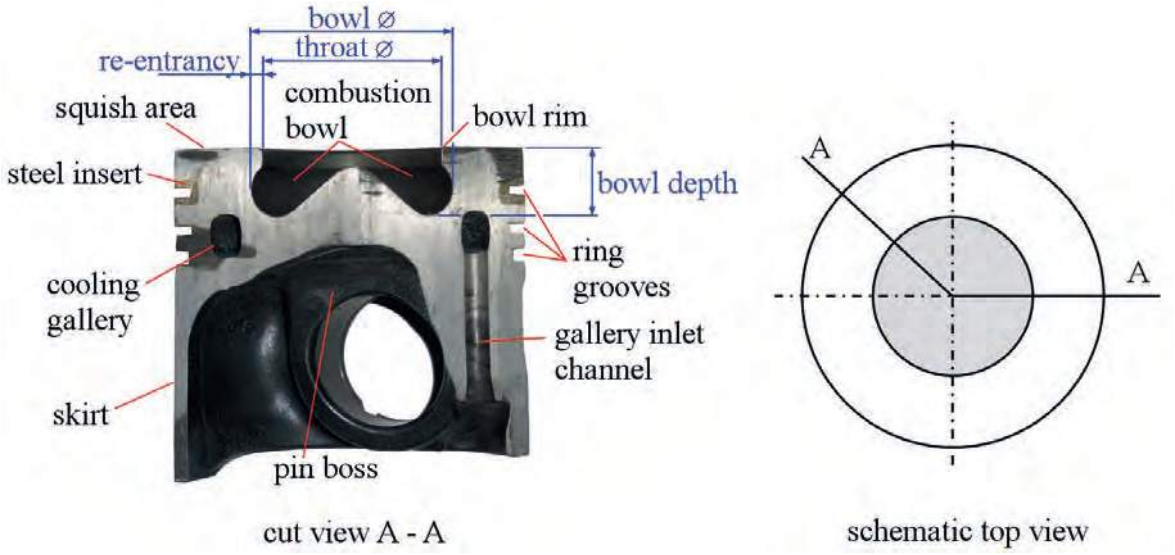

Fig. 2.3 Cross-section cut view of diesel piston identifying important design features and view plane A – A

2.2 Processes in diesel engines

2.2.1 Diesel combustion and in-cylinder temperatures

Since the first introduction of internal combustion engines to vehicles at the beginning of the 20^{th} century there were continuous improvements of performance and specific power (Cousins and Bueno, 2007). Until the end of the 1980's the main fuel delivery to the cylinder in small sized diesel engines (cylinder volumes of 500 cm^3 or less) was by indirect diesel injection (*IDI*). Materials and technologies available limited the improvement in specific power, while total power output could be increased by larger engine sizes. In the 1990's direct

injection (*DI*) was introduced for small diesel engines and a very rapid increase in specific power occurred (Kamp, 2008; Kolbenschmidt, 2001).

Maassen et al. (2005) indicated that the first generation of direct injection diesel engines had a specific power of 25 $kW/litre$. This contrasts today's engines with specific powers of 75 $kW/litre$ as stated by Kenningley and Morgenstern (2012). This increase has allowed a reduction of engine size, while maintaining the same power output and reducing fuel consumption as shown by von Rüden (2004) and was also a main driver in today's legislation.

While the specific power is suitable for engine comparisons, it is not a direct indicator for the load on the engine components. During the design process the peak cylinder pressure need to be considered. Rakopoulos et al. (2002) stated that the peak cylinder pressures of 220 *bar* to 230 *bar* may be reached with optimised dynamic injection processes, although not all of the benefits of the high pressure may be harnessed due to increased friction. Maassen et al. (2005) also showed that values of up to 220 *bar* can be achieved for passenger car engines or Light Duty Vehicle (*LDV*) with cylinder volumes of around 500 cm^3. Values for peak pressures for the development of heavy goods vehicles (*HGV*) engines with cylinder volumes of around 2000 cm^3 were given with up to 300 *bar* by Aoyagi et al. (2006), although the actual peak pressure in the cylinder may only reach 200 *bar*. Such values were also given by Son et al. (2009), highlighting the trend towards higher cylinder pressures.

The pressure inside the cylinder can be linked to the combustion gas temperature. The gas temperature needs to be considered because of heat transfer to the components, raising the component temperature and in turn reducing material strength. Numerical analysis by Chiodi and Bargende (2001) revealed significant differences in local temperatures, whereby peak temperatures of the burned gas zone were determined with 2800 K and that of the unburned gas zone with 900 K. Both temperatures were found simultaneously inside the cylinder volume and numerical investigations can provide such detailed information. Common experimental technologies, such as thermocouples, lack the possibility to deliver such high detailed results and only the mean gas temperature may be measured. It was shown to be sufficient accurate for heat transfer calculations. Kosaka and Arai (2011) determined flame and mean gas temperature in a medium diesel engine with average values of 1900 K, and 1250 K respectively. Such high in-cylinder temperatures during combustion were also determined by Kuzuyama et al. (2012) and Das and Roberts (2013).

Wenzel (2006) and Chatterjee et al. (2008) found that the combustion temperature can be linked to the formation of NOx emissions. Emission laws limit the maximum exhaustion of NOx (and other gases) and avoidance is desired to minimise expensive after treatment reduction technology. A reduction of combustion temperature would reduce NOx, but for conventional combustion technologies this would also reduce engine performance. Alternative combustion processes (Singh and Agarwal, 2012) and alternative fuels (Han et al., 2015) are in development and show promising results, but are not ready for mass produced engines yet.

Cao et al. (2009), Prasad et al. (2011), Rajamani et al. (2012), Mobasheri and Peng (2013) and Quazi et al. (2015) showed that the combustion bowl strongly influences the formation of emissions, especially NOx and particulates. Re-entrant combustions bowls generally showed a trend to lower NOx and particulates. The bowl rim overhang increases the squish area between piston top and cylinder head and generates increased air velocities. This supports faster combustion through improved in-cylinder air movement and minimises potential fuel jet wall impingement.

2.2.2 Heat transfer to piston

There are two principal mechanisms to transfer heat from the hot combustion gas inside the cylinder to the piston:

- Heat convection, and
- Heat radiation.

Heat convection occurs when the hot gas generated during combustion sweeps over the surface of the combustion chamber walls, e.g. piston crown and bowl. Direct measurements of heat flux inside combustion chambers are difficult to achieve due to the limited access to the walls of the chamber and cost implications. Therefore the heat flux is usually calculated from temperature measurements.

Alternatively models were developed to predict and analyse heat transfer independent of measurements for heat loss estimation. The most commonly used heat transfer model was developed by Woschni (1970). Although developed in the 1970's, this model is still heavily used to determine the heat losses in combustion engines. The model was based on the heat transfer in a tube under turbulent flow regime and expanded to include engine specific parameters, such as cylinder pressure, gas temperature and gas velocity. The results were

validated against calculations made on components and compared well, although it required adaption to specific engine types (diesel or petrol). The advantage of the model was that it provided very quick reliable predictions, which allowed the inclusion of the model into engine process simulations (Ricardo, GT-Power, AVL Boost). The model was improved by Bargende (1991) with respect to crank-angle based representation of the heat transfer values, while maintaining the performance. The models of Woschni (1970) and Bargende (1991) provided good results for heat loss estimations, when only surface averaged heat transfer was of interest. Although simple and quick to solve, these models did not predict local heat transfer, e.g. to analyse local component peak temperatures.

Eiglmeier and Merker (2000) developed a model that made use of phenomenological description of the processes inside the cylinder, employing also separation of the combustion chamber walls into several surfaces. This allowed not only an analysis of the total heat flux, but also local variations. The model showed that the region below the piston bowl rim and the lower piston bowl were areas of highest heat flux due to the close proximity between burned gas and wall. These predictions were confirmed with measurements by Eiglmeier et al. (2001).

During the combustion process soot particulates are produced, which have approximately the temperature of the flame and are of black colour. The formation of soot is undesired, but cannot be avoided due to the injection process, where locally liquid fuel meets the flame. Soot concentration reduces during the expansion stroke due to post combustion oxidisation (Wenzel, 2006) and overall cylinder temperature reduces in combination with the expanding volume. It is, however, important not to underestimate the heat radiated to components during the high pressure phase of the engine cycle, as the particulates have a relative high mass compared to the combustion gas. Heat radiation is taking place between bodies without direct contact. Musculus (2005) measured peak soot temperatures as high as 2400 K for injection timing turned to early, conditions present during high power demands from the engine. Zha et al. (2012) measured values of average soot temperatures as high as 2050 K for crude oil based diesel fuel and 2100 K for a 20% bio-diesel blend fuel, the latter being of importance as renewable fuels seeing increased market presence. The mechanical loading from high power demand and the thermal loading from heat transfer need to be considered in combination for development.

As the piston approaches the top dead centre the clearance between piston squish area and cylinder head reduces, generating an air movement perpendicular to the central cylinder axis, known as tumble. Fridriksson et al. (2014) showed in a numerical study that not only the squish-area induced tumble controlled heat transfer, but also in-cylinder swirl, an air movement around the central cylinder axis. It was found that at full load operating conditions the total heat flux was approximately 60% higher with low swirl in comparison to no swirl. The total heat flux was even up to 125% higher with high swirl, although no specific values of low and high swirl in terms of swirl ratios were given. Swirl is an essential requirement for an optimum combustion process, but will also lead to high heat transfer into the combustion chamber components. Surface insulation, acting as heat barrier, can help reducing heat transfer to the piston top surface. Rupangudi et al. (2014) have shown the benefits of a ceramic coated piston. Experiments showed reduced fuel consumption, increased overall thermal efficiency and increased exhaust gas temperature relative to an uncoated piston, indicating reduced heat loss during combustion.

A numerical approach to determine heat transfer during diesel combustion was proposed by Eiglmeier and Merker (2000) and Eiglmeier et al. (2001). The model employed a multi zone approach, incorporating the individual effects of convective and radiation heat transfer and showed a ratio of 3:1 towards convection. Lopez et al. (2012) investigated the heat transfer on a current mass-produced diesel engine, employing improved injection technology resulting in lower formation of soot. The heat transfer due to radiation could be reduced to 17% of all combustion chamber heat transfers (convection and radiation). Although a significant reduction, it is still a source of heat to be considered.

An attempt to measure direct heat flux between combustion gas and cylinder head wall was performed by Kavtaradze et al. (2012), using a specially developed sensor. It was pointed out that such sensors could also be used in pistons, but with limited life time, ranging from 10 hours to 12 hours. The complex layered sensor design and tolerances in the layer thickness introduced an uncertainty, but it was found that increased soot deposition on the sensor surface posed a much larger uncertainty. The soot layer acted as an insulation barrier, potentially falsifying measured heat transfer coefficients.

The insulation effect of the soot layer was also noted by Köpple et al. (2014). It was stated that the deposition layer led to reduced heat flux, due to the increased surface temperature. In addition the measured temperatures decreased during operation, as the thickness of the soot

layer increased. This problem was overcome by temperature measurement at an alternative reference position inside the combustion chamber. A clean non-soothed temperature sensor was inserted into the combustion chamber and the engine was motored without combustion, while the temperature was measured. The apparent temperature difference between soothed and non-soothed probe was used to compensate for the deposited soot layer offset.

2.2.3 Piston material and limitations

Improvement of diesel engines is partially limited by the material properties of pistons. Röhrle (1995), Chen and Worden (2000), Mahadevan and Gopal (2008) and Mahle (2012) provided information concerning the change of material strength with increase in temperature, clearly indicating limitations encountered at high temperature. For all materials the strength decreased significantly at elevated temperatures, as shown in Figure 2.4. For casting aluminium (M124, M138 and M244) the strength reduced to a quarter at temperatures found at full-load engine operation conditions. At the same time the Young's modulus also decreased, leading to increased deformations. The same behaviour was visible for steel, although strength and Young's modulus exhibit higher absolute values. Steel is mainly used for piston crowns, whereby Micro-Alloyed Steels (MAS) are medium carbon steels, but exhibit a finer grain structure and hence increased surface hardness (Chen and Worden, 2000). Esfahanian et al. (2006) stated that the highest temperature of any point in the piston should not exceed 66% of the melting temperature of the material. With temperature differences in the piston also occur variations in deformation due to thermal expansion, subsequently resulting in thermal stresses. These will add to the stress from the pressure loading. An example of high temperature fatigue failure was presented by Chen and Worden (2000), as shown in Figure 2.5. The elevated temperatures combined with the high pressure caused high temperature fatigue as shown by Silva (2006), concluding that sufficient cooling is required. Morgan et al. (2013) also investigated bowl rim stress and found identical fatigue crack behaviour on a piston with re-entrant bowl edge. The manufacturing process of the piston had also a strong influence on the fatigue behaviour of the material, as shown by Reichstein et al. (2005). The casting process in particular required a high control of each phase of the process to avoid material oxidation and defect inclusion, as this increased kerb sensitivity and initiated cracks.

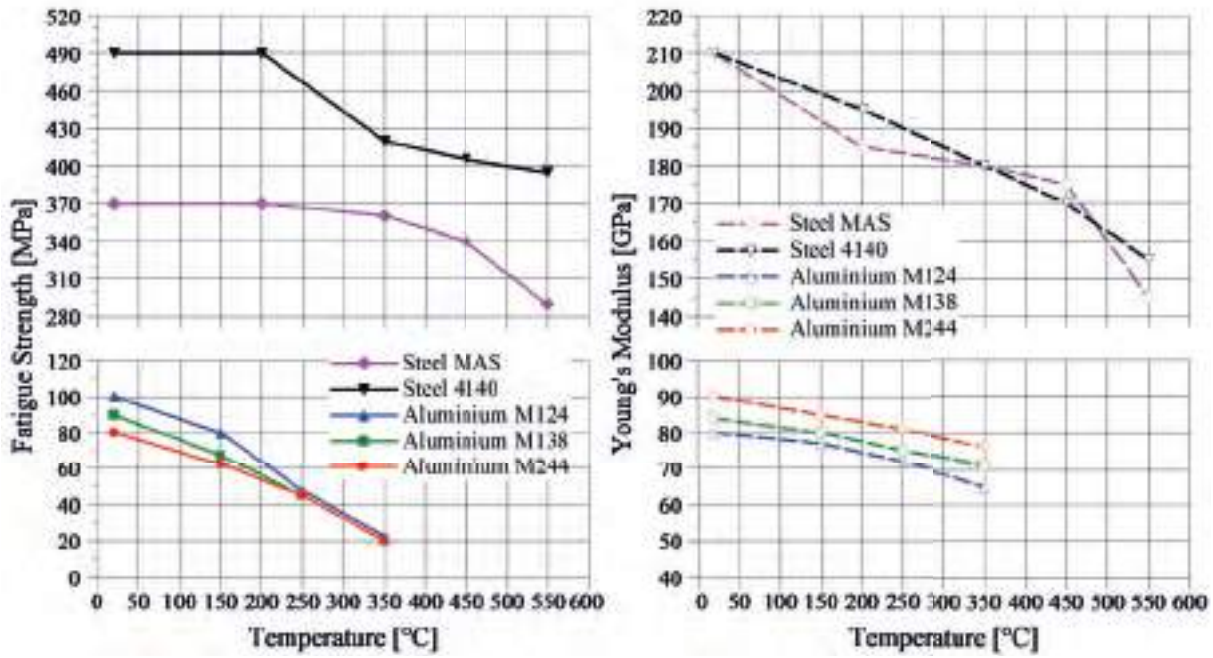

Fig. 2.4 Temperature dependent material behaviour of various piston materials

Data taken from Chen and Worden (2000) and Mahle (2012) and graphically prepared for better overview

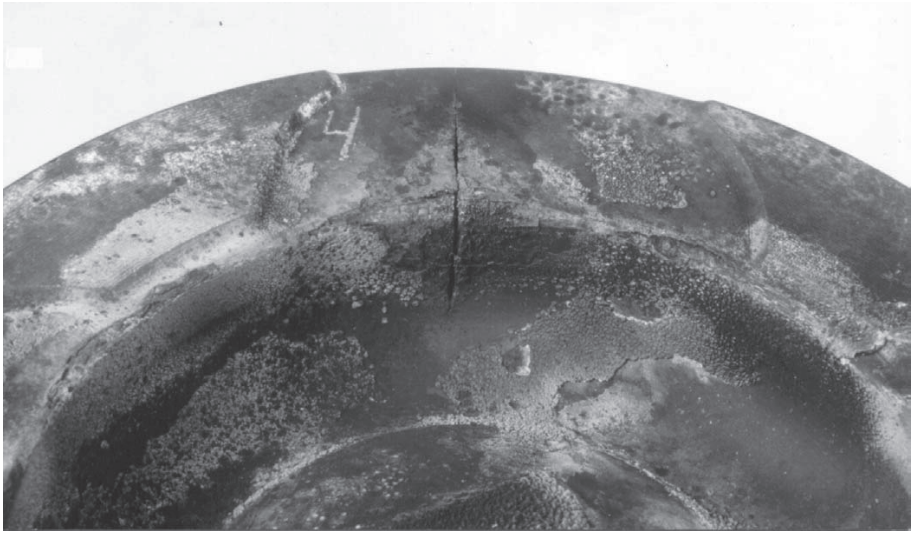

Fig. 2.5 Fatigue crack of open combustion bowl diesel piston at bowl rim edge near pin boss (Chen and Worden, 2000)

Tanihata et al. (2006) employed high pressure casting, rather than the standard gravitation casting process. The advantage of the described process was the increased cooling rate of the material, leading to a finer metallic grain structure at microscopic level. This in turn allowed

the increased use of alloying elements, such as nickel, leading to an increase in fatigue stress between 50% and 80% at temperatures of 525 K and 575 K respectively. A similar behaviour was found for the tensile strength. The use of high pressure also reduced the formation of material inhomogeneity (air bubbles) and porosity, while improving the production quality. The combination of increased tensile strength and fatigue strength allowed an optimisation of the piston design, leading to 4.4% lower friction and 2.2% lower specific fuel consumption as compared to gravity cast pistons.

Material fatigue can also be reduced by employing alternative manufacturing processes together with material composition, as shown by Mahadevan and Gopal (2008) and Wu and Li (2010). Large bore pistons were produced using a squeeze casting process with the inclusion of alumina-silicate fibre reinforcement. This resulted in a change in the material structure at microscopic level (grain level) compared to gravity cast pistons, leading to a light weight piston, due to lower combined density, with higher fatigue resistance. There was, however, no evaluation of the cost implication of such a changed process, which may be the reason why such pistons have limited application in mass produced engines as a standard.

2.2.4 Piston temperature

Combustion bowls of diesel engines can be described as omega-like shaped and can be re-entrant (overhanging) at the bowl rim. This feature is of high importance to combustion efficiency, but also a major region of concern due to the high mechanical and thermal loading of it. Knowing the temperature of the rim during engine operation allows assessment of how close the material is to its limits and if potential failure of the rim occurs. The material accumulation on the bowl rim also results in a larger surface area, leading to increased heat transfer into the piston (Wenzel, 2006) and longer heat transfer paths inside the piston to the cooler heat sink boundaries.

Piston temperature measurement has been performed under operating conditions to a large extend, but it is not an easy task and only few measurement locations can be investigated at once. Flynn and Underwood (1945) were among the first to investigate the temperatures of pistons with jet impingement cooling on the under crown. The piston investigated did not contain an internal cooling gallery, but focus shifted towards engine oil as medium for controlling piston temperatures. Especially high power output was of particular interest, as

low power output conditions generally lead to lower piston temperatures. Various methods and strategies have been employed, as shown by Kato and Moritsugu (2001), Pan et al. (2005), Ladommatos et al. (2005), Thiel et al. (2007), Zhang (2011), Kenningley and Morgenstern (2012) and Luff et al. (2012). The investigators found that the highest temperatures were generally found in the region of the combustion bowl rim, with cyclic average temperatures ranging from 260° C up to 375° C, whereby Kenningley and Morgenstern (2012) measured instantaneous temperatures of up to 390° C. These temperatures were also dependent on cooling being actively employed or not. It was clearly shown by Luff et al. (2012) and Kenningley and Morgenstern (2012) that the cooling of the piston did lower the peak temperatures with differences of up to 25° C and 100° C respectively.

With the in-cylinder conditions changing during the engine operation cycle the heat transfer changes and can be linked to the piston cycle position, resulting in surface temperature variations. When the piston is near the top dead centre and combustion takes place the temperature in the piston surface increases. With progress in the operating cycle the combustion finishes and cooler fresh air is drawn into the cylinder, causing a reduction in surface temperature. Based on piston temperature measurement by Kenningley and Morgenstern (2012) and Köpple et al. (2014) it was found that cyclic variation could be as high as 25° C. This change in temperature caused cyclic thermal loading and could lead to fatigue failure.

Thiel et al. (2007) investigated the effects of various gallery shape concepts and oil jet nozzles with regards to piston temperatures, concluding that the gallery shape, in particular the total gallery surface, did have an effect on temperature. The use of two oil jets, as compared to the common single jet arrangement, showed improved cooling of the piston, leading to a reduction by 20° C at the bowl rim for identical flow direction, meaning that both gallery halves contained normal flow from inlet to outlet. At opposing flow directions, with one gallery half having flow from inlet to outlet and the other half from outlet to inlet, reduction by 25° C were achieved. In all cases the total flow rate was identical, highlighting the advantage of the concept.

To reduce the amount of heat being transferred to the piston an artificial thermal barrier could be used, e.g. by application of a ceramic layer on the surface. This has been shown by Modi (2012), although with limited success on surface temperatures and limited information on lifetime stability of the barrier material.

Traditionally, the measurement of piston temperatures is common in engine development, but in the early development stage of an engine a physical specimen may not be available, as prototyping is a cost and time intensive process. The expense of physical testing, has led to the effort to develop analytical or numerical models to predict temperatures prior to prototype testing of engines to optimise performance and design.

Analytical models have the advantage that they deliver results fast, but may lack accuracy. These models are sometimes referred to as semi-empirical models. Torregrosa et al. (2006) proposed a detailed model for the prediction of wall temperatures of cylinder components, but relied on Woschni's heat transfer model, which was an empirically developed model and in turn heavily relied on the knowledge of the thermal boundary conditions. Results were validated against measured data and proved good accuracy. The shortcoming was the lack in local peak temperatures to predict life time expectancy and the lack of taking cooling into consideration.

The results from any simulations should be validated by comparison with measured data to assess the quality and reliability of the results, but lack of test data means that validations are based usually on one specific case. Sangeorzan et al. (2011) investigated and developed a full engine thermal management model to predict thermal performance especially in view of cold start temperature control. It was found that little general information was available for heat transfer coefficients and that most 1-dimensional models only delivered average temperatures, rather than peak temperatures. The developed model did, however, consider active cooling in the form of oil jets cooling the bottom of the piston.

2.2.5 Heat transfer away from piston

The heat transfer away from the piston (piston to cylinder wall) is mainly based on heat conduction, when no active piston cooling is employed. Woschni et al. (1998) stated that the highest heat transfer away from the piston (up to 50% of total) occurred at the piston rings, especially the top ring. It was also pointed out that approximately one third of the overall engine friction occurred at the rings, which caused further heat generation. According to Kajiwara et al. (2003) up to 70% of the heat was transferred across the piston rings to the cylinder liner, when no oil jet cooling was applied. Pan et al. (2005) stated values of similar magnitude, although for slightly different piston designs. A tight relation consisted between

combustion related heat transfer and friction caused heat transfer, which may explain the difference in the heat transfer values given by Woschni et al. (1998) and Kajiwara et al. (2003) and Pan et al. (2005), where frictional heat generation was not considered.

The use of active cooling changed the heat path and transfer mechanisms. So called under-crown cooling was investigated as early as 1945 by Flynn and Underwood (1945). A fixed nozzle at the bottom of the crank case was used to eject an oil jet towards the inside of the piston, impacting on the bottom of the piston crown, as shown in Figure 2.6b. While the oil was flowing along the piston bottom, convection took place, taking heat away from the piston, while the heat transfer across the rings reduced. This type of cooling is mainly applied to spark ignition engines, which possess an almost flat crown (top surface) and demands light pistons due to the higher engine speeds. An attempt to validate simulated heat transfer and to determine reliable heat transfer coefficients for under-crown cooled piston was made by Agarwal et al. (2011) employing a thermal imaging method to capture piston temperatures. The piston was set up in a controlled environment (not inside engine) to eliminate unwanted effects from the variability of the engine operation. The results showed the benefit of the cooling, indication a reduction of crown temperature by 35° C to 40° C, thereby showing good comparisons between measured and simulated data.

The most common active cooling method in current diesel engines is through an internal cooling gallery, as shown in Figure 2.6c. A nozzle in the crank case ejects an oil jet towards the bottom of the piston. Instead of ejecting onto the piston bottom surface, the oil enters through a channel into an annular cavity, the so-called cooling gallery. The oil then flows through the gallery, until it leaves at the opposite side through another channel to return to the oil sump. With the internal cooling gallery being actively used, the heat path changes. The majority of the heat is transferred away from the piston by the oil in the channel and a significantly reduced amount still passes across the rings. Kajiwara et al. (2003) stated that 60% to 70% of the heat was transferred away by the cooling gallery. Pan et al. (2005) stated around 75% total heat transfer by the gallery for a similar piston design with steel crown. This reduced to only 45% for an aluminium piston design with 34% still being transferred across the rings due to the better heat conductivity of aluminium. An additional benefit of gallery cooling is that heat could also be removed from sensitive locations, such as top land, top ring groove and pin boss (Kajiwara et al., 2003). This trend was also confirmed by Kenningley

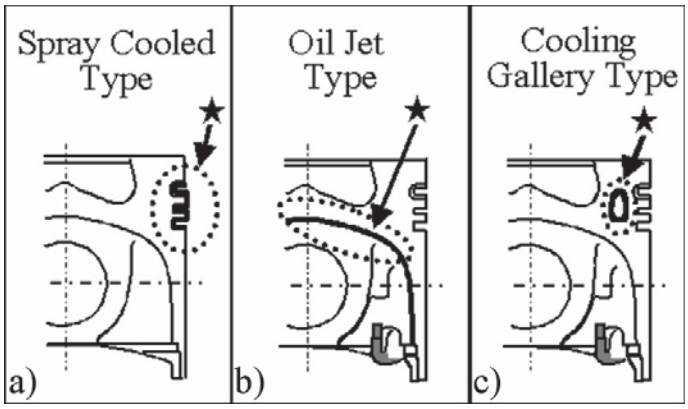

Fig. 2.6 Pistons with different cooling concepts indicating area of highest heat rejection, a) splash cooled, b) under-crown cooled, c) internal gallery cooled

(Kajiwara et al., 2003)

and Morgenstern (2012), showing a relative average temperature reduction of 100° C around the combustion bowl.

Although piston heat transfer was a very important area of investigation, direct measurements of the heat transfer coefficient could not be conducted due to the complexity of measurement. This was especially the case for the internal cooling gallery, where the heat transfer coefficients could only be determined analytically or numerically from temperature measurements. Thus far no information is available for direct experimental determination of heat transfer coefficients inside the cooling gallery.

It was commonly acknowledged that the amount of heat transferred may be linked to the transfer surface area and an increase of the gallery surface would therefore be beneficial. Larger galleries would achieve a larger surface for heat transfer, but also weaken the structure, as the wall thickness may reduce within a fixed piston size. Placing the gallery closer to high temperature regions, such as the pin boss and ring area, could increase the heat transfer at these locations. An analysis of the performance of this concept was conducted by Thiel et al. (2007) and showed an average temperature reduction by 10° C from critical piston locations. Although the gallery volume and surface area were less than the standard gallery, it was assumed that the reduction was more a result of the improved surface velocities due to the gallery shape. Unfortunately no heat transfer coefficients were determined.

The advancements in computing power and numerical flow modelling methods, namely Computational Fluid Dynamics (*CFD*), have led to an expansion of heat transfer analyses,

allowing more detailed results in comparison to the more simplistic analytical models. Kajiwara et al. (2003) used *CFD* to investigate the heat transfer within an open cooling gallery, exploring parameters such as gallery height, oil flow rate and engine speed. The average Heat Transfer Coefficients (*HTC*) were found within a range of 1500 W/m^2K at low engine speeds (960 rpm) and medium oil flow rate, up to 5500 W/m^2K at high speeds (1920 rpm) and low oil flow rate. While there was a reasonable comparison between experimental and numerical results (960 rpm only), there were significant differences at low oil flow into the gallery, overestimating the heat transfer. It was believed that the change of oil temperature was not appropriately taken into account. It did however highlight the necessity for data validation. Furthermore the results were also used to derive simplified analytical relations to determine the heat transfer coefficients, separating effects into shaker cooling, forced convection type heat transfer and conduction like heat transfer. It was found that an increasing oil flow rate reduced the shaker cooling effect in a parabolic way, leading to a dramatic reduction of heat transfer.

Pan et al. (2005) also determined the heat transfer coefficients for an internally cooled piston using numerical methods (*CFD*) and focused on the link with gallery oil filling. Although no validation data was available, it was found that the heat transfer coefficient changed depending on the circumferential position of the gallery. The highest *HTC* were found at the gallery top and inside wall near then combustion bowl with instantaneous values as high as 4000 W/m^2K and as low as 200 W/m^2K, indicating the cyclic variation. The lowest HTC was found at the bottom of the gallery with maximum and minimum values of 1000 W/m^2K and 50 W/m^2K respectively, showing comparable cyclic behaviour. These values were obtained for one specific case at 2100 rpm, but undisclosed engine load, limiting the transferability of the absolute values to other findings. It was also shown that the oil filling has an effect on the *HTC*, but the relation to gallery filling showed significant differences to the findings of Kajiwara et al. (2003), with low *HTC* at low gallery filling. At high filling the HTC showed comparable dramatic reduction in value.

Takeuchi et al. (2006) conducted numerical investigations determining piston temperatures and heat transfer coefficients linking Computational Fluid Dynamics (*CFD*) and Finite Element Analysis (*FEA*) simulations. Results for temperature were validated against experimental obtained temperatures and showed good comparison. The heat transfer coefficient, however, showed significant difference being larger than 30%, raising questions about the

correctness of boundary conditions for the simulation. Attempts were made to validate the calculated gallery filling with real life data from flow visualisation, but no information was presented on how well this was achieved.

Yi et al. (2007) also used *CFD* to determine heat transfer coefficients of an internally cooled piston gallery, identifying the location of oil inside the gallery and the piston position in its cycle as governing parameters. It was found that large amounts of oil would not necessarily lead to high heat transfer coefficients. A high oil fill level inside the gallery reduced the oil sloshing (shaking) and the heat transfer mechanism changed from convection to conduction. This led to higher oil temperatures inside the gallery at the wall and reduced heat transfer away from the piston top to the bottom, confirming previous findings.

Du (2012) used a numerical wavelet neural network (*WNN*) method to determine heat transfer in a piston with internal cooling gallery. The *WNN* model consisted of interlinking functions, where feed forward data and feedback data was used to determine a desired output, either as single value or group of values. The model, however, required pre-conditional analysis to train the model, a disadvantage, when new models were created, although expansion of an established model may yield advantages later. The *WNN* derived heat transfer coefficients were used to predict the temperature distribution using additional software. Results were compared to experimental data, showing good comparison. For the internal gallery the overall HTC were found between 1250 W/m^2K and 1700 W/m^2K, although no details of engine speed and engine loading were given.

In the past alternative attempts have been made to control the heat transfer away from the piston more precisely to maintain low temperatures. It was noted that the use of cooling oil has limitations, as the surrounding conditions of the oil jet and high velocity of the piston led to complex and less controllable behaviour. Investigations were focused on the introduction of closed volume heat pipes, filled with a specific boiling point liquid. Although comparable to internal cooling galleries, the closed volume allowed for precise control of the amount of the liquid present.

Cao and Wang (1995) changed the design of a common diesel piston to replace the horizontally circumferential cooling gallery with a vertical heat pipe, partially filled with oil. Although experimental tests were performed on a test rig (not in fired engine) and at low engine speed (480 rpm), the results showed comparable temperatures at the piston top to conventional cooling, therefore proving the benefits of the system. Ling et al. (1998)

expanded on the work of Cao and Wang (1995) and conducted a parametric study on the dimensions of the heat pipe to find the critical minimum required frequency of the heat pipe to operate. Comparisons were made with experimental results and very good correlation was found. The frequencies found were equivalent to engine speeds in the range of 250 rpm to 500 rpm, well below the operating speeds of engines. This meant that heat pipes should work for engines. Wang et al. (2000) also expanded on the previous work, but changed the vertical pipe design into an annular cavity, very much like standard cooling galleries. The concept proved to reduce the temperature gradient as well as the peak temperatures at the ring belt. Although the method proved to be capable to control temperature, a practicable application did not occur outside experimental studies.

With the advancements of technologies and tailored fluids, the concept of heat pipes was investigated again by Wang et al. (2015). Although being a study of principle and to validate simulations, it was found that the use of a nanofluid, a mixture of liquid (water) with nano-sized particles (SiO_2), provided better heat transfer in comparison to pure water. The reason was found in the higher heat capacity and the higher inertia of the particles. While the higher inertia meant that the particles would impact more with the boundary surfaces, extracting more heat that a pure liquid, the interaction with the water improved heat transfer to the water. The suitability for pistons could only be assumed, as no comparison to oil jet cooling with internal galleries was available. In terms of energy consumption and oil stability this concept had certainly advantages, although these had to offset the additional cost of manufacturing.

Besides the determination of the heat transfer inside the piston, overall engine thermal management simulation may be used to identify specific areas of cooling loss and cooling reliability. The majority of such simulations use either simplified 1-dimensional models for heat flow or semi-empirical formulations for heat transfer, or combinations of both. The heat transfer from combustion gas to piston is still relying on the semi-empirical model of Woschni (1970) and thus far is still the most commonly used model. Although improvements and expansions have been made to the model, it is unable to predict local peak temperatures and does not consider two-way cooling effects, such as gallery cooling. It relies heavily on thermal boundary conditions, such as the wall temperature, which by itself is influenced by the heat transfer. Furthermore, due to the overall averaging behaviour of the model, it over-estimates the heat transfer as shown by Sharief et al. (2008). This was also confirmed by Kono et al.

(2012), which used the model to determine in-cylinder heat transfer and considered internal piston cooling effects, but there was no direct relation to the conditions inside the gallery, therefore lacking actual heat sink effects of the oil.

Modern development tools for engine process simulation, such as Ricardo Wave and GT-Power, include sub-models to analyse thermal losses and engine component temperatures, e.g. for the piston. At the current state of development these models only determined losses based on fixed values submitted by the user (Ricardo, 2012). The implementation of advanced heat transfer sub-models using the proposed models of Kajiwara et al. (2002), Torregrosa et al. (2006) or Sangeorzan et al. (2011) could provide an improvement to the development process. The model of Sangeorzan et al. (2011) was capable to predict average temperatures, but still had limitations, especially with respect to the amount of oil inside the cooling gallery, which controlled the heat transfer mechanism inside the gallery, as shown above. Another disadvantage may be found in the expense of long calculation time, eliminating one of the main advantages of these development tools.

2.3 Internal gallery cooling, conditions and behaviour

2.3.1 Cooling gallery related dimensionless numbers

It has been established that the gallery filling does influence the heat transfer coefficient inside the cooling gallery significantly. Assessing the filling accurately is therefore important to accurately model thermal conditions. Specific ratios are important to express the effectiveness of the oil flow capturing and oil retaining within the gallery. These are not efficiencies and only express the behaviour of flow capturing.

Oil fill ratio

Heidrich (2003) and Kajiwara et al. (2003) defined the oil fill ratio by means of a quasi-steady state height of oil at the gallery bottom relative to the height of the gallery. It can be determined by

$$OFR_h = \frac{h_{oil}}{h_{gallery}} \tag{2.1}$$

where h_{oil} is the height of the oil and $h_{gallery}$ is the height of the gallery. Such an approach limits the application to near rectangular cross-sections only and to approximately horizontal

fill levels. More complex shapes with varying width would lead to reduced *OFR*, if the gallery was significantly wider at the bottom. Pan et al. (2005) redefined the oil fill ratio as the volume of the oil inside the gallery relative to the total gallery volume. It can be calculated by

$$OFR_v = \frac{V_{oil}}{V_{gallery}} \tag{2.2}$$

where V_{oil} is the volume of the oil inside the gallery and $V_{gallery}$ is the volume of the gallery.

Gallery catch ratio

Heidrich (2003) defined the gallery catch ratio (*GCR*) as the ratio of oil volume flow exiting from the nozzle and exiting the gallery at the outlet opening and is a measurement of the effectiveness of the gallery to pass flow through the gallery. It can be determined by

$$GCR = \frac{\dot{V}_{out}}{\dot{V}_n} \tag{2.3}$$

where $\dot{V}_{out}$ is the volumetric flow rate from the gallery exit and $\dot{V}_n$ the flow rate from the nozzle. It incorporates several effects concerning the flow into and out of the gallery, such as short circuiting at the inlet and re-entrant flow at the outlet. Optimum values will be near 100%.

Inlet catch ratio

The flow at the gallery inlet may be considered individually to assess the effectiveness of the flow into the gallery, as short circuiting flow or misalignment of the jet plays a crucial role in the gallery filling. It can be determined by

$$ICR = \frac{\dot{V}_{in}}{\dot{V}_n} \tag{2.4}$$

where $\dot{V}_{in}$ is the volumetric flow rate through the gallery inlet. The optimum values will be near 100%, meaning that all oil ejected from the nozzle enters and remains in the gallery.

2.3.2 Design of cooling galleries and studies of filling and flow behaviour

The first appearance of a concept to reduce temperature of highly heat-loaded moving components inside combustion engines relates to a patent by Heron (1923). Although more aimed at the cooling of exhaust valves of supercharged aero engines, it was mentioned that this method could also be extended to other moving components, such as pistons. The concept involved a closed internal cavity, partially filled with a non-volatile medium, such as mercury, potassium, lithium or sodium. A precise amount of filling was not given and only stated as considerable quantity. Heron (1931) patented also a piston design for internal combustion engines involving an internal chamber explicitly for cooling of the piston, whereby the chamber may be sealed or tightly closed. The cooling medium was identified as a material that is solid at room temperature and liquid at engine operating temperatures. The above materials were specified, but engine oil was not considered. The movement of the liquid inside the chamber was explained and reasoned, but the amount of filling desired was not disclosed. The above described gallery type is generally termed closed gallery, as the fluid inside is retained, as opposed to an open gallery, which allows flow into and out of the gallery during movement.

Bush and London (1965) primarily investigated the heat transfer coefficients on a piston-like model with internal cavity, using the description of 'cocktail shaker' to describe the liquid behaviour. The cavity shape under investigation was cylindrical (diameter to height ratios of 0.56 to 2.1), rather than torus-like as found in modern pistons. It was partially filled with a variety of liquids, such as water, glycerine mixtures and mercury, but not engine oil, with filling ratios from $^{1}/_{8}{}^{th}$ to $^{7}/_{8}{}^{th}$. It was implied that the gravitational forces on the liquid are always less that the oscillation induced dynamic forces. It was also noted that for small gallery sizes the surface tension forces becomes important relative to the dynamic forces, limiting the minimum height of the cavity.

Stotter (1966) investigated different types of cooling methods experimental. An engine with bore and stroke of 165.1 *mm* and 203.2 *mm* respectively was driven by an electric motor with speeds of 358 rpm, 566 rpm and 873 rpm, while thermally loaded at the piston top by a propane flame. The testing included jet cooling and a pseudo-gallery cooling, where an oil retaining tray was mounted on the piston underside. It was found from *HTC* analysis that the engine speed was more important than the filling of the pseudo-gallery, which itself was not determined.

French (1972) investigated the heat transfer on a piston fitted to a rig, representing an engine with bore, stroke and speed of 203.2 *mm*, 304.8 *mm* and 410 *rpm* respectively. The study concentrated on the effectiveness of cooling and *HTC*. It was found that the use of a completely filled internal gallery produced lower *HTC* as compared to a partially filled gallery, concluding that the addition of air into the fluid provides superior cooling of cocktail shaker type. The optimum ratio between liquid and gas was, however, not investigated.

Evans (1977) investigated the cocktail shaker cooling effects in an open gallery using video capturing techniques. It was found that various flow regimes occurred inside the gallery, including flow along surfaces, surface impingement and detached surface flow. An empirical correlation for the heat transfer was proposed based on the Reynolds number, Prandtl number and velocity components of the flow, including consideration of the flow regime, but gallery filling was not included.

Pimenta and Filho (1993) based their study of heat transfer and temperature distribution on an engine of 137 *mm* bore and 165 *mm* stroke with engine speed at 1200 *rpm* and 1900 *rpm*. The *HTC* analysis included the correlation by Evans (1977), but expanded into finite element analysis (*FEA*) on the piston. The experimental and numerical data generally compared well (less than 10% difference) for the majority of the measurement points, but showed significant difference with regards to the inside of the gallery (20%). Gallery filling was not explicitly determined.

An increase of the gallery surface increases the area for heat transfer capability. This can be achieved by larger sized galleries, but may weaken the structure, as the wall thickness reduce within a fixed piston size. An alternative solution was patented by Martin and Thieme (2000), adopting a wave-shaped gallery, as shown in Figure 2.7. It was stated that the gallery can be placed closer to high temperature regions, such as the pin boss and ring area, increasing heat transfer at these locations. Issler (2000) also patented a piston with a cooling gallery, but in comparison to Martin and Thieme (2000) the surface area was increased by ribs protruding vertically from the bottom into the cooling channel. Further improvements to the manufacturing of such pistons were patented by Eichel et al. (2001) and Wellmann (2001). Finished pre-manufactured cooling gallery volumes were added to a die prior to the casting process the centre of the cast allowing a precise positioning and definition of the gallery.

Kajiwara et al. (2002) and Kajiwara et al. (2003) used computational fluid dynamics (*CFD*) to determine heat transfer coefficients (*HTC*), whereby the gallery filling was determined

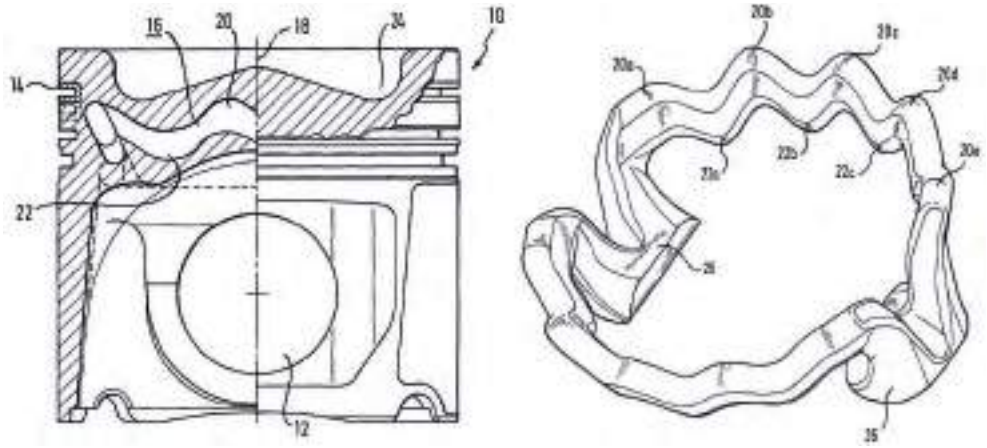

Fig. 2.7 Wave-shaped cooling gallery to improve heat transfer from piston via increased surface area

(Martin and Thieme, 2000)

using hydraulic equations based on inlet and outlet mass flow over time. The outlet flow from the gallery was calculated from piston acceleration, oil height inside gallery and outlet area. The inlet was calculated from nozzle exit pressure and area, oil density and flow loss coefficient. The latter was assumed to be constant, but its meaning was not explained explicitly and may refer to the gallery catch ratio (*GCR*) or to loss of flow from friction in the nozzle. The height of oil, being used to express the oil fill ratio, was calculated from the inlet and outlet flow in an iteration process. Unfortunately no comparison to physical data of filling was available. The simulation results of the flow behaviour, however, revealed that the majority of the oil was located at the gallery top near *TDC* and at the bottom at *BDC* with transitional mid-gallery positions in between, confirming regimes identified by Evans (1977).

Heidrich (2003) conducted visual studies using a strong non-transparent dye to enhance flowing liquid visibility, as shown in Figure 2.8. This provided a strong contrast to the air, allowing identification of clear interface boundaries between the oil and air. A $^3/_4$–model was used, which provided a cross-sectional view of the gallery and hence could be used to identify the fill level across the gallery as well and the flow behaviour. Due to the visibility of the inside of the gallery, without the distortions of the curved gallery shape, it can be seen that the flow inside the gallery is of 3–dimensional behaviour and a non-transparent oil will cause difficulties in analysing the fill level, especially when air bubbles are entrained in the oil, but cannot be detected. Unfortunately no information was available about the investigated

parameters and outcomes from the study. The flow near the inlet is highly turbulent with high entrainment of air into the oil, potentially changing the behaviour of the oil, especially when high amounts of small air bubbles dissolve into the oil. This phenomenon is not desired, as the air inside the oil may be taken to the oil sump and can enter the lubrication circuit. Pan

Fig. 2.8 Gallery cross-sectional flow visualisation

(Heidrich, 2003)

et al. (2005) conducted a numerical analysis (*CFD*) on a specific built gallery to determining *OFR* and *HTC*. For one case *HTC* were validated by comparison with measured temperatures. The flow behaviour inside the gallery determined by Kajiwara et al. (2003) was confirmed. It was also found that the *OFR* changes within the crank cycle relative to piston position with higher filling during the downward stroke and lower filling during upward stroke. The absolute values of filling were, however, not validated against actual data.

Heidrich et al. (2006) returned to the concept of a closed gallery employing easy vaporising media, such as water, ammoniac or glycol. The patented concept considered an annular gallery together with heat pipes extruding from the underside of the piston. The advantage of the design was seen in the availability of sufficient amount of cooling liquid, independent of the position of the piston within the crank cycle, although it was not specified how much filling would be sufficient.

Takeuchi et al. (2006) conducted experimental studies using a mixture of a fluorescent dye (Coumarin-6) and oil in combination with a Xenon flash light and a high speed camera. A transparent acrylic plastic model of the piston was used. During the tests the oil flow rate from the nozzle and the flow from the gallery exit were recorded to determine the catch rate of the oil jet, indication that only 63% to 78% of the oil enters the gallery depending on engine

speed. It was also found that a strong dependency between oil flow behaviour and piston position occurred, depending on the position in the crank cycle, as shown in Figure 2.9. The underlining link was attributed to the relation of piston acceleration and oil inertia. The results of the visual experiment were compared to numerical simulations (*CFD*) in the same annular cooling gallery. The simulations showed that less than 80% of the oil jet mass flow entered the gallery for the case of 3000 rpm and 2.0 l/min flow rate. Although no actual values for *OFR* were presented, the comparison between actual and numerical results showed good correlation and also highlighted that the gallery filling was not constant throughout the gallery length. A progressing wave effect was noticeable. A comparison of average gallery surface *HTC* from experiment and simulation showed high differences (up to 30%). It was indicated that this may be a result of the heat transfer calculations. Yi et al. (2007) conducted a *CFD*

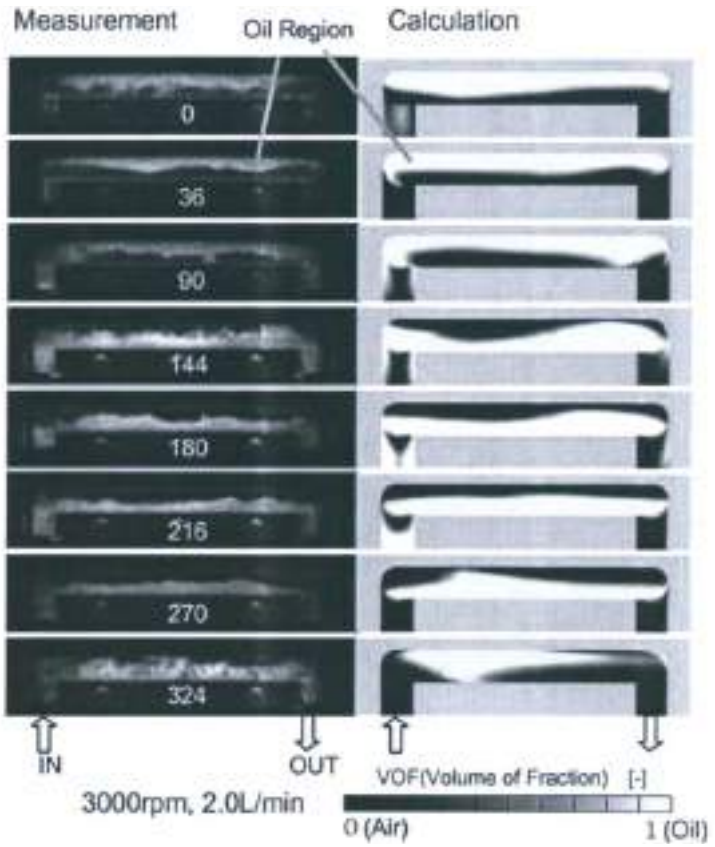

Fig. 2.9 Comparison of physical visualisation and simulation of oil flow in gallery

(Takeuchi et al., 2006)

study to investigate *OFR* and *HTC*. The cooling gallery was split into sections to investigate the filling along the gallery. The results showed strong variation of *OFR* of up to 10% in the

individual sections during the crank cycle. This was a significant change considering that the average *OFR* for the overall gallery was only approximately 20%. It was also indicated that cycle-averaged *OFR* increased from inlet towards outlet and that the *OFR* stabilised within ten consecutive crank cycles, a very low number of cycles, considering the highly transient inflow and outflow behaviour with recirculating and re-entry flows.

As mentioned before, concepts were developed to increase the gallery surface area, e.g. through a wave-like gallery shape. An experimental analysis of the performance of this concept was conducted by Thiel et al. (2007) and showed an average temperature reduction by 10° C from critical piston locations. Although the gallery volume and surface area were less than the standard (non-waved) gallery, it was assumed that the reduction in temperature was more a result of the improved surface velocities due to the shape. Unfortunately no heat transfer coefficients were determined and neither flow behaviour nor filling was investigated, as the study primarily focused on temperature measurement. The different gallery concepts did show that small changes in the design can have a significant impact on the cooling.

Komiya et al. (2011) investigated the flow behaviour on two different gallery layouts, a 2–dimensional and 3–dimensional gallery shape. Both galleries used the same gallery cross-section of 19 *mmx*10 *mm* and a length of 518 *mm*. The 2–dimensional gallery model is shown in Figure 2.10. It was allowing for a better viewing of the flow pattern in the gallery, while eliminating some of the flow effects, such as circular sloshing due to the slightly oval gallery shape. During the static test conditions it was found that the impingement of the jet at the end of the inlet channel reduced the kinetic energy of the liquid significantly, before flow into the channel occurred. Investigation under dynamic conditions revealed the same loss of kinetic energy as found in the static condition study. Additionally a clouding of the liquid was observed at the investigated speed of 1000 *rpm*, potentially indicating strong mixing with the gas phase. A further study by Komiya et al. (2011) was performed on a 3–dimensional model, as shown in Figure 2.11. It was found that the conditions found at the inlet of the 2-dimensional channel still applied. Furthermore the 3–dimensional gallery led to spiral flow inside the gallery, while strong collision of flows at the intersection between the gallery branches and exit channel occurred, which would be expected, as the flows have to be unified again. The study was conducted at a rig speed of 1000 *rpm* and used water instead of oil to provide flow conditions that can be matched to engine speed conditions at 4000 *rpm*. Although the Reynolds number increased, it was stated that the gallery should also

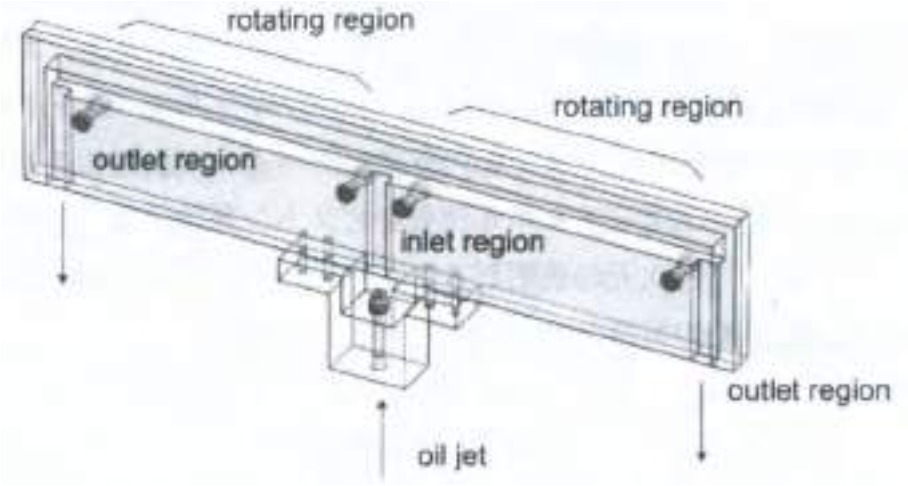

Fig. 2.10 2-dimensional gallery model to investigate oil channel flow behaviour

(Komiya et al., 2011)

be 2.5 times larger to match the Reynolds numbers at 4000 *rpm* with oil as the coolant. Lv

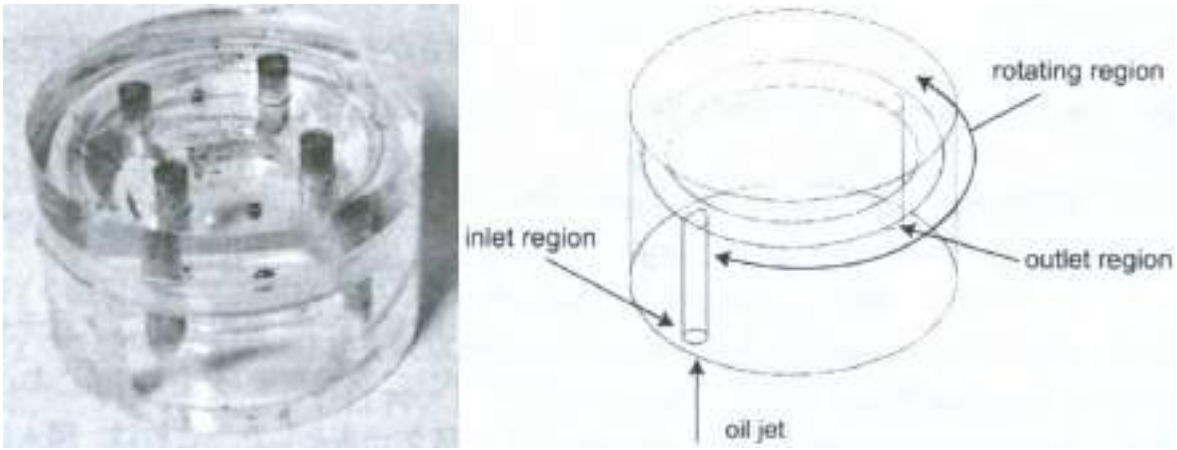

Fig. 2.11 3–dimensional gallery model to investigate oil channel flow behaviour

(Komiya et al., 2011)

et al. (2015) experimentally studied the flow behaviour inside a rectangular-shaped straight gallery. The closed transparent gallery design was partially filled with various levels of water and exposed to set oscillating frequencies. It was found that at a certain frequency, between 6 Hz and 8 Hz (equivalent to engine speeds of 360 rpm to 480 rpm) the flow pattern changed dramatically. At 6 Hz or below the inertia effects were too small to cause a breakup of the bulk flow, as shown in Figure 2.12. The water was mainly sloshing in the horizontal direction, without significant turbulent mixing. The behaviour changed for frequencies beyond

8 Hz, when independent droplet and air bubbles occurred. An increase in oscillating speed further increased breakup and mixing, especially in the centre of the gallery, although it was unclear, if this was a result of wall friction or low illumination quality. At high fill ratio (80%) the mixing movement inside the gallery became obstructed by the water itself, limiting impact with the top and bottom wall. It was assumed that this would reduce heat transfer, an assumption supported by findings of Kajiwara et al. (2003), Pan et al. (2005) and Yi et al. (2007). Although the results may have allowed some estimation about the behaviour inside a real piston gallery, there were still limits in the transferability. The probe gallery was closed and no liquid entered and left the internal volume. However, this would create an inflow driven flow from the inlet and therefore introduced additional flow velocity. The straight shape did not represent the gallery flow either, as the annular curvature introduces extra swirling from side wall impacts. Furthermore the viscosity of the water was significant lower than that of oil, as well as coalescence effects with the wall. Wang et al. (2015) used the same closed

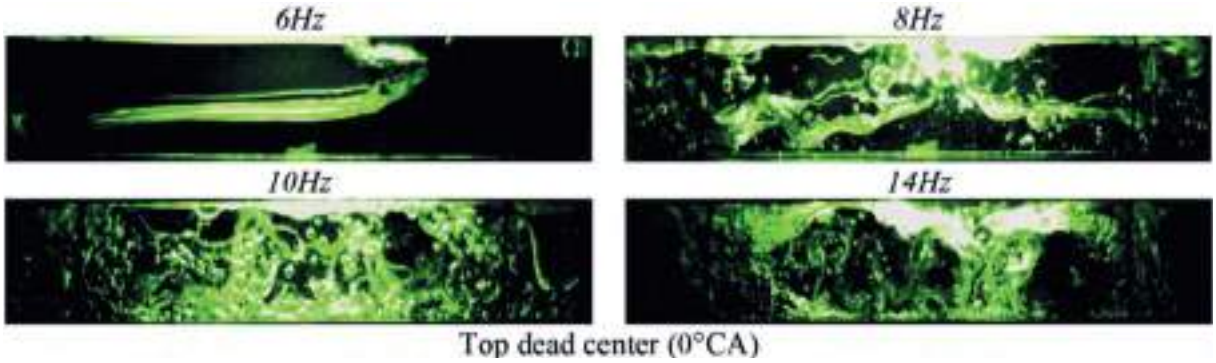

Fig. 2.12 Example of flow condition inside gallery at *TDC* position with 60% water filling and oscillating at various frequencies

(Lv et al., 2015)

box-section volume and equipment as above, but investigated the effect of nanofluids inside the volume. Comparisons were made to pure water with respect to flow behaviour and heat transfer. The flow behaviour of the pure water was virtually identical to the results of Lv et al. (2015) and the nano-particle loaded water, containing SiO_2 nano-particles, showed generally the same behaviour. The investigators concluded that the main drive of the flow was inertia based, but that the dispersed nano-particles seemed to reside longer at the impinging gallery wall. Also the solid particles improved the breakup of the static boundary layer due to higher impact inertia in comparison to a liquid. The flow was also modelled using *CFD*, employing

various models for multi-phase flow, as shown in Figure 2.13. It became apparent that not all models represented the flow accurately, although no information was given on how the images for comparison were selected. It was stated that the flow reached a cyclic repetitive behaviour, but, unfortunately, no specific information was given on the definition of cyclic, which may refer to the vertical flow patterns of the oil, as a result of the oscillating motion. The frequency of the cycle would be identical to the frequency of the gallery movement. Analysing Figure 2.13a it can be seen that a substantial amount of liquid can be found to the left part of the volume. Should this liquid move to the right and back to the left, then another cyclic behaviour would be present. Such horizontal movement may be over a number of work cycles, where the frequency would be potentially a multiple of the vertical cyclic frequency.

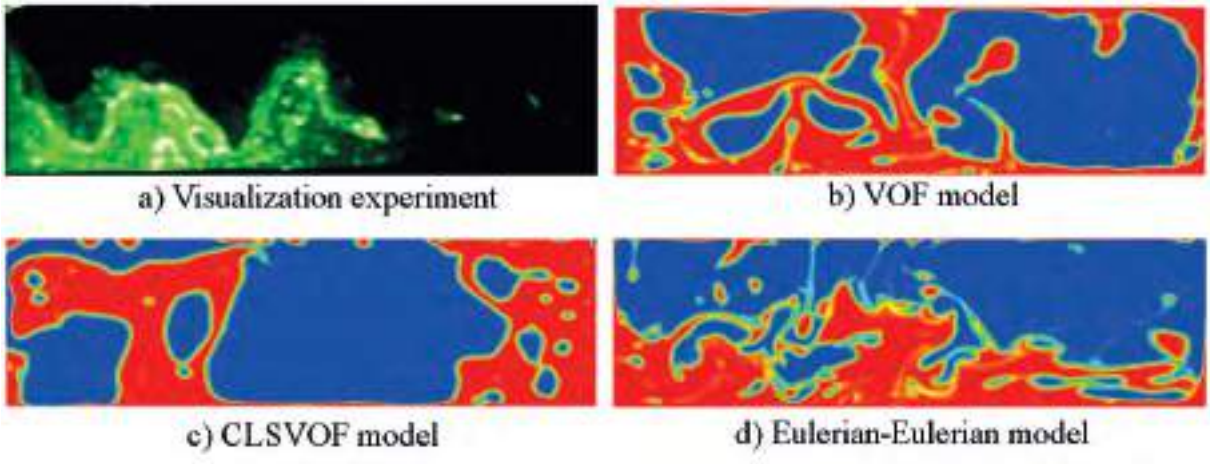

Fig. 2.13 Example of the flow patterns predicted by different multiphase models at *TDC* position and engine speed of 200 *rpm*, 40% filling and 5% nano-particle loading

(Wang et al., 2015)

2.4 Parameters influencing gallery filling

There are various parameters that influence the filling of the piston cooling gallery and the magnitude of influence varies severely. The following parameters were identified.

2.4.1 Engine speed

The engine speed was identified as a major influence in many sources. Heidrich (2003) indicated that an increase in engine speed reduced the oil fill ratio, as the catch rate of the oil

jet on the inlet channel to the gallery reduced. This behaviour was also confirmed by Yi et al. (2007). With increased engine speed, the piston speed between the dead centres increased. On the downward movement the oil jet was forced into the gallery as the relative velocity between jet and piston was high. On the upward stroke the relative velocity between jet and piston reduced leading to less oil entering the gallery. In the extreme, at high engine speeds, the piston could move at a higher velocity that the oil jet and hence no oil entered the gallery on the upward stroke.

Kajiwara et al. (2003), Pan et al. (2005) and Torregrosa et al. (2010) also mentioned engine speed as an influential factor, but no data was presented and purely a tendency was given.

2.4.2 Oil flow rate

The flow rate may be expressed in two ways, either as mass flow rate or as volume flow rate. There was no clear differentiation which method was more representative to indicate desired behaviour. Heidrich (2003) indicated that an increased mass flow rate increased the fill ratio, as more oil was entering the gallery inlet. Kajiwara et al. (2003) found the same behaviour. This seemed to be a reasonable statement, as more oil would reach the gallery inlet. Pan et al. (2005) showed that there occurred a limit in flow rate, beyond which no increase in oil fill ratio occurred. It was identified that increased flow rates would lead to a divergence of the jet (jet breakup) as the jet velocity increased accordingly, resulting in negative effect on fill ratio. Yi et al. (2007) and Agarwal et al. (2011) confirmed the findings in general, although the focus was more on the velocity of the jet leaving the nozzle. Assuming the oil to be a non-compressible fluid at low pressure, the velocity of the jet may be expressed as a function of flow rate for a fixed diameter nozzle.

2.4.3 Gallery entry and exit geometry

The gallery entry does play an important role in gallery filling, as it was identified in many sources (Heidrich, 2003; Kajiwara et al., 2003; Komiya et al., 2011; Pan et al., 2005; Thiel et al., 2007). There were, however, no specific details available what this meant. No reference was made to dimensions or shape of the inlet, leaving room for questions. Thiel et al. (2007) investigated pistons with separated gallery branches (two halves) with one nozzle for each

branch. The entrance and exit of the gallery was formed in a way to allow the entering or exiting oil to flow along the gallery wall, rather that impinging or hitting the wall and splitting the flow in two halves. The galleries did show a reduction of temperatures, but without providing information about the filling of the gallery. Komiya et al. (2011) also concluded that the inlet sections leading to the channels should be designed in a matter that allowed smooth flow to avoid stagnant conditions.

The influence of the exit geometry was more detailed. Heidrich (2003) and Kajiwara et al. (2003) showed that an increase of the exit diameter furthers the flow from the gallery reducing the gallery filling.

2.4.4 Piston position during crank cycle

Depending on the position of the piston in the crank cycle the relative velocity between oil jet and piston changes and could lead to the oil jet not reaching the gallery entry. This would change the filling during the crank cycle leading to varying fill ratios during upward and downward stroke. This was clearly shown in numerical studies performed by Pan et al. (2005) and Yi et al. (2007). In both cases comparable gallery designs were analysed. Although it cannot be clearly identified, if the conditions were identical, it did show comparable behaviour of gallery filling, even in terms of the absolute fill values. Torregrosa et al. (2010) also identified the position as a parameter, but no specific data was given.

2.4.5 Nozzle geometry and jet impingement

Pan et al. (2005) identified the quality of jet alignment as a factor to filling, which was confirmed by Thiel et al. (2007). A misaligned nozzle would cause the oil jet to miss the inlet of the gallery and hence reduce filling. It was pointed out that in some circumstances this could be a desired condition. The oil jet was aligned with the gallery inlet for the lower positions of the piston (near *BDC*), but when the piston reached positions near the *TDC* the jet missed the inlet and impinged on the underside of the piston taking heat away from the piston centre. As the gallery was concerned with the cooling of the outer locations of the piston (bowl rim and rings), it did not cool the bowl centre. The misalignment was therefore employed to overcome the locally restrained cooling of the internal gallery.

Considering the flow in a straight circular pipe the cross-sectional flow velocity profile would be axi-symmetric parallel to the pipe centreline and depend only on the nature of flow, laminar to turbulent. When a jet would be ejected from a straight nozzle, e.g. the exit of a sufficient long straight pipe, then the jet would be projected further along the direction of the nozzle centre line, if no additional forces acted upon the jet after exit. The impingement position on a surface at distance from the nozzle exit would coincide with a point through which the nozzle exit centreline would pass. Nozzles used in current engines contain a curvature before the exit, as the fixing location of the nozzle in the crank case would be offset from the piston. This can change the exit flow direction relative to the nozzle exit centreline. Verkaik et al. (2009) investigated the flow behaviour in bend pipes. It was not only found that the velocity profile showed an increase in velocity towards the outside of the bend, it was also found that secondary flow in the cross-section occurred, causing an increase of pressure at the outside surface of the bend. If the exit of a nozzle would coincide with the end of the bend, then the ejected jet would not protrude along the nozzle exit centreline, but diverge from it. Unfortunately little information was available on the effect of pre-exit curvature of open ended pipes with regards to the directional divergence of the jet from the projected flow direction and no study relating to oil jet nozzles was available. Experimental and numerical studies concentrated exclusively on straight nozzles. An experimental and numerical study by Triep et al. (2013) on a venom channel of a spitting cobra with a sharp 90°bend prior to the exit found that a divergence angle between the jet centre and the direction normal to the exit occurred. The impingement position of the jet on a surface at a longitudinal distance from the nozzle exit would experience similar effects and a lateral offset would occur, with the lateral offset being depended on the flow rate and therefore on the velocity at the exit.

The significance of this behaviour may be linked with the variation of the flow rate with engine speed from the engine oil pump. When the oil jet would be aligned with the gallery inlet relative to low flow rates, then the impingement position may change with increasing flow rate, leading to reduced oil catch ratio and lower gallery filling.

2.4.6 Oil viscosity

The viscosity of the oil is highly sensitive to the temperature and reduces with increasing temperature. Yi et al. (2007) showed that the oil temperature changed along the gallery,

with the highest temperatures being near the gallery exit, when it had accumulated heat from passing through the gallery. Analysing the change of temperature in relation to the absolute temperature revealed that the viscosity change was relative small, generating actually reasonable small changes in viscosity. A potential effect of viscosity on the gallery filling was also mentioned by Torregrosa et al. (2010), although no specifics are presented.

It may be assumed that the viscosity does have an effect on the fill ratio, as the oil temperature changes depending on the engine operation conditions. The relative influence on filling or flow behaviour in relation to the engine speed and flow rate could still not be assessed.

2.4.7 Piston stroke and connecting length

The piston stroke has a direct link to the distance between nozzle and gallery inlet. This distance can be reduced using a cut-out in the piston skirt or increased by locating the nozzle lower in the crank case. There was no information available about the effect of the distance on gallery filling. Kneer and El-Khawankey (2010) showed that the jet diverges with flow rate and oil temperature. The increased breakup of oil jets at higher temperatures, even at low flow rates, may reduce the amount of oil directly entering the gallery. A large distance between nozzle and gallery may therefore reduce the filling. Any vibration of the engine and subsequent introduction of lateral momentum to the exit flow was not even considered.

A change in conrod length changes the behaviour of the piston movement and therefore the velocity and acceleration of it. A reduction in conrod length leads to increased piston acceleration at the *TDC*, while a reduction occurs at *BDC*. This in turn would change the inertia forces on the oil inside the gallery and therefore may affect the internal gallery flow with potential obstruction of flow at inlet and outlet. Torregrosa et al. (2010)) stated that there was an influence from the relative velocity between jet and piston, hence conrod length did play a role, although no specific information was provided.

2.4.8 Gallery shape

Kajiwara et al. (2003) identified the gallery shape as a parameter, although there was no specific information about the meaning of gallery shape. This could be the annual diameter, cross-section area or shape. Komiya et al. (2011) also mentioned the cross-sectional shape of

the gallery as an influencing factor, stating that vertical stirring can be improved by the shape. Although the gallery size was acknowledged as a factor, no specific information about the actual volume was provided. Yi et al. (2007) also mentioned gallery shape as a factor. Again it was not clear what was meant by shape, but it was indicated that the gallery length and indirectly the annual diameter of the gallery was influential.

2.4.9 Oil jet breakup

Although jet breakup occurs in the space between nozzle and gallery entry, hence outside the gallery, it has a strong effect on the catch ratio and therefore on the gallery filling. The subject of 'breakup of free jets' is studied very thoroughly and the knowledge is very wide ranging. There was, however, no information publicised about the relationship between jet breakup and gallery filling. The ejection of a liquid, such as water or oil, from a nozzle into a stationary gas produces a free surface jet. The breakup behaviour may be classified simply as Rayleigh regime (e.g. dripping), transitional regime and atomisation regime (e.g. spray), depending on the velocities of jet and surrounding environment medium.

Eggers and Villermaux (2008) stated that breakup of free jets was caused by the velocity difference at the interface surface between gas and liquid, leading to shear stress at the interface or more specifically in a shear layers of the interface. Fellouah et al. (2009) also stated that the cross-section of a free liquid jet surrounded by a gas could be treated as three regions, namely an outer region, a shear layer region and a centreline region, whereby the outer region was in contact with the gas and could include strong vortices. It was implied that the vorticity generation in the gas shear layer became the driving force of the breakup, when the inertia effect were larger than the surface tension. The ratio between inertia forces and surface tension could be expressed by the Weber number as

$$We = \frac{\rho u^2 l}{\sigma_s} \tag{2.5}$$

where ρ is the density, u the velocity, σ the surface tension and l the characteristic length. For the breakup of round jets l can be assumed to be the diameter, d, of the jet. At $We < 1$ the breakup is characterised by formation of droplets with size predominantly controlled by surface tension. This is the Rayleigh breakup regime, with formation of droplets at approximately jet diameter and very little surface rippling, as explained by Farvardin and

Dolatabadi (2013). At $We > 1$ the effects in the shear layer lead to surface rippling and rupture with possible gas entrainment into the jet, but a clear identification of the breakup regime between transitional (jetting) and atomisation cannot be made.

The behaviour of the exiting jet can also be linked to the flow character, being laminar, transitional or turbulent, which determines the velocity profile across the jet at the nozzle exit. To determine the flow character the Reynolds number can be used. It describes the ratio of inertia and viscous forces and can be calculated by

$$Re = \frac{\rho u l}{\mu} \tag{2.6}$$

where ρ is the density, u the velocity, l the characteristic length and μ the dynamic viscosity. For experimental pipe flow laminar conditions are assumed for $Re < 2000$ and turbulent conditions for $Re > 4000$, with transitional behaviour in between. With respect to numerical analysis the transitional flow condition cannot be modelled because of its chaotic character and a value for the Reynolds number to distinguish laminar and turbulent flow is required. Versteeg and Malalasekera (2007) indicated that a change from laminar to turbulent flow in pipes may be assumed at Reynolds numbers of 2000, while Andersson et al. (2011) stated that this change may be considered at a Reynolds numbers of 2100.

Whilst the Weber number characterises the stability of droplets in relation to relative velocity and surface tension, it does not take account of viscosity effects to counteract droplet breakup. The dimensionless Ohnesorge number represents the ratio of viscous forces to surface tension and inertia forces and can be used to describe the stability of a droplet. It can also be expressed as a ratio of the square rooted Weber number and the Reynolds number.

$$Oh = \sqrt{\frac{\mu}{\sigma \rho l}} = \frac{\sqrt{We}}{Re} \tag{2.7}$$

where ρ is the density, σ the surface tension, l the characteristic length and μ the dynamic viscosity. Li (2008) explained that energy induced to a moving droplet may be dissipated by the internal viscous effects inside the droplet and obstructs droplet formation. This behaviour occurred at high Ohnesorge numbers. On the opposite, low Ohnesorge numbers indicate that induced energy is converted to surface tension energy and allows formation of droplets. The Ohnesorge number may be used on its own to assess the droplet formation probability, but Liu

(1999), Delteil et al. (2011) and Farvardin and Dolatabadi (2013), Agrawal (2013) highlighted that the breakup regime of a jet can be identified using a Reynolds number vs Ohnesorge number diagram. An overview of the relation between breakup regimes, Reynolds number and Ohnesorge number is shown in Figure 2.14. The breakup of a liquid jet with Weber

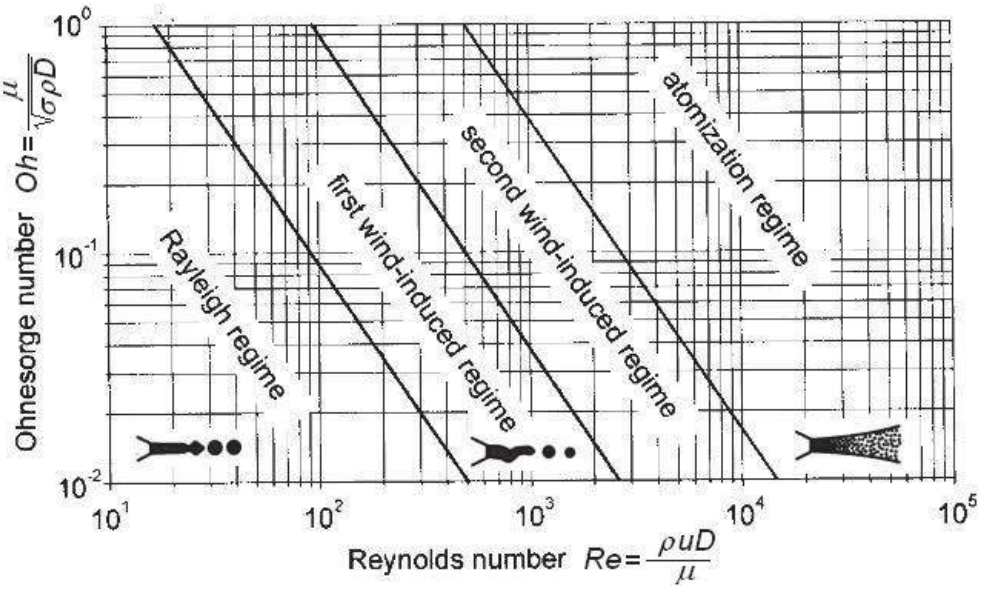

Fig. 2.14 Indication of breakup regimes as a function of Reynolds number and Ohnesorge number

(Martínez, 2014)

numbers larger than unity led to a widening of the jet cross-section as shown by Fellouah et al. (2009). The widening can be expressed as the plume angle or jet opening angle, ϕ, as shown in Figure 2.15. The escaping jet from the nozzle may be initially smaller in diameter, but with increasing distance from the nozzle the jet diameter increases. When the jet diameter exceeds the gallery inlet diameter only partial entry of the jet occurs, leading to low oil catch ratio and reduced gallery filling. Kneer and El-Khawankey (2010) indicated that the oil temperature has a significant effect on the jet breakup. It was shown that at low oil temperatures and high flow rate only little breakup occurred, leading to a narrow oil jet improving gallery inlet hit accuracy. In the contrary at higher temperatures with lower flow rates an increase the breakup was noticed, leading to an increase in plume angle and reducing hit accuracy. This may have negative effects on the gallery filling.

Besides the natural breakup of a jet, pulsating flow can also encourage breakup, as mentioned by Eggers and Villermaux (2008). Manring and Kasaragadda (2003) and Huang

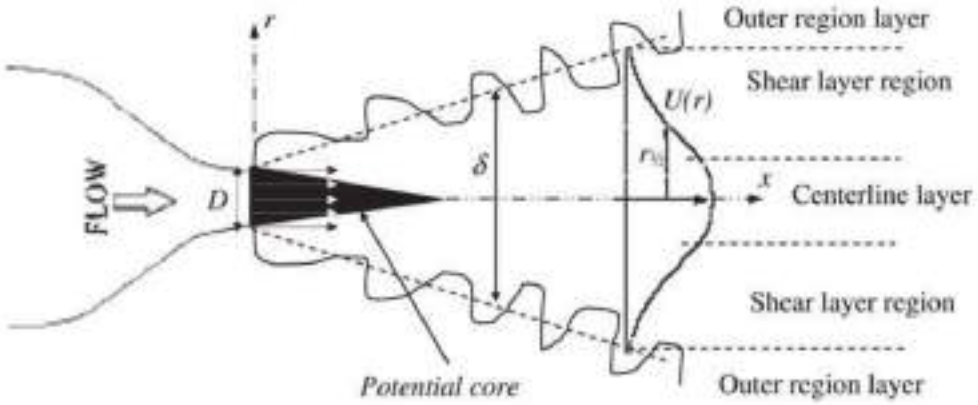

Fig. 2.15 Jet opening angle and jet layers

(Fellouah et al., 2009)

and Lian (2009) stated that external spur gear pumps, as found in engines, produced time dependent pulsating flow. The magnitude of pulsation depended strongly on the design of the oil pump. Pumps with relief grooves reduced the pulsation magnitude significantly and produced a flow with almost absolute positive sinusoidal variation. Huang and Lian (2009) experimentally determined peak flow rate fluctuations of 4.0% above and 7.1% below from the mean flow rate for an external spur gear pump.

Pulsating flow behaviour also occurs from vane type pumps. Harrison et al. (2014) showed that an interruption of delivery occurs as the vanes move from the suction side to the delivery side and vice versa. This resulted in volumetric flow pulsation, although values were not disclosed. Pulsating vane pump mass flow behaviour was also determined by Jones et al. (1998), He and Kong (2013) and Zanetti-Rocha et al. (2013). It was shown that the pulsation of the flow rate from the average flow rate depended very strongly on the rotational speed, delivery pressure and the design with respect to number of vanes and dimensions. The analysis of aforementioned publications on vane pumps also highlighted that no comparable pulsation pattern between investigations were found and the design of the individually studied pumps must be very influential on the behaviour.

2.5 Environmental concerns and gallery filling

2.5.1 Parasitic losses from piston cooling

The drive for improved fuel economy attracts attention not only of primarily necessary systems, such as camshafts, but also of secondary systems, such as oil pumps. Although necessary to deliver the engine with lubricant, the oil pump also supplies the nozzles for piston cooling. While delivering oil to the bearings of the engine, some of the oil flow is redirected towards the cooling nozzles.

Lasecki and Cousineau (2003) determined that the amount of oil ejected from the cooling nozzles was as high as 12% of the total flow for a heavy-duty diesel engine with a specific flow rate of 8 l/min. A performance comparison of a conventional and electrically driven oil pump found that power requirement on the pump could be reduced the by 50%, as the flow rate may be adapted to the actual flow requirement. Staley et al. (2007) indicated that the oil pump constitutes between 1% and 3.5% of engines fuel consumption and proposed the use of variable flow oil pumps to address the flow demand more accurately. This was also proposed by Loganathan and Govindarajan (2011), who concluded that variable flow pumps would yield larger gains that optimisation of fixed flow rate pumps.

It highlights that the maximum performance gains from variable flow rate pumps could only be harnessed, if the flow rate was adjusted accordingly to the requirements. Continuously feeding oil to the cooling gallery would require higher flow rates than the actual demand for filling. Less may mean more in the sense that a lower oil flow rate from the pump could reduce losses, while lower flow rates lead also to reduced jet breakup and possibly increased oil catch rate of the gallery for better gallery filling. It should also be noted that cooling of pistons is not always required, but only during high power demand from the engine. Switch-off of cooling jets may be implemented as well to reduce pumping losses.

2.5.2 Effects on oil during engine operation

Piston cooling may be a major concern to performance improvement engineers, but further issues arise through the use of the engine oil as coolant. The main task for the oil is to lubricate the engine. At high temperature the oil changes its molecular structure and the long-chain

molecules required for lubrication are broken down (cracked), reducing the lubrication ability of the oil and leading to potential engine failure.

Moritani and Nozawa (2003) measured temperatures at the piston ring land as high as 170° C. This was usually no temperature to be concerned about, but due to the high concentration of hydrocarbons and oxygen from the combustion chamber the degradation rate of the oil accelerated. Pan et al. (2005) mentioned that prolonged exposure of the oil to high temperatures can lead to carbon deposits on the piston leading to higher fuel consumption and increased blow-by at the piston rings. Phillips (2006) also stated that at temperatures above 300° C thermal degradation combined with oxidation occurred, especially referring to the piston ring zone of diesel pistons.

Moritani and Nozawa (2003), Phillips (2006) and Kim and Park (2012) also linked degradation to pressure, stating that an increase in pressure increased the degradation rate. This was particular the case in diesel engines with high cylinder pressures, although the high combustion pressures may not occur at the piston rings. The result of the oil degradation was increased wear due to oil thinning, also known as dieselization.

Alternative fuels, such as biodiesel, also caused dilution of oil used to lubricate and cool as shown by Fang et al. (2007), Tsuji and Neto (2008), Steinschütz et al. (2010) and Zha et al. (2012). The reduced oil quality led to increased engine wear. Zha et al. (2012) showed that the use of bio-diesel blends increased the temperature of soot inside the cylinder (10° C to 30° C higher) and the formation of localised high intensity soot clouds. The high soot temperature increased the oxidation of the soot in the exhaust system (after being expelled from cylinder) with excess air, leading to fewer emissions, but the higher temperature in the cylinder led to increased heat radiation to the piston and other components and potential contamination of the oil film on the cylinder walls.

2.6 Summary

This chapter introduced the reasons, needs and requirements for piston cooling. For further improvement of diesel engine output performance the cylinder pressure needs to be increased, requiring higher material strength. This means that piston temperature must be reduced, or, if not possible, at least controlled to a limit, relying heavily on reliable heat transfer. Therefore piston cooling is a vital part of engine thermal management to guarantee reliable operation

with maximum fuel efficiency and minimum emission impact. Modern diesel engines require active cooling of the piston, employing internal cooling galleries to extract heat specifically at high temperature areas, such as combustion bowl rim, pin boss and ring carrier. The knowledge of the heat transfer coefficients is critical to assess the thermal conditions and subsequently resulting temperatures. Heat transfer coefficients depend also on the gallery filling level in terms of the thermal inertia of the oil to extract heat, but also on bulk flow speed, as this controls the speed and amount of heat that can be transferred.

The majority of investigations on internal gallery flow and heat transfer referred to large cylinder sizes of 2000 cm^3 or above. Pistons for smaller engine sizes, as found in passenger vehicles, with cylinder volumes of approximately 500 cm^3 are mainly investigated with focus on temperature measurements. The majority of analyses conducted use numerical techniques (simulations) to determine the heat transfer coefficient. Heat transfer, piston temperatures and gallery filling show strong inter-relations. The problem arises with the validation of numerical results. While temperatures can be validated reasonable well through direct measurements on operating engines, the heat transfer coefficients are virtually impossible to determine directly through measurements.

The direct measurement of the oil fill level inside the cooling gallery of an operating engine is also virtually impossible due to lack of suitable sensors and technique, as any variation in temperature will change the properties of the oil and therefore the flow behaviour. It was shown that flow behaviour can be determined, when transparent piston and gallery models are created and tested outside engines with high speed video equipment. The findings from isothermal tests have highlighted a further issue, adding to the complexity of the problem. The flow inside the gallery is not steady, but of highly transient behaviour, making comparison of results between experiment to simulation even more difficult.

Although there are shortcomings in the validations of numerical models, these are still the most efficient way for design improvements. A clear assessment of the reliability, constraints and limitations of numerical analysis with regards to experiments would be beneficial, while also obtaining information about the filling and flow behaviour inside the gallery itself.

Through the literature the most influential parameters concerning gallery filling were identified. The strongest effects were attributed to engine speed and oil flow rate, while geometric features on gallery, nozzle and engine were seen as less influential, but not insignificant.

CHAPTER 3 NUMERICAL METHODS

Computational Fluid Dynamics (*CFD*) software is widely used nowadays to solve complex flow phenomenon. This chapter is concerned with the theory and requirements of numerical methods to solve flow phenomenon in general and multi-phase flow in particular. It is aimed to introduce the reader to the principles of numerical flow modelling and to highlight some of the consideration of the selection in the model development process.

The principles of fluid flow modelling are set forth and specific considerations relating to the problem to be investigated are explained and discussed, concerning the subjects of meshing, turbulence, time dependence, multi-phase flow, interface tracking and boundary conditions. Relations to published work on piston cooling are made where possible to emphasise the importance of described methods and to support the selection process of modelling techniques with regards to the problem. Occasionally reference is made to specific conditions or requirements of the software used. These are then explicitly stated. The software used in this study was ANSYS Fluent V14 ©.

3.1 Introduction and Governing Equations

The bases of most computational fluid dynamic simulations are the Navier-Stokes-Equations, which describe the flow within a domain based on conservation of mass, momentum and energy. Thereby the equations consider three spatial directions, namely the x, y and z direction for 3–dimensional domains and time, t.

Mass conservation

For a given volume of specified size the mass continuity has to be satisfied, meaning that no mass can be generated or lost and inflowing or outflowing masses have to be reflected by the increase or reduction in mass within the volume. This is dealt with by the mass continuity equation. The equation can be written in a differential form Versteeg and Malalasekera (2007)

for an infinitesimal small control volume as

$$\frac{\partial \rho}{\partial t} + \frac{\rho \partial (u)}{\partial x} + \frac{u \partial (\rho)}{\partial x} + \frac{\rho \partial (v)}{\partial y} + \frac{v \partial (\rho)}{\partial y} + \frac{\rho \partial (w)}{\partial z} + \frac{w \partial (\rho)}{\partial z} = 0 \tag{3.1}$$

where ρ is the density and u, v, w are the velocities in the x, y, z direction respectively. The equation may be written in short vector notation as

$$\frac{\partial \rho}{\partial t} + \nabla(\rho \mathbf{u_i}) = 0 \tag{3.2}$$

As mass is a scalar only one equation is required. This equation is valid for compressible and incompressible flows, as it accounts for changes of velocity and density with regards to time and space. In the case of incompressible flow, where the density is constant throughout the control volume, the differentials of density are zero and the equation reduces to

$$\frac{\partial (u)}{\partial x} + \frac{\partial (v)}{\partial y} + \frac{\partial (w)}{\partial z} = 0 \tag{3.3}$$

Momentum conservation

Momentum is a vector and therefore requires the evaluation in the specific directions. In a Cartesian coordinate system the directions are x, y and z, hence there are three momentum equations. For the x–direction the equation (Versteeg and Malalasekera, 2007) is

$$\frac{\partial (\rho u)}{\partial t} + \nabla(\rho u \mathbf{u_i}) = -\frac{\partial p}{\partial x} + \frac{\partial \tau_{xx}}{\partial x} + \frac{\partial \tau_{yx}}{\partial y} + \frac{\partial \tau_{zx}}{\partial z} + S_{Mx} \tag{3.4}$$

with τ being the stresses in the fluid and S_{Mx} a source term accounting for gravitational and body forces acting on the fluid. For Newtonian fluids there occur three normal stresses

$$\tau_{xx} = \lambda(\nabla \mathbf{u_i}) + 2\mu \frac{\partial u}{\partial x}, \quad \tau_{xx} = \lambda(\nabla \mathbf{u_i}) + 2\mu \frac{\partial v}{\partial y}, \quad \tau_{xx} = \lambda(\nabla \mathbf{u_i}) + 2\mu \frac{\partial w}{\partial z} \tag{3.5}$$

and six shear stresses

$$\tau_{xy} = \tau_{yx} = \mu \left[\frac{\partial v}{\partial x} + \frac{\partial u}{\partial y} \right], \quad \tau_{xz} = \tau_{zx} = \mu \left[\frac{\partial u}{\partial z} + \frac{\partial w}{\partial x} \right], \quad \tau_{zy} = \tau_{yz} = \mu \left[\frac{\partial w}{\partial y} + \frac{\partial v}{\partial z} \right] \tag{3.6}$$

whereby μ is the dynamic viscosity and λ is the second viscosity coefficient, with the relation

$$\lambda = -2/3\mu \tag{3.7}$$

The complete momentum equation then becomes

$$\frac{\partial(\rho u)}{\partial t} + \nabla(\rho u \mathbf{u_i}) = -\frac{\partial p}{\partial x} + \frac{\partial}{\partial x}\left(\lambda(\nabla \mathbf{u_i}) + 2\mu\frac{\partial u}{\partial x}\right) + \frac{\partial}{\partial y}\left(\mu\left[\frac{\partial v}{\partial x} + \frac{\partial u}{\partial y}\right]\right)$$

$$+\frac{\partial}{\partial z}\left(\mu\left[\frac{\partial u}{\partial z} + \frac{\partial w}{\partial x}\right]\right) + S_{Mx} \tag{3.8}$$

The simplified equations of momentum conservation in y–direction and z–direction are

$$\frac{\partial(\rho v)}{\partial t} + \nabla(\rho v \mathbf{u_i}) = -\frac{\partial p}{\partial y} + \frac{\partial \tau_{xy}}{\partial x} + \frac{\partial \tau_{yy}}{\partial y} + \frac{\partial \tau_{zy}}{\partial z} + S_{My} \tag{3.9}$$

$$\frac{\partial(\rho w)}{\partial t} + \nabla(\rho w \mathbf{u_i}) = -\frac{\partial p}{\partial z} + \frac{\partial \tau_{xz}}{\partial x} + \frac{\partial \tau_{yz}}{\partial y} + \frac{\partial \tau_{zz}}{\partial z} + S_{Mz} \tag{3.10}$$

Energy conservation

The energy equation evaluates all energies transferred across the boundaries of the volume. The energy is regarded as a scalar, hence there is a single equation. The equation includes energy due to work on the control volume (e.g. from pressure on the fluid or shear), heat transfer (from external sources and from internal heating, such as viscous heating) and the change of internal energy (on a molecular basis and from the flow itself). The equation can be written for total energy as (Versteeg and Malalasekera, 2007)

$$\frac{\partial(\rho E)}{\partial t} + \nabla(\rho E \mathbf{u_i}) = +\frac{\partial}{\partial x}\left(k\frac{\partial T}{\partial x}\right) + \frac{\partial}{\partial y}\left(k\frac{\partial T}{\partial y}\right) + \frac{\partial}{\partial z}\left(k\frac{\partial T}{\partial z}\right) - \frac{\partial(pu)}{\partial x} - \frac{\partial(pv)}{\partial y}$$

$$-\frac{\partial(pw)}{\partial z} + \frac{\partial(u\tau_{xx})}{\partial x} + \frac{\partial(u\tau_{yx})}{\partial y} + \frac{\partial(u\tau_{zx})}{\partial z} + \frac{\partial(v\tau_{xy})}{\partial x} + \frac{\partial(v\tau_{yy})}{\partial y}$$

$$+\frac{\partial(v\tau_{zy})}{\partial z} + \frac{\partial(w\tau_{xz})}{\partial x} + \frac{\partial(w\tau_{yz})}{\partial y} + \frac{\partial(w\tau_{zz})}{\partial z} + S_E \tag{3.11}$$

The above equation contains a general description of energy in the variable of E. Expressions for kinetic energy, as well as internal energy can be written explicitly. Additional sources are covered through the source term S_E.

It may be noted that the momentum and energy equations, although suitable for compressible time-dependent flow, do not take turbulence into consideration.

Flow domain

The above equations are solved for a finite number of control volumes, representing the flow domain, as shown in Figure 3.1. The entirety of the control volumes is also called mesh. The following methods can be used to consider the control volumes in the flow domain:

- Lagrangian method,
- Eulerian method, and
- Lagrangian-Eulerian method.

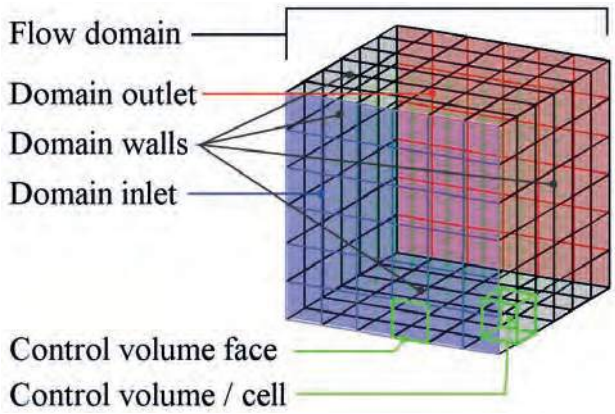

Fig. 3.1 Terminology of basic flow domain boundaries and treatment

The Lagrangian method considers the control volumes to be material parcels of fixed mass travelling along a flow path, while the Eulerian method generally uses control volumes of fixed size and position through which the flow passes. Both methods may be combined to utilise the advantages, which led to the Lagrangian-Eulerian method.

Hirt and Nichols (1981) stated that discontinuities occur on the boundary of the surfaces involving free phase flows, such as two-phase flow. For such multiphase flows Hui and Xu (2012) stated that the Lagrangian method would be better suited, as it allows the sharp modelling of interfaces, with the control volumes containing only one phase with clear boundary surfaces, as shown in Figure 3.2a. The phases interface is represented by the boundaries of control volumes, where both phases connect. The Eulerian method considers

the phases as passing media through the control volumes, causing a blurring of the interface, as shown in Figure 3.2b. This leads potentially to inaccuracies in the solution with coarse meshes and requires special modelling, or tracking, of the interface inside the cells. Although the Lagrangian method may appear as more suitable for multi-phase flow, Donea et al. (2004) indicated that problems arise, when large deformations of the control volumes occur, e.g. due to high vortices or shear flows. This requires constant reproduction of the flow domains control volumes, which increases simulation time. As a consequence the Eulerian method is more suitable to deal with this problem due to the fixed control volumes in space and size. The flexible mesh of the Lagrangian method with its sharp interfaces and the Eulerian

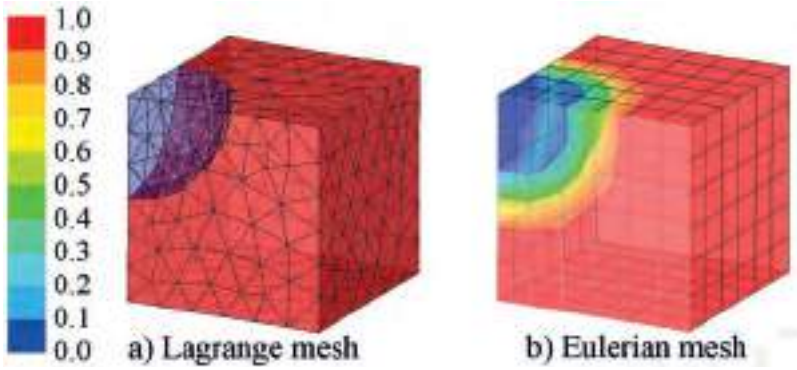

Fig. 3.2 Lagrangian mesh and Eulerian mesh for multi-phase flow considering identical volumes of liquid (red) and gas (blue)

method with improved calculation time led to a combination of both, resulting in the Arbitrary Lagrangian Eulerian (*ALE*) method. The flow can be modelled in the flexible mesh as a function of position and time and is then transferred to the fixed mesh for solving, being finally transferred back to the flexible mesh for post processing. Such a method was used by Fu et al. (2006) investigating the cooling effect inside a reciprocating piston gallery. The investigation, however, was conducted with air as the cooling medium (single–phase only) and in 2–dimensional space. The disadvantage of this process was mainly in the transfer mechanism between methods, requiring analytical functions to be developed specifically for this application. It was therefore not considered as a viable option for this study.

3.2 Volume meshing

To obtain values for the flow field variables, such as velocities, temperatures and pressure, the flow domain is split into cells (control volumes in 3D), also known as the mesh. Meshes

can be divided into a number of categories, whereby a flow domain geometry can be meshed with structured, unstructured or hybrid meshes, as shown in Figure 3.3. The advantages of

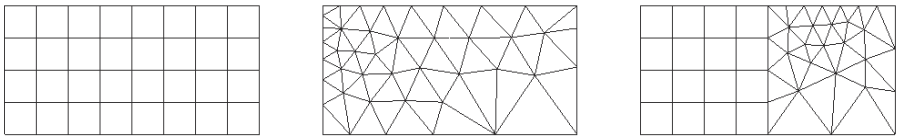

Fig. 3.3 Different types of meshes

structured meshes are in the connection and interactions of cells with each other, which leads to an efficient and accurate representation of the flow field. The problem arises with complex geometries, where these cells may become extremely deformed (skewed). Unstructured meshes allow easy meshing of complex geometry. The connection between cells is more random (not aligned with flow direction) and extra information about the cell connection is required. This increases the memory demand and leads to higher computational expense. The application of hybrid meshes uses the advantage of both mesh types, where the structured mesh is employed on simpler areas of geometry and complex areas are covers with an unstructured mesh.

Three are various shapes of the cells, namely hexahedrons, wedges, pyramids and tetrahedrons, as shown in Figure 3.4. These are all for 3–dimensional space. Equivalent of hexahedrons and tetrahedrons exits in 2–dimensional space and are namely squares and triangles respectively. While hexahedral cells are predominantly used for structured 3–dimensional meshes, tetrahedrons are used for unstructured meshes, although structured meshes are possible. Ferziger and Peric (2002) and Peric (2004) stated that hexahedral cells provide the best

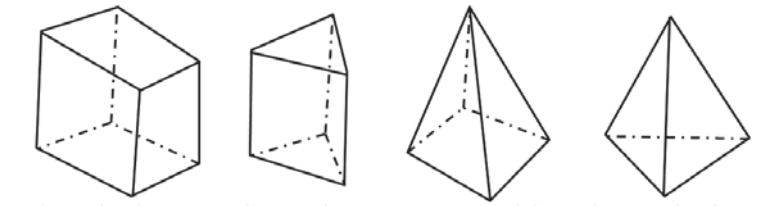

Fig. 3.4 Cell types in 3–dimensional space

performance in terms of efficiency and accuracy as compared to tetrahedral cells, but also acknowledges that the generation of high quality structured meshes are difficult to achieve,

if at all. At least three quality indicators of the mesh cells should be considered, orthogonal quality, skewness and aspect ratio.

The orthogonal quality relates to geometric relationship of neighbouring cells with respect to their cell centres and cell boundaries across which fluxes are calculated. Ferziger and Peric (2002) explained that although complex geometry shapes led generally to non-orthogonal meshes, the aim should always be to create meshes as orthogonal as possible, highlighting the importance of the angle between a cell surface normal vector and the vector of cell centres of neighbouring cells sharing that face. The reason can be found in the higher truncation error on non-orthogonal (and non-uniform) grids and increased interpolation errors. Juretic (2004) also showed that the truncation error is minimal for orthogonal meshes improving the order of accuracy. The orthogonal quality Q_o can be determined by

$$Q_o = \frac{\overrightarrow{A_i} \cdot \overrightarrow{f_i}}{|\overrightarrow{A_i}| \cdot |\overrightarrow{f_i}|} or \frac{\overrightarrow{A_i} \cdot \overrightarrow{c_i}}{|\overrightarrow{A_i}| \cdot |\overrightarrow{c_i}|} \tag{3.12}$$

where A_i is the face normal vector, f_i the vector from the cell centre to the face edge and c_i the vector between neighbouring cell centres, as shown in Figure 3.5. The calculation has to be performed for all cells and faces in the flow domain and the lowest value will be used for the quality assessment. Orthogonal meshes will return only values of 1 indicating the highest quality, while non-orthogonal meshes have values lower than unity with the poorest quality mesh returning values near zero. The skewness relates to the angular deviation of the edges of a faces from its equilateral angles. On quadrilateral faces, as found on hexahedrons, the equilateral angle in 90°. The lowest skewness and therefore best quality is represented for values of 0, while highly skewed faces return a value of 1. Bakker (2012) stated that for hexahedral cells that values of above 0.85 should be avoided.

Another measurement of mesh suitability is the aspect ratio of the cells. It is the ratio of the longest edge to the shortest edge of the cell and has the optimum value of 1. Hexahedral cells may be adjusted (or trimmed) in shape allowing one dimension of the cell being longer in the direction of flow, increasing the aspect ratio (Bakker, 2012). The increased length in the flow direction allows for larger simulation time steps for transient flow modelling and therefore reduced calculation time. Although one dimension of the cell changes, this does not necessary increase the cell skewness, if the cell angles remain near constant. Such trimmed

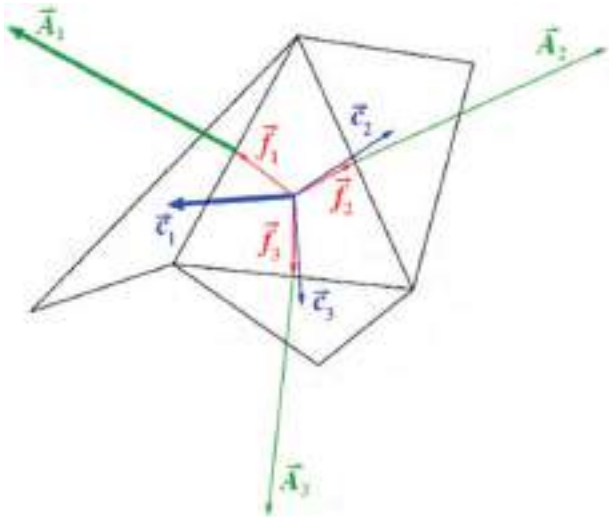

Fig. 3.5 Vectors used to determine orthogonal quality

(ANSYS, 2013a)

cells are especially necessary useful, where larger velocity gradients are apparent, e.g. normal to walls.

If effects of surface tension are of high importance, then a 3–dimensional hexahedral mesh should be employed, as the tetrahedral mesh may produce inaccurate results (ANSYS, 2011). Structured meshes are preferred for faster calculation and the potential use of Graphic Processing Units (*GPU*) on graphic cards as solver cores, as these can reduce simulation time and have a significant lower cost per solver core in comparison to Central Processing Units (*CPU*). Corrigan et al. (2009) have employed *GPU*'s successful on an unstructured mesh modelling flow over a wing profile and determined reductions in simulation time as high as 100%. Despite the potential gains, Slagter (2014) stated that the use of *GPU*'s is at the moment unsuitable for transient simulations.

3.3 Volume phase modelling and interface tracking

As mentioned in the previous section, the mesh representing the flow domain can be implemented using the Lagrangian or Eulerian method. The software used in this study uses the Eulerian mesh method and only models for multiphase flow on a fixed mesh will be considered.

Brennen (2005), Andersson et al. (2011) and Bakker (2012) highlighted the most common models to simulate multiphase flows as:

- Euler–Lagrange (for dispersed phase),
- Euler–Euler,
- Mixture (or algebraic slip mixture model, *ASMM*),
- Volume–of–Fluid (*VOF*) and
- Level–Set (*LSM*).

The Euler–Lagrange model considers one fluid as a continuous phase and the second phase as a dispersed phase, whereby the second phase is considered as individual particles. For each particle the path of movement is modelled, as well as interactions with the continuous phase. With increasing volumetric content of the secondary phase the computational demand also increases. Chen (2004) stated for bubble laden flow that the computational power requirement can not only be linked to the mesh size, but also to the number of bubbles to be tracked in the flow. This is the main disadvantage of the model, which was also explained by Andersson et al. (2011).

The following multiphase flow models have in common that the sum of all phase fractions in each cell need to be unity or mathematically expressed as

$$\sum_{q=1}^{n} \alpha_q = 1 \tag{3.13}$$

where q is the phase identifier, n is the number of phases present in the domain and α_qq is the volume fraction identifier. The volume fraction identifier represents the amount of a particular phase in a cell and takes values from 0 (cell empty of phase) to 1 (cell full of phase). The multiple phases also lead to an expansion of the continuity equations for mass, momentum and energy. The modified mass conservation equation was used as an example for the below explained models. Tryggvason (2010) also explained that the momentum equations may be expanded by an additional term involving the interface forces, whereby the force may include drag, lift, gravitational, pressure or any other force. Such additional forces could be included into software code as user defined functions for enhancement of the breakup of free jets or formation of bubbles and droplet due to coalescence.

The Euler–Euler model is suitable for the majority of mixing flows, but especially for flows with phase interaction, where exchange of momentum occurs. This model is also very

demanding on computational power and memory, as continuity and momentum equations have to be solved for each phase individually. The advantage is that it allows for better tracking of phase changes and interphase drag and lift coefficients. Wang et al. (2015) used the model to determine the flow inside a closed gallery-like model and found it superior to the *VOF* model in predicting the flow behaviour. It was implied that the model performed better, as three phases were modelled, a solid one for nano-particles, a liquid one for water and a gaseous on for air. Here the momentum interaction between phases plays a crucial role. The mass conservation equation is

$$\frac{\partial}{\partial t}(\alpha_q \rho_q) + \nabla(\alpha_q \rho_q u_q) = \sum_{p=1}^{n} (\dot{m}_{pq} - \dot{m}_{qp}) \tag{3.14}$$

Where p and q are the index referring to the number of phases, ρ_q is the density, u_q the velocity, $\dot{m}$ the mass transfer between phases from q to p and p to q. Needless to say that for two phases two sets of equations have to be solved, increasing memory and processor demand.

The Mixture model is a variety of Euler–Euler model and allows penetration and mixing of the phases, being better suited for mixing flows where no clear phase separation is present, such as in particle laden flow and dispersed small bubbles flows. The model employs mixture equations for momentum, continuity and energy, while also containing extra equations to calculate the secondary phases, from which relative velocities of the phases can be determined. It is simpler that the Eulerian model due to the reduced number of equations, but more demanding than the *VOF* model, although sharing some commonalities, such as a single momentum equation for the phases. The mass conservation equation is

$$\frac{\partial}{\partial t}(\rho_m) + \nabla(\rho_m u_m) = 0 \tag{3.15}$$

where the mixture velocity and mixture density can be determined by

$$u_m = \frac{\sum_{p=1}^{n} (\alpha_p \rho_p u_p)}{\rho_m} \qquad \textit{and} \qquad \rho_m = \sum_{p=1}^{n} (\alpha_p \rho_p) \tag{3.16}$$

The solving of one set of continuity equations leads to reduced computational demand and shorter simulation times as compared to the Euler–Euler model.

The Volume–of–Fluid (*VOF*) model is based on developments by Hirt and Nichols (1981). It allows the tracking of phase interfaces and is suited to flows where the fluids do not mix (immiscible) and the position of the interface is of interest. This includes open surface flows, as well as jet breakup and large bubble flow. The model uses a single mass conservation equation in the form of

$$\frac{1}{\rho_q}\left[\frac{\partial}{\partial t}(\alpha_q\rho_q)+\nabla(\alpha_q\rho_q u_q)=\sum_{p=1}^{n}(\dot{m}_{pq}-\dot{m}_{qp})\right] \tag{3.17}$$

For accurate interface tracking additional models are required, especially for strongly curved interfaces and coarser meshes. The *VOF* model is the most widely used model to track phase interfaces, especially for time-dependent solutions (ANSYS, 2011; Bakker, 2012) and was employed by Pan et al. (2005), Yi et al. (2007) and Wang et al. (2015) for gallery flow analysis. It is also the least demanding model method with respect to computational power, as only one set of momentum equations is required. Kositgittiwong et al. (2010) pointed out that the *VOF* model has its limitations in the shared equation approach, when high velocity differences between the phases occur. Furthermore, Andersson et al. (2011) stated that a sufficiently fine mesh is required for accurate interface tracking, leading to increased memory demand and computational time, which may offset the gains from its simplicity.

Another method based on the Eulerian flow field is the Level-Set method (*LSM*). Osher (2001) stated that the method was primarily developed to compute and analyse the motion of a surface within a velocity field. The Level-Set relates to a function describing the shape of a surface in relation to any arbitrary point in the flow domain. For the surface boundary the solution to the function is zero, while positive and negative values relate to position either inside or outside the boundary.

Osher (2001) and Ménard et al. (2007) stated the most significant advantage as the capability of the method to easily compute the splitting and joining of surfaces as found on jet breakup. A.Berlemont et al. (2012) also stated that geometric information about the surface is easy to obtain, although this does not necessarily mean easy numerical implementation. The main disadvantage is that it is not mass conserving in under–resolved regions, where large stretching of the surface occurs, as stated by Ménard et al. (2007). This was also stated by

A.Berlemont et al. (2012) and the reason was found in the re-distancing algorithm required for strongly stretched surfaces.

Alternatively the Level-Set method may be coupled with the *VOF* method to utilise the benefits of the accurate interface tracking of the *LSM* with the mass conservative solution of the *VOF*, as shown by Ménard et al. (2007) and A.Berlemont et al. (2012) for jet breakup investigations.

The models described above may be used to predict the location of the phases within the flow domain and also for the interface tracking, although lacking the accuracy of the precise representation of the interface position. More accurate interface reconstruction schemes were developed that link with the *VOF* model. Common interface reconstruction schemes are:

- Compressive scheme,
- Compressive Interface Capturing Scheme for Arbitrary Meshes (*CICSAM*) scheme,
- Higher Resolution Interface Capturing (*HRIC*) scheme,
- Simplified Line Interface Calculation (*SLIC*) scheme and
- Piecewise-Linear Interface Calculation (*PLIC*) or geometric-reconstruction scheme.

Although all of these schemes can be used for interface reconstruction, not all of them are suitable for the problem under investigation. ANSYS (2011) recommended for cases where sharp interface between phases are important the Compressive, *PLIC* or *CICSAM* schemes. Seo (2014) identified the same schemes to produce sharp and accurate interfaces. It was also highlighted that these schemes had the disadvantage of long computing times and demanded high quality meshes with low skewness. Besides accuracy and sharpness of the interface, computational time and stability of the simulation were also identified and key factors for the selection of the interface tracking scheme.

Waclawczyk and Koronowicz (2006) showed for a breaking wave problem that the *VOF* model with the *CICSAM* and the *HRIC* schemes provide good comparison results to the Level-Set model with regards to shape preservation and interface capturing, but also highlighted the strong dependency of the time step of the transient solution. Waclawczyk and Koronowicz (2008) expanded their previous study and compared results from experimental investigations of forced water sloshing within a tank to simulation results using the *VOF* model with the *CICSAM* and *HRIC* scheme. Both models were found to provide initially good comparison of the main flow features, although with increasing sloshing periods the accuracy of the flow

features deteriorated slightly as a result of the increasingly dispersed flow. It was also noticed that the *CICSAM* scheme produced a sharper interface. Unfortunately no specific information was provided for both cases on the computational time requirement.

The Piecewise-Linear Interface Calculation (*PLIC*) scheme reconstructs the interface within a cell that contains at least two phases, reducing the diffusion of the interface by keeping the interface within one cell. Rider and Kothe (1995) stated that the *PLIC* scheme outperforms several *VOF* methods, including *SLIC*. In their investigated cases the interface remained sharp, although larger cells delivered less accurate results due to the linear character of the reconstruction, when a strong interface curvature occurs within a cell. It was also stated that lost curvature information from the linearization could not be recovered and only a refined mesh can improve results, whereby linearization errors may still remain on a cell level. Zhang et al. (2014) also stated the sharp interface maintaining as an advantage, but described the processes involved as complicated and challenging for unstructured 3–dimensional meshes.

The accurate capturing of interface dynamic requires the inclusion of the surface tension modelling. Two methods to implement surface tension were available, namely the Continuum Surface Stress (*CSS*) method and the Continuum Surface Force (*CSF*) method.

The continuum surface force (*CSF*) method was proposed by Brackbill et al. (1992) to overcome the difficulties in modelling the interface with complex shapes. It is stated that the force at the interface is not considering the boundary of the phases as a discontinuity, but rather as an interface with finite thickness representing the transition from one fluid to another. It is therefore modelled as a volume force and is submitted to the momentum equation as a source term. The surface force has to be determined for each surface pair, even including separation of different materials within a phase, e.g. oil water flow, which allows a wide range of applications. For two phases in direct contact the conditions are identical on both sides and the force equation can be given as (Andersson et al., 2011; ANSYS, 2011)

$$F_{CSF} = \sigma_s \kappa \nabla \alpha \tag{3.18}$$

where σ is the surface tension, κ the surface curvature and α the volume fraction. As the interface is treated as a continuum, rather than a discontinuity, a requirement is that the thickness of the interface layer is sufficiently small to capture the curvature of the interface accurately.

The continuum surface stress (*CSS*) calculates the surface force based on the divergence of the capillary stress tensor as stated as stated by Boger et al. (2010), Sultana (2012) and Albert et al. (2012). The force can be calculated from

$$F_{CSS} = \nabla T = \nabla \sigma_s \left[|\nabla \alpha| I - \frac{\nabla \alpha \times \nabla \alpha}{|\nabla \alpha|} \right] \tag{3.19}$$

where T is the capillary stress tensor and I a unit tensor. The advantage of the *CSS* is that it avoids the explicit calculation of curvature of the interface and relies mainly on the gradients of the volume fractions. For gravity-driven wall-film flow Albert et al. (2012) also stated that the internal vortex structure of the flow was predicted insufficiently accurate, which can affect results of heat and mass transfer simulations.

It may be noted that there are two interfering methods involved affecting the shape and position of the interface. Outside the gallery the breakup of the jet and formation of droplets follow the physical principle involving the surface tension. Sirignano (1999) states that for Weber numbers below a critical value the surface tension controls the distortion of the surface, dominating the aerodynamic forces which tend to disintegrate the surface. This behaviour was also shown by Delteil et al. (2011), where surface tension is used to predict Rayleigh breakup with low velocity differences between phases. Here the implementation of the surface tension does play a crucial role.

Inside the gallery the case is different. Pan et al. (2005) stated that the velocities at the interface maybe assumed as nearly identical and air resistance at the interface is less of a driving factor of the breakup. The shape of the phase interface surface inside the gallery may be more dictated by externally created forces on the flow, such as gravitational and acceleration forces from gallery movement. These are implemented as body forces. Bush and London (1965) stated that the influence from the piston acceleration is at least four times higher in comparison to the gravitational force. Surface tension may play an even smaller role inside the gallery, but may still be considered.

3.4 Transient modelling

A time-dependent solution is required for all transient flow conditions. The time advancement step is of high importance to reach stable and converged solutions. If the time step between

calculation time points is too large, the flow may pass through a large number of control volumes and some effects may not be treated or considered, potentially leading to inaccuracies or even solver instabilities. There are two methods to introduce time stepping, namely an implicit scheme and an explicit scheme.

The implicit scheme calculates flow variable values at the present (new) time step by considering previous and present time step values. This makes this approach very stable with regards to the size of the time step. Although this allows for large time steps and therefore fast approach of solutions, the solving process requires intermediate iteration steps with regards to the interaction between pressure and velocity field in the domain, which increases the calculation time and memory requirement.

The explicit scheme calculates the flow variables at the present time step based only on previous time step values. This strongly limits the time step size and may lead to longer simulations times. Employing the geo–reconstruct scheme for the interface tracking requires the explicit *VOF* model.

The pressure and velocity field need to be corrected for each time step calculation and various methods and algorithms are available. The *SIMPLE* (Semi Implicit Method for Pressure Linking Equations) scheme is one of the most common approaches. Versteeg and Malalasekera (2007) stated that the transient *SIMPLE* scheme and its derivatives are implicit schemes that need to be solved iteratively at the end of each time step. Marshall and Bakker (2001) and Tu et al. (2012) explained that for the solving the momentum equation the pressure distribution is only guessed or used from the converged solution of the previous time step. A pressure field correction equation based on the mass continuity equation is solved after the momentum equation. The corrected pressure field can then be used to correct the velocity field, which in turn can be used to solve the momentum equation. This process is repeated until a sufficient accurate solution is obtained. An alternative method is the transient *PISO* (Pressure Implicit with Splitting of Operators) scheme. It is a non–iterative algorithm solved at the end of each time step, which can help to speed up the solution process. Issa (1986) showed that for small time steps the *PISO* scheme can produce sufficient quality results.

The selection of the time step is governed by the Courant–Friedrichs–Lewy conditions, expressed in the Courant–Friedrichs–Lewy number (*CFL* number). It determines the maximum time step viable to obtain stable and correct solutions of explicit time schemes. The

time step can be calculated as

$$\Delta t = \frac{CFL\,\Delta x}{u} \tag{3.20}$$

where Δx the directional control volume length and u the directional flow velocity. Bhaskaran and Collins (2013) state that the explicit scheme is stable for *CFL* numbers ≤ 1. Although the *CFL* number should not exceed unity, it should be small enough to capture the interface accurately, but should also be large enough to reduce computational time, allowing in some instances to increase the *CFL* above unity. A too large *CFL* number can lead to solver divergence, especially with regards to mass continuity.

3.5 Turbulence modelling

The equations of mass continuity, moment and energy may be used to describe turbulent flow. Turbulent eddies, or vortex-like movement, in fluid movement possess a characteristic length and time scale. Large turbulent eddies break into smaller eddies through dissipation of kinetic energy. The process of breakdown eventually reaches the eddy sizes, where the viscous forces become higher than the inertia forces. This is the Kolmogorov scale, which refers to the smallest turbulent eddies, as shown in Figure 3.6. Andersson et al. (2011) stated size and lifetime of some smallest scale eddies as 50 μm and 5 *ms* respectively. Theoretically the mesh must be fine enough the capture such small eddies, if only above equations were to be used to predict flow and to capture turbulent effects correctly. The use of such fine

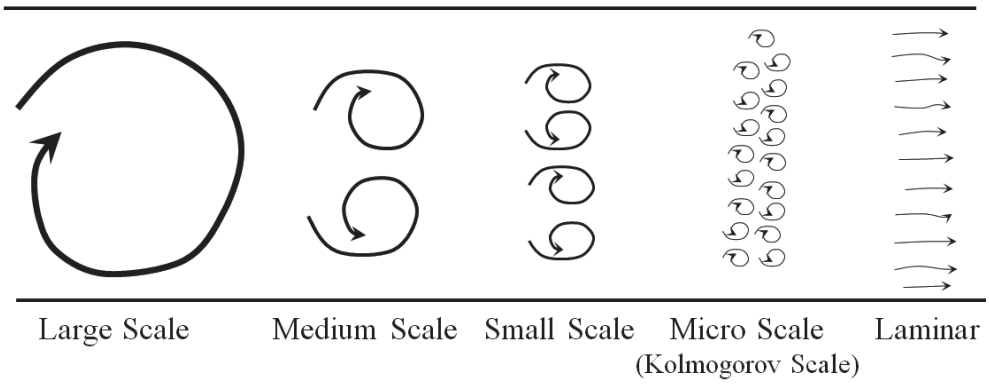

Fig. 3.6 Turbulence scales in flow

meshes and time steps led to Direct Numerical Simulation (*DNS*), but this comes at a high computational cost. Shinjo and Umemura (2010) modelled the breakup of a liquid jet, including the formation and tracing of break-away droplets using *DNS*. The simulation was

contained within a domain size of 14.6 *mm x* 4.5 *mm x* 4.5 *mm* at a grid size of 0.35 *mm* at the finest resolution. This amounted to a total of 6 billion cells, a problem size only suitable to be solved by supercomputer. Although 5760 cores were used, the simulation still required 410 hours to provide a full set of solutions. A.Berlemont et al. (2012) also showed the capabilities of *DNS* to solve the breakup of liquid gasoline jet. Based on a domain size of 0.36 *mm x* 1.44 *mm x* 1.44 *mm* and mesh size on 1.44 μm, totalling 256 million cells, the typical simulation time was given with 20 hours on 1024 cores and 2000 time steps. It can be seen that the resulting computational demand and therefore cost implications limit the application to few problems.

Alternative models to introduce turbulence on larger mesh sizes were developed. Vectorial flow properties, such as velocity or momentum, need to be considered in the x, y and z direction for a Cartesian coordinate system. For laminar flow conditions, where no fluctuations of velocities occur, the determined velocities are the time averaged velocities for the solved time step at any location and time. Considering the x–direction only and turbulent conditions, the velocity u consists of a mean flow velocity and velocity fluctuation due to the turbulence and can be expressed as

$$u = \frac{1}{\Delta t}\int_0^{\Delta t} \bar{u}(t)dt + \frac{1}{\Delta t}\int_0^{\Delta t} u'(t)dt = \bar{u} + u' \tag{3.21}$$

whereby $\bar{u}$ is the mean velocity, u' the fluctuation velocity and Δt the time step interval. For the y and z direction the respective equations can be found. The momentum equation containing velocity differentials in the form of $\nabla(\rho u \mathbf{u_i})$ requires the inclusion of the velocity fluctuation with

$$\nabla(\rho u \mathbf{u_i}) = \nabla(\rho \overline{u}\,\overline{\mathbf{u_i}}) + \nabla(\rho \overline{u'\mathbf{u_i'}}) \tag{3.22}$$

with

$$\nabla(\rho \overline{u'\mathbf{u_i'}}) = \frac{\partial(\rho \overline{u'u'})}{\partial x} + \frac{\partial(\rho \overline{u'v'})}{\partial y} + \frac{\partial(\rho \overline{u'w'})}{\partial z} \tag{3.23}$$

The solving of these extra terms by integration will lead to three additional normal stresses and six additional shear stresses of the form of

$$\tau_{xx} = -\overline{\rho u'^2} \qquad and \qquad \tau_{xy} = \tau_{yx} = -\overline{\rho u'v'} \tag{3.24}$$

to represent just three. These are known as Reynolds stresses. The time averaging and inclusion of the Reynolds stresses leads to Reynold-Averaged Navier-Stokes (*RANS*) models, which are also known as the $k-\varepsilon-model$ and its derivatives, where k is the turbulent kinetic energy and ε the turbulence dissipation. The turbulent kinetic energy per unit mass can be calculated with

$$k = \frac{1}{2}(\overline{u'^2} + \overline{v'^2} + \overline{w'^2}) \tag{3.25}$$

where u', v' and w' are the velocity fluctuations, and the energy dissipation with

$$\varepsilon = C_\mu^{3/4} \frac{k^{3/2}}{l_t} \tag{3.26}$$

where C_μ is a dimensionless constant and l_s the turbulent length scale of the eddies. Versteeg and Malalasekera (2007) stated that the length scale can be estimated as $l_s = 0.07L$ with the L being the characteristic length.

Another quantification of the turbulence is found in the turbulence intensity, expressed as

$$I = \frac{u'}{\bar{u}} = \frac{\sqrt{2/3k}}{\bar{u}} \tag{3.27}$$

It can be used to determine the turbulence of flows entering the domain when conventional calculations of the flow field based on fluctuation between cells is not possible.

Although the standard $k-\varepsilon-model$ is one of the most widely used models, due to its robustness, ANSYS (2011) stated that it has shown shortcoming with regards to swirling flows and axisymmetric jets. The dissipation equation is not suitable to describe the shear in certain circumstances accurately, e.g. at lower Reynolds numbers, where the turbulence is not isotropic. In order to overcome this problem, Shih et al. (1995) proposed the realizable $k-\varepsilon-model$. The model does not use a constant value for C_μ. It is calculated as

$$C_\mu = \frac{1}{A_0 + A_s \frac{kU^\star}{\varepsilon}} \tag{3.28}$$

where $U^\star$, A_0 and A_s are derived constants from the angular velocity of the turbulent field (ANSYS, 2011).

For completeness some alternatives to the above models maybe briefly mentioned, namely the Large Eddy Simulations (*LES*) and Reynolds Stress equation models (*RSM*). The lack of

information about implementation in the field of this study limits the assessment of suitability and these are therefore not used. *LES* attempts to solve mainly the larger turbulence eddies and introduce the smaller eddies back at a sub-grid level. Wang et al. (2008) modelled round jets with variable density for a single-phase gaseous jet, primarily investigating the evolution of the jet. The results provided good comparison to experimental data, indicating that *LES* may be suitable for modelling round jets with the benefit of larger meshes and therefore reduce simulation time.

The *RSM* model contains seven equations to model turbulence. Versteeg and Malalasekera (2007) explained that the *RSM* model provided a better description of the Reynolds stresses in comparison to the $k-\varepsilon-model$, especially for complex flows with large body forces and complex strain fields. Mahmoud et al. (2010) used the *RSM* model and $k-\varepsilon-model$ to simulate the evolution of a round co-flowing jet. A comparison of the results with experimental data concluded that both models predict the jet velocities and turbulence well, although the $k-\varepsilon-model$ required adaption, while still being computational less expensive. This was in line with Versteeg and Malalasekera (2007), which stated that the increase in computational load for the *RSM* model is limiting its application.

3.6 Near-wall flow and treatment

With respect to the problem to be solved the flow friction at the walls had to be considered for two specific cases, the flow inside the nozzle with single phase flow and the flow within the gallery as two–phase flow. Generally, the turbulent condition near a wall changes significantly and needs to be considered carefully. No-slip condition, meaning zero velocity at the wall, lead to large gradients of flow bound variables. While viscous damping reduces the tangential velocity fluctuations, kinematic blocking reduces velocity fluctuations normal to the wall (ANSYS, 2011).

The near-wall region can be subdivided into three sub-layers, as shown in Figure 3.7. Dimensionless variables are used to describe relevant layer properties. The thickness of the layer is given as y^+ and the mean velocity is given as U^+. Both can be determined by

$$y^+ = \frac{\rho u_\tau y}{\mu} \tag{3.29}$$

$$U^+ = \frac{U}{u_\tau} \qquad with \qquad u_\tau = \sqrt{\frac{\tau_w}{\rho}} \tag{3.30}$$

where U is the free stream velocity, y the distance from the wall, u_τ the wall friction velocity and τ_w the wall shear stress.

The change in flow conditions can be represented by separating the region at the wall into three layers, as show in Figure 3.7. Adjacent to the wall is the viscous sub-layer, where the flow is nearly laminar and viscous effects are dominant. Andersson et al. (2011) and Tu et al. (2012) stated that for $y^+ < 5$ the velocity in the layer can be assumed to linearly increase with the wall distance and follows $U^+ = y^+$.

The laminar viscous sub-layer is followed by the buffer sub-layer, where turbulence is present together with viscous effects, followed by the third fully turbulent layer, where turbulence plays the major role in the flow conditions. Andersson et al. (2011) suggested the thickness of the buffer layer with $5 < y^+ < 30$, followed by a fully turbulent sub-layer with $30 < y^+ < 400$. Tu et al. (2012) did not imply such a distinction and stated the thickness of the turbulence sub-layers as $30 < y^+ < 500$. The velocity in the fully turbulent layer can be calculated by

$$U^+ = \frac{1}{\kappa_{vK}} ln(y^+) + B \tag{3.31}$$

where B is an empirically derived constant and κ_{vK} is the von Karman constant. Trinh (2010) showed that the von Karman constant varies depending on the flow conditions, but also the surrounding atmospheric conditions. It was found from other studies that the constant can range from 0.35 to 0.46, but a value of 0.4 is deemed as the universal number.

A common approach to solve the flow in the near-wall zone is through wall-functions, which ignores the presence of the three different layers and represents the condition near the wall by employing semi–empirical formulas. The advantages are that the turbulence models don't need to be modified (e.g. to account for the laminar conditions in the viscous sub-layer) and the laminar flow near the wall can be determined for a single mesh layer at the wall, rather than multiple layers. This improves the calculation speed, as fewer cells need to be modelled. It is, however, very important to select the correct height of the laminar mesh layer. The height should fall into the buffer sub-layer. ANSYS (2011) stated a value of 11.225 for y^+, which represents the intersection of the linear and logarithmic dimensional velocity

lines in Figure 3.7. Versteeg and Malalasekera (2007) recommended a value of 11.63, while Andersson et al. (2011) generally recommended values lower than 30.

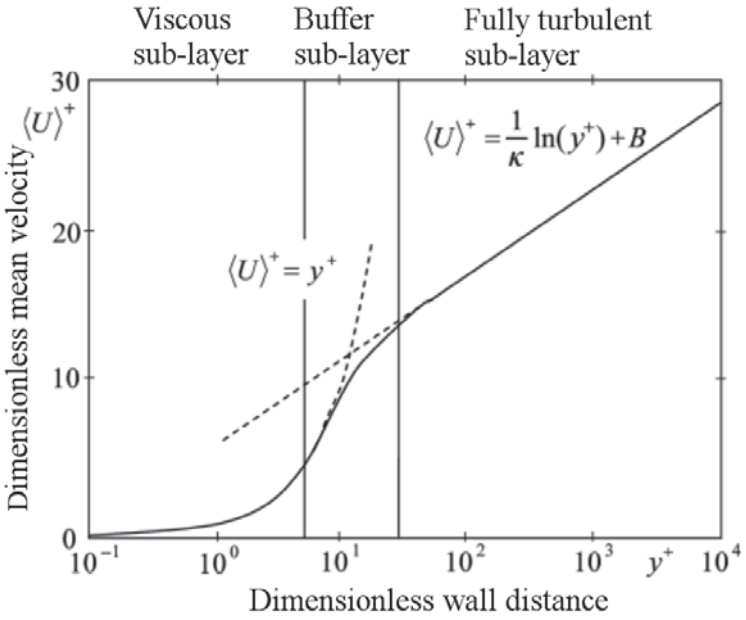

Fig. 3.7 The law of the wall

(Andersson et al., 2011)

In order to overcome problem with too low y^+ values, a non-equilibrium wall function model was developed by Kim and Choudhury (1995). The model uses two layer cells to represent the near-wall region. The mean velocity function was expanded to include pressure gradients and turbulence kinetic energy in neighbouring cells are taken into account.

Yeoh and Tu (2010) indicated that there is no direct or straight forward rule for what type of wall function should be applied for multi-phase flow, although non-equilibrium or enhanced wall-functions are recommended. It was also explained that too strong refinement of the cells near the wall can even lead to worse results for shear stresses, as artificial turbulences may be introduced. The rigorous assessment of the more sophisticated wall-functions for different multi-phase flows was recommended.

Should wall functions fail to predict the flow behaviour near the wall accurately, then more refined meshing is required, leading to boundary layer meshes. The flow inside the gallery may be considered as a flow without transverse pressure gradient. This is distinctly different from pipe flow, where the pressure forcing the flow also produces pressure gradients. For the determination of the boundary layer dimensions the theory of a flat plate can be used.

Equation 3.29 can be rearranged to yield the thickness, y, by

$$y = \frac{\mu y^+}{\sqrt{\tau_w \rho}} \tag{3.32}$$

Schlichting (1979) stated that the wall shear stress can be determined by

$$\tau_w = 0.5\, C_f \rho u_x^2 \tag{3.33}$$

where u_x is the free steam velocity and C_f the skin friction coefficient for flat plates without transverse pressure gradient. It can be calculated by

$$C_f = (2\, log(Re_x) - 0.65)^{-2.3} \tag{3.34}$$

where R_{ex} is the Reynolds number in the boundary layer. It can be calculated as

$$Re_x = \frac{\rho u_x L_{BL}}{\mu} \tag{3.35}$$

where L_{BL} is the distance from the wall at which 99% of the free stream velocity are reached. Values for y^+ may be used accordingly to determine the thickness of the first mesh layer of the boundary mesh (e.g. $y^+ = 11.63$) and the total thickness of the boundary layer (e.g. $y^+ = 300$). With the thickness of the first layer known, the thickness of the following layers can be calculated, whereby a thickness increase of 20% for each subsequent layer can be introduced, until the total thickness is reached. This approach of a very refined mesh near the wall increases the mesh size significantly and therefore increases the computation time.

For completeness it may be noted that the above description considered mainly the flow in the near-wall region, but the use of the wall functions also extends to the modelling of other flow variables and scalar variables, such as temperature. The proposed study did not consider temperature variations and hence a more rigorous modelling approach to satisfy criteria for heat transfer in the boundary layer was not considered.

3.7 Summary

This chapter introduced numerical methods of fluid flow simulation. The underlying principles and particular modelling techniques with regards to multiphase flow were explained and analysed.

There is a trade-off between accuracy and complexity of the models, directly affecting the computing performance and subsequently the computational time requirement. While Lagrangian (moving fluid parcel) methods capture the interface between two fluids most precisely, the computational demand is high and highly curved interfaces can lead to highly deformed meshes and inaccuracies. The Eulerian (fixed control volume) methods can also be used to capture the interface between fluids, with the phase modelling being performed by the volume-of-fluid (*VOF*) method. To enhance the interface capturing the piecewise-linear interface calculation (*PLIC*) scheme was identified as the best option, although a sufficiently fine mesh is required to capture interface features accurately.

Previous works on gallery flow analysis relied on the standard $k-\varepsilon-model$, as it provides a robust numerical process. The introduction of the oil jet into the model required consideration of the high shear forces involved at the surface of the jet. The identified shortcomings of the standard $k-\varepsilon-model$ for this case led to the selection of the realizable $k-\varepsilon-model$. The use of the alternative turbulence models was considered, but the increased complexity, marginal gains expected and limitations of computation resources permitted their useful application.

The transient character of the investigation requires a compromise of the time step between fast time advancement and a robust and accurate numerical process. Too much forward stepping in time may lead to short simulation times, but insufficient capturing of flow behaviour. Too small time steps provide high phase interaction and flow capturing, but also lead to long simulation time. A compromise between time demand and accuracy needs to be found for simulation processes, as no clear rules apply.

CHAPTER 4 EXPERIMENTAL APPARATUS

This chapter focuses on the design and build of a suitable test rig and apparatus to obtain experimental data for comparison simulation data. Details of components and subsystems of the test rig will be explained and discussed, and reasons for their choice stated. Particular reference will be made to the selection, design and limitation of the mechanism providing the required movement of test bodies, including the dimensioning process of the used components. The study will focus on two specific gallery shapes, for which the material and manufacturing selection process are stated. These gallery models will be referred to as the small gallery model (*SGM*) and the large gallery model (*LGM*). Finally the test rig instrumentation and visual recording system is described.

4.1 Test bench general description

The test rig was based on two separate frames, each having a distinct purpose. These will be referred to as lower frame and upper frame, as shown in Figure 4.1.

4.1.1 Lower frame, systems and components

The lower frame was available at the university faculty's facilities to investigate the cooling effect of under-crown and internal cooling on static (non–moving) pistons. It was built for the purpose of delivering oil at high continuous flow rates and at constant temperature and made from box-section steel tube (50 *mm x* 50 *mm*) with overall dimensions of 1100 *mm* width x 1500 *mm* height x 1600 *mm* depth. It also contained an electric power supply panel, oil tank, oil pump, oil drainage tray, cooling circuit, flow control and monitor panel, and provides space for additional measurement equipment, if required. Each of these components will be specified below. A schematic of the hydraulic circuit is shown in Figure 4.2.

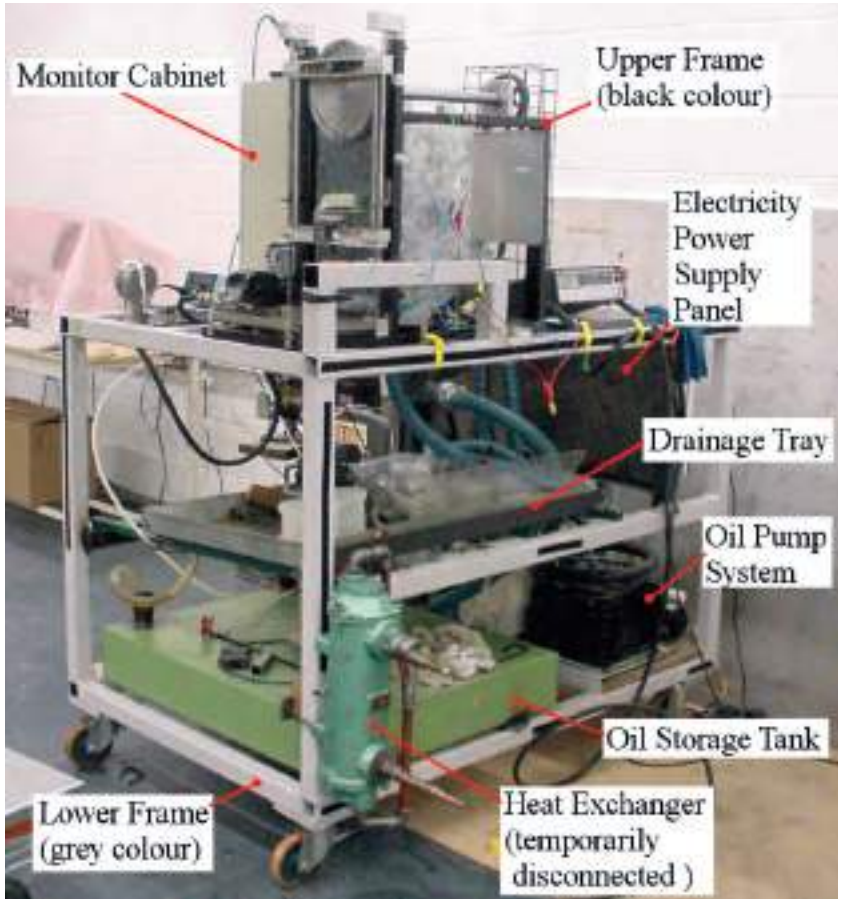

Fig. 4.1 Complete test rig with upper and lower frame

The oil was stored in an open vented tank (**1**) near the frame bottom, 900 *mm* length, 900 *mm* depth and 200 *mm* height, holding approximately 80 *litres* of oil. One K–type thermocouple was used to monitor the oil temperature inside the tank.

The oil delivery system used a rotary internal vane pump (**2**), which was driven by a 415 V three-phase motor (**3**). The maximum flow rate and pressure supplied were 20 l/min and 18 *bar* respectively, the latter being controlled by an internal pump bypass with relieve valve. The pump drew the oil from the tank via a metal mesh filter element (**4**) and delivered flow at a constant rate. A variable three-way valve (**5**) was used to control the flow after the pump. Some of the oil was directed towards the oil nozzle with the remainder short circuiting back to the tank. It was mainly used to reduce the load on the instruments and flexible lines.

Although pressure load was reduced, the pumping process still added heat to the oil. Such behaviour was also noted by Lasecki and Cousineau (2003). During short operation times (typically less than 10 minutes) the large thermal capacity of the oil stored in the tank kept the temperature variation well within 1° C. This was the smallest incremental change the

temperature measurement instrument showed. The change of the viscosity at such temperature change was significantly small enough to be neglected.

For longer periods of operation with temperature changes larger than 1° C, additional cooling was achieved by means of a water-oil cooler (**7**) with the flow being controlled by a manual three-way valve (**6**). The water for the heat exchanger was drawn from an engine test facility external water circuitry. The temperature of the water was controlled by cooling towers (**8**) of the external engine test facility, which eliminated the need for water flow adjustment to control the temperature of the exiting oil.

A simple adjustable one-way valve (**9**) was used to control the flow rate of oil, followed by a temperature sensor (**10**), pressure gauge (**11**) and mass flow meter (**12**), before delivering oil to the nozzle (**13**) inside the upper frame assembly (**14**). After the oil exited the nozzle it entered the model gallery (**15**), flowing through it and leaving at the gallery exit. It returned via a catch tray (**16**) and strainer (**17**) at the bottom of the upper test rig, before draining into the drainage tray (**18**), where the majority of the air contained within the oil was removed. Finally it returned to the storage tank (**1**) via gravity driven flow.

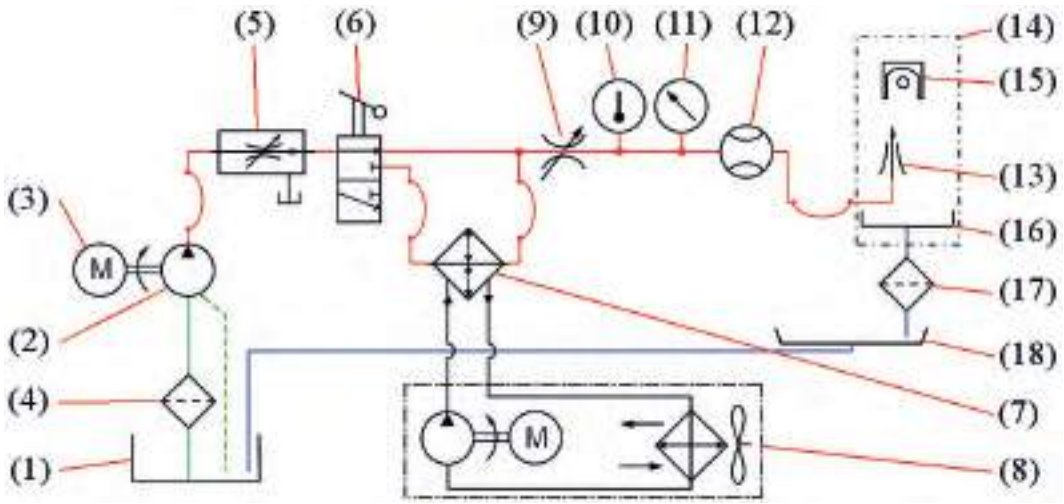

Fig. 4.2 Schematic of hydraulic circuit

4.1.2 Upper frame, systems and components

Motion transfer mechanism

An electric motor was used as the source of motion for the piston models. Prior to the design and built the type of motion conversion mechanisms was to be determined to transfer of

the rotational motion of the motor to the reciprocating motion of the gallery models. Two mechanisms were considered:

- Common crank mechanism with conrod, and
- Scotch yoke mechanism.

The behaviour of both systems can be described and analysed for piston position, velocity and acceleration by the same set of equations, with the difference being that the Scotch yoke mechanism will generate a nominally sinusoidal motion and the crank mechanism generates only a sinusoidal-like motion, as a result of the conrod length. The approximate position of a piston for a crank mechanism can be calculated by

$$s_p = R\left[1 - \cos(\omega t) + \frac{R}{2L_{CR}}\sin^2(\omega t)\right] \tag{4.1}$$

where R is the crank radius, L_{CR} the conrod length, ω the angular velocity and t the time. The product of angular speed and time can also be expressed as crank angle (CA), α. The position was calculated relative to the TDC. It can be seen that the conrod length has an influence on the position. When the conrod length would be increased, in the limit the second term inside the bracket converges towards zero, leading to a nominally sinusoidal motion. Thus the use of an infinite long conrod represents the yoke mechanism, while any other length refers to a crank mechanism.

The conrod had also an effect on the piston velocity. The equation can be derived by differentiating the position equation with respect to time, which leads to

$$v_p = R\omega\left[\sin(\omega t) + \frac{R}{2L_{CR}}\sin(2\omega t)\right] \tag{4.2}$$

It can be seen that the conrod length has the same effect on velocity than it has on the position. The piston velocity was identified as an influential parameter on the oil jet entering gallery. If the gallery model velocity was larger than the oil jet velocity, then oil would not enter the gallery. This may occur during part of the upward movement, while during the downward movement the velocity of the oil jet and gallery model summarize and lead to increased oil flow into the gallery.

Further differentiation by time yields the equation for the piston acceleration, as is given by the expression

$$a_p = R\omega^2 \left[\cos(\omega t) + \frac{R}{2L_{CR}} \cos(2\omega t) \right] \tag{4.3}$$

The existence of two cosine terms introduced a super positioning of terms at the dead centres per se. The second cosine term, however, contributes at twice the crank angle, indicating that different accelerations at *TDC* and *BDC* occur, with the peak acceleration at the *TDC* (0° *CA* and 360° *CA*). The acceleration had an effect on the oil flow behaviour inside the gallery. Higher accelerations would contribute to higher inertia driven flow behaviour, subsequently influencing not only flow behaviour, but also flow velocities on internal surfaces.

The use of a conrod would introduce significant side loads due to the varying conrod angles during the crank cycle, which in turn would require sufficient strengthening of the sliding surfaces to support the additional loads. This would also require an improved continuous lubrication system to allow sliding of the gallery model supporting component along this surface. Engine–based systems can provide such a mechanism, where a dedicated lubrication system is already employed. The variability in terms of stroke length does also pose a problem due to the length of the sliding surface and a requirement to change the crank radius. Furthermore, such systems are also difficult to balance, due to the second order vibration introduced by the conrod.

In contrast, the absence of a conrod for the Scotch yoke mechanism would reduce the complexity of the test rig and also reduce the loads on components, allowing for smaller dimensions of bearings and test rig components. In addition the better suitability with regards to varying strokes and resulting simpler balancing highlighted the superior design of the yoke mechanism in comparison to the crank mechanism. Although the demand was initially for real piston motion and the conrod length was identified as potential factor influencing gallery filling, the main focus of the study was aimed at the determination of the flow behaviour inside the gallery and comparison to numerical equivalent studies, whereby identical conditions would be required, regardless of the motion transfer mechanism.

Upper Frame Design

The upper frame was made from box-section steel tube (50 *mm x* 25 *mm*) with additional strengthening rails at the bottom of 50 *mm x* 50 *mm*. The raised position from the mounting surface also allowed for the space to bolt the upper frame to the lower frame via six bolts of

M10 size. A schematic of the upper frame and the components is shown in Figure 4.3. Larger sized and detailed views are shown in Appendix A.

The upper frame consisted of the following sub-systems:

- Drive / electric motor with speed controller,
- Transmission,
- Yoke mechanism with flywheel,
- Sliding frame and
- Oil control and guide system.

The highest performance power source available in the department to drive the test bench was a shunt-wound direct-current motor with dedicated speed controller. The specifications of the electric motor and controller are given in Table 4.1.

Table 4.1 DC motor and speed controller specifications

Electric motor	
Motor type	Shunt wound DC, separate shunt field & armature windings
Maximum voltage	240 V AC
Rated power	0.6 HP (447 W)
Speed at rated power	2400 rpm
Maximum torque (n $\tilde{0}$ rpm)	2.9 Nm
Speed controller	
Voltage input	240 V AC
Max input current (fused)	13 A
Frequency	50 Hz
Voltage output	0 . . . 250 V DC
Max shunt field current	2.75 A
Control type	Potentiometer for armature current control
Voltage conversion	Rectifier for armature and shunt circuit

The motor speed was set by adjustment of a potentiometer, which consisted of three inter-linked subsystems, namely a rectifier circuit for the shunt field, a rectifier for the armature and a potentiometer for the armature. A schematic circuit is shown in Figure 4.4. The use of armature control allowed the safe operation of the electric motor, as the mechanical connection system of the potentiometer first provided current to the shunt field, before the armature. In this way an armature burn out was avoided, as the low resistance would lead to high current, if no electric field from the shunt was present. The speed was adjusted by control of the

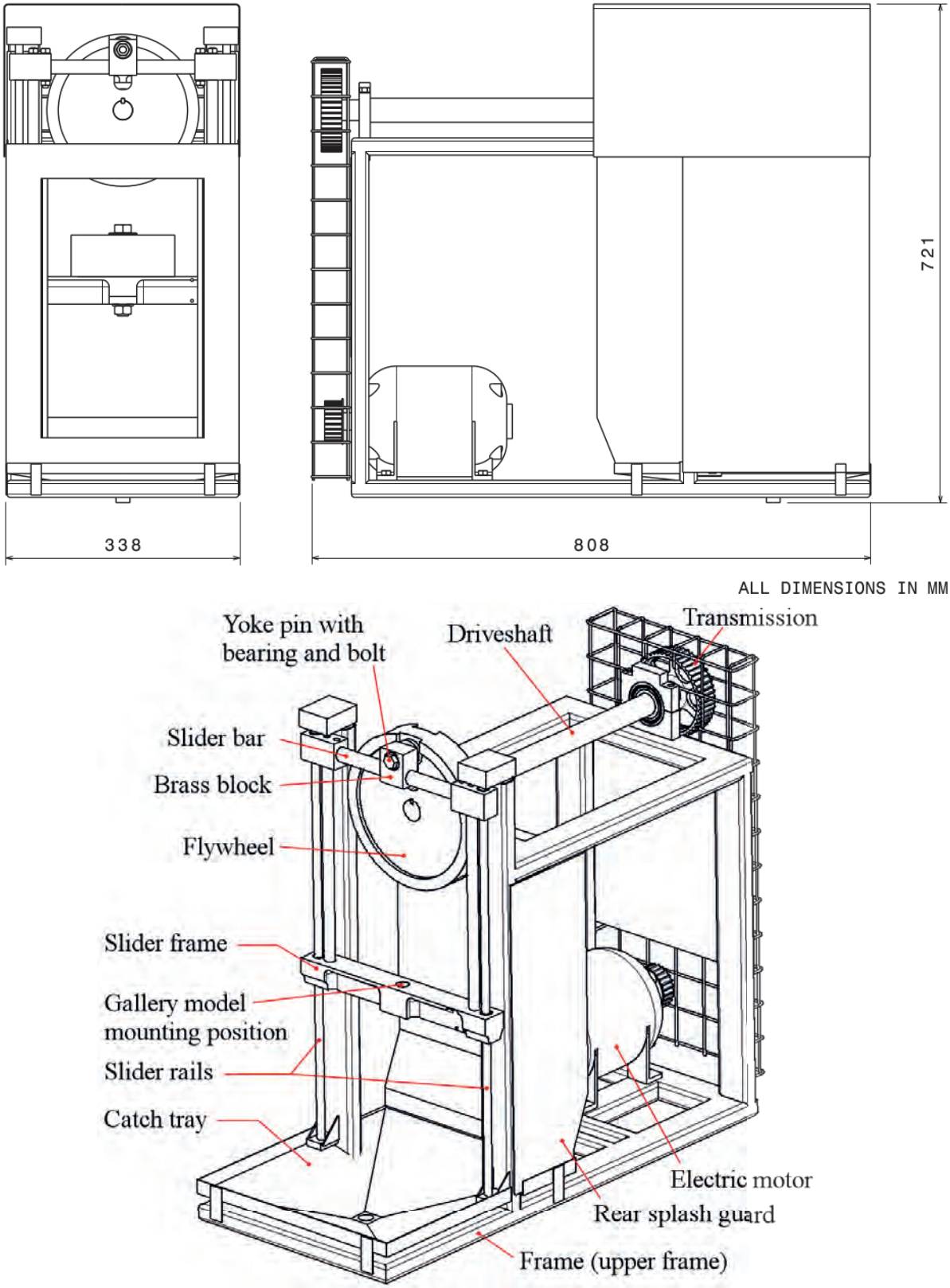

Fig. 4.3 Side and front view of upper frame with overall dimensions and isometric view without front splash guard cover

resistance of the potentiometer, which adjusted the current delivered to the armature, whereby the potentiometer position was linearly proportional to the motor speed.

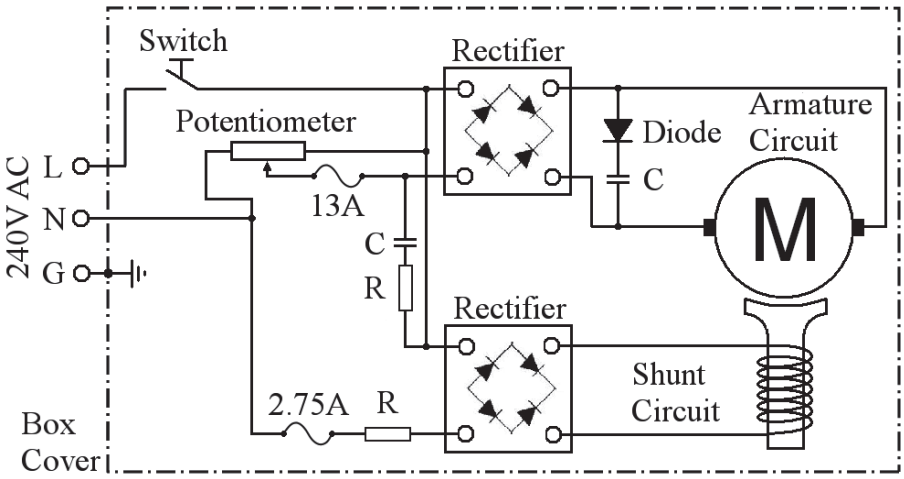

Fig. 4.4 Schematic circuit of rheostat controller and electric motor

After modelling the initial concept of the test bench with the *CAD* software CATIA, a dynamic analysis was performed to assess the ability of the performance of the electric motor to satisfy speed demands and to allow dimensioning of components. The software used was ADAMS, a dedicated software tool for solid-body dynamic (*SBD*) analysis. In order to reduce computing demand (in terms of geometric complexity) the model in ADAMS was reduced to simple basic volumes. The software did not require accurate description of the geometric shape, but rather depended on correct inertia based values (e.g. masses, centre of gravity location, moment of inertia, etc.). These were obtained from CATIA and transferred to ADAMS. Figure 4.5 shows the model, identifying the model components.

The input data was adjusted accordingly to accommodate the different piston strokes and component weights, specific to the large and small gallery model. The required data were masses and inertias. The inertias, namely I_{ox}, I_{oy} and I_{oz}, were relative to the centre of gravity of each component and related to the directions, x, y and z, of the reference coordinate system respectively. A summary of the applied component data is given in Table 4.2.

An initial investigation took place to determine the motor rotor inertia, based on rotor acceleration measurements. Torque values were then determined by measurements of the acceleration of the motor rotor with an additional solid steel disc of known inertia. From the measurement values an approximation function of the torques was derived. The optimum fit

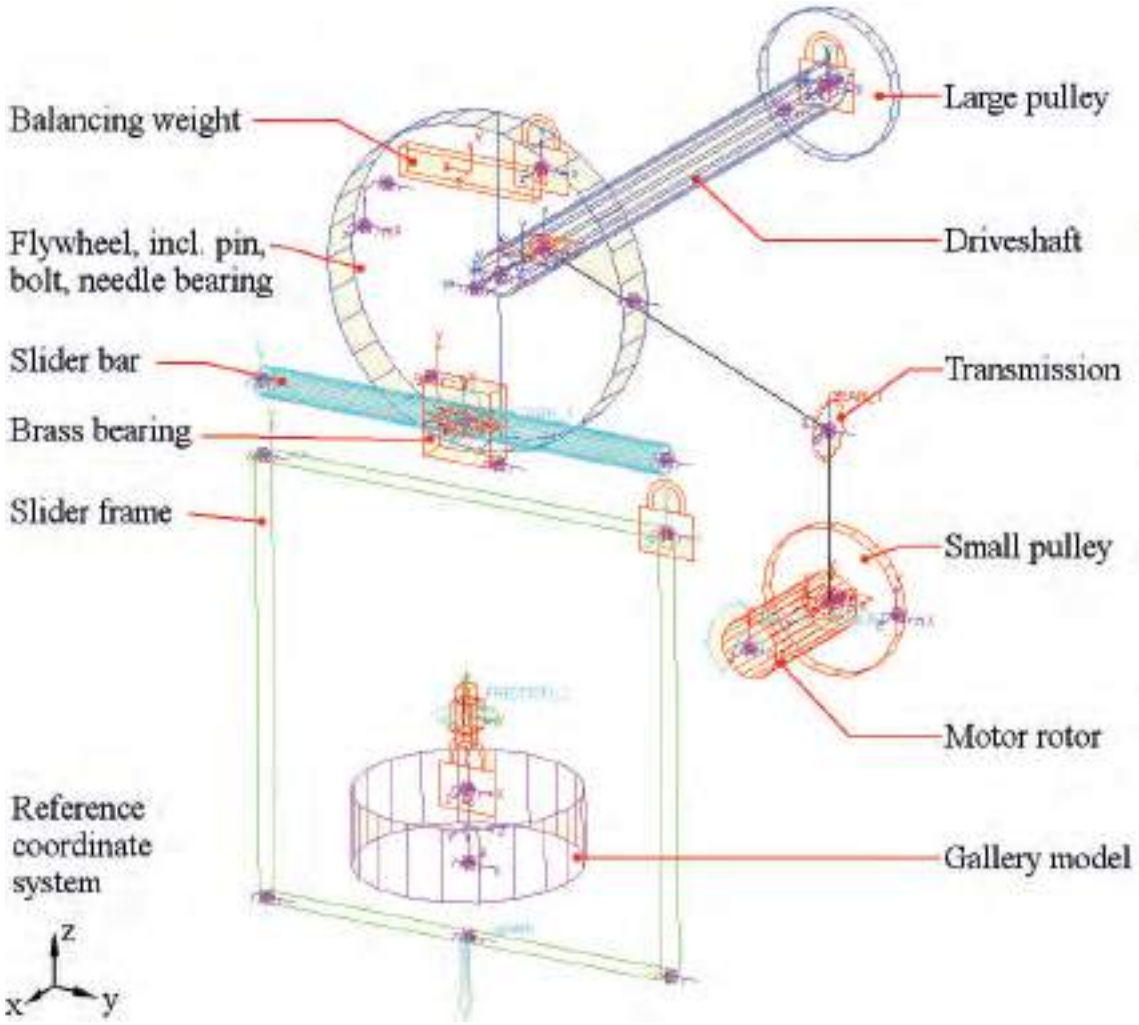

Fig. 4.5 Simplified mass-inertia model representing test bench for multi-body dynamic analysis

Table 4.2 Dynamic model component input data

	Component name	Mass	I_{ox}	I_{oy}	I_{oz}
		kg	$kg \cdot cm^2$	$kg \cdot cm^2$	$kg \cdot cm^2$
A	Rotor of motor	3.4	19.32	55.12	55.12
B	Small pulley	0.42	1.81	1.32	1.32
C	Large pulley	0.57	14.15	7.36	7.36
D	Shaft with main bearings	3	3.72	653.5	653.5
E	Flywheel	8.5	569	270.9	315.6
F	Pin, bolt and needle bearing	0.31	0.31	1.39	1.39
G	Brass sliding bearing	0.27	0.93	0.75	1.16
H	Balancing weight	0.6	1.35	1.31	0.62
I	Slider bar	0.64	38.05	0.32	38.05

was provided by a second-order polynomial and can be given as

$$T\left(n_{em}\right) = -1.07 \times 10^{-7}\, n_{em}^{2} \;-\; 2.35 \times 10^{-4}\, n_{em} \;+\; 2.9 \tag{4.4}$$

where n_{em} is the rotational speed in revolutions per second with the torque in *Nm*. The torque was modelled as a function of rotor speed, as shown in Figure 4.6. It was included in the solid body dynamics simulation model to determine the maximum crank speed for both gallery models. Although the approximation may not represent the correct torque value at very low and high speeds, it was seen as appropriate for the purpose of the study, as the prediction were conservative.

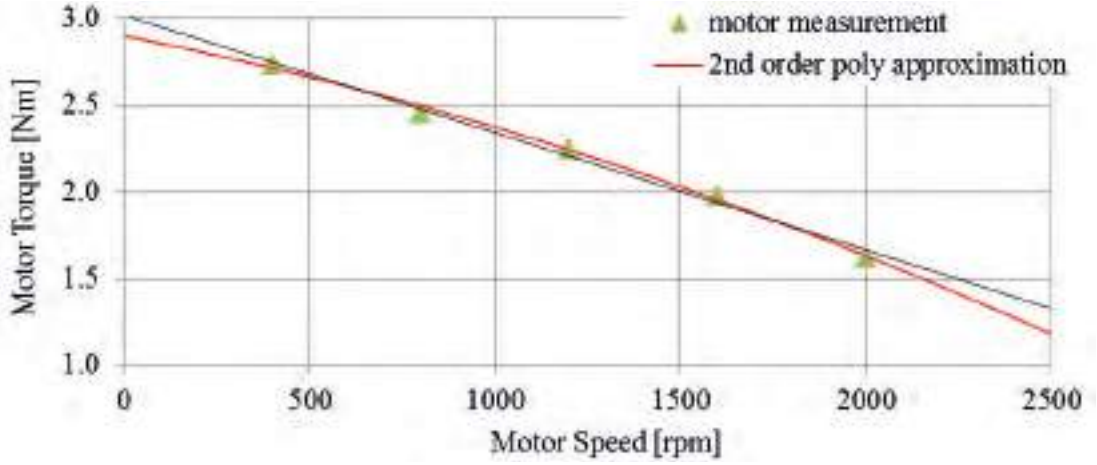

Fig. 4.6 Electric motor torque as a function of speed

The dynamic model also included friction at the sliding contacts between the brass bearing and sliding rod, and sliding frame and guide rods, as these had an effect on the maximum speed. Static and kinetic friction were included. Kuchling (1986) provided a friction coefficient between brass and steel with an oiled surface contact as 0.07. Haberhauer and Bodenstein (2005) stated a kinetic friction coefficient for a lubricated contact between brass and steel of 0.03 to 0.08. Chowdhury et al. (2012) also showed that the friction coefficient was dependent on sliding velocity. A constant values of 0.07 was used, as no specific data for speed dependent kinetic friction coefficients were available, especially with the extra uncertainty of lubricated contact surfaces. Static friction was also included, with identical values to kinetic friction. This simplification was also attributed to lack of reliable data. All roller bearings were treated without friction, as the rolling friction coefficient was significantly smaller than the sliding friction coefficient.

An investigation of the maximum achievable test rig speeds at varying transmission ratios was performed, which identified the highest speed for the *SGM* at a ratio of 2:1 as 1650 *rpm* and for the *LGM* as 760 *rpm*. The behaviour of both gallery models is shown in Figure 4.7. It can be clearly seen that the speed also varied within the cycle. The reasons can partially be found in the gravity acting on the slider frame, contributing to increased downward speed and reduced upward speed, but also in the friction effects. The speed variation within the crank cycle was approximately $\pm 10\%$ from the mean speed for the large gallery model and $\pm 5\%$ for the small gallery model. This indicated that a larger mass and longer stroke lead to increased variation.

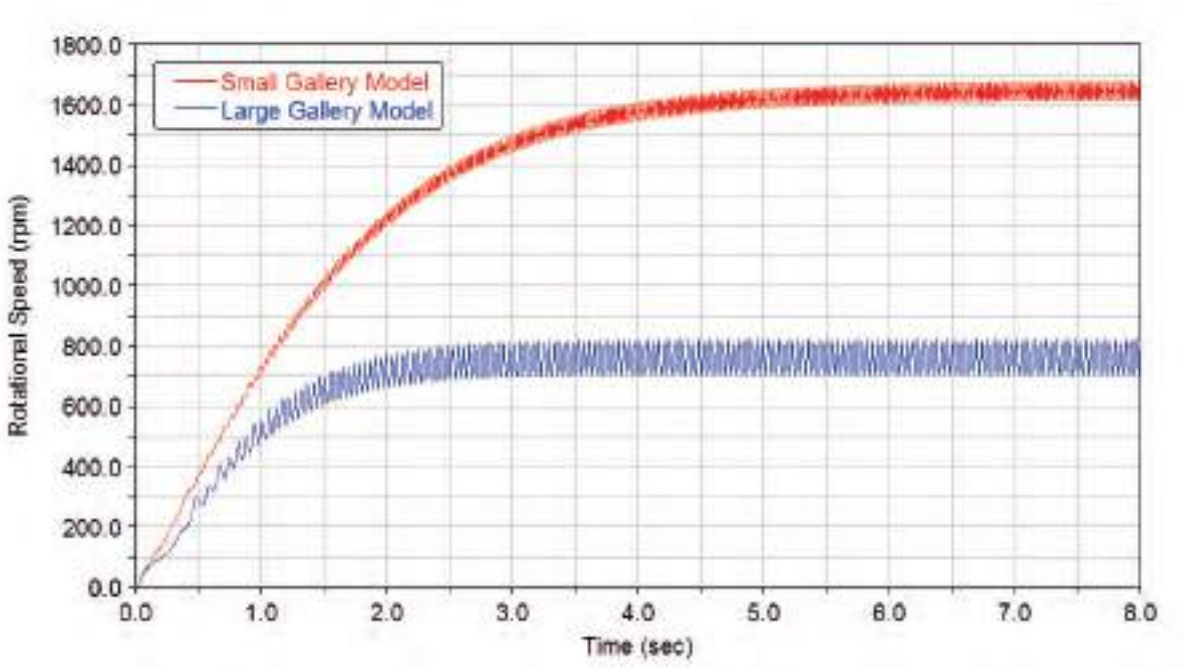

Fig. 4.7 Maximum theoretical speed for both models and transmission ratio 2:1

The maximum predicted average crank speed for the *SGM* of 1650 *rpm* was on the lower end of the speed range where real engines achieve their maximum torque output. This would also be an engine speed, where cooling of the piston may be required. The motor speed at this condition would be 3300 *rpm* with a transmission ratio of 2:1, but it was limited to a maximum no–load speed of 2400 *rpm*. The discrepancy can be attributed to the torque approximation function, which delivers values beyond the no–load speed. Such behaviour is impossible and the test rig would achieve only a maximum rotational speed of 1200 *rpm*. This was still deemed acceptable for the purpose of gallery flow determination.

The maximum component accelerations and highest joint loads (bearings) were determined for the dimensioning of the main components of the test rig. Care was taken in the adjustment of inertia values for different piston sizes and strokes, as summarised in Table 4.3.

Table 4.3 Maximum theoretical speed and resulting bearing loads and acceleration

Piston model	Max. mean disc speed	Main shaft bearing load	Pin bearing load	Sliding rod load	Sliding frame acceleration
	rpm	N	N	N	m/s^2
LGM	760	1925	2341	2163	633
SGM	1650	4883	4170	3783	1399

The transmission consisted of two standard pulleys with 24 teeth and 48 teeth respectively, giving the optimum transmission ratio of 2:1. Both pulleys were connected by a toothed belt eliminating slippage of the belt. The tension of the belt could be adjusted through the position of the motor by variation of mounting height. While one pulley was connected to the motor output shaft, the second pulley was connected to a driveshaft, located to the top of the upper frame. At the opposite end of the driveshaft the flywheel was connected that held the yoke pin of the Scotch yoke mechanism.

Two deep groove ball bearings supported the driveshaft at either end. The bearings had a maximum speed and a maximum dynamics load rating of 12000 rpm and 20.3 kN respectively. While the maximum speed of the shaft was well below the bearings rating, the load rating had to be taken into consideration to allow continuous and safe operation. Both bearings were of sealed design, eliminating the need for extra lubrication. The peak load at the flywheel experienced during operation was determined as 4.9 kN, which was well below the load rating. The bearing at the pulley end was exposed to a lower load. Use was made of common component usage on both ends to keep cost and component diversity low.

The driveshaft was located on top of the frame, which also placed the flywheel at the top. This was not ideal for the weight distribution. The benefits were that the piston was pulled up, rather than pushed up. This provided free undisturbed clearance below the gallery model. Furthermore, the rotating flywheel was not in contact with the oil during operation and therefore oil splashing was limited to a minimum. This was especially important, as a clear undisturbed view of the piston models was important for the flow visualisation.

The analytical equations for position, velocity and acceleration were idealised representations and did not contain influences from inertia and friction effects during operation. The dynamic analysis using ADAMS revealed that the movement of the gallery models on the test rig would significantly differ from the theoretical predictions (analytical), as shown in Figure 4.8. For better comparability between different strokes and speeds the accelerations were normalised relative to the maximum acceleration found on the theoretical sinusoidal movement. It can be seen that the crank mechanisms would generate acceleration values that were up to 30% higher at *TDC* and 35% lower at *BDC* than the nominally sinusoidal accelerations of the yoke mechanism. The ADAMS model predicted an even larger difference for the *LGM* at *BDC* (approximately 50%), but a reduced difference at *TDC* (25%). This highlighted the shortcomings of the analytical model, but also indicated that there will be variations in the behaviour of the crank mechanisms.

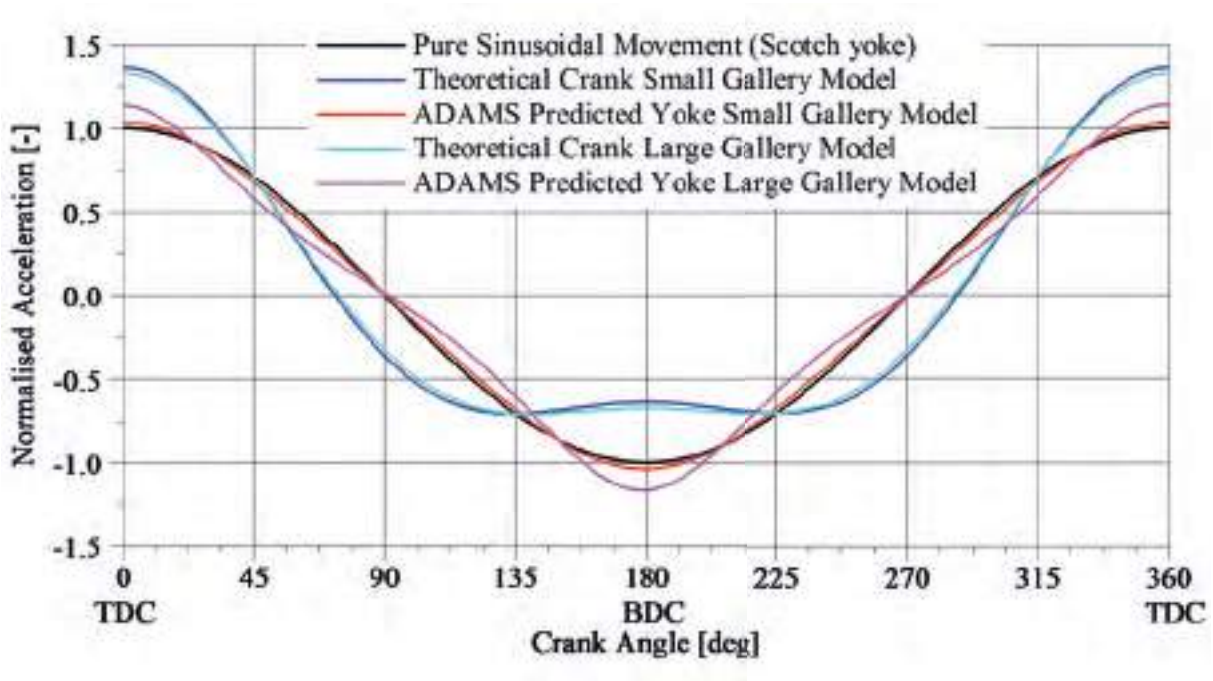

Fig. 4.8 Comparison of normalised acceleration vs. crank cycle for various systems for small gallery model at 1650 *rpm* and large gallery model at 760 *rpm*

The flywheel was manufactured with a slot to accommodate the yoke pin and to allow continuous variable stroke length between 84 *mm* and 182 *mm*. This covered for a large range of engine stroke sizes, usually found on small passenger car engines and large heavy goods vehicles. Figure 4.9 shows the arrangement of pin positions for maximum and minimum stroke. The flywheel was initially balanced for rotational masses only, but additional masses

could be bolted onto the flywheel to balance the yoke pin, needle bearing and part of the sliding block, as well as partial reciprocating masses inherited from the slider mechanism.

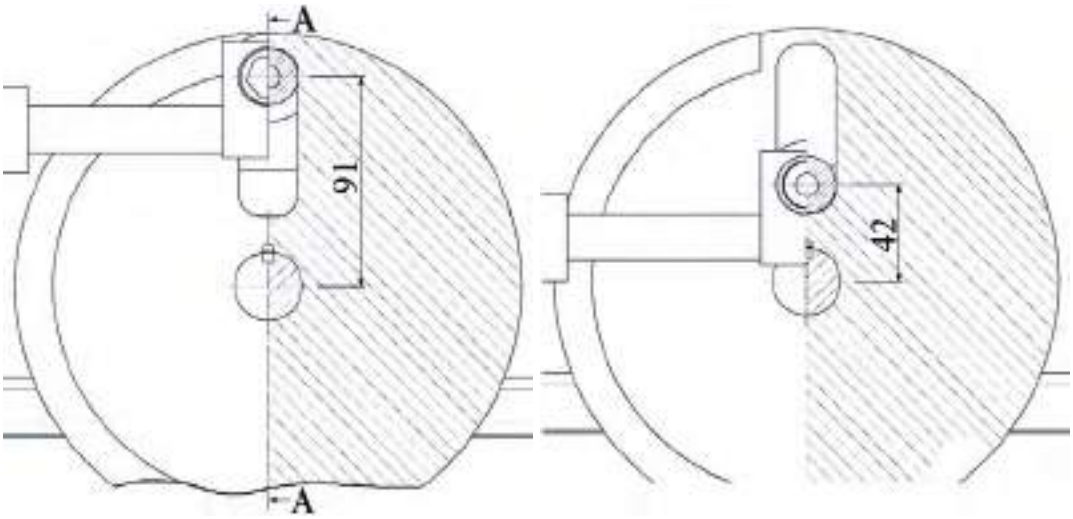

Fig. 4.9 Maximum and minimum position of yoke pin

A cross-sectional view of the final design of the yoke mechanism is shown in Figure 4.10. The bearing used was a drawn cup needle roller bearing with dimensions of 20 *mm* inner

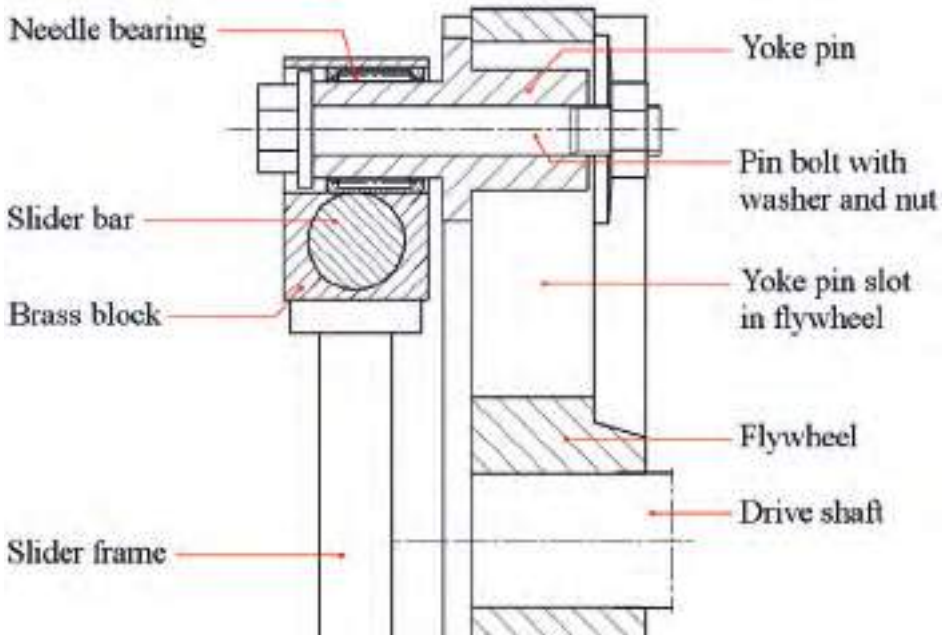

Fig. 4.10 Cross-section of motion conversion mechanism central unit

diameter, 26 *mm* outer diameter and 20 *mm* width. The maximum speed range was given as 14000 *rpm*, well below maximum operating speed of the rig. The maximum dynamic loading was given with of 15.1 *kN*, while the determined peak load at the pin bearing was 4.2 *kN*,

also below the bearing's rating. The needle bearing also reduced friction between yoke pin and sliding block and minimised lubrication requirements, although accurate alignment of the flywheel and slider frame was important to avoid bearing overloading. The drawn cup type retained some lubricant in the cup during operation, maintaining constant lubrication without the need for additional permanent oil feed. The needle bearing was fitted to the sliding block using a press fit, necessary for the bearing to reduce the clearances with the precision made yoke bolt race and also to remove the need for an extra securing mechanism.

The sliding block was made from brass for its self-lubrication properties, when lubrication may become scarce. The mating slider bar surface was made from steel with a hard–chromed surface finish, to minimize friction and improve long term resistance to wear. Lubrication was via drip feeding onto the top surface. This was sufficient for the test procedure, although care had to be taken with regards to heat, as the drip feed of oil was not sufficient for cooling. Attempts of using linear roller bearings instead of the sliding contact proved inadequate. At higher operating velocities of the slider frame the inertia effect on the balls inside the linear bearing stopped the rotation of the balls, leading to sliding contact. This increased the frictional loss in the bearing, but more importantly, also broke the contact surface of the ball rolling surface, which led to increased clearance from wear and jerk after some time of operation.

As described earlier, the Scotch yoke mechanism reduced the side loads to a minimum, where only the friction force between sliding block and rod caused loads lateral to the gallery model movement direction. This allowed for small sized slider rails to be used in conjunction with brass bearings. The slider rails were made from steel with a polished surface, and supported at three position to the upper frame's vertical rails. Thereby two supports were on either end, whilst the third support was at the middle distance of the rod length. This also helped to avoid guide rod deformation due to vibrations.

The slider frame was comprised of an upper slider bar, a lower horizontal gallery mounting cross member and tubes, through which the bolts were passing and holding the frame together. The frame was designed with minimum weight in mind, but keeping the strength as high as possible to avoid any backlash during operation. The assembled slider frame is shown in Figure 4.11.

The gallery models were fixed to the lower cross member with a centrally located bolt of size M16. The arrangement also allowed rotation of the gallery model, providing visual

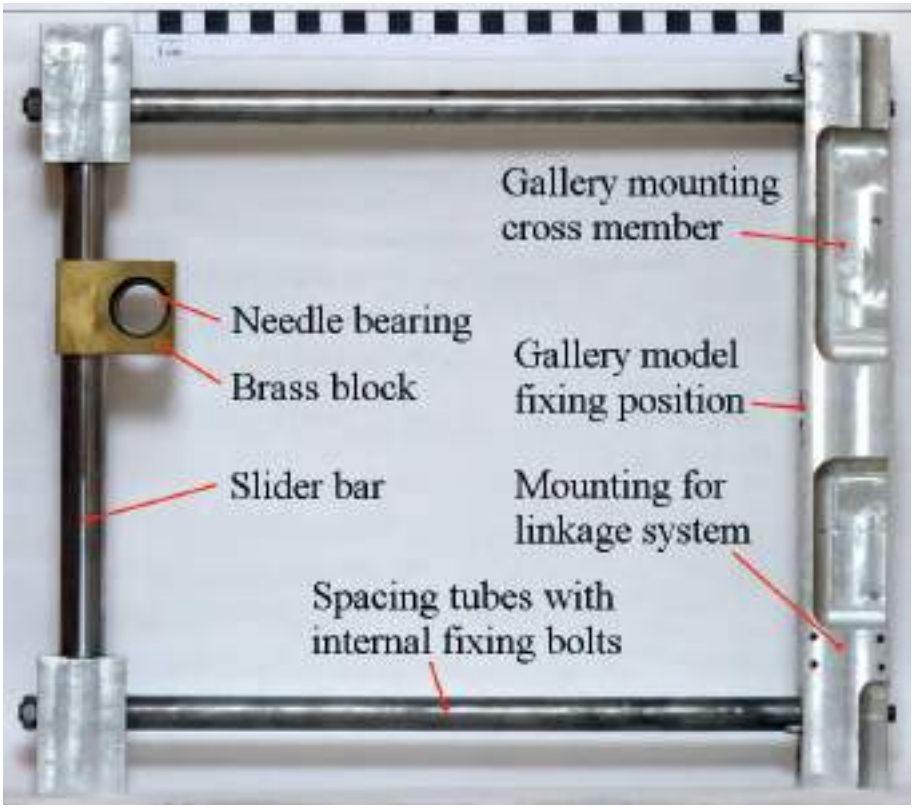

Fig. 4.11 Assembled slider frame with brass bearing (square size 1 $cm \times 1$ cm)

access to all sides of the gallery model for image recording. In order to avoid reflections of the light sources during image recording a matt black guard was fitted to the slider frame. As the slider frame cross member was narrower at the bottom the guard was also angled, which also reduced reflections. Provision was made for additional instrumentation via a linkage system, if required.

Oil nozzles and oil return

Oil was delivered to the gallery models via a flexible hose and a mounting block holding the nozzle. The mounting block was supported through a steel bar, which was held in a vice located beside the upper frame, allowing for adjustment of the nozzle to suit the piston visualisation position. Adjustment was available for three directions and three rotations, giving full flexibility. The block accommodated for both nozzles, although only one nozzle was used at the time depending on the gallery model investigated, while the holes for the other nozzle were blocked.

An oil collection tray was located below the oil nozzle. The inverted pyramid shape contained a central hole through which the oil was guided back to the lower frame oil tray. Before the oil arrived at the lower frame tray it passed a strainer (medium woven steel filter

with size 0.7 mm) that allowed for the removal of the majority of the air entrained in the returning oil before entering the tank.

The complete yoke mechanism was covered by a housing to reduce contamination of the near environment with oil during testing. The cover fully enclosed the sides, back and top. The front side contained an opening for visual access to the gallery model. Initially a transparent plastic shield was employed to eliminate splash oil exiting through the front. During the operation some oil impacted with the splash shield, causing obstructed and distorted view of the gallery models. The removal of the splash shield showed negligible oil contamination of the environment, which allowed the operation without it for best results.

4.2 Piston gallery models

4.2.1 Small gallery piston overview

The smaller piston of the investigated gallery designs was based on a passenger car diesel piston for direct injection with a cylinder volume of 500 cm^3, as shown in Figure 4.12. The internal gallery was located between the second piston ring and the lower area of the re-entrant bowl. The overall volume of the gallery was 12 cm^3, excluding the inlet and outlet channel. A torus–like salt core was used to create the gallery inside the piston, creating a rough casting surface. The inlet and outlet channel for the gallery were manufactures by centre drilling after the casting.

Fig. 4.12 Small gallery piston (left) and cut section view of piston, exposing inlet channel (centre) and exit channel (right)

4.2.2 Small gallery model (*SGM*) preparation for visualisation

A transparent model of the piston gallery was required to visually determine the filling and flow behaviour inside the cooling gallery. Visual purity of the material was very important in order to obtain high quality, non-distorted images of the flow. Manufacturing and surface finish of the gallery surfaces had also be taken into consideration. Furthermore the material needed to be resistant to oil and robust enough to withstand the acceleration forces occurring from the test bed.

Two manufacturing processes were taken into account, moulding and machining. Moulding offered an exact replica of the gallery including the surface roughness. This however was also the main disadvantage of this method. With a certain surface roughness the visibility into the gallery became very limited and hence the fluid flow could not be examined thoroughly. The ideal surface would need to be polished. The material choice was therefore limited to clear transparent acrylic (Perspex). The machining process had the advantage of gallery surfaces polishing, but the disadvantage that the gallery model required splitting into at least two separate parts. Model body splitting could be vertical or horizontal. In order to reduce view distortion caused by the splitting and based on the fact that the gallery needed to be highly transparent, machining with a vertical split was employed.

The gallery model was developed as a three-part design, consisting of an outer ring, an inner ring and an inlet channel section, as shown in Figure 4.13. Each of the rings held half of the gallery. Both halves were created with a small overlap to provide a push fit interference. Before the assembly the interfering surfaces were also coated with an adhesive to provide extra contact strength to avoid any dislocation. The mass of the model without fixtures was 190 *grams*.

A centrally located tapped M16 hole was used to fix the model with a bolt to the lower cross member of the sliding frame of the test rig. The central bolt and the backward facing part of the gallery showed high interference on the visibility of the flow in the front facing part of the gallery. Therefore an intermediate annular groove between bolt and gallery was manufactured, as shown in Figure 4.14. A non-transparent material was added to the outside surface of the groove to block the view beyond the groove. To enhance the contrast of the oil inside the gallery, several blocking material colours were investigated, including white, yellow, green, blue and red. White showed the best results, as the camera would only record black

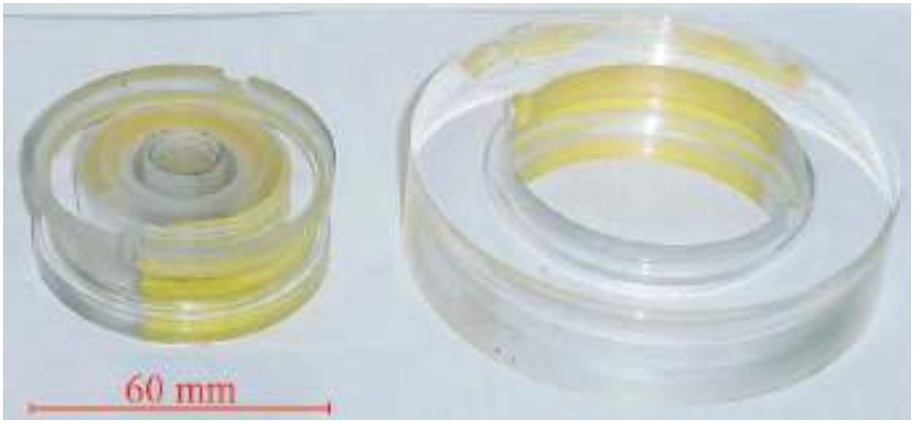

Fig. 4.13 Gallery model inner and outer ring for visual investigations

and white images and a colour different from white was producing a grey shade reducing the contrast of the oil.

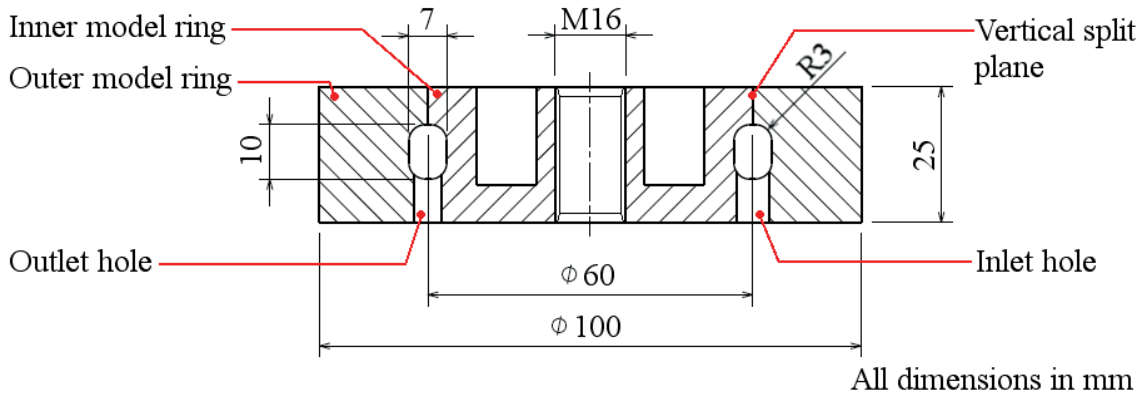

Fig. 4.14 Major dimensions of small gallery model

The original piston design contained a dedicated inlet and outlet channel. The inlet channel was included in the model design through the attachment of a 25 *mm* block at the inlet and outlet side, as shown in Figure 4.15. Markers were applied to the outside surface of the gallery model for better outline of the gallery, indicating the top and bottom limits.

4.2.3 Small gallery nozzle

The oil nozzle used for the small gallery model was a mass-production nozzle, as fitted in current diesel engines. It is shown in Figure 4.16. The total length of the nozzle pipe was approximately 55 *mm*, where the last 25 *mm* had an internal diameter of 2.0 *mm*. Approximately 13 *mm* from the nozzle exit was a bend of 65°with a curvature radius of 5 *mm*. The production nozzle contained a spring operated ball valve opening at a supply pressure of

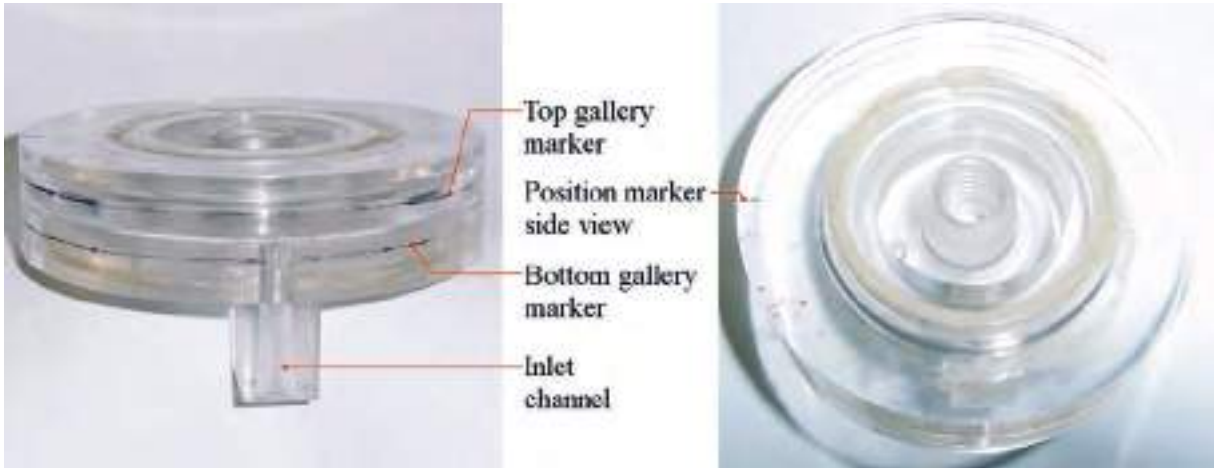

Fig. 4.15 Assembled small gallery model for visual investigation

approximately 1.8 *bar* to avoid oil flow at low engine lubrication system pressures. For the investigation the ball valve was removed to avoid introduction of pulsation from the valve.

Fig. 4.16 Oil nozzle for small gallery model with 2.0 *mm* nozzle exit diameter

4.2.4 Large gallery piston overview

The large gallery investigated was from a heavy–duty direct–injection diesel engine with a cylinder volume of 2650 cm^3. The piston application ranged from heavy goods vehicles to earth moving equipment and to power generators for stationary applications and locomotives. The articulated piston was consisting of two parts, the piston crown and piston skirt. The gudgeon pin was the connecting link between skirt, crown and conrod.

In the production case the piston crown, containing the cooling gallery, was made from steel. The crown consisted initially of two separate halves, one being exposed to the combustion chamber and the other being exposed to the crankcase and containing the pin bosses. Both were machined including the appropriate gallery half. Friction welding was used to combine the halves creating a welding burr on the outside of the piston and two more on the

inside of the gallery. While the burrs on the outside could be removed during machining, these on the inside of the gallery remained, as shown in Figure 4.17. Kolbenschmidt (2007) indicated that the burrs could be removed, if the piston was manufactured in a combination of forging and friction welding. This removal would improve the flow characteristic of the oil inside the gallery. The shape of the gallery was of a complex nature, as shown in Figure 4.18, following the shape of the combustion bowl. The gallery was also of closed design with separate inlet and outlet hole, having a volume of 220 cm^3.

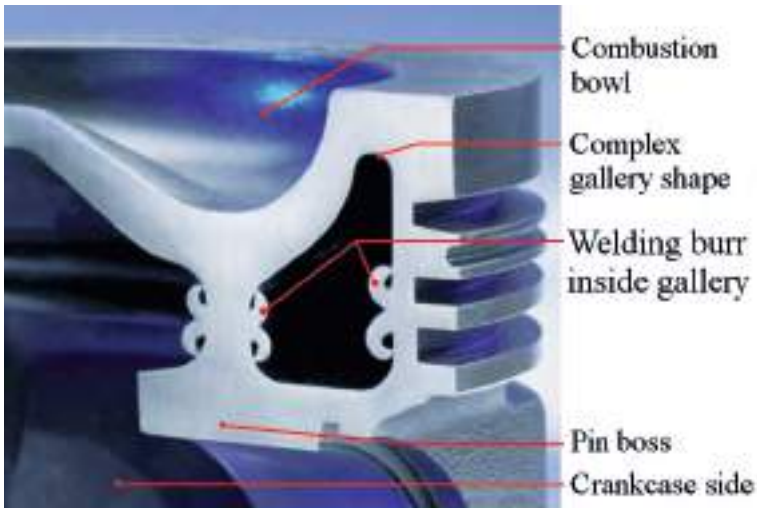

Fig. 4.17 Cut view of common piston crown exposing gallery shape with manufacturing burr inside gallery

(Baberg et al., 2012)

4.2.5 Large gallery model (*LGM*) preparation for visualisation

A transparent model of the gallery was manufactured for fill level and flow pattern investigation. The same considerations for manufacturing processes and material choice were taken into account, as discussed for the small gallery model. This led to the same choice of material, which was transparent acrylic (Perspex).

The large gallery model was designed with a horizontal gallery split, as opposed to the small gallery model with a vertical split. Hence the model consisted of a top gallery part and a bottom gallery part as shown in Figure 4.18. In this design the horizontal split of the gallery did introduce a visibility obstruction, but the effect was evaluated to be negligible with respect to the gallery height. Besides the better manufacturability of the complex shape, the

horizontal split would also allow for the inclusion of a representative part for the welding burr, if required. This would partially obstruct the view into the gallery and was therefore not implemented in the current study. An additional advantage of the machining was the comparable gallery surface finish to built piston designs. The model outside and inner gallery surfaces were polished to improve visibility into the gallery.

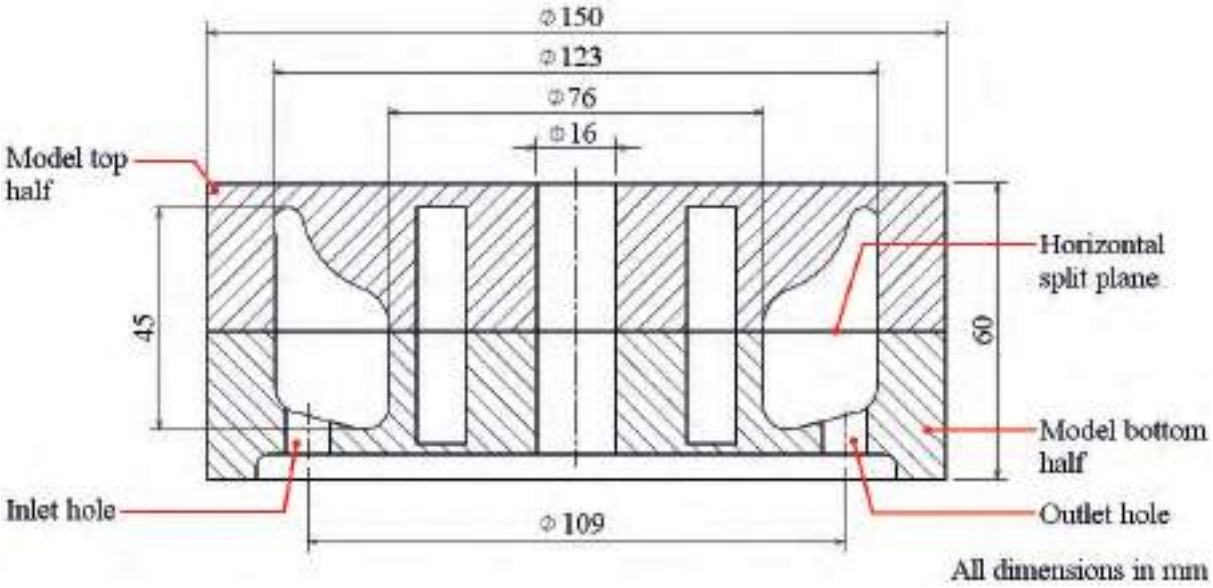

Fig. 4.18 Cross-sectional view of gallery model with major dimensions

The model contained no inlet or outlet channel, as the production piston did not contain such features, and were 9 *mm* in diameter. A conical cover was attached to the inlet side to reduce oil splashing from the impact between oil jet and gallery model during piston movement. The cover was sufficiently large in width as to not interfere with the flow of oil from the nozzle. The outlet did not require any splash cover. The gallery halves were held together by a centrally located steel bolt, as shown in Figure 4.19. It fixed the model also to the sliding frame cross member of the test rig. The mass of the model without fixtures was 870 *grams*.

The large gallery model also contained a groove, as found on the small gallery model, to add a non-transparent material between the front facing gallery and backward facing gallery and centre bolt. The material was used to enhance visibility of the oil flow and to avoid visibility of the bolt.

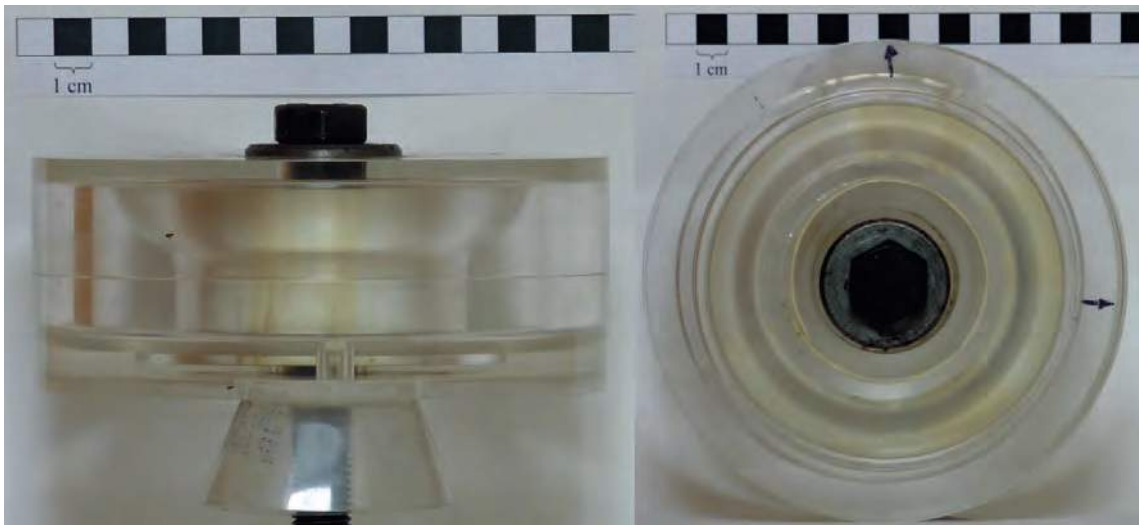

Fig. 4.19 Assembled large gallery model for visual investigation with centrally located bolt

4.2.6 Large gallery nozzle

The oil nozzle for the large gallery model was a standard mass-production nozzle as fitted to current engines, as shown in Figure 4.20. It was of an open flow design, without a valve to disable flow at low system oil pressure. The total length of the nozzle pipe was 50 *mm* with a curvature radius of 15 *mm* at an angle of 70°. The final 15 *mm* before the nozzle exit had a constant diameter of 3.0 *mm*.

Fig. 4.20 Oil nozzle for large gallery model with 3.0 *mm* nozzle exit diameter

4.3 Instrumentation and sensors

Pressure sensor

The used analogue pressure gauge had a range from 0 *bar* to 10 *bar*.

Flow sensor

The flow meter was of paddle wheel type with a frequency output proportional to volumetric

flow rate. The instrument overview is given in Table 4.4.

Table 4.4 Flow meter specifications

Property	Description
Model type	RFO-2500 series
Signal generation	Hall sensor
Input signal	4.5 V to 24 V DC, continuous
Output signal	4.5 V to 24 V DC, pulsed
Output frequency	25 Hz to 250 Hz
Flow rate range	5.7 l/min to 45.4 l/min
Max pressure	6.9 bar (100 psig)
Temperature range	-28° C to +82° C
Max viscosity	38 mPa·s
Connection port size	0.5 inch

(GEMS, 2014)

Speed sensor

An inductive sensor was fitted near the toothed region of the large pulley. The signal was transmitted to a frequency meter, where it was converted to rotational speed and displayed. The speed was set and adjusted manually, based on the readings from the speed display. The constant conditions during operation showed no long term effects on speed and the high flywheel inertia kept the cycle–to–cycle angular speed variation within $\pm 2\%$.

Temperature sensor

The oil temperature at the nozzle and inside the tank were measured using K–type thermocouples. The thermocouples were calibrated at water melting point (0° C) and boiling point (99.3° C at 98.859 *mbar*) for accuracy.

4.4 High speed camera

The camera system used was a Kodak Ektapro HS4540mx High Speed Motion Analyser, as schematically shown in Figure 4.21. The complete system consisted of:

- imager (camera head),
- processor, controlling and storing the recordings,
- keypad to control the processor,
- monitor (Sony 1442 QM) for direct image view,

- video recorder (Panasonic MD830) for video storage,
- video printer (Mitsubishi P500E) for image printing,
- computer (Dell), incl monitor, keyboard and mouse for image storage and transfer,
- Canon TV Zoom Lens V6x16 with focal length 16–95 mm and focal ratio f/2.0,
- 2 halogen lamps (2 x 50W)

shows an overview of the camera system.

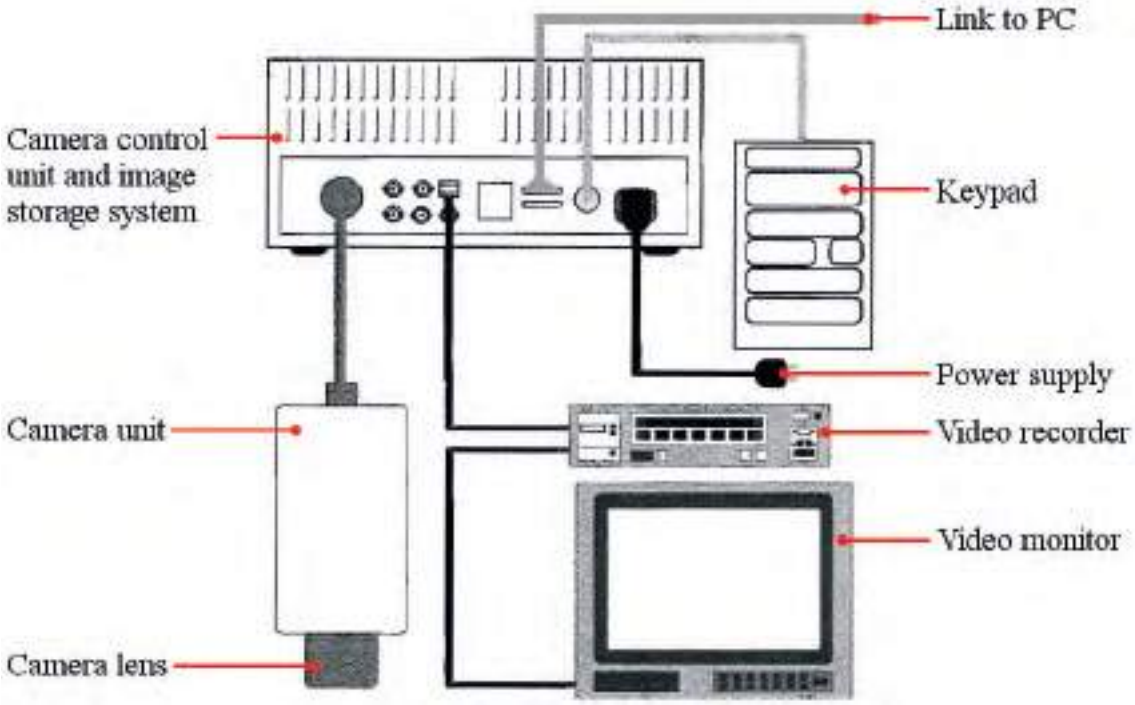

Fig. 4.21 Kodak Ektapro HS4540mx High Speed Motion Analyser wiring diagram

(Kodak, 1999)

The camera uses a CCD sensor (charge-coupled device) and records images with a maximum full size resolution of 256×256 pixels at 256 grey shades up to a speed of 4500 frames per second (*fps*). The maximum frame rate is 40500 *fps*, but at reduced image size. The internal memory was 192 *Mb*, which was sufficient for storage of 3072 full sized images. Kodak (1999) stated the available recording settings as given in Table 4.5. The quality of the images greatly affected the quality of results, especially with regard to analysing the flow behaviour. Where possible the highest resolution was used to capture the flow with highest detail.

The camera recorded and stored the image frames in the control unit memory as soon as the camera was set to 'record mode'. Once the memory was fully used, the control unit would

Table 4.5 Available recording image sizes and frame rates of Kodak EktaPro camera

Recording rate	Image resolution (horizontal x vertical)	Max number of images stored	Recorded time
fps	*No of pixels*	–	*sec*
30 to 4500	256 x 256	3072	0.6824
9000	256 x 128	6144	0.6826
13500	128 x 128	12288	0.9101
18000	256 x 64	12288	0.6826
27000	128 x 64	24576	0.9102
40500	64 x 64	49152	1.2136

(Kodak, 1999)

initiate the deletion of the earliest image. This process would continue, until a trigger for image retaining occurred. The trigger could be from the keypad or via an external signal to synchronise with events, such as lasers and strobe lights. Use was made of the keypad trigger. In addition the images were also recorded on video tape for safe keeping and backup.

4.5 Summary

This chapter explained the development and built process for the test rig for the experimental part of this study.

One focal point was on the design of the test bodies. Two specific pistons were identified for the study, representing the wide range of engine applications. Both contained highly different cooling gallery designs, which were analysed and described. The designs, material selection and manufacturing process of the test specimens were explained and discussed.

The second focal point was on the design process of the test rig, explaining the reasoning of choices made, including the mechanism generating a representative motion for the test bodies. The selected yoke mechanism satisfied the requirement for variability of stroke length, test body size, rotational speed. The absence of a conrod meant that the movement was not identical to real engine motion, but this was evaluated as acceptable in light of reduced complexity of the system and aim of the study being concerned with the evaluation of experimental and numerical flow study.

CHAPTER 5 EXPERIMENTAL RESULTS

This chapter focuses on the determination and evaluation of experimental results using the test rig and instrumentation discussed in the previous chapter.

The first section concentrates on the determination of the oil properties and the investigation of the flow behaviour as the oil jet exits the nozzle. The knowledge of the oil jet behaviour is required for the assessment of the relationship between the oil jet and gallery inlet and to provide information for definition of the boundary conditions for the numerical study.

The next section specifies the visual arrangement, flow settings and speed settings for the large gallery model (*LGM*). A detailed examination of the in-gallery flow behaviour with respect to bulk flow and gallery filling is performed for one representative operating condition case of 4.0 l/min and 600 rpm, which is also used as the comparison case for the numerical investigation. The study and description of the differences and commonalities of the in-gallery flow behaviours for all investigated speed and flow rate cases for the *LGM* closes the section.

The last section of this chapter details the visual arrangement, flow settings and speed settings for the small gallery model (*SGM*) and the examines the in-gallery flow behaviour with respect to bulk flow and gallery filling for the case of 1.65 l/min and 750 rpm. This is also a comparison case for the numerical investigation. A study and description of the differences and commonalities, as for the *LGM*, is also performed. The chapter closes with a summary of the findings from this chapter.

5.1 Introduction and terminology

An initial analysis of the recorded images showed that there were air bubbles of various sizes present inside the gallery. These will be referred to in the following way. Air bubbles with a size of less than approximately 0.5 *mm* are referred to as micro-sized. These are

mainly suspended in the oil and cannot be identified or tracked individually, but have a significant effect on the translucence of the oil. Small-sized bubbles refer to a size up to approximately 3 *mm*, which can be identified clearly and tracked in the flow, unless they are hidden within the bulk oil. The definition of the medium-sized and large-sized bubbles are linked to gallery height and relate to up to half gallery height and near full gallery height respectively. Boundaries of such are clearly identifiable.

The flow directions were determined from three consecutive recorded images. The analysis was carried out by manually assessing the movement of flow features, which may be small-sized air bubbles dragged along in the oil flow or/and the movement of oil air interfaces for medium-sized and large-sized air bubbles. This resulted in a time consuming process, but was the most accurate method to determine the flow directions. Although utmost care was taken in the flow analysis, there may be some underlying flow behaviour, which cannot be detected, if sufficiently sized and traceable air bubbles are not present.

In order to improve the quality of flow direction results and to reduce analysis time Particle Image Velocimetry (*PIV*) was considered and an initial study performed. However, the three–dimensional shape of the gallery and the resulting complex non-planar flow characteristic prohibited any useful analysis of the velocities and directions, as some of the features used for the analysis disappeared from the visible range of the camera viewing position (moving into the centre of the gallery away from visible outside) or the change in position changed the grey-tone of flow features and falsified the results. It was therefore decided to pursue the manual tracking method.

Furthermore, all presented photographs show only a limited view of the flow behaviour, but represent a good encapsulation of the flow behaviour found for a wider range of test conditions. Additional information about in-gallery behaviour including positions before and after *BDC* and *TDC* is provided in Appendix B.

The flow behaviour was found to vary depending on the position inside the gallery. Figure 5.1 shows the representation of a gallery highlighting the specific sections referred to in this chapter.

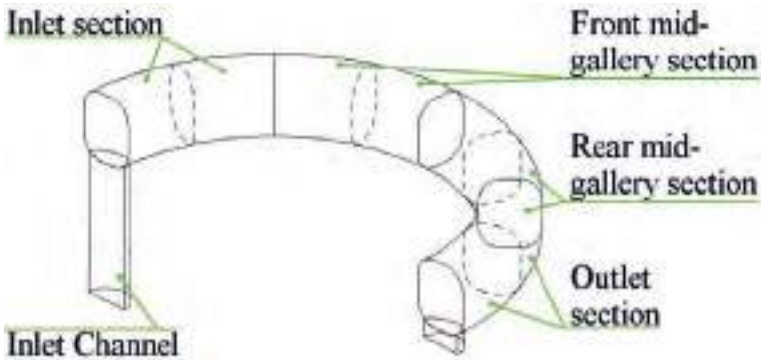

Fig. 5.1 Definition of gallery sections naming

5.2 Oil properties and oil jet behaviour study

5.2.1 Oil properties

The oil used during the tests was a mixture of hydraulic oils to mimic the behaviour of engine oil at operating conditions, a method also used by Schwarz and Adolph (2001) to investigate oil nozzle flow behaviour. The used oil mixture required the determination of the density, viscosity and surface tension.

Oil density and viscosity

The density was determined using the gravimetrical method, measuring the mass for a volume of 1000 cm^3 at various temperatures. Statistical analysis of ten measurements was used to assess the uncertainties and measurement error. The viscosity was determined using the falling ball method. The Hagen-Poiseulle[1] method was considered, but could not be implemented with sufficient accuracy, as the small oil volumes involved caused significant change in temperatures during the measurements. Measurements were conducted at the same temperatures as for the density measurements. Statistical analysis of ten measurements was used to assess the uncertainties and measurement error. The determined values are given in Table 5.1.

Pimenta and Filho (1993) determined for a standard engine oil of $15W40$ grade the dynamic viscosity and density as 11.9 *mPas* and 847 kg/m^3 respectively for a temperature of 100°C. Saadi et al. (2013) investigated the temperature effects on oil properties and found values for dynamic viscosity and density of engine oil at 100°C as 10 *mPas* and 810 kg/m^3

[1] Viscosity determined from time dependent flow of a defined volume of liquid through a pipe with fixed length and diameter.

Table 5.1 Properties of used oil mixture

Temperature	Density	Dynamic viscosity
$°C$	$kg \cdot m^{-3}$	$mPa \cdot s$
5	850.3	18.58
17	842.1	13.79
20	840.1	12.56
26	836.3	10.46

respectively. These compare well with the properties of the used oil, hence representing conditions at engine operation.

Oil – air surface tension

A sufficient accurate value of the surface tension of the oil could not be determined, with the magnitude of deviation of results at the same level as the measurements. It was decided to assume a value based on comparable oils. Table 5.1 provides a range of values for surface tension taken from Jones and Wedeven (1971) and Kaldonski et al. (2011). The synthetic and super-refined oils refer to engine oils, while the SN-650 and Molylube oil refer to a base oil for engines and a gearbox oil respectively.

Table 5.2 Values of surface tension for selected oils at various temperatures

Temperature	Synthetic paraffinic oil[a]	Super-refined naphthenic mineral oil[a]	Super-refined paraffinic mineral oil[a]	SN-650[b]	Molylube[b]
$°C$	*mN/m*	*mN/m*	*mN/m*	*mN/m*	*mN/m*
23	25.6	25.6	29.8	–	–
25	–	–	–	30.5	27.6
40	–	–	–	29.4	26.4
50	–	28.7	27.2	–	–
100	25.6	25.6	23.4	15.8	22.4
150	22.2	22.2	20.0	–	–

(Jones and Wedeven, 1971)[a], (Kaldonski et al., 2011)[b]

As mentioned previously, the oil used for the investigation was a mixture of hydraulic oil to mimic the behaviour of engine oil at $100°C$. It can be seen that the temperature has a strong effect on surface tension, but variation between different oil types was small in comparison. For the further study a value of 26 mN/m was used.

5.2.2 Flow from nozzle and flow meter calibration

The flow meter was calibrated for each nozzle to improve accuracy of flow rate, as recommended by GEMS (2014). During calibration the temperature was monitored and controlled to minimise variation of viscosity and density.

Mass flow calibration was preferred over volume flow calibration. It minimises the skewing of results due to air entrainment into the oil, a consequence of the breakup of the oil jet. Care was taken to eliminate as much air from the oil before measurement. Large bubbles were eliminated quickly by short shock waves (from vessel impact) prior to measurement, but micro-sized air bubble elimination would take significant longer under ambient conditions. The air bubble induced error can be assumed negligible, as the specific weight ratio between oil and air was approximately 700:1.

The following procedure was employed to determine the volume flow rate for both nozzles:

1. The oil flow control valve was set to obtain a specific reading from the flow meter display.
2. A container (volume of approximately 1.2 $litres$) was filled with oil near to top without spilling and the fill time, pressure and temperature were recorded.
3. The container including oil was weighted and the mass recorded.
4. The container was drained and the empty mass recorded.
5. The procedure was repeated for a minimum of nine more recordings.
6. The mass flow rate was calculated by

$$\dot{m}_o = \frac{m_f - m_e}{t_f} \tag{5.1}$$

   Where m_f is the mass of the filled container, m_e the mass of the empty container and t_f the fill time.
7. The volume flow rate was calculated by

$$\dot{V}_o = \rho_o \, \dot{m}_o \tag{5.2}$$

   Where ρ_o is the density of the oil.
8. The process was repeated for increased flow rates up to maximum conditions of nozzle flow rate.

The relation between flow meter display reading and flow rate was established to provide input settings for flow rate during testing. Figure 5.2 shows the relation between flow meter display reading and volumetric flow rate for each nozzle. The difference in meter reading at identical flow rates through the nozzles was a result of the application of a flow limiter at the sensor input for the smaller gallery nozzle in order to increase the velocity at the sensor wheel. This was necessary to stabilise the readings and to reduce effects from internal friction of the sensor wheel. This was also the reason for the offset between the curves in the overlapping flow rate region.

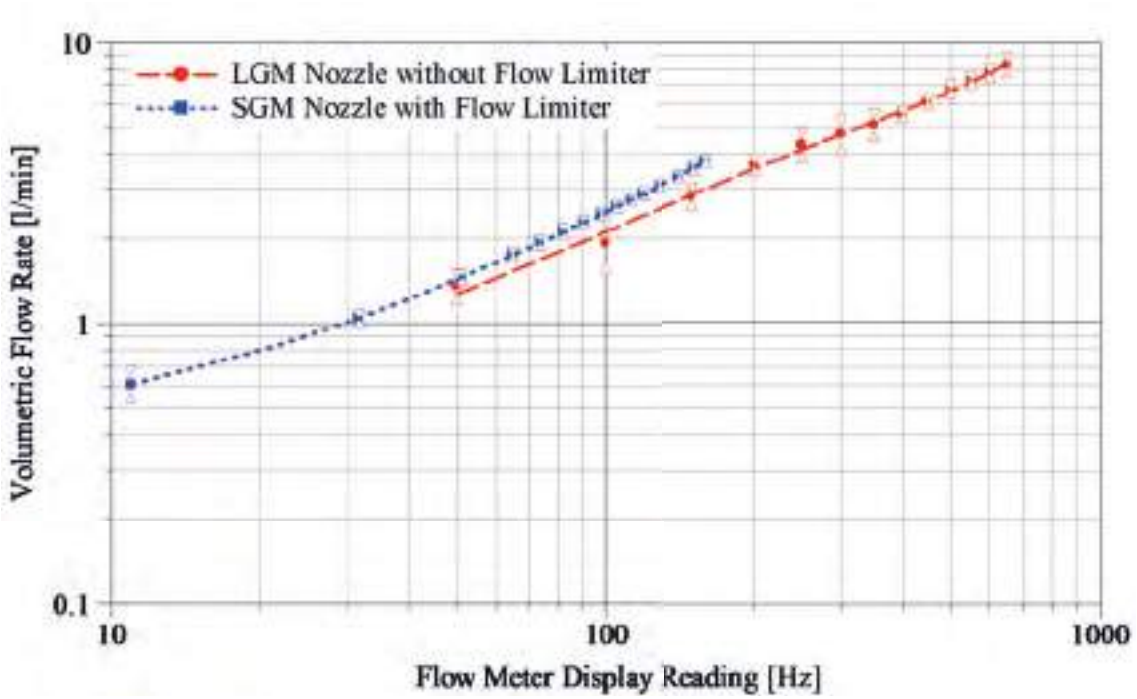

Fig. 5.2 Flow meter display reading vs. volumetric flow rate for both nozzles

There also occurred volumetric flow at a display reading of zero. This was seen as correct, as the flow indicator required a minimum flow to overcome the friction in the rotor bearings and the leakage (bypass) around the rotor. The precise shut–off point was not investigated, as this was producing flow rates below the minimum flow rates defined.

For the large gallery model nozzle a 3^{rd} order polynomial approximation provided the best fit to determine flow rate and can be given as

$$f_{iLGM} = -0.917\,\dot{V}_o^3 + 16.258\,\dot{V}_o^2 + 2.7667\,\dot{V}_o + 27.343 \tag{5.3}$$

where $\dot{V}_o$ refers to the oil flow rate to be set. For the small gallery model nozzle a 2^{nd} order polynomial approximation was used and can be given as

$$f_{iSGM} = 0.384\,\dot{V}_o^2 + 45.952\,\dot{V}_o - 16.677 \tag{5.4}$$

The supply pressure to the nozzle played also an important role in the oil jet behaviour, as increasing pressure differences would lead to surface breakup. Figure 5.3 shows the relationship between volumetric flow rate and supply pressure. With increasing flow rate the pressure increased exponentially, converging towards a maximum flow rate, as the flow resistance increased, especially with the onset of turbulent flow.

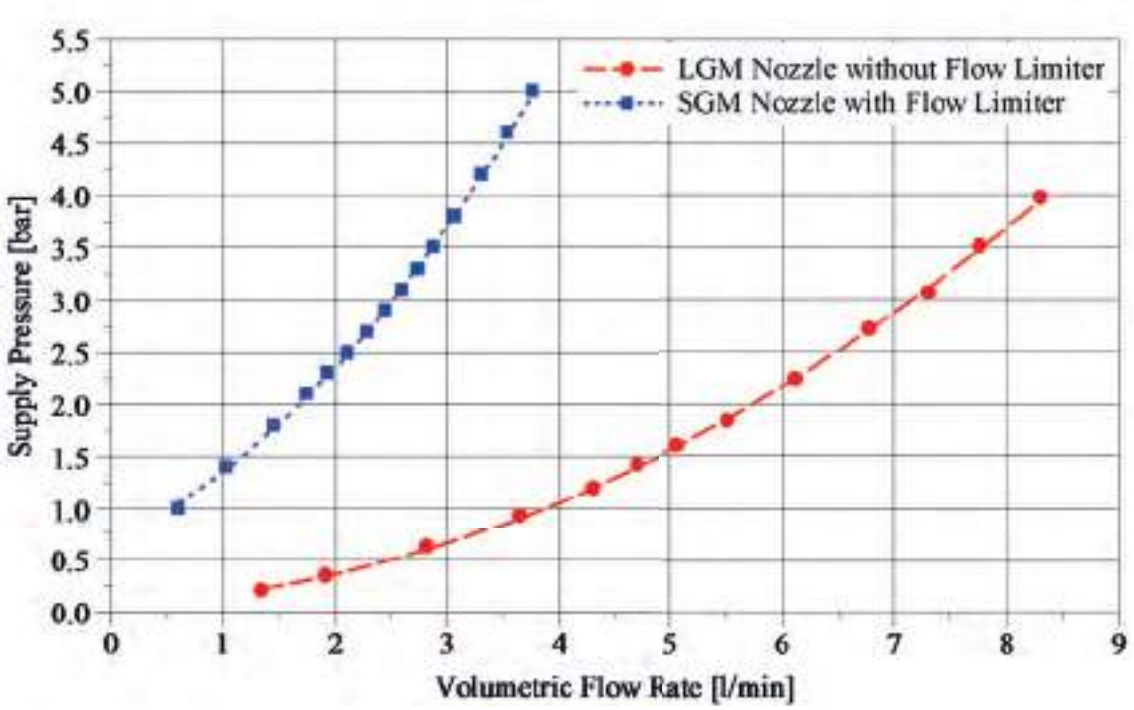

Fig. 5.3 Pressure vs. flow rate relationship from nozzle calibrations

The relationship between volumetric flow rate and nozzle exit velocity of the oil jet was linear, as the oil was an incompressible fluid at such low pressures and the law of continuity applies. The oil jet exit velocity can be calculated as

$$v = \frac{4\,\dot{V}_o}{\pi\,d_n^2} \tag{5.5}$$

where $\dot{V}_o$ is the volumetric flow rate and d_n the nozzle exit diameter.

The Reynolds number can be used to determine the flow conditions at the nozzle exit. For the large gallery model nozzle the onset of transition conditions ($Re \leq 2000$) was initiated at a flow rate of 4.25 l/min and for the small gallery model nozzle at a flow rate of 2.25 l/min, as shown in Figure 5.4. This related to average exit velocities of 10.5 m/s and 15.7 m/s respectively.

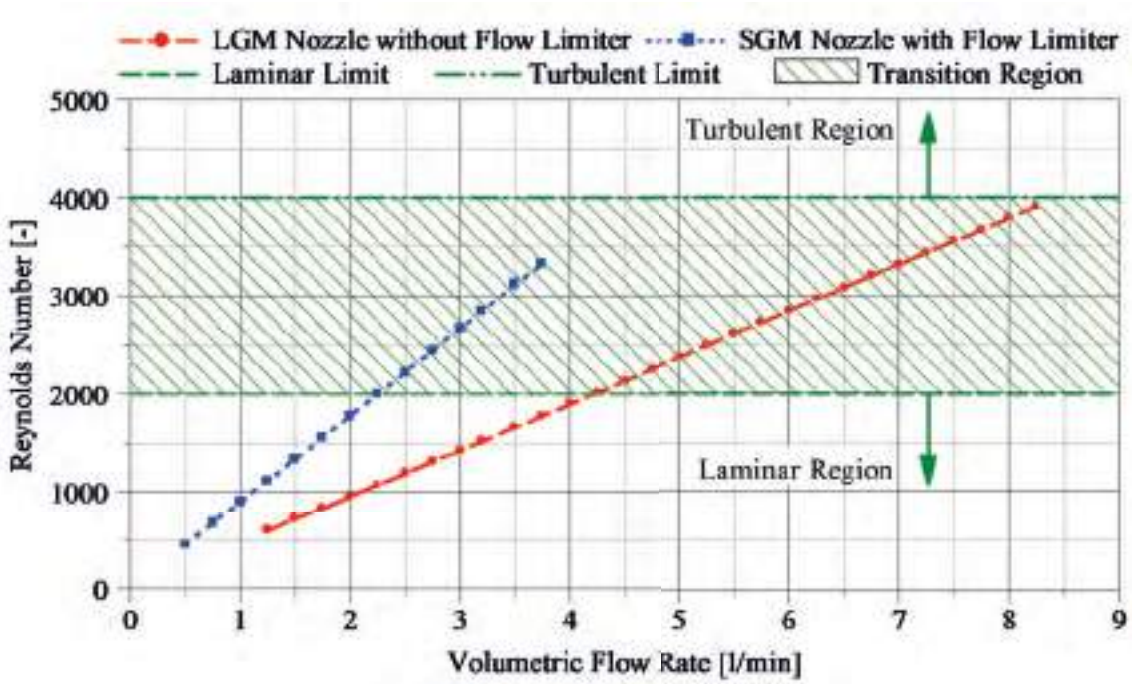

Fig. 5.4 Reynolds numbers for nozzle exit flow and theoretical laminar flow distance of jet from nozzle exit

5.2.3 Large gallery model nozzle flow behaviour

The behaviour of the free–steam oil jet influenced the galley filling. Tests were conducted to investigate the oil jet behaviour, where oil was freely ejected from the nozzle vertically into undisturbed stationary air. A back plate with dedicated markings for distance from nozzle and angle from vertical was placed behind the jet, as shown in Figure 5.5. The jet was aligned with the centre marking of the plate. A halogen lamp was used to increase the contrast of the oil and to aid the camera recordings, as the short exposure time interval inherently produced dark images. A curved deflector was used to guide the oil away from the front face of the back plate in order to avoid potential returning oil blocking the view onto the oil.

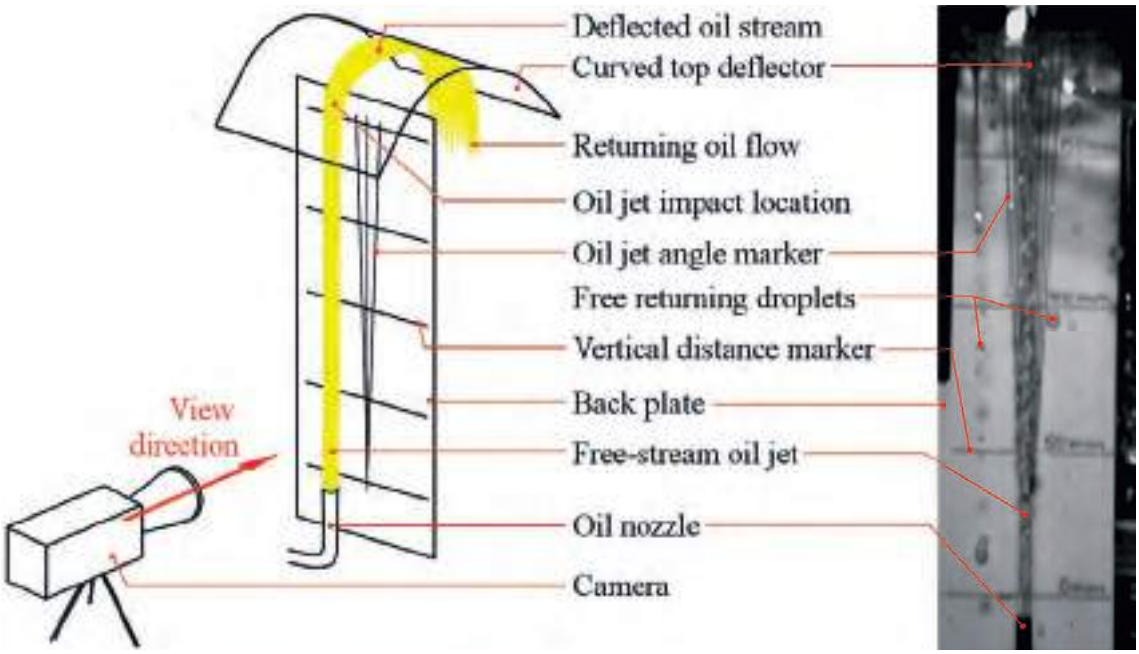

Fig. 5.5 Schematic of oil jet imaging setup and actual recorded image

A comparison of oil jets for different flow rates is shown in Figure 5.6. Some of the larger scale rippling of the surface may be linked to the pulsating supply pressure from the vane oil pump, as shown by Zhang et al. (2006). Images were taken at a recording rate of 9000 fps at a resolution of 256 $\times$ 128 $pixels$. The oil jet surface boundaries were manually redrawn to enhance jet visibility. It can be clearly seen that an increase in the flow rate also increased the jet widening angle. This led to larger impingement areas at further distance from the nozzle exit. At the highest flow rate of 8.0 l/min the jet widening angle was determined to be approximately 5°. This would be significant to the oil catch ratio. Taking into consideration that the distance inside the engine between nozzle exit and gallery inlet at *TDC* was approximately 250 *mm* (170 *mm* stroke + skirt length) the impingement diameter could reach values of 25 *mm*. This is significantly larger than the gallery inlet hole diameter of 9 *mm*.

It was also found that the impingement location of the oil jet relative to a point exactly above the nozzle changed. This behaviour was only found at flow rates less than 4.0 l/min and was linked to the influence of nozzle curvature just before the exit. As the jet started to break up more on the outside surface, the change of the impingement position at the distance was negligible.

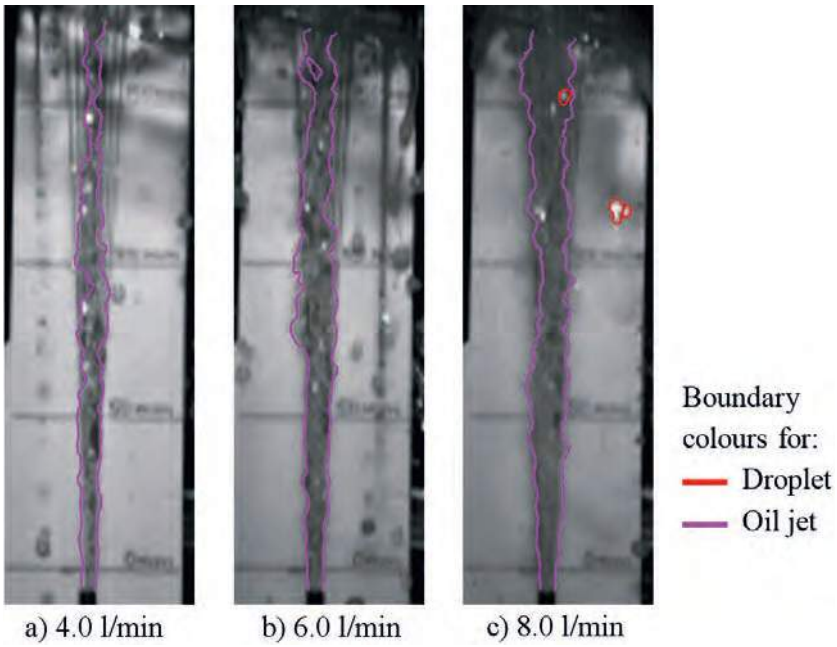

Fig. 5.6 Schematic of oil jet imaging setup and actual recorded image

Figure 5.7 shows three images, identifying the position of the same oil particle inside the oil jet at different vertical distance markers for jet velocity determination. An analysis of the velocity for the lower section (0 *mm* to 50 *mm*) cannot be made, as a particle cannot be identified. The oil jet was still in a transitional state near laminar conditions (including low outside surface rippling), which showed little jet breakup and particle formation.

The intervals between Figure 5.7a and b, and Figure 5.7b and c were 32 frames and 35 frames respectively. The recording frame rate was set to 9000 fps, equating to a time interval, t between frames of seconds. With the distance of 50 *mm* between marker lines the average velocity can be determined as

$$v_{a\to b} = \frac{0.05m}{32 \times 1.\bar{1} \times 10^{-4}s} = 14.1\frac{m}{s}$$

and

$$v_{b\to c} = \frac{0.05m}{35 \times 1.\bar{1} \times 10^{-4}s} = 12.9\frac{m}{s}$$

It can be seen that the jet velocity reduced with increasing distance from the nozzle, which was expected, as gravity and air friction would pose a resistance to the jet flow. Using the

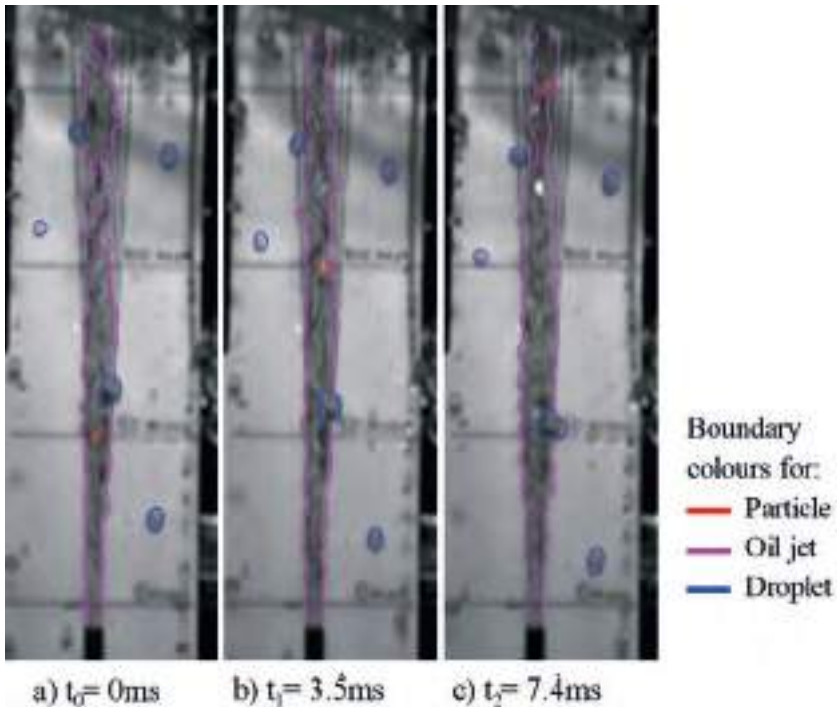

Fig. 5.7 Movement of oil particle in vertical direction at 5.0 l/min

flow data from the test the average nozzle exit velocity, v_e, of the oil jet can be calculated as

$$v_e = \frac{4\,\dot{V}_o}{\pi\,d_n^2} = \frac{4 \times 5\;l/min}{\pi\,0.003^2 m^2} = 11.8\frac{m}{s}$$

where $\dot{V}_o$ and d_n are the volumetric flow rate and nozzle exit diameter respectively. The calculated nozzle exit velocity of the jet of 11.8 m/s and the velocity determined from the images of 14.1 m/s were in good comparison, given that the real jet nozzle exit velocity was not constant across the nozzle diameter. Either laminar or turbulent flow conditions at the nozzle exit would generate a velocity profile with higher velocity towards the jet centre as compared to the velocities near a wall. The velocity from the images reflected this behaviour, while the above given method assumes constant exit velocity, leading to a lower value.

5.2.4 Small gallery nozzle flow behaviour

The mechanical shut–off valve inside the small gallery nozzle was removed to reduce flow instabilities, resulting from the movement of the valve during operation. The experimental setup of the jet behaviour study was identical with the large gallery nozzle. During testing it became clear that the lower quality imaging with the high speed camera would not provide

sufficient quality images for analysis. Large jet breakup and smaller droplet size led to highly blurred images. A different camera with higher resolution was used to capture the jet behaviour, but with the disadvantage of slow consecutive image recording without interval time control, making velocity analysis impossible.

As volumetric flow rate increased the oil jet showed a significant change in breakup behaviour, as shown in Figure 5.8. At low flow rates of 1.4 l/min the jet showed near laminar behaviour independent from jet length. It can be seen, that with increasing flow rate the oil jet showed initial rippling of the jet surface, before a distinct breakup occurred between 2.1 l/min and 2.6 l/min. Further increase in flow rate led to extreme breakup of the jet, culminating in the formation of small droplets. It can also be seen that the lateral impingement position of the oil jet changed. As the flow rate increased the location moved in the direction away from the nozzle inflow position (inflow from left, impingement moved to the right). It can be assumed that the change in the cross-sectional velocity profile and the resulting inertia effects influenced the exit angle of the jet, as shown by Triep et al. (2013).

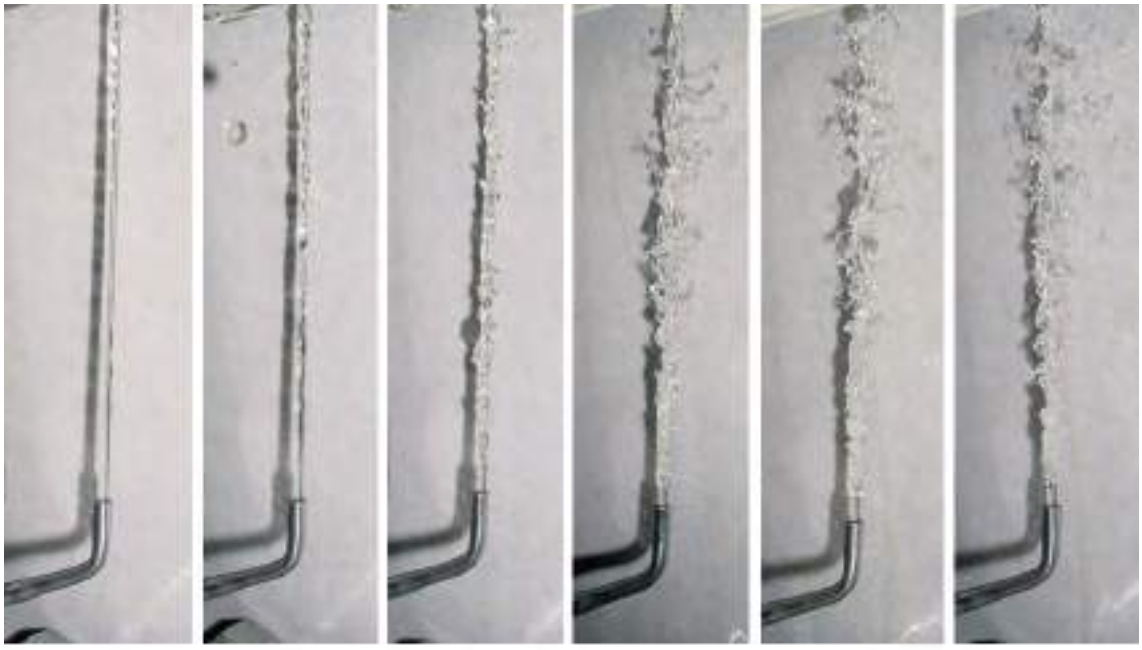

Fig. 5.8 Comparison of small gallery nozzle oil jets for different flow rates

Based on the strong breakup of the jet the test range was bound between 0.5 l/min and 2.1 l/min, as higher values were evaluated as unsuitable for reasonable gallery filling following the very large jet angle. The jet widening angle at pressure up to 2.1 l/min was

determined as approximately 2.5°. Taking into consideration that the distance inside the engine between nozzle exit and gallery inlet at *TDC* was approximately 120 *mm* (88 *mm* stroke and skirt length) the impingement diameter could reach values of 7.2 *mm*. This was slightly larger than the gallery inlet channel diameter of 7 *mm*.

5.2.5 Jet breakup regime

The breakup of a free stream jet leads to an increase of the effective cross-sectional diameter of the jet with increasing distance from the nozzle. Depending on the jet velocity the breakup ranges from Rayleigh breakup (dripping) at low velocities to atomisation at high velocities. In order to achieve an optimal oil catch ratio the jet diameter should not exceed the inlet hole diameter to the gallery. The breakup regime could be used to determine the breakup behaviour and to draw conclusions about the suitability of flow rates on the delivery of oil to the gallery. The regime can be identified using a Reynolds number vs Ohnesorge number diagram, as stated by Liu (1999), Farvardin and Dolatabadi (2013), Agrawal (2013) and Delteil et al. (2011).

Table 5.3 shows the values of the average nozzle exit velocities and flow regime determining dimensionless numbers of both nozzles. The operating range was indicated by minimum and maximum flow rate, whereby the maximum flow rate was limited to a delivery pressure of 4 *bar*. Although the velocity changed with flow rate, the Ohnesorge number was constant, since the viscous forces increased at the same rate as the square-rooted inertia forces, leading to a constant ratio of both. It can also be seen that there occurred transition from laminar to turbulent conditions for both nozzles.

Both nozzle jets can be classified as jets with mainly 2^{nd}–wind induced breakup, as highlighted in Figure 5.9. This breakup regime was characterised by a wave–like outer shape with widening of the jet, whereby the rippling of the surface was a result of the velocity difference between jet and surrounding stationary air. Both jets also showed an increase in the jet widening angle with increasing flow rate as found by Ménard et al. (2007).

As the flow rate increased, so did the velocity difference, leading to an increase in the turbulence in the outer jet layer, where the contact with the air existed. This was in accordance with findings from Fellouah et al. (2009) and also implied that increased amounts of air were

Table 5.3 Velocity and dimensionless number range for large and small gallery nozzles

LGM nozzle	Flow rate	Velocity	Reynolds-No.	Ohnesorge-No.
	l/min	*m/s*	–	–
min $\dot{V}_o$	4.00	9.43	1892	4.91×10^{-2}
	4.44	10.47	2100	4.91×10^{-2}
max $\dot{V}_o$	8.00	18.86	3785	4.91×10^{-2}
SGM nozzle	**Flow rate**	**Velocity**	**Reynolds-No.**	**Ohnesorge-No.**
	l/min	*m/s*	–	–
min $\dot{V}_o$	1.38	7.36	985	6.01×10^{-2}
	2.37	12.55	2100	6.01×10^{-2}
max $\dot{V}_o$	3.20	16.96	2669	6.01×10^{-2}

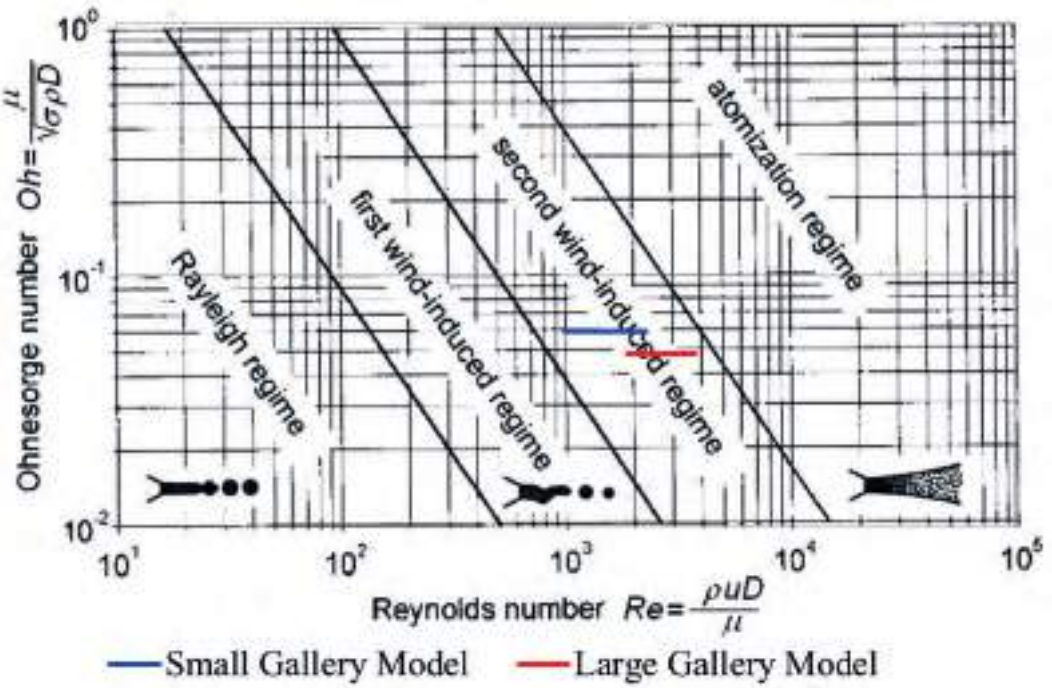

Fig. 5.9 Breakup regime range of jets for both nozzles

(Martínez, 2014)

drawn into the jet. Such behaviour was noted during mass flow calibration of the jets, where increased amounts of micro-sized air bubbles (< 0.5 *mm* diameter) were noted.

It was noted that the jet for the small gallery nozzle exhibited more severe breakup behaviour (Figure 5.8f) in comparison to the large gallery nozzle, although the breakup regime ranges were comparable. The small gallery nozzle jet portrayed a behaviour that may be described as close to atomisation at the highest flow rate. An alternative nozzle design was investigated, where only the last 5 *mm* before the nozzle exit were of constant cross-sectional diameter (2.0 *mm*), rather than the last 25 *mm*. The recorded jets exhibited significant differences in the jet breakup at identical flow rates, as shown in Figure 5.10. The largest differences were found at the highest flow rate. As the test conditions, such as flow

Fig. 5.10 Oil jet breakup at flow rate of 3.2 l/min for different nozzle designs

rate, temperature, density, viscosity, etc., were identical in both cases the difference in the jet behaviour can be linked to the nozzle design.

It was also shown previously that the curvature of pipes caused a difference in the cross-sectional velocity, whereby the higher velocities were found on the outer curvature surface of the bend (Triep et al., 2013). The superposition of the higher flow velocity in the bend from the reduced cross-section and the higher velocity on the outer surface in the bend would lead to the highest jet exit velocity on the extension of the outer surface. The higher exit velocity of the free stream jet induced more shear into the contact layer between air and oil, leading to stronger breakup. On the contrary, at the inner surface of the pipe bend the velocity would be

lower, leading to a lower exit velocity at the extension of the inner surface at the nozzle exit and therefore reduced shear between air and oil and less breakup.

Based on the findings it can be derived that the breakup analysis using the Reynolds and Ohnesorge numbers has significant shortcomings when curvatures and cross-sectional changes occur in the proximity of the nozzle exit. The majority of published results from jet studies considered free, gravity driven and straight nozzle flow, where no disturbance from pump pulsation or pipe curvature was present. Such analyses should therefore only be used as a guideline.

5.3 Large gallery model tests

5.3.1 Investigation cases for visualisation

The visual recordings provided reference information for the oil behaviour inside the gallery, especially with respect to bulk flow and filling conditions. Four cases were specified for investigation, based on volumetric flow rate and rotational crank speed.

The flow rates were selected based on the demand to generate an oil jet with low to medium boundary breakup to provide a high catch rate and to reduce high impact splash of the jet on the gallery model. Tests with higher flow rates produced high levels of sideward droplet splashing, significantly affecting the visibility of the gallery by interfering with the viewing direction from the camera. The rotational speed was restricted by the power of the electric motor and limitation of balancing. The test cases are shown in Table 5.4.

Table 5.4 Flow assessment cases for large gallery model

Test	Rotational crank speed	Volumetric flow rate	Stroke	Flow regime
	rpm	*l/min*	*mm*	–
1	300	4.0	170	laminar
2	300	6.0	170	turbulent
3	600	4.0	170	laminar
4	600	6.0	170	turbulent

Images were recorded near the dead centres at a recording rate of 4500 *fps* with a resolution of $256 \times 256 pixels$. Higher recording speeds were considered, but were found to significantly reduce image resolution and thereby the visual sensitivity for flow identification and analysis.

The camera was placed at approximately one meter from the piston model. The distance was required to avoid oil splashing onto the camera lens, since the use of a splash screen guard was not practical due to the oil drops interfering with the view. In addition to improve the visibility of the flow and to enhance the contrast of the oil air separation surface, two 50 *W* halogen lamps were used. These were at the same distance as the camera to avoid safety issues with the temperature of the lamp and any potential splashing oil droplets.

The gallery was axi–symmetric with exception of the inlet and outlet holes, allowing recording of only one branch of the gallery as the flow in the other branch was deemed to be mirrored behaviour.

The test rig splash guard allowed only visibility of the moving gallery model from one outside direction. In order to investigate the in-gallery flow the model was rotated on the sliding frame cross-member. For each viewing position the nozzle position was rearranged to align the oil jet with the new position of the inlet hole. Care was taken to achieve identical impingement positions at the inlet hole for *TDC* and *BDC* position of the model.

Four camera positions were selected for the recording of the oil flow behaviour, as shown in Figure 5.11. The choice of recording positions was based on a preliminary visual study, investigating the flow behaviour along the gallery branch. The inlet position (**A**) was chosen because of the inflow of the jet and the high turbulence and mixing of flows. The outlet position (**D**) was of major interest because of the interference of exiting and re-entering flow of oil. The viewing position at 45°from the gallery inlet (**B**) was selected, as the oil flow showed a strong reduction of the turbulence. The position at 45°from the gallery outlet (**C**) was chosen due to the flow incorporating strong large-scale mixing of oil and air.

A fifth position was considered in the central part of the gallery branch (90°from the inlet), but could not be implemented due to limitations of oil nozzle arrangement. With the gallery model fitted to the top of the sliding frame cross-member the central viewing position led to the covering of the inlet and outlet of the gallery.

Figure 5.12 shows a cross-section of the gallery model defining the specific walls of the gallery. In particular the inward tilting surface of the outer gallery wall played a crucial role in the flow behaviour.

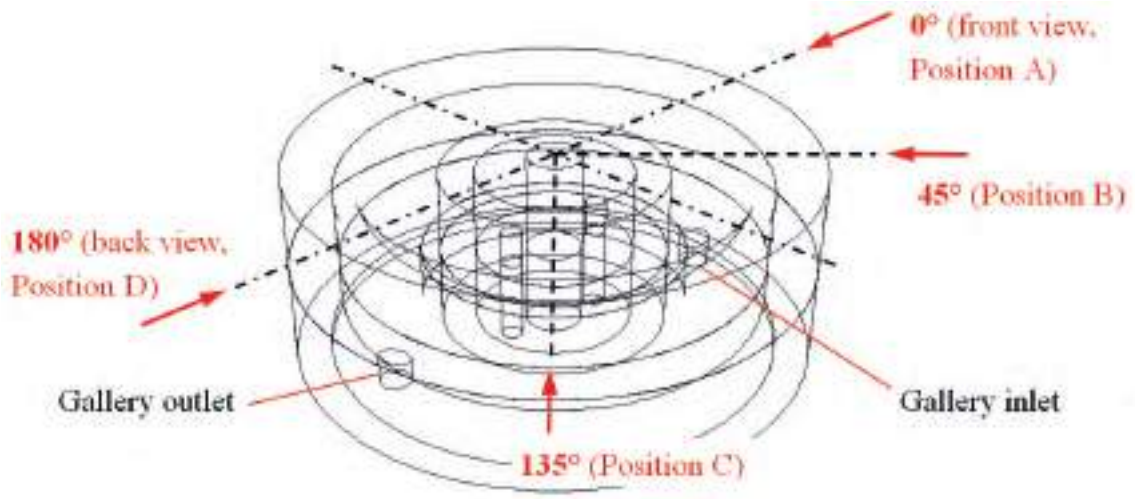

Fig. 5.11 Camera positions for flow recording of large gallery model

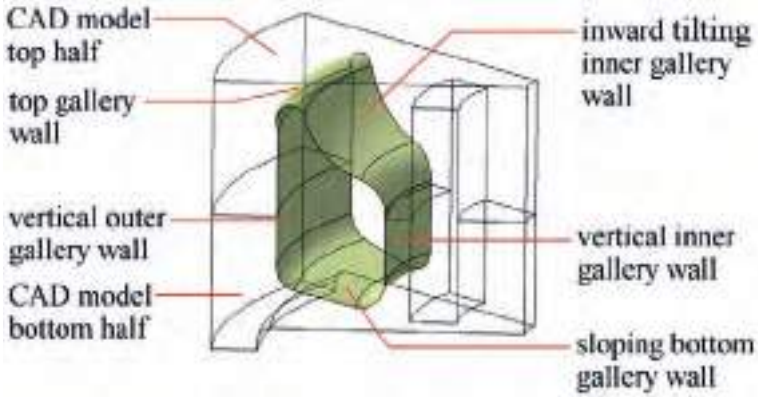

Fig. 5.12 Section of large gallery model with specified wall identifiers

The circular shaped outside surface of the gallery model required extra consideration with regards to the area of the gallery suitable for flow analysis. The recorded images would still show gallery flow in areas of the outer limits of the model, although no gallery was present in this location. The reason can be found in the refraction of light at the interface between the solid transparent gallery model material and the air outside the gallery. This led to a distorted view towards the outer part of the gallery prohibiting the analysis of the full gallery width. The problem is highlighted for a particular case shown in Figure 5.13. The top portion shows the cross-section of the *CAD* model, indicating the outer limit position of the internal gallery within the model. The bottom portion shows an image from the high-speed recording with internal flow pattern. It can be clearly seen that an air bubble is visible near the outside of the recorded image of the gallery model, although the gallery did not exist in this area.

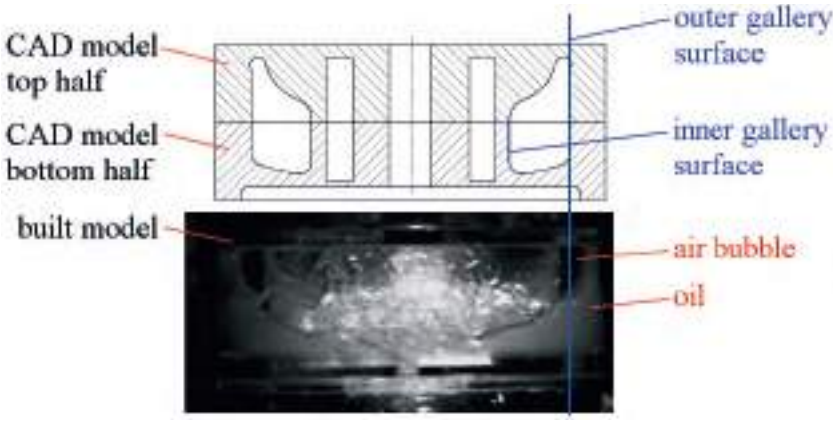

Fig. 5.13 Image showing distorted flow towards edge of large gallery model

The gallery height of 45 *mm* was covered by approximately 70 pixels. The movement of a flow feature, e.g. air bubble boundary, can only be traced within one pixel accuracy, or approximately 0.64 *mm*, which equated to a relative error of 1.4%. Besides the pixel resolution error, the presence of flow features outside the gallery surfaces introduced an additional error, which may be termed a viewing position error. Assuming a direct view towards the gallery centre (symmetry axis) the refraction did not produce an error, as the entry and exit angles were perpendicular to the surface. As the viewing direction moved towards the outside of the model the refraction angle changed and a viewing position error was introduced, until the maximum refraction angle was reached. There were also two refractions, one on the outside surface of the model and one at the outer gallery surface. For viewing positions between the centre axis and 35.6 *mm* from the centre axis, the recorded flow related to flow between the inner and outer gallery surface. This position was termed maximum outside view, as shown in Figure 5.14. Beyond this point the recorded flow should be treated with care.

In order to keep the viewing position error at a minimum to allow good comparability with simulation data it was decided that the error should not be larger than one pixel of the image resolution. The safe distance was found to be approximately 22.5 *mm* from the centre axis, allowing for a safe image analysis width of 45 *mm*, giving a total error from pixel resolution and refraction as 2.8%. This was deemed sufficient accurate for the study.

In order to identify larger air bubbles in the gallery that may be hidden within the oil flow, the use of a laser was considered, but the aeration from the jet breakup prior to entering the gallery and the strong mixing of oil and air at the inlet section prohibited the view of the laser-enhanced flow pattern inside the gallery. Furthermore the refraction of the laser at

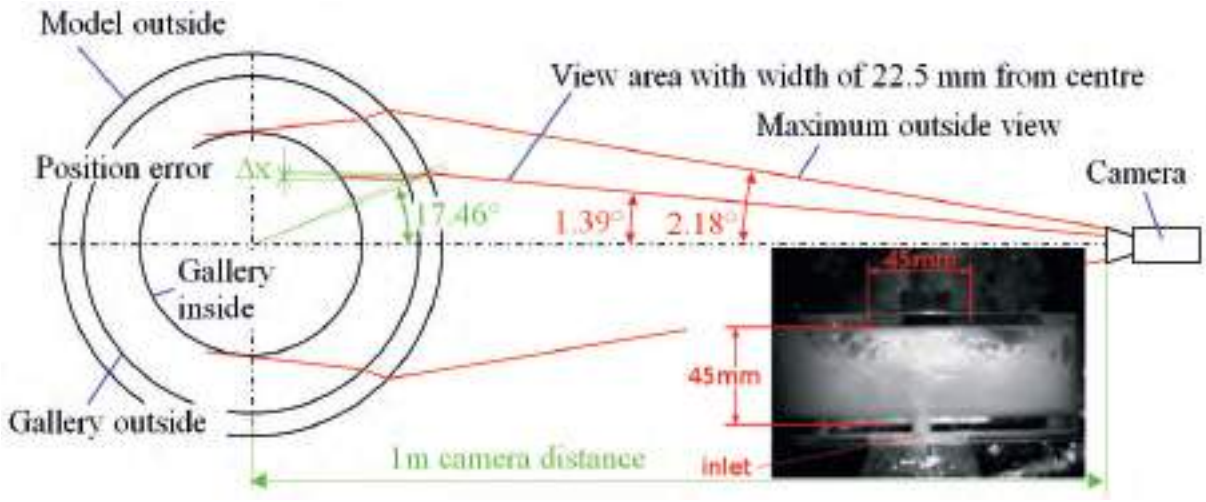

Fig. 5.14 Schematic of maximum suitable view angle and usable width for flow analysis of large gallery model

the gallery surface also led to a reduction in laser brightness and did not lead to images of sufficiently improved quality for analysis. Therefore the laser was not used.

5.3.2 Results at *BDC*, *600 rpm* and *4.0 l/min*

The following images show the bulk flow behaviour inside the gallery of the large gallery model. The arrows indicate the direction of the flow, either for the air oil interface (blue colour) or the bulk oil flow (red colour).

Figures 5.15 to 5.17 show a selection of images highlighting the flow behaviour of the oil and air within the gallery from various view angles at *BDC*. During the downward stroke the oil inside the gallery occupied the full space from top to bottom only with larger air bubbles appearing near the gallery exit. As the gallery approached the *BDC* the oil started to move towards the bottom of the gallery primarily as a result of the deceleration of the gallery approaching the standstill at *BDC*. The flow behaviour can be seen along the gallery length, from inlet to exit. Additional information about gallery filling including positions before and after *BDC* and *TDC* is shown in Appendix B.

At the inlet section the oil jet was passing through the layer of oil located at the bottom of the gallery (**A**) at all times, as shown in Figure 5.15. The oil jet had also sufficient momentum to force its way through the gallery bottom oil layer to impact on the inward facing inner gallery wall. The impact diverted the flow away from the inlet hole into the gallery (**B**) with partial circulation in the bottom oil layer near the inlet (**C**). This flow was also encouraged

by the large amount of air at the top of the gallery, especially after the *BDC*. Furthermore, despite the inertial movement of oil towards the bottom of the gallery, there was little oil exiting through the inlet hole (**D**), as compared to the outlet, also indicating the high jet inertia relative to the inertial oil movement.

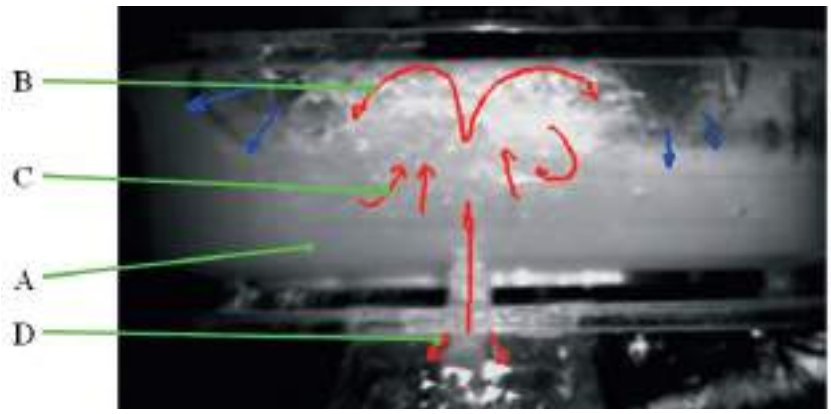

Fig. 5.15 Flow behaviour large gallery model inlet sections at *BDC* for 600 rpm and 4 l/min flow rate (front view)

Due to the translucence of the oil it was unfortunately not possible to identify the precise conditions at the inlet hole, whether air drawn into the gallery by the jet built an extra separation layer between internal gallery oil and entering jet.

Figure 5.16 shows the movement and deformation of the larger air bubbles in the mid-gallery sections (**E**). The air movement was mainly dictated by the flow of the oil, which itself was dictated by the inertial forces on the oil (**F**) and the availability of space (air bubbles). The smaller-sized air bubbles were dragged along in the oil stream and followed the main oil bulk flow (**G**). A clear size difference between the independent moving air bubbles and oil flow driven air bubbles could not be determined due to insufficiencies in the images resolution.

There was strong oil outflow from the outlet (**H**) during the whole *BDC* position range, as a result of the deceleration of the gallery model before *BDC* and acceleration after *BDC*. This outflow continued during parts of the upward movement. There was also “back-lash” or “swirl” induced oil flow towards the outlet of the gallery, best visible where large air bubbles were present (**I**), as indicated in Figure 5.17.

As the oil was distributed across the gallery height during the downward stroke, the deceleration near the *BDC* forced the oil onto the gallery bottom surface at *BDC*, but due to a larger oil mass at the gallery outside and the sloping bottom gallery surface, the oil

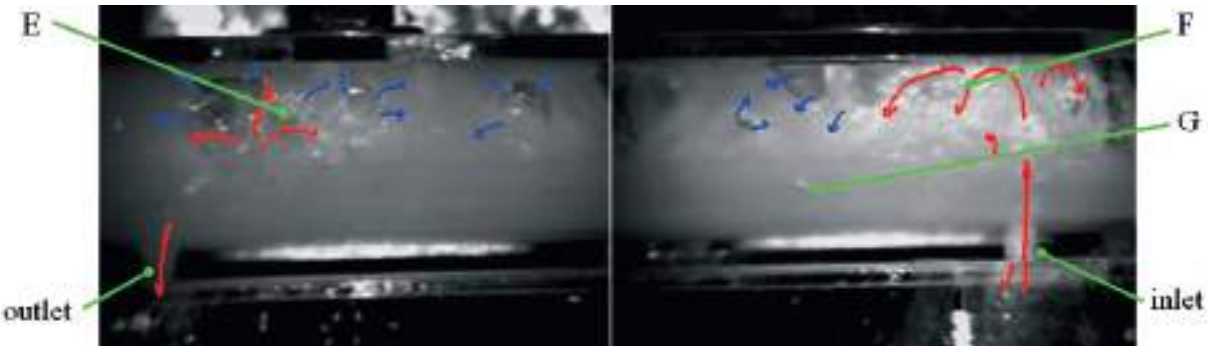

Fig. 5.16 Flow behaviour large gallery model mid-gallery sections at *BDC* for 600 rpm and 4 l/min flow rate (135° and 45° view from inlet)

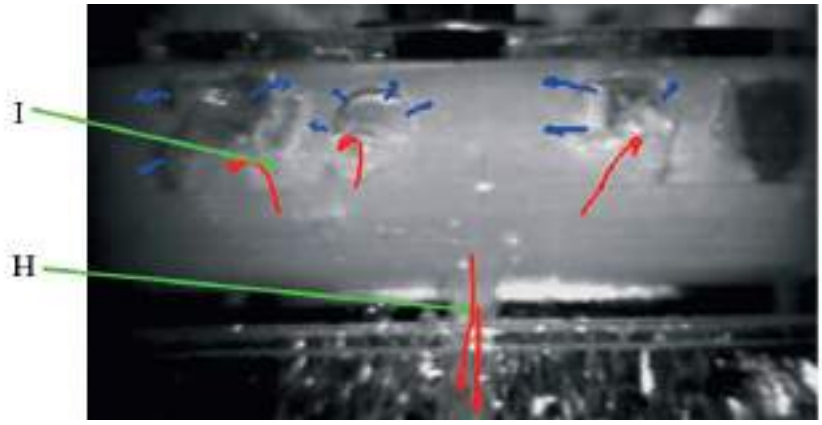

Fig. 5.17 Flow behaviour large gallery model exit sections at *BDC* for 600 rpm and 4 l/min flow rate (rear view)

flowed towards the inner gallery surface and was pushed up the inside and then towards the centre due to the inward tilting inner gallery wall. Figure 5.18 highlights the flow behaviour in the cross-section, identifying stages of occurrence. As can be seen in Figure 5.17 and indicated in Figure 5.18, there occurred an upward swirl inside the gallery, eventually leading to insufficient amounts of oil at the exit, leading to a reduced outflow and breakup.

The onset of forced outflow as a result of internal flow behaviour, not gravitational pull, occurred at approximately 60° *bBDC* and had a near constant flow rate behaviour until 40° *aBDC*. After this the flow rate reduces, until at half stroke (90° *aBDC*) the outflow almost terminated.

5.3.3 Results at *TDC*, *600 rpm* and *4.0 l/min*

Figures 5.19 to 5.21 show the behaviour of air and oil inside the gallery at *TDC*. Additional images showing also the behaviour before and after *TDC* are provided in Appendix B.

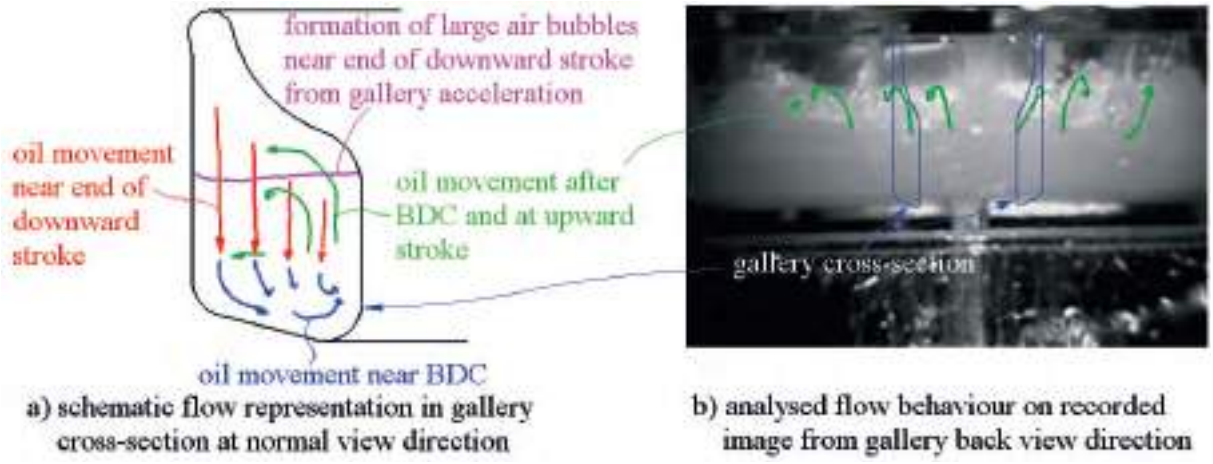

Fig. 5.18 Flow inside gallery cross-section; a) schematic representation of flow near *BDC*, b) recorded flow conditions at gallery exit 30° *aBDC*

Overall it can be seen that when the gallery reached the *TDC* the majority of the oil was distributed across the height of the gallery, with larger air bubbles present near the inlet and in the further sections of the gallery. The distribution was a result of the reduction of the gallery velocity approaching *TDC*, where the inertia forces dictated the movement. The gallery cross-section had a reduced radial depth at the top in comparison to the gallery bottom, which was significantly broader. The reduced space at the gallery top provided less space for the oil and the only flow was therefore towards the air bubbles pushing them downwards inside the gallery. The locations of the air bubbles played a crucial role in the direction of the flow.

Air was drawn into the gallery together with the oil jet (**J**), as the oil jet had widened as a result of the jet breakup and the larger distance between gallery inlet and nozzle. This also caused turbulence at the inlet (**K**), as indicated by the formation of many small-sized air bubbles (**L**) (white spots due to reflection of light), shown in Figure 5.19. The larger-sized air bubbles at the gallery bottom (**M**) were a result of the large content of air present inside the gallery top at *BDC*, but not from the jet entry.

As the oil was pushed upward in the mid-gallery sections (**N**) the smaller width at the top and hence lower volume prohibited collection on top, as shown in Figure 5.20. The oil was flowing to the areas of lowest resistance, which were the large air bubbles in the later mid-gallery sections (**O**). This also introduced a flow towards the gallery exit (**P**). The large air bubbles were broken down and formed a low layer at the gallery bottom (**R**), which moved towards the exit, but also back towards the inlet channel leading to some circulation of the air

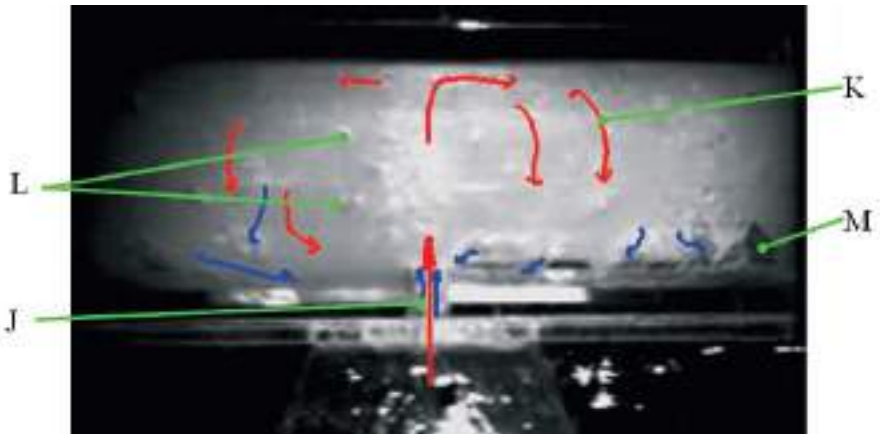

Fig. 5.19 Flow behaviour large gallery model inlet sections at *TDC* for 600 rpm and 4 l/min flow rate (front view)

in the mid-gallery sections. This caused a circulating flow over the full crank cycle between the inlet and the later mid-gallery sections.

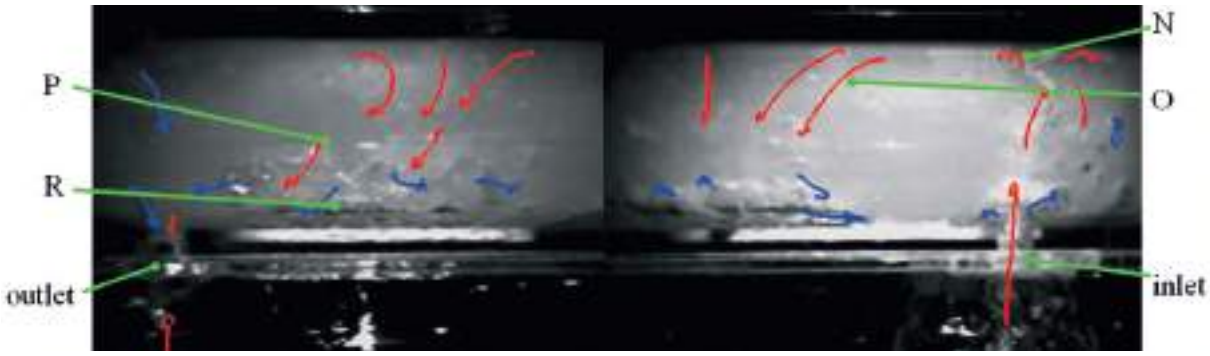

Fig. 5.20 Flow behaviour large gallery model mid-gallery sections at *TDC* for 600 rpm and 4 l/min flow rate (135° and 45° view from inlet)

The breakup of the air bubbles at the bottom and the mixing with some of the oil led to a forced movement of both towards the exit channel (**S**), as indicated in Figure 5.21. The result was a combined flow of oil and air exiting the gallery through the outlet channel. Whilst the flow of air was mainly outward, the flow of oil showed both, in and outflow (T).

During the upward stroke oil was flowing out of the exit hole, but still with a resulting upward movement direction, although with a lower velocity than the gallery model velocity. While the gallery velocity was dictated by the driving conditions and was prescribed by the rotational crank speed, the oil velocity was a function of the outflow velocity and the experienced gravitational forces and did not follow the rules of the gallery velocity. This resulted in upward moving oil, while the gallery was at standstill at *TDC*, leading to an impact between exiting (downward flowing) internal gallery oil and entering (upward moving)

external oil. Depending on the position of the upward moving oil, which depended on the direction of the outflow during the upward stroke, there occurred pure outflow, pure inflow or a mix of both.

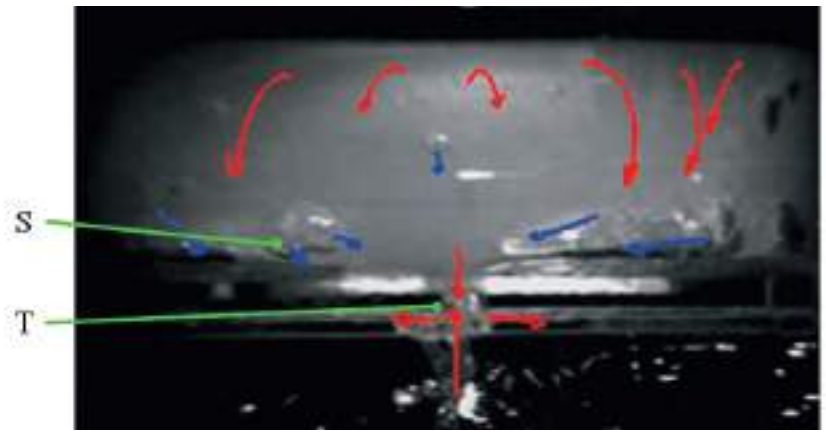

Fig. 5.21 Flow behaviour large gallery model exit sections at *TDC* for 600 rpm and 4 l/min flow rate (back view)

Figure 5.22 shows a schematic representation of the movement of oil in the full gallery branch explicitly highlighting the colliding flows of oil from the inlet and exit sections.

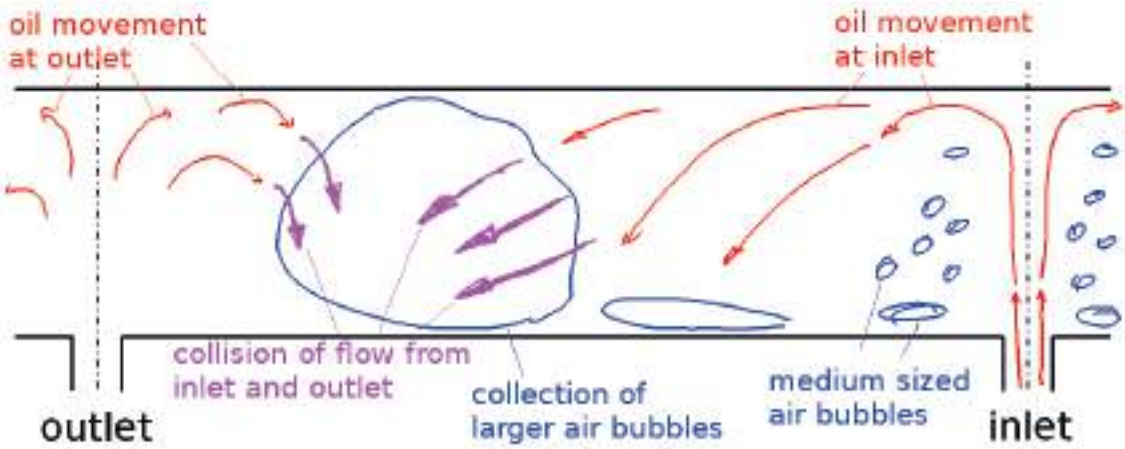

Fig. 5.22 Schematic representation of oil flow direction inside gallery after *TDC*

5.3.4 Commonalities and differences between cases

Figures 5.23 to 5.26 highlight the gallery filling and air distribution for the investigated cases identified in Table 5.4 on page 109.

At the *BDC* the largest air content in the gallery inlet sections was located at the gallery top wall, as shown in Figure 5.23. As shown previously, the inertia driven flow was the

source of positioning the oil at the gallery bottom. Although the inertia effects increased with rotational speed the oil jet showed similar behaviour of piercing through the bottom oil layer, indicating sufficient high momentum to control inflow. There was consistency in the flow behaviour for all flow rates and engine speeds, but the filling height showed variations with a tendency of slightly lower filling at higher flow rates, whereby the rotational speed had less influence on filling.

While the inertia effects placed the oil at the gallery bottom in the inlet sections, there was still oil distributed across the gallery height in the outlet sections, as shown in Figure 5.24. The reason was found in the collision of the flows from both gallery branches. The amount of oil flowing in the gallery branches towards the outlet was significantly more than the amount of oil being able to pass through the outlet channel, whereby the non-exiting oil was partially pushed upwards in the gallery. The air bubbles were defined with sharper boundaries, indicating a reduced turbulence with less air bubble surface breakup. It can also be seen that the largest amount of air was present for the lower crank speeds, which was the opposite condition to the inlet section.

As the inertia driven flow also led to swirling flow inside the gallery, the reduced crank speed caused lower inertia forces and reduced velocities, collecting more oil at the inlet, which otherwise would be circulated away from it, as indicated in Figure 5.22. The swirling behaviour in the radial cross–sections at *BDC* was also present, although larger gallery filling reduced the effect.

When the gallery was at the *TDC* the majority of the air was located at the bottom of the gallery, as shown in Figure 5.25. The stationary condition of the gallery at *TDC* allowed the inertia driven flow of the oil to progress to the top of the gallery. There was minimal difference in the actual location of the larger air bubbles between the various conditions and the frontal size of them did not differ significantly. It can also be seen that there were more medium-sized air bubbles present for the lower flow rates, although no significant influence of the engine speed could be determined. It may be noted that the flow velocities may be different between the cases, but a sufficient accurate determination of the velocities was not possible from the recorded still frames.

As identified previously the inertia effects on the oil determined the position of the air bubbles in the gallery outlet sections with low effects of the gallery flow from the inlet. Figure 5.26 shows that at 600 *rpm* the majority of the air was located at the gallery bottom,

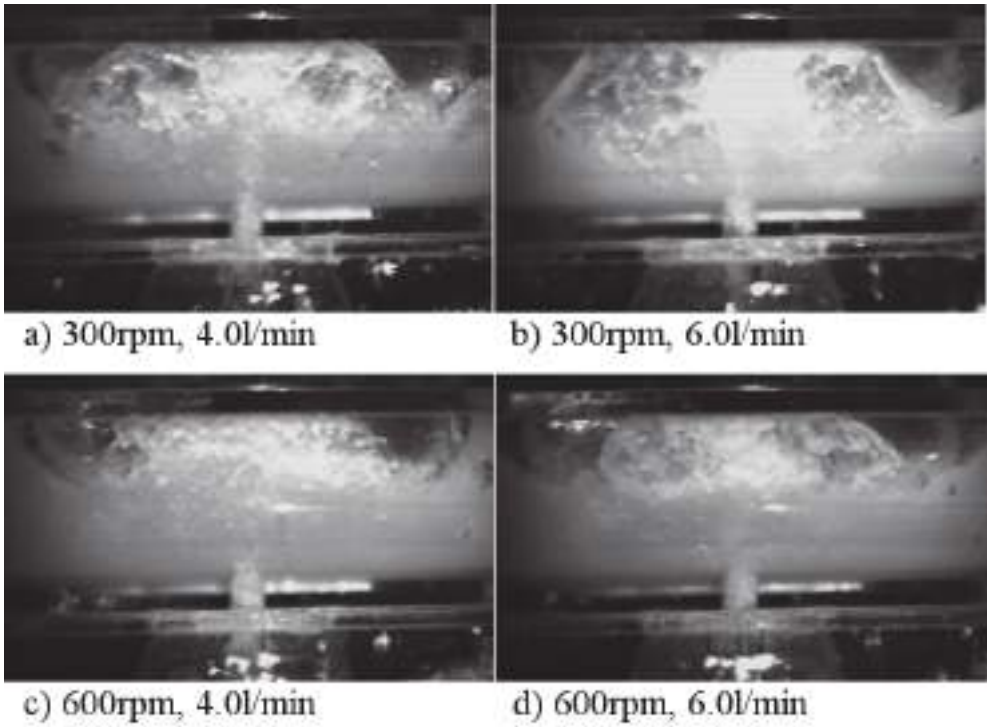

Fig. 5.23 Large gallery model filling of inlet sections at *BDC* and for different flow rates and crank speeds

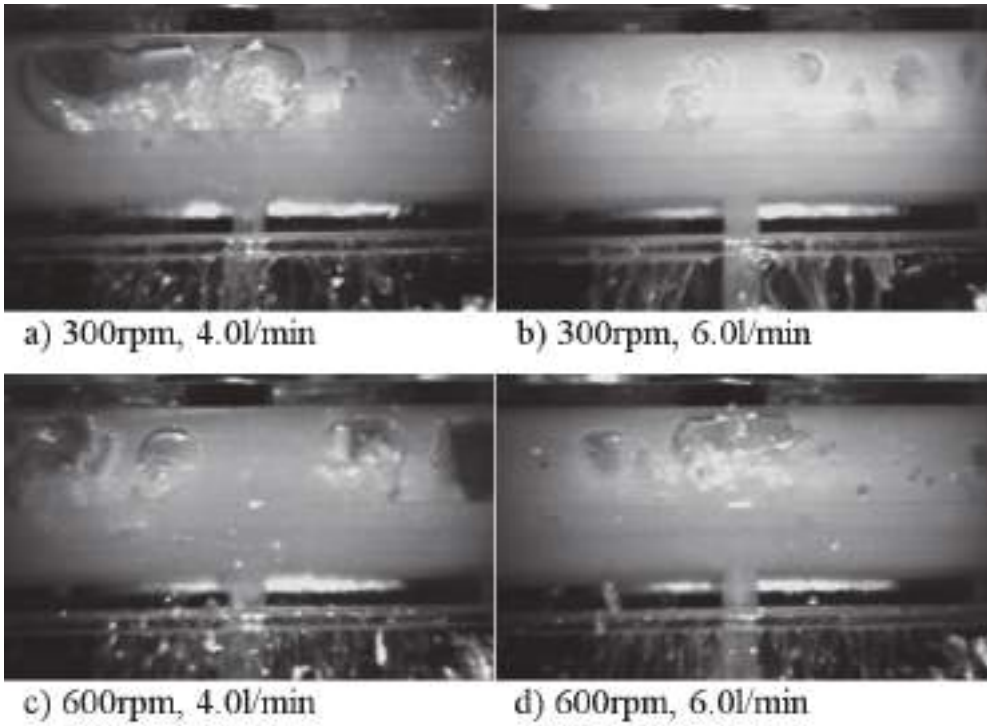

Fig. 5.24 Large gallery model filling of outlet sections at *BDC* and for different flow rates and crank speeds

while at 300 *rpm* the air was still in transit and had not fully reached the gallery bottom. This indicated that with higher rotational crank speed the inertia effects were increasingly controlling the flow inside the gallery, particular with the absence of the forced inflow conditions from the oil jet.

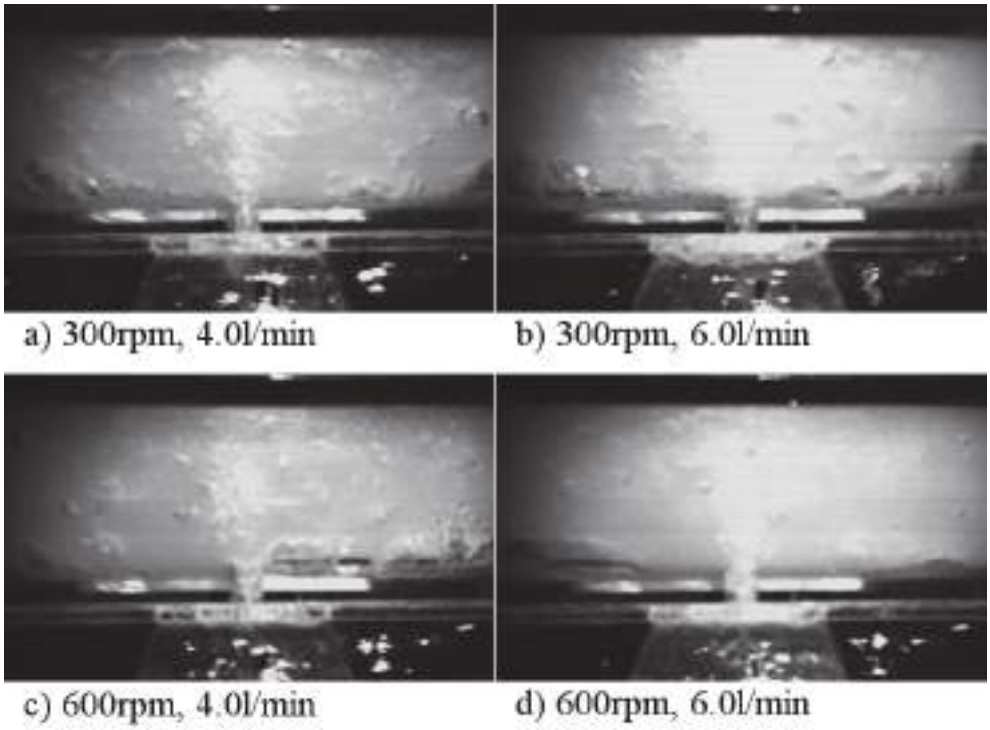

Fig. 5.25 Large gallery model filling of inlet sections at *TDC* and for different flow rates and crank speeds

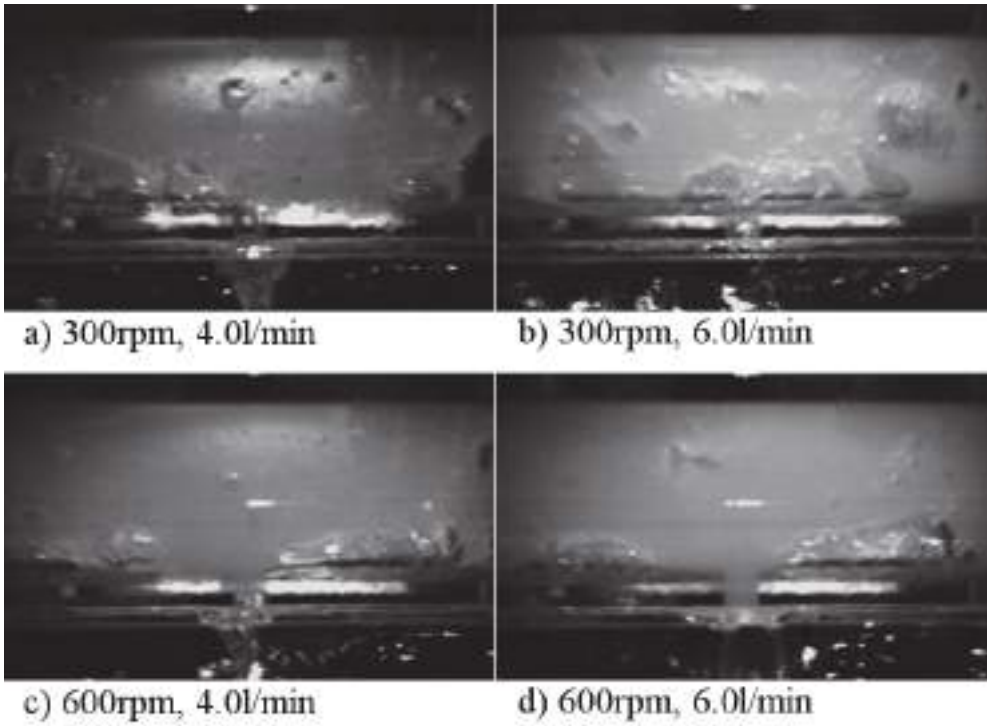

Fig. 5.26 Large gallery model filling of outlet sections at *TDC* and for different flow rates and crank speeds

5.4 Small gallery model tests

5.4.1 Investigation cases for visualisation

The higher possible speed range for the small gallery model allowed the investigation of a wider range. The selected test cases are shown in Table 5.5.

Table 5.5 Flow assessment cases for large gallery model

Test	Rotational crank speed	Volumetric flow rate	Stroke	Flow regime
	rpm	*l/min*	*mm*	–
1	750	1.651	88	laminar
2	500	1.105	88	laminar
3	500	2.121	88	laminar
4	1000	1.105	88	laminar
5	1000	2.121	88	laminar

The axi-symmetric cross–section of the small gallery model allowed for the recording of the flow behaviour within one gallery branch. The flow was deemed to be of symmetric behaviour, as highlighted for the large gallery model. Images were taken at 4500 *fps* with a resolution of 256 $\times$ 256 pixels. The small height of the gallery and the short stroke in relation to the gallery diameter allowed the recording of the full stroke length at once, allowing analysis of the flow inside the gallery during a complete crank cycle.

The reduced height of the model also allowed the fixation at the bottom of the slider frame cross–member, providing viewing conditions for the inflow and outflow without obstruction or limitation in visibility and flow for different viewing positions. Furthermore the gallery was smaller in diameter, as compared to the large gallery model, with the consequence that three viewing positions of the gallery were sufficient to capture the flow. Figure 5.27 shows the viewing position setup for imaging. The rearrangement of the jet with regards to the inlet hole was necessary for each view position, as found for the large gallery model. The arrangement was conducted at static conditions for *BDC* and *TDC* position. Extra care was taken to reproduce identical flow conditions inside the gallery before commencement of transient image recording.

Figure 5.28 shows the definition of the wall names of the small gallery model for better understanding of the description of the flow behaviour inside the gallery.

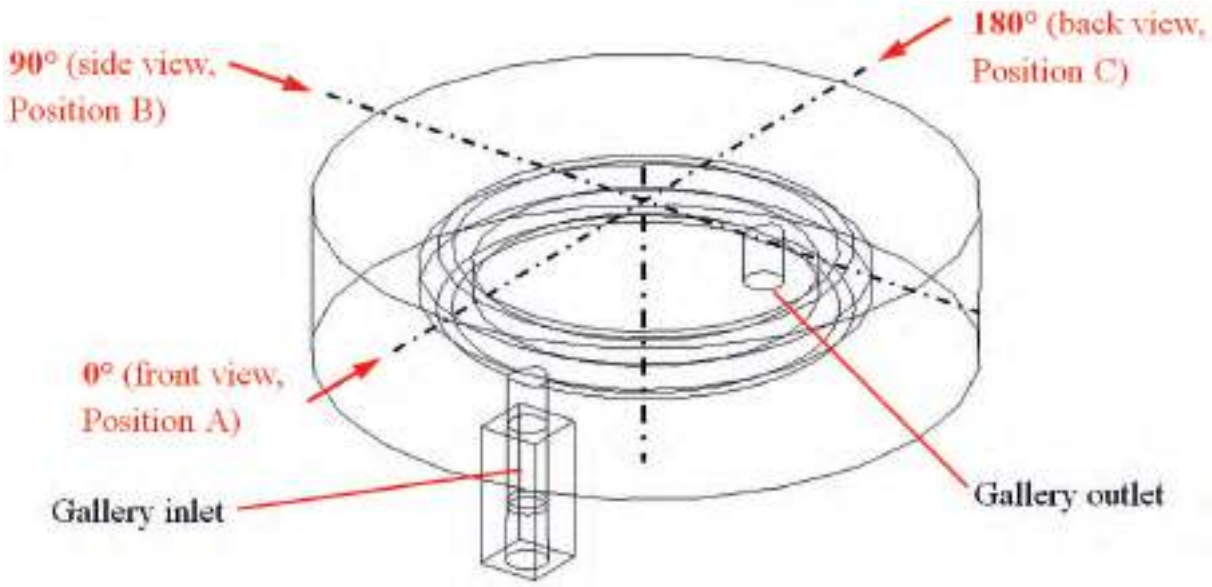

Fig. 5.27 Camera positions for flow recording o small gallery model

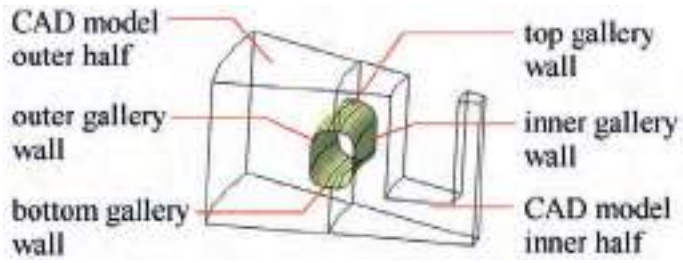

Fig. 5.28 Section of small gallery model with specified wall identifiers

There were limitations concerning the suitable view width for analysis, as experienced with the larger gallery model. The refraction of the light, as it passed from inside the gallery into the model material and then out of the model again to the camera, caused a distorted view of the inside. Figure 5.29 shows a comparison between the gallery model cross-section and a recorded image of the conditions inside the gallery, clearly identifying the area of the gallery, where the highest distortions occurred. It can be seen that there were still flow features visible, although there was no physical gallery present.

The gallery height of 10 *mm* was covered by approximately 22 pixels. The movement of a flow feature, e.g. air bubble boundary, could only be traced within one pixel, or approximately 0.46 *mm*, which equated to a relative error of 4.6%.

With increasing distance from the centre axis the induced viewing position error due to refraction on the outer model surface curvature also increased, as described previously for the large gallery model. In order to keep the viewing position error at a minimum to allow

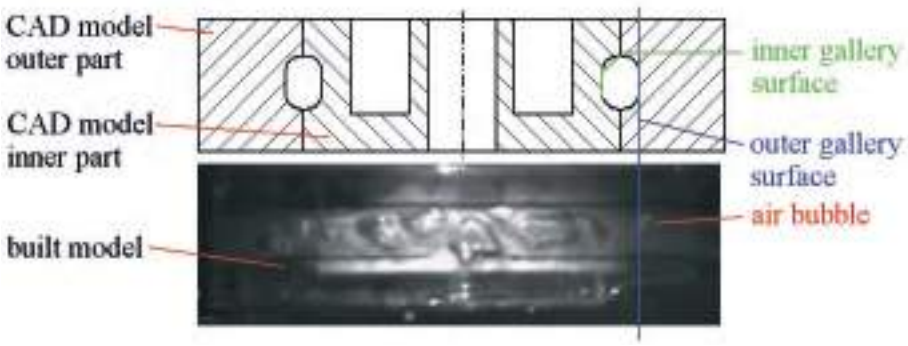

Fig. 5.29 Image showing distorted flow towards edge of small gallery model

good comparability with simulation data it was decided that the error should not be larger than one pixel of the image resolution. The safe distance was found to be approximately 23.2 *mm* from the centre axis, as shown in Figure 5.30. This allowed for a safe image width of 46.4 *mm*, giving the total pixel resolution error and refraction error as 9.2%. It was still deemed sufficient accurate for the study, given the limitation of the camera resolution.

Figure 5.30 also shows the relative view angle of the gallery for the safe viewing condition. At a total view angle of 27.6°to the left and right of the centre axis (full section width 55.2°) the angle was deemed large enough to allow three recording positions. The maximum outside view was determined as 32 *mm* from the centre and any flow captured beyond this point should be treated with care.

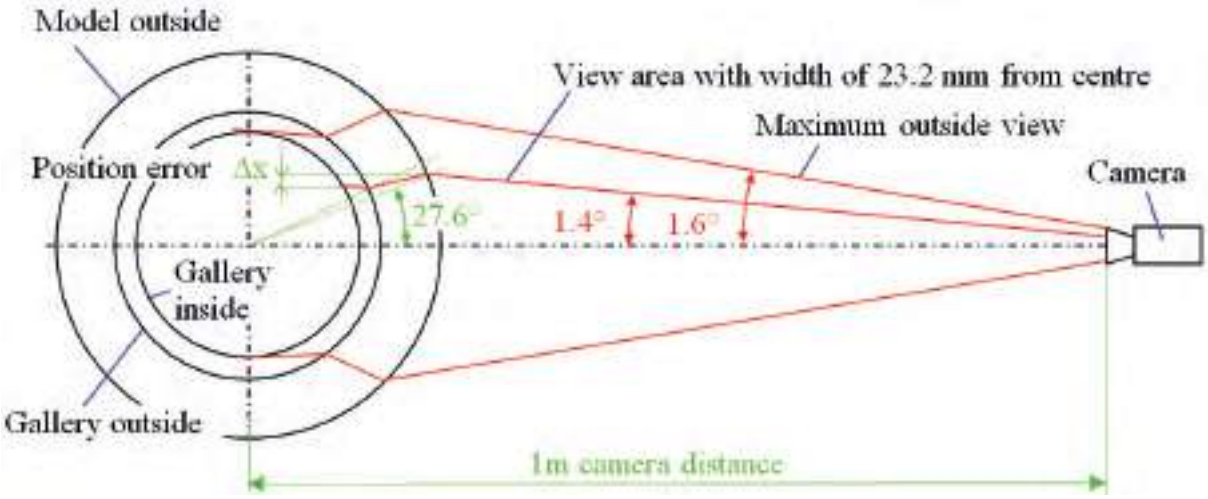

Fig. 5.30 Schematic of maximum suitable view angle and usable width for flow analysis of small gallery model

It should also be noted that there was a positioning error occurring due to the curvature of the gallery at the top and bottom. As the gallery was investigated for the position of air and

oil along the length, this error might be omitted. If gallery filling analysis with respect to oil fill ratio should be conducted, then this should be included.

5.4.2 Conditions at *BDC*, *750 rpm* and *1.65 l/min*

For the gallery movement from before *BDC* to after *BDC* permanent oil inflow occurred (**A**), impacting on the top wall of the gallery. The flow deflected sideways into the gallery branches (**B**) showing features of strong oil and air mixing, and subsequent features of high turbulence. While approaching the *BDC* the deceleration of the gallery forced a wall-bound downward flow (**C**). Although it cannot be attributed to gallery deceleration, the opposing movement of the gallery may have produced a direction driven surface reflection, leading to a combination of sideways deflection and downward reflection as shown in Figure 5.31. At the *BDC* the flow changed to a more horizontal direction along the gallery top, as the opposing movement reflection was eliminated.

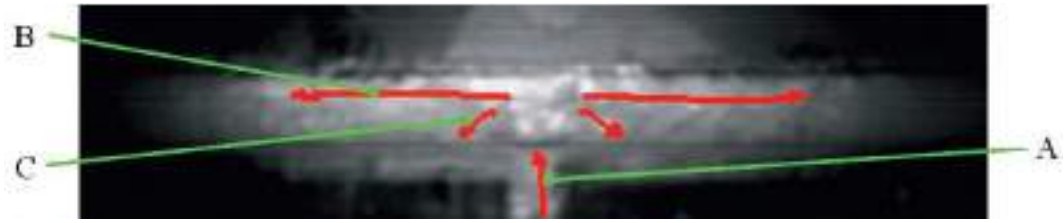

Fig. 5.31 Flow behaviour small gallery model inlet sections at *BDC* for 750 rpm and 1.651 l/min flow rate (front view)

Approximately 60°into the gallery branch from the inlet channel the turbulent features deteriorated and the formation of larger air bubbles occurred (**D**). As the gallery approached *BDC* the oil was forced to the bottom of the gallery due to deceleration (**E**). The small gallery size forced the air bubbles to move in the same direction as the inflow driven oil flow (**F**), as indicated in Figure 5.32. The bulk flow velocities of oil and air were different, with the latter being slower, producing a slight bubble rotation effect.

As the flow reached the outlet section the majority of outflow was oil (**G**), as the air bubbles were located and collecting at the gallery top (**H**), as shown in Figure 5.33. There was still continuing push on oil and air from the mid-gallery section and both moved towards the outlet (**I**).

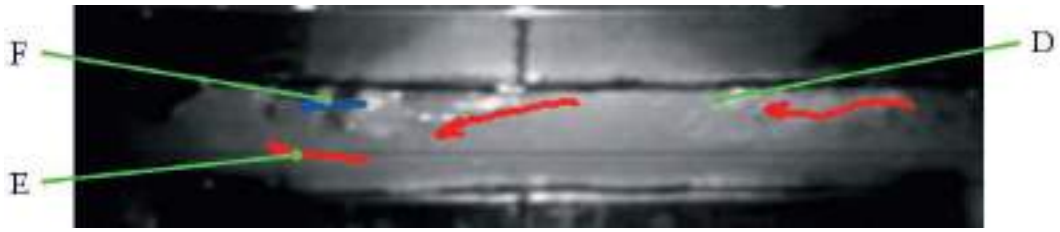

Fig. 5.32 Flow behaviour small gallery model mid-gallery sections at *BDC* for 750 rpm and 1.651 l/min flow rate (side view)

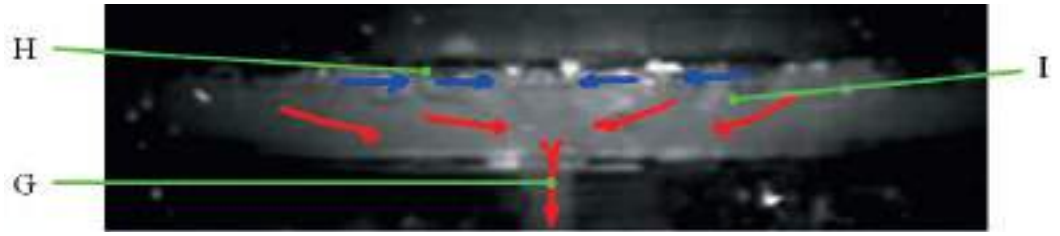

Fig. 5.33 Flow behaviour small gallery model outlet sections at *BDC* for 750 rpm and 1.651 l/min flow rate (back view)

5.4.3 Conditions at *TDC*, *750 rpm* and *1.65 l/min*

At the inlet section the flow near the *TDC* showed a shorter high turbulence region. In comparison to the *BDC*, the distance from the inlet channel was only 40°. There was still a mixture of oil and air entering the gallery (**J**), as shown in Figure 5.34. The increased distance of the inlet from nozzle exit reduced the strength of the inflow and therefore the protruding length of the turbulence region. At the same time the approaching of the *TDC* caused a movement of the oil towards the gallery top, resulting in a horizontal oil flow into the gallery due to the oil jet (**K**) and forcing air bubbles into the mid-gallery section (**L**).

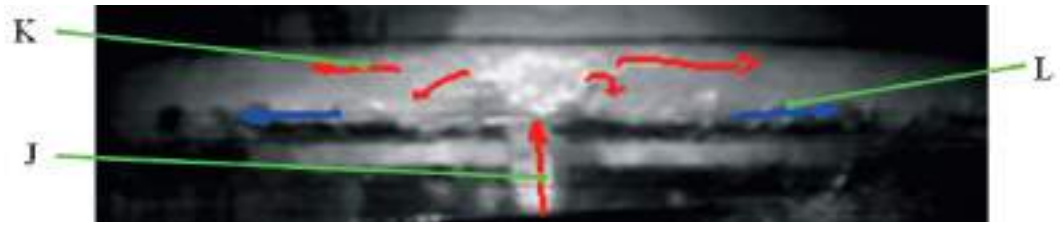

Fig. 5.34 Flow behaviour small gallery model inlet sections at *TDC* for 750 rpm and 1.651 l/min flow rate (front view)

Beyond the high turbulence region the formation of larger scale air bubbles took place. The air bubbles were located at the bottom of the gallery due to the inertia effects on the oil (**M**). These were sufficiently strong to balance the height of air bubbles at the *TDC* across the gallery length, as shown in Figure 5.35. Although inertia played a strong role in the flow

behaviour inside the gallery, particularly on the position of air, the flow was mainly driven by the oil inflow into the gallery (**N**). The small gallery size did not allow for large scale vertical flow, as seen in the large gallery model.

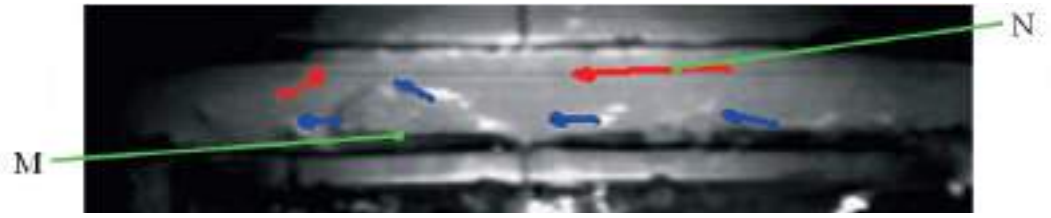

Fig. 5.35 Flow behaviour small gallery model mid-gallery sections at *BDC* for 750 rpm and 1.651 l/min flow rate (side view)

Figure 5.36 shows the flow in the outlet sections at *TDC*. During the upward movement of the gallery a permanent flow of air and oil towards the exit occurred (**O**), but only near the *TDC* the inertia effects on the oil were strong enough to force the flow. The majority of the air was found at the gallery bottom (**P**) and as the gallery came to a standstill the outflow changed from oil to air until the larger air bubbles had exited. Simultaneously there was still flow of air and oil from the mid-gallery sections towards the outlet channel. When the gallery started to move downward, the outflow changed to a combination of oil and air again, depending on the amount of air present and the flow conditions in the mid-gallery section.

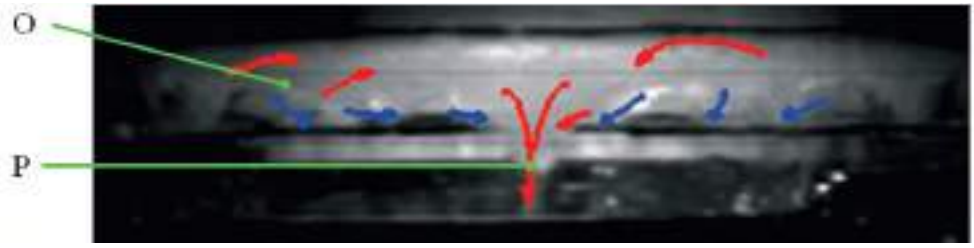

Fig. 5.36 Flow behaviour small gallery model inlet sections at *BDC* for 750 rpm and 1.651 l/min flow rate (front view)

5.4.4 Commonalities and differences between cases

The main location of the air inside the gallery at *BDC* was at the top of the gallery and was common for all crank speeds, flow rates and gallery branch positions, as shown in Figure 5.37. There occurred fairly clear oil bulk flow for the lowest flow rates of 1.105 l/min, indicating little mixing of the oil and air, particularly with regards to air entrainment. At a crank speed of (500 rpm) were also medium-sized air bubbles present at the inlet (front view), which

started to combine into larger-sized air bubbles approximately 40°from the inlet channel. This position also coincided with the end of the inflow generated turbulence region, which was the driving factor for the air combination.

With increasing flow rate the amount of entrained air increased, clearly indicated by the translucent gallery filling. In addition the length of the turbulence region caused by the jet entry increased. The longest distance of turbulence was found for 500 rpm and 2.212 l/min, which reached nearly 80°from the inlet. A comparable length was also found for 750 rpm at 1.651 l/min, indicating that the crank speed had a smaller influence on the inlet turbulence than the flow rate and jet velocity respectively.

The lowest flow rate of 1.105 l/min showed the highest amount of oil in the gallery, with the location of the air in the gallery being at near identical positions, indicating an independence from crank speed as well.

At the *TDC* the air was found on the gallery bottom along the gallery length, as shown in Figure 5.38, due to the inertia forces on the oil, as the direction of the gallery changed. Furthermore the same air entrainment in the oil was present as for the *BDC*. The increased distance of the nozzle from the gallery did not have a significant effect on the air entrainment.

There occurred less length of inlet turbulence region from the inlet channel. In comparison to the *BDC* cases with a maximum furthest distance of 80°, the turbulence region length at *TDC* was only approximately 40°from the inlet channel. The increased distance from the nozzle exit led to reduction in oil jet velocity and momentum due to longer occurrence of air resistance on the outside of the jet and partially by gravitational effects. The increased distance also led to widening of the jet cross-section as it reached the inlet channel, further reducing momentum due to channel wall contact effects.

A comparison of air content revealed that an increase of crank speed, at constant flow rate, led to lower amount of air. This can be seen particularly at the side view, where a comparison of 500 rpm and 1000 rpm, both at 1.105 l/min, showed an air occupation of approximately 80% and 50% of the gallery height respectively. An increase in flow rate at constant speed showed an increase in oil filling, although the increased air entrainment would contribute to the overall air content. The combination of jet inflow driven forward flow and inertia controlled air positioning resulted in a majority of the air escaping through the outlet hole, before the oil was exiting.

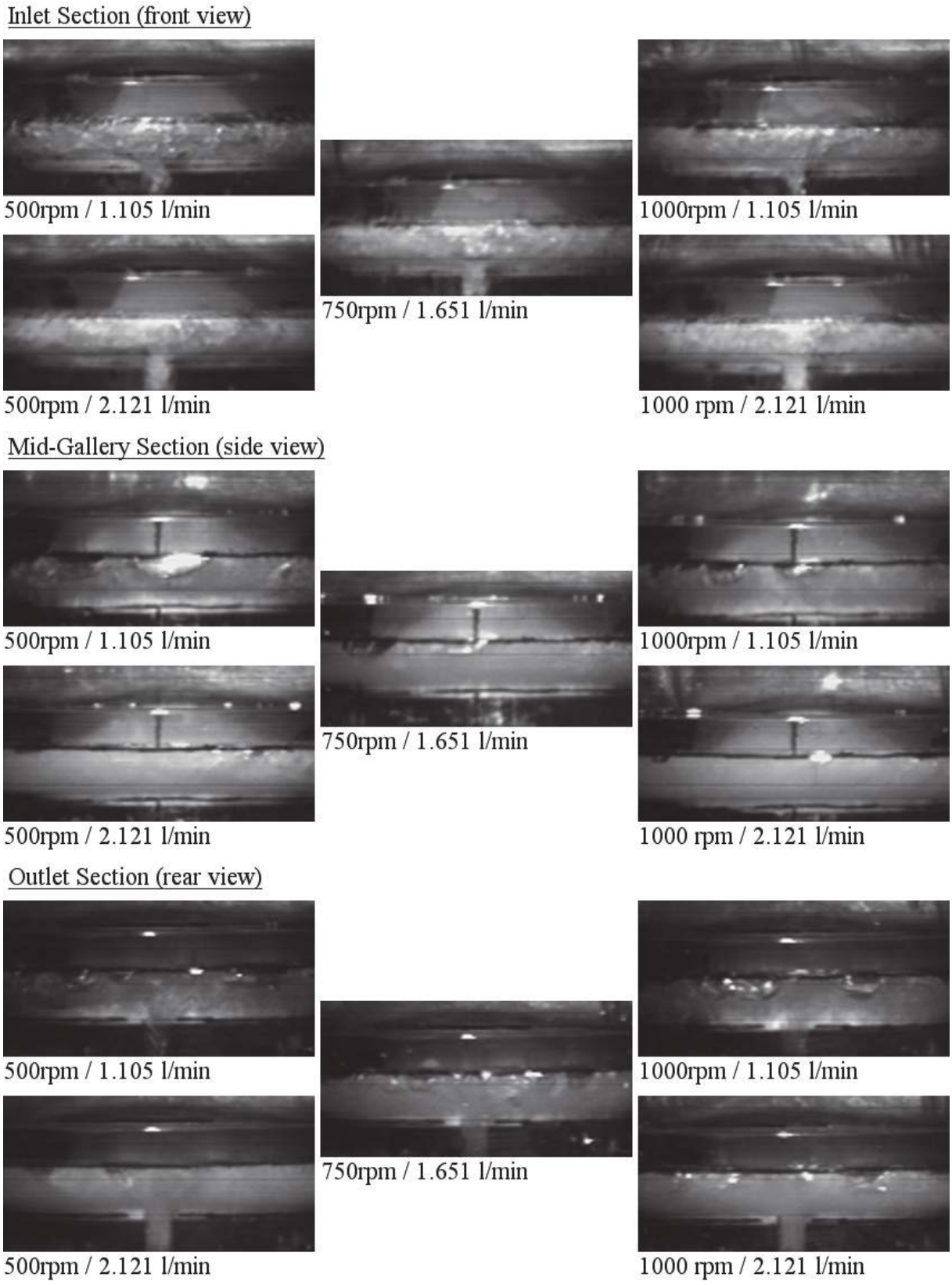

Fig. 5.37 Flow behaviour in gallery of small gallery model at BDC for recorded rotational crank speeds and oil flow rates

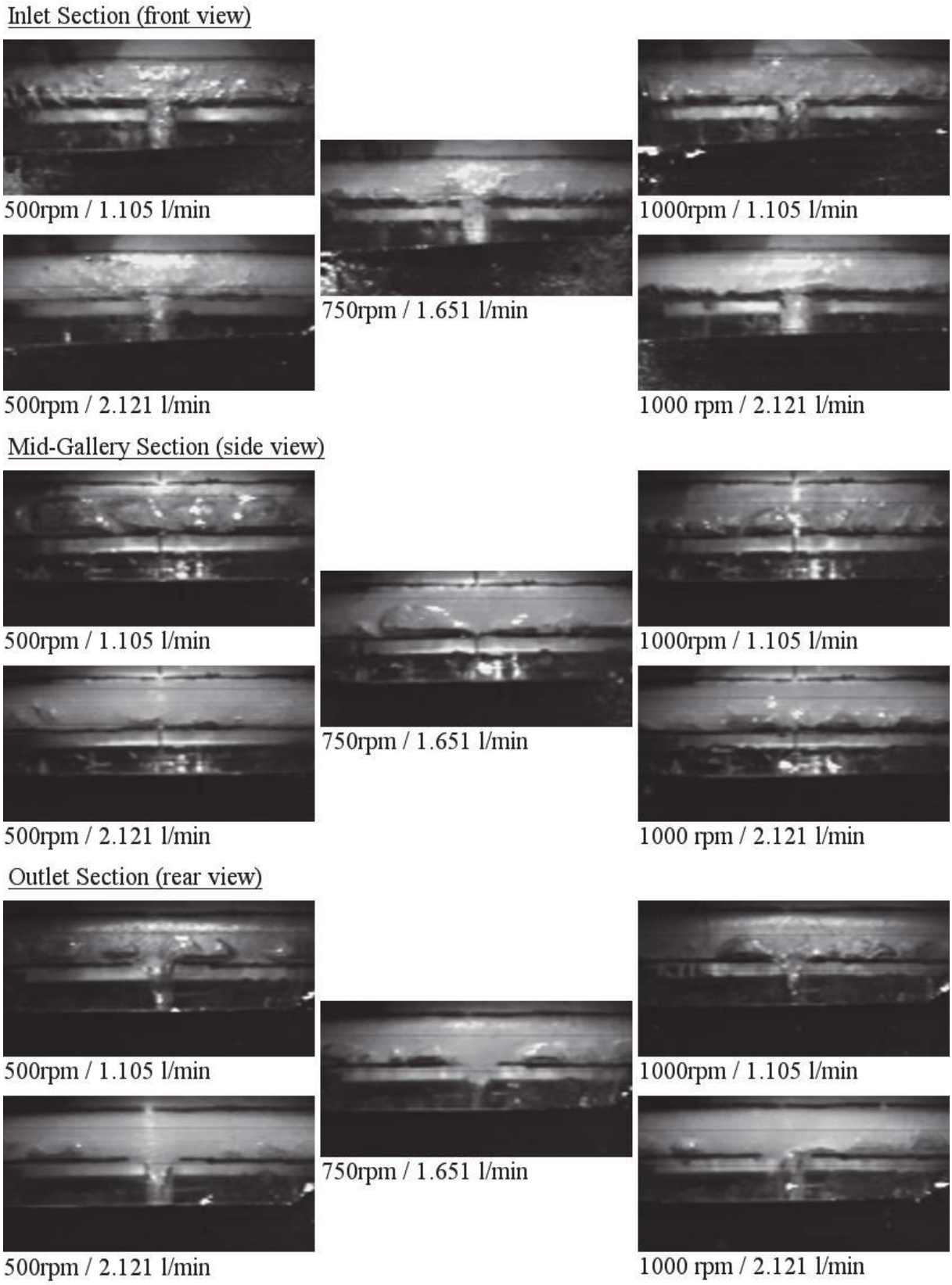

Fig. 5.38 Flow behaviour in gallery of small gallery model at TDC for recorded rotational crank speeds and oil flow rates

5.5 Summary

This chapter focused on the determination and analysis of the behaviour of the oil jets ejected from the nozzles and the flow behaviour inside the large and small gallery models at various operating conditions.

Both oil jets exhibited similar breakup behaviour, which can be described as wave-like and led to an increase in cross-sectional area with increase in distance from the nozzle. Higher flow rates increased the jet widening angles and led in some instances to jet diameters larger than the diameter of the gallery inlet. This was accompanied with an increase in air entrainment into the jet. The breakup was also greatly influenced by the nozzle design, especially the design of the nozzle tip.

Both galleries showed similarities in the internal flow behaviour, but also distinct flows, which could be linked to the gallery size and shape.

The vertical movement of oil inside the galleries was primarily driven by inertia, as a result of the acceleration and deceleration of the gallery models near the dead centres. The main location of the oil at *TDC* was found near the gallery top and at *BDC* near the gallery bottom. The movement of the oil from top to bottom and vice versa occurred during the second half of a stroke and finished after the dead centre position. This effect was more visible in the large gallery than the small gallery, which can be attributed to the difference in gallery volume. The larger gallery may contain a similar oil fill ratio (percentage), but the absolute volume of air was higher, allowing for increased freedom of movement. Additionally the cohesion of air bubbles in the smaller gallery formed air bubbles of a size that obstructed some of the oil movement, as the surface tension effects counteracted breakup. There was no indication that gravitational force affects the vertical movement inside the gallery.

At the inlet section of both galleries high turbulences occurred due to the entering oil jet, being expressed by strong air and oil mixing. The jet momentum for all investigated cases was sufficiently high to pass through any oil layer inside the gallery, and impacted on the gallery top surface. After the impact the flow was deflected and the gallery shape controlled the direction of the flow. While the inward facing inner gallery wall of the large gallery produced a circulating flow near the inlet channel, the horizontal top surface of the small gallery showed a direct flow into the gallery branch. The distance between nozzle exit and gallery inlet had an effect on the size of the turbulence region in the gallery. While the longest turbulence region

length at *BDC* reached almost the mid-gallery length, the length was significantly shorter at *TDC*.

In the mid-gallery sections, beyond the inflow based high turbulence region, occurred formation of large air bubbles. The horizontal flow was mainly a result of the deflected flow from the inlet section. The gallery shape again controlled the flow behaviour. The more race-track shaped cross-section of the smaller gallery produced a smoother wall-bound flow, while the large gallery with an inward facing inner wall did not allow for such smooth wall-bound flow and showed more chaotic and sloshing flow behaviour. There was a more directed forward flow of oil and air in the smaller gallery, due to the lower volume and the reduced ability of the oil to break the air bubbles down (surface tension). In the large gallery the bigger volume allowed for the air to be swirled around locally, rather than transported along the gallery.

The flow in the outlet section was influenced by the flow from the gallery branches, as well as the condition outside the gallery outlet. During the upward stroke the majority of the exiting oil was from the gallery outlet, but still with an upward directed movement following the gallery. The gravitational forces slowed the outside oil down and delayed the impact with the gallery outlet until the downward stroke (after *TDC*), leading to some re-entrance of oil into the gallery, but also air.

An increase in flow rate generally led to an increase in filling and air entrainment, although the effects were much less for the large gallery.

The effect of the engine speed on the filling varied with gallery size and flow rate. While there appeared to be an increase in filling of the small gallery at lower flow rate and with increase in speed, there was negligible effect at higher flow rate. The effect of crank speed on the large gallery filling was generally small, only showing slight variation in the inlet section of the gallery. Overall the crank speed showed little effect on the location of the air and oil within the gallery.

CHAPTER 6 NUMERICAL RESULTS

This chapter is concerned with the numerical study of the identical gallery shapes and cases as identified in the experimental study.

The first part investigates the flow from a nozzle to assess the conditions surrounding the oil jet and the best method to achieve appropriate results, but also at minimum required computational expense to use the software license most efficient.

The second part is concerned with the investigation of the large gallery model (*LGM*). After the description of the model setup, a mesh sensitivity study is performed, followed by an assessment of the uncertainties. A suitable mesh model is used to perform an analysis of the flow inside the gallery for the corresponding cases to the experimental investigation in the previous chapter.

The third part is focused on the small gallery model (*SGM*) and follows the same procedures as for the large gallery model, although lessons learned from the large gallery model were used in order to reduce the number of initial studies of mesh independence. The corresponding cases to the experimental study were performed and the flow analysed. The chapter then closes with a summary of the findings.

6.1 Model assumptions overview

Based on findings from the literature review and available modelling techniques of the software the following assumptions were made for the model:

- The *realisable* $k-\varepsilon-model$ was used in order to improve representation of the breakup of the free round oil jet from the crankcase nozzle. This was different from Pan et al. (2005) study using the standard $k-\varepsilon-model$, as their investigation did not include a free jet.

- The *VOF* model was used for the tracking of the interface, as it allowed sharper oil air interface presentation and enhanced phase separation. Care was taken with regards to mesh size, as large elements may cause underestimation or overestimation of cell filling due to the linear piece-wise interpolation of the method. This was especially true for large surface curvature and small sized droplets.
- Surface tension was included, as it was a controlling factor for jet breakup and was expected to affect the in-gallery flow.
- The flow was isothermal. There was no heat transfer between boundaries and fluids. This would require detailed knowledge of the heat transfer conditions, which were currently solved only by adapting models to suite few measurement points, while internal gallery flow conditions were not fully investigated and validated.
- The viscosities of the fluids were constant, as the temperature was constant. For the inclusion of heat transfer, and subsequent changes in density and viscosity, the correct boundary conditions would be required (see above), which were unknown or could only be derived from simulations. Oil temperature during the validation tests was constant in order to reduce viscosity changing effects.
- Phases of oil and air were incompressible. The investigated domain of the gallery represented an open channel connected to a constant pressure ambient reservoir. The space outside the gallery was modelled to include effects concerning the low pattern outside the inlet and outlet channel of the gallery and any interaction with the internal gallery flow.
- Wall boundaries were not modelled with boundary layers, as the driving force from the gallery movement was significantly larger than the frictional forces on the wall and no heat transfer was included. Wall function (enhanced wall-functions) allowed for coarser mesh, while still maintaining consideration of shear flow near wall boundaries.
- The flow was transient and the movement of the gallery model was sinusoidal to represent the movement during experimental investigation.
- The flow from the nozzle was at a constant flow rate, neglecting pulsating effects from the oil pump delivery. The nozzle exit velocity was represented by a cross-sectional profile to represent the differences of laminar or turbulent conditions found at the nozzle exit.

6.2 Nozzle Flow

The experimental results showed a breakup of the oil jet for various flow rates. Prior to the gallery modelling it was decided to investigate the effects of pump pulsation on the behaviour of the oil jet. In particular the jet development and breakup was of interest, as the diameter of the oil jet played an important role in the amount of the oil entering the gallery and therefore the oil catch ratio. In the experiments the oil was delivered by a vane-type pump. Positive displacement pumps, such as vane pumps, inherently produce time-dependent pulsating flow, as shown by Jones et al. (1998), Giuffrida and Lanzafame (2005) and Bianchini et al. (2009). It was stated that the magnitude of pulsation strongly depended on the design of the pump and the pulsation magnitude may be reduced by design features, such as relief grooves, which would also generate flow with almost solely sinusoidal behaviour.

The oil jet behaviour in an undisturbed unconstrained environment (free flow) was investigated for one specific case in order to assess the requirements to generate sufficient accurate jet representation, but also to minimise computational expense with regards to the jet modelling in the gallery models. The numerical study of the jet behaviour was based on the large gallery nozzle only, as the experimental study for this nozzle provided the best results in terms of pulsation frequency and jet behaviour consistency. The flow domain is shown in Figure 6.1. The dimensions were taken directly from the large gallery nozzle. The flow domain consisted of a cylindrical core jet volume (including the nozzle) and a cylindrical far-field, representing the environment around the jet. Use was made of symmetry to further reduce computational demand. The generated hexahedral mesh consisted of a finer mesh in the jet core and jet surface area and a coarser mesh at a distance of $^1/_2$ the jet diameter. One mesh refinement step was performed capturing the jet and jet surface mesh in order to analyse the influence on the jet breakup behaviour. Thereby all cells in the refinement area were split into eight hexahedral cells.

An analysis of the recorded experimental images showed that consecutive jet breakup pattern occurred at identical image positions at an interval of 9 images. At a recording rate of 9000 *fps* this equated to a pulsation frequency of approximately 1000 Hz. Unfortunately the variation of pressure or flow rate could not be recorded and an approximation had to be made. Bianchini et al. (2009) found for a combustion engine lubrication pump a maximum and minimum variation of discharge pressure of +4% and -7% respectively from the average

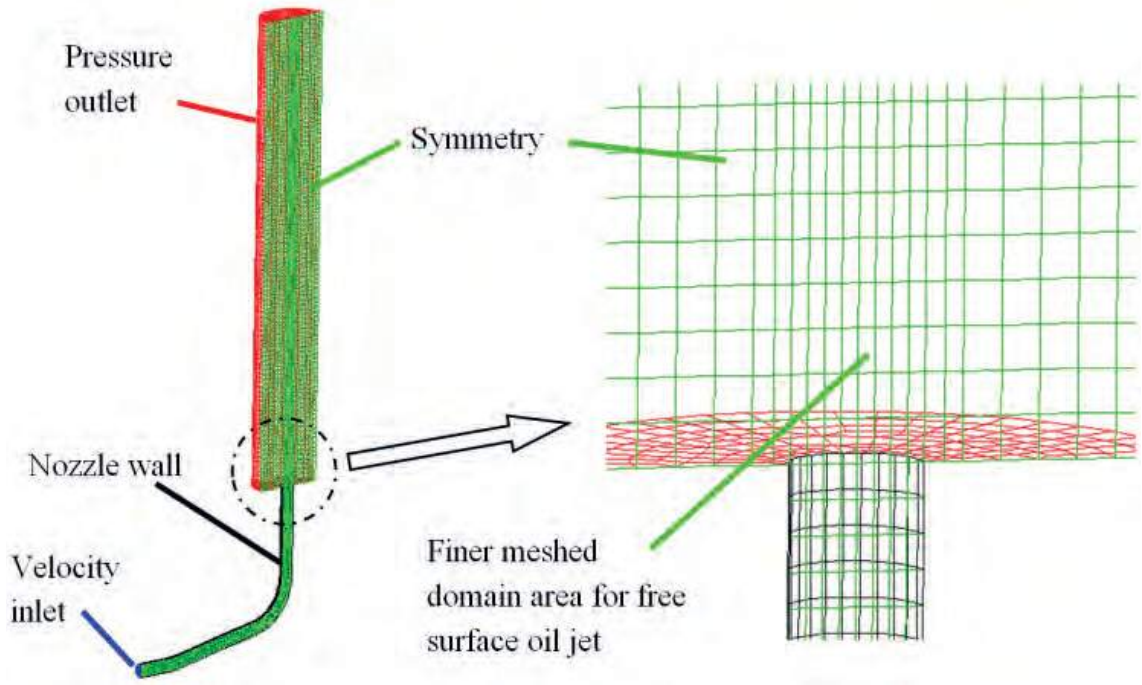

Fig. 6.1 Domain for oil jet behaviour modelling

pressure. Eight cases were investigated, of which four cases were with a curved nozzle, as shown in Figure 6.1, and four cases with a straight nozzle at the following conditions:

a) curved nozzle with constant flow, no refinement,
b) curved nozzle with constant flow, with refinement,
c) curved nozzle with pulsating flow at 1000 Hz frequency, no refinement,
d) curved nozzle with pulsating flow at 1000 Hz frequency, with refinement,
e) straight nozzle with constant flow, no refinement,
f) straight nozzle with constant flow, with refinement,
g) straight nozzle with pulsating flow at 1000 Hz frequency, no refinement,
h) straight nozzle with pulsating flow at 1000 Hz frequency, with refinement,

There was no additional modelling of any machinery or test rig vibration. Only the jet behaviour due to pulsation and the curved nozzle was of interest. All cases were conducted at the same average volumetric flow rate of 4.0 l/min. The fluctuations from the average flow rate were +4.0% and -7.0% to produce maximum and minimum flow rate respectively. The oil was assumed to be incompressible at such low pressures and the domain inlet was defined by an inlet velocity with a time profile as shown in Figure 6.2. At the prescribed flow conditions the inflow was still laminar with a Reynolds number of 1892 for an exit velocity of

9.43 m/s. At the model inlet a laminar profile was specified, reflecting the inlet conditions more accurately, with the velocity at the wall being zero and maximum in the centre of the flow.

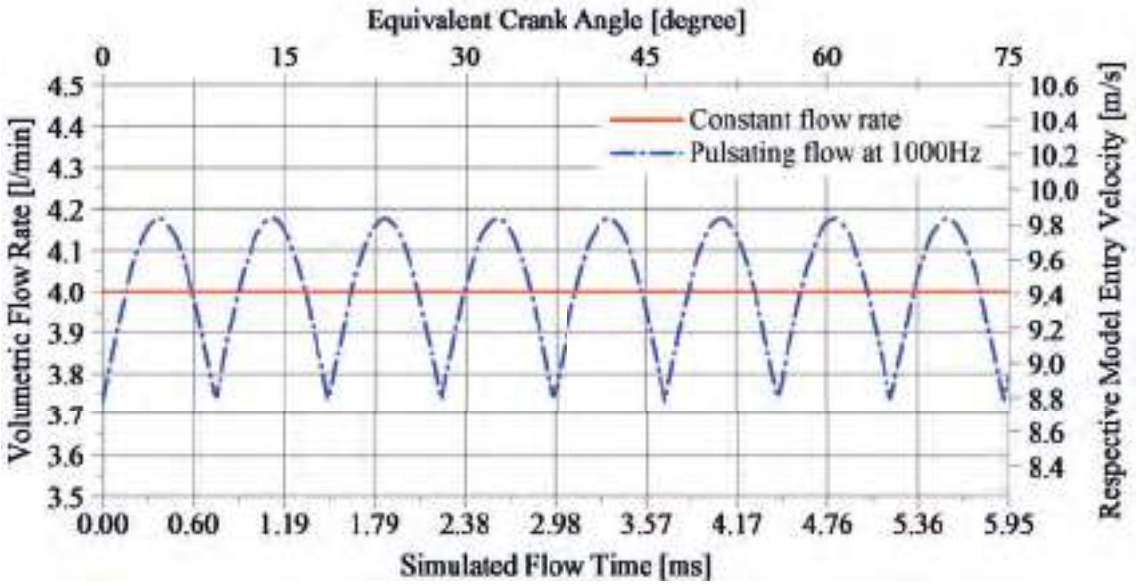

Fig. 6.2 Nozzle entry velocity profiles

In order to model jet breakup accurately the domain relies strongly on the mesh density, as shown by Pai et al. (2008), Shinjo and Umemura (2010), Delteil et al. (2011) and A.Berlemont et al. (2012). A very fine mesh is required to allow accurate tracking of small droplet separation and impact, which leads to the breakup. This mesh dependency is one of the drawbacks of the *VOF* model, as the interface tracking is based on the evaluation of the phases inside a mesh cell, as shown by Delteil et al. (2011). For too coarse meshes the individual droplets detaching from the main bulk flow cannot be captured and only interface diffusion occurs. The behaviour of the interface diffusion can be noticed for all cases, where the standard meshes indicated interface surface rippling, while the refined meshes allowed for a better capturing of the surface and some of the surface rippling was eliminated. This effect was best noticeable by comparison of Figure 6.3e & f, where the refined mesh did not show any signs of surface rippling. The effect of the entry conditions on the jet behaviour between curved nozzle and straight nozzle were marginal, although noticeable.

For continuous inflow conditions (Figure 6.3a, b, e & f) the jets showed few signs of surface rippling or breakup. Any indicated breaking of the surface could be attributed to the diffusion behaviour of the coarser mesh, rather than actual breakup. The introduction of

pulsation to the inflow (Figure 6.3c, d, g & h) did lead to some rippling of the jet surface, especially for the curved nozzle entry, but also did not significantly increase the jet diameter to highlight any jet breakup conditions.

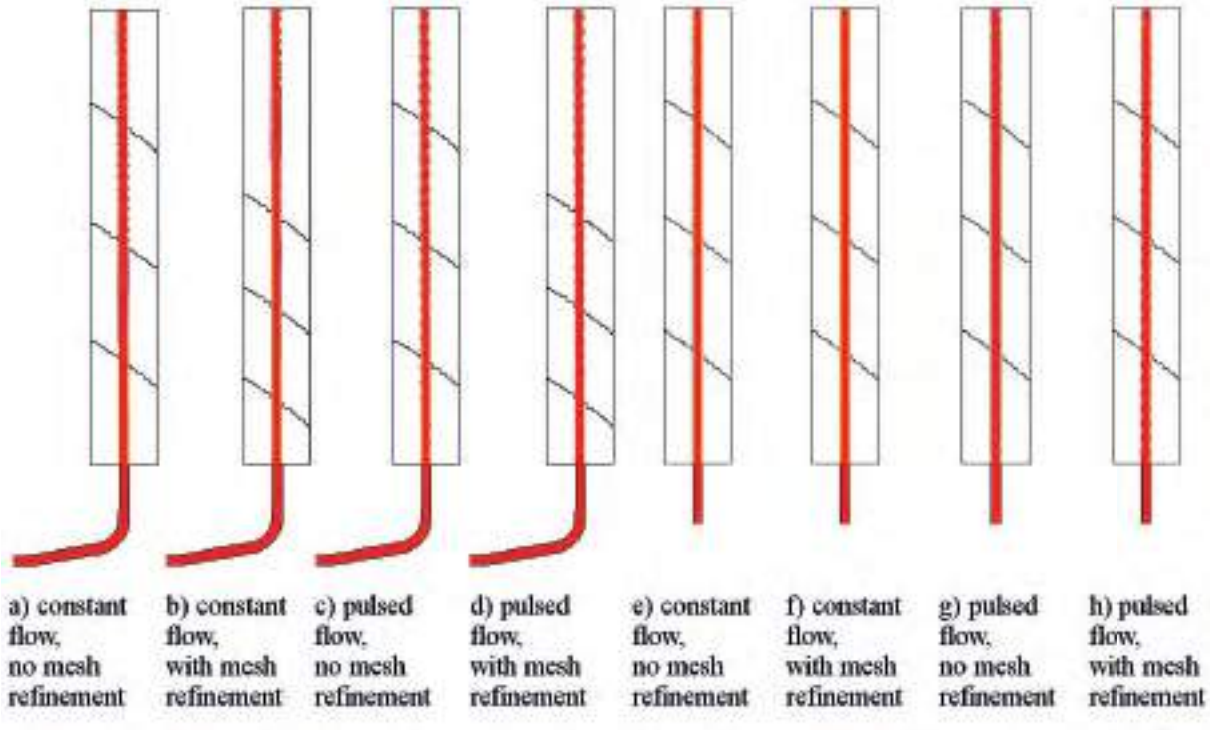

Fig. 6.3 Oil jet behaviour for average volume flow rate of 4.0 l/min at different inlet flow conditions and mesh densities

A comparison of the jets showed that although there occurred rippling of the surface with pulsation, the width of the oil jet did not change significantly in comparison to the conditions with constant flow rate. Even at large distance from the nozzle exit the jet diameter did not increase. The refinement of the mesh was only leading to a more detailed interface representation, but with identical jet behaviour. Based on the findings from the jet behaviour study it was decided that modelling of the oil jet with a refined mesh for the gallery filling investigation was not necessary. The jet cross-section did not show any significant increase in diameter or divergence from the vertical flow path to justify the incurred extended simulation time of the finer mesh. Furthermore the results from the curved nozzle showed that the curvature did not change the jet behaviour significantly and a straight nozzle would be sufficient to generate an appropriately represented oil jet for the filling investigation. In addition the curved nozzle, pulsating flow and finer mesh would also have a negative effect by

prolonging the simulation time and increasing hardware requirement, which could not justify the marginal gains.

6.3 Large gallery model setup and initial study

6.3.1 Geometry

The gallery flow domain was regarded as symmetrical, with the symmetry plane passing though nozzle, inlet channel and outlet channel centres, necessitating only half of the flow domain to be modelled. The gallery model was also split into sub-domains to aid meshing and to define appropriate section properties. The sub-domains were nozzle, inlet-free-flow, gallery sections and outlet-free-flow, as shown in Figure 6.4. The gallery sub-domain was further divided into sub-sections providing a better mesh control and also allowed investigating the flow behaviour in different sections, as executed by Pan et al. (2005) and Yi et al. (2007). The gallery was split into eight identical sections, all with an angle of 22.5°. The inlet and outlet sections included a short channel, representing the inlet and outlet hole.

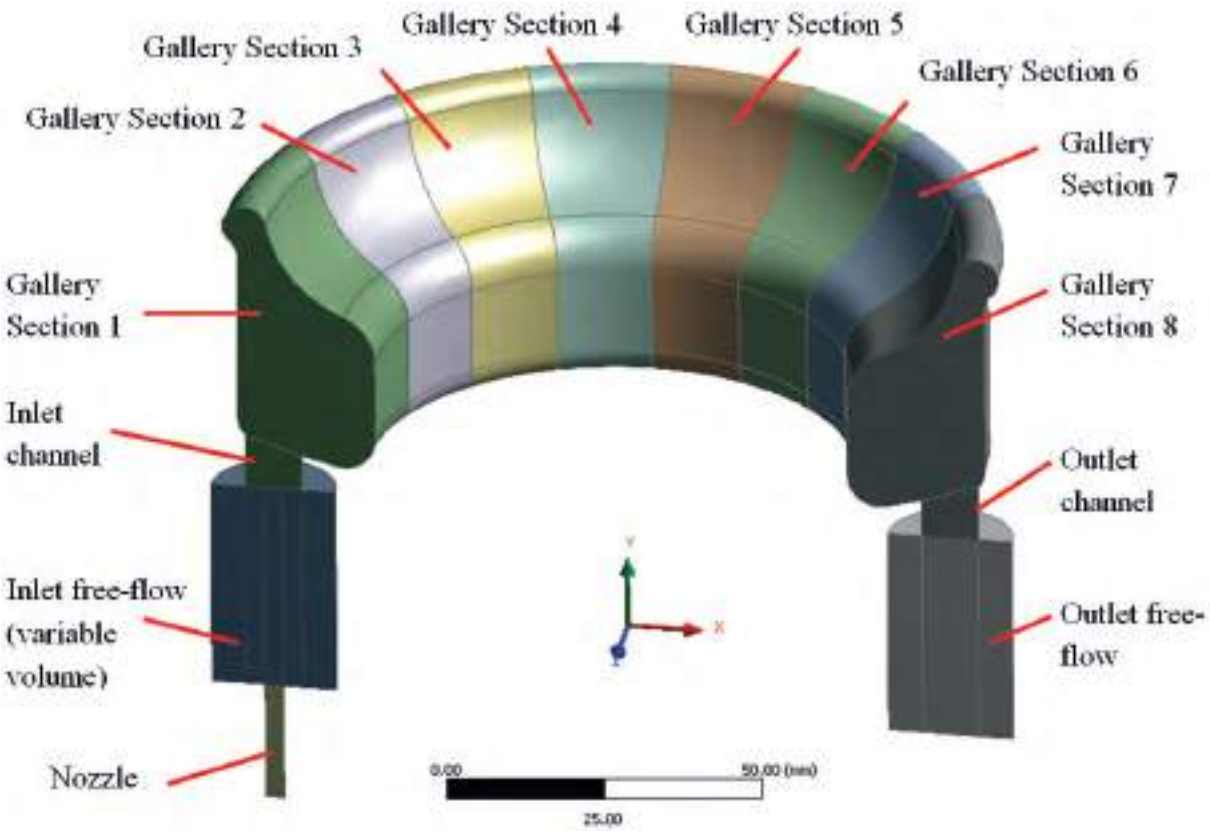

Fig. 6.4 Large gallery model geometry

Torregrosa et al. (2010) indicated that the relative velocity of the jet between nozzle exit and gallery inlet has an effect on gallery filling. This could be linked directly to engine speed, but also to stroke length, which affects the jet breakup in terms of jet width and velocity at gallery entry. Previous investigations by Pan et al. (2005) and Yi et al. (2007) modelled the jet inlet as a simple face split of the inlet channel entry, where the jet was represented by a velocity inlet of diameter of the nozzle. The remaining gallery inlet was modelled as a pressure outlet. The experimental results did shown that backflow from the gallery influenced the flow behaviour at the inlet and outlet section. This backflow behaviour would not be included, when the jet entry was modelled as a direct entry as explained above. It was therefore decided to include a part of the flow domain outside the gallery containing the oil jet.

The inclusion of the re-entry effect at the inlet side was achieved by modelling a dynamically changing free-flow domain volume, connecting a stationary fixed nozzle and a moving gallery. The diameter of the free-flow domain should be sufficiently large to avoid influences from the opening boundary conditions and to keep exiting oil in close proximity to model backlash effects. Homma et al. (2006) used a ratio between the jet diameter and domain diameter of 1:10, while Delteil et al. (2011) used a ratio of 1:6.8 for jet breakup modelling. The diameter of the inlet-crank sub-domain was set to 21 *mm*, giving a ratio of 1:7. The same dimension was used for the outlet-free-flow domain, whereby the domain had a fixed volume size and moved with the gallery.

6.3.2 Boundary conditions

The boundary conditions of the model included inlets and outlets for flow, as well as walls and symmetries. Each will be described in detail below.

Flow domain inlet

The oil entered the model domain at the nozzle, as shown in Figure 6.5. The entry was modelled as a velocity inlet and the inflow medium was incompressible oil. The average velocities were derived from the experimental settings, based on the volume flow rates of the *LGM* of 4.0 l/min and 6.0 l/min, giving Reynolds numbers of 1892 and 2838 respectively. The velocity profile of the flow within the nozzle therefore depended upon laminar or turbulent conditions and required adjustment accordingly.

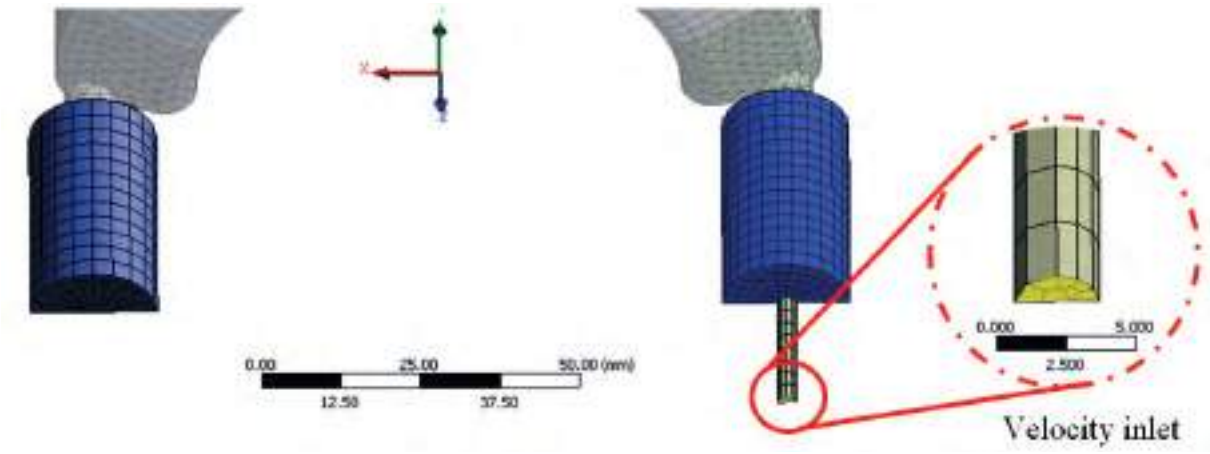

Fig. 6.5 Model inlet large gallery model

While the flow at 4.0 l/min could be assumed laminar, the flow at 6.0 l/min was transitional, whereby either laminar or turbulent condition could occur. Joseph and Yang (2010) have also shown that within this range the wall friction coefficient behaves rather randomly. Although this would be sufficient to describe the behaviour in the experiment, it was insufficient for numerical simulation and a defined boundary between laminar and turbulent was necessary. Versteeg and Malalasekera (2007) indicated a change from laminar to turbulent flow in pipes at a Reynolds number of 2000, while Andersson et al. (2011) stated the onset of transition for $R > 2100$. Therefore for condition below $Re < 2100$ the flow was assumed laminar, and for $Re \geq 2100$ the flow was assumed to be turbulent. In both cases, laminar and turbulent, the inflow conditions were described as a 3–dimensional user defined function profile to reflect the nature of the flow more accurate, as compared to an average velocity profile as employed by Pan et al. (2005).

The laminar flow velocity profile can be expressed as a parabolic function taking the form of

$$v_{p\ lam}(r) = v_{max\ lam}\left(1 - \frac{r^2}{R_n^2}\right) \tag{6.1}$$

with

$$v_{max\ lam} = 2\ v_{avg}$$

where R_n is the radius of the nozzle exit, r the radial coordinate variable of the exit, $v_{max\ l}$ the maximum laminar flow velocity and v_{avg} the average flow velocity at the nozzle cross-section. The value of v_{avg} was derived from volumetric flow rate, density and nozzle area. The radial

distance r from the nozzle centre position is

$$r(x,z) = \sqrt{x^2 + y^2} \tag{6.2}$$

Kudela (2012) stated that the maximum inlet velocity for turbulent flow can be determined by the equation

$$v_{max\ t} = v_{avg}(1 + 1.33\sqrt{f}) \tag{6.3}$$

where f is the friction coefficient, which can be calculated from various approximation function, such as developed by Nikuradse, Prandtl, Colebrook, Haarland and Brkic (Brkić, 2011). While Nikuradse's and Prandtl's equation were independent from the surface roughness and delivered good correlations for smooth pipes, the equations of Colebrook, Haarland and Brkic included surface roughness and allowed for a larger range of applications. The correlation by Brkić (2011) was given as

$$f = -2.0\ log\left[\frac{1.25603}{\sqrt{-\frac{0.0015702}{ln(Re)} + \frac{0.3942031}{ln^2(Re)} + \frac{2.5341533}{ln^3(Re)}}} + \frac{\varepsilon_s}{3.71d}\right] \tag{6.4}$$

where Re is the Reynolds number, ε_s the surface roughness and d the pipe diameter. With a nozzle diameter of 3 mm and determining the surface roughness of the nozzle based on a cold drawn process with a value of 1.6 μm (Marrs, 2011), the friction factor yielded a value of 0.04482. A comparison of the friction factors from all above correlations showed a variation below 2% and extending to the maximum velocity of the profile a variation as low as 0.2% was determined. This was deemed sufficiently accurate, given that the wall friction concerned the flow inside the nozzle and the main focus was on the jet breakup.

The velocity profile for turbulent flow can be described as a function of radial position from the axial nozzle centre by the equation

$$v_{p\ t} = v_{max\ t}\left(1 - \frac{r}{R}\right)^{1/n_0} \tag{6.5}$$

The exponent n_0 was determined with a value of 5, based on data given by Johnson and Bushnell (1970) and Kudela (2012). Based on equation (6.1) and equation (6.5) the appropriate

velocity profile for the simulation was determined. The normalised velocity profiles are shown in Figure 6.6, whereby normalised refers to the ratio of the varying profile velocity depending on the radial position to the average exit velocity.

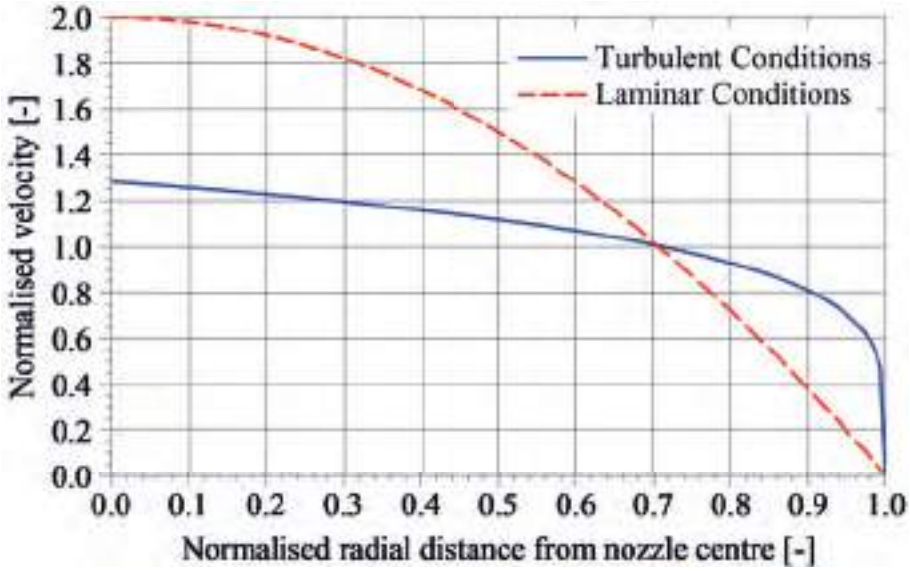

Fig. 6.6 Normalised inlet velocity profile comparison relative to average velocity for laminar and turbulent conditions

The profiles were applied to the nozzle inlet surface using a user–defined function (see Appendix C.1 and C.2 for examples). The resulting representative inlet velocity distribution for turbulent conditions is shown in Figure 6.7.

The condition within the nozzle sub-domain was adapted accordingly to reflect the flow conditions. For turbulent conditions the inflow turbulent intensity was set to 5% following recommendations of Versteeg and Malalasekera (2007) and the hydraulic diameter for the fully developed flow was 3 *mm*.

Flow domain outlets

All outlets of the model flow domain were specified as pressure outlets, as shown in Figure 6.8. Oil and air were present in the sub-domains of inlet free-flow and outlet free-flow. It was assumed that any oil exiting the sub-domains would not re-enter the sub-domain and only air was permitted to re-enter to maintain constant pressure in the flow domain.

The velocity difference at the interface between oil jet and surrounding air leads to turbulent flow of air within the inlet free-flow sub-domain. These turbulences were assumed to be swirls of constant size. The re-entry of air into the flow domain was assumed to be at turbulent conditions, as the movement of the gallery model would create air movement beyond

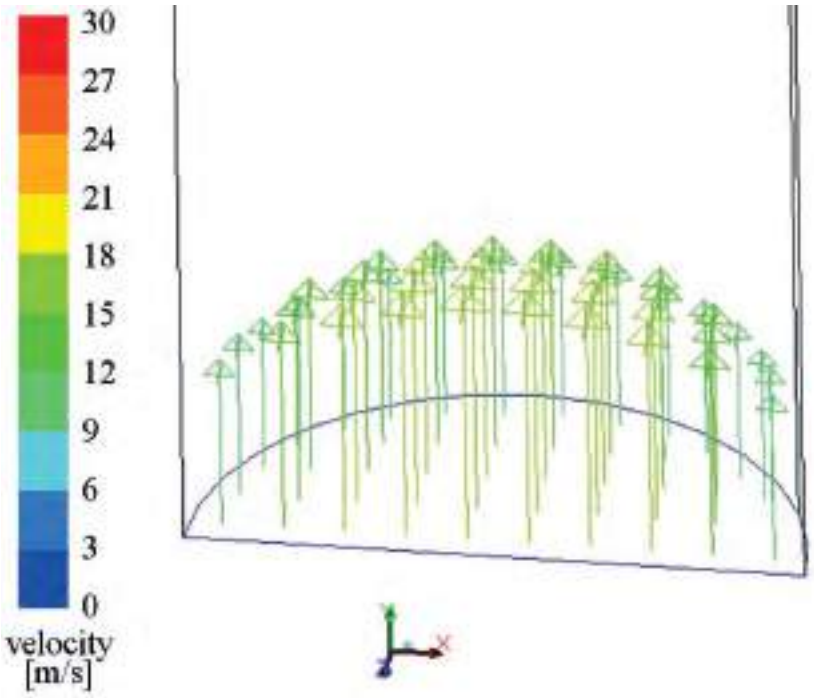

Fig. 6.7 Turbulent inlet velocity boundary conditions at 6.0 l/min

the modelled flow domain. The backflow turbulence was estimated based on the maximum inlet free-flow length when at *TDC* and the maximum piston velocity causing the air to swirl. The backflow turbulence intensity was considered to be 5%, following recommendations of ANSYS (2013b). The hydraulic diameter of the backflow was assumed as 10 *mm*, as the largest swirl within the inlet free-flow could only be of the size of the space between the jet and the outlet boundary. The same conditions were used on all other outlets.

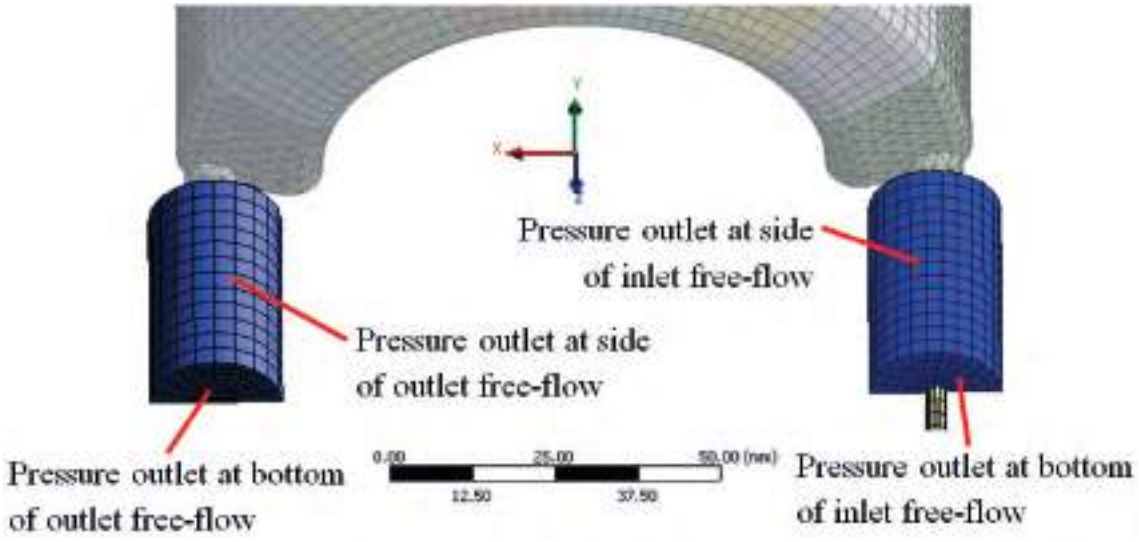

Fig. 6.8 Model outlets at gallery inlet and outlet side for large gallery model

Flow domain walls

All gallery domain walls were modelled with a surface roughness of 32 μm, representing the average roughness of the machined reference body in the experiments. This included the surfaces of the gallery, as well as the surfaces of the inlet channel and outlet channel. The gallery walls were split into wall sections, representing the main heat transfer areas, as shown in Figure 6.9. Although heat transfer was not considered, wall wetting of these sections may be analysed.

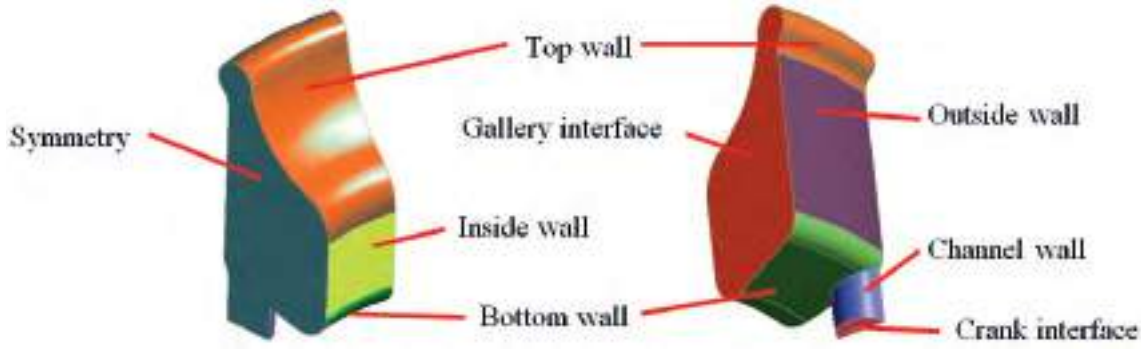

Fig. 6.9 Identification of wall surfaces for LGM on example of sub-domain Section 1

Flow domain symmetry and interfaces

The sub-domains were connected by interfaces. The use of symmetry in the model also introduced symmetry boundaries. Figure 6.10 shows the interface and symmetry planes of the model.

6.3.3 Materials

The material properties of the oil were taken from the experimental data for transferability of results. The properties of the oil during the experimental phase were determined at a temperature of 20°C within a temperature controlled environment. Table 6.1 shows the main properties. All were assumed constant.

Table 6.1 Material properties of oil and air

Material	Temperature	Density	Dynamic viscosity	Surface tension
	$°C$	$kg \cdot m^{-3}$	$mPa \cdot s$	N/m
oil	20	840	12.56	0.026
air	20	1.2	0.0183	0.026

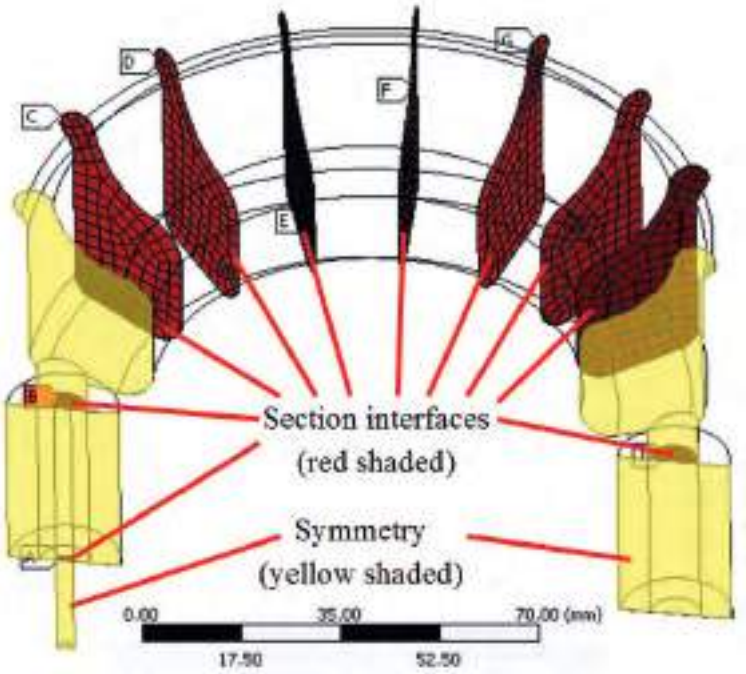

Fig. 6.10 Identification of interfaces and symmetry boundaries for *LGM*

6.3.4 Initial meshes

A structured hexahedral mesh was the primary target for the full flow domain. Beside the best performance of the hexahedral mesh, it also provided the best control volume shape for the *VOF* model (ANSYS, 2011). However, it was found that no sufficient quality mesh for the sections interfacing the sub-domains of gallery entry (Section 1) and the inlet free-flow, as well as for the sub-domains of gallery exit (Section 8) and outlet free-flow could be generated. The reason for this problem was the highly curved and sharply angled surface areas at the intersection between gallery bottom walls and inlet channel wall. The highest distorted elements were therefore found in this area, with minimum orthogonal quality[1] of 0.08, indicating an unsuitable quality mesh for stable and accurate simulated flow.

A tetrahedral mesh was used for the gallery inlet and outlet sections (Sections 1 and 8 respectively), as shown in Figure 6.11a for the inlet section. The advantage was that the orthogonal quality in these sections was improved to a value of 0.3 from 0.08. The disadvantage of this element type was found in the increased number of control volumes and numerical expense in tracking of the phase interface, leading to increased simulation time, and less accurate treatment of surface tension effects using the *VOF* model.

[1]Orthogonal quality values of 1 correspond to best quality and values close to 0 correspond to low quality.

Taking the disadvantages of the tetrahedral mesh into considerations it was decided to investigate the use of a hexahedral mesh. As mentioned before, a direct application of a hexahedral mesh to the gallery inlet and outlet section geometry was not possible. The sections were therefore split at the intersection between gallery and inlet channel to generate two separate volumes, as shown in Figure 6.11b. This also generated an additional section interface. Attempts to generate a mesh with conform[2] interface shape and size resulted in equally skewed and deformed mesh elements. The use of non-conform[3] interfaces allowed the connection of sub-domains, although they do not share connection features, e.g. boundaries, nodes or edges. The mesh minimum orthogonal quality was increased to a value of 0.618 from 0.08 in comparison to the initial hexahedral mesh and the amount of elements reduced by 70% relative to the tetrahedral mesh, also reducing the computational expense (memory and time).

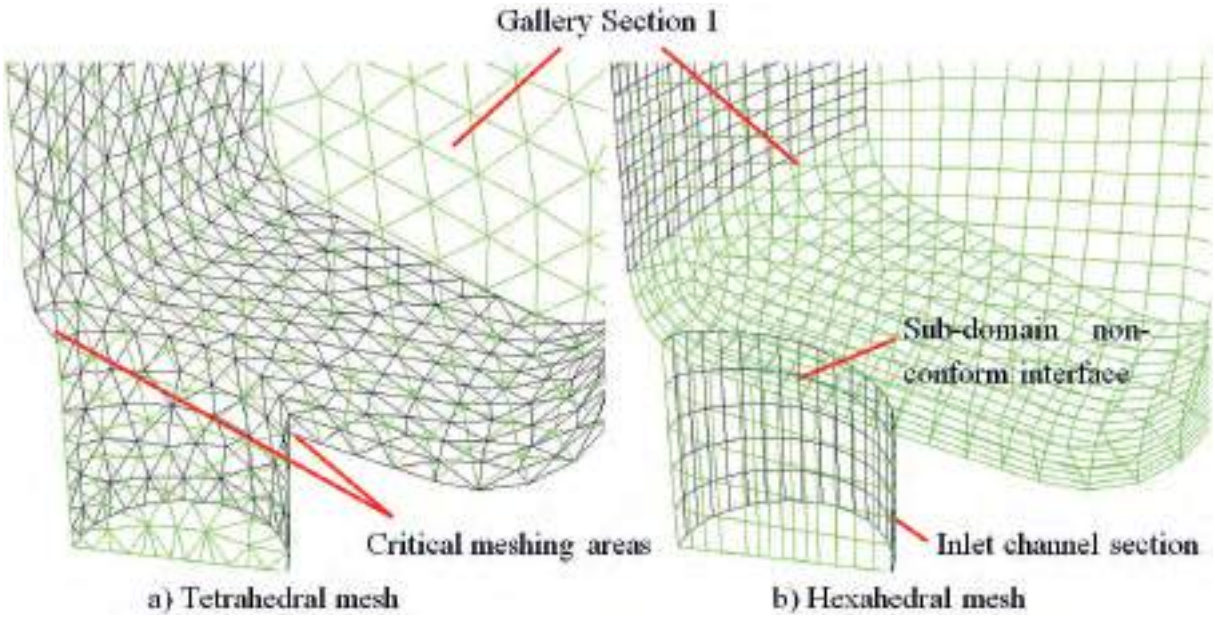

Fig. 6.11 Mesh types employed at gallery inlet section and inlet channel

An attempt was made to apply identical conditions for both meshes with respect to element length and quality where possible. The differences for the sub-domains containing the hexahedral mesh (Sections 2 to 7) were therefore very little. For the sub-domains with different meshes (Sections 1 and 8 of the gallery) the same outline conditions were used. This

[2]A conform interface mesh means the meshes of two adjoined volumes share identical geometrical and control volume boundaries, e.g. the mesh edges coincide with the geometry edges and both are conform.

[3]With a non-conform interface mesh geometry and mesh of two adjoined volumes do not share the same boundaries. The mesh is not conform to the geometric boundaries.

assured that the edge lengths were nearly identical, but the volumes of the tetrahedrons were approximately $1/4$ that of the volumes of the corresponding hexahedrons.

6.3.5 Convergence study and uncertainty assessment

There are three specific convergence criteria to be considered:

- Time step convergence,
- Transient model convergence and
- Mesh independence convergence.

All will be considered and described separately below.

Time step convergence (time step simulation convergence)

The values of each variable within a time step are calculated using an iterative solution process. At the end of each iteration step the scaled absolute residuals, representing the numerical errors from the equation solving process, are evaluated. A time step has converged results, when the residuals satisfy a set criteria. This can be a threshold value specifying a minimum error, or a minimum difference between iteration steps, or any other user defined criteria.

A time step was considered to have converged, when the residuals for velocities, mass continuity, turbulent energy and turbulent energy dissipation achieved values below the threshold of 10^{-3} and for energy with values below 10^{-6}. Given the transient behaviour of the conditions it was also found that for some cases this criteria was not achieved and a constant residual value occurred. For these cases an additional criterion was that the residuals must reduce at least by order of magnitude 10^3 with a maximum residual value of 10^{-1}.

Higher residual values can be a result of a large time step size. In order to stabilize the simulation a variable time step sizing was implemented, where the next time step was recalculated at the end of a time step, based on velocities, cell length and global Courant number. This allowed for improved simulation time, when low velocities occurred, but also stable calculation at higher speed flows. The maximum time steps were also limited to $1/10$ of a crank angle for better flow stabilisation.

Transient model convergence

Transient model convergence refers to the achievement of set criteria of flow variables for a prescribed number of consecutive crank cycles.

The investigated problem contained highly transient and unstable flow behaviour. Although the domain inlet boundary conditions can be classified as constant for the nozzle exit flow, the behaviour around the gallery inlet and outlet depended strongly on the conditions inside the gallery, as well as the exchange of fluid between gallery inside and the free-flow volumes outside the gallery. This generated problems with convergence definitions in the sense that small changes between consecutive cycles may occur.

The first generated and stable running model employing a conform-interface (tetrahedral mesh in Sections 1 and 8) was used to obtain initial fill data for the absolute filling and filling behaviour of the gallery. The modelled conditions were 600 rpm crank speed, 4.0 l/min flow rate, 170 mm stroke and sinusoidal piston motion (infinite length conrod, Scotch yoke). The entry flow at the nozzle inlet was modelled using the laminar profile, as the Reynolds number was below 2100.

Two distinct criteria for model convergence were considered:

1. cyclic averaged overall gallery (sections 1 to 8) oil fill ratio or *gallery filling* and
2. cyclic averaged individual gallery section oil fill ratio or *section filling*.

Convergence refers in this instance to the conditions of defined variation limits of the gallery filling over a range of consecutive cycles. The first (initial) model was used to determine the approximate time constant of the gallery filling behaviour to estimate the response of the gallery to the change of filling.

Figure 6.12 shows the filling behaviour of the overall gallery with regards to time. The filling can be separated into two periods, an initial filling period and a settling period. The initial filling period was used to determine the time dependent condition for the (transient) model convergence in order to minimise computational expense.

The initial gallery filling behaviour can be modelled as a step function response of a first order time dependent system, with the oil flow representing the step input, while all other parameters are constant. The behaviour of the gallery filling can be described by an exponential function as

$$OFR(t) = K\left(1 - e^{-t/\tau}\right) \tag{6.6}$$

where K is the gallery filling after the filling period, τ the time constant (time until 63.2 % of K were reached) and t the flow time. The values for K and t were determined using the above equation together with a standard deviation estimation, whereby the standard deviation

between step response function and simulation data was reduced to a minimum. The best fit data was determined as 71.5% for the maximum gallery filling and 2.1 *s* for the time constant (equivalent of 21 cycles) with a standard deviation of 1.4%. The step response is shown in Figure 6.12.

Each simulation model would be evaluated based on the conditions of 21 consecutive cycles and if the criterion of convergence was achieved the simulation was halted and declared converged.

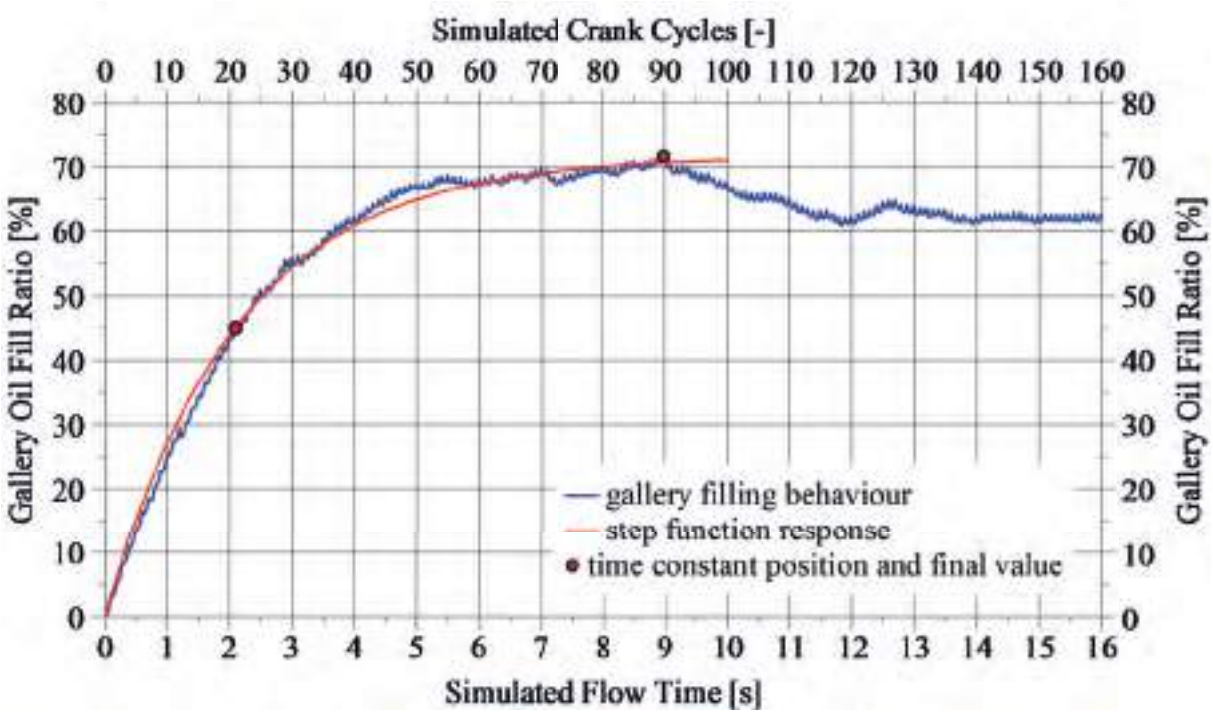

Fig. 6.12 Gallery filling and time behaviour for intial *LGM* mesh model at 600 *rpm* crank speed and 4.0 *l/min* flow rate

Analysing the flow behaviour inside the gallery also revealed the underlining behavioural change between the initial filling period and the settling period. During the filling period the flow was unstructured and chaotic, indicated by the more chaotic directions of the flow vectors, as shown in Figure 6.13a. The chaotic flow, especially in the gallery mid-sections, led to additional flow obstruction causing an increase in filling.

Figure 6.13b indicates the flow directions during the (transient) settling period. An established repetitive flow pattern existed, indicated by the more structured flow direction vectors in the mid-gallery sections. The flow was more structured and larger amounts of oil were guided through the gallery until equilibrium between inflow and outflow was achieved and the gallery oil filling showed a cyclic varying, but overall constant average value. The

colours of the flow direction arrows represent the velocity magnitude of the flow. Little differences in the velocity values for both time dependent cases were found, indicating that the strongest effect driving the oil movement may be found in the inflow of the oil, rather than the inertia effects.

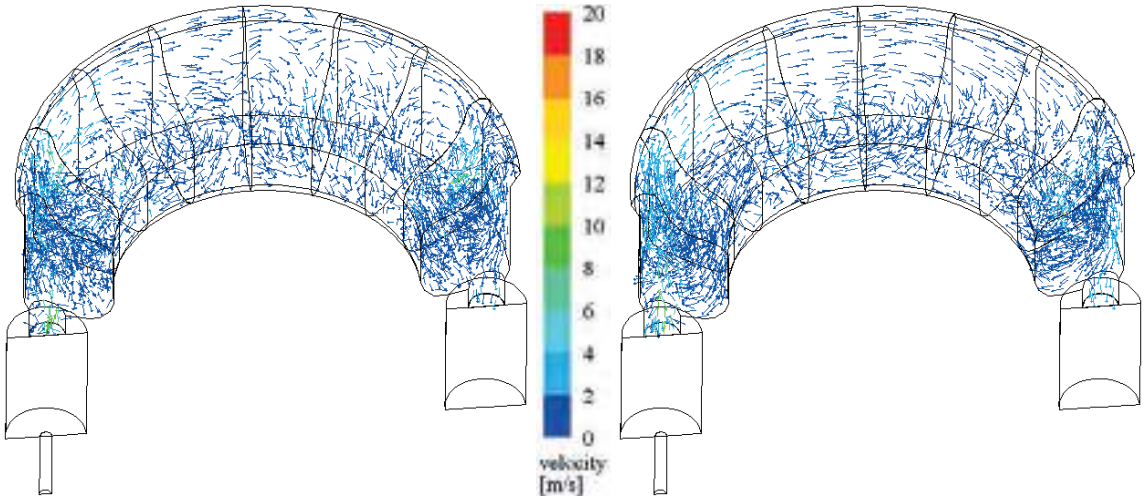

a) flow time 5.0 s (50 cycles) b) flow time 15.0 s (150 cycles)

Fig. 6.13 Gallery flow pattern and flow velocites for intial *LGM* mesh model at 600 *rpm* crank speed and 4.0 *l/min* flow rate and for different flow times

The opposing demands of low computational time and accuracy were considered in the collection of data. The variable time stepping allowed for the optimum simulation time, while maintaining a stable solution as well. For data analysis and manipulation the data should be collected at consistent crank angles in the cycle, whereby the number of data points per cycle should not be too low to eliminate flow behaviour effects, but also not too high to increase simulation time for the crank cycle. Appropriate simulation performance and accuracy was found at five crank angle interval data recording, resulting in 72 values per cycle.

Figure 6.14 highlights the difference in filling behaviour within the gallery. While the variation of the overall gallery filling was very small (2%), the variation within the sections was significantly higher with peak variations of up to 60%. For better visibility the data is represented with different zero markers, whereby the incremental scale is identical (10%). While the behaviour of the overall gallery *OFR* would be easy to assess and may indicate a converged filling behaviour, the filling of the gallery sectors may not have converged and visual assessment of convergence would be difficult to achieve. Therefore the assessment of convergence was based on the determination of the deviation of the *OFR* from the average values. First the cycle average oil fill ratio for each crank cycle was calculated using the

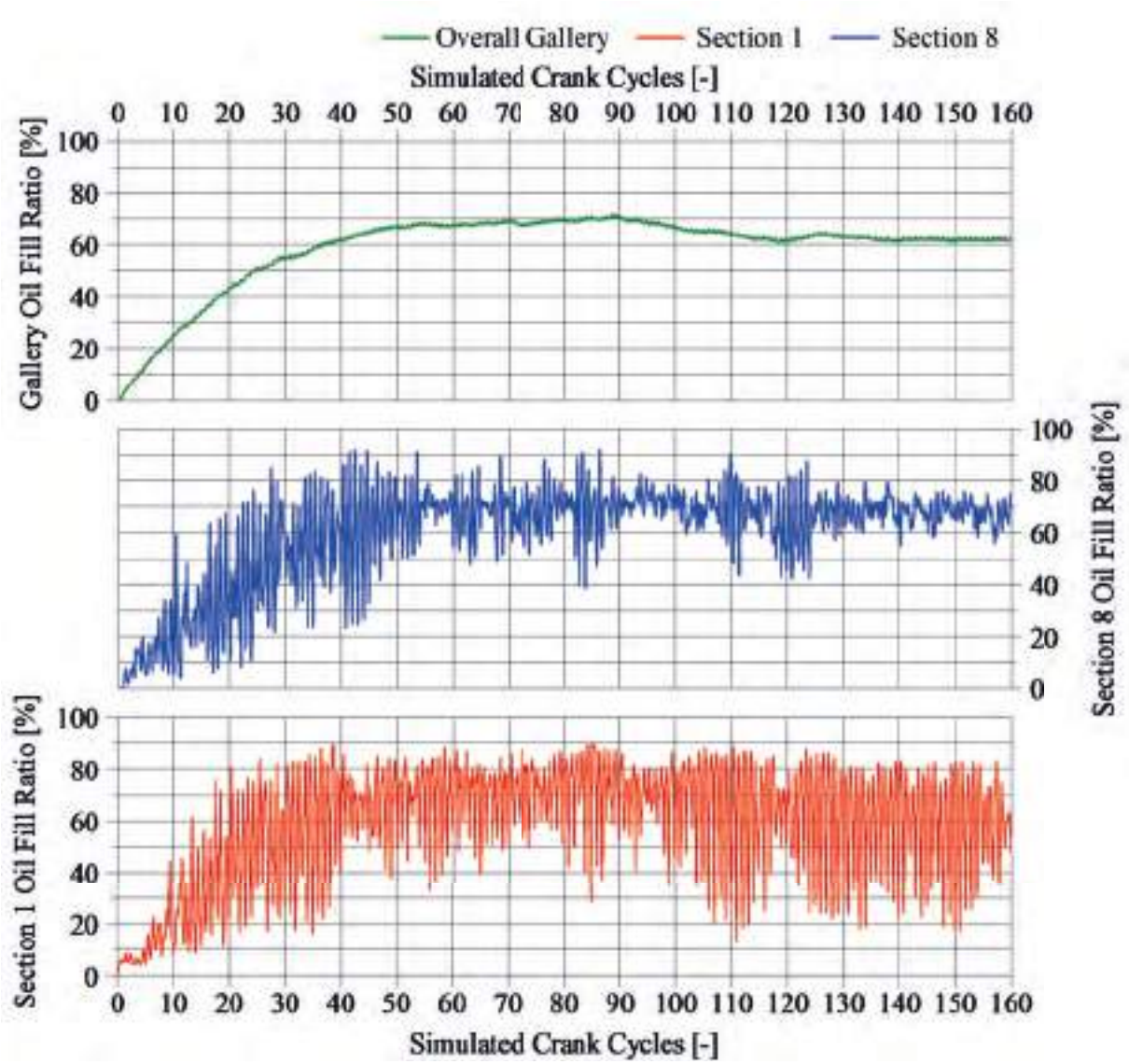

Fig. 6.14 Internal gallery filling behaviour for overall gallery and sections 1 and 8

equation

$$OFR = \frac{1}{72} \sum_{cas=1}^{72} OFR^*_{cas} \tag{6.7}$$

where OFR^*_{cas} is the gallery OFR for every recorded fifth crank angle during a full crank cycle. Then the standard deviation of the OFR for each crank cycle was calculated with the equation

$$\sigma_{OFR} = \sqrt{\frac{1}{72} \sum_{cas=1}^{72} (OFR - OFR^*_{cas})^2} \tag{6.8}$$

The average value from standard deviation of the 21 consecutive crank cycles was then determined by

$$\overline{\sigma}_{OFR} = \frac{1}{21} \sum_{noc=1}^{21} (\sigma_{OFR})_{noc} \tag{6.9}$$

This was the first criteria for the convergence assessment and represented the deviation of the *OFR* from the cycle averages, but excluding the variation of the *OFR* for consecutive cycles.

The second assessment criteria addressed the deviation of the *OFR* based on a cycle-by-cycle consideration. The average of the *OFR* for 21 consecutive cycles was calculated by

$$\overline{OFR} = \frac{1}{21} \sum_{noc=1}^{21} OFR_{noc} \tag{6.10}$$

from which the standard deviation of the 21 consecutive cycle average was determined by

$$\sigma_{\overline{OFR}} = \sqrt{\frac{1}{21} \sum_{noc=1}^{21} \left(\overline{OFR} - OFR_{noc}\right)^2} \tag{6.11}$$

If large variation of the *OFR* with the range occurred, then the standard deviation would indicate this behaviour, regardless if the variation was small and continuous or abrupt.

The overall gallery filling was declared converged, when the standard deviation of the average of 21 consecutive cycles was less than the average standard deviation of 21 consecutive cycles

$$\overline{\sigma}_{OFR} < \sigma_{\overline{OFR}} \tag{6.12}$$

The calculation process was also repeated for each individual sector (sector 1 to 8) to assess sectoral filling convergence. The simulation process was only terminated, when overall and sectoral convergence was achieved. If such criterion was not achieved, then the simulation was terminated after 200 cycles (approximately 10 time constants) of the settling period phase and all evaluation was based on averaging over the 200 cycles.

Mesh independence convergence

The method of *CFD* builds on the division (discretisation) of the flow domain into small control volumes (cells), for which the flow equations are solved. As shown previously, the time step for a calculation greatly depends on the size of the cells. Large cells allow therefore for larger time steps and can lead to shorter overall simulation times to solve a problem. On the contrary, small cell sizes require smaller time steps, prolonging the overall simulation

time, but improve simulation accuracy as smaller flow phenomenon and flow features can be captured more accurately. Neither of the cell limits offers the best performance considering accuracy, simulation time and cost. The optimum lies somewhere in between.

Roache (1997), de Souza (2002), Celik et al. (2008) and Delteil et al. (2011) strongly encourage the investigation of mesh convergence and model sensitivity to assess the quality of the results. It was postulated that grid convergence is achieved, if a refinement in the mesh size does not yield further change in solution variables. Roache (1997) also stated that without thorough investigation of the model uncertainties, expressed as mesh based errors, results should not be presented in publications. Furthermore it was recommended that there should be at least three different mesh sizes for analysis, with the size of the finer mesh being half the height (length) of the coarser mesh. This can be achieved in two ways, either by mesh refinement or by coarsening. Mesh refinement posed fewer problems in the application, as elements could be easily split, rather than combined. However, the splitting increased element numbers by a factor of 8 (2^3) per refinement step. This led to very fine meshes, which required significantly increased computing power for solving and partially caused problems with regards to computation time.

de Souza (2002) used splitting the cells into cells with half the edge size as a refinement method to investigate mesh independence. For 3–dimensional meshes each tetrahedron was split into eight new tetrahedra cells and each hexahedron was split into eight new hexahedra, leading to a cell volume reduction by 87.5%. It was also postulated that the selection of the dependent parameter for mesh convergence relied strongly on the type of problem investigated. For the simulation of jet breakup Pai et al. (2008) identified the Weber number as the defining parameter for mesh independence analysis. The cell splitting method also had a negative side, where with progressing refinement steps parallel computing capabilities are a must in order to solve such problems within a reasonable computing time.

Delteil et al. (2011) therefore employed a variation of the method to validate a liquid jet breakup model. The sizes of the cells in the full flow domain were initially reduced by 30% through adjustment of cell volume and re-meshing. The process was repeated twice with reductions at 50%. With increase in mesh density the results converged towards a final value, which then compared well with experimental data, confirming the accuracy of the model and the approach.

Slagter (2008) proposed a comparable method, but starting with the finest mesh representing the level of tolerance required in the model, and then progressing by combining cells into larger ones. This would lead to coarser meshes and deviation behaviour from the converged fine mesh results. Bakker (2012) indicated that some of the shortcomings of coarser meshes may be overcome by employing higher order calculation schemes, although these are not as stable and may have a higher computational cost.

An alternative method for mesh refinement was presented by A.Berlemont et al. (2012). Particular areas of the flow field were re-meshed, to capture the occurring phenomenon more accurately, while generally maintaining a large mesh for fast solution. The method was applied to the tracking of the interface of two phases, where the area near the interface was re-meshed with finer cells to capture the rippling of the interface. This reduced the solution process time and resource requirement, making this approach more economical in comparison to the other methods.

For the problem under investigation a mesh convergence test was conducted to assess the mesh sensitivity. Following the approach by de Souza (2002), an initially coarse mesh was used, followed by refinement of the full domain in several steps. The initial mesh was reduced based on modification of cell edge length, rather than cell spitting. An initial study with the cell splitting approach showed a generation of an amount of cells, which led to unsustainable long calculation times, as a result of restricted available resources (computer specifications). Therefore, for a refinement step the cells edge lengths were reduced approximately by $\sqrt[3]{0.5}$ reducing the cell volume to 50% of the original size. Roache (1997) recommended performing at least two refinements to obtain three solutions for the analysis of the convergence, if the exact solution was not known.

The mesh convergence test was conducted on both mesh-type models, the mixed mesh model (gallery section 1 and 8 with tetrahedra and 2–7 with hexahedra), and pure hexahedral mesh model. Besides the mesh sensitivity analysis, the performance of the meshes with regards to computational time was also assessed to identify the best performing model for the comparative study simulations. It may be noted here that there was an additional model for the non-conform interface models. The declared converged model was also investigated with regards to the boundary layer influence. For better overview the mesh statistics for this model is included here. Table 6.2 shows an overview of the models used for the convergence study.

[4]BL = Boundary Layer

Table 6.2 Mesh sizes and quality for *LGM* with conform and non-conform interfacs

Mesh size	Minimum Number of Cells (BDC)	Maximum Number of Cells (TDC)	Maximum Cell Skewness	Minimum Orthogonal Quality	Maximum Aspect Ratio	Average Gallery Cell Size
	–	–	–	–	–	mm^3
Non-conform interface models						
Very coarse	15758	18893	0.802	0.251	15.22	16.28
Coarse	22392	49082	0.897	0.296	17.30	14.78
Medium	50451	67437	0.802	0.321	14.75	5.24
Fine	77042	96507	0.876	0.213	24.40	3.07
Very fine	125880	152570	0.925	0.125	17.30	1.85
Non-conform interface models						
Very coarse	2572	3948	0.596	0.701	5.91	52.46
Coarse	11577	14029	0.616	0.618	6.62	14.66
Medium	25533	36073	0.696	0.696	7.36	5.38
Fine	43789	57899	0.604	0.712	7.56	2.98
Very fine	78684	99254	0.581	0.735	8.37	1.62
Fine BL^4	112073	123693	0.864	0.366	14.67	1.14

Figure 6.15 and 6.16 show the direct comparison between the average cell sizes of all mesh models. It can be seen that the average cell size was almost halving with each step. The intended refinement step could not be achieved for the very coarse conform interface mesh, because the already large cell size for the coarse mesh could not be increased significantly due to limitations of mesh skewness. The significant smaller cell size for the boundary layer model was a result of the small near wall cells representing the boundary layer. The core cell size was identical to the fine mesh.

For many simulations, including highly turbulent flow and heat transfer, boundary layers are used at the wall in order to determine the flow and transport conditions more accurately. Although turbulent flow may be the predominant flow in a domain, near the wall a laminar boundary layer was present and required careful consideration.

As stated previously, equation 3.32 allowed estimation of the distance y representing the height of the first cell of the boundary layer at the wall, leading to

$$y = \frac{\mu\, y^+}{\rho u_\tau} = \frac{\mu\, y^+}{\sqrt{\rho\, \tau_w}} \tag{6.13}$$

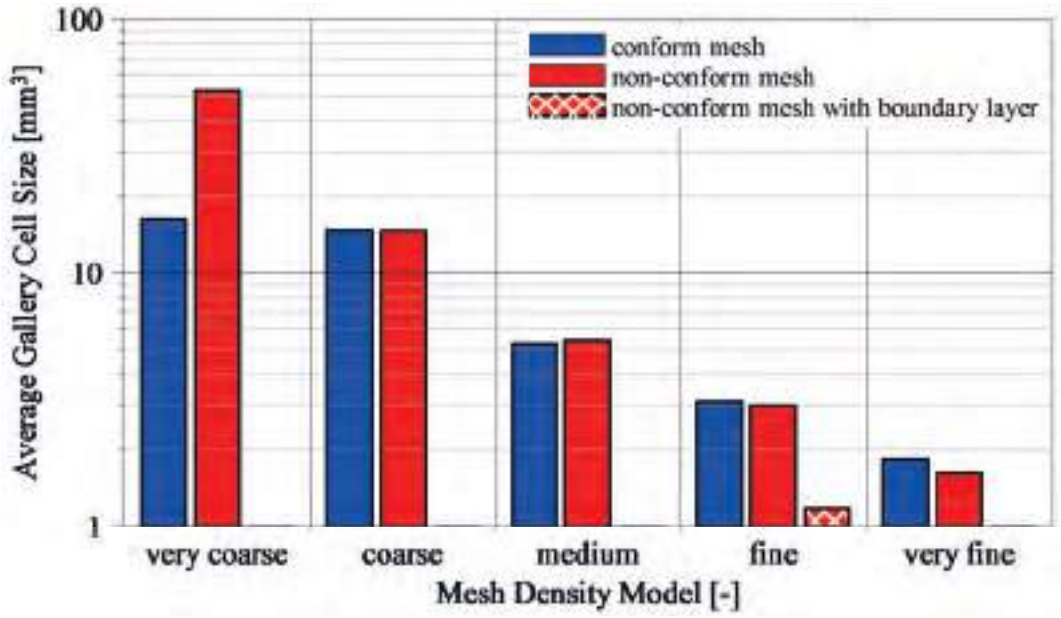

Fig. 6.15 Average cell size for mesh inside gallery for investigated *LGM* models

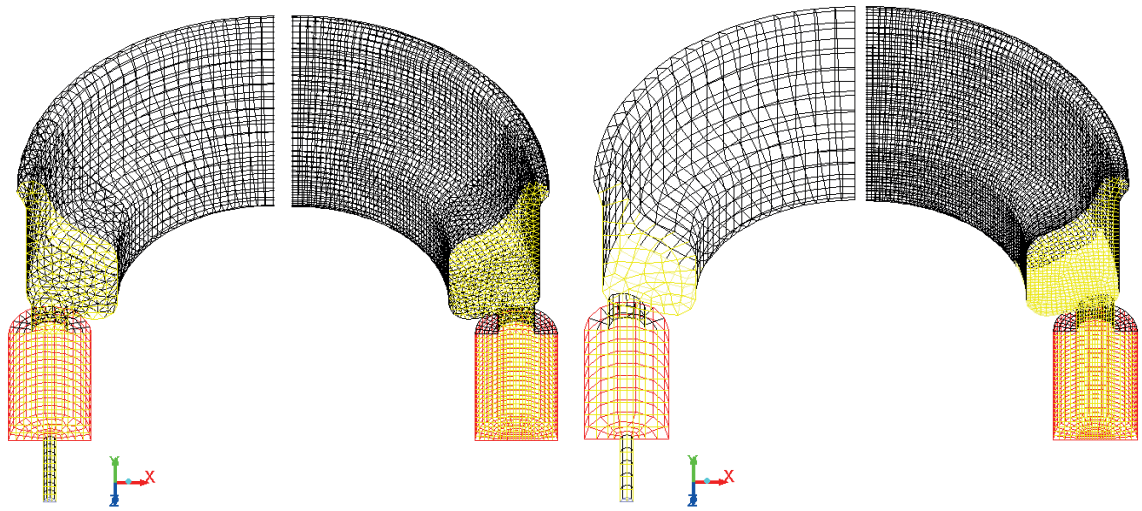

a) conform mesh b) non-conform mesh

Fig. 6.16 Mesh difference between conform interface and non-conform interface model, indicating coarsest mesh (left) and finest mesh (right)

with

$$u_\tau = \sqrt{\frac{\rho}{\tau_w}} \tag{6.14}$$

where μ is dynamic viscosity, ρ the density, u_τ the velocity parallel to the wall, τ_w the wall shear stress and y^+ is the dimensionless wall distance. The value for y^+ was set to 11.63, based on recommendation of the thickness of laminar and buffer layer by Andersson et al. (2011) and Versteeg and Malalasekera (2007).

An initial analysis of the flow velocities inside the model gallery without the boundary layer was performed and revealed an unstructured distribution of the highest velocities across the gallery sections, ranging from 1.9 m/s to 23.9 m/s. The average velocity was determined as 8.4 m/s over one complete crank revolution cycle and was used as the free steam velocity for the estimation of the first boundary layer mesh height.

The thickness of the first cell in the boundary layer was determined as 0.18 *mm* with a total thickness of the boundary layer of 4.66 *mm*, resulting in a total of 10 layers to represent the boundary layer. The meshing of the gallery with a boundary layer at the determined conditions showed severely deformed and skewed cells, especially in the upper part of the gallery. An adjustment of the dimensions and number of layers was necessary. A sufficiently fine boundary layer was found with 5 layers and a total thickness of 1.34 *mm*, which achieved a skewness and orthogonal quality of 0.864 and 0.366 respectively. The meshes with and without boundary layer are shown in Figure 6.17. The detailed view of the mesh with boundary layer also highlights the area of concern with regards to the skewness, as highly deformed cells can be found near the boundary layer.

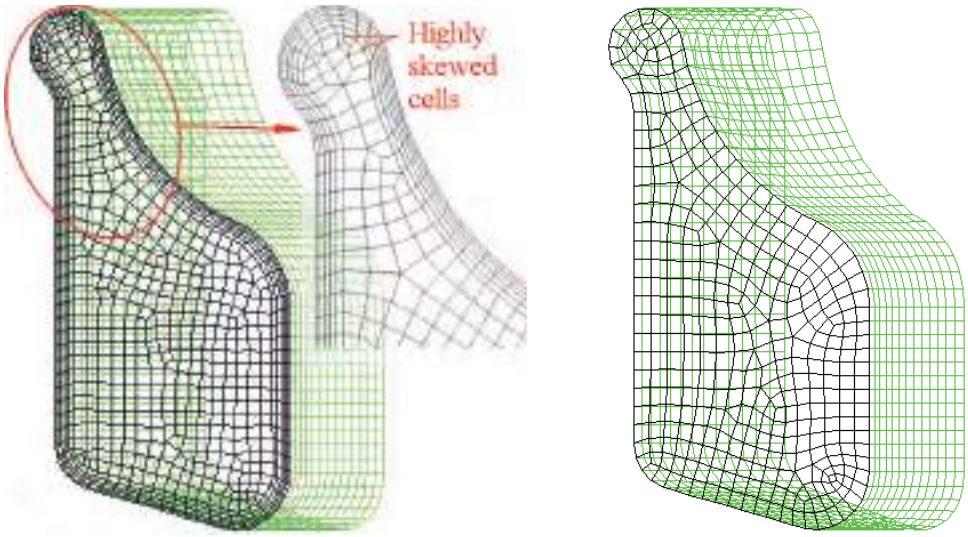

a) Mesh with boundary layer and detailed view b) Mesh without boundary layer

Fig. 6.17 Mesh comparison between *LGM* model with and without boundary layer inside gallery

Figure 6.18 shows the converged *OFR* for all investigated mesh refinement models. It can be seen that the refinement of the mesh led towards a final gallery filling value of approximately 80%, independent of the mesh type. It can also be seen that when boundary layers were included in the model, it did not yield significant different results in comparison

to the same mesh density model without the boundary layer. Although only present for one specific case, this result was deemed sufficient to exclude the boundary layer from the comparative models.

The very fine mesh for the conform-interface model did not yield a converged result, due to the excessive computation time as a result of the large number of cells.

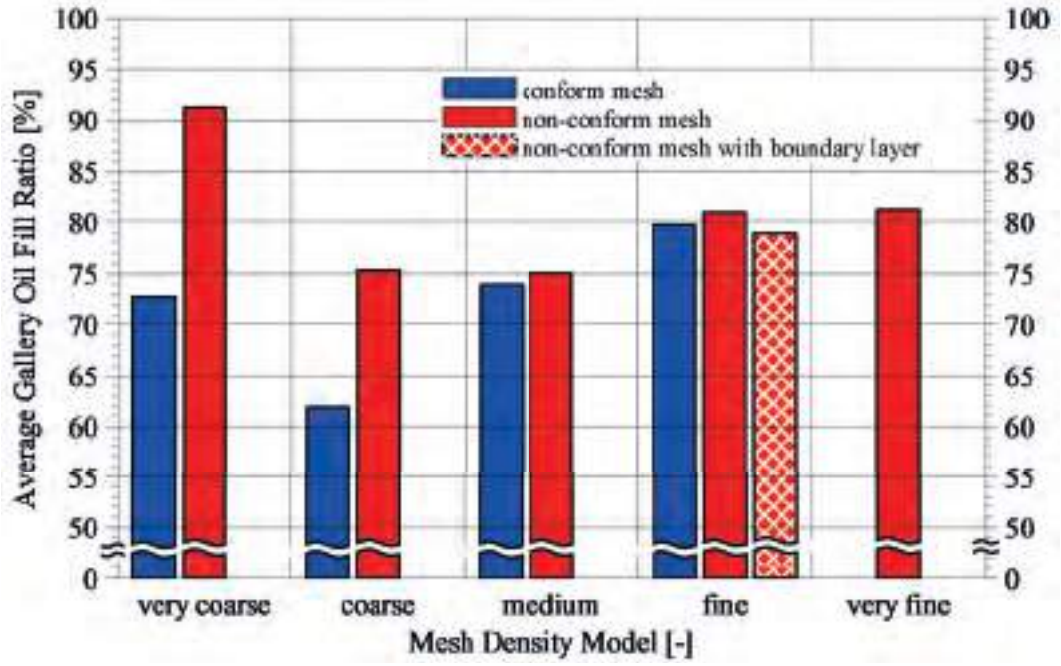

Fig. 6.18 Average gallery filling *LGM* for various mesh models

It may be noted that all models were run on the same computer in sequential order so that the results could be directly compared. To place the computational times in prospective, the computer and software specifications were:

- Intel i7 3770K 3^{rd} generation multi-core processor at 4.1 GHz,
- Memory of 16 GB at 1600 MHz,
- Seagate hard drive with 1TB storage space at 7200 rpm,
- ANSYS Fluent R14 Parallel at 2 physical cores with 2 integer cores each (4 partitions).

Figure 6.19 shows a comparison of the time required per crank revolution cycle. The non-conform fine mesh showed the best performance in terms of computation time, which can be attributed to the lower number of cells. Although the difference in the simulation time between the non-conform fine and very fine model was only 1h 56m, the minimum number of 21 cycles was needed to determine convergence. This amounted in a simulation

time difference of approximately 1.6 days. It was also noticed that some models produced faster reduction in residuals and hence reached the time step convergence target much quicker. This also accounted for the difference in simulation time. Care was taken that the solutions converged at every integration step by either reaching the target (generally 10^{-3}, but 10^{-6} for energy) or residuals falling at least a magnitude of 10^3.

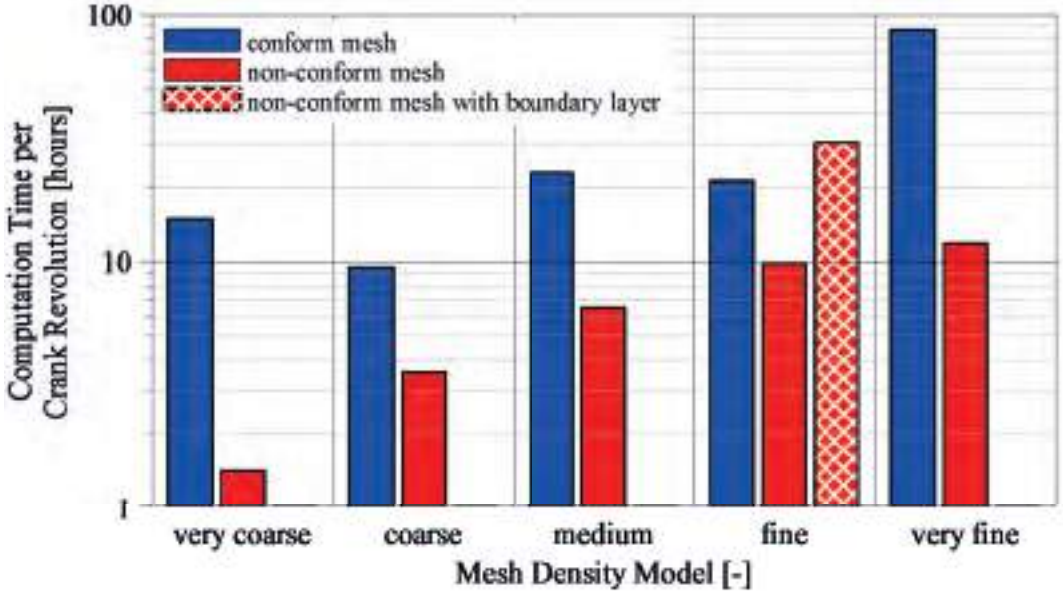

Fig. 6.19 Simulation time for one crank cycle for various meshes on *LGM*

Uncertainty Assessment

An uncertainty assessment was conducted to assess the quality of the numerical results and achievement of mesh independence of the results. Roache (1997), Eca and Hoekstra (2006) and Ali et al. (2009) suggested the determination of mesh convergence using a Grid Convergence Index, a modified version of the Richardson extrapolation (Richardson and Gaunt, 1927). The mesh data and results of target variables, such as velocity, from the solved mesh models maybe used to determine the Grid Convergence Index (*GCI*). Additionally to the *GCI* the order of accuracy p, approximate relative error e_a, and convergence ratio R could be calculated to assess, if convergence was achieved. A detailed explanation of the theory and process can be found in Appendix D. For the presented study the *OFR* was used as the investigated variable of the uncertainty assessment.

While the convergence ratio R indicated the type of convergence, the *GCI* was a measure of the resolution level and how close the solution would approach an approximated final value. The aim was to refine the mesh until smaller values of the *GCI* were obtained, although the

value for the *GCI* was dependent on the requirements of the study and had to be set on an individual basis.

Eca and Hoekstra (2006) and Ali et al. (2009) stated different types of convergence conditions, where:

- for $0 < R < 1$, monotonic convergence is indicated,
- for $-1 < R < 0$, oscillatory convergence is indicated,
- for $R > 1$, divergence is indicated and
- for $R < -1$, oscillatory divergence. is indicated

Examining the results in column 1 of the non-conform interface models in Table 6.3 it can be seen that the convergence ratio R was very small, but indicating monotonic convergence. The *GCI* for the second refinement step (GCI_{fine}) showed a value of less than 1%, indicating that the solution had converged. The convergence order of accuracy p, however, was very high and therefore out of the order of reliable convergence, so called super-convergence. Eca and Hoekstra (2006) suggested, when large values for the order of accuracy were found, to set the order to a value of two and recalculate again. The recalculated results are shown in column 2 of the non-conform interface models in Table 6.3. The *GCI* values increased, but for the fine grid step (GCI_{fine}) was still at a value below 1%, and convergence could be declared.

The values for the conform interface modes in Table 6.3 show the results of the equivalent mesh sizes models to the non-conform interface models. The convergence ratio R showed monotonic behaviour with an accuracy order near unity, which meant that accuracy was only of linear quality. The *GCI* showed high values for the coarse and fine step and could not be classified as converged yet. An extra refinement step was performed (very fine mesh), but the excessive computation time permitted any reliable results to be obtained.

Table 6.3 *GCI* Analysis

Interface Model	Non-conform		Conform
	Medim–Fine–Very fine		Coarse–Medium–Fine
p	15.83	2 (set)	1.065
e_a	0.37%	0.37%	7.3%
GCI_{coarse}	0.598%	22.3%	16.2%
GCI_{fine}	0.022%	0.97%	16.0%
R	0.04	0.043	0.98

The boundary layer model was omitted in the uncertainty study, as only one model was investigated and good comparison with the model without the boundary layer was determined.

6.4 Large gallery model filling behaviour study during crank cycle

The non-conform interface model with fine mesh and without boundary layer was used to investigate the influence of flow rate and rotational crank speed on the gallery oil filling. This model was used, based on the outcomes of the convergence study, as it provided the best performance with regards to computational stability, relative accuracy and computing time.

The images presented in the following text provide an overview of the conditions inside the gallery for one case only. More images highlighting the flow conditions inside the gallery for all investigated cases can be found in Appendix E.1 to E.4.

6.4.1 Flow behaviour at *BDC*, *600 rpm* and *4.0 l/min*

Figure 6.20 shows the air distribution inside the gallery at the *BDC* position of the crank cycle. The images highlight the main positions of the air bubbles inside the gallery from various viewing positions and were superimposed from ten consecutive crank cycles. It can clearly be seen that there occurred cycle-by-cycle variation of size and position of the air, indicating a strong time dependent behaviour. It may be noted that the difference in colour strength does not indicate higher probability of the air bubble being in this position. It is rather a result of the superimposing image process from the post-processing, although overlapping air bubbles will produce darker shading.

From the images shown in Figure 6.20 it can also be seen that the vertical position of air in the gallery changed along the horizontal gallery position. Two effects controlled the air position. As the gallery reached the *BDC* the oil was forced to the gallery bottom by inertia effects, pushing the air upwards. This effect was predominant in the mid-gallery and outlet sections of the gallery.

At the gallery inlet sections the effect of the entering oil jet controlled the position of the air. The oil jet pierced through the bottom oil layer and impacted on the gallery inside top wall, from where it was pushed into the gallery branch. The continuous oil jet entry provided

a source for the flow into the gallery branch and also caused flow of oil along the gallery walls. This created an oil layer at the wall and suspended the air near the gallery centre. The inlet-driven wall-guided circulating flow at the inlet also retained the majority of air at the inlet sections. Smaller amounts of air separated from the collected air content at the inlet and moved into the mid-gallery sections to continue travelling towards the exit. At the outlet the bottom oil layer blocked the air from exiting, leading to increased amounts of air above the outlet, but little air exiting.

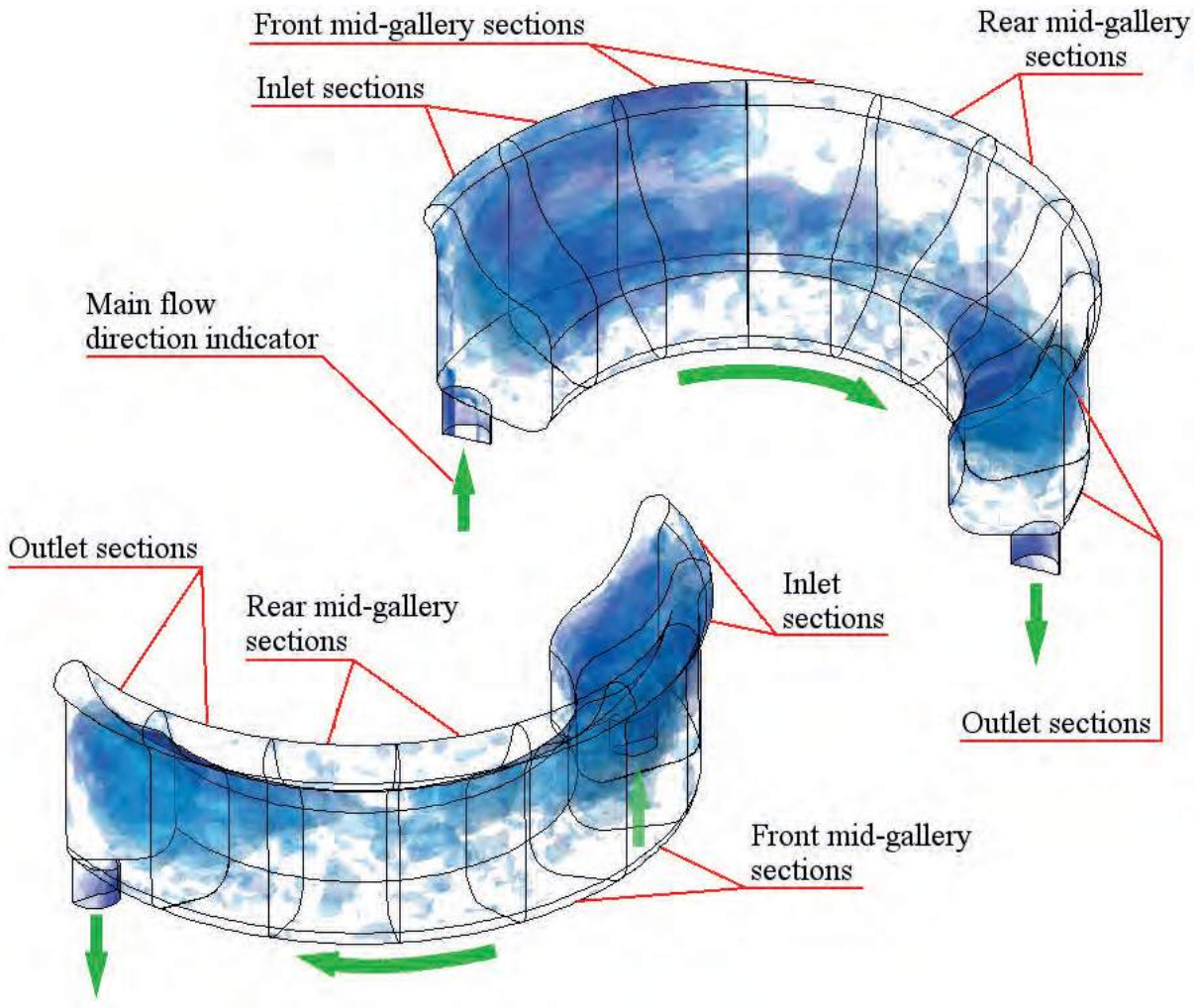

Fig. 6.20 Main positions of air inside the *LGM* gallery at *BDC* position (superposition of consecutive 10 cycles)

Figure 6.21 shows a representative flow condition inside the gallery at the *BDC* position from the consecutive cycles used for the above image. The presented case is a representative encapsulation of the flow conditions encountered. The air position was superimposed by flow direction vectors of oil and air, shown as red and blue coloured arrows respectively. At the

inlet sections the flow was mainly driven by the oil entering through the gallery inlet. The high momentum of the oil jet allowed the oil to pierce through the bottom oil layer (**A**) and impact on the inner gallery top surface (**B**). The wall impact deflected the oil jet and led to flow into the galley branch (**C**), whereby the flow was partially controlled by the gallery wall. The combination of the inertia forced flow and the oil jet driven wall-bound flow also generated a circulating swirling flow of the oil towards the gallery inlet (**D**). Furthermore the deflected flow and the swirling movement encouraged strong mixing effects.

The flow progressed through the gallery branch and became more inertia controlled, as the effects from the entering oil jet reduced. The horizontal movement (**E**) could still be linked to the oil inflow, but the vertical movement (**F**) was a combination of the inertia effects due to gallery model velocity changes and the movement of air bubbles. The combination of both (inertia and air) led to a swirling oil movement (**G**) in the front mid-gallery sections with some flow back to the inlet sections.

The flow in the rear mid-gallery sections showed little influence from the forward flow from the inlet sections. The main flow behaviour could be attributed to inertia controlled flow with little horizontal movement, leading to more cross-sectional movement (**H**), especially when larger air bubbles were present. The direction of the swirl was dictated by the gallery shape, as the amount of oil located at the outer vertical gallery surface was larger, pushing the lower amount at the inner vertical gallery wall upward.

At the outlet sections the inertia effect was the main driver to push the oil towards the outlet channel (**I**). This also forced the collected air upward (**J**) and controlled the oil flow out of the gallery. Comparable cross-sectional flow behaviour as in the adjacent sections can be found. The higher amount of oil on the outer gallery carried more inertia than the oil at the inner gallery wall. This led to downward moving oil on the outside wall (**K**) and upward moving oil on the inside wall (**L**). The cross-sectional area of the outlet hole was also too small to allow fast enough drainage of the oil to allow concentrated exit flow and the remaining oil aided the inner wall upward oil flow.

6.4.2 Flow behaviour at *TDC*, *600 rpm* and *4.0 l/min*

Figure 6.22 shows the air distribution inside the gallery at the *TDC* position of the crank cycle based on ten consecutive crank cycles. During the upward stroke from *BDC* the majority of

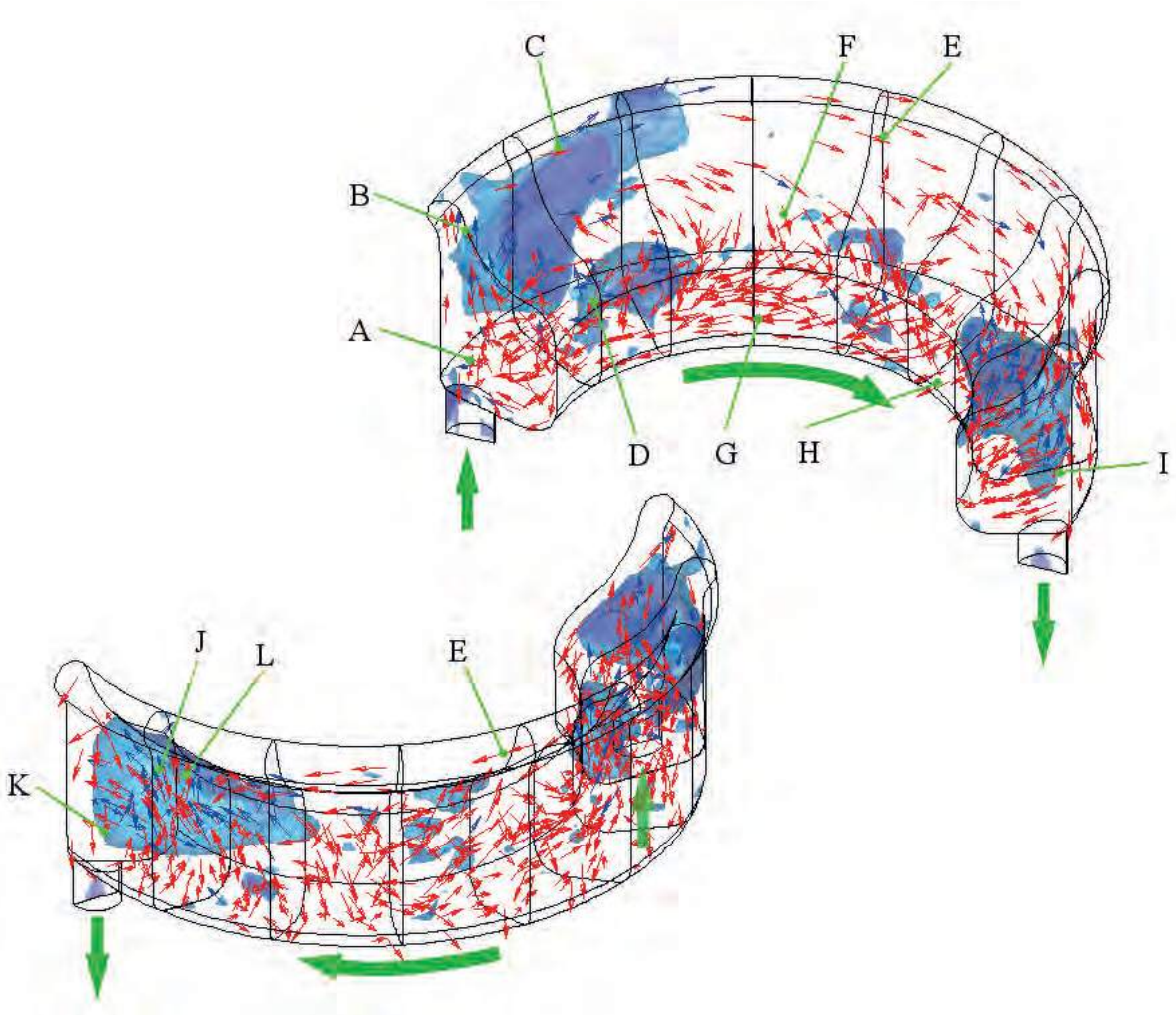

Fig. 6.21 Air position and flow direction of oil and air inside *LGM* gallery sections at *BDC* for one representative cycle

oil was located at the gallery bottom. When the gallery approached the *TDC* the velocity of the gallery model reduced. The reduction in velocity was not transmitted to the oil and the remaining inertia forces on the oil forced a movement of the oil towards the gallery top, while forcing the air downwards. The start of this process occurred before the *TDC*, but the most consistent air locations were found near the *TDC*. Although the inertia effects on the oil generally resulted in downward movement of air to the bottom, the internal flow paths of the oil also carried smaller sized air bubbles back towards the gallery top.

The cycle-by-cycle variation of air location resembled the condition as found at the *BDC* position, highlighting the strong transient instability. The distribution of the air along the gallery branch showed significant difference. The majority of the air was found at the mid-gallery and outlet sections, with the inlet sections portraying the lowest air content. The

largest variation of air location can be found in the mid-gallery sections. The interaction between forward flow from the inlet sections (entering oil jet) and backward flow from the outlet sections caused a mixing that led to the inconsistent transient air positions.

The lower amount of air at the inlet sections can be attributed to the reduced impact energy of the oil jet, leading to reduced forward flow into the gallery. The collection of the air at the gallery bottom allowed also for more space to be filled by oil.

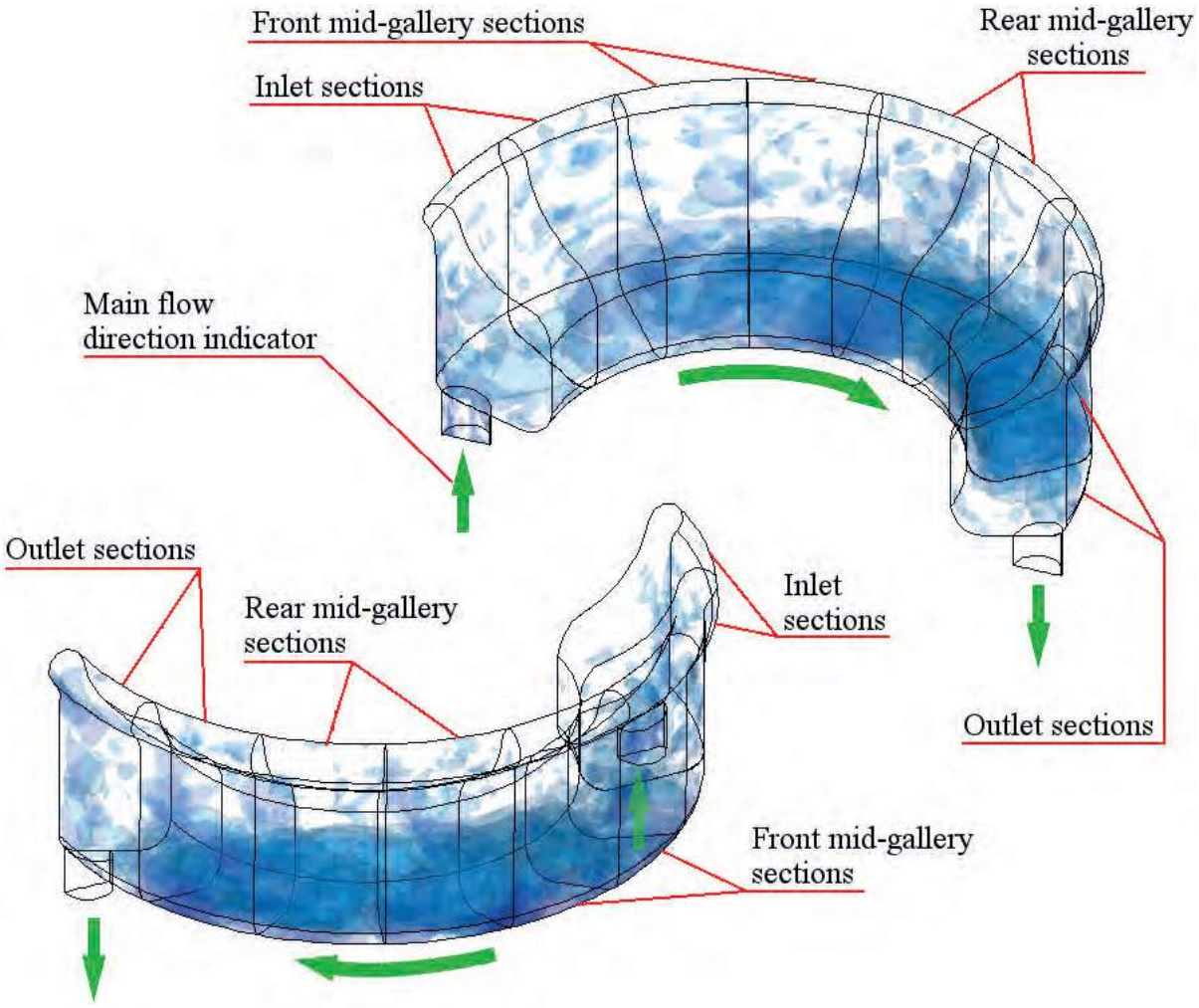

Fig. 6.22 Main positions of air inside the *LGM* gallery at *TDC* position (superposition of consecutive 10 cycles)

Figure 6.23 shows one representative flow condition inside the large gallery at the *TDC* position from the ten consecutive cycles used for the above image. The presented case is a representative encapsulation of the flow conditions encountered. The air position was superimposed by flow direction vectors of oil and air, shown as red and blue coloured arrows respectively.

The entering oil jet caused a collection of oil at the inlet sections that allowed little formation of air pockets (**A**). In comparison to the conditions at *BDC* the oil present in the gallery moved upward and the inflowing oil impacted on the bulk oil formation (**B**). This forced the oil sideways into the gallery branch due to lack of space (**C**) and caused a circulating flow (**D**) in the first half of the of the gallery branch. The circulating flow pushed the air into the lower areas of the mid-gallery sections (**E**) and also forced flow of oil along the gallery bottom (**F**).

The main flow direction in the outlet sections was upward (**G**) as the gallery came to a standstill at the *TDC* position. Although the oil generally moved away from the gallery bottom, hence from the outlet channel, the limited space at the gallery top only allowed for a flow direction back into the gallery branch (**H**).

In the mid-gallery sections the larger air bubbles controlled the flow, as these provided the least resistance to the oil. There occurred two distinct flow streams, initiated from the inlet section and the outlet section. While source of the flow from the inlet was found in the entering jet and inertia effects, the flow from the outlet section was mainly caused by the combining flows at the outlet channel and from inertia effects. At the collision of the flows the oil was forced downward (**I**) mainly on the outer gallery wall. As the flow from the inlet contained the larger kinetic energy due to the jet inflow, the location of the collision was found in the rear mid-gallery sections (**J**), beyond the half gallery length.

6.4.3 Gallery sections oil filling during crank cycle at *600 rpm* and *4.0 l/min*

Figure 6.24 shows the cycle averaged filling for each individual gallery section (green bars). The cycle averaged *OFR* for the overall gallery was determined as 80.9%, as indicated by the dashed line. It can be clearly seen that the cycle averaged section *OFR* varied, with a maximum difference found at 4.5% (difference of average *OFR* between section 1 and 4). This was small compared to the variation of the *OFR* within each individual gallery section during the crank cycle, indicated by the side bar (blue and red). The largest variation was found for section 1 at the inlet, where a total variation between maximum and minimum filling of 30% occurred. It should be noted that the bars indicate the averaged minimum

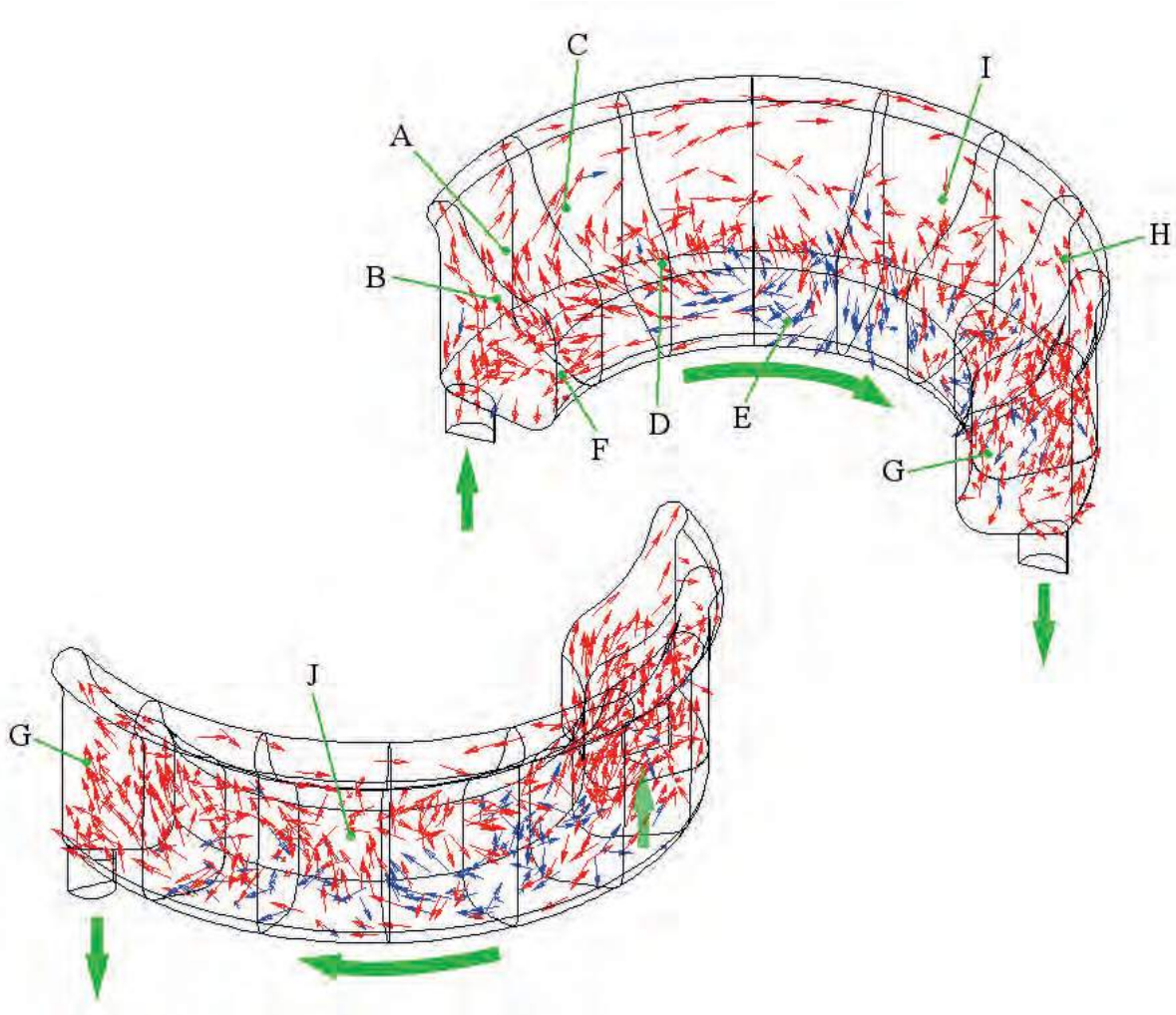

Fig. 6.23 Air position and flow direction of oil and air inside *LGM* gallery sections at *TDC* for one representative cycle

and maximum section filling occurring during the cycle. This is not standard deviation or variability and only shows the variation of *OFR* within the cycle.

The oil filling behaviour of each individual section is shown in Figure 6.25. The solid lines represent the cyclic section filling during the crank cycle and the dash-dot lines represent the average filling over the cycle. The average data was obtained by averaging results from 100 consecutive cycles.

The black dashed lines refer to the theoretical normalised entry velocity of the oil jet as it entered the gallery. The normalisation of the velocity was performed to emphasise the increase in entry velocity as the gallery moved downward and a reduction in entry velocity as the gallery moved upward. Normalisation was performed with respect to nozzle exit velocity

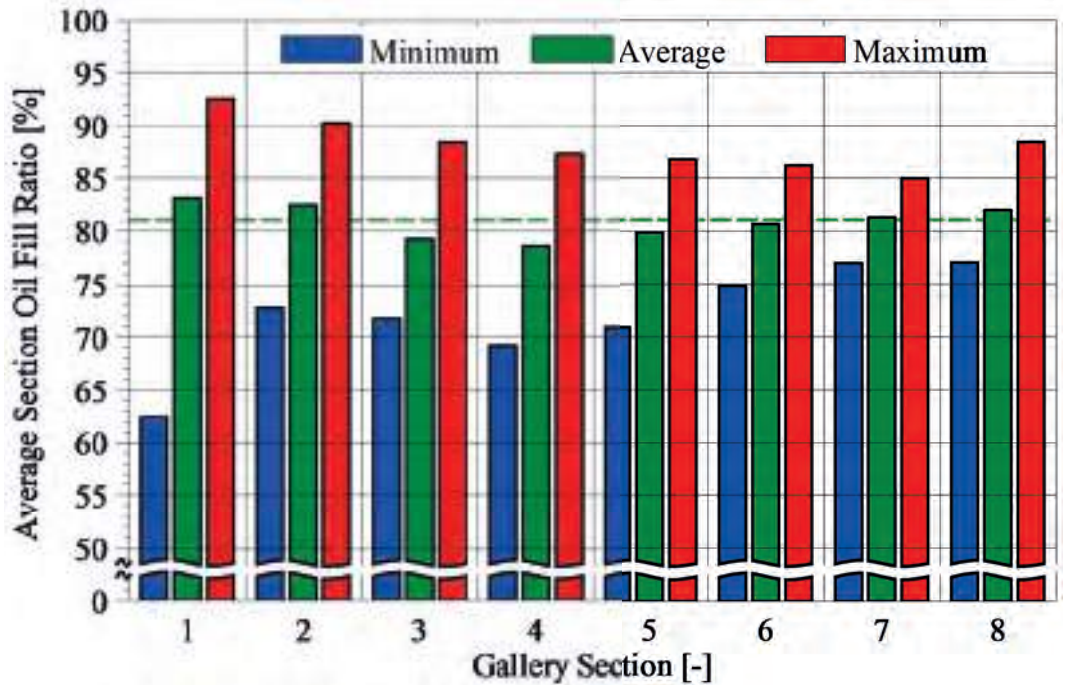

Fig. 6.24 Gallery section *OFR* for *LGM* and deviation from cycle averaged mean (average of 100 cycles)

of the oil jet and a value of one indicates that the entry velocity was identical to the nozzle exit velocity.

The high variation at the inlet sections can be attributed to the influence of the entering oil jet and gallery movement. During the upward stroke less oil entered the gallery due to the lower velocity difference between jet and gallery, leading to a reduction of filling in the inlet section. The opposite effect occurred during the downward stroke, where the upward facing jet was forced at a higher relative velocity into the gallery, delivering an increased amount of oil.

The mid-gallery sections showed the smallest variation in filling. The inertia driven change in oil position together with varying forward flow from the inlet and backward flow from the outlet section meant that the majority of air was forced to circulate in the gallery, rather than being pushed to the outlet and exit. This circulation was constrained to the amount of air present and hence lower variation occurred.

The outlet section showed comparable cyclic behaviour to the inlet section, as the flow patterns were comparable. As the gallery moved upward the oil was exiting, reducing filling. During the downward stroke oil was delivered from the gallery branch to the outlet increasing filling, while some re-entry of oil from outside the gallery occurred, adding to the increase.

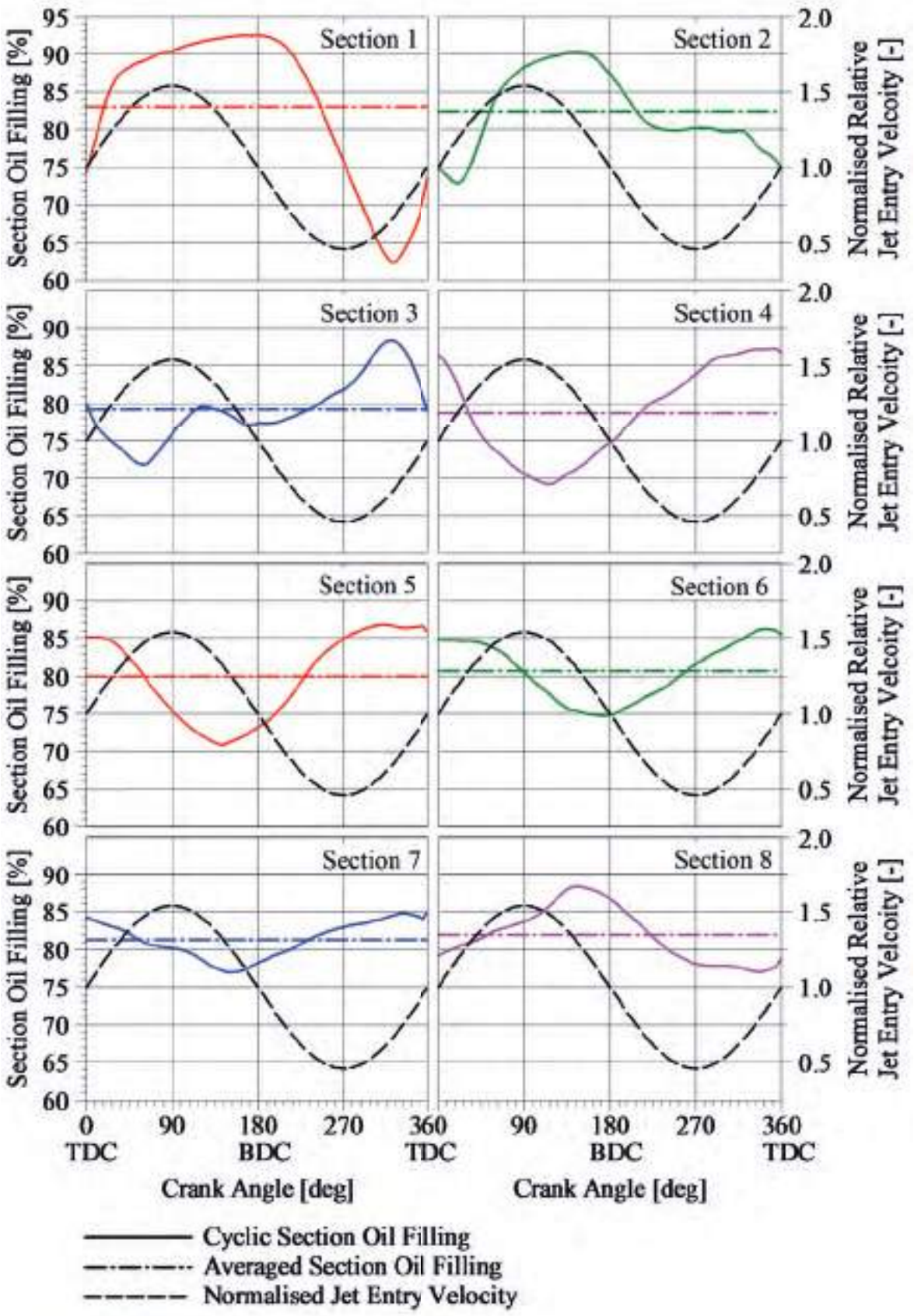

Fig. 6.25 Section oil filling behaviour during complete crank cycle for *LGM* (average of 100 cycles)

Figure 6.26 shows the oil flow behaviour during the crank cycle, highlighting key effects. The oil jet showed a convoluted shape, as shown in Figure 6.26a. Oil exiting from the inlet section during the upward stroke impacted on the oil jet and caused a divergence from the straight path. The extent of side movement of the jet depended on the amount and location of the rejected oil and varied by crank cycle.

The crank angle of the lowest oil fill ratio in the mid-gallery sections (sections 3 to 7) changed at near constant interval and indicated a movement of air bubbles through the gallery. The movement of a large air bubble is shown in Figure 6.26b to d. At the *TDC* the air was located at the gallery bottom in the central mid-gallery sections. During the downward stroke the inertia driven oil flow together with the inlet flow pushed the air towards the inlet section and onto the inner galley wall, as shown in Figure 6.26b. At the same time oil re-entered the gallery through the outlet channel as the downward gallery velocity was higher than the falling velocity of the oil outside the gallery.

The approach of the *BDC* position increased the inertia effects and the air in the gallery was driven upwards, while the exit flow from the outlet was at maximum, as shown in Figure 6.26c. During the upward stroke the oil flow at the gallery bottom and the entering oil jet at the inlet forced the air along the gallery top into the rear mid-gallery sections, as shown in Figure 6.26d. At the same time oil exited during the whole upward stroke, although the amount exiting reduced beyond the half stroke position, as the outlet section emptied and little flow from section 7 occurred. The movement of air continued along the gallery top until the approach of the *TDC* position, where inertia effects forced the oil to the gallery top again.

A similar behaviour of circulating air movement was also observed at the rear mid-gallery sections and outlet sections, but with a smaller air size. The air bubble position in the sections 7 and 8 compared well with the centre air movement in sections 3, 4 and 5 and can be clearly seen in Figure 6.26c and 6.26d.

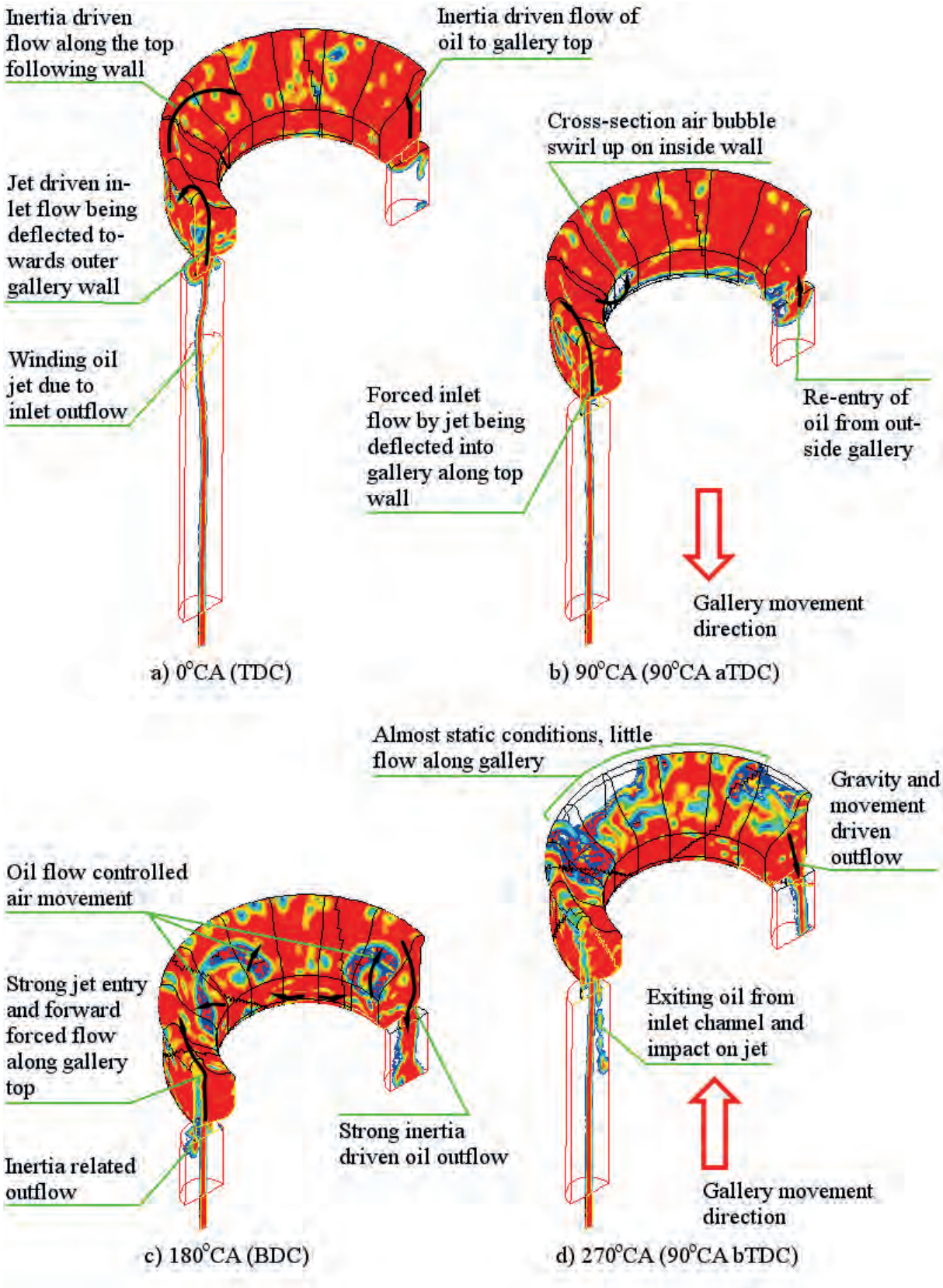

Fig. 6.26 Gallery filling and internal flow behaviour of *LGM* during crank cycle at 600 rpm and 4.0 l/min

6.5 Small gallery model setup and initial study

6.5.1 Geometry

The small gallery model (*SGM*) was generated following the same procedure as the large gallery model (*LGM*) and is shown in Figure 6.27. The gallery was split into eight sections, with an inlet and outlet channel connecting to free-flow volumes. The inlet channel was modelled with a longer geometry than the outlet channel to reflect the experimental model. Use was made of symmetry to reduce computational demand.

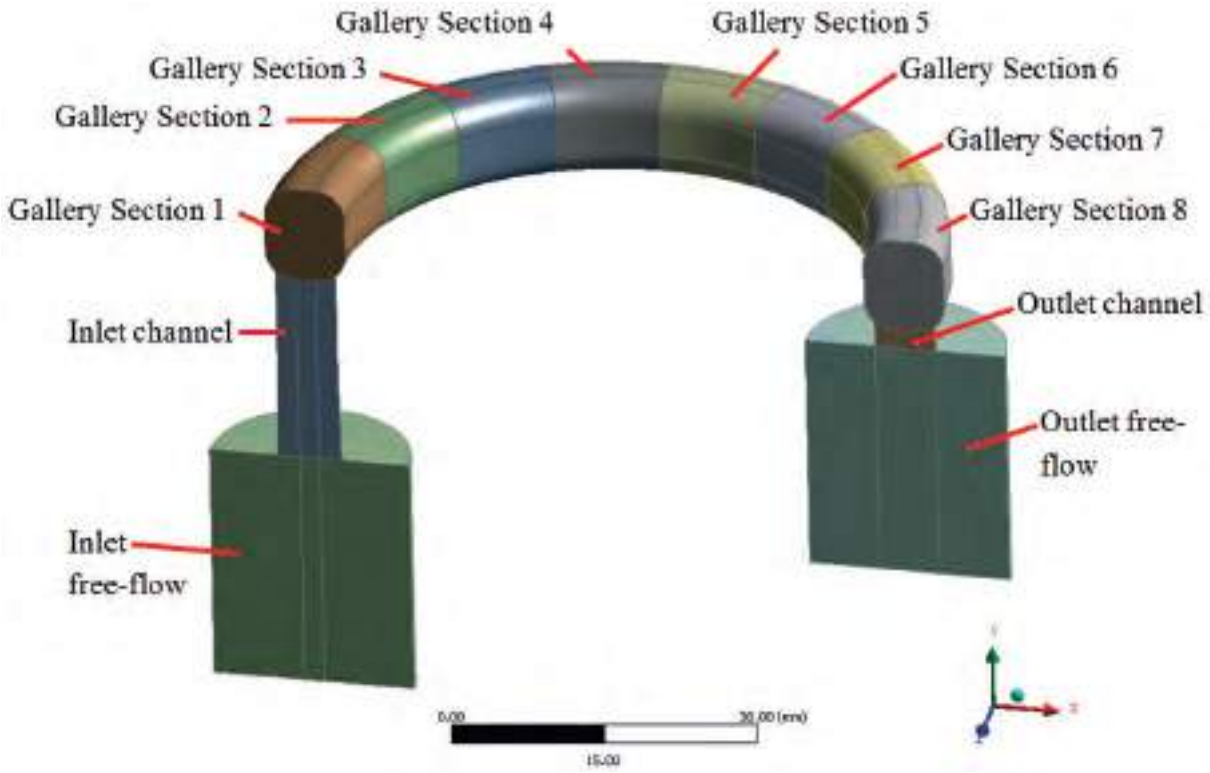

Fig. 6.27 Small gallery model geometry

6.5.2 Boundary conditions

The similarity between both galleries allowed transfer of boundary conditions to the small gallery model, especially with regards to walls, interfaces and outlets.

Walls

The walls were generated identically to the *LGM* with the same conditions described in Section 6.3.2, page 141. The named gallery walls are shown in Figure6.28.

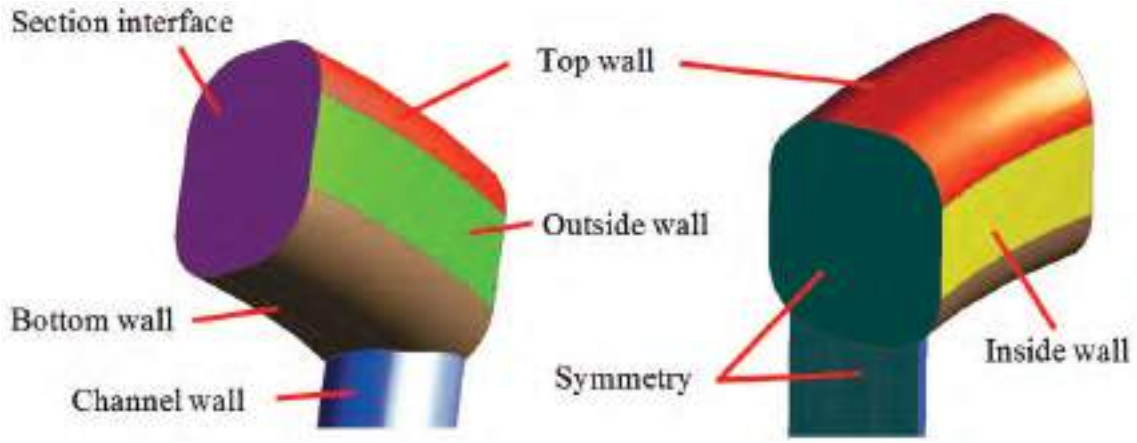

Fig. 6.28 Wall surfaces on small gallery model

Model inlet and outlets

Figure 6.29 highlights the inlet and outlets of the *SGM*. The inlet was modelled as a velocity inlet, using the same profile description for turbulent or laminar inflow conditions, as for the *LGM* (Section 6.3.2, page 141). The profile was adjusted to reflect the 2 *mm* inlet diameter. The additional nozzle volume, as used on the *LGM*, was not included. The direct application of the velocity profile at the inlet free-flow was found to sufficiently model the jet behaviour and also reduced the model size. The outlets were pressure outlets using identical conditions to the *LGM* with 5% turbulence intensity and 10 *mm* backflow hydraulic diameter.

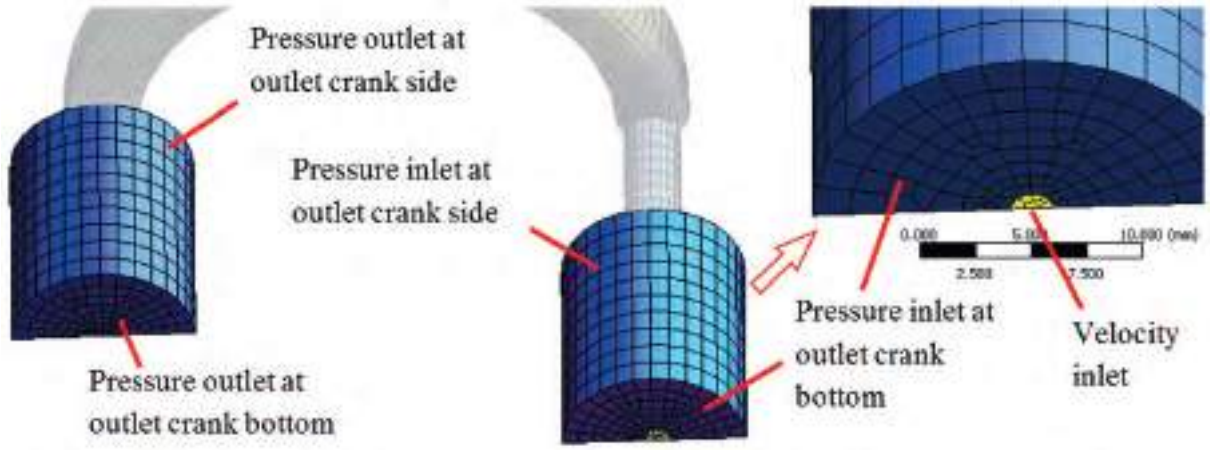

Fig. 6.29 Model outlet and inlet for small gallery model

Symmetry and interfaces

The model sub-domains (sections, channels, etc.) were connected by interfaces, as shown in red in Figure 6.30. All interfaces were of conform type, except for the interfaces between the

inlet channel and gallery section 1 and outlet channel and gallery section 8, which were of non-conform type. Use was also made of the gallery's symmetry.

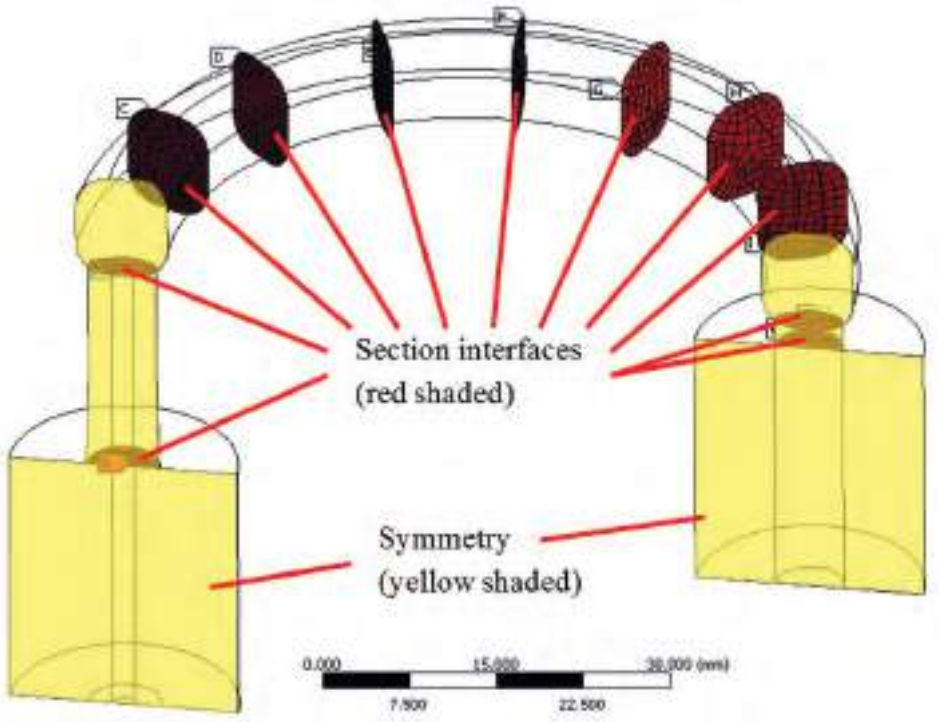

Fig. 6.30 Small gallery model interfaces and symmetry

6.5.3 Materials

The same values of density and viscosity for oil and air were used, as described in Section 6.3.3 on page 146.

6.5.4 Meshing

The mesh sensitivity study on the *LGM* determined a sufficient fine mesh for converged oil fill ratio results and good phase interface tracking capability. However, the significant difference between both gallery sizes raised the issue, if the same mesh size could be used to obtain equally reliable results from the *SGM*. The small gallery exhibited a larger gallery surface to volume ratio, potentially resulting in higher influence of friction from the wall bounded flows inside. A mesh convergence study was therefore conducted.

An initial coarse mesh was generated, using a hexahedral mesh, and refinement was executed by splitting each cell into eight new cells to obtain the medium mesh. The process

was repeated to the mesh again, resulting in the fine mesh. A fourth mesh was generated, aimed to resemble approximately the mesh size of the converged large gallery model. To keep the skewness within acceptable limits there had to be a compromise and the generated mesh was more in line with the fine mesh of the *LGM*. A final fifth mesh was generated showing the core properties of the initial coarse mesh, but employing a 1 *mm* boundary layer thickness at the gallery walls. Table 6.4 shows an overview of all mesh models.

Table 6.4 Mesh sizes and quality for *SGM* with non-conform interfaces

Mesh size	Minimum Number of Cells (BDC)	Maximum Number of Cells (TDC)	Maximum Cell Skewness	Minimum Orthogonal Quality	Maximum Aspect Ratio	Average Gallery Cell Size
	–	–	–	–	–	mm^3
Coarse	2482	4550	0.667	0.534	11.47	3.73
Medium	18684	24039	0.798	0.481	7.79	0.47
Fine	137712	146252	0.952	0.676	16.67	0.06
LGM-eq.	7672	12488	0.571	0.748	9.53	1.26
Coarse-BL[5]	6259	10219	0.667	0.622	1.26	1.39

The inlet free-flow sub-domain employed a varying size mesh to provide the link between nozzle opening and moving gallery, as shown in Figure 6.31 for the medium mesh. All other sub-domains used a fixed size mesh.

In comparison to the large gallery model the calculation time was less, as the total number of cells was lower. There was a significant increase in the calculation time between coarse, medium and fine mesh, due to refinement, but as only the gallery was refined by cell-splitting the time increase did not increase proportionally.

Figure 6.32 shows that the calculation time from the medium mesh to the fine mesh increased approximately by a factor of 4.3, while the number of cells increases by a factor of six based on the *TDC* mesh size. Similar factors should be expected for the coarse mesh to medium mesh refinement. The mesh size increased by a factor of 5.3, while the computation time increased only by a factor of two. This meant that the coarse mesh model was slower in relation to the mesh size. Although the governing equations were solved for each cell in the model, the use of a multi-core solving process added extra requirements to the solving process. For a multi-core process the model was split into partitions (software driven), with one partition for each solving core. Each partition had to be interlinked with the adjacent

[5]BL = Boundary Layer

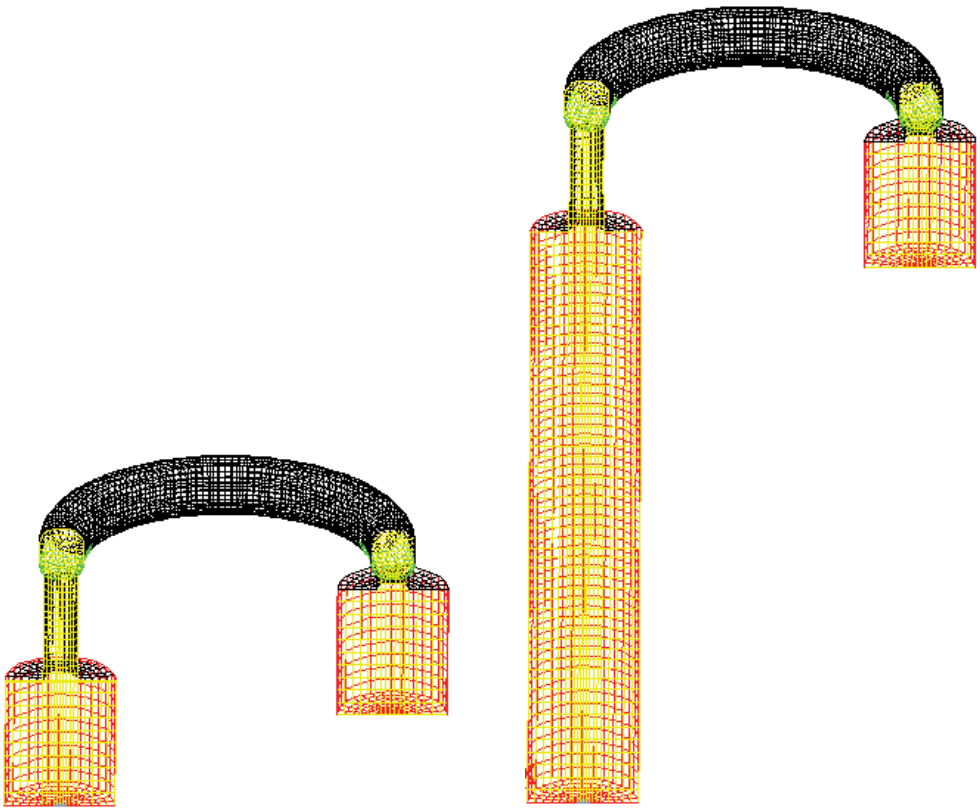

a) mesh for gallery at BDC b) mesh for gallery at TDC

Fig. 6.31 Small gallery model mesh at *BDC* and *BTDC*

partition. On coarse meshes the solving time may be low, but the interlinking process added to the total solving time and did not increase proportional with mesh size, therefore leading to longer overall time relative to finer meshes.

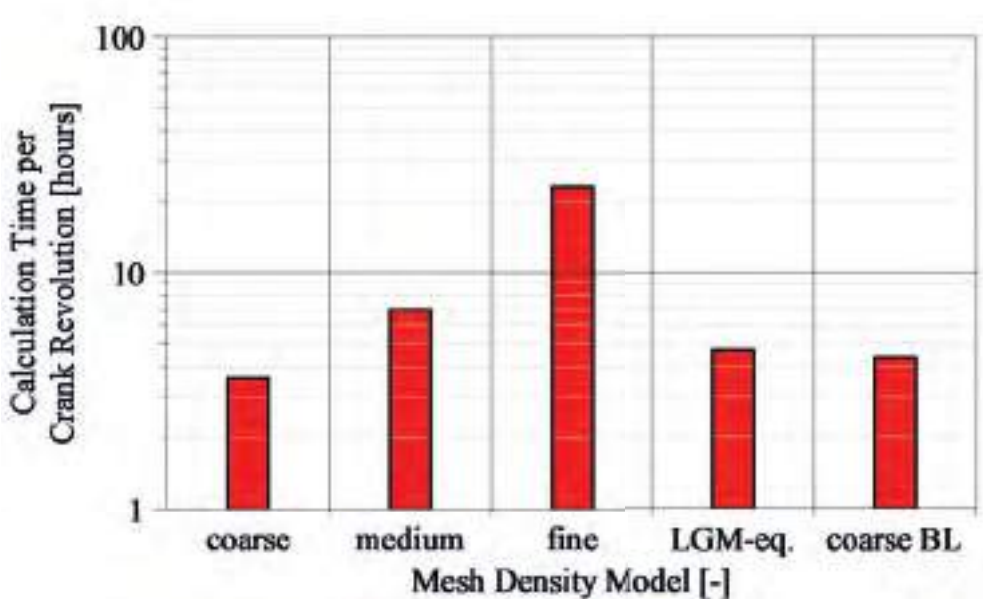

Fig. 6.32 Simulation time for one crank cycle for investigated meshes on *SGM*

6.5.5 Convergence study

The same averaging method, averaging range (21 consecutive crank cycles) and convergence assessment criteria, as used for the *LGM* and described in Section 6.5.5, was used for the *SGM*. While the coarse mesh models did not reach convergence and data averaging was performed over 200 cycles, the fine mesh model converged after 82 cycles, approximately half the cycles of the medium mesh model. The fine mesh model may seem the better option for analysis, but the significant increase in simulation time (approximately 35 days) made its use impractical. All coarse and medium mesh models showed similar respective values for the cycle averaged oil fill ratio within a range of 6%, as shown Figure 6.33. The fine mesh model in comparison showed a higher value for *OFR*, exceeding the coarse models by at least 8% and the medium mesh models by 14%. There was little difference in *OFR* between coarse model with and without boundary layer, indicating that the boundary layer may be omitted, if no heat transfer was included.

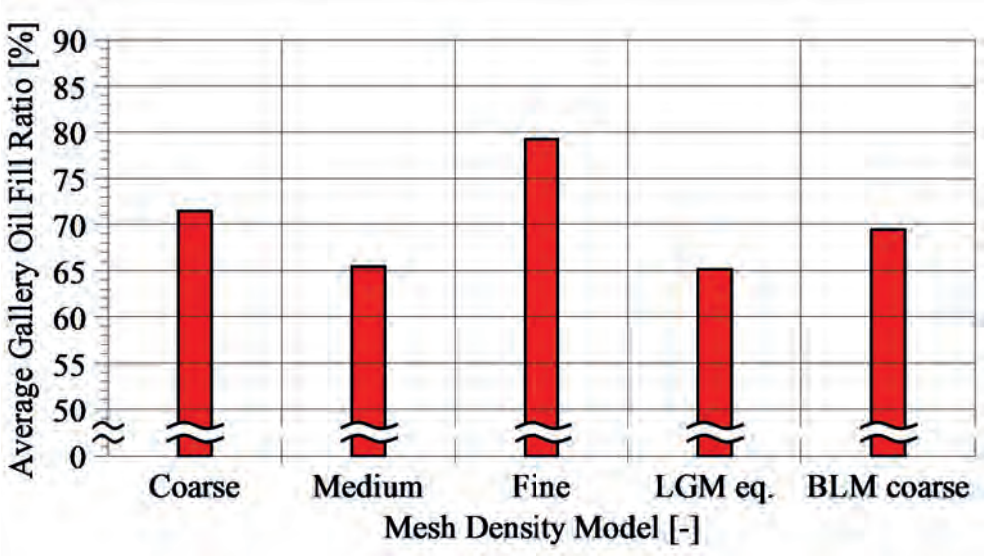

Fig. 6.33 Average gallery filling for investigated meshes on *SGM*

An uncertainty assessment should be performed to assess the quality of convergence of the *OFR* with respect to mesh density, but significantly different *OFR* value between the mesh models did not yield reasonable results. A further refinement of the mesh was also impractical, given the long calculation time for the fine mesh. The implementation of a coarser mesh as an alternative to an additional mesh refinement step was attempted, but led to a highly distorted mesh causing issues with solver stability. As a compromise between computing power and

sufficient reliable results the priority was given to the model employing cell size of the *LGM*, as the suitability of the mesh was shown previously.

6.6 Small gallery model filling behaviour study during crank cycle

The model with the *LGM* equivalent mesh size was used to investigate the influence of flow rate and rotational crank speed on the gallery oil filling. This model was used, based on the outcomes of the convergence study, as it provided the best performance with regards to computational stability, relative accuracy and computing time.

The images presented in the following text provide an overview of the conditions inside the gallery for one specific case only. More images highlighting the flow conditions for all investigated cases can be found in Appendix E.5 to E.8.

6.6.1 Flow behaviour at *BDC*, *750 rpm* and *1.65 l/min*

Figure 6.34 shows the distribution of air inside the small gallery at the *BDC* position of the crank cycle along the gallery length. The images highlight the main locations of air, based on the superposition of results from ten consecutive cycles. It can be seen that the air was mainly distributed along the top of the gallery, which was mainly a result of the inertia effects and supported by gravity. As the gallery approached zero velocity at the *BDC* position, the oil was forced to the bottom and the air collected at the gallery top.

The largest amount of the air was found at the inlet sections, covering sections 1 and 2. There was good consistency of the general air locations, but it can also be seen that strong variation of the position of air bubbles especially in the rear mid-gallery sections occurred. This could be attributed to the transient effects influencing the actual inflow and outflow of the gallery openings.

Figure 6.35 shows one representative flow condition inside the gallery at the *BDC* position from the ten consecutive cycles used for Figure 6.34. It can be seen that as the oil jet entered through the inlet, it pierced through the bottom oil layer and impacted on the gallery top (**A**). There was also some air drawn into the gallery along with the oil jet (**B**). Due to the close distance between nozzle and gallery, the jet diffusion was marginal, leading to a narrow jet in

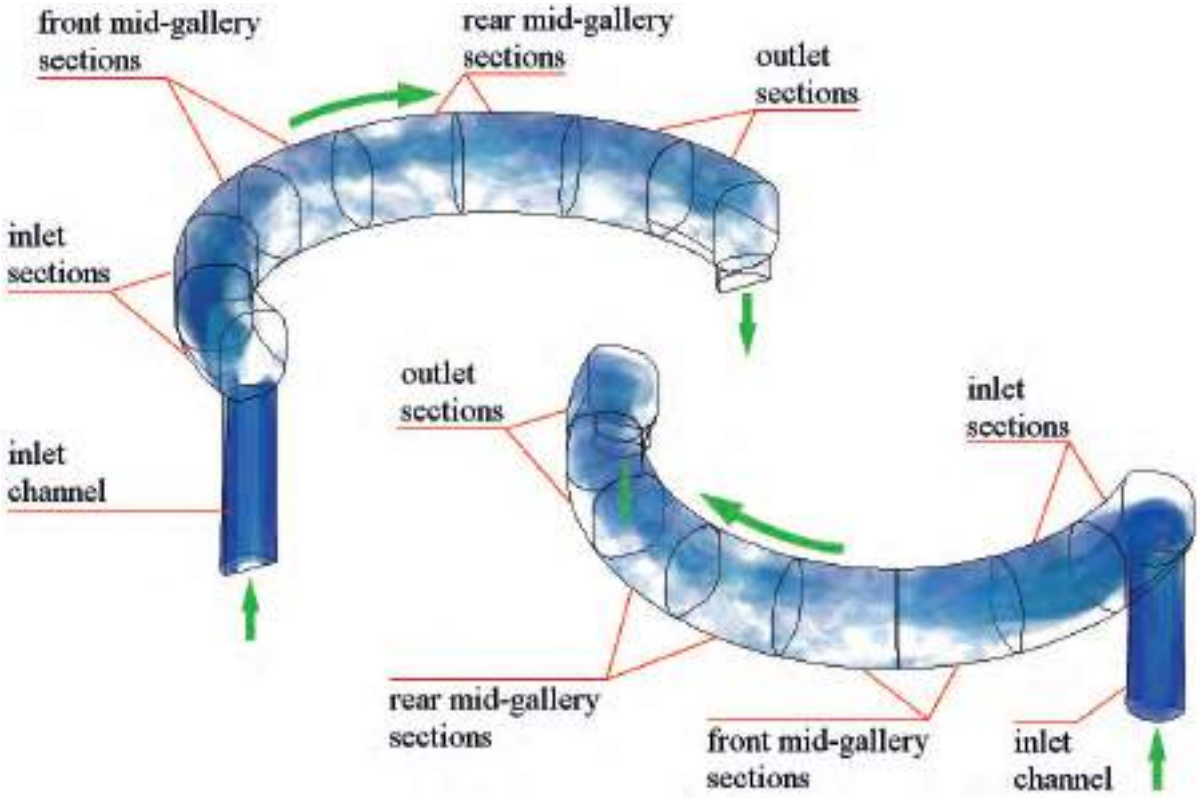

Fig. 6.34 Main positions of air inside the *SGM* gallery at *BDC* position (superposition of consecutive 10 cycles)

the inlet channel cross-section centre. In some instances oil was exiting from the gallery at the same time by flowing along the inlet channel wall. At the top gallery wall the oil jet deflected and progressed horizontally into the gallery branch. The smaller cross-section and smaller diameter of the gallery led to wall-bound flow along the outer gallery wall (**C**), creating a movement from top to bottom that progressed to the half-length of the gallery branch. The oil flow also controlled the location of the air bubbles, which collected on the inner gallery wall in the inlet sections (**D**) and near the gallery cross-section centre, as oil in the gallery was pulled to the bottom by inertia effects and the entering oil jet created a layer at the top.

In the front mid-gallery sections the flow still showed wall-bound forward flow (**E**), driven by the jet inflow. In the rear mid-gallery sections the flow slowed down significantly, generating a cross-sectional swirling flow, whereby upward flow occurred (**F**) on the inside gallery wall. As gravitational effects would generally produce downward flow of the oil, the effects of the curvature around the centre axis together with the inlet flow pushed the oil up.

The flow in the gallery outlet sections showed mainly horizontal forward flow behaviour (**G**) with little cross-sectional swirling. At the intersection of both gallery branches the main

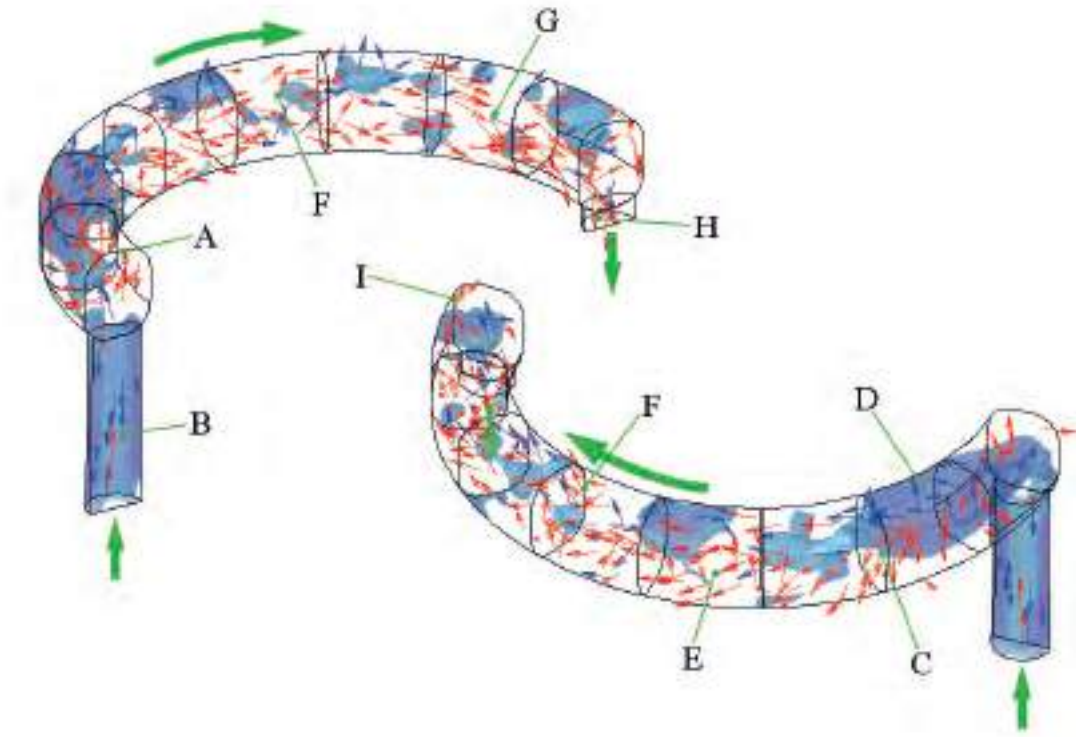

Fig. 6.35 Air position and flow direction of oil and air inside SGM gallery sections at BDC for one representative cycle

flow was through the outlet channel (**H**), mainly as a result of the colliding branch flows, but also because of the inertia effects. In some instances some upward flow was noticeable (**I**), the reason being that the outlet channel could not provide sufficient flow cross-section for both branch flows, as the amount of oil from each gallery branch was larger than the outlet channel itself.

6.6.2 Flow behaviour at *TDC*, *750 rpm* and *1.65 l/min*

Figure 6.36 shows the distribution of air inside the small gallery at the *TDC* position of the crank cycle along the gallery length. The images highlight the main locations of air, based on the superposition of results from ten consecutive cycles. The air was mainly located on the gallery bottom, as the inertia forces on the oil were significantly larger than the gravitational forces pushing the oil to the gallery top.

The increased distance between nozzle exit and inlet channel entry (and gallery respectively) generated a slightly winding[6] behaviour of the oil jet, reducing the momentum of the oil jet (top right corner of Figure 6.36). The result was increased oil content in gallery section 1 adjoined to the inlet channel, indicated by the small amount of air bubbles. The reduction in inflow momentum had also an impact on the front mid-gallery sections, where less stable and repeatable flow conditions led to a distribution of air bubbles across the gallery height.

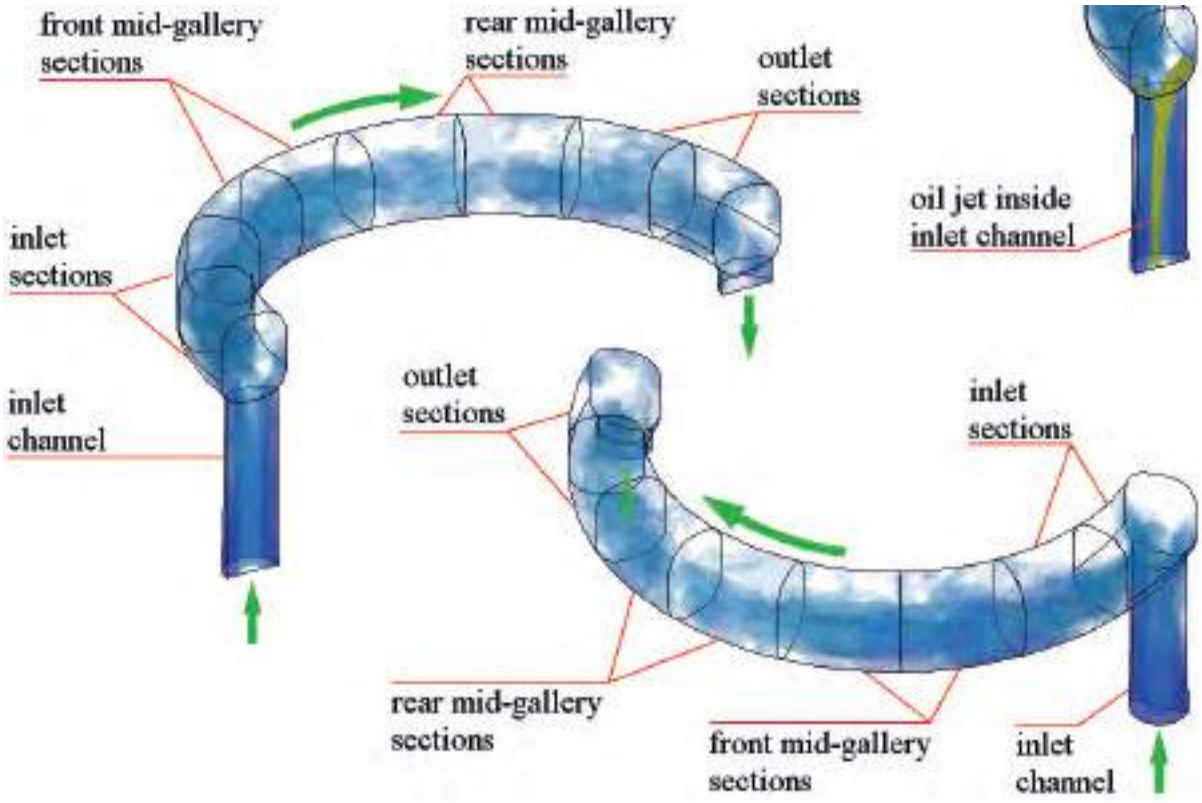

Fig. 6.36 Main positions of air inside the *SGM* gallery at *TDC* position (superposition of consecutive 10 cycles) and diverted jet in inlet channel

There were also some randomly distributed air bubbles near the top gallery wall, especially in the outlet sections. The amount of oil exiting during the upward stroke influenced the flow conditions in the outlet sections and subsequently the re-entrant of oil, which in turn affected the flow in the gallery.

Figure 6.37 shows a representative flow condition inside the gallery at the *TDC* position from the consecutive cycles used for the above image. As shown previously, the inertia effect was the controlling factor for the positioning of air and oil, with the air being forced to the

[6]The oil jet diverted from the straight vertical flow behaviour and portrayed a snaking behaviour. This is different from jet breakup.

gallery bottom and the oil to the top. The majority of air was found in the inlet sections of the gallery and was comparable to the amount of air as found at the *BDC* position.

The increased distance between nozzle exit and inlet channel entry, resulting in the winding of the oil jet, led to interaction with oil present on the inlet channel walls flowing out of the gallery (**A**) and reduced jet momentum. When the oil jet entered the gallery it impacted on the bulk oil mass located on the gallery top and forced the bulk oil to move into the branch (**B**). This reduced velocity and momentum further and hence circulating flow near the inlet hole occurred. In the front mid-gallery sections the flow was more unstructured or

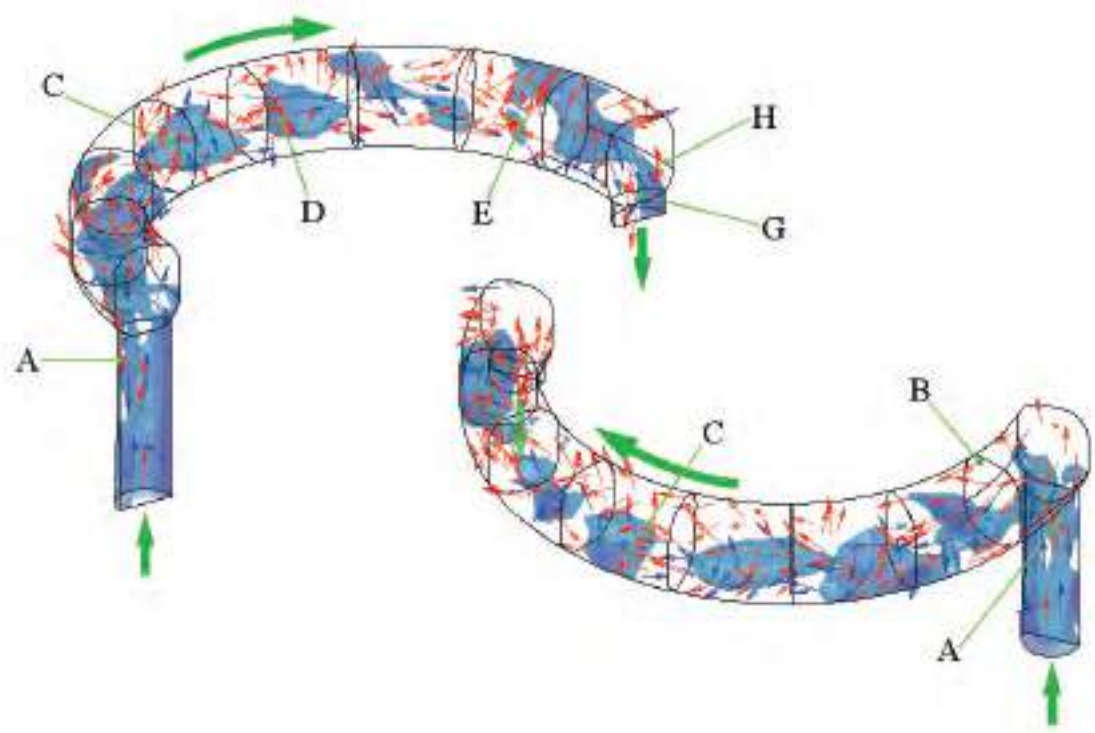

Fig. 6.37 Air position and flow direction of oil and air inside *SGM* gallery sections at *BDC* for one representative cycle

chaotic (**C**), rather than directed as found at the *BDC* position. The reduced velocity at the inflow and therefore less forward flowing oil led to a more inertia controlled flow behaviour. It was noticeable that the air was not entirely at the bottom of the gallery and was still moving towards the gallery bottom (**D**) with slight forward movement. The gallery velocity reduction at the end of the upward stroke caused the oil to move to the gallery top, but mainly flowing along the gallery walls. This forced the air downward into the gallery cross-section centre. The reduced cross-section of the gallery had also an effect on the air and oil movement, where

the reduced space did not allow for more unrestricted flow, as seen on the *LGM*. The bulk oil flow was not able to split the larger air bubbles and led to more wall bound oil flow with the air being suspended in the gallery centre. The restriction also caused a delay in the air movement to reach the gallery bottom, which occurred after the *TDC* position.

At the gallery outlet sections the flow was partially directed towards the outlet channel with strong cross-sectional swirling (**E**) towards the gallery top. The driving factor was again the inertia force on the oil. In comparison to the mid-gallery sections the flow was more structured and directed. This was only possible due to the lower oil content near the outlet channel, as the gallery outlet sections were emptied during the upward stroke. There was a mixture of oil and some air exiting from the gallery (**G**), as the inertia moved some oil away from the outlet (**H**).

6.6.3 Gallery section oil filling during crank cycle at *750 rpm* and *1.65 l/min*

Figure 6.38 shows the cycle averaged oil fill ratio for each gallery section. It can be seen that the *OFR* increased with distance from the inlet channel with near constant *OFR* from the mid-gallery sections up to the outlet channel. The largest variation between maximum and minimum section *OFR* occurred at the outlet section and was a result of the forward flow from the mid-gallery sections and the cycle depending exit flow through the outlet.

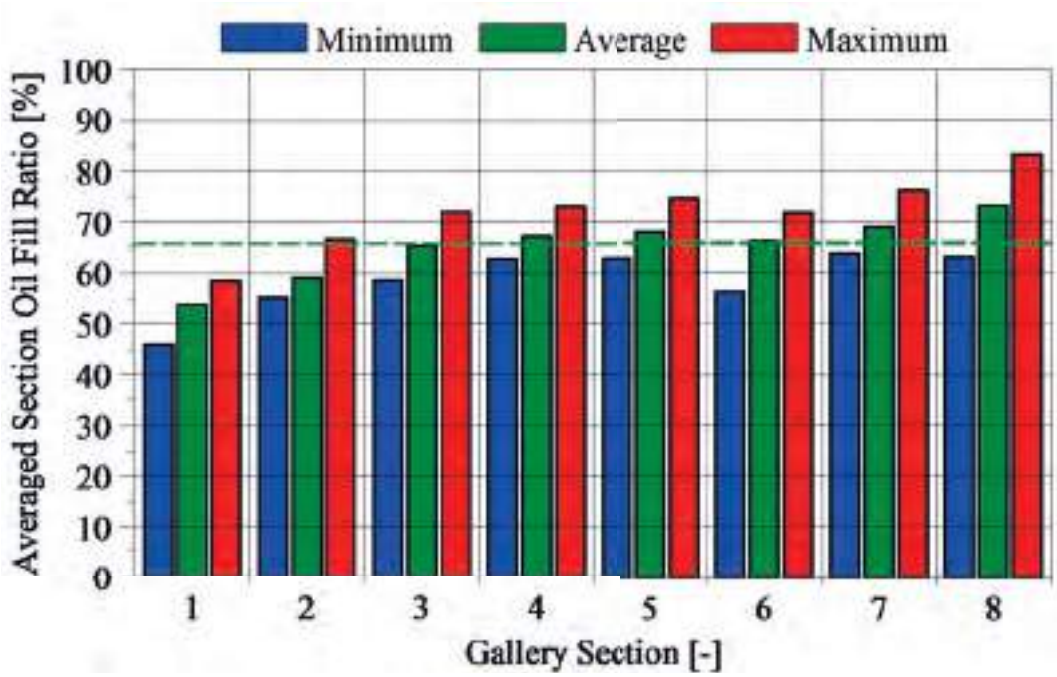

Fig. 6.38 *SGM* section oil filling (average of 100 cycles)

Figure 6.39 highlights the oil filling behaviour for one complete crank cycle, based on the average of 100 consecutive cycles. Figure 6.40 further highlights some of the flow feature. The same normalisation process of the jet entry velocity into the gallery was performed as for the *LGM* gallery. When the gallery moved downwards the filling of the inlet section adjoined to the inlet channel (Section 1) reduced. The opposite effect occurred during the upward stroke, where the filling of Section 1 increased. This behaviour would not be expected, as the opposing velocities of upward jetting oil and downward moving gallery should cause entry of larger amounts of oil into the gallery leading to increased *OFR*. A closer inspection of the flow in the inlet sections of the gallery revealed that the entering oil jet caused a forced movement of oil residing in Section 1 prior to the downward movement, pushing into Section 2 and 3 of the gallery, leading to an increase in *OFR* in these sections during the downward stoke of the gallery. Although oil was permanently delivered to the inlet section, there was some short-circulating flow (direct exit from inlet) also contributing to the reduction in *OFR*, as shown in Figure 6.40b.

During the upward stroke the filling of Section 1 increased. Less oil entered through the inlet channel due to the lower relative jet entry velocity, also reducing flow momentum. The curvature of the gallery changed the oil flow position from the gallery top to the gallery bottom and allowing for collection of oil in the inlet section. In addition some backward flow on the gallery bottom wall from Section 2 occurred, as shown in Figure 6.40d. This led to a reduction of *OFR* in Section 2.

Figure 6.39 also shows the results of inertia effects at and after *BDC*, where the oil was forced to the gallery bottom wall, in particular seen in Figure 6.40c and d. Together with the entering oil jet driven forward flow a surging wave occurred, represented by the occurrence of peak section fillings at varying crank angles. While the peak *OFR* in Section 2 occurred at approximately 90°CA *aTDC*, the peaks for Section 2 and 3 were found at approximately 140°CA *aTDC* and 190°CA *aTDC*. The variation of the *OFR* in the second half of the gallery was not as distinct as in the gallery front half, as the momentum of the flow reduced. The forward flow almost stalled in the mid-gallery sections producing an oil swirl around the gallery cross-section, before continuing with increased velocity towards the outlet.

While the flow and *OFR* in the rear mid-gallery sections still followed the surging wave, the variation of the *OFR* in the outlet section (Section 8) was controlled by the outflow of oil. At the *BDC* occurred strong inertia driven outflow from the gallery, as shown in Figure 6.40c.

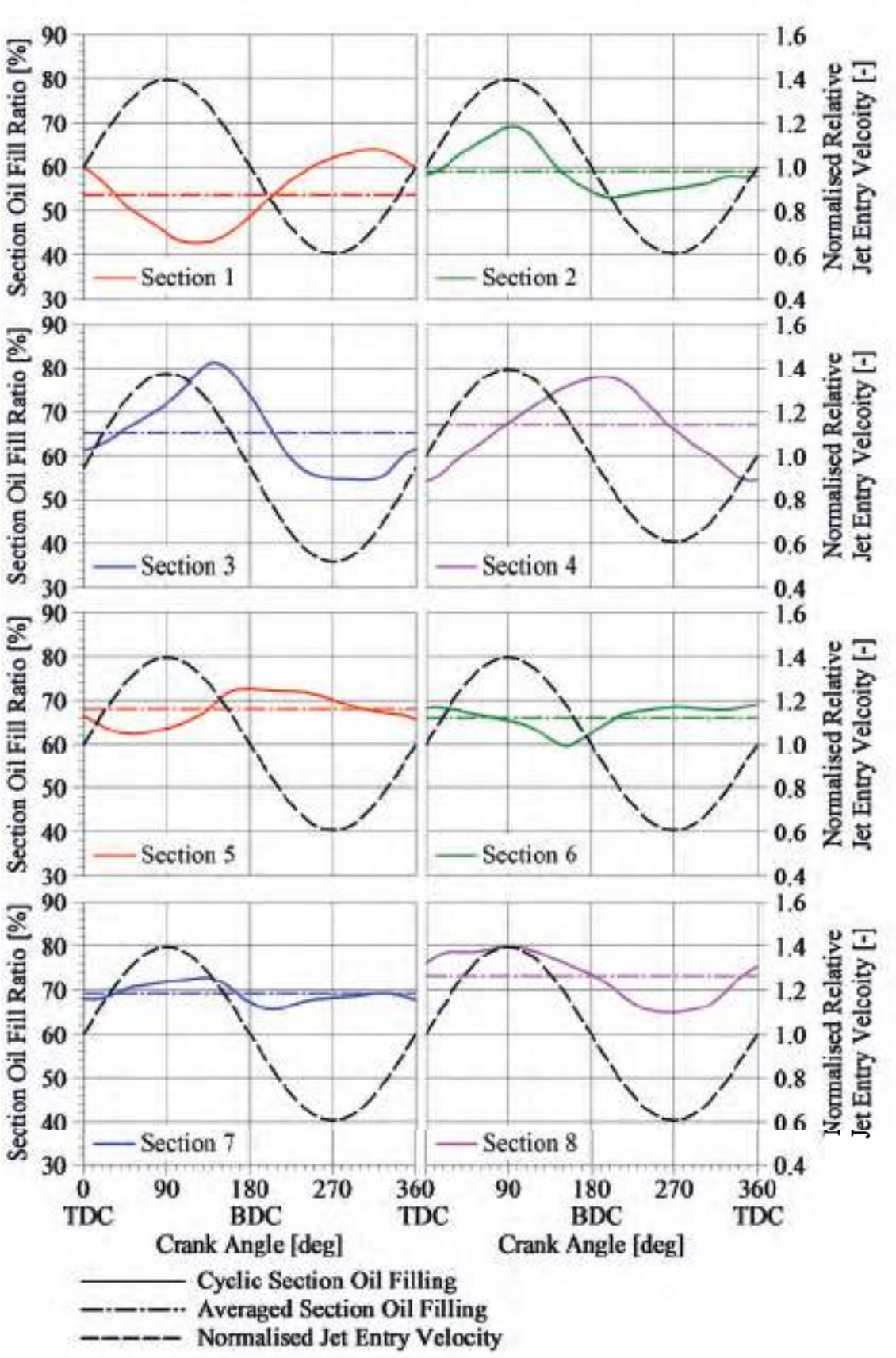

Fig. 6.39 Section filling behaviour during crank cycle for *SGM* (average of 100 cycles)

The outflow reduced during the upward stroke, as shown in Figure 6.40d. This led overall to a continuing emptying during the upward stroke. During the downward stroke little oil exited the gallery and the filling increased, as shown in Figure 6.39. The majority of oil was delivered by forward flow from the mid-gallery sections, but there occurred also re-entry of oil through the outlet channel, which was a remainder of the exiting oil from the upward stroke.

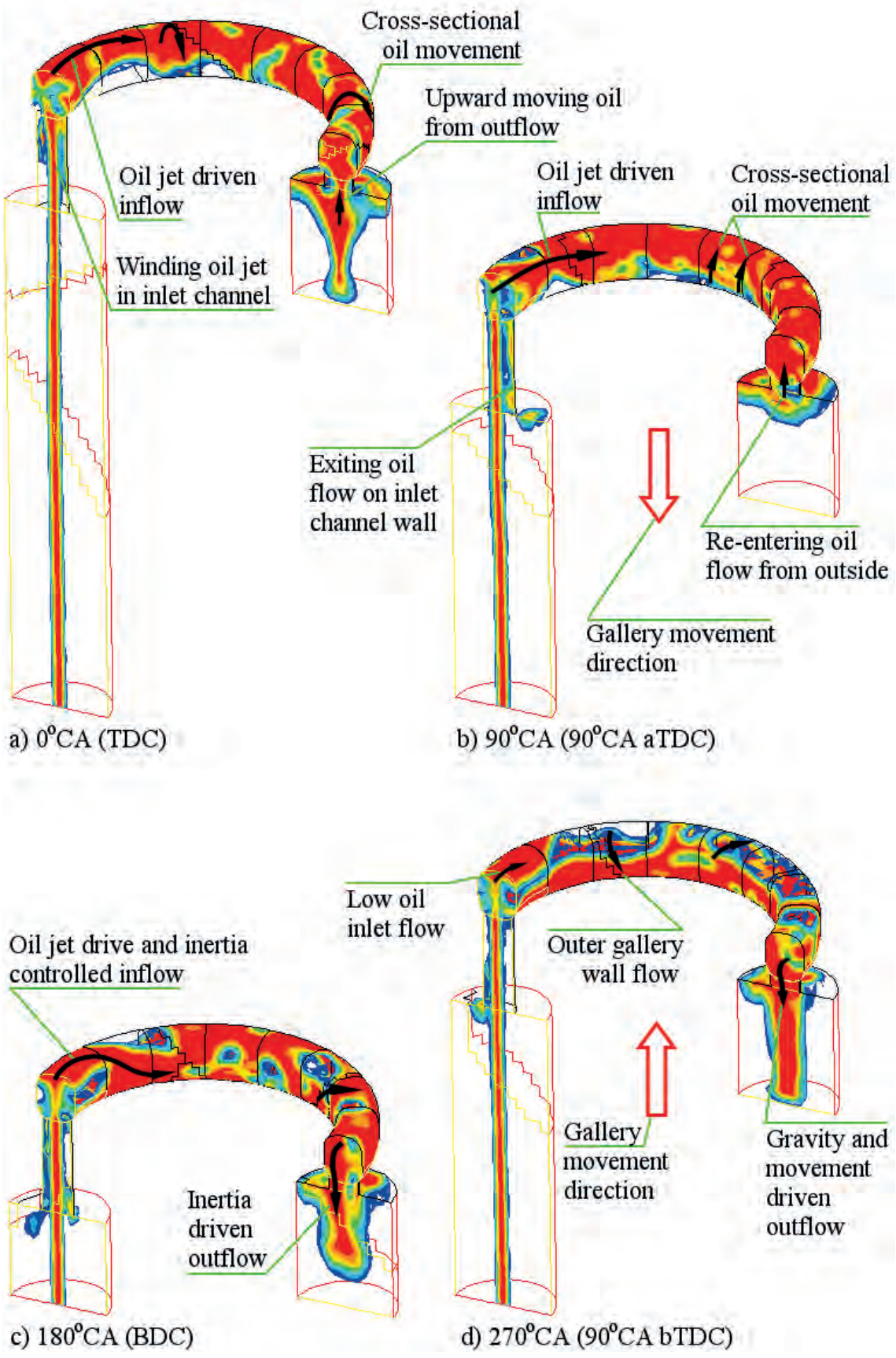

Fig. 6.40 In-gallery filling and behaviour for *SGM* during crank cycle at 750 rpm and 1.65 l/min

6.7 Summary

This chapter was concerned with the numerical investigation of the flow behaviour for two gallery models.

In the first part a study of a free-flow oil jet was conducted to determine the requirements on the computational domain (mesh density) to appropriately represent the jet. The conditions surrounding one nozzle were investigated for a constant average volumetric flow rate, but at varying fluctuation frequencies representative of that found on oil pumps. The pump equivalent pulsation did generate a breaking of the otherwise smooth jet surface, but a detailed jet breakup as found on the experiments was not achieved, as the requirements on the fineness of the domain grid was well out of the computational capabilities of the available hardware. However, it was found that for the investigated cases the variation of the jet cross-section was marginal and a coarser mesh would be sufficient to model the oil jet behaviour.

The second part was concerned with the large gallery model (*LGM*). The free-flow oil jet was employed to represent oil delivery conditions to the gallery more appropriately, as significant oil return flow was found in the experimental study, indicating strong interaction between jet and gallery model. It was found that short circuiting in the gallery and inlet outflow did impact on the jet, causing diversion effects during the gallery upward movement.

The relative large gallery volume and subsequent formation of large air bubbles of the size of the gallery width allowed for turbulent mixing, but low restriction flow. The walls were partially controlling the flow inside the gallery, whereby the cross-section shape and annular curvature contributed to the flow behaviour. The inward facing inner gallery top wall caused unbalanced amounts of oil between the outer and inner gallery wall, with larger amounts being allowed to collect on the outside wall.

The inertia effects therefore generated a stronger effect on the outside, pushing the inner wall oil into the centre due to the inner wall curvature and creating a cross-sectional swirl. This was also supported by the annular curvature, especially in the first half of the gallery. The gallery movement direction also controlled greatly the filling of the inlet and outlet sections of the gallery, whereby in the mid-gallery sections close to the inlet a strong back and forth air movement was noticed. A similar, but less strong effect was noticed in the outlet sections, whereby the re-entry of oil during the downward stroke contributed to the filling.

In the third part the small gallery model (*SGM*) was investigated. It was modelled based on the same principles as the large gallery model, also including a free-flow oil jet. The analysis of the small gallery model revealed similar oil movement behaviour with respect to wall bound flows. The annular curvature and race-track like cross-section of the gallery encouraged a more smooth flow, lacking some of the turbulences experienced on the large gallery model. Furthermore, the smaller sized gallery did not allow for the air bubble breakup seen at the *LGM* and caused a slight damping effect on the flow, expressed as significant lower oil fill ratio fluctuations in the mid-gallery sections.

CHAPTER 7 COMPARISON OF EXPERIMENTAL AND NUMERICAL RESULTS

This chapter focuses on the comparison of the experimental and numerical findings.

The first part is concerned with the large gallery model. The commonalities and differences between experimental and numerical results in the gallery filling and flow behaviour inside the gallery will be analysed based on one specific, but representative case. This is followed by comparison of experimental and numerical results in the representation of internal gallery filling for varying conditions of rotational crank speed and nozzle oil flow rate. Commonalities and differences are identified, analysed and explained.

The second part follows the structure and underlying methodology of the first part, but concentrates on the results from the small gallery model.

The chapter then closes with a summary of the findings.

7.1 Introduction

The presented experimental flow images for the *LGM* and *SGM* are identical to the images shown in the experimental results chapter (5). All flow indicating arrows were obtained by manual assessment of the flow from three consecutive images. Arrows coloured red indicate the flow direction of oil and blue arrows indicate the flow direction of the interface between air and oil.

The images showing results from the numerical study of the *LGM* and *SGM* are based on the same simulation models, reflecting the experimental conditions. For the *SGM* the images of inlet sections, mid-gallery sections and outlet sections are identical to the images of the numerical results chapter. For the *LGM* the images of inlet sections and outlet sections are also identical to the numerical results chapter, but the images for the front mid-gallery

sections and rear mid-gallery sections were additionally generated for better comparability to the experimental images.

Colour coding is also used to distinguish the commonalities and differences between experimental and numerical results. Pointers highlighting commonalities are coloured green and pointers for differences are magenta coloured.

One specific flow rate and crank speed case is presented in detail for comparison. The results are typical representations of the flow in the galleries. Variations occurring with change of rotational crank speed and nozzle oil flow rate are highlighted, rather than described, in order to minimise repetition of the same underlying behaviour.

7.2 Large gallery model

7.2.1 Experimental and numerical result comparison at *BDC* for 600 *rpm* and 4.0 *l/min*

Overall there was good comparison between the air position in the experiment and in the simulations. The majority of the air was located at the gallery top to both sides of inlet channel, extending into the front mid-gallery sections, as shown in Figure 7.1. The experimental results indicated a larger collection of air in the right branch of the gallery in comparison to the simulation results. This should be treated with care, as the position error due to the refraction effect of the gallery curvature increases with increasing distance from the vertical image centre. In comparison the simulation did not contain such an error. Therefore features close to the left and right visible edge of the gallery may not be used for the comparison of air at the inlet.

The continuous inflow of the oil jet did not allow significant collection of air directly above the inlet hole. The deflection of the oil jet on the inner inward-tilting top gallery wall led to forced flow of oil into the gallery branches. As the oil jet entered the gallery the momentum exchange with the bottom oil layer also created a small scale swirl contained to the inlet section. This feature was present in the results of the experimental and numerical study, although stronger visible in the experimental flow results, as seen in Figure 7.1. Furthermore there was air drawn into the gallery with the entering oil jet for both studies.

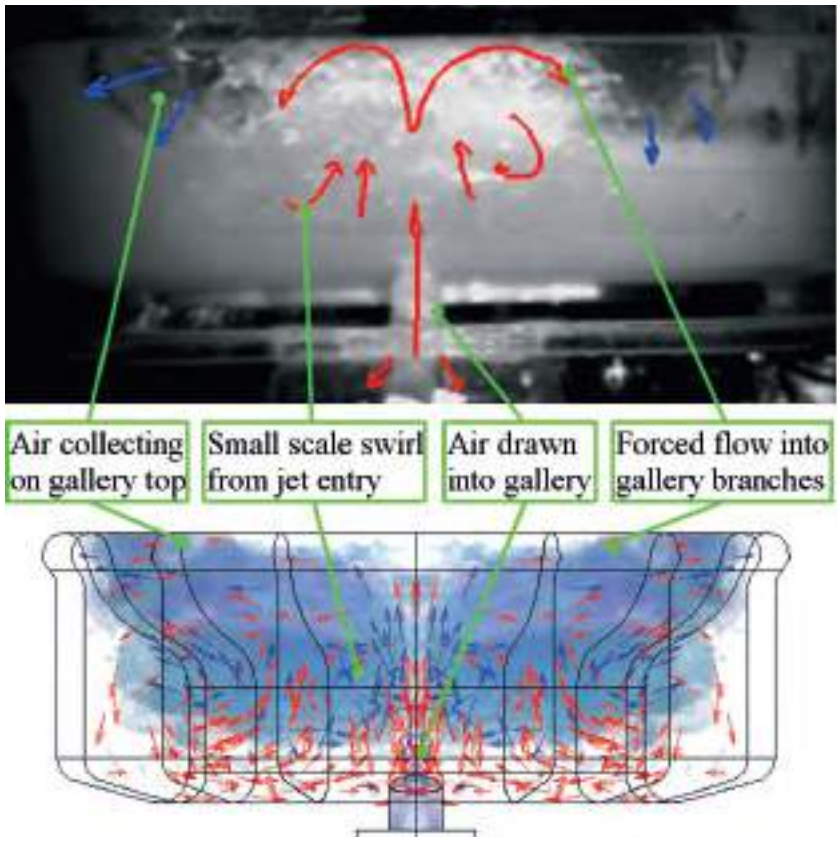

Fig. 7.1 Experimental and numerical results of inlet sections for *LGM* at *BDC*, 600 *rpm* and 4.0 *l/min*

There were differences with regards to the predicted air location by the simulation at half the height of the gallery in comparison to the experimental results, where air was not shown in this position. The predicted location of the air was at the inside wall of the gallery and was visible due to the portraying of the air, rather than the oil. The experiment would not allow such an option and the correctness of the air being in this position cannot be assured.

The location of the visible air at the gallery top in the front mid-gallery sections showed good comparison between experimental and numerical results, as shown in Figure 7.2. The majority of air was found near the gallery top. The simulation indicated larger air pockets at half the gallery height, but this would not be visible in the experimental image, as explained previously. The experimental result did show the outline of a medium sized air bubble and the darker central shade indicated that it may expand throughout the gallery width onto the opposite gallery wall. This would be in line with the end of the predicted centrally located air bubbles shown in the simulation result.

The main oil flow direction along the top of the gallery was also in good comparison. The experiments showed an entering oil jet forcing a flow along the top of the gallery, before

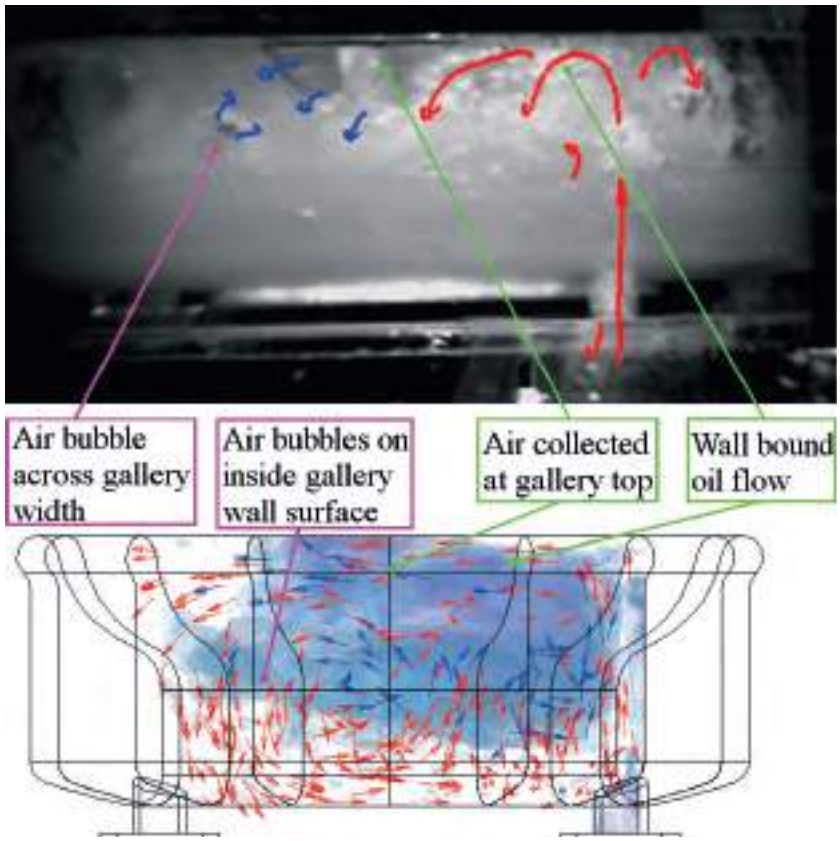

Fig. 7.2 Experimental and numerical results of front mid-gallery sections for *LGM* at *BDC*, 600 *rpm* and 4.0 *l/min*

being pushed downward on the gallery wall and allowing the air to collect on the top of the front mid-gallery sections. A similar behaviour was indicated by the simulations, although the downward forced flow was less developed compared to the experiment. The upward indicated flow direction near the gallery bottom in the simulation occurred mainly at the inner gallery wall, but insufficient data was available for the gallery bottom in the experiment to verify this flow direction.

In the rear mid-gallery sections the air locations differed strongly between experiment and simulation, as shown in Figure 7.3. There was a tendency in the simulation for the air to be pushed to the gallery top, but the arrival at this position occurred after the *BDC* position in the crank cycle. Although the simulation predicted the location of air at a lower gallery height, it can be seen that there occurred a comparable column of oil at the beginning of the rear mid-gallery sections. An analysis of the flow behaviour of the full gallery also revealed that the oil column was a result of two oil flow streams clashing, whereby one stream was initiated from the gallery inlet side and the other stream from the gallery outlet side.

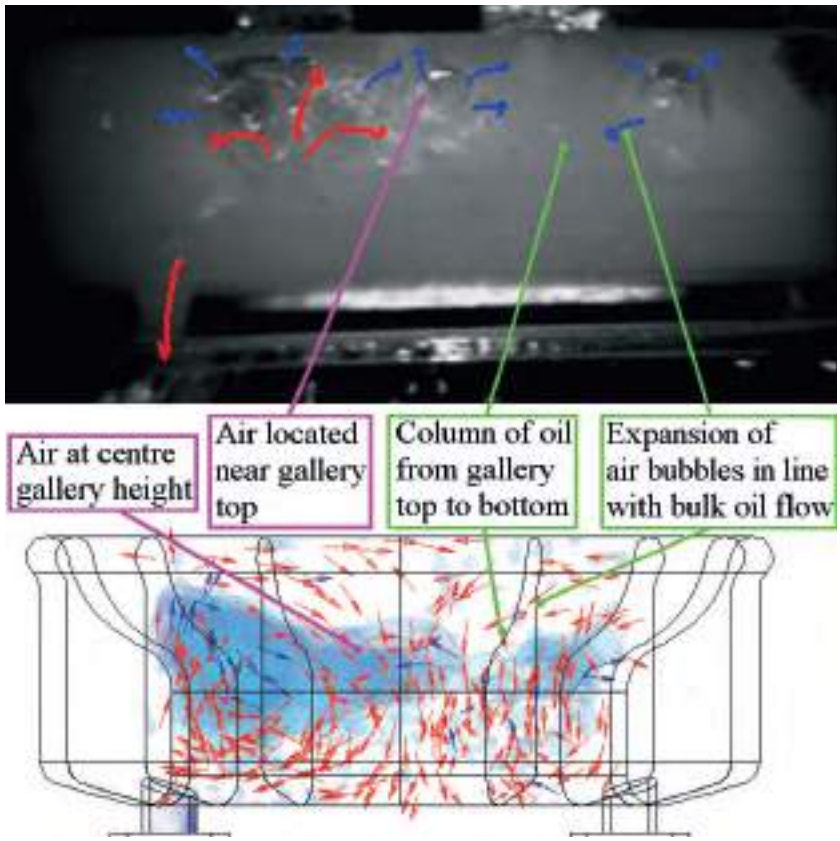

Fig. 7.3 Experimental and numerical results of rear mid-gallery sections for *LGM* at *BDC*, 600 *rpm* and 4.0 *l/min*

The flow vectors of the expanding air bubbles in the experiment may be used to estimate the directional flow of the oil. The direction of the air bubbles at the upper right end of the gallery (right side from the oil column) indicated a flow to the left side towards the gallery exit sections. As air was present in the upper gallery region left to the oil column the flow must be downwards. A comparable flow pattern was seen in the simulation, where the flow was from the top right of the gallery towards the left bottom of the gallery. The upward indicated flow in the simulation was found to be at the inside gallery wall, whereby the downward flow occurred on the outside gallery wall, also producing a cross-sectional swirl in the gallery.

The locations of the air pockets in the gallery outlet sections were also predicted at a lower gallery height position in comparison to the experimental data, as shown in Figure 7.4. The indication by the air direction vectors was, however, that the air moved towards the gallery top.

The experimental results allowed for identification of two different oil flow behaviours, exiting flow through the outlet channel and wall controlled flow along the gallery inside wall. There was good comparison in the flow behaviour from the gallery through the outlet for

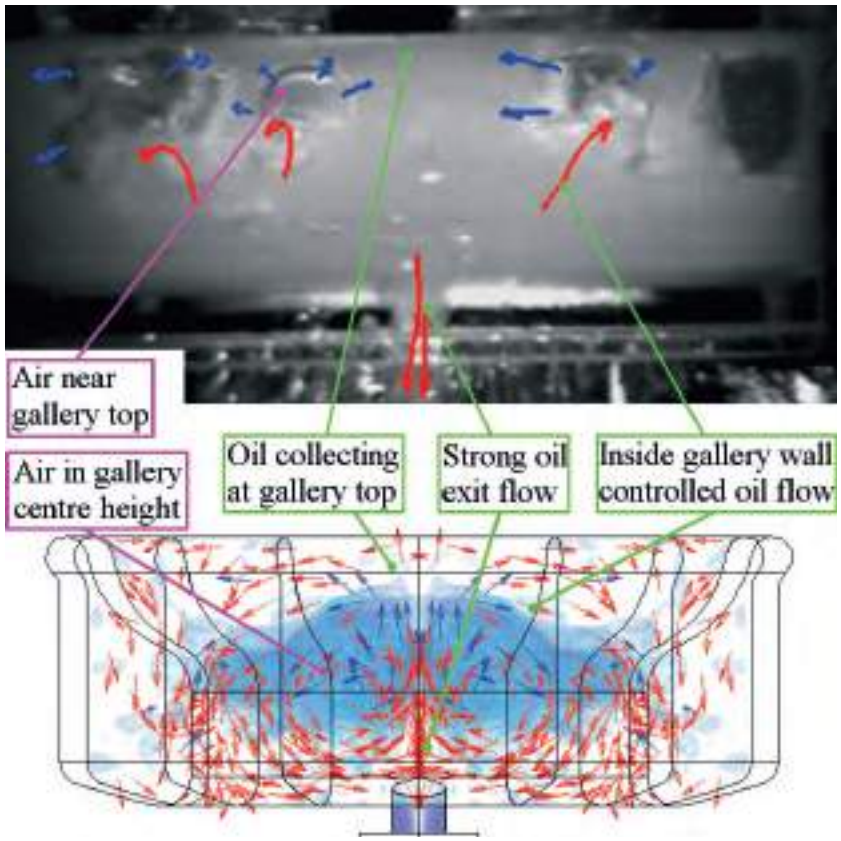

Fig. 7.4 Experimental and numerical results of outlet sections for *LGM* at *BDC*, 600 *rpm* and 4.0 *l/min*

both studies. The extension of the oil flow stream from the mid-gallery sections generated an increased collection of oil near the outlet, forcing the majority of the oil out. The numerical results also highlighted that there was not sufficient outlet area and part of the oil was pushed towards the gallery top.

The most significant difference in oil flows was found in the sections adjoined to the outlet. While the experiment showed oil piercing through the air bubbles from the gallery inside wall to the gallery outside wall (radial direction), the simulation did not show such behaviour, but rather a circulating flow along the outside wall (tangential direction). Overall the flow in the outlet sections was more structured and directed in the simulations as compared to a more chaotic and turbulent flow found in the experiment.

7.2.2 Experimental and numerical result comparison at *TDC* for 600 *rpm* and 4.0 *l/min*

Overall there was good comparison between the air position in the inlet sections between the experiment and the simulation, as shown in Figure 7.5. Both results showed the majority of the air at the bottom of the gallery, as expected due to inertia effects. Experiment and simulation also showed good comparison with regard to the formation of small-sized air bubbles. The non-symmetric occurrence of the air near the location of the inlet channel was a result of the effects surrounding the entering oil jet. Although care was taken in the arrangement of the oil jet, the large distance between nozzle exit and gallery inlet did generate variation on the gallery entry behaviour, especially with consideration of the influence of partial outflow of oil during the upward stroke. With the simulation being only a half model, the non-symmetric effect of jet entry point variation did not occur.

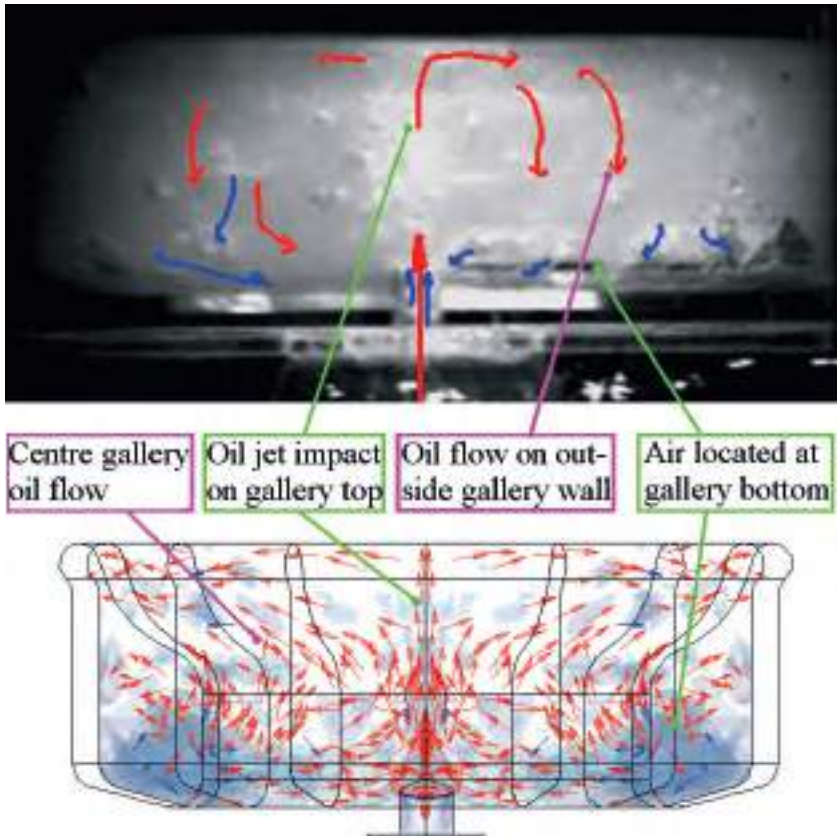

Fig. 7.5 Experimental and numerical results of inlet sections for *LGM* at *TDC*, 600 *rpm* and 4.0 *l/min*

A circulating flow in the inlet sections was determined for the experimental results, whereby the entering oil jet impacted on the gallery top wall and then deflected into the gallery

branches. With the oil being present on the gallery top due to the inertia effects, the flow was deflected downward and circulating oil flow was experienced mainly near the gallery outside wall. An inspection of the simulation results revealed similar flow behaviour, although the circulation did not appear to be of the same scale as indicated by the experiment, but slightly larger, expanding into the front mid-gallery sections. The returning flow can be seen at the gallery bottom.

The largest amount of the air was found near the half length of the gallery branch at the end of the front mid-gallery sections, as shown Figure 7.6. Experiment and simulation also showed comparable behaviour of the air flow towards the inlet. The air flow could be linked to the large scale circulating flow of the oil that rose from the inlet up to the gallery top, where it deflected into the gallery branch. The experiment showed stronger oil flow behaviour towards the gallery bottom along the outside wall of the gallery. The simulation did not highlight such a flow at the same gallery location, although backflow behaviour was noticed at the gallery bottom. Both studies, experimental and numerical, also indicated a region of low oil movement, whereby the circulating flow represented the boundary. It should be noted that absence of large scale vertical or horizontal flow does not mean motionless, as circulating flow can introduce rotational flow behaviour and consequently turbulence.

The occurrence of small-sized air bubbles near the inflow was also present in experimental and numerical studies, including the distribution along the flow direction, whereby the reduced motion area contained the lowest amount of air.

Figure 7.7 shows the air locations and flow directions in the rear mid-gallery sections for experiment and simulation. There was good comparison in the air location, which was found at the gallery bottom and consisted of large-sized air bubbles. The main flow direction of air inside the gallery was towards the outlet section, but a minor flow also occurred along the gallery bottom towards the gallery half length.

The main flow behaviour of the oil was also in good comparison. Two streams of inertia driven oil flow along the gallery top wall collided in the regions of the rear mid-gallery sections, forcing the flow of oil downwards. This collision appeared in a similar position to the collision of streams at the *BDC* position, but in contrast to the *BDC* position a column of oil was not formed as a result of the inertia effects on the oil. The flow direction of the oil after the collision showed also good consistency between experiment and simulation, being towards the gallery outlet and pushing the air towards the outlet as well. Although there was

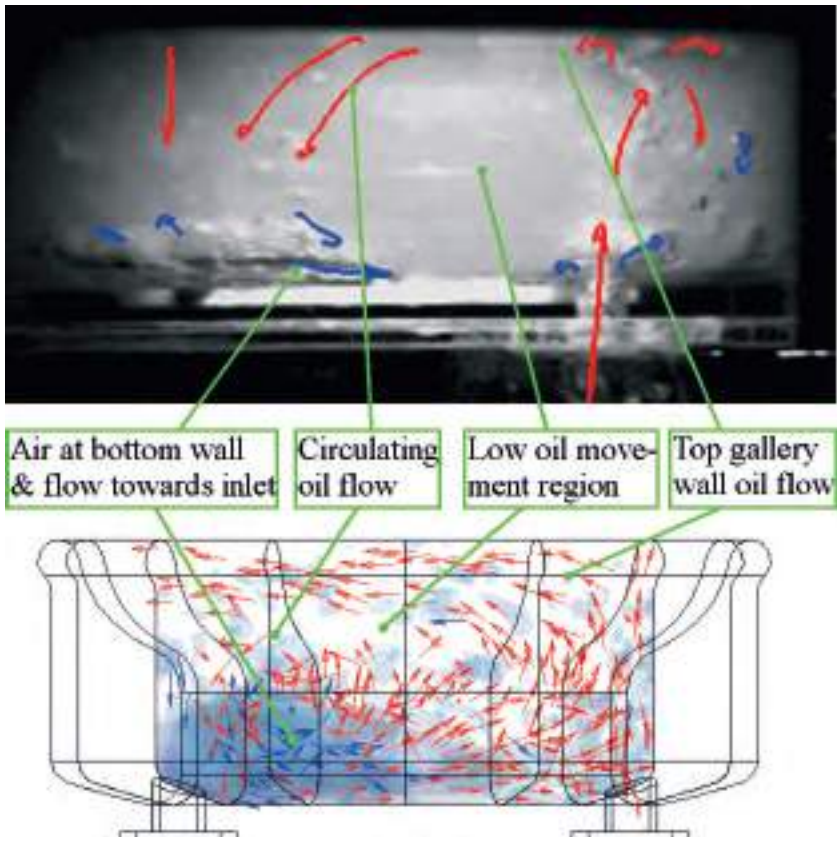

Fig. 7.6 Experimental and numerical results of front mid-gallery sections for *LGM* at *TDC*, 600 *rpm* and 4.0 *l/min*

indication in the simulation of upward pointing flow at the collision region, a closer inspection revealed that the flow occurred at the inside gallery wall, which would not be noticeable in the experimental results.

The location of the larger air bubbles in the experiment and in the simulation showed good consistency, as shown in Figure 7.8. There occurred non-symmetrical distribution of the air in the experiment, which can be attributed to the variation of flow splitting into the gallery branches at the inlet. It was also found that the air bubbles did not reach the outlet channel at the *TDC*, which was consistent in both studies, experimental and numerical, although the oil flow passing over the air bubbles forced the air to move towards the outlet channel. While the inertia driven in-gallery bulk oil flow was towards the gallery top wall there was still oil exiting the gallery through the outlet channel and was partially obstructed by oil outside the gallery.

The simulation indicated a strong inertia driven upward directed oil flow above the outlet channel that was deflected on the inner inward-tilted top gallery wall and pushed into the gallery branch. This led to the downward flow of the oil on the outside gallery wall. There

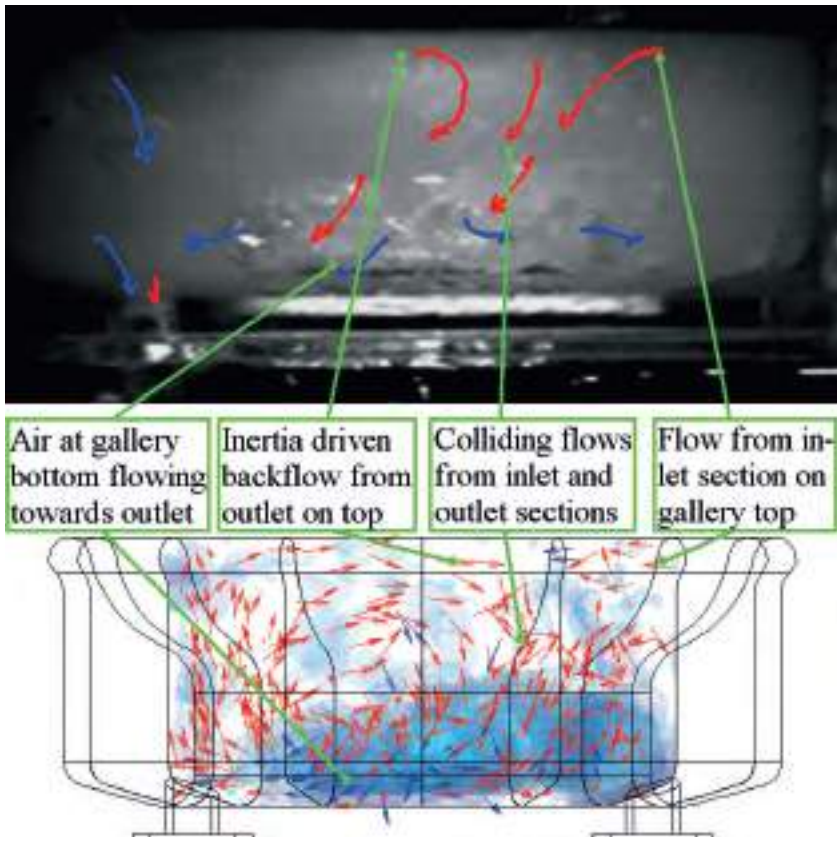

Fig. 7.7 Experimental and numerical results of rear mid-gallery sections for *LGM* at *TDC*, 600 *rpm* and 4.0 *l/min*

was similar flow behaviour in the experiment with visible indication of the flow on the outer gallery wall being downwards. It may be assumed reasonable, that the downward forced flow at the outer gallery wall was a result of the flow in the centre of the gallery cross-section. As the inertia forces on the oil would primarily generate an upward movement, the wall guided flow may overcome this force and counteract the inertia-driven flow, leading to the downward wall flow. This would be consistent with the main indicated flow direction of the simulation.

7.2.3 Commonalities and differences between *LGM* cases with different crank speeds and flow rates at *BDC*

Figure 7.9 shows a comparison experimental and numerical results of the inlet gallery sections filling behaviour at the *BDC* based on the parametric variation of rotational crank speed and nozzle oil flow rate. There was good comparison between experiment and simulation, and the trend of filling behaviour was represented well.

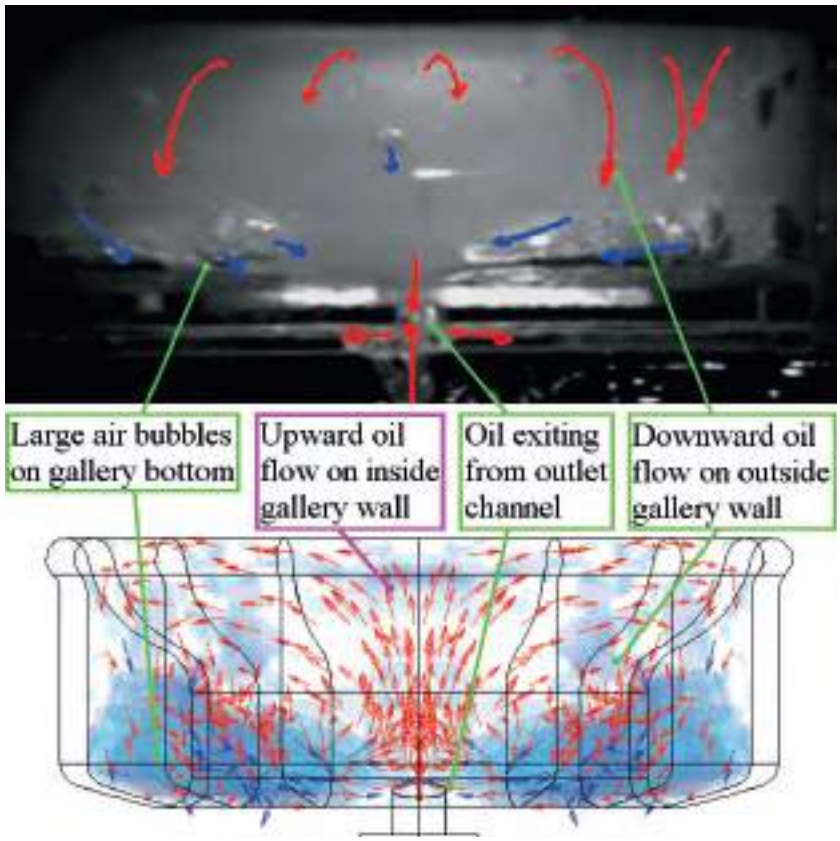

Fig. 7.8 Experimental and numerical results of rear mid-gallery sections for *LGM* at *TDC*, 600 *rpm* and 4.0 *l/min*

The majority of the oil was found at the gallery bottom due to inertia effects as the gallery model came to a standstill at *BDC*. All results show that the entering oil jet held sufficient high momentum to pierce through the bottom oil layer and impacted on the inward-tilting inner gallery wall. This behaviour was visible in the experimental result images by the oil reaching the gallery top. The absence of air in the simulations, represented by blue shaded areas above the inlet channel, meant that oil was reaching the gallery top. All images also portrayed a jet deflection on the tilted inner gallery wall into the gallery branches, followed by flow along the gallery top, before wall-guided downward oil flow on the outside gallery wall occurred.

The results generally showed a collection of large air bubbles on the gallery top adjoined to the jet entry area, which was clearly visible during the experiments and was well represented by the simulations. In addition the trend of gallery filling seen in the experiments was also visible in the simulations, whereby the lowest oil content could be found for the case of 300 rpm and 6.0 l/min. The air content at 300 rpm & 4.0 l/min and 600 rpm & 4.0 l/min was nearly identical, although the experimental images showed more diluting of the oil layer

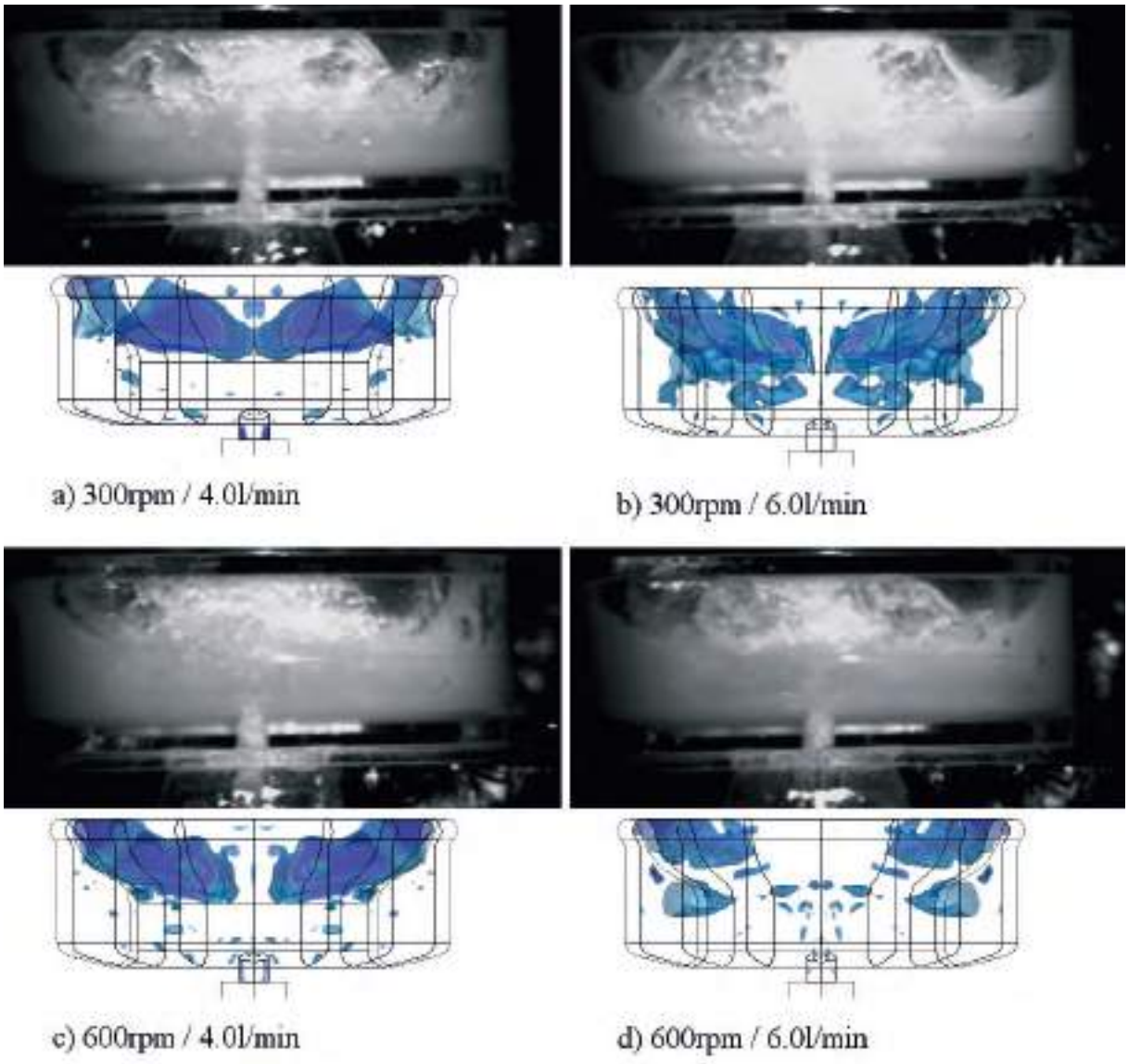

Fig. 7.9 Experimental and numerical results of inlet sections for *LGM* at *BDC* for different crank speeds and oil flow rates

with medium-sized air bubbles at the lower speed. A comparable effect was visible in the simulation results, where similar amounts and distribution of air was found. In contrast the oil flow path did show differences expressed by the different formation of the air boundaries. The lowest air content in the inlet section was found at highest crank speed and flow rate of 600 rpm and 6.0 l/min respectively with good similarities between experimental and simulation results.

At the outlet sections the experimental results showed the majority of the oil collecting at the gallery bottom, although some oil was also found at the gallery mid-height and top, as shown in 7.10. As the gallery approached *BDC* and the velocity reduced two effect occurred,

inertia effects and colliding flows. The inertia effects had the strongest influence on the oil movement towards the gallery bottom, as explained previously. In additions, the collision effects of the combining flows from the two gallery branches led to oil being unable to exit and therefore being forced upward. Only approximately 40°*CA* after *BDC* the full top air layer was achieved. This behaviour was consistent for all speeds and flow rates in the experiments.

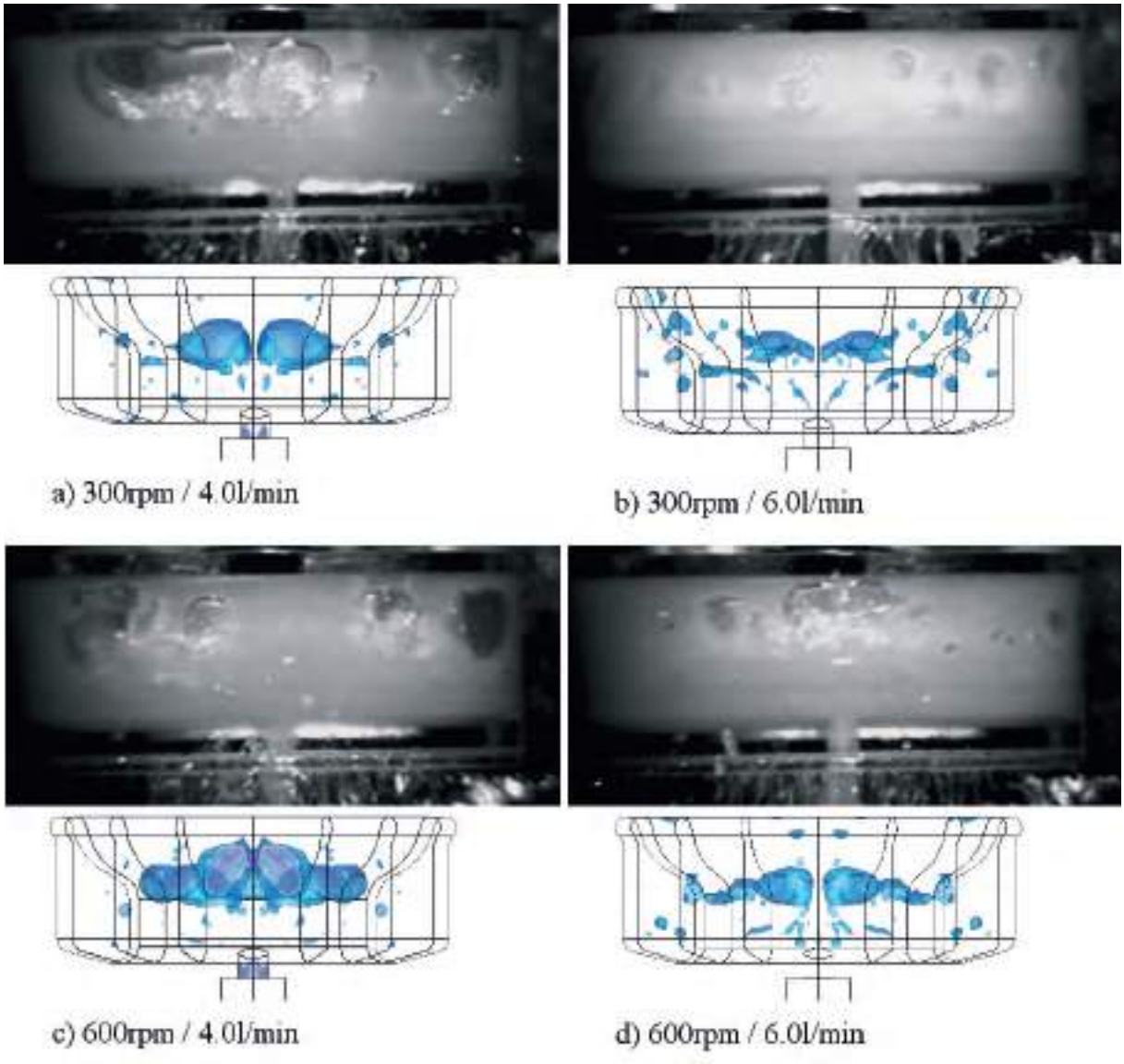

Fig. 7.10 Experimental and numerical results of outlet sections for *LGM* at *BDC* for different crank speeds and oil flow rates

The simulation results did not predict this behaviour well. The air location was predicted at a lower gallery height position with oil being present at the gallery top wall. The best prediction in terms of air content was found for 600 rpm and 4.0 l/min, with the other cases showing significant differences. It should be noted that the air content in the simulation may

be higher than the visible air shown, as the software does not render small scale air bubbles (smaller than mesh size), although numerically the cells contain air. Both results, experimental and simulation, showed a tendency of lower oil content in the gallery outlet sections for lower oil flow rates.

The simulation predicted the movement behaviour and top wall collection of air similarly to the experiments, but delayed with respect to crank angle. A closer inspection of the results at 600 rpm and 4.0 l/min revealed that the air was reaching the gallery top at approximately 60°CA after BDC with a formation of a constant air layer at the gallery top being further delayed.

7.2.4 Commonalities and differences between *LGM* cases with different crank speeds and flow rates at *TDC*

There was generally good comparison between the numerical and experimental results of gallery filling in the inlet sections at *TDC*, as shown in Figure 7.11. The flow of oil within the gallery was still in transition from the bottom to the top, as the gallery velocity reduced while approaching *TDC*, initiating the formation of larger air bubbles at the gallery bottom.

The increased distance between nozzle exit and gallery inlet together with the distribution of oil across the gallery height led to the formation of small-sized to medium-sized air bubbles, as the oil jet entered the gallery and caused strong mixing between the air contained in the jet surface layer and the oil in the gallery. This behaviour was found for all speed and flow rate cases and was in good comparison between experimental and simulation results. There was also a tendency in both studies of the formation of larger-sized air bubbles at the gallery bottom, but at distance from the inlet channel, except for the case of 600 rpm and 4.0 l/min, where both showed that the air reached the inlet channel.

Figure 7.12 shows the distribution of air in the outlet sections of the gallery at *TDC* position. The experiments showed that the majority of the oil was distributed across the gallery height with some formation of larger-sized air bubbles. The crank speed had an effect on the position and formation of the air bubbles. While at lower speed the air bubbles had a tendency towards more circular shapes, at higher speeds the air bubbles were more of conical shapes pointing towards the outlet channel, highlighting the underlying inertia effects during gallery slowdown approaching *TDC*. The effect of varying air bubble heights with changing

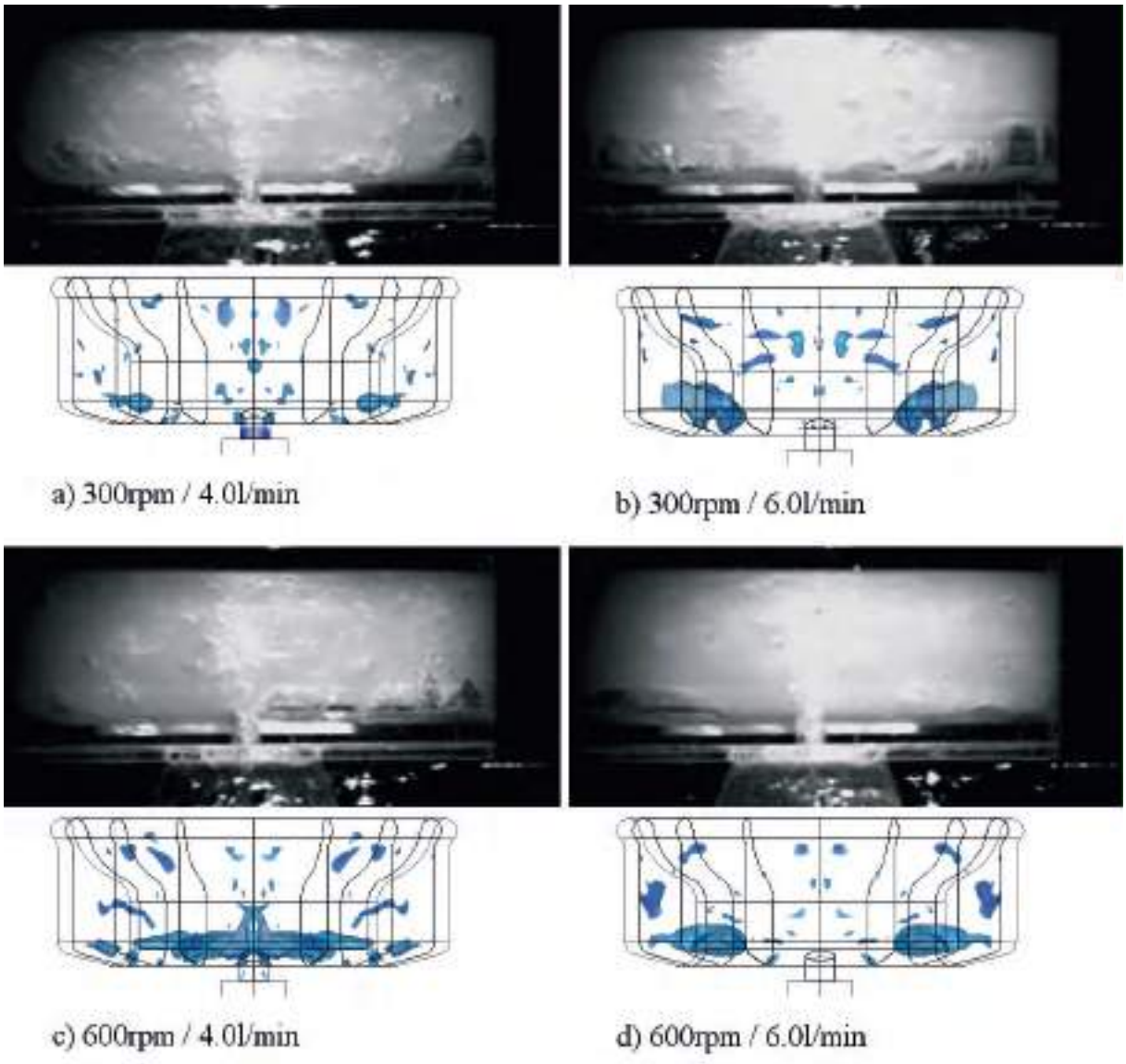

Fig. 7.11 Experimental and numerical results of inlet sections for *LGM* at *TDC* for different crank speeds and oil flow rates

velocity was also visible in the simulation results, although the conical shapes were not as explicit.

In all cases there was also a tendency of less small-sized to medium-sized air bubbles suspended in the flow, as compared to the inlet sections. The only exception was the case at 300 rpm and 6.0 l/min, where strong mixing of the oil and air occurred. A closer inspection of the experimental results showed that the gallery was only filled with oil half height and the large amount of air allowed for unstructured mixing effect. In all other cases significantly more oil was found in the outlet gallery section, leading to more directed oil movement.

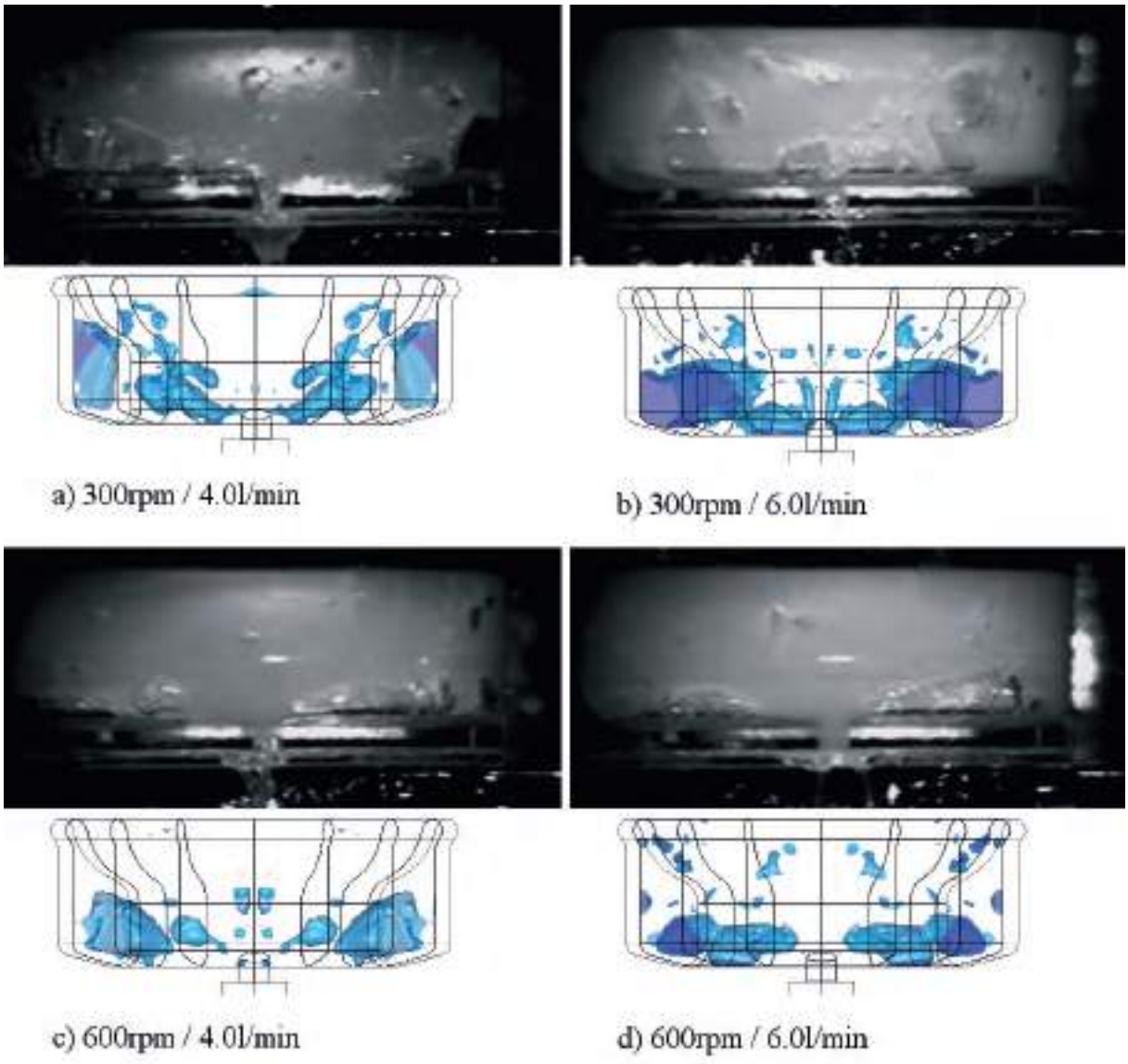

Fig. 7.12 Experimental and numerical results of outlet sections for *LGM* at *TDC* for different crank speeds and oil flow rates

7.3 Small gallery model

7.3.1 Experimental and numerical result comparison at *BDC* for 750 *rpm* and 1.65 *l/min*

Figure 7.13 shows strong turbulent flow behaviour at the inlet protruding into the adjoined gallery sections. The extent can still be seen in the side view (Figure 7.14) and can be estimated as $^1/_3$ of the gallery branch length (approximately 60° from inlet). The close proximity of the nozzle to the gallery resulted in strong oil jet entry into the gallery, culminating in significant

amount of air being drawn into the gallery as well. Such behaviour was also represented by the low volumetric sector filling as shown in Figure 6.38 on page 185.

Strong turbulence was also found in the numerical results and showing a comparable, but slightly shorter length, expressed by the extension of the air representation. For both studies, experimental and numerical, the indication was also that with progressing distance the turbulence became more present at the gallery top. With increasing distance from the inlet channel the flow velocity and mixing of oil and air reduced, causing a decrease in turbulence. In addition the reduced momentum allowed the inertia (and gravitational) effects to control the collection of oil at the gallery bottom.

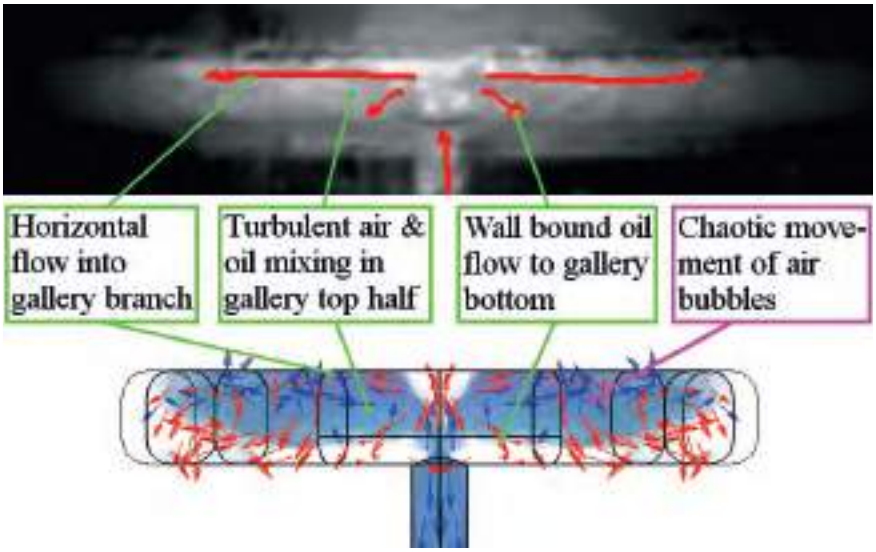

Fig. 7.13 Experimental and numerical results of inlet sections for *SGM* at *BDC*, 750 *rpm* and 1.65 *l/min*

The flow near the inlet was mainly driven by the entering oil jet. The jet impacted on the gallery top wall and separated horizontally to protrude into the gallery branches. This behaviour could be found in the experiment and the simulation. There occurred some swirling flow near the inlet, which was found in both results. The main flow of the oil was downward along the outer gallery wall, adding to the bottom gallery oil layer. As the oil flow reached the gallery bottom the impact with the already present oil also created flow backward towards the inlet (interface sector 1 – 2). This was shown in the simulation, but could not be identified sufficiently clear in the experiment.

Figure 7.14 shows the oil and air flow in the side gallery sections. The air was only found at the gallery top due to the inertia effects on the oil. The position of the air in the numerical

predictions did compare very well with the experiment, where the majority of the air occurred after the gallery mid-length.

The mid-gallery sections also highlighted a change in the air flow behaviour. The air in the front mid-gallery sections showed turbulence controlled movement, expressed by many smaller air bubbles. In contrast, the air in the rear mid-gallery sections highlighted formation of larger air bubbles with distinct interface boundaries, as a result of the lower turbulence.

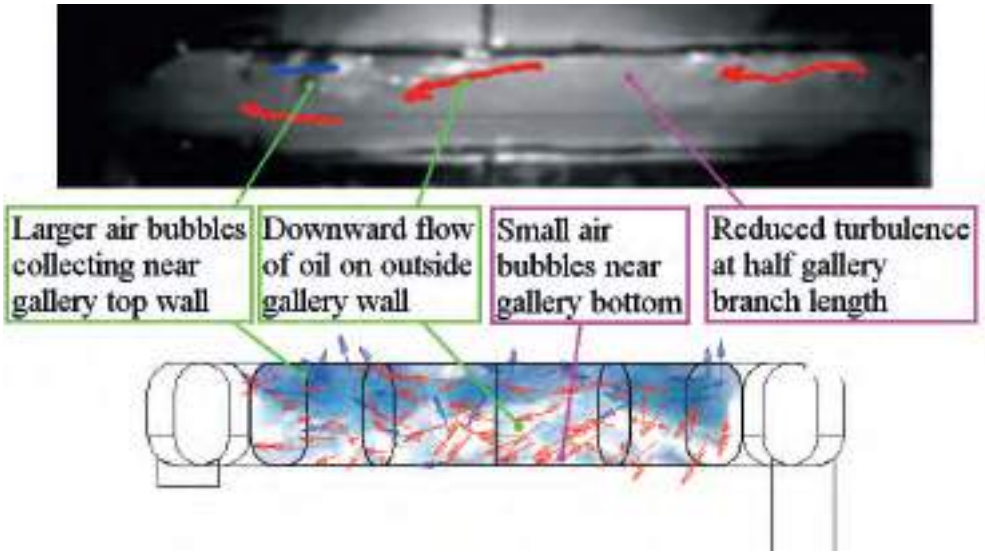

Fig. 7.14 Experimental and numerical results of mid-gallery sections for *SGM* at *BDC*, 750 *rpm* and 1.65 *l/min*

The flow direction in the mid-gallery sections showed good consistency between experiment and simulation. This was especially apparent for locations with sufficient highlighted features, where the flow could be analysed with good reliability. The main flow direction in both studies showed a forward flow from the inlet to the outlet without significant flow swirling. The flow was partially wall bound (mainly along outer gallery wall) and consisted of a circular movement around the gallery cross-section centre.

The same behaviour of air and oil was also found in the outlet sections of the gallery, as shown in Figure 7.15. In both studies, experimental and numerical, the air was distributed along the length of the gallery top, without any distinct formation of larger air bubbles. Both studies also indicated that part of the air was drawn towards the outlet channel, highlighting the strong flow current.

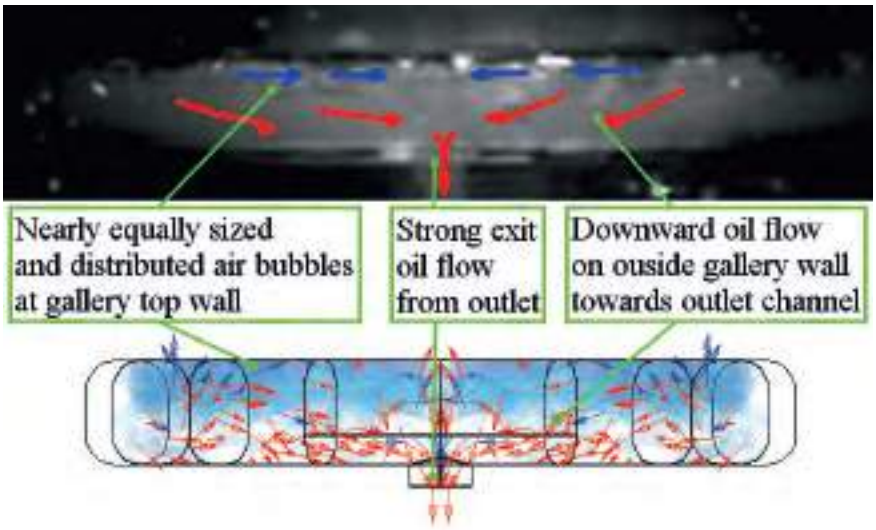

Fig. 7.15 Experimental and numerical results of outlet sections for *SGM* at *BDC*, 750 *rpm* and 1.65 *l/min*

The main flow direction of the oil for both cases was from the gallery branches with a slight downward movement along the outer gallery wall towards the outlet channel. The flows from both branches combined and forced the oil outflow through the outlet channel.

The smaller gallery volume of the *SGM* in comparison to the *LGM* did not allow for the split of the oil flow, where part of the oil exited through the outlet channel and the remaining oil was recirculated into the gallery branch. The combining flows from the gallery branches combined and exited the gallery, while the air was collecting at the gallery top.

7.3.2 Experimental and numerical result comparison at *TDC* for 750 *rpm* and 1.65 *l/min*

Figure 7.16 shows the comparison of air locations and flow vectors for the gallery inlet sections at the *TDC*. A comparison of the air locations showed good consistency between both, experimental results and numerical predictions. The experiment showed turbulence in the gallery near the inlet channel, but with a lower intensity in comparison to the *BDC* behaviour, resulting in less protrusion of the turbulent mixing zone into the gallery branch. The majority of the oil was at the top of the gallery, with the larger air bubbles being at the gallery bottom. As the gallery came to a rest at the *TDC*, the inertia force pushed the oil upwards to the gallery top. This type of oil and air distribution can also be found for the simulation results.

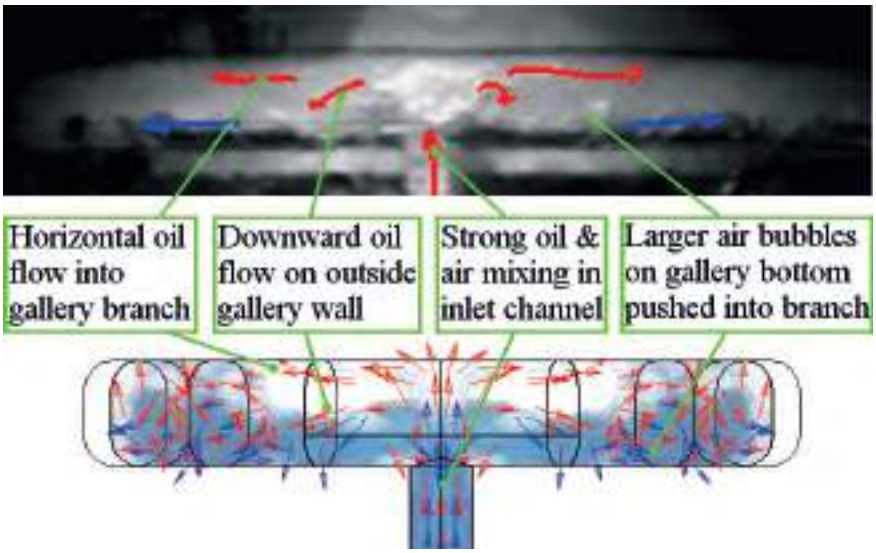

Fig. 7.16 Experimental and numerical results of inlet sections for *SGM* at *TDC*, 750 *rpm* and 1.65 *l/min*

The comparison of the flow directions also showed good similarities. The oil jet entering through the inlet channel led to upward oil flow, before impacting on the top gallery wall. The impact forced an oil jet breakup, splitting the flow into both gallery branches, whereby wall-bound flow on the outer gallery wall was predominant. In the adjoined mid-gallery sections downward flow occurred as a result of the gallery curvature. The race-track shaped cross-section also supported smooth flow. Only near the inlet channel some circulation occurred, which can be found for experiment and simulation cases. Both studies also showed consistent air flow behaviour, whereby the air located at the gallery bottom was pushed into the gallery branches.

Figure 7.17 shows the experimental and numerical results of the flow behaviour in the mid-gallery sections of the gallery at *TDC*. The main air location was found at the bottom of the gallery, as seen previously. While the experimental results showed a large air bubble at the rear mid-gallery sections, the numerical results predicted a more even spread of the air across the gallery length with indication of increased air content at the front mid-gallery sections. This difference may seem substantial, but should be treated with care. The practical limitations of the image capturing system prohibited the collection data from multiple crank cycles and the image only represents experimental result from one individual crank cycle. In contrast the numerical study allowed the capture of flow behaviour from multiple crank cycles. A detailed analysis of the numerical results showed that in one out of ten consecutive

cycles occurred also an air bubble of similar size in the gallery mid-section, although on the gallery inside wall, rather than across the full gallery width.

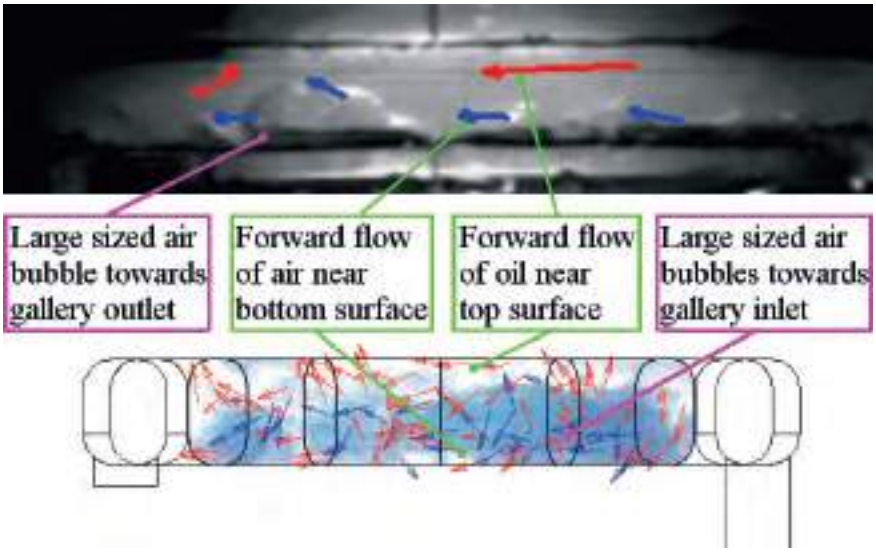

Fig. 7.17 Experimental and numerical results of mid-gallery sections for *SGM* at *TDC*, 750 *rpm* and 1.65 *l/min*

There was some consistency in the comparability of the flow direction between experiment and simulation, although the simulation predicted more chaotic flow in the mid-gallery sections, as opposed to more structured forward flow found in the experiment. In the rear mid-gallery sections occurred swirling flow, which was found for both investigations. The flow direction of the air showed good comparison, as the main direction of the air flow was towards the gallery outlet.

The position of the air at *BDC* (Figure 7.14) and at the *TDC* (Figure 7.17) after the mid-gallery length seemed to indicate a stationary behaviour of the air at this location. A detailed frame by frame analysis of the cycle did, however, show that the air bubble was not the same. The formation of the air bubble was due to the oil movement from the gallery top to the bottom and vice versa. There occurred also an additional forward forced flow of oil and air inside the gallery near the dead centre of the cycle, resulting in the visible air being moved forward a significant distance.

Figure 7.18 shows the behaviour of oil and air flow in the gallery outlet sections. As found in the inlet and mid-gallery sections, the experimental results showed that the oil resided mainly at the gallery top, while the air was constrained to the gallery bottom forming distinctly sized air bubbles. The distribution and size of the air bubbles in the simulation

showed reasonable comparison with the experimental results, whereby some small-sized air bubbles occurred at the gallery mid-height near the outlet channel and at the gallery top in the sections adjoined to the outlet. These occurred in the centre of the gallery cross-section, so if present in the experiment would not be detected due to the opaque oil colour.

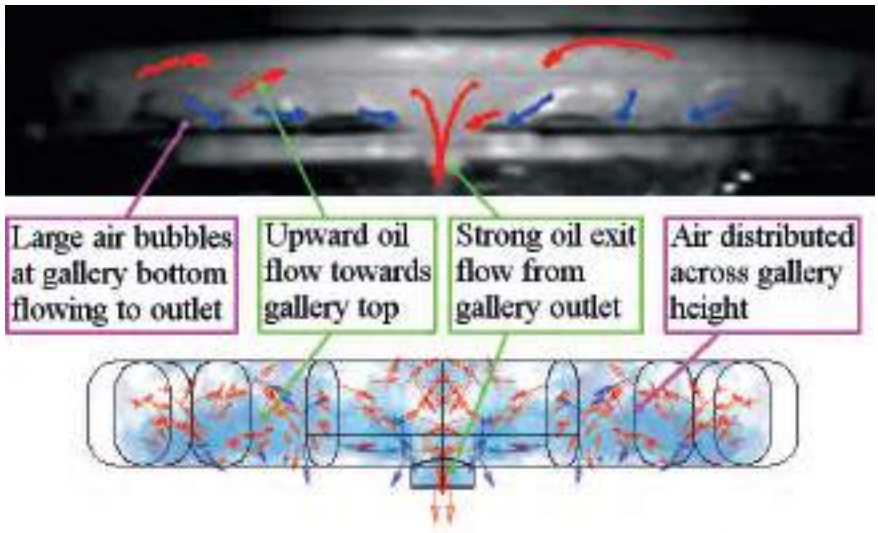

Fig. 7.18 Experimental and numerical results of outlet sections for *SGM* at *TDC*, 750 *rpm* and 1.65 *l/min*

The main flow direction of air was towards the outlet channel along the gallery bottom. Both studies, experiment and simulation, showed the same behaviour with good comparability in direction and position. As the oil streams from the gallery branches collided, a downward flow out of the outlet channel occurred. This flow behaviour was present in both studies, although the simulation results indicted also upward flow along the outside gallery wall, which was not present in the experiment. The main flow in the cross-section centre was consistent with the experiment, that is, being towards and out of the gallery outlet channel.

Considering the full gallery length of the *SGM* there was constant forward flow with little backward circulation, as seen for the large gallery model (LGM). The reduced cross-sectional area, as compared to the *LGM*, prohibited such behaviour, as there was insufficient space to allow deviation from the main flow direction.

7.3.3 Commonalities and differences between *SGM* cases of different crank speed and flow rate at *BDC*

Generally there was good comparison of the air distribution between experiment and simulation, although there appeared significant differences in the representation of the air behaviour in the inlet sections, as shown in Figure 7.19. While the experiment showed strong turbulent air and oil mixing, generated by the entering oil jet, the simulation predicted formation of larger-sized air bubbles. This may be attributed to the coarseness of the domain mesh, which cannot be used to visibly show small-sized air bubbles. The boundaries of the air bubbles in the simulation did produce comparable boundaries to the air loaded swirling region in the experiment.

All parametric cases showed turbulent mixing in the inlet sections of the gallery, whereby higher flow rates increased the length of the turbulent region, as found when comparing results for cases a) and d), as well as cases e) and c) in Figure 19. At the same time an increase in rotational crank speed counteracted this effect, reducing the length of the region, as found for cases a) and e), as well as d) and c).

The experimental results in Figure 7.19 also show fewer micro-sized air bubbles for conditions of 500 rpm and 1.105 l/min, indicated by more transparent oil content in comparison to the other cases. A comparable result can be seen for 1000 rpm and 1.105 l/min, although the onset of formation of micro-sized air bubbles was present.

As stated previously, the simulation could not model the air and oil mixing behaviour in detail, as found for the experimental results, but rather highlighted areas of collected air in the form of air bubbles. A comparison of the turbulent regions in the experiments with the predicted air bubbles did show similarities in the position and extend. Thereby the simulation generally showed formation of an oil layer at the gallery bottom and the air collecting near the gallery top. The largest difference from all behaviours was seen for the lowest speed and highest flow rate (500 rpm and 2.121 l/min), where the momentum from the jet entry was high enough to push the air to the gallery bottom. For this case the jet entry could therefore be evaluated as having a higher effect on the gallery flow behaviour than the inertia effects due to the stopping of the gallery.

A detailed analysis of the gallery inlet sections highlighted the significant difference in flow behaviour with increased volumetric oil flow rate, as shown in Figure 7.20. Figure 7.20b

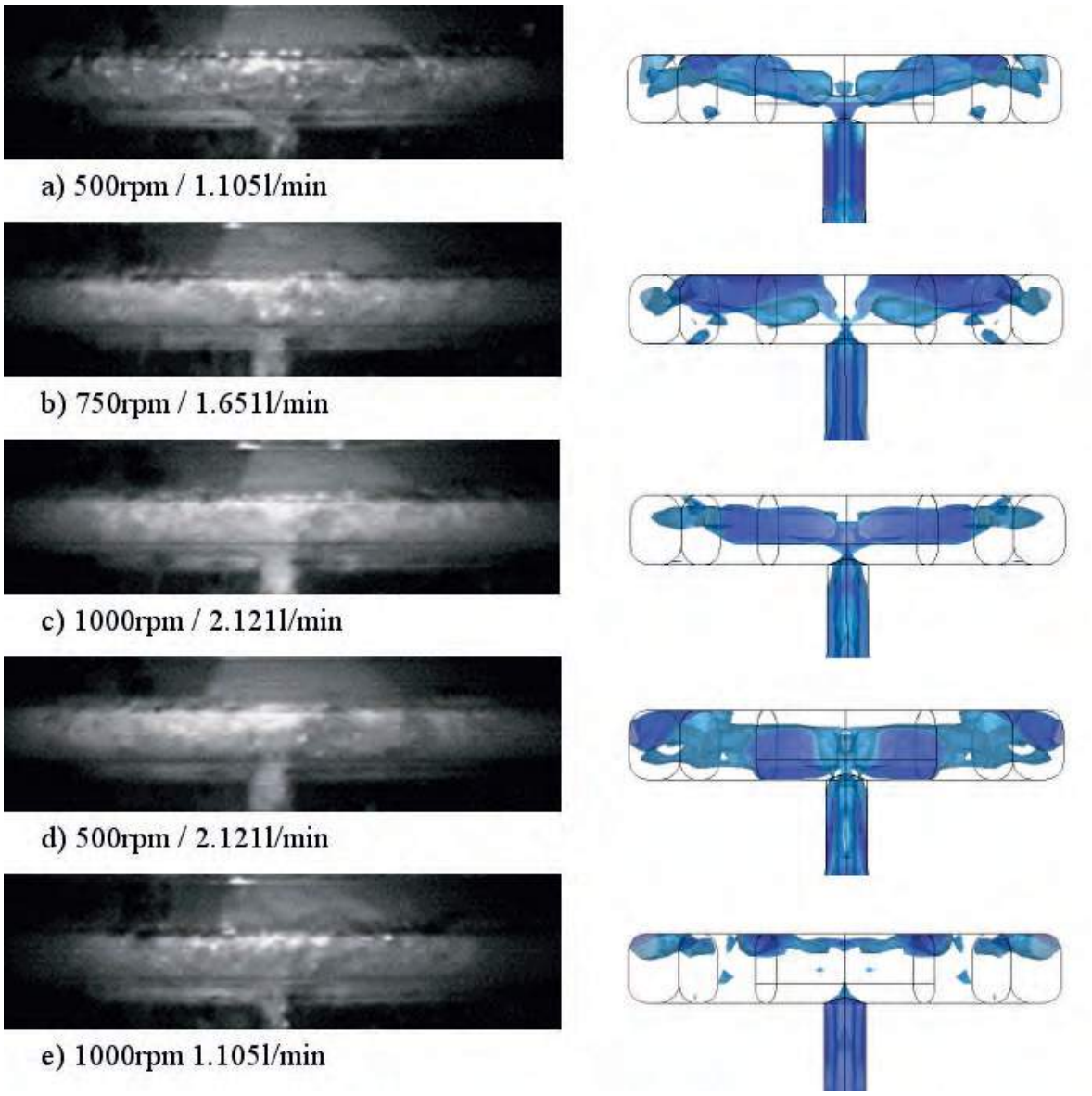

Fig. 7.19 Experimental and numerical results of inlet sections for *SGM* at *BDC* for different crank speeds and oil flow rates

shows that there appeared strong top wall bound flow as a result of the faster jet entry velocity at the higher flow rate, passing over centrally located air bubbles and keeping them away from the top. At the same time increased mixing of oil and air took place, expressed by the increased presence of centre legend colours. At the lower flow rate a stronger separation of air and oil occurred. The separation was indicated by the increased presence of the blue and red colours, representing pure air and oil respectively, as shown in Figure 7.20a.

Figure 7.21 shows a comparison of gallery filling at various rotational crank speeds and volumetric oil mass flow rates. The experimental images indicated that no significant mixing region was found in the outlet sections and the flow showed more laminar behaviour. The

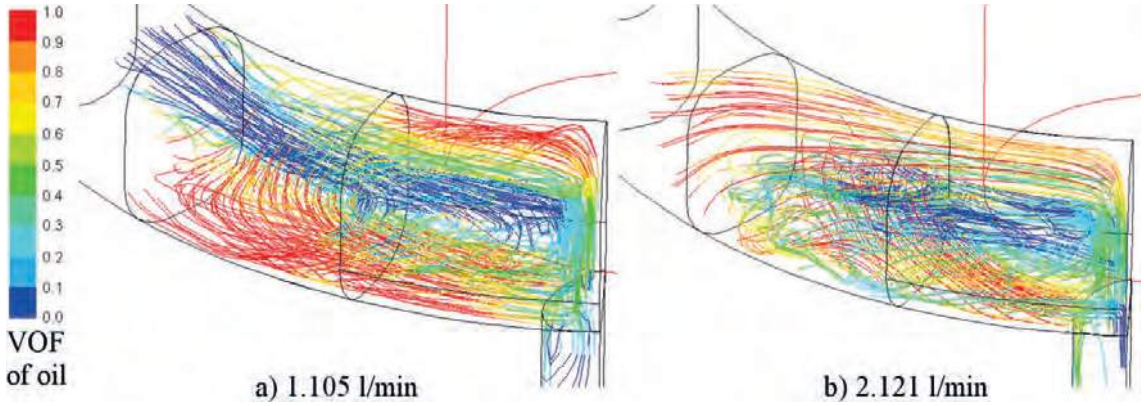

Fig. 7.20 Comparison of flow behaviour in gallery inlet sections of *SGM* showing *VOF* of oil along path lines at 500 *rpm* and different oil flow rates

consistency in opaqueness of the oil in comparison to the gallery inlet sections indicated that no or very little coalescence of the micro-sized air bubbles occurred. The micro-sized air bubbles were carried along with the bulk oil flow and also exited with the oil. There was clear formation of larger-sized air bubbles in comparison to the inlet. This may be a result of the combination of medium-sized air bubbles due to the low turbulence in the outlet sections allowing coalescence effects to control the formation.

The comparison between experiment and simulation did show a good consistency with regards to air location and size. The majority of the air was located at the gallery top, highlighting the strong inertia effect on the oil. The largest gallery filling may be assumed at lowest crank speed and highest flow rate, indicated by the absence of large-sized air bubbles in experiment and simulation results, although the volume of the micro-sized air bubbles cannot be determined, but may not be neglected. The presence of micro-sized air bubbles in the majority of the investigated cases may be used to assume identical amounts of air being suspended in the oil.

7.3.4 Commonalities and differences between *SGM* cases of different crank speed and flow rate at *TDC*

Figure 7.22 shows the gallery filling in the inlet sections at the *TDC* for various crank speeds and flow rates. For all cases the majority of air was located at the gallery bottom, indicating the largest effect from inertia forces initiated by the gallery slowdown towards the *TDC* position. The mixing region was smaller in comparison to the *BDC*, which was expected, as

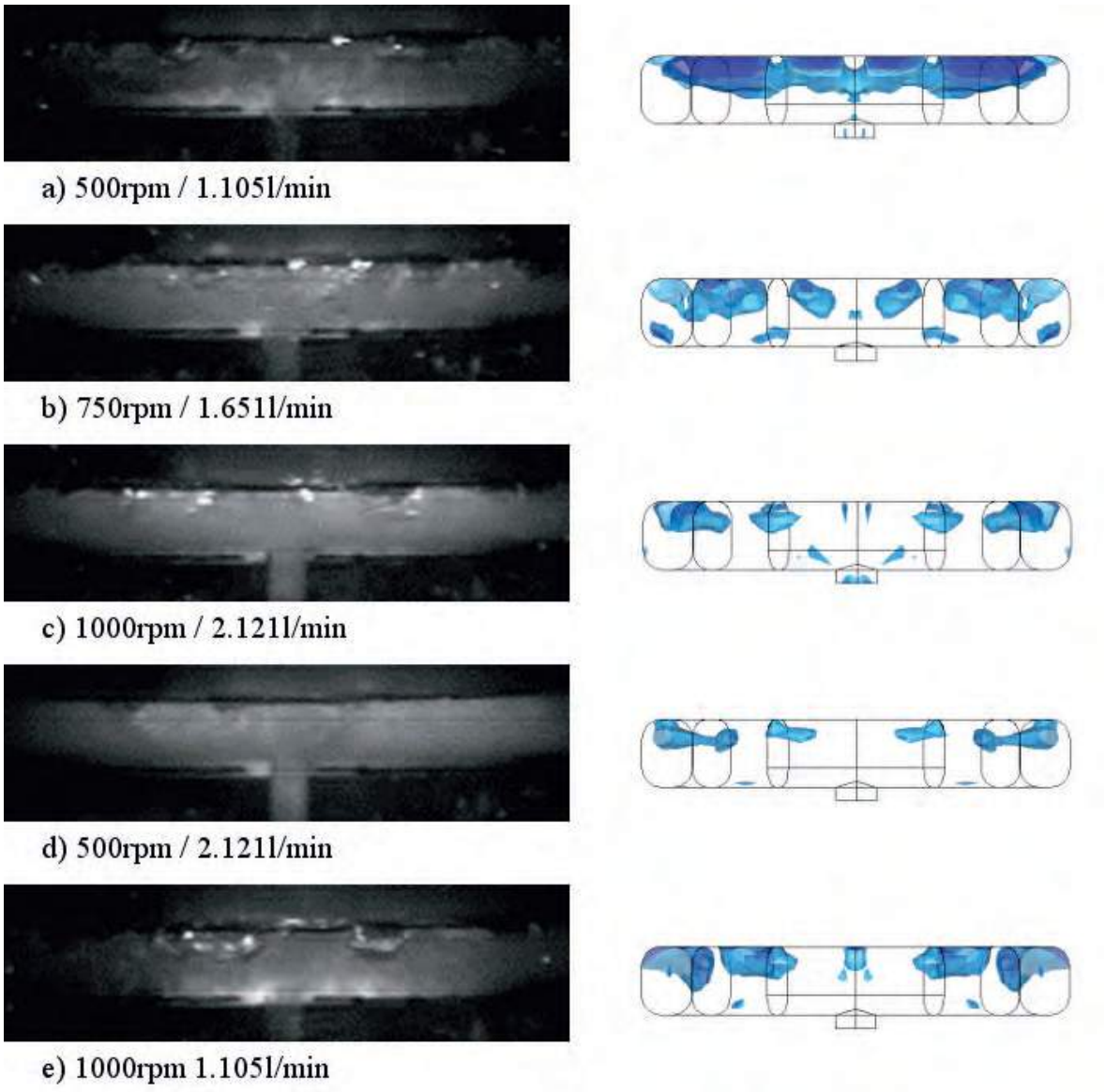

Fig. 7.21 Experimental and numerical results of outlet sections for *SGM* at *BDC* for different crank speeds and oil flow rates

the increased distance between nozzle and gallery meant loss of jet momentum. In addition the impact of the oil jet on the oil layer present at the gallery top acted as a damping element to the flow, before the oil jet could impact on the top gallery wall.

There was generally good comparison between the larger-sized air bubble locations when comparing the predicted locations with the experimental results. A significant difference was only found in the air location for the lowest speed and highest flow rate (500 rpm and 2.121 l/min). The higher flow rate meant increased upward velocity of the jet and the lower gallery speed allowed the jet to enter the gallery at a higher velocity, therefore carrying more momentum. This led to jet breakup and a forced flow into the gallery branches. At the same

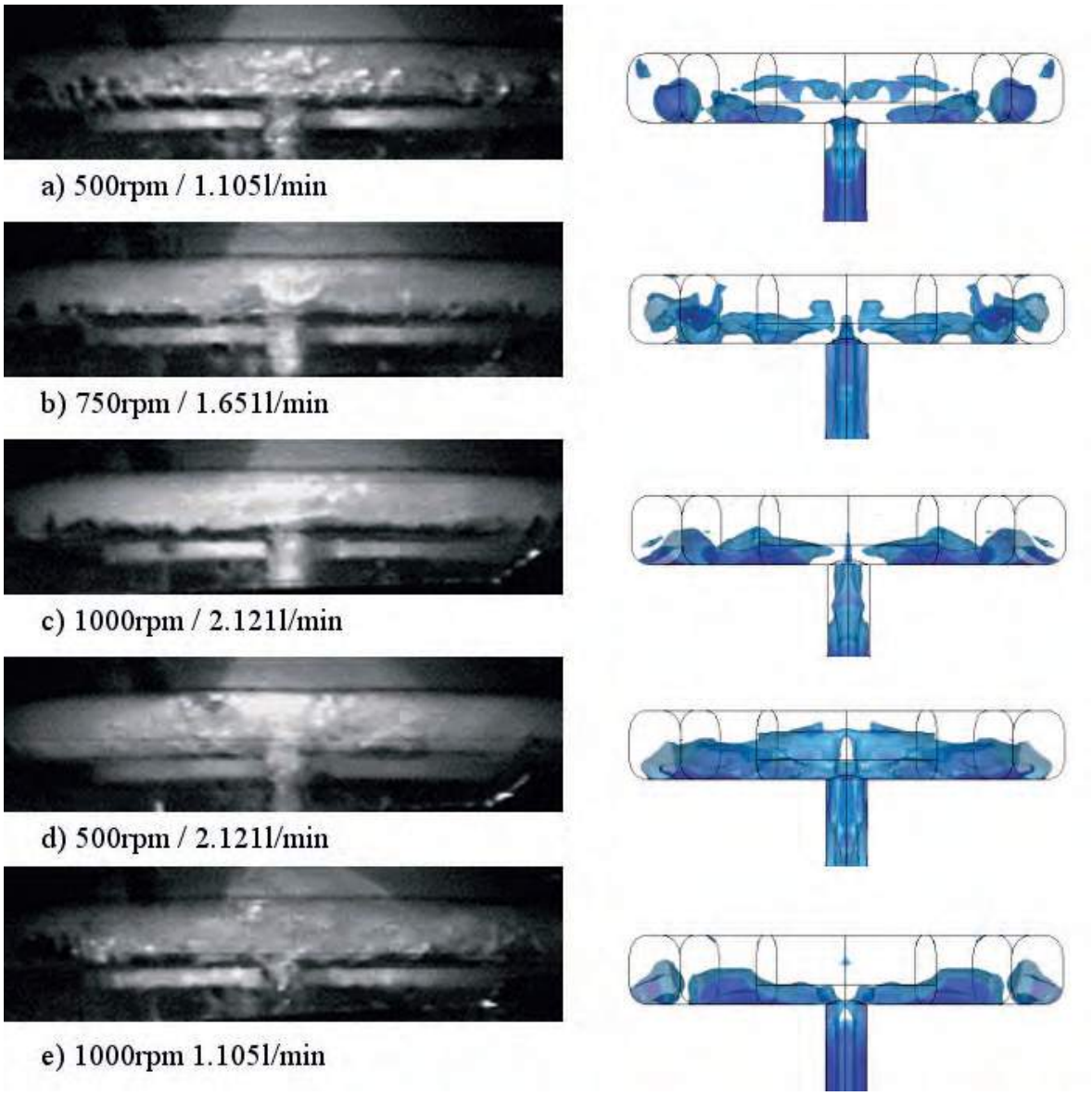

Fig. 7.22 Experimental and numerical results of inlet sections for *SGM* at *TDC* for different crank speeds and oil flow rates

time the oil present on the top surface in the gallery branch forced a downward flow of the oil and air, creating a strong mixing effect on the gallery bottom.

The difference in the variation of gallery filling at low speed and varying oil flow rate can be seen in Figure 7.23. The higher momentum of the oil jet at higher flow rates produced a less diverting jet and a more structured and persistent flow through the gallery, indicated by the consistent colour scheme sown in Figure 7.23b. This was also indicated by the formation of a larger sized air bubble at the gallery bottom as a result of the wall bound flow. The behaviour of the flow in the gallery at the lower flow rate (Figure 7.23a) showed a much stronger variation of the colour scheme, indicating less stable flow and formation of air

bubbles at varying positions along the gallery branch. The increased appearance of blue colour also highlights the presence of increased air content.

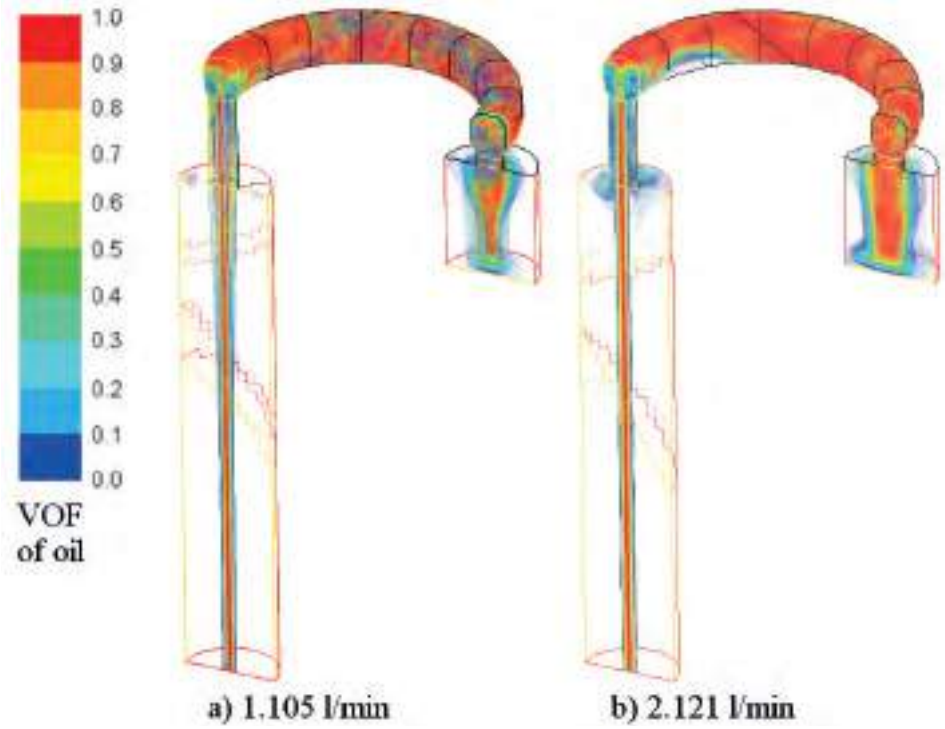

Fig. 7.23 Oil jet and gallery filling indicating VOF at TDC for 500 rpm and varying volumetric oil flow rate

The comparison of the experimental and simulation results showed a reasonable good comparison with regards to air bubble size, but also with respect to filling, as shown in Figure 7.24. The experiments showed the lowest filling at lowest speed and lowest flow rate (Figure 7.24a), with formation of large-sized air bubbles. These were a result of the coalescence of the medium-sized air bubbles found at the inlet section, whereby micro-sized air bubbles were still suspended in the bulk oil flow, if present at the inlet. The majority of the large-sized air bubbles were found at the gallery bottom, due to inertia effects.

The highest gallery filling was found at lowest speed and highest flow rate (Figure 7.24d), whereby the filling at highest speed and flow rate (Figure 7.24c) showed very similar results. At the lowest flow rate a comparable behaviour was also found, where the lower speed (Figure 7.24a) showed nearly similar filling to the highest speed (Figure 7.24e). This behaviour was not correctly predicted by the simulation, which overestimated the air content for the lowest flow rate and speed case (Figure 7.24a).

The experimental and numerical results indicated that the oil flow rate had a more significant effect on gallery filling of the outlet sections at lower crank speed with lower oil filling was present for the lower flow rate. This can be clearly seen by comparison of Figure 7.24a and 7.24d. This behaviour was opposed to the behaviour at the inlet sections, where a higher air content was determined at the lower crank speed. The higher momentum of the entering jet at higher flow rates would generate a wall bound flow along the gallery walls, causing a slowdown and collection of oil in the rear mid-gallery and outlet sections.

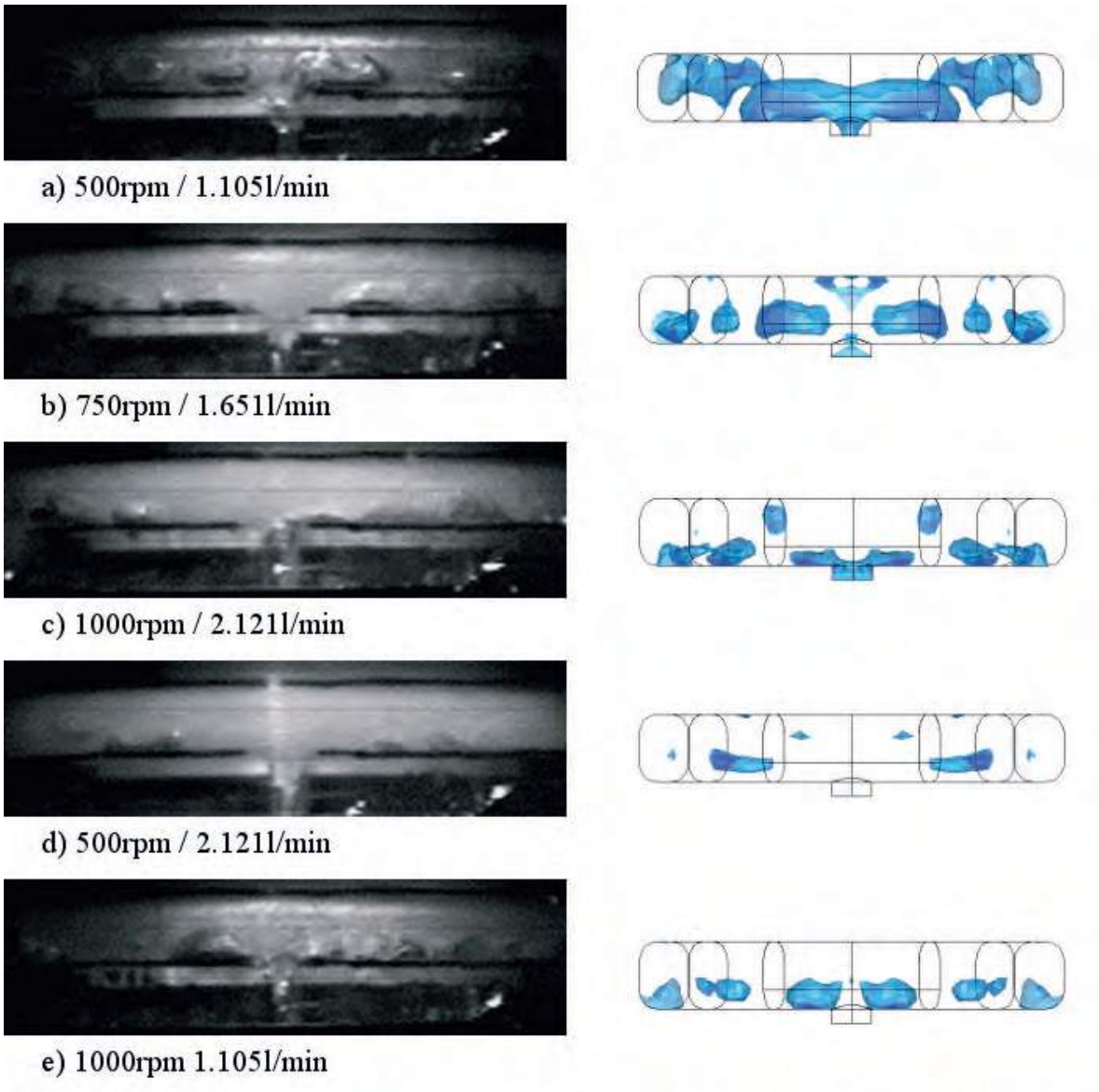

Fig. 7.24 Experimental and numerical results of outlet sections for *SGM* at *TDC* for different crank speeds and oil flow rates

At higher crank speeds occurred little variation of the air content, indicating a low influence of the crank speed on the filling of the outlet sections, whereby the results from both studies

also compared well. The reason for the low difference in filling can be related to the flow behaviour at the inlet sections. Although lower amounts of oil entered at lower flow rates during the upward stroke of the gallery, the opposing movement of gallery and oil jet during the downward stroke led to increased oil entry. At high oil flow rates and high crank speeds the superposition of the velocities led to a limitation of the amount of oil entering the gallery branches and some short circuiting and exiting through the inlet occurred. This led to the collection of near identical amounts of oil at the higher crank speed, seen in both studies.

The crank speed did, however, have an influence on the position of the air in the gallery. At lower crank speeds the air was not fully bound to the gallery bottom wall, but was found to be located more toward the gallery centre, as found in Figure 7.24a.

7.4 Summary

This chapter was concerned with the comparison of experimental and numerical results portraying the gallery filling and internal gallery flow behaviour for two differently sized and shaped gallery models. The commonalities and differences from the results were analysed and discussed for one specific representative case with fixed rotational crank speed and oil flow rate, as well as for a range of cases with varying rotational crank speeds and oil flow rates.

It was found that generally there was good comparison between the experimental results and numerical predictions of the gallery filling and internal gallery flow behaviour.

At the *BDC* the experimental results for the large gallery model (*LGM*) clearly showed air collecting at the gallery top surface as a result of inertia effects on the oil during the reduction of gallery velocity while approaching the *BDC*. In contrast the numerical results did not determine the air location accurately in all sections of the gallery. While the predicted air location at the inlet sections were in good comparison with the experimental results, the prediction of air positions at the mid-gallery and outlet sections were significantly lower in the gallery than the experimental results showed. Although the prediction of the air position showed shortcomings, the main flow directions showed good consistency to the experimental results, highlighting the occurring oil movement and allowing detailed understanding of the oil flow inside the gallery.

The filling and flow conditions of the *LGM* at the *TDC* were well predicted by the simulations with the size and behaviour of the air bubbles contained in the gallery showing good similarities to the experimental results. Both, experimental and numerical studies, showed the strong effect of the inertia driven flow as the gallery approached *TDC*, leading to distinct swirling flows in the gallery, while allowing air to collect at the gallery bottom.

The inaccurate prediction of the air position in the gallery outlet sections at the *BDC* was also present in all parametric cases, while at the inlet sections at *BDC* and for all sections at the *TDC* good comparison was found. Unfortunately the precise cause of this inaccuracy of the prediction at the *BDC* could not be determined. It was, however, found that the breakup of larger air bubbles was not in the same manner as found in the experiment. While the experiment showed a stronger air bubble rippling surface, the simulation retained a much smoother surface. The reasons for the difference may be linked with phase interface treatment and tracking in the software, or potentially with insufficient fine mesh to model the air bubble surface with oil protrusions before breakup. Both reasons cannot be identified with sufficient high certainty as the main cause.

The predictions of air position and oil flow behaviour in the small gallery model (*SGM*) showed good similarities to the experimental results. The inertia effects mainly controlled the location of the air bubbles, as found for the *LGM*, and the simulation results did portray this behaviour well in terms of size and position.

The smaller volume and hence reduced height of the *SGM* had a stronger control on the formation, breakup and flow behaviour of the air bubbles in the gallery. The smaller volume led to bubble sizes with the largest ones found to be at the self-sustaining size controlled by the surface tension. This size was present in the experiment predictions and simulation results. The surface tension led to air bubbles of size sufficiently large to be dragged along in the flow without splitting into smaller air bubbles, particularly in the mid-gallery and outlet gallery sections.

A difference between simulations and results was also found in the high turbulence region of the gallery inlet sections. The generation of smaller-sized air bubbles as shown in the experimental results was not found in the numerical results, although the outlines of predicted air bubbles was in good comparison with the turbulent region of the experiment. This limitation of the numerical results was mainly bound to the mesh density, whereby too

coarse mesh sizes cannot predict the breakup and formation of smaller air bubbles accurately enough, while large air bubbles can still be accurately tracked.

Overall the simulations were capable of predicting the bulk oil flow inside the gallery accurately enough and also the position of air bubbles, including the formation and breakup of the air bubbles in the larger sized gallery.

CHAPTER 8 CONCLUSIONS

The main aims of this research, as stated at the beginning of this thesis, were to determine the flow behaviour of oil inside a diesel piston cooling gallery under dynamic conditions and to assess the quality of numerical analysis data in comparison to experimental data. It can be concluded that the overall aims were achieved. In particular the following.

Oil Jet Behaviour and Influence

- The experimental results have shown that not only does the nozzle exit velocity of the oil jet have a strong influence on the jet breakup (jet widening), but also that the design of the nozzle exit is crucial. Nozzle shape induced turbulence played an important role in the jet breakup and standard calculations using Reynolds number and Ohnesorge number based on average flow velocities have limitations in the prediction of the breakup scheme and should be used with caution.
- The numerical results showed that jet breakup behaviour can be reproduced, but required a very fine mesh at least at the interface between oil and air. In contrast the increased simulation time of a refined mesh did not justify the gains from jet breakup modelling for the investigated case. Similar jet breakup behaviour can be modelled through the introduction of pulsating flow.
- The modelling of the free jet together with the gallery has shown that backflow from the gallery inlet influences the formation of the jet. In particular the exiting oil at the *BDC* deflected the jet near the nozzle exit and strong deviation from the gallery inlet resulted.

Gallery and Gallery Section Fill Level during Crank Cycles

- The experimental determination of accurate or even approximate values for the oil fill ratio (*OFR*) of the gallery cannot be performed for dynamic operating conditions using the visual method. The micro-sized air bubbles in the oil beyond transitional jet exit

flow regimes led to an opaque colour of the the oil-air mixture, within which even larger sized air bubbles cannot be detected, unless these are located at a visible gallery wall. The strong turbulence at the inlet section of the gallery and subsequent mixing of air and oil also prohibited reasonable analysis of oil fill ratio. For the mid-gallery and outlet sections the filling may be approximated, but only for *BDC* and *TDC* crank cycle positions and with compensation for the 3–dimensional gallery shape (refraction error).

- The simulations showed that very similar results of *OFR* were obtained for meshes with and without the boundary layer, indicating that the boundary layer may be omitted in the modelling of the flow without heat transfer. In addition a finer mesh was required to improve the numerical tracking of the interface. The generally low flow velocities inside the gallery also support this modelling approach, as the quasi-laminar layer near the wall extended sufficiently far to be covered by the first mesh layer. On the other hand the use of a finer mesh had the adverse effect of long simulation times in order to obtain results. In comparison to the wall boundary layer mesh, the variation of volumetric oil flow rate and rotational crank speed did have a significantly larger effect.
- The numerical results highlighted a highly transient behaviour of gallery filling and fill level settling. In particular the large gallery model (*LGM*) showed strong cyclic transient fill level variations, where the overall *OFR* varied during one crank cycle only by approximately 2%, but *OFR* variation over multiple consecutive cycles of up to 10% occurred. The variation frequency did not occur as a multiple of crank speed, but with random frequencies and magnitudes. The variations were strongly influenced by the conditions at the gallery inlet and gallery outlet, especially the impingement of oil backflow from the inlet causing deviation of the jet from the straight ejection path.
- There were significant differences in the gallery *OFR* with regards to location inside the gallery and position within the crank cycle. The average total gallery *OFR* showed relatively small values in the range of approximately 2% for large gallery and approximately 5% for small gallery. An analysis of the average section *OFR* showed very different results with variation during the crank cycle of up to 50% for the *LGM* and up to 30% for the small gallery model (*SGM*). The reason was found in the movement of air between gallery sections, especially in the inlet and mid-gallery sections, where the entering oil jet added a driving force to the inertia driven flow.

Air and Oil Flow Behaviour inside the Gallery

- Overall the experimental and numerical results were in good comparison, highlighting the effects of the jet driven forward flow and the wall-guided inertia driven swirling flow in both galleries during the whole crank cycle. The bulk flow directions were also represented well, with the exception of turbulence regions with air bubbles smaller than the mesh size. The only strong difference was found in the prediction of the air bubble position in the large gallery model (*LGM*) at the mid-gallery and outlet sections near the *BDC*.
- For the gallery inlet section the numerical results predicted the conditions reasonably well with the bulk flow directions in both galleries showing comparable features to the experiment, including shortcut swirling, but it also highlighted the shortcomings of the simulation with regards to the representation of the air bubble size. While the experiment showed a distinct turbulence region expressed by fast moving medium-sized air bubbles, the simulations predicted larger continuous air bubbles. The occurrence of these larger air bubbles can be attributed to the mesh density, where air bubbles of size of the mesh cells are grouped together as a result of the interface tracking process, rather than individually shown.
- In the mid-gallery sections the reduced turbulence and the formation of larger-sized air bubbles led to improved comparability of numerical and experimental results. Both analyses showed similar bulk flow behaviour and air bubble sizes, but also showed the distinctive differences between the flow in the *LGM* and *SGM*. The larger volume of the *LGM* together with the complex gallery cross-sectional shape allowed for chaotic flow, as large air bubbles presented little resistance to the inertia driven oil flow. In contrast the smaller more regular shaped volume of the *SGM* only allowed air bubbles, where surface tension forces controlled the behaviour and partially prevented breakup, leading to wall-guided forward flow.
- The inertia effects of the gallery movement predominantly controlled the flow behaviour in the outlet sections of both galleries, small and large. The majority of the oil outflow occurred near the *BDC* and reduced during the upward stroke, ceasing at *TDC*. During the downward stroke a combination of air and oil entrance occurred, generally leading to the formation of large-sized air bubbles. These conditions were in good comparison

between experiment and simulation. The only significant difference occurred for the prediction of the air position in the *LGM*, which was at mid-gallery height, rather than gallery top as seen in the experiment.

CHAPTER 9 RECOMMENDATIONS

The following recommendation for improvements and expansions on the current work are:

- The test rig should be updated or rebuilt to raise the crank speed range to engine operating range limits. The highest demand for piston cooling is found at maximum engine power output, due to the highest heat losses from combustion.

- Validation of the simulation results against experimental results should be performed with respect to in-gallery flow velocities. This may be implemented by 3–dimensional particle image velocimetry (PIV) analysis and the use of particle trackers. The method would allow determining the flow velocities in specific gallery sections and also provide an overall view of the bulk oil flow. In addition the trackers may be used to determine the residence time of the oil in the gallery.

- The experimental and numerical studies were performed at isothermal conditions, but the heat transfer inside the gallery during engine operation influences the material properties, such as viscosity, density and heat capacity. The effect of varying viscosity and density should be investigated in general, but also with respect to the effects on sectional flow behaviour and filling. The introduction of heat transfer does require analysis of the boundary layer effects, although the present study determined no effect on the flow or filling.

- The shortcomings found in the modelling should be addressed and reasons investigated. For pure flow analysis the effects of the suspended micro-sized air bubbles may be omitted, but with introduction of thermal effects any insulation effects due to the micro-sized bubbles needs to be investigated. Also the different air position to the experiment at *BDC* in *LGM* needs further analysis. With the air not rising into the upper and smaller cross-sectional width region the surface tension and/or wall adhesion effects may play a

role in the modelling and should be addressed. Both cases may need a refined mesh and it is strongly recommended options of upgraded parallel processing or even clustering are investigated.

- The study should also be expanded with regards to the identified parameters controlling gallery filling. Although effects of engine speed and oil flow rate were investigated, the range was limited to match the experimental conditions, but should be expanded to match the operating ranges of engines. In addition the effect of a conrod should be investigated, as this affects the maximum velocity and the maximum acceleration of the piston, which indirectly affects the inertia driven flow.

- Furthermore the two gallery shapes have shown that the flow inside the gallery was influenced by the gallery shape. Even derivation from the torus-like shape has been proposed and may also be included. There are a variety of gallery shapes on the market. The cross-sectional shape does influence the flow behaviour and should be investigated further.

REFERENCES

A.Berlemont, Bouali, Z., Cousin, J., Desjonquères, P., M.Doring, and T. Ménard and, E. N. (2012). Simulation of liquid/gas interface break-up with a coupled level set/VOF/ghost fluid method. *Seventh International Conference on Computational Fluid Dynamics, July 9-13*. Big Island, Hawaii, USA.

ACEA (2015). Diesel penetration. Technical report, European Automobile Manufacturers' Association, http://www.acea.be/statistics/article/diesel-penetration; last accessed 17.04.2015.

Agarwal, A. K., Goyal, S. K., and Srivastava, D. K. (2011). Time resolved numerical modeling of oil jet cooling of a medium duty diesel engine piston. *International Communications in Heat and Mass Transfer*, 38(8):1080–1085. Elsevier.

Agrawal, K. S. (2013). Breakup of liquid jets. *International Journal of Emerging Technologies in Computational and Applied Sciences (IJETCAS)*, 13:487–496. Elsevier.

Albert, C., Raach, H., and Bothe, D. (2012). Influence of surface tension models on the hydrodynamics of wavy laminar falling films in volume of fluid-simulations. *International Journal of Multiphase Flow*, 43:66–71. Elsevier.

Ali, M. S. M., Doolan, C. J., and Wheatley, V. (2009). Grid convergence study for a two-dimensional simulation of flow around a square cylinder at a low reynolds number. In *Seventh International Conference on CFD in the Minerals and Process Industries CSIRO*, Melbourne, Australia 9 - 11 December.

Andersson, B., Andersson, R., Håkansson, L., Mortensen, M., Sudiyo, R., and Van Wachem, B. (2011). *Computational fluid dynamics for engineers*. Cambridge University Press, Cambridge, UK, 1 edition. ISBN: 9781107018952.

ANSYS (2011). *ANSYS FLUENT Theory Guide, Release 14*. ANSYS Inc., Canonsburg, PA, USA.

ANSYS (2013a). *ANSYS FLUENT Meshing Guide, Release 15*. ANSYS Inc., Canonsburg, PA, USA.

ANSYS (2013b). *ANSYS FLUENT User Guide, Release 15*. ANSYS Inc., Canonsburg, PA, USA.

Aoyagi, Y., Osada, H., and Misawa, M. (2006). Advanced diesel combustion using of wide range, high boosted and cooled EGR system by single cylinder engine. *SAE International*. SAE Technical Paper 2006-01-0077.

Baberg, A., Freidhager, M., Mergler, H., and Schmidt, K. (2012). *Aspekte der Kolbenmaterialwahl bei Dieselmotoren*. *MTZ-Motortechnische Zeitschrift*, 73(12):964–969.

Bakker, A. (2012). Applied computational fluid dynamics, lecture 16–free surface flows. online lecture notes, url: http://bakker.org/dartmouth06/engs150/16-fsurf.pdf, last accessed: 17.04.2015.

Bargende, M. (1991). *Ein Gleichungsansatz zur Berechnung der instationären Wandwärmeverluste im Hochdruckteil von Ottomotoren*. Dr.-Ing. thesis, Technische Universität, Darmstadt, Germany.

Bhaskaran, R. and Collins, L. (2013). Introduction to cfd basics. online Notes, Cornell University, Sibley School of Mechanical & Aerospace Engineering, New York, url: http://dragonfly.tam.cornell.edu/teaching/mae5230-cfd-intro-notes.pdf, last accessed: 15.11.2013.

Bianchini, A., Ferrara, G., Ferrari, L., Paltrinieri, F., Tosetti, F., and Milani, M. (2009). Design and optimization of a variable displacement vane pump for high performance ic engine lubrication: Part 1-experimental analysis of the circumferential pressure distribution with dynamic pressure sensors. *SAE International*. SAE Technical Paper 2009-01-1045.

Boger, M., Schlottke, J., Munz, C. D., and Weigand, B. (2010). Reduction of parasitic currents in the DNS VOF code FS3D. In *12th Workshop on Two-Phase Flow Predictions*, Stuttgart, Germany, March.

Brackbill, J. U., Kothe, D. B., and Zemach, C. (1992). A continuum method for modeling surface tension. *Journal of computational physics*, 100(2):335–354. Elsevier.

Brennen, C. E. (2005). *Fundamentals of Multiphase Flow*. Cambridge University Press, New York, USA. ISBN: 978-0-521-84804-6.

Brkić, D. (2011). New explicit correlations for turbulent flow friction factor. *Journal of Nuclear Engineering and Design*, 241(9):4055–4059. Elsevier.

Bush, J. and London, A. (1965). Design data for "cocktail shaker" cooled pistons and valves. *SAE International*. SAE Technical Paper 650727.

Cao, L., Bhave, A., Su, H., Mosbach, S., Kraft, M., Dris, A., and McDavid, R. M. (2009). Influence of injection timing and piston bowl geometry on PCCI combustion and emissions. *SAE International*. SAE Technical Paper 2009-01-1102.

Cao, Y. and Wang, Q. (1995). Piston cooling with shaking-up heat pipes (SUHP) and thermal analysis of the cooling system. *SAE International*. SAE Technical Paper 950526.

Celik, I. B., Ghia, U., Roache, P. J., and Freitas, C. J. (2008). Procedure for estimation and reporting of uncertainty due to discretization in cfd applications. *Journal of Fluids Engineering*, 130(7). Elsevier.

Chatterjee, S., Walker, A. P., and Blakeman, P. G. (2008). Emission control options to achieve Euro IV and Euro V on heavy duty diesel engines. *SAE International*. SAE Technical Paper 2008-28-0021.

Chen, P. (2004). *Modeling the fluid dynamics of bubble column flows*. Doctoral dissertation, Sever Institute of Washington University, Missouri, USA.

Chen, Y.-C. and Worden, J. A. (2000). Evaluation of microalloyed steel for articulated piston applications in heavy duty diesel engines. *SAE International*. SAE Technical Paper 2000-01-1232.

Chiodi, M. and Bargende, M. (2001). Improvement of engine heat-transfer calculation in the three-dimensional simulation using a phenomenological heat-transfer model. *SAE International*. SAE Technical Paper 2001-01-3601.

Chowdhury, M. A., Nuruzzaman, D. M., and Hannan, A. (2012). Effect of sliding velocity and relative humidity on friction coefficient of brass sliding against different steel counterfaces. *International Journal of Engineering Research and Applications*, 2(2):1425–1431. Elsevier.

Corrigan, A., Camelli, F., Löhner, R., and Wallin, J. (2009). Running unstructured grid based CFD solvers on modern graphics hardware. *19th AIAA Computational Fluid Dynamics Conference*, pages 22–25. American Institute of Aeronautics and Astronautics, Reston, VA, USA.

Cousins, S. H. and Bueno, J. G. andCoronado, O. P. (2007). Powering or de-powering future vehicles to reach low carbon outcomes: the long term view 1930—2020. *Journal of Cleaner Production*, 15(11):1022–1031.

Das, S. and Roberts, C. (2013). Factors affecting heat transfer in a diesel engine: Low heat rejection engine revisited. *SAE International*. SAE Technical Paper 2013-01-0875.

de Souza, A. (2002). *How To – Plan a CFD Study*. NAFEMS Ltd., Glasgow, UK.

Delteil, J., Vincent, S., Erriguible, A., and Subra-Paternault, P. (2011). Numerical investigations in rayleigh breakup of round liquid jets with VOF methods. *Journal of Computers & Fluids*, 50:10–23. Elsevier.

Donea, J., Huerta, A., Ponthot, J.-P., and Rodríguez-Ferran, A. (2004). Arbitrary lagrangian–eulerian methods. *Encyclopedia of Computational Mechanics*, 34(2004). John Wiley & Sons, Ltd.

Du, J. (2012). A wavelet neural network method to determine diesel engine piston heat transfer boundary conditions. *SAE International*. SAE Technical Paper 2012-01-1760.

Eca, L. and Hoekstra, M. (2006). Discretization uncertainty estimation based on a least squares version of the grid convergence index. 2nd Workshop on CFD Uncertainty Analysis, Lisbon, October 2006.

Eggers, J. and Villermaux, E. (2008). Physics of liquid jets. *Reports on Progress in Physics*, 71(3):142–151. Elsevier.

Eichel, D., Huang, Y., and Kopp, M. (2001). Kolben mit einem ringförmigen kühlkanal. Deutsches Patent– und Markenamt, München, Germany. Patent no: DE 10015709, 11.08.2001.

Eiglmeier, C., Lettmann, H., Stiesch, G., and Merker, G. P. (2001). A detailed phenomenological model for wall heat transfer prediction in diesel engines. *SAE International*. SAE Technical Paper 2001-01-3265.

Eiglmeier, C. and Merker, G. (2000). *Neue Ansätze zur phänomenologischen Modellierung des gasseitigen Wandwärmeübergangs im Dieselmotor*. *MTZ-Motortechnische Zeitschrift*, 61(5):324–335.

Esfahanian, V., Javaheri, A., and Ghaffarpour, M. (2006). Thermal analysis of an SI engine piston using different combustion boundary condition treatments. *International Journal of Applied Thermal Engineering*, 26(2006):277–287. Elsevier.

Evans, C. A. (1977). Cocktail shaker. *Journal of*. Heat Transfer Science Library, University of Nottingham.

Fang, H. L., Whitacre, S. D., Yamaguchi, E. S., and Boons, M. (2007). Biodiesel impact on wear protection of engine oils. *SAE International*. SAE Technical Paper 2007-01-4141.

Farvardin, E. and Dolatabadi, A. (2013). Numerical simulation of the breakup of elliptical liquid jet in still air. *Journal of Fluids Engineering*, 135. Paper No: FE-12-1515.

Fellouah, H., Ball, C., and Pollard, A. (2009). Reynolds number effects within the development region of a turbulent round free jet. *International Journal of Heat and Mass Transfer*, 52:3943–3954. Elsevier.

Ferziger, J. H. and Peric, M. (2002). *Computational Methods for Fluid Dynamics*. Springer-Verlag Berlin Heidelberg, Germany, 3 edition. ISBN: 978-3-642-56026-2.

Flynn, G. and Underwood, A. F. (1945). Adequate piston cooling - oil cooling as a means of piston temperature control. *SAE International*. SAE Technical Paper 450167.

French, C. C. J. (1972). Piston cooling. *SAE International*. SAE Technical Paper 720024.

Fridriksson, H. S., Tuner, M., Andersson, O., Sunden, B., Persson, H., and Ljungqvist, M. (2014). Effect of piston bowl shape and swirl ratio on engine heat transfer in a light-duty diesel engine. *SAE International*. SAE Technical Paper 2014-01-1141.

Fu, W.-S., Lian, S.-H., and Hao, L.-Y. (2006). An investigation of heat transfer of a reciprocating piston. *International Journal of Heat and Mass Transfer*, 49:4360–4371. Elsevier.

GEMS (2014). *RFO / RFA 2500 Series Continuous Output*. Gems Sensors and Controls, Plainville, CT, USA. Instruction Bulletin No. 157258, Rev. J.

Giuffrida, A. and Lanzafame, R. (2005). Cam shape and theoretical flow rate in balanced vane pumps. *Journal of Mechanism and Machine Theory*, 40(3):353—369. Elsevier.

Haberhauer, H. and Bodenstein, F. (2005). *Maschinenenelemente: Gestaltung, Berechnung, Anwendung*. Springer Verlag, Berlin Heidelberg, Germany, 13 edition. ISBN:.

Han, X., Wang, M., and Zheng, M. (2015). Study of low temperature combustion with neat n-butanol on a common-rail diesel engine. *SAE International*. SAE Technical Paper 2015-01-0003.

Harrison, J., Aihara, R., Eshraghi, M., and Dmitrieva, I. (2014). Modeling engine oil variable displacement vane pumps in 1d to predict performance, pulsations, and friction. *SAE International*. SAE Technical Paper 2014-01-1086.

He, Y. Y. and Kong, F. Y. (2013). Numerical calculation and analysis of radial force on the single-action vane pump. *IOP Conference Series: Materials Science and Engineering*, 52(3). IOP Publishing Ltd.

Heidrich, P. (2003). *Numerische Simulation von Strömungs– und Transportprozessen*. Presented at Technische Universität Stuttgart, April 2003 (unpublished material).

Heidrich, P., Lochmann, R., and Estrum, T. (2006). Kühlkanalkolben für einen verbrennungsmotor mit wärmerohren. Deutsches Patent– und Markenamt, München, Germany. Patent no: WO 2006015585, 16.02.2006.

Heron, S. D. (1923). Improvements in the cooling of valves or other moving parts of internal combustion engines that are subject to high temperature. European Patent Office. Patent no: GB 224288, 07.08.1923.

Heron, S. D. (1931). Improvements in or relating to pistons and method of making the same. European Patent Office. Patent no: GB 396249, 07.11.1931.

Hirt, C. W. and Nichols, B. D. (1981). Volume of fluid (VOF) method for the dynamics of free boundaries. *Journal of Computational Physics*, 39(1):201–225. Elsevier.

Homma, S., Koga, J., Matsumoto, S., Song, M., and Tryggvason, G. (2006). Breakup mode of an axisymmetric liquid jet injected into another immiscible liquid. *Chemical engineering science*, 12(61):3986–3996. Elsevier.

Huang, K. J. and Lian, W. C. (2009). Kinematic flowrate characteristics of external spur gear pumps using an exact closed solution. *Journal of Mechanism and Machine Theory*, 44:1121–1131.

Hui, W.-H. and Xu, K. (2012). *Computational Fluid Dynamics Based on the Unified Coordinates*. Springer–Verlag Berlin Heidelberg, Germany. ISBN: 978-3-642-25895-4.

Issa, R. I. (1986). Solution of the implicitly discretised fluid flow equations by operator-splitting. *Journal of Computational Physics*, 62(1):40–65. Elsevier.

Issler, W. (2000). Gekühlter kolben für verbrennungsmotoren. Deutsches Patent– und Markenamt, München, Germany. Patent no: DE 19926568, 14.12.2000.

Johnson, C. B. and Bushnell, D. M. (1970). Power-law velocity-profile-exponent variations with reynolds number, wall cooling, and mach number in a turbulent boundary layer. Technical Note D-5753, NASA, Langley Research Centre, Hampton, VA, USA.

Jones, B. L., Johnston, D. N., and Longmore, D. K. (1998). Simulation of suction flow ripple in power steering pumps. *SAE International*. SAE Technical Paper 982023.

Jones, W. R. and Wedeven, L. D. (1971). *Surface-Tension Measurements in Air of Liquid Lubricants to 200°C by the Differential-Maximum Bubble-Pressure Technique*. Nasa Technical Note, Lewis Research Center Cleveland, Ohio, USA.

Joseph, D. D. and Yang, B. H. (2010). Friction factor correlations for laminar, transition and turbulent flow in smooth pipes. *Physica D: Nonlinear Phenomena*, 239(14):1318–1328. Elsevier.

Juretic, F. (2004). *Error analysis in finite volume CFD*. Doctoral dissertation, Imperial College London (University of London).

Kajiwara, H., Fujioka, Y., and Negishi, H. (2003). Prediction of temperatures on pistons with cooling gallery in diesel engines using CFD tool. *SAE International*. SAE Technical Paper 2003-01-0986.

Kajiwara, H., Fujioka, Y., Suzuki, T., and Negishi, H. (2002). An analytical approach for prediction of piston temperature distribution in diesel engines. *Japan SAE Review*, 23(4). Society of Automotive Engineers of Japan.

Kaldonski, T. J., Gryglewicz, L., Stanczyk, M., and T., K. (2011). Investigations on lubricity and surface properties of selected perfluoropolyether oils. *Journal of KONES Powertrain and Transport*, 18(1):207. Elsevier.

Kamp, H. (2008). Neue Kolbentechnologien. Technical report, KS Kolbenschmidt GmbH, Neckarsulm, Germany. presentation: Wilhelm-Maybach–Schule Stuttgart, Germany, March 2008.

Kato, N. and Moritsugu, M. (2001). Piston temperature measuring technology using electromagnetic induction. *SAE International*. SAE Technical Paper 2001-01-2027.

Kavtaradze, R., Zelentsov, A., Gladyshev, S. P., Kavtaradze, Z., and Onishchenko, D. (2012). Heat insulating effect of soot deposit on local transient heat transfer in diesel engine combustion chamber. *SAE International*. SAE Technical Paper 2012-01-1217.

Kenningley, S. and Morgenstern, R. (2012). Thermal and mechanical loading in the combustion bowl region of light vehicle diesel alsicunimg pistons; reviewed with emphasis on advanced finite element analysis and instrumented engine testing techniques. *The name of the journal SAE International*. SAE Technical Paper 2012-01-1330.

Kim, J. and Park, S. (2012). A study on sensor design for measurement of automobile engine oil degradation and level. *International Proceedings of Computer Science & Information Technology*, 28:11–16. IACSIT Press, Singapore.

Kim, S.-E. and Choudhury, D. (1995). A near-wall treatment using wall functions sensitized to pressure gradient. *Journal of Separated and Complex Flows*, 1995:273–280. Elsevier.

Kneer, R. and El-Khawankey, S. (2010). Bedarfsgerechte Kolbenkühlung. Technical report, Lehrstuhl für Wärme- und Stoffübertragung, RWTH Aachen, Germany. poster presentation.

Kodak (1999). *User's Manual Kodak EKTAPRO HS Motion Analyser, Model 4540mx*. Eastman Kodak Company, San Diego, CA, USA.

Kolbenschmidt (2001). Kolbentechnologie für Pkw-Dieselmotoren – Höchste Leistungsdichte mit KS-Kolben. Technical report, KS Kolbenschmidt GmbH, Neckarsulm, Germany.

Kolbenschmidt (2007). Neue Werkstoffe und Prozesse für Pkw-Dieselmnotoren. Technical report, KS Kolbenschmidt GmbH, Neckarsulm, Germany.

Komiya, A., Moriya, S., Kobari, T., Kosaka, S., Nakano, Y., and Maruyama, S. (2011). Pisuton kurinu chaneru nairu dou no kashika. *Transactions of Society of Automotive Engineers of Japan*, 42(1):149–154.

Kono, M., Basaki, M., Ito, M., Hashizume, T., Ishiyama, S., and Inagaki, K. (2012). Cooling loss reduction of highly dispersed spray combustion with restricted in–cylinder swirl and squish flow in diesel engine. *SAE International*. SAE Technical Paper 2012-01-0689.

Köpple, F., Seboldt, D., Jochmann, P., Hettinger, A., Kufferath, A., and Bargende, M. (2014). Experimental investigation of fuel impingement and spray-cooling on the piston of a GDI engine via instantaneous surface temperature measurements. *SAE International*. SAE Technical Paper 2014-01-1447.

Kosaka, H. and Arai, T. (2011). Simultaneous measurements of temperatures of flame and wall surface in a combustion chamber of diesel engine. *SAE International*. SAE Technical Paper 2011-01-2047.

Kositgittiwong, D., Chinnarasri, C., Julien, P., Ruff, J., and Meroney, R. (2010). Multiphase flow models for 2d numerical modeling of flow over spillways. Colorado State University, Fort Collins, Colorado, USA.

Kuchling, H. (1986). *Taschenbuch der Physik*. VEB Fachbuchverlag, Leipzig, Germany. ISBN:.

Kudela, H. (2012). Turbulent flow. online Notes on Fundamentals of Fluid Mechanics, Politechnika Wrocławska, , url: http://fluid.itcmp.pwr.wroc.pl/ znmp/fundmech.htm, last access: 10.08.2015.

Kuzuyama, H., Machida, M., Kawae, T., Tanaka, T., Aoki, H., Sugiyama, Y., and Umehara, T. (2012). High efficiency and clean diesel combustion concept using double premixed combustion. *SAE International*. SAE Technical Paper 2012-01-0906.

Ladommatos, N., Xiao, Z., and Zhao, H. (2005). The effect of piston bowl temperature on diesel exhaust emissions. In *Proceedings of the Institution of Mechanical Engineers, Part D: Journal of Automobile Engineering*, volume 219 of *3*.

Lasecki, M. P. and Cousineau, J. M. (2003). Controllable electric oil pumps in heavy duty diesel engines. *SAE International*. SAE Technical Paper 2003-01-3421.

Li, D. (2008). *Encyclopedia of Microfluidics and Nanofluidics*. Springer Science & Business Media, Berlin, Germany. ISBN: 978-0-387-32468-5.

Ling, J., Cao, Y., and Wang, Q. (1998). Critical working frequency of reciprocating heat-transfer devices in axially reciprocating mechanisms. *International Journal of Heat and Mass Transfer*, 41(1):73–80.

Liu, H. (1999). *Science and Engineering of Droplets: Fundamentals and Applications*. William Andrew Publishing, Norwich, New York, USA. ISBN: 0-8155-1436-0.

Loganathan, S. and Govindarajan, S. (2011). Design and development of vane type variable flow oil pump for automotive application. *SAE International*. SAE Technical Paper 2011-28-0102.

Lopez, J. J., Garcia-Oliver, J. M., Martin, J., Chemisky, J. P., and Bouet, A. (2012). A soot radiation model for diesel sprays. *SAE International*. SAE Technical Paper 2012-01-1069.

Luff, D. C., Law, T., Shayler, P. J., and Pegg, I. (2012). The effect of piston cooling jets on diesel engine piston temperatures, emissions and fuel consumption. *SAE International*, pages 1300–1311. SAE Technical Paper 2012-01-1212.

Lv, J., Wang, P., Bai, M., Li, G., and Zeng, K. (2015). Experimental visualization of gas–liquid two-phase flow during reciprocating motion. *Journal of Applied Thermal Engineering*, 79:63—-73. Elsevier.

Maassen, F., Bick, W., and Haubner, F. (2005). Lightweight engine concepts for a passenger car diesel engine with 200 bar peak pressure. *SAE International*. SAE Technical Paper 2005-01-0659.

Mahadevan, R. and Gopal, R. (2008). Selectively reinforced squeeze cast pistons. In *68th World Foundry Congress*, pages 379–384. Chennai, India.

Mahle (2012). *Pistons and engine testing*. Vieweg + Teubner Verlag, Springer Fachmedien, Wiesbaden, Germany, 1 edition. ISBN: 978-3-8348-1590-3.

Mahmoud, H., Kria, W., Mhiri, H., Le Palec, G., and Bournot, P. (2010). A numerical study of a turbulent axisymmetric jet emerging in a co-flowing stream. *Journal of Energy Conversion and Management*, 51:2117–2126. Elsevier.

Manring, N. D. and Kasaragadda, S. B. (2003). The theoretical flow ripple of an external gear pump. *Journal of Dynamic Systems, Measurement, and Control*, 125:396—404. ASME Transactions.

Marrs, J. (2011). *Machine Designers Reference*. Industrial Press, South Norwalk, CT, USA. ISBN: 9780831191405.

Marshall, E. M. and Bakker, A. (2001). Computational fluid mixing. Technical report, Technical Notes, Fluent Inc., Lebanon, New Hampshire, USA.

Martin, E. and Thieme, S. (2000). Flüssigkeitsgekühlter Kolben. Deutsches Patent– und Markenamt, München, Germany. Patent no: DE 19930630, 26.10.2000.

Martínez, I. (2014). Combustion kinetic. online lecture notes Universidad Politecnica Madrid, url: http://webserver.dmt.upm.es/ isidoro/bk3/, last accessed: 25.09.2014.

Ménard, T., Tanguy, S., and Berlemont, A. (2007). Coupling level set/VOF/ghost fluid methods: Validation and application to 3d simulation of the primary break-up of a liquid jet. *International Journal of Multiphase Flow*, 33:510–524. Elsevier.

Mobasheri, R. and Peng, Z. (2013). CFD investigation of the effects of re-entrant combustion chamber geometry in a HSDI diesel engine. *International Journal of Mechanical, Aerospace, Industrial and Mechatronics Engineering*, 7(4). World Academy of Science, Engineering and Technology.

Modi, A. J. (2012). Experimental study of energy balance in thermal barrier coated diesel engine. *SAE International*. SAE Technical Paper 2012-01-0389.

Morgan, W., Barnes, S., Ryu, K. H., Jun, S., and Shim, W. (2013). A non-linear finite element approach applied to diesel piston combustion bowl rim strength assessment. *SAE International*. SAE Technical Paper 2013-01-0293.

Moritani, H. and Nozawa, Y. (2003). Oil degradation in second–land region of gasoline engine pistons. *Journal of Synthetic Lubrication*, 38:36–43. R&D Rev. Toyota CRDL.

Musculus, M. P. B. (2005). Measurements of the influence of soot radiation on in-cylinder temperatures and exhaust nox in a heavy-duty di diesel engine. *SAE International*. SAE Technical Paper 2005-01-0925.

Osher, S. andkiw, R. P. (2001). Level set methods: an overview and some recent results. *Journal of Computational Physics*, 169(2):463–502. Elsevier.

Pai, M. G., Desjardins, O., and Pitsch, H. (2008). Detailed simulations of primary breakup of turbulent liquid jets in crossflow. *Center for Turbulence Research, Annual Research Briefs*, 34(2010):451–466. Stanford University, Stanford, CA, USA.

Pan, J., Nigro, R., and Matsuo, E. (2005). 3–D modeling of heat transfer in diesel engine piston cooling galleries. *SAE International*. SAE Technical Paper 2005-01-1644.

Peric, M. (2004). Simulation of flows in complex geometries: new meshing and solution methods. *Proceedings NAFEMS seminar: "Simulation of complex flows (CFD) – Application and trends"*. NAFEMS, Niedernhausen, Wiesbaden, Germany.

Phillips, W. D. (2006). The high–temperature degradation of hydraulic oils and fluids. *Journal of Synthetic Lubrication*, 23(1):39–70. Wiley Online Library.

Pimenta, M. and Filho, R. (1993). Cooling of automotive pistons: Study of liquid-cooling jets. *SAE International*. SAE Technical Paper 931622.

Prasad, B. V. V. S. U., Sharma, C. S., Anand, T. N. C., and Ravikrishna, R. V. (2011). High swirl-inducing piston bowls in small diesel engines for emission reduction. *Journal of Applied Energy*, 88(7):2355–2367.

Quazi, M. A., Singh, S. K., and Jadhao, M. (2015). Effect of piston bowl shape, swirl ratio and spray angle on combustion and emission in off road diesel engine. *SAE International*. SAE Technical Paper 2015-26-0142.

Rajamani, V. K., Schoenfeld, S., and Dhongde, A. (2012). Parametric analysis of piston bowl geometry and injection nozzle configuration using 3d CFD and DoE. *SAE International*. SAE Technical Paper 2012-01-0700.

Rakopoulos, C., Hountalas, D., Koutroubousis, A., and Zannis, T. (2002). Application and evaluation of a detailed friction model on a DI diesel engine with extremely high peak combustion pressures. *SAE International*. SAE Technical Paper 2002-01-0068.

Reichstein, S., Hofmann, L., and Kenningley, S. (2005). *Entwicklung von Kolbenwerkstoffen für moderne Hochleistungsdieselmotoren*. *Giesserei–Praxis*, 2005(10):380–384.

Ricardo (2012). *WAVE Help Manual*. Ricardo Ltd, Shoreham-by-Sea, UK.

Richardson, L. F. and Gaunt, J. A. (1927). The deferred approach to the limit. part i. single lattice. part ii. interpenetrating lattices. *Philosophical Transactions of the Royal Society of London, Series A, containing papers of a mathematical or physical character*, pages 299–361.

Rider, W. J. and Kothe, D. B. (1995). Comments on modeling interfacial flows with volume-of-fluid methods.

Roache, P. J. (1997). Quantification of uncertainty in computational fluid dynamics. *Annual Review of Fluid Mechanics*, 29(1):123–160. Palo Alto, CA, USA.

Röhrle, M. D. (1995). *Pistons for Internal Combustion Engines: Fundamentals of Piston Technology*. Verlag Moderne Industie, Landsberg/Lech, Germany.

Rupangudi, S., Ramesh, C., Veerabhadhrappa, K., and V, R. (2014). Study of effect of coating of piston on the performance of a diesel engine. *SAE International*. SAE Technical Paper 2014-01-1021.

Saadi, M. S., Ismail, M., Fotowat, S., Quaiyum, M. A., and Fartaj, A. (2013). Study of motor oil cooling at low reynolds number in multi-port narrow channels. *SAE International Journal of Engines*, 2(6). SAE Technical Paper 2013-01-1643.

Sangeorzan, B., Barber, E., and Hinds, B. (2011). Development of a one-dimensional engine thermal management model to predict piston and oil temperatures. *SAE International*. SAE Technical Paper 2011-01-0647.

Schlichting, H. (1979). *Boundary–Layer Theory*. McGraw–Hill, New York, USA, 7 edition. ISBN: 0-07-055334-3.

Schwarz, R. and Adolph, J. (2001). *Optimierung von Ölspritzdüsen zur Kolbenkühlung*. *MTZ-Motortechnische Zeitschrift*, 62(3):236–239.

Seo, J. (2014). Multiphase flow modeling with free surfaces flow. Presented at the 2014 Korea Convergence Conference.

Sharief, A., Chandrashekar, T. K., Antony, A. J., and Samaga, B. S. (2008). Study on heat transfer correlation in IC engines. *SAE International*. SAE Technical Paper 2008-01-1816.

Shih, T.-H., Liou, W., Shabbir, A., Yang, Z., and Zhu, J. (1995). A new eddy-viscosity model for high reynolds number turbulent flows - model development and validation. *Computers & Fluids An International Journal*, 24(3):227–238. Elsevier.

Shinjo, J. and Umemura, A. (2010). Simulation of liquid jet primary breakup: Dynamics of ligament and droplet formation. *International Journal of Multiphase Flow*, 36(7):513–532. Elsevier.

Silva, F. S. (2006). Fatigue on engine pistons: A compendium of case studies. *International Journal of Engineering Failure Analysis*, 13(2006):480–492. Elsevier.

Singh, A. P. and Agarwal, A. K. (2012). An experimental investigation of combustion, emissions and performance of a diesel fuelled HCCI engine. *SAE International*. SAE Technical Paper 2012-28-0005.

Sirignano, W. A. (1999). *Fluid dynamics and transport of droplets and sprays*. Cambridge University Press, New York, USA, 1 edition. ISBN: 0-521-63036-3.

Slagter, J. W. (2008). Examining spatial (grid) convergence, nparc alliance verification and validation coordinators. http://www.grc.nasa.gov/WWW/wind/valid/tutorial/spatconv.html, last access: 22.01.2014.

Slagter, W. (2014). How to speed up ANSYS 15.0 with GPUs. online ANSYS IT Solutions Webcast Series, url: http://www.ansys.com/, last accessed: 25.02.2014.

Son, J. H., Jung, S. S., Yoon, W. H., An, S. C., and Ha, M. Y. (2009). Design and application of composite piston for high power diesel engine. *SAE International*. SAE Technical Paper 2009-01-0192.

Staley, D., Pryor, B., and Gilgenbach, K. (2007). Adaptation of a variable displacement vane pump to engine lube oil applications. *SAE International*. SAE Technical Paper 2007-01-1567.

Steinschütz, K., Geringer, B., Jech, M., Urbanek, M., Wopelka, T., and Besser, C. (2010). Impact of oil aging on wear of piston ring and cylinder liner system. *SAE International*. SAE Technical Paper 2010-32-0124.

Stotter, A. (1966). Heat transfer in piston cooling. *SAE International*. SAE Technical Paper 660757.

Sultana, Z. (2012). *Finite Element Simulation of Interfacial Flows on Unstructured Meshes using a Second-Order Accurate VOF Method*. Doctoral dissertation, University of Toronto, Canada.

Takeuchi, Y., Akimoto, K., Noda, T., Nozawa, Y., and Yamada, T. (2006). Experimental and numerical investigation of heat absorption characteristics by engine oil in piston cooling channel. In *Proceedings of 31st, World automotive congress; FISITA 2006*, Yokohama, Japan. Paper Number F2006P154.

Tanihata, A., Sato, K., and Furukawa, K. (2006). Development of high–strength piston material with die casting. *SAE International*. SAE Technical Paper 2006-01-0986.

Thiel, N., Weimar, H.-J., Kamp, H., and Windisch, H. (2007). Advanced piston cooling efficiency: A comparison of different new gallery cooling concepts. *SAE International*, pages 776–790. SAE Technical Paper 2007-01-1441.

Torregrosa, A., Broatch, A., Olmeda, P., and Martín, J. (2010). A contribution to film coefficient estimation in piston cooling galleries. *Journal of Experimental Thermal and Fluid Science*, 34(2010):142–151. Elsevier.

Torregrosa, A., Meda, P., Degraeuwe, B., and Reyes, M. (2006). A concise wall temperature model for DI diesel engines. *International Journal of Applied Thermal Engineering*, 26(2006):1320–1327. Elsevier.

Triep, M., Hess, D., Chaves, H., Brücker, C., Balmert, A., Westhoff, G., and Bleckmann, H. (2013). 3d flow in the venom channel of a spitting cobra: do the ridges in the fangs act as fluid guide vanes? *Public Library of Science (PLOS) one*.

Trinh, K. T. (2010). On the karman constant. arXiv preprint arXiv:1007.0605, url: http://arxiv.org/abs/1007.0605, last accessed: 06.07.2014.

Tryggvason, G. (2010). Multiphase flow modeling. online Notes on Computational Fluid Dynamics I, Worcester Polytechnic Institute, Worcester, MA, USA, url: http://users.wpi.edu/ gretar/me612.htm, last accessed: 09.11.2013.

Tsuji, F. K. and Neto, L. D. (2008). Influence of vegetable oil in the viscosity of biodiesel -– a review. *SAE International*. SAE Technical Paper 2008-36-0170.

Tu, J., Yeoh, G. H., and Liu, C. (2012). *Computational fluid dynamics: a practical approach*. Butterworth-Heinemann, Oxford, UK. ISBN: 978-0-08-098243-4.

Verkaik, A. C., Beulen, B. W. A. M. M., Bogaerds, A. C. B., Rutten, M. C. M., and van de Vosse, F. N. (2009). Estimation of volume flow in curved tubes based on analytical and computational analysis of axial velocity profiles. *Journal of Physics of Fluids*, 21. Elsevier.

Versteeg, H. and Malalasekera, W. (2007). *An Introduction to Computational Fluid Dynamics: The Finite Volume Method*. Prentice Hall, Harlow, Essex, UK, 2 edition. ISBN: 978-0131274983.

von Rüden, K. (2004). *Beitrag zum Downsizing von Fahrzeug-Ottomotoren*. Dr.-Ing. thesis, Fakultät V - Verkehrs- und Maschinensysteme, Technische Universität Berlin, Berlin, Germany.

Waclawczyk, T. and Koronowicz, T. (2006). Modeling of the wave breaking with CICSAM and HRIC high resolution schemes. In *Proceedings of the European Conference on Computational Fluid Dynamics,*, Egmond aan Zee, The Netherlands, September 5-8, 2006.

Waclawczyk, T. and Koronowicz, T. (2008). Comparison of CICSAM and HRIC high-resolution schemes for interface capturing. *Journal of theoretical and applied mechanics*, 46(2):325–345. Elsevier.

Wang, P., Fröhlich, J., Michelassi, V., and Rodi, W. (2008). Large-eddy simulation of variable-density turbulent axisymmetric jets. *International Journal of Heat and Fluid Flow*, 29:654–664. Elsevier.

Wang, P., Lv, J., Bai, M., Li, G., and Zeng, K. (2015). The reciprocating motion characteristics of nanofluid inside the piston cooling gallery. *Journal of Powder Technology*, 274:402—417. Elsevier.

Wang, Q., Cao, Y., Wang, R., Mignano, F., and Chen, G. (2000). Studies of a heat-pipe cooled piston crown. *Journal of Engineering for Gas Turbines and Power*, 122(1):99–105.

Wellmann, N. (2001). Kolben mit einer verbindung von einem kühlkanal zu einer kolbenbolzenbohrung. Deutsches Patent– und Markenamt, München, Germany. Patent no: DE 19954725, 23.05.2001.

Wenzel, S. P. (2006). *Modellierung der Ruß- und NO_x-Emissionen des Dieselmotors*. Dr.-Ing. thesis, Fakultät für Maschinenbau, Otto-von-Guericke Universität Magdeburg, Magdeburg, Germany.

Woschni, G. (1970). Die Berechnung der Wandverluste und der thermischen Belastung der Bauteile von Dieselmotoren. *MTZ-Motortechnische Zeitschrift*, 31(12):491–499.

Woschni, G., Klaus, B., and Zeilinger, K. (1998). *Untersuchung des Wärmetransportes zwischen Kolben, Kolbenringen und Zylinderbüchse*. *MTZ-Motortechnische Zeitschrift*, 59(9):556–563.

Wu, S. and Li, J. (2010). Application of ceramic short fiber reinforced al alloy matrix composite on piston for internal combustion engines. *China Foundry*, 7(4):408–412. China Foundry.

Yeoh, G. and Tu, J. (2010). *Computational Techniques for Multiphase Flows*. Butterworth Heinemann, Oxford, UK. ISBN: 978-0-08-046733-7.

Yi, Y., Reddy, M., Jarret, M., Shyu, P., Kinsey, C., Alcenius, T., and Inal, K. (2007). CFD modeling of the multiphase flow and heat transfer for piston gallery cooling system. *SAE International*. SAE Technical Paper 2002-01-0068.

Zanetti-Rocha, L., Gerges, S., Johnston, D., and Arenas, J. (2013). Rotating group design for vane pump flow ripple reduction. *International Journal of Acoustics and Vibration*, 18(4):192–200. Elsevier.

Zha, K., Yu, X., Florea, R., and Jansons, M. (2012). Impact of biodiesel blends on in-cylinder soot temperature and concentrations in a small-bore optical diesel engine. *SAE International*. SAE Technical Paper 2012-01-1311.

Zhang, D., Jiang, C., Liang, D., Chen, Z., Yang, Y., and Shi, Y. (2014). A refined volume-of-fluid algorithm for capturing sharp fluid interfaces on arbitrary meshes. *Journal of Computational Physics*, 274:709–736. Elsevier.

Zhang, D., Perng, C.-Y., and Laverty, M. (2006). Gerotor oil pump performance and flow / pressure ripple study. *SAE International*. SAE Technical Paper 2006-01-0359.

Zhang, Z. (2011). Piston temperature measurement using voltage recorder and numerical simulation of the temperature field. *SAE International*. SAE Technical Paper 2011-01-2230.

APPENDIX A DRAWINGS OF TEST RIG COMPONENTS

A.1 List of rig components

Table A.1 List of test rig components

Name	Number	Name	Number
Piston Motion Test Rig	RPC-100-0000	Hex-Bolt M8x50mm 8.8	RPC-X00-0001
Test Rig Frame	RPC-101-0000	Hex-Nut M8 8.8	RPC-X00-0002
Oil Catch Tray	RPC-101-0021	Hex-Bolt M16x120mm 8.8	RPC-X00-0003
Top Sliding Rail Support	RPC-101-0026	Hex-Nut M16 8.8	RPC-X00-0004
Sliding Rail	RPC-101-0027	Washer M8 Ø17mm	RPC-X00-0005
Rear Spash Guard	RPC-101-0029	Washer m16 Ø50mm	RPC-X00-0006
Rear Belt Guard	RPC-101-0031	Washer M16 Ø30mm	RPC-X00-0007
Inner Belt Guard	RPC-101-0032	Large Pulley	RPC-X00-0010
Slider Bar	RPC-102-0001	Bearing HK2020	RPC-X00-0011
Slider Bar Connector	RPC-102-0002	Hex-Nut M10 8.8	RPC-X00-0012
Slider Bearing	RPC-102-0003	Washer M10 Ø24mm	RPC-X00-0013
Cross Member	RPC-102-0004	Hex-Bolt M10x100 8.8	RPC-X00-0014
Spacing Tube	RPC-102-0005	Washer M10 Ø38mm	RPC-X00-0015
Threaded Rod M8-390mm	RPC-102-0006	Key 4.75x15x5	RPC-X00-0016
Centre Disk	RPC-103-0001	Hex-Bolt M8x100 8.8	RPC-X00-0017
Crank Pin	RPC-103-0002	Hex-Bolt M8x25 8.8	RPC-X00-0018
Brass Bearing	RPC-103-0003	Dowel Pin Ø6x15mm	RPC-X00-0019
Driveshaft	RPC-103-0004	Bearing 6205-2RS	RPC-X00-0020
Bearing Support	RPC-103-0005	Electric Motor	RPC-X00-0021
Gallery Model	RPC-105-0000	Small Pulley	RPC-X00-0022

Only the components shown in the drawings provided are given.

A.2 Drawings

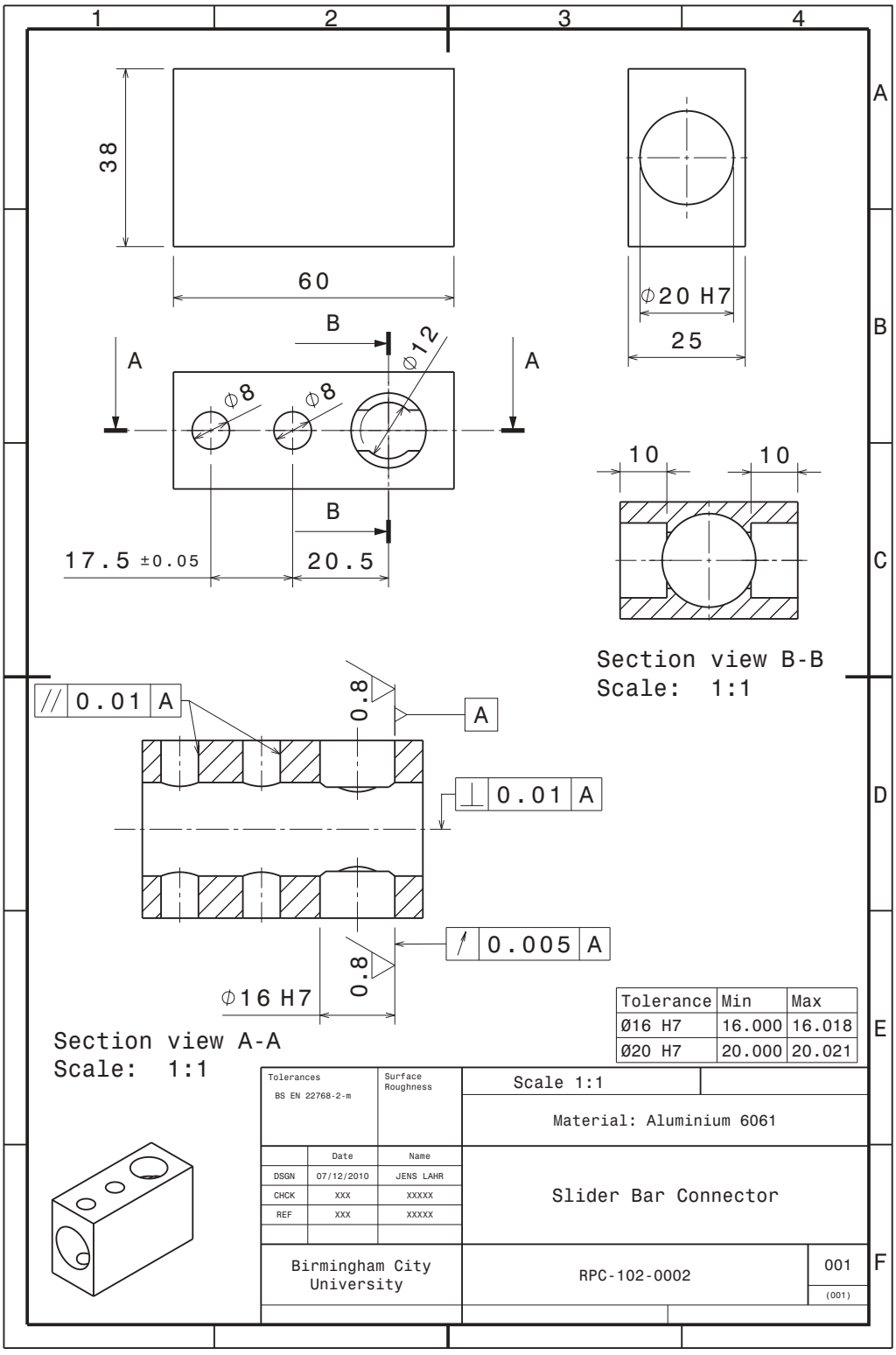
38
60
B
A
A
ϕ12
ϕ8
ϕ8
B
17.5 ±0.05
20.5
ϕ20 H7
25
10
10
Section view B-B
Scale: 1:1
0.01 A
0.8
A
0.01 A
0.005 A
0.8
ϕ16 H7
Section view A-A
Scale: 1:1
Tolerance | Min | Max
Ø16 H7 | 16.000 | 16.018
Ø20 H7 | 20.000 | 20.021
Tolerances BS EN 22768-2-m
Surface Roughness
Scale 1:1
Material: Aluminium 6061
Date | Name
DSGN | 07/12/2010 | JENS LAHR
CHCK | XXX | XXXXX
REF | XXX | XXXXX
Slider Bar Connector
Birmingham City University
RPC-102-0002
001
(001)
1 2 3 4
A B C D E F

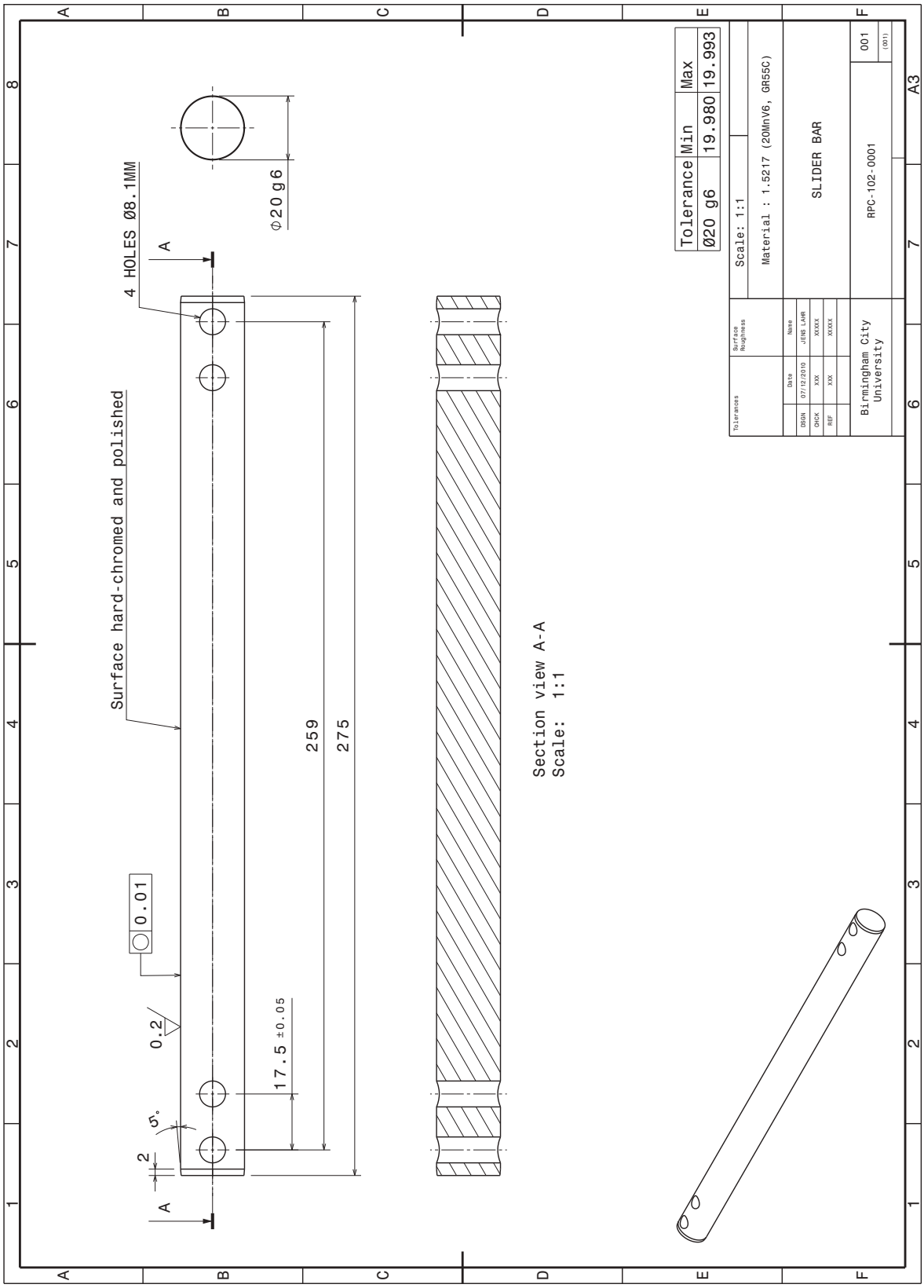
4 HOLES Ø8.1MM
Surface hard-chromed and polished
0.01
0.2
17.5 ±0.05
259
275
2
5°
A
Section view A-A
Scale: 1:1
Tolerance Min Max
Ø20 g6 19.980 19.993
Scale: 1:1
Material : 1.5217 (20MnV6, GR55C)
SLIDER BAR
RPC-102-0001
001
Birmingham City University
Tolerances
Surface Roughness
DRGN 07/12/2010 JENS LAHR
CHCK XXX XXXX
REF XXX XXXX
A3

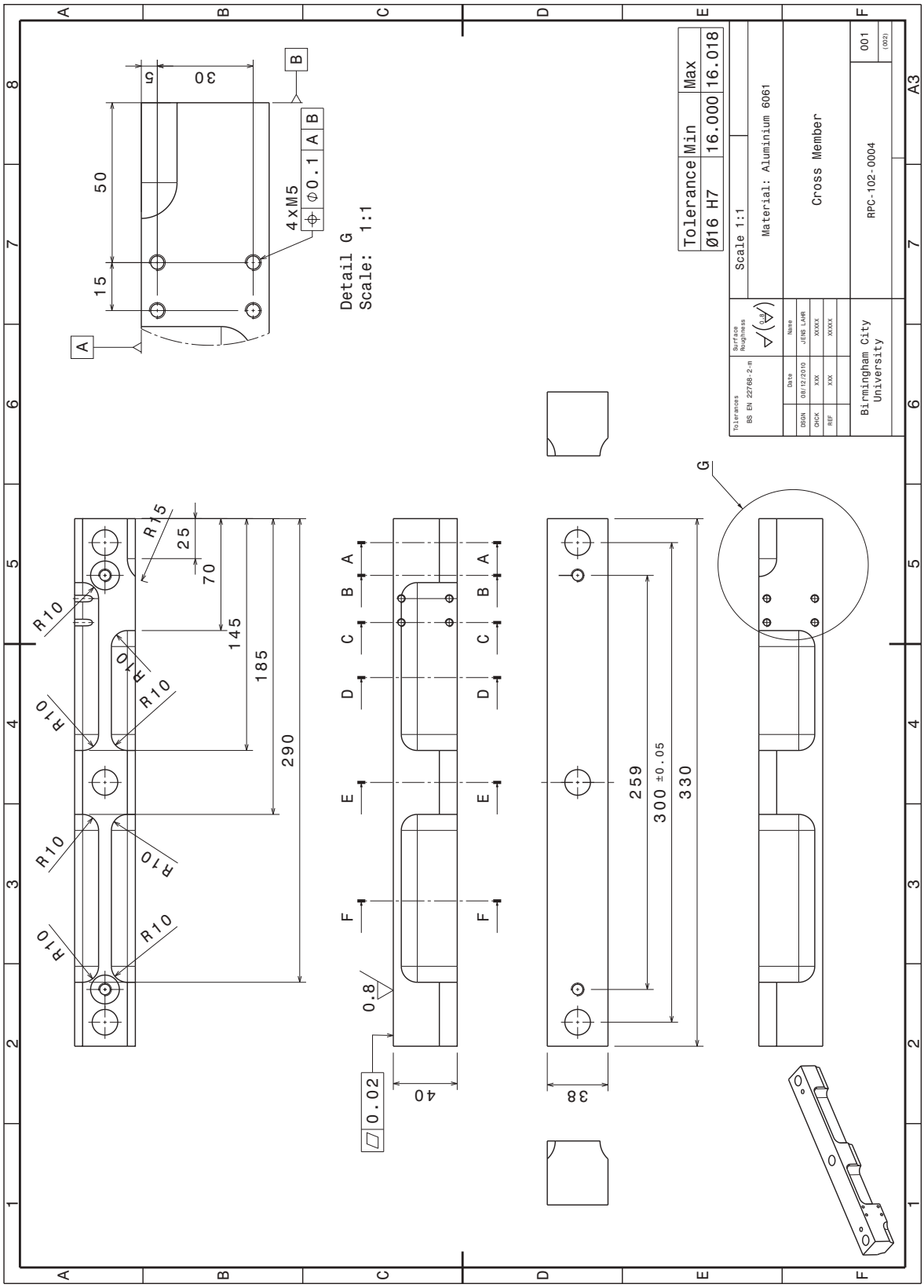
Detail G
Scale: 1:1
4xM5
Ø0.1 A B
Tolerance Min Max
Ø16 H7 16.000 16.018
Scale 1:1
Material: Aluminium 6061
Cross Member
RPC-102-0004
001
Birmingham City University
Tolerances
BS EN 22768-2-m
DRGN 08/12/2010 JENS LAHR
CHCK XXX XXXX
REF XXX XXXX
R15
R10
25
70
145
185
290
259
300 ±0.05
330
40
38
0.8
0.02

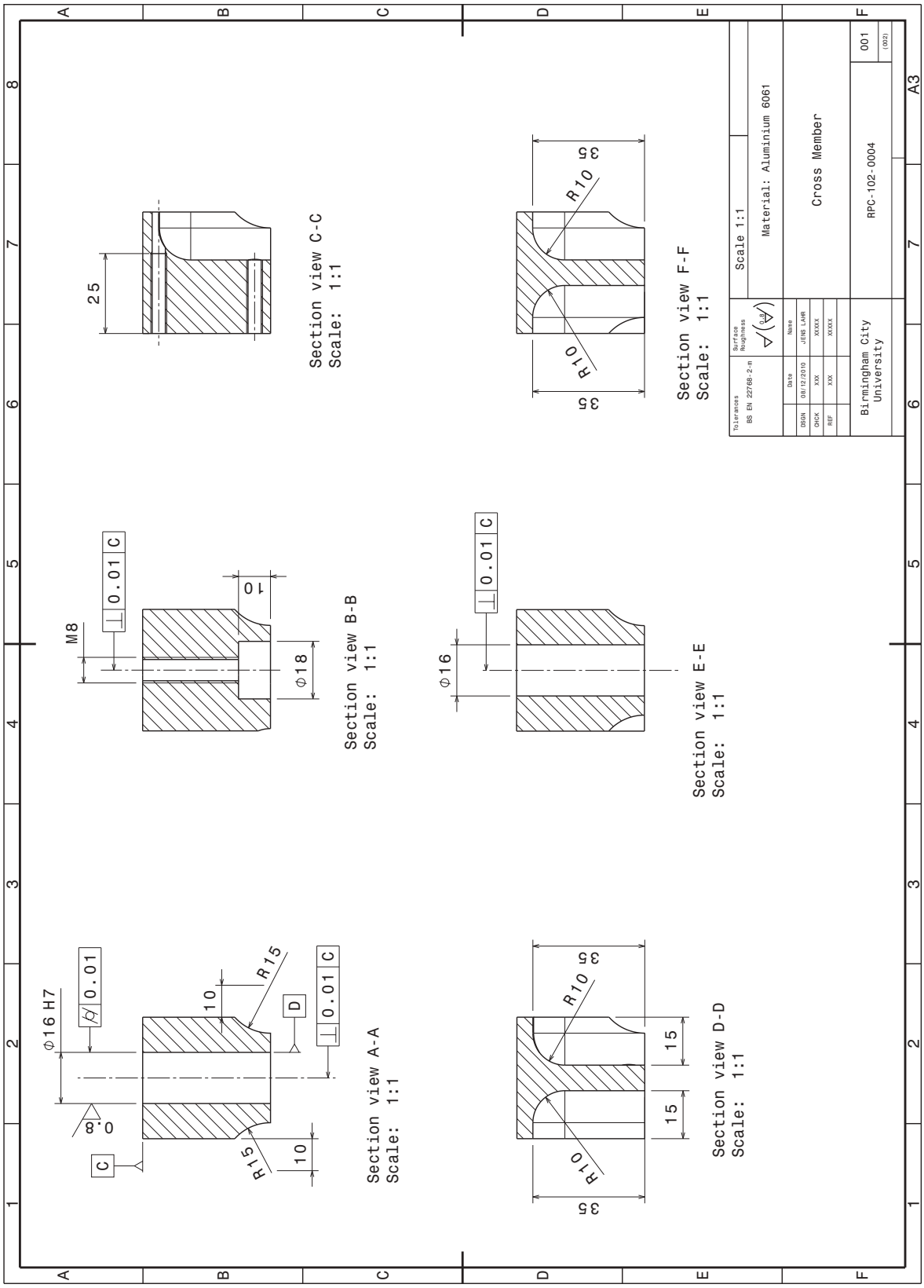
Section view C-C
Scale: 1:1
25
Section view F-F
Scale: 1:1
R10
35
Section view B-B
Scale: 1:1
M8
0.01 C
10
Φ18
Section view E-E
Scale: 1:1
Φ16
Section view A-A
Scale: 1:1
Φ16 H7
0.01
0.8
R15
D
Section view D-D
Scale: 1:1
15
Tolerances
BS EN 22768-2-m
Surface Roughness
Scale 1:1
Material: Aluminium 6061
Cross Member
DRGN
CHCK
APP
Date
08/12/2010
XXX
XXX
Name
JENS LAHR
XXXX
XXXX
Birmingham City University
RPC-102-0004
001
(002)
A3

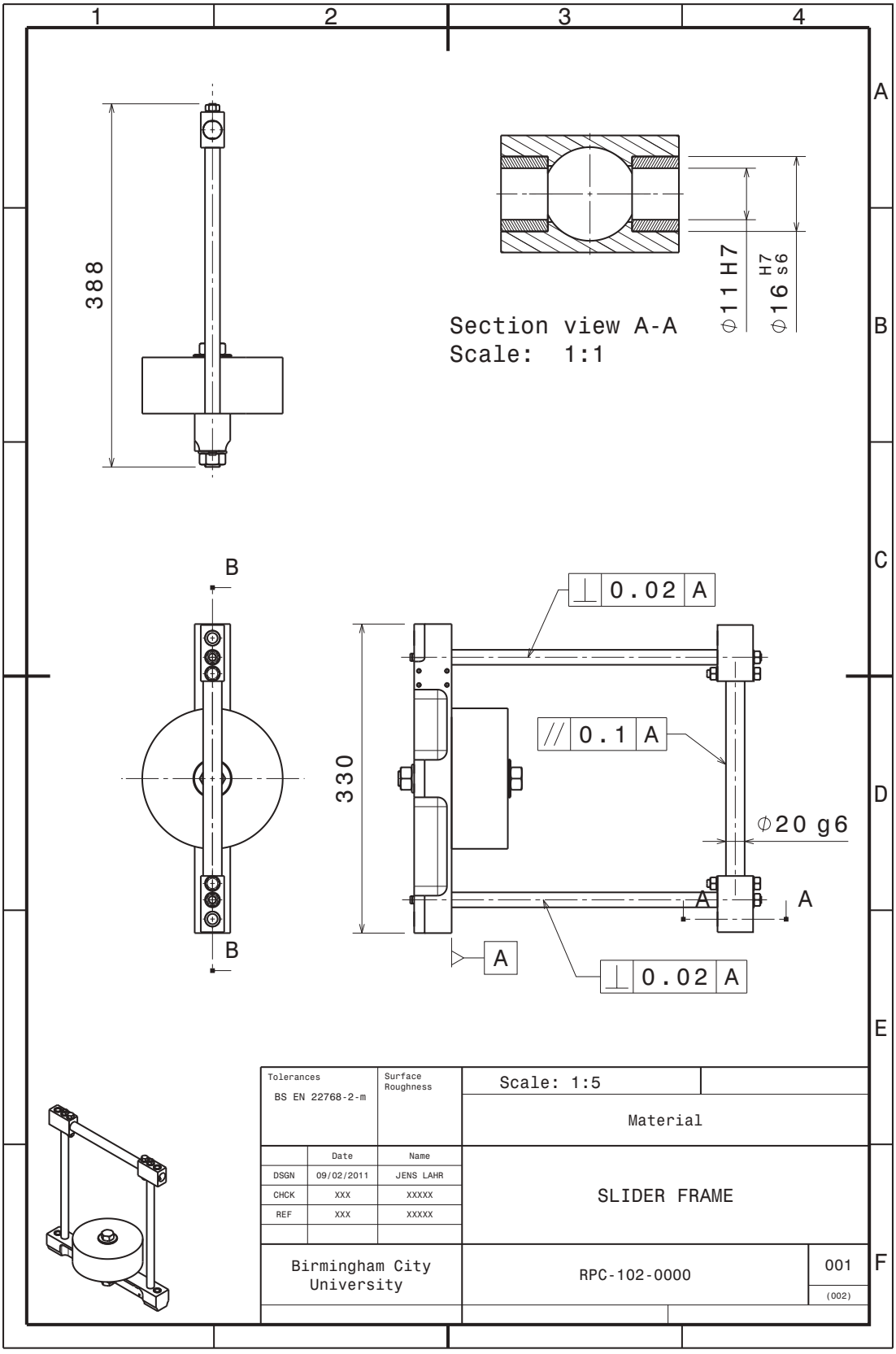
1
2
3
4
A
B
C
D
E
F
388
Section view A-A
Scale: 1:1
ϕ11 H7
ϕ16 H7 s6
B
B
330
0.02 A
0.1 A
ϕ20 g6
A
A
A
0.02 A
Tolerances
BS EN 22768-2-m
Surface Roughness
Scale: 1:5
Material
Date
Name
DSGN
09/02/2011
JENS LAHR
CHCK
XXX
XXXXX
REF
XXX
XXXXX
SLIDER FRAME
Birmingham City University
RPC-102-0000
001
(002)

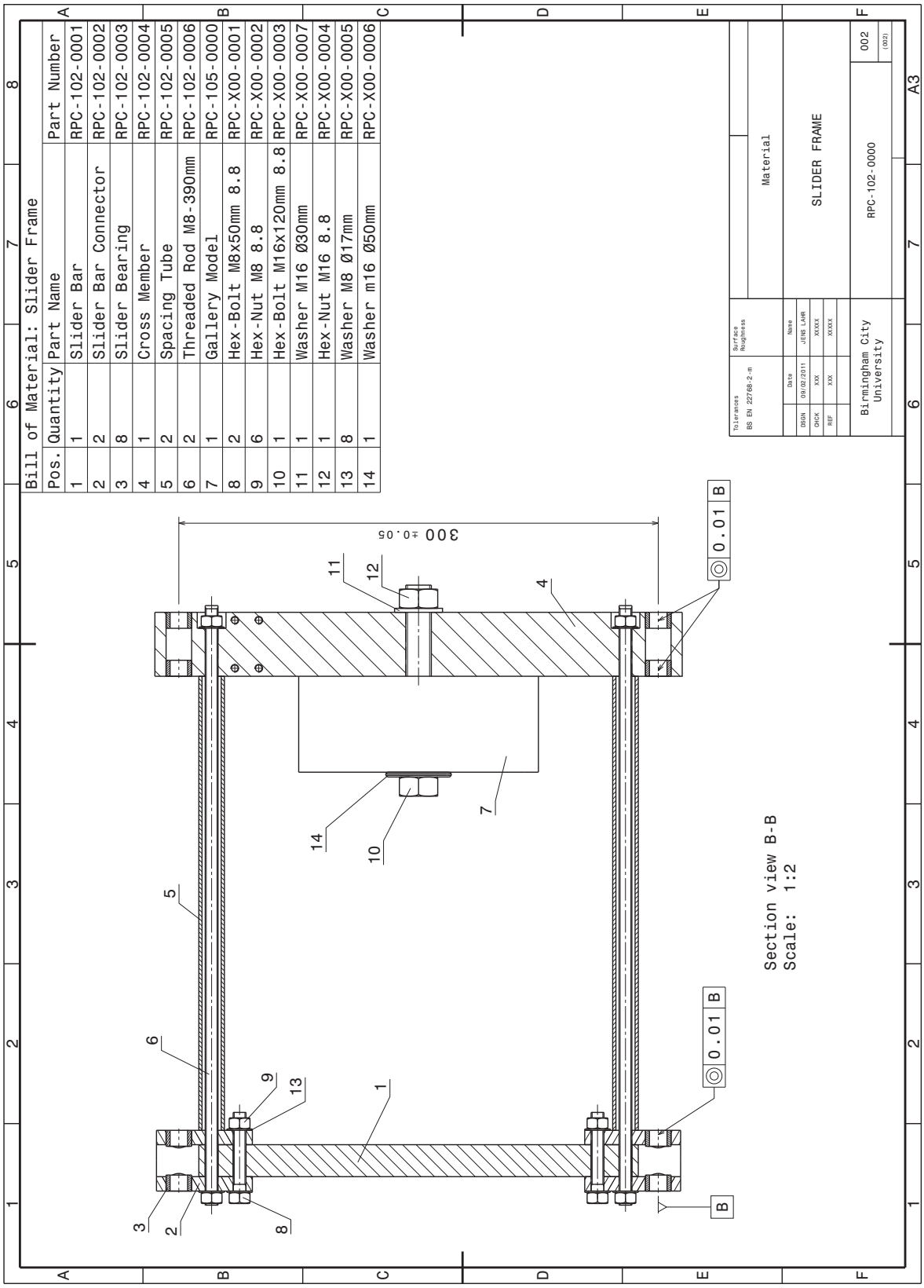

Bill of Material: Slider Frame

Pos.	Quantity	Part Name	Part Number
1	1	Slider Bar	RPC-102-0001
2	2	Slider Bar Connector	RPC-102-0002
3	8	Slider Bearing	RPC-102-0003
4	1	Cross Member	RPC-102-0004
5	2	Spacing Tube	RPC-102-0005
6	2	Threaded Rod M8-390mm	RPC-102-0006
7	1	Gallery Model	RPC-105-0000
8	2	Hex-Bolt M8x50mm 8.8	RPC-X00-0001
9	6	Hex-Nut M8 8.8	RPC-X00-0002
10	1	Hex-Bolt M16x120mm 8.8	RPC-X00-0003
11	1	Washer M16 Ø30mm	RPC-X00-0007
12	1	Hex-Nut M16 8.8	RPC-X00-0004
13	8	Washer M8 Ø17mm	RPC-X00-0005
14	1	Washer m16 Ø50mm	RPC-X00-0006

Tolerances BS EN 22768-2-m

Surface Roughness

Material

	Date	Name
DRGN	09/02/2011	JENS LAHR
CHCK	XXX	XXXX
REF	XXX	XXXX

SLIDER FRAME

Birmingham City University

RPC-102-0000

002 (002)

A3

300 ±0.05

0.01 B

Section view B-B
Scale: 1:2

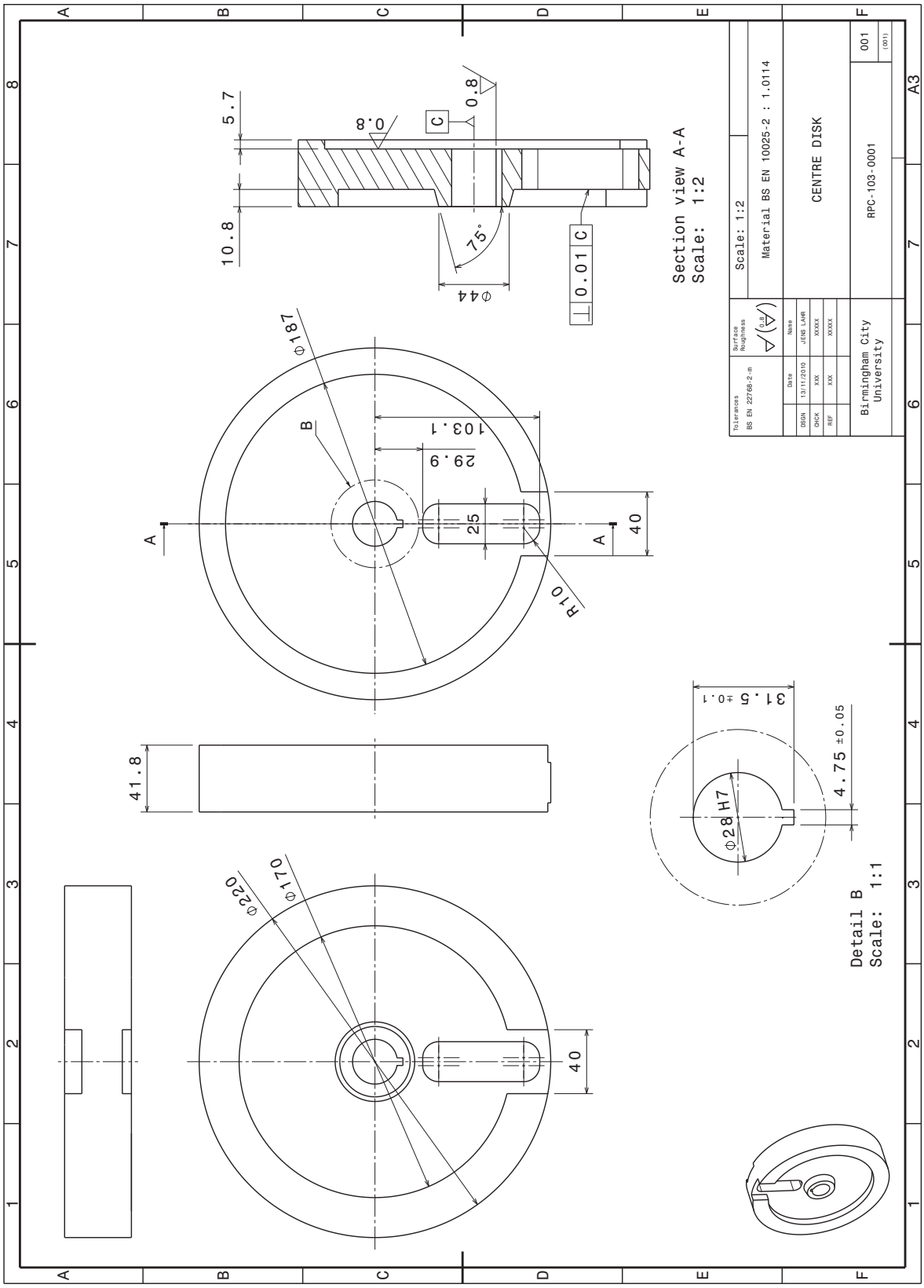
Section view A-A
Scale: 1:2
Detail B
Scale: 1:1
CENTRE DISK
RPC-103-0001
001
Material BS EN 10025-2 : 1.0114
Scale: 1:2
Birmingham City University
Tolerances BS EN 22768-2-m
Surface Roughness
DRGN JENS LAHR
CHCK XXX
REF XXX
Date 13/11/2010
Name XXXX
XXXX
Ø187
Ø170
Ø220
Ø44
103.1
29.9
25
40
R10
41.8
5.7
10.8
0.8
75°
0.01 C
31.5 ±0.1
Ø28 H7
4.75 ±0.05

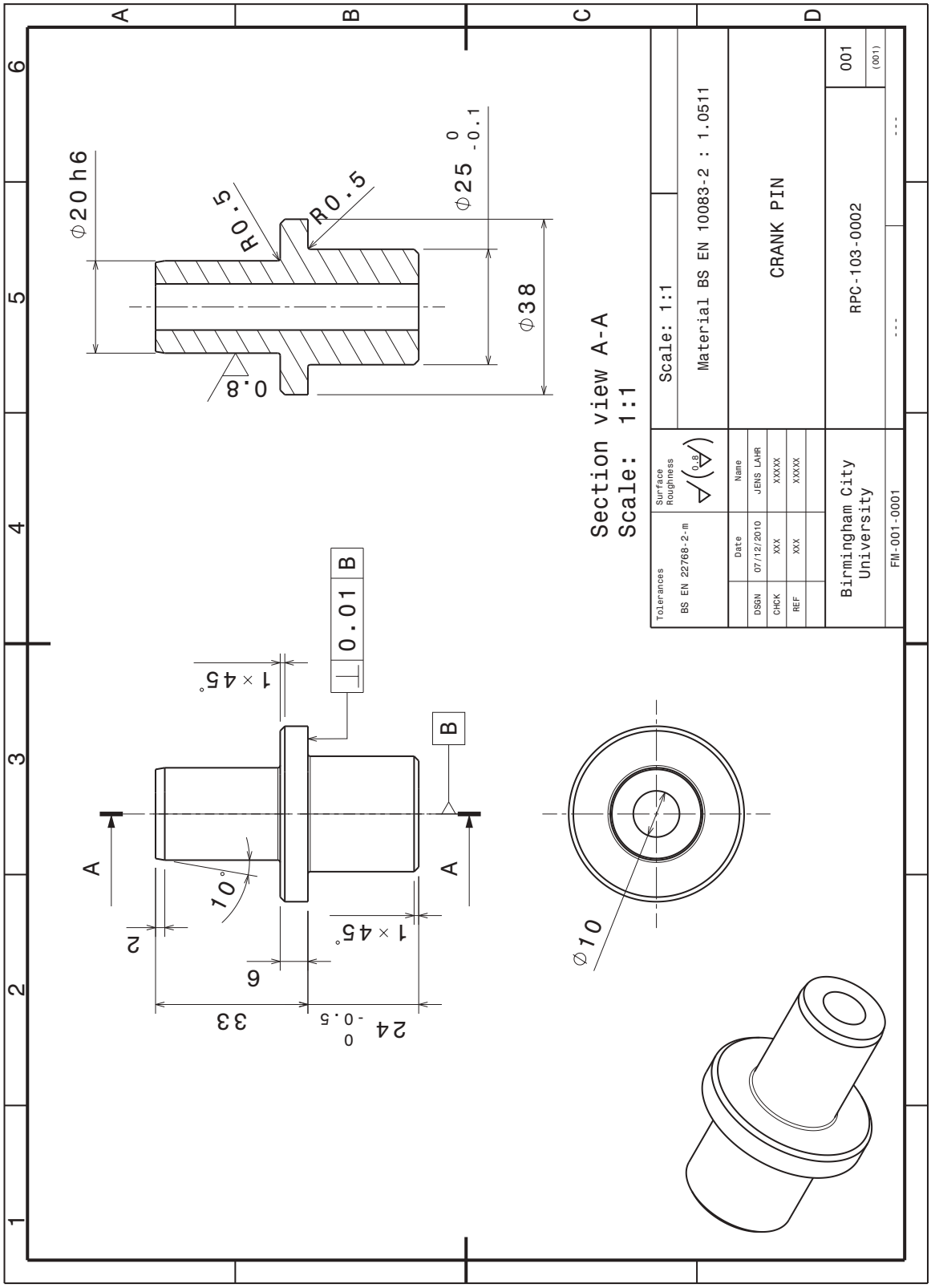
Section view A-A
Scale: 1:1
Scale: 1:1
Material BS EN 10083-2 : 1.0511
CRANK PIN
RPC-103-0002
001
Birmingham City University
FM-001-0001
Tolerances
BS EN 22768-2-m
Surface Roughness
Date
Name
DSGN
07/12/2010
JENS LAHR
CHCK
XXX
XXXXX
REF
XXX
XXXXX
φ20 h6
R0.5
R0.5
φ25 0 -0.1
φ38
0.8
0.01 B
B
1 × 45°
1 × 45°
10°
A
A
2
6
33
24 0 -0.5
∅10

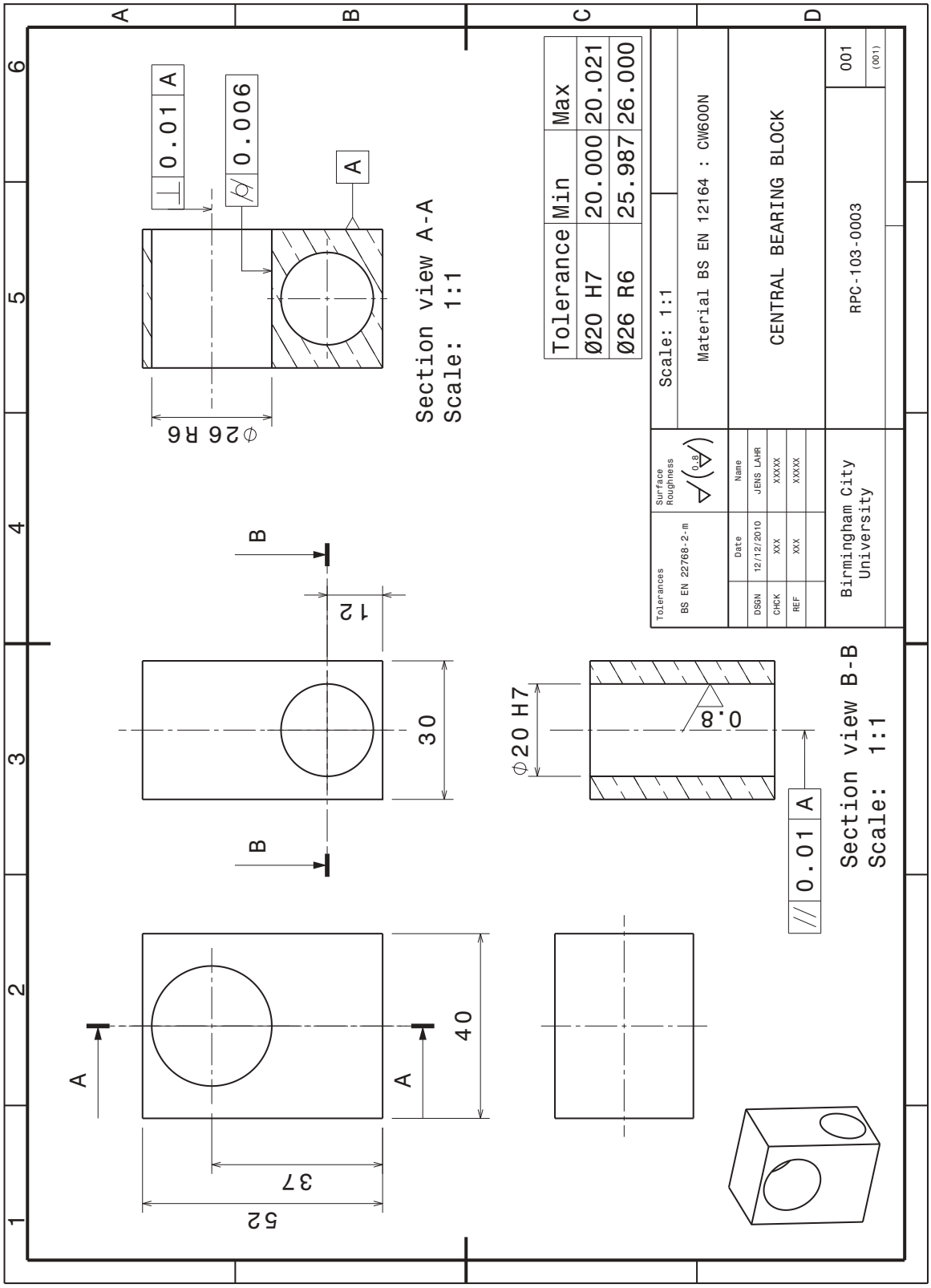
Section view A-A
Scale: 1:1
Section view B-B
Scale: 1:1
Tolerance Min Max
Ø20 H7 20.000 20.021
Ø26 R6 25.987 26.000
Scale: 1:1
Material BS EN 12164 : CW600N
CENTRAL BEARING BLOCK
RPC-103-0003
001
Birmingham City University
Tolerances
BS EN 22768-2-m
Surface Roughness
DSGN 12/12/2010 JENS LAHR
CHCK XXX XXXXX
REF XXX XXXXX
0.01 A
0.006 A
0.01 A
Ø26 R6
Ø20 H7
0.8
12
30
40
52
37

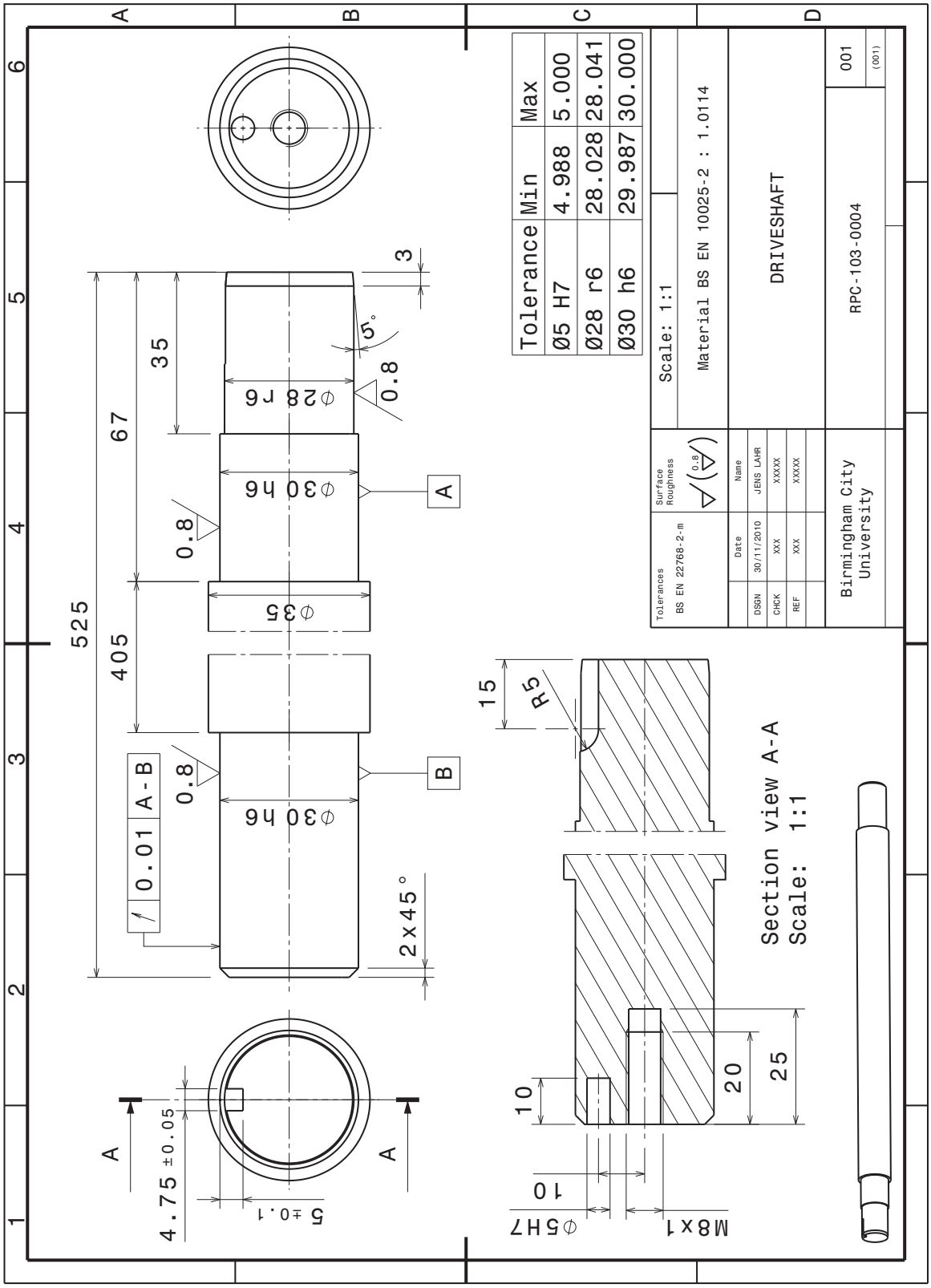
A
B
C
D
1
2
3
4
5
6
Tolerance | Min | Max
Ø5 H7 | 4.988 | 5.000
Ø28 r6 | 28.028 | 28.041
Ø30 h6 | 29.987 | 30.000
Scale: 1:1
Material BS EN 10025-2 : 1.0114
DRIVESHAFT
RPC-103-0004
001
(001)
Tolerances
BS EN 22768-2-m
Surface Roughness
0.8
Date
Name
DSGN 30/11/2010 JENS LAHR
CHCK XXX XXXXX
REF XXX XXXXX
Birmingham City University
525
405
67
35
3
5°
Ø28 r6
Ø30 h6
Ø35
0.8
0.01 A-B
2x45°
A
B
4.75 ±0.05
5 ±0.1
15
R5
10
20
25
Ø5H7
M8x1
Section view A-A
Scale: 1:1

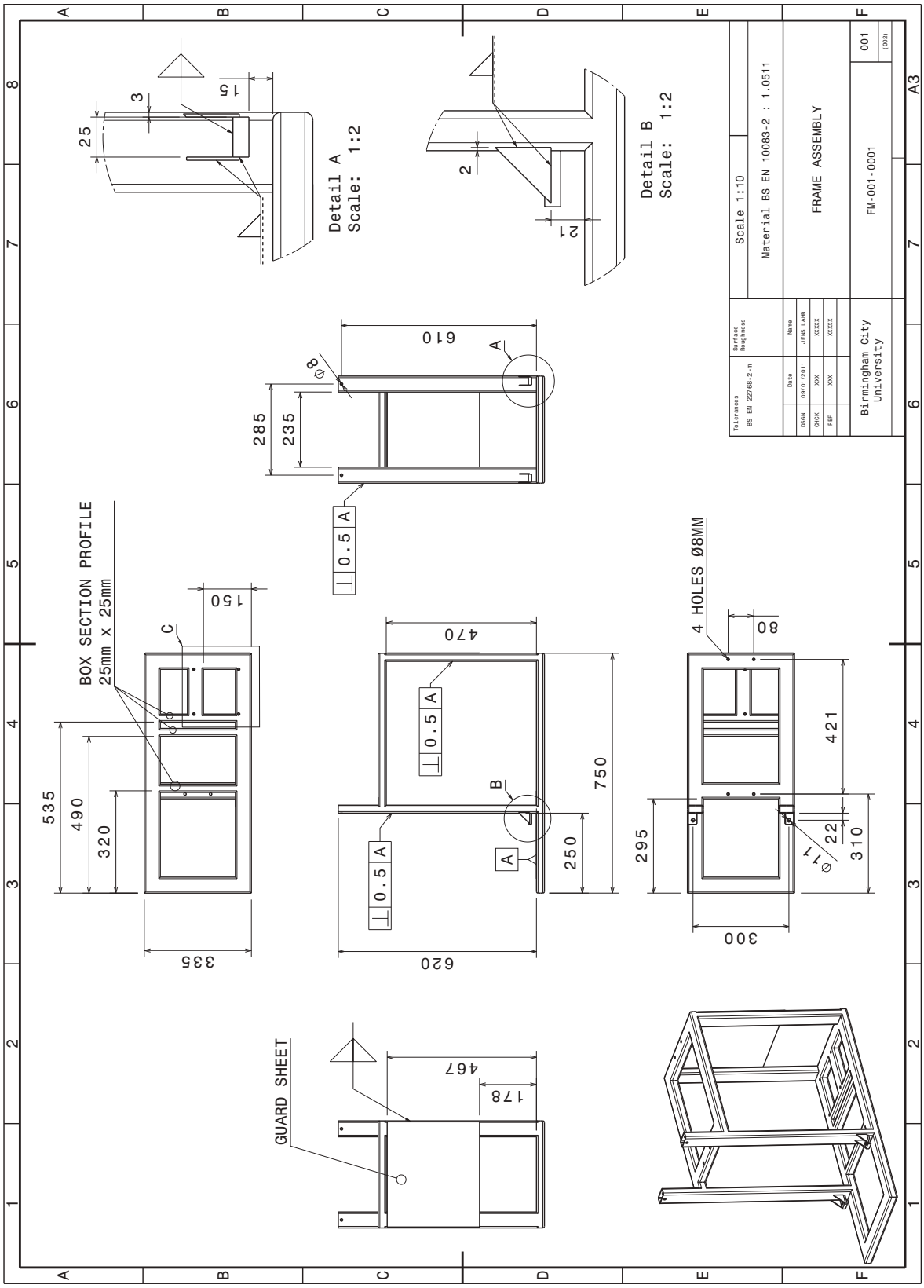
Detail A
Scale: 1:2
Detail B
Scale: 1:2
Scale 1:10
Material BS EN 10083-2 : 1.0511
FRAME ASSEMBLY
FM-001-0001
001
Birmingham City University
Tolerances BS EN 22768-2-m
Surface Roughness
DRGN 09/01/2011 JENS LAHR
CHCK XXX XXXX
REF XXX XXXX
BOX SECTION PROFILE
25mm x 25mm
4 HOLES Ø8MM
GUARD SHEET
610
470
467
178
620
335
300
150
80
535
490
320
285
235
750
250
421
310
295
25
3
15
2
1
22
0.5 A

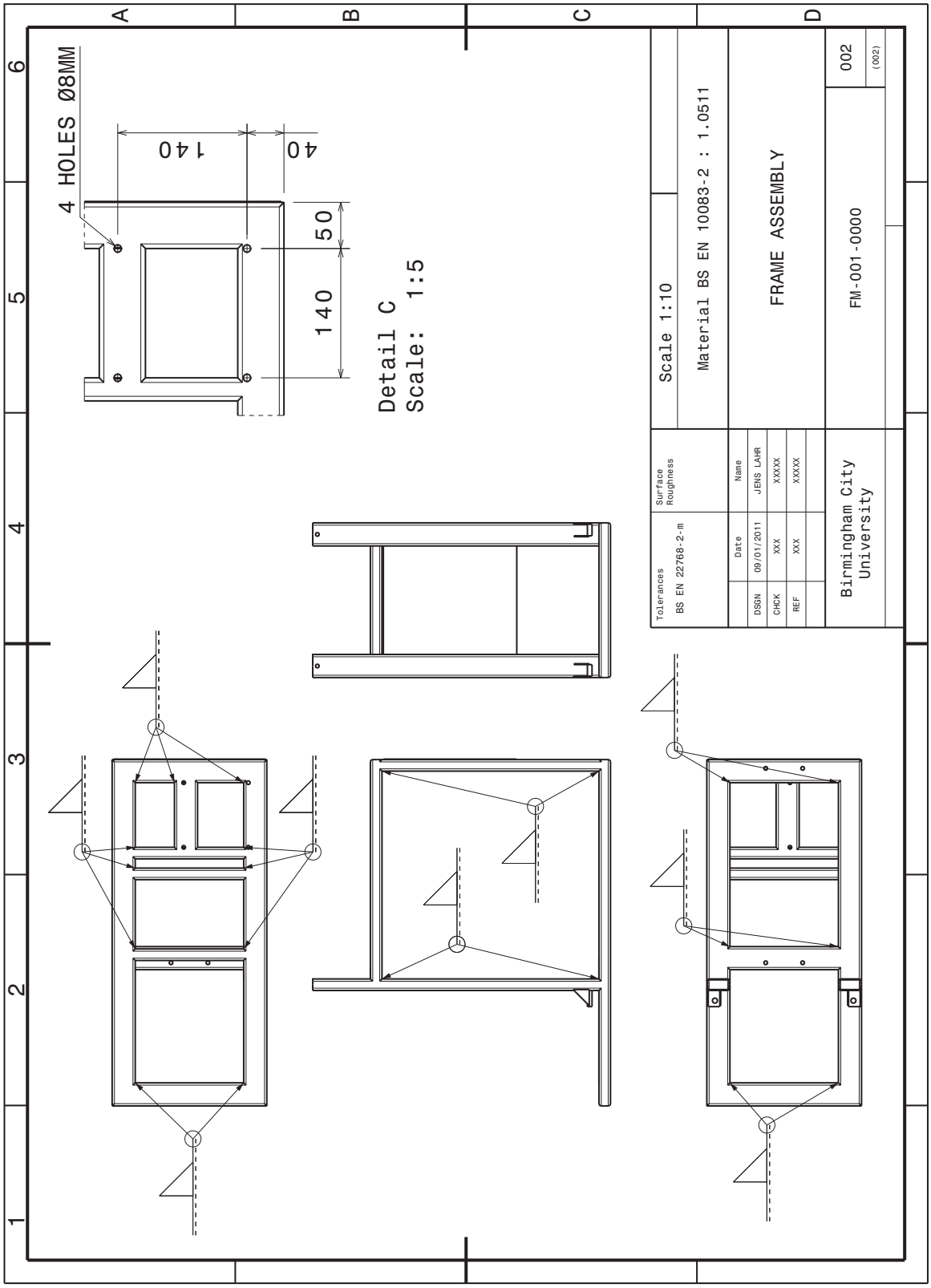
4 HOLES Ø8MM
140
40
50
140
Detail C
Scale: 1:5
Scale 1:10
Material BS EN 10083-2 : 1.0511
FRAME ASSEMBLY
002
(002)
FM-001-0000
Tolerances
BS EN 22768-2-m
Surface
Roughness
Date
Name
DSGN
09/01/2011
JENS LAHR
CHCK
XXX
XXXXX
REF
XXX
XXXXX
Birmingham City
University

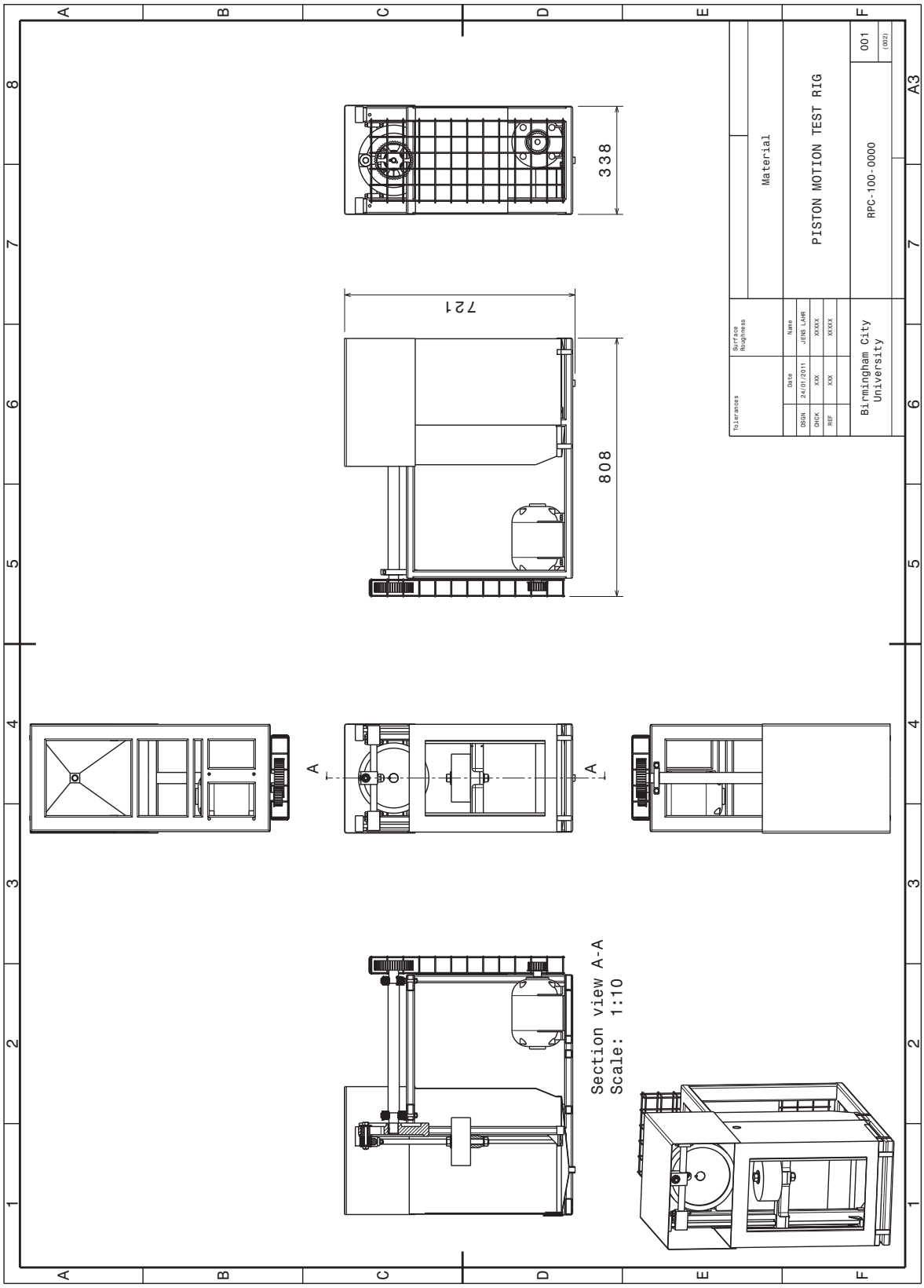
338
721
808
A
A
Section view A-A
Scale: 1:10
Material
PISTON MOTION TEST RIG
RPC-100-0000
001
(002)
Birmingham City University
Tolerances
Surface Roughness
DRGN 24/01/2011 JENS LAHR
CHCK XXX XXXX
REF XXX XXXX
A3

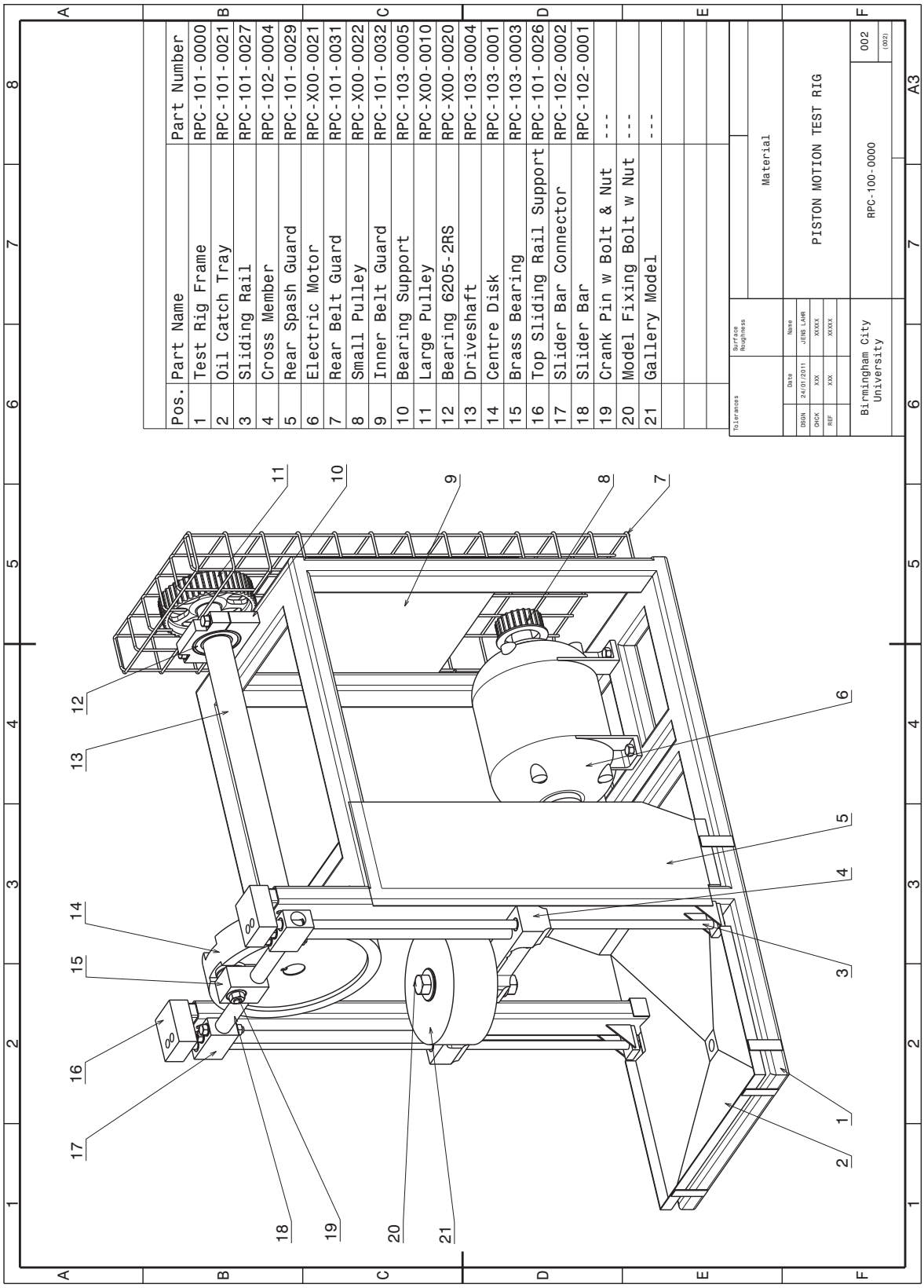
Pos. Part Name Part Number
1 Test Rig Frame RPC-101-0000
2 Oil Catch Tray RPC-101-0021
3 Sliding Rail RPC-101-0027
4 Cross Member RPC-102-0004
5 Rear Spash Guard RPC-101-0029
6 Electric Motor RPC-X00-0021
7 Rear Belt Guard RPC-101-0031
8 Small Pulley RPC-X00-0022
9 Inner Belt Guard RPC-101-0032
10 Bearing Support RPC-103-0005
11 Large Pulley RPC-X00-0010
12 Bearing 6205-2RS RPC-X00-0020
13 Driveshaft RPC-103-0004
14 Centre Disk RPC-103-0001
15 Brass Bearing RPC-103-0003
16 Top Sliding Rail Support RPC-101-0026
17 Slider Bar Connector RPC-102-0002
18 Slider Bar RPC-102-0001
19 Crank Pin w Bolt & Nut ---
20 Model Fixing Bolt w Nut ---
21 Gallery Model ---
Tolerances
Surface Roughness
Material
Date Name
DRGN 24/01/2011 JENS LAHR
CHCK XXX XXXX
REF XXX XXXX
PISTON MOTION TEST RIG
Birmingham City University
RPC-100-0000
002
(002)
A3

APPENDIX B EXPERIMENTAL RESULTS OF FLOW BEHAVIOUR INSIDE GALLERIES

B.1 Small gallery model at *BDC*

30°*CA bBDC* | *BDC* | 30°*CA aBDC*
conditions: 500 *rpm*, 1.105 *l/min*

30°*CA bBDC* | *BDC* | 30°*CA aBDC*
conditions: 500 *rpm*, 2.121 *l/min*

30°*CA bBDC* | *BDC* | 30°*CA aBDC*
conditions: 750 *rpm*, 1.651 *l/min*

30°*CA bBDC* | *BDC* | 30°*CA aBDC*
conditions: 1000 *rpm*, 1.105 *l/min*

conditions: 1000 *rpm*, 2.121 *l/min*

Fig. B.1 Flow in SGM at various conditions, inlet sections

30°*CA bBDC* | *BDC* | 30°*CA aBDC*

conditions: 500 *rpm*, 1.105 *l/min*

30°*CA bBDC* | *BDC* | 30°*CA aBDC*

conditions: 500 *rpm*, 2.121 *l/min*

30°*CA bBDC* | *BDC* | 30°*CA aBDC*

conditions: 750 *rpm*, 1.651 *l/min*

30°*CA bBDC* | *BDC* | 30°*CA aBDC*

conditions: 1000 *rpm*, 1.105 *l/min*

30°*CA bBDC* | *BDC* | 30°*CA aBDC*

conditions: 1000 *rpm*, 2.121 *l/min*

Fig. B.2 Flow in SGM at various conditions, mid-gallery sections

30°*CA bBDC* | *BDC* | 30°*CA aBDC*
conditions: 500 *rpm*, 1.105 *l/min*

30°*CA bBDC* | *BDC* | 30°*CA aBDC*
conditions: 500 *rpm*, 2.121 *l/min*

30°*CA bBDC* | *BDC* | 30°*CA aBDC*
conditions: 750 *rpm*, 1.651 *l/min*

30°*CA bBDC* | *BDC* | 30°*CA aBDC*
conditions: 1000 *rpm*, 1.105 *l/min*

30°*CA bBDC* | *BDC* | 30°*CA aBDC*
conditions: 1000 *rpm*, 2.121 *l/min*

Fig. B.3 Flow in SGM at various conditions, outlet sections

B.2 Small gallery model at *TDC*

30°*CA bTDC* | *TDC* | 30°*CA aTDC*
conditions: 500 *rpm*, 1.105 *l/min*

30°*CA bTDC* | *TDC* | 30°*CA aTDC*
conditions: 500 *rpm*, 2.121 *l/min*

30°*CA bTDC* | *TDC* | 30°*CA aTDC*
conditions: 750 *rpm*, 1.651 *l/min*

30°*CA bTDC* | *TDC* | 30°*CA aTDC*
conditions: 1000 *rpm*, 1.105 *l/min*

30°*CA bTDC* | *TDC* | 30°*CA aTDC*
conditions: 1000 *rpm*, 2.121 *l/min*

Fig. B.4 Flow in SGM at various conditions, inlet sections

30°*CA bTDC* | *TDC* | 30°*CA aTDC*

conditions: 500 *rpm*, 1.105 *l/min*

30°*CA bTDC* | *TDC* | 30°*CA aTDC*

conditions: 500 *rpm*, 2.121 *l/min*

30°*CA bTDC* | *TDC* | 30°*CA aTDC*

conditions: 750 *rpm*, 1.651 *l/min*

30°*CA bTDC* | *TDC* | 30°*CA aTDC*

conditions: 1000 *rpm*, 1.105 *l/min*

30°*CA bTDC* | *TDC* | 30°*CA aTDC*

conditions: 1000 *rpm*, 2.121 *l/min*

Fig. B.5 Flow in SGM at various conditions, mid-gallery sections

30°*CA bTDC* | *TDC* | 30°*CA aTDC*

conditions: 500 *rpm*, 1.105 *l/min*

30°*CA bTDC* | *TDC* | 30°*CA aTDC*

conditions: 500 *rpm*, 2.121 *l/min*

30°*CA bTDC* | *TDC* | 30°*CA aTDC*

conditions: 750 *rpm*, 1.651 *l/min*

30°*CA bTDC* | *TDC* | 30°*CA aTDC*

conditions: 1000 *rpm*, 1.105 *l/min*

30°*CA bTDC* | *TDC* | 30°*CA aTDC*

conditions: 1000 *rpm*, 2.121 *l/min*

Fig. B.6 Flow in SGM at various conditions, outlet sections

B.3 Large gallery model at *BDC*

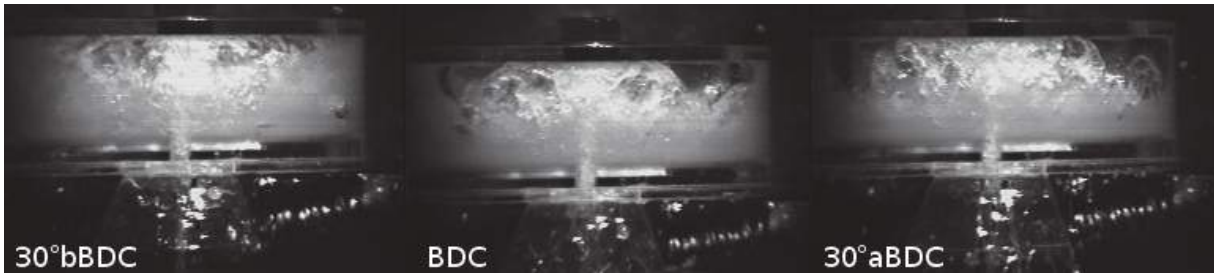

conditions: 300 *rpm*, 4.0 *l/min*

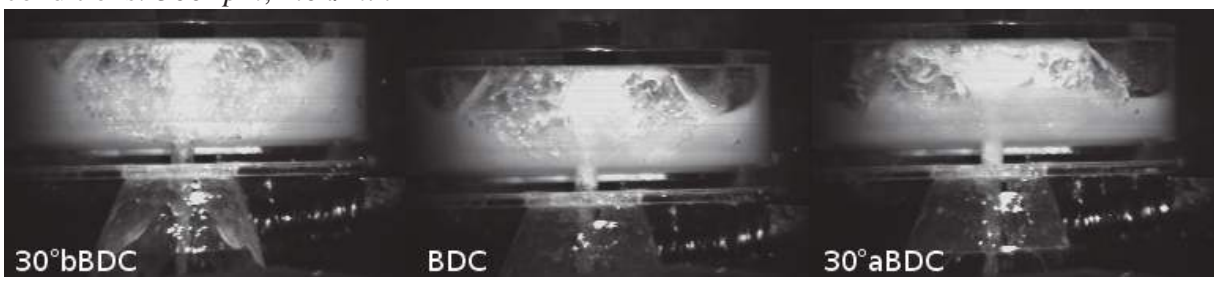

conditions: 300 *rpm*, 6.0 *l/min*

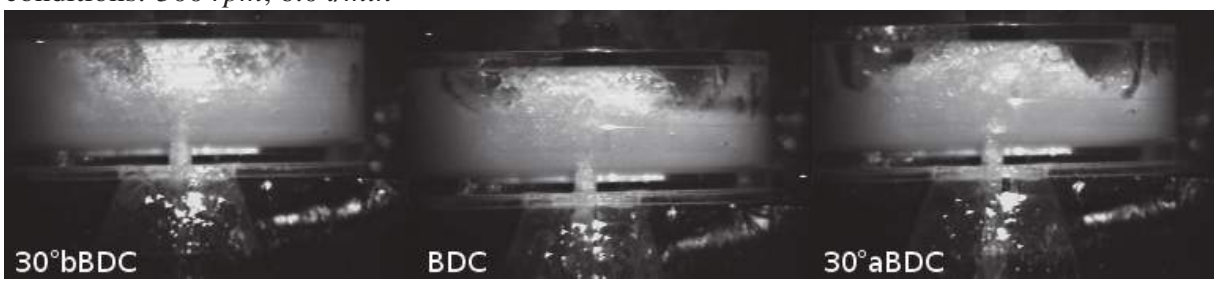

conditions: 600 *rpm*, 4.0 *l/min*

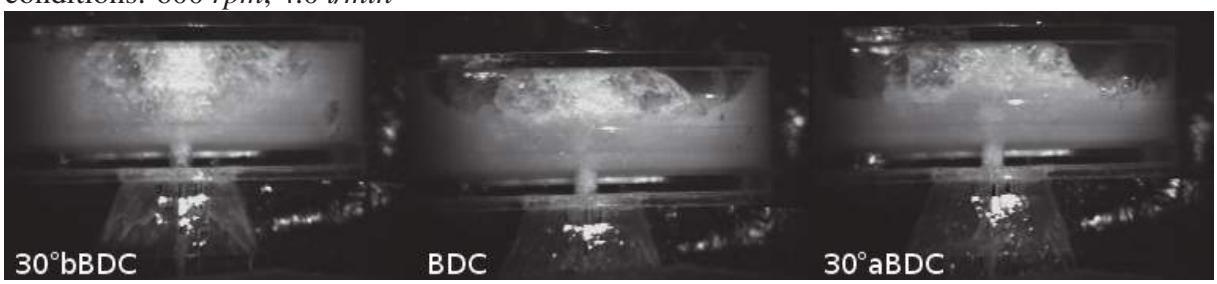

conditions: 600 *rpm*, 6.0 *l/min*

Fig. B.7 Flow in LGM at various conditions, inlet sections

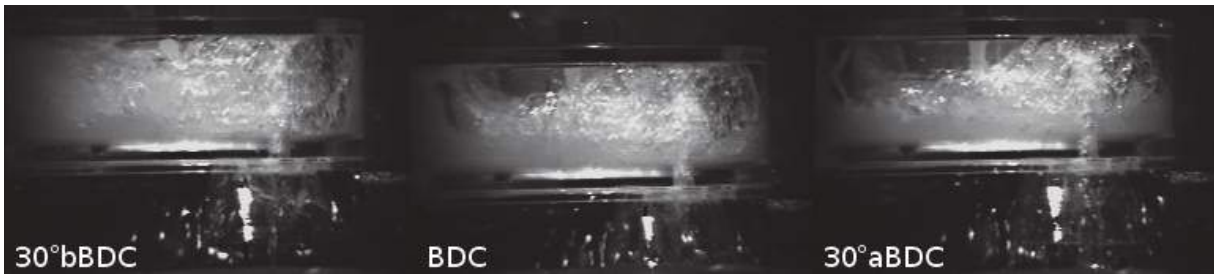

conditions: 300 *rpm*, 4.0 *l/min*

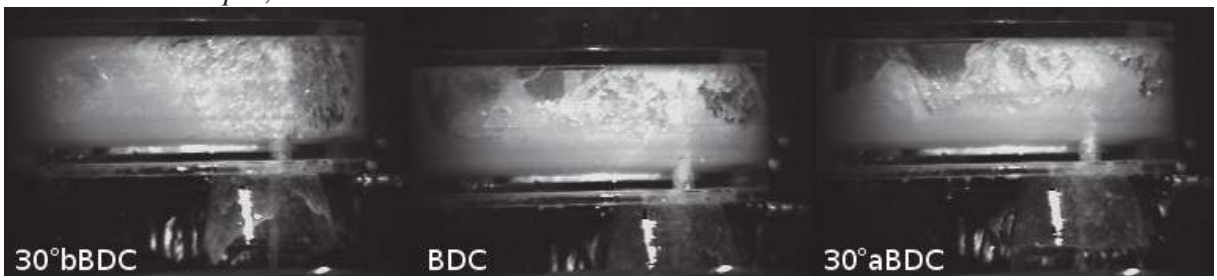

conditions: 300 *rpm*, 6.0 *l/min*

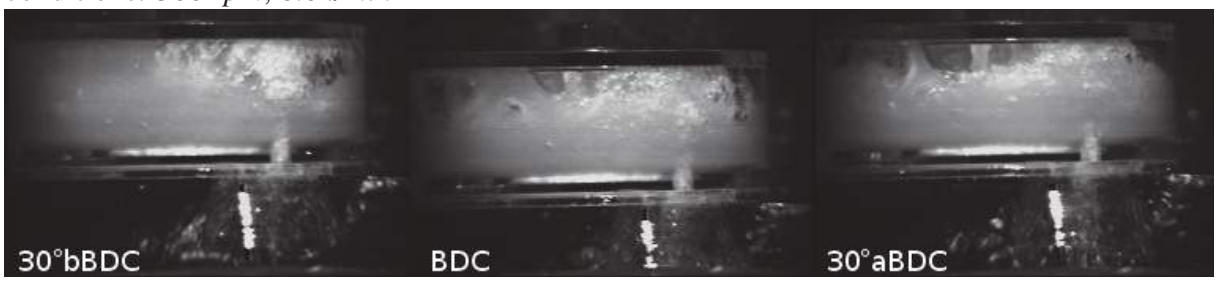

conditions: 600 *rpm*, 4.0 *l/min*

conditions: 600 *rpm*, 6.0 *l/min*

Fig. B.8 Flow in LGM at various conditions, rear mid-gallery sections

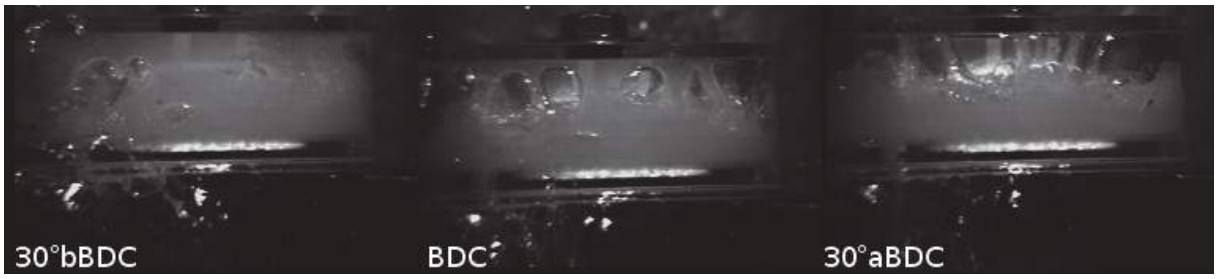

conditions: 300 *rpm*, 4.0 *l/min*

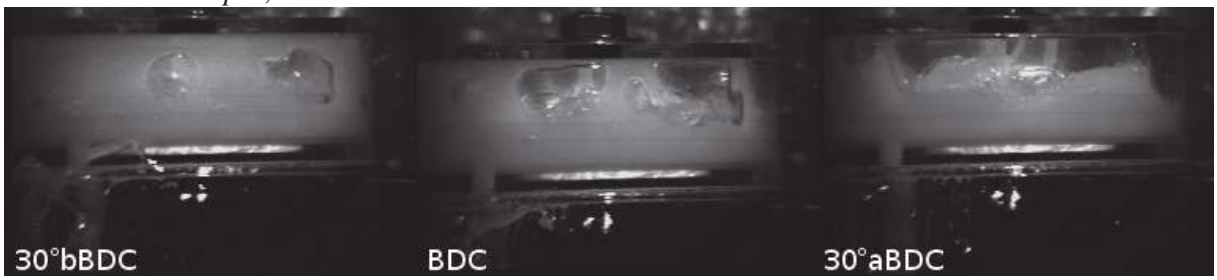

conditions: 300 *rpm*, 6.0 *l/min*

conditions: 600 *rpm*, 4.0 *l/min*

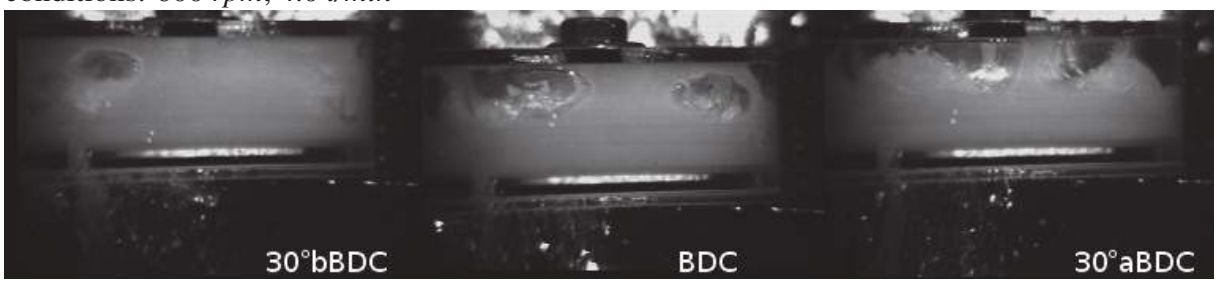

conditions: 600 *rpm*, 6.0 *l/min*

Fig. B.9 Flow in LGM at various conditions, front mid-gallery sections

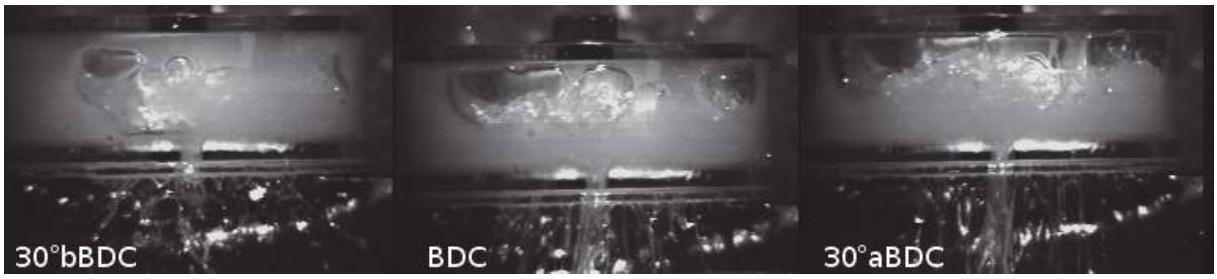

conditions: 300 *rpm*, 4.0 *l/min*

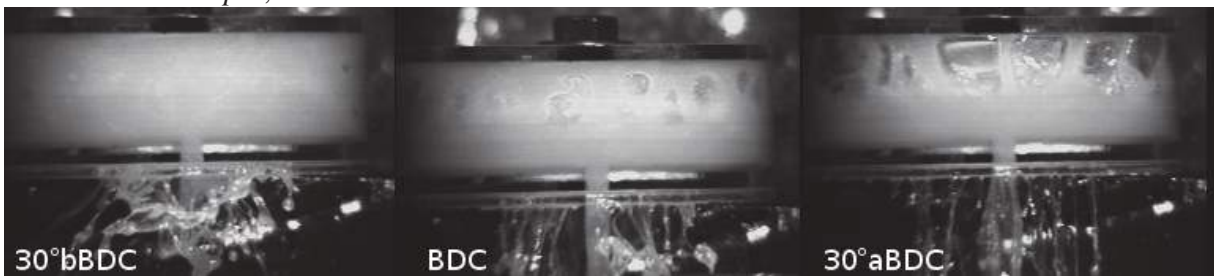

conditions: 300 *rpm*, 6.0 *l/min*

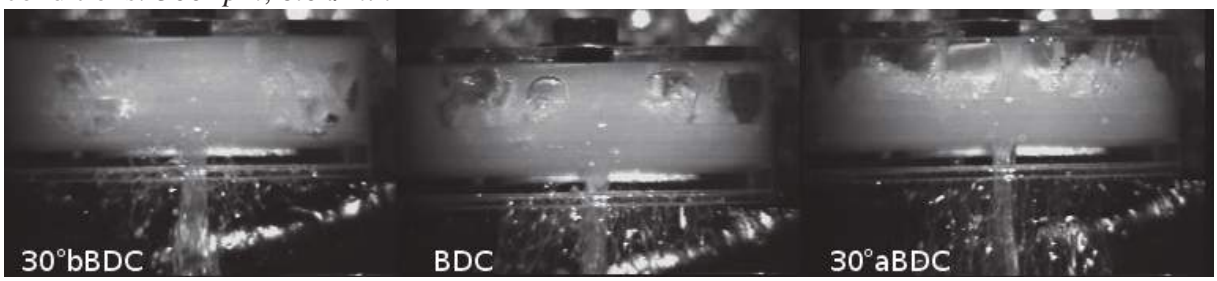

conditions: 600 *rpm*, 4.0 *l/min*

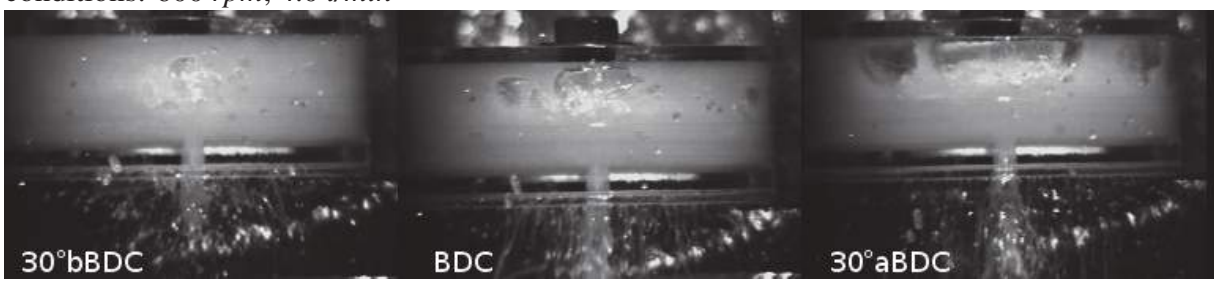

conditions: 600 *rpm*, 6.0 *l/min*

Fig. B.10 Flow in LGM at various conditions, outlet sections

B.4 Large gallery model at *TDC*

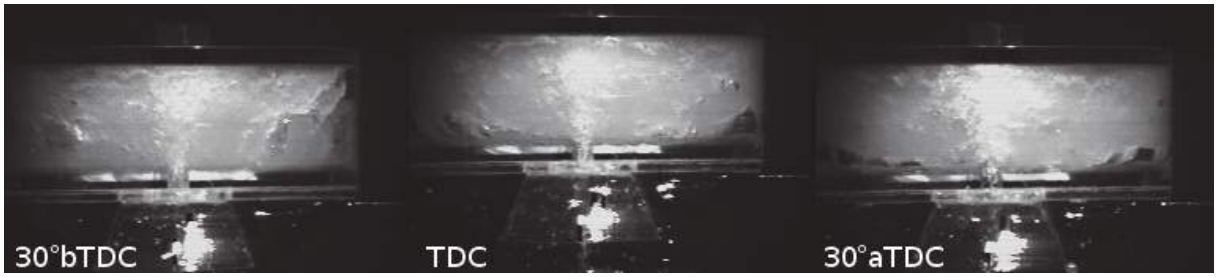

conditions: 300 *rpm*, 4.0 *l/min*

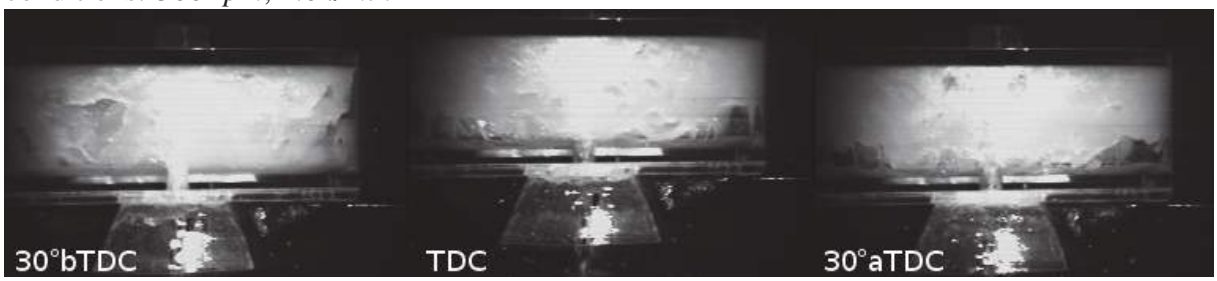

conditions: 300 *rpm*, 6.0 *l/min*

conditions: 600 *rpm*, 4.0 *l/min*

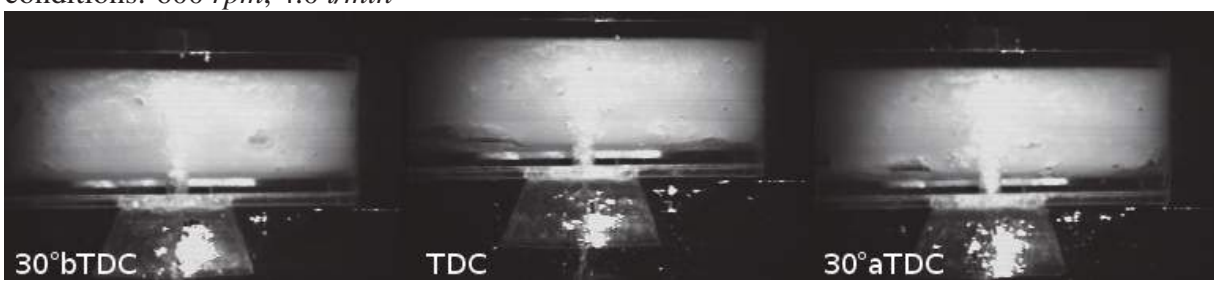

conditions: 600 *rpm*, 6.0 *l/min*

Fig. B.11 Flow in LGM at various conditions, inlet sections

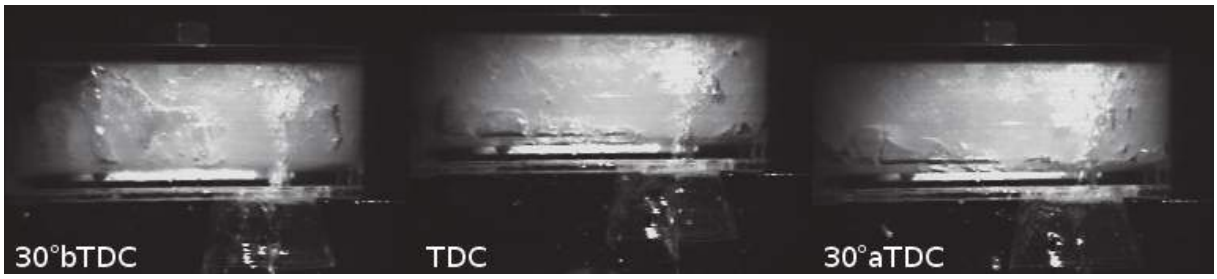

conditions: 300 *rpm*, 4.0 *l/min*

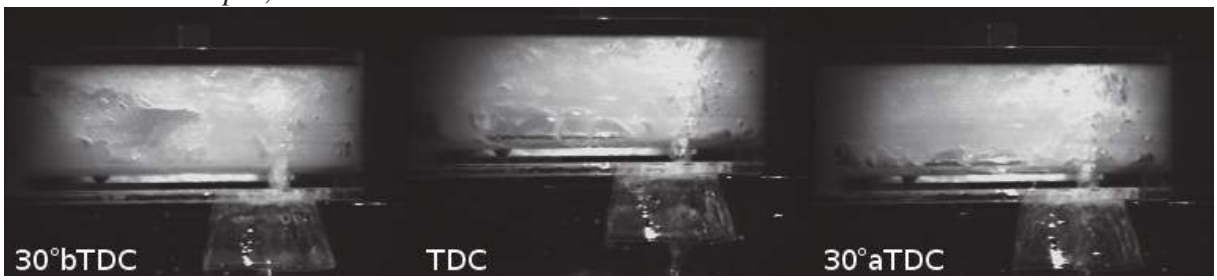

conditions: 300 *rpm*, 6.0 *l/min*

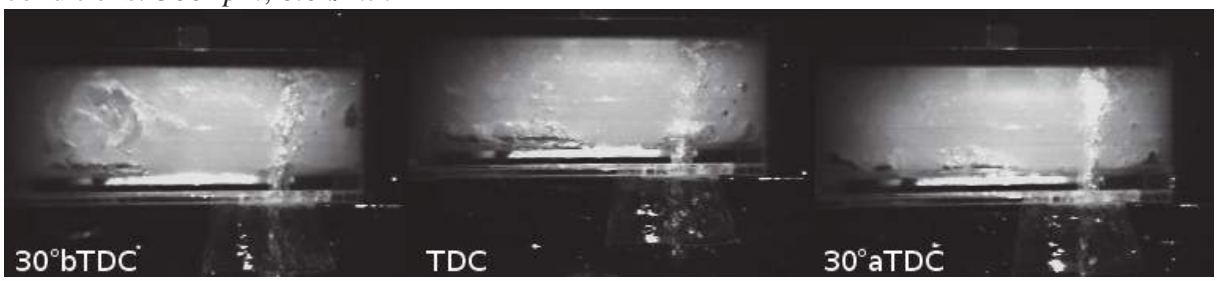

conditions: 600 *rpm*, 4.0 *l/min*

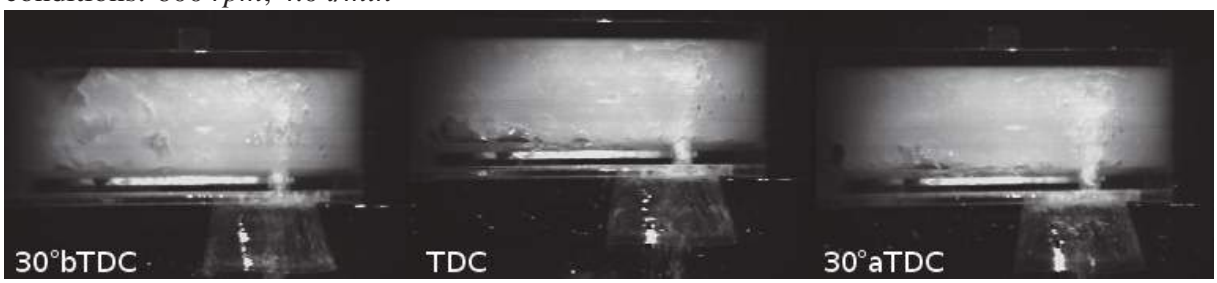

conditions: 600 *rpm*, 6.0 *l/min*

Fig. B.12 Flow in LGM at various conditions, rear mid-gallery sections

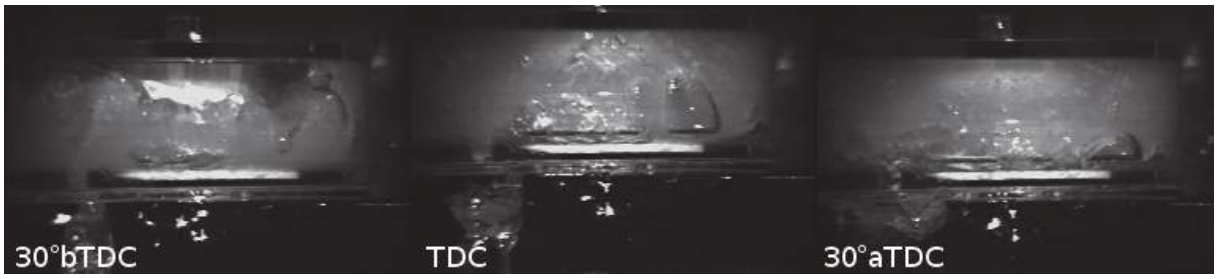

conditions: 300 *rpm*, 4.0 *l/min*

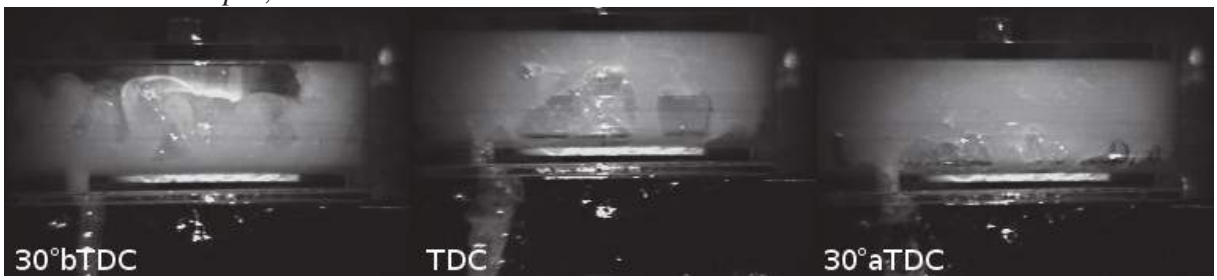

conditions: 300 *rpm*, 6.0 *l/min*

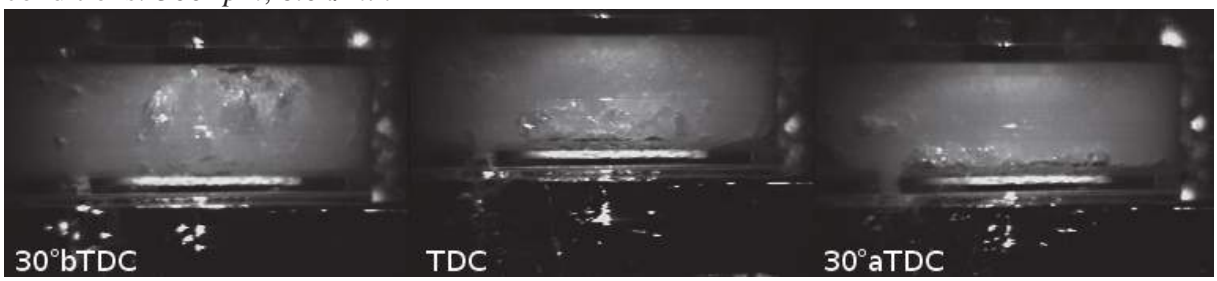

conditions: 600 *rpm*, 4.0 *l/min*

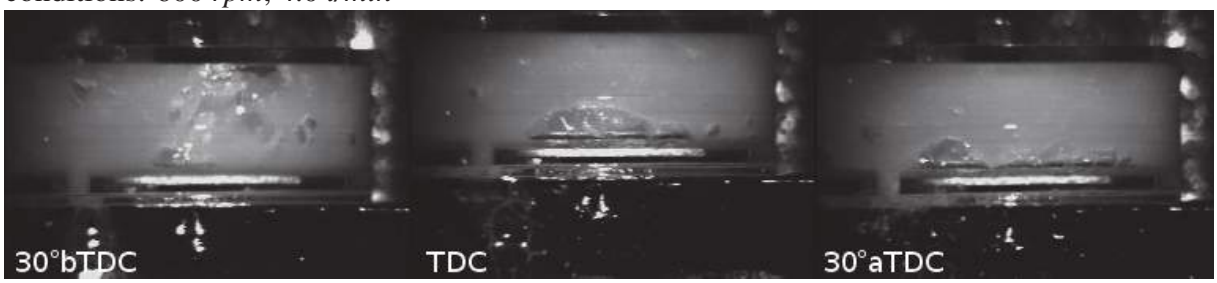

conditions: 600 *rpm*, 6.0 *l/min*

Fig. B.13 Flow in LGM at various conditions, front mid-gallery sections

conditions: 300 *rpm*, 4.0 *l/min*

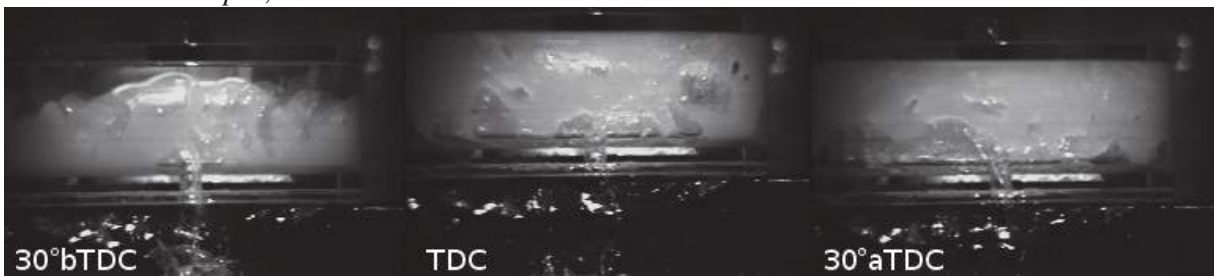

conditions: 300 *rpm*, 6.0 *l/min*

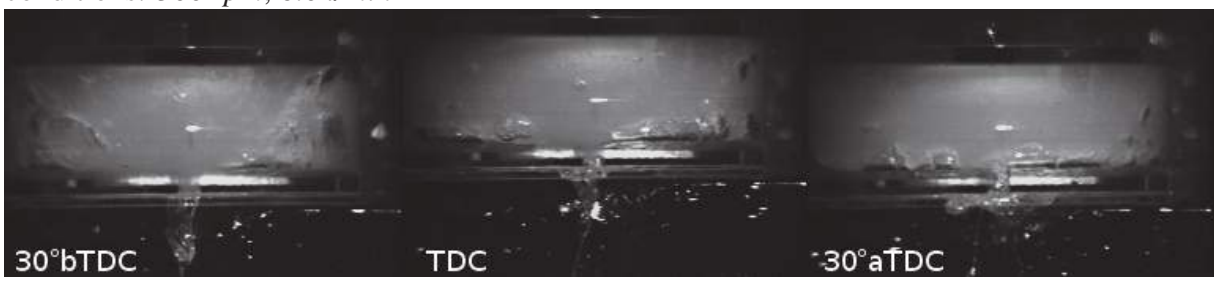

conditions: 600 *rpm*, 4.0 *l/min*

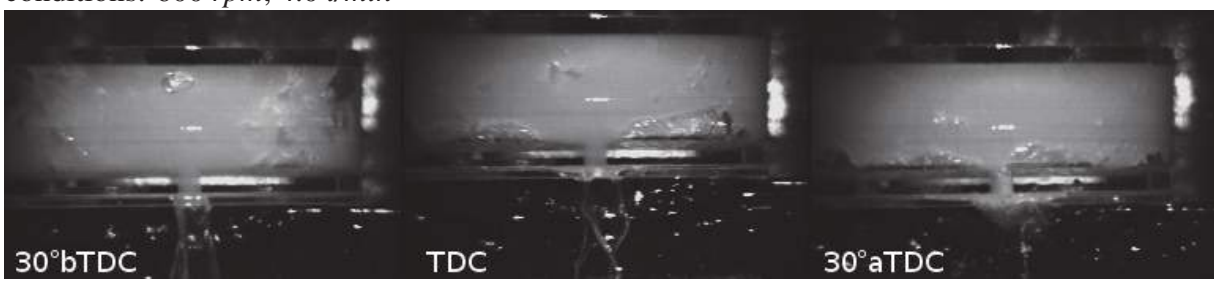

conditions: 600 *rpm*, 6.0 *l/min*

Fig. B.14 Flow in LGM at various conditions, outlet sections

APPENDIX C USER-DEFINED FUNCTION FOR INLET VELOCITY PROFILE

C.1 Laminar conditions

```
/************************************************************************
y-vel-profile.c \\
UDF for specifying steady-state velocity profile for nozzle inlet
The profile is parabolic for laminar conditions at 4 l/min (Re=1892)
************************************************************************/

\#include "udf.h"

DEFINE\_PROFILE}(inlet\_y\_velocity\_L, thread, position)
{
real x[ND_ND];    /* position vector 0=x, 1=y, 2=z */
real zz;          /* zz is a real number */
real xx;          /* xx is a real number */
real r;           /* r is a real number */
real NR;          /* NR is a real number */
real vym;         /* vym is a real number */
real xo;          /* xo is a real number */
vym = 9.431464;   /* vym is the max velocity for 3mm inlet and 4l/min
flow rate */
NR = 0.0015;      /* NR is the nozzle radius in m */
xo = -0.054365;   /* xo is the x-direction offset of the inlet from
the model origin */
face_t f;

begin_f_loop(f, thread)
{
F_CENTROID(x,f,thread);
xx = x[0];                              /* xx is the x-coordinate */
zz = x[2];                              /* zz is the z-coordinate */
r = pow(pow((xx-xo),2)+pow(zz,2),0.5);   /* calculate position at
inlet for polar CS */
F_PROFILE(f, thread, position) = vym*(1-((r*r)/(NR*NR)));
/* this calculates the laminar y-velocity based on inlet position */
```

```
}
end_f_loop(f, thread)
}
```

C.2 Turbulent conditions

```
/************************************************************************
y-vel-profile.c
UDF for specifying steady-state velocity profile for nozzle inlet
The profile is parabolic for turbulent conditions at 6 l/min (Re=2838)
************************************************************************/

#include "udf.h"

DEFINE_PROFILE(inlet_y_velocity_T, thread, position)
{
real x[ND_ND];    /* position vector 0=x, 1=y, 2=z */
real zz;          /* zz is a real number */
real xx;          /* xx is a real number */
real r;           /* r is a real number */
real NR;          /* NR is a real number */
real vym;         /* vym is a real number */
real xo;          /* xo is a real number */
real n;           /* n is the exponent for power law of turbulent profile*/
vym = 18.0798;    /* vym is calculated for 3mm inlet and 6l/min flow rate*/
NR = 0.0015;      /* NR is the nozzle radius and is 0.0015m */
n = 5;            /* exponent interpolated from
xo = -0.054365;   /* xo is the x-direction offset of the inlet from the
model origin */
face_t f;

begin_f_loop(f, thread)
{
F_CENTROID(x,f,thread);
xx = x[0];                              /* xx is the x-coordinate */
zz = x[2];                              /* zz is the z-coordinate */
r = pow(pow((xx-xo),2)+pow(zz,2),0.5);   /* calculate position at inlet
for polar CS */
F_PROFILE(f, thread, position) = vym*pow( (1-(r/NR)) , (1/n) );
/* this calculates the turbulent y-velocity based on inlet position */
}
end_f_loop(f, thread)
}
```

APPENDIX D UNCERTAINTY ASSESSMENT OF GRID DEPENDENT VARIABLE

The grid convergence index (GCI) can be determined for any parameter of interest ϕ, e.g. in the present case for the gallery oil fill ratio (*OFR*). The calculations shown below relate to the medium, fine and very fine mesh model, whereby N_i is the number of cells for each model represents, with the index i referring to the mesh model, where 1 indicates the finest mesh and 3 the coarsest mesh. The process was based on recommendations by Roache (1997) and Celik et al. (2008) and was adapted to the presented case accordingly. The first step involved the calculation of the average cell height, h_i with

$$h_i = \left(\frac{V_i}{N_i}\right)^{\frac{1}{3}} \tag{D.1}$$

Roache (1997) stated that the grid stepping should be $r \approx 2$. This meant that the length of the element sides should be halved, leading to 8 hexahedrons or 8 tetrahedrons respectively. The height step ratio, r, and convergence result step, ε can be calculated by

$$r_{12} = \frac{h_2}{h_1} \qquad and \qquad r_{23} = \frac{h_3}{h_2} \tag{D.2}$$

and

$$\varepsilon_{32} = \phi_3 - \phi_2 \qquad and \qquad \varepsilon_{21} = \phi_2 - \phi_1 \tag{D.3}$$

The coefficients p and q for a two step convergence analysis are

$$p = \frac{1}{ln(r_{21})}\left|ln\left(\left|\frac{\varepsilon_{32}}{\varepsilon_{21}}\right|\right) + q(p)\right| \tag{D.4}$$

and

$$q(p) = ln\left(\frac{r_{21}^p - s}{r_{32}^p - s}\right) \tag{D.5}$$

with

$$s = -1\left(\frac{\varepsilon_{32}}{\varepsilon_{21}}\right) \tag{D.6}$$

As can be seen above, the equations for p and q are implicit and can only be evaluated by iteration. With the p and q the extrapolated values of the investigated convergence parameter

can be determined for each step as

$$\phi_{21.ext} = \frac{r_{21}^{p}\phi_1 - \phi_3}{r_{21}^{p} - 1} \tag{D.7}$$

and

$$\phi_{32.ext} = \frac{r_{32}^{p}\phi_2 - \phi_3}{r_{32}^{p} - 1} \tag{D.8}$$

Now the approximate relative error, e_a, and extrapolated relative error, e_{ext}, for the fine grid refinement step can be determined and assessed for each step by

$$e_{a.21} = \frac{\phi_1 - \phi_2}{\phi_1} \qquad and \qquad e_{ext} = \frac{\phi_{21.ext} - \phi_1}{\phi_{21.ext}} \tag{D.9}$$

The same process is used for the coarse grid step respectively. The *GCI* for the fine and coarse grid step can then be calculated as

$$GCI_{fine} = \frac{1.25e_{a.21}}{r_{21}^{p} - 1} \qquad and \qquad GCI_{coarse} = \frac{1.25e_{a.32}}{r_{32}^{p} - 1} \tag{D.10}$$

Finally the convergence rate, R, can be calculated to determine, if convergence is present.

$$R = \frac{GCI_{fine}}{GCI_{coarse}} \tag{D.11}$$

Eca and Hoekstra (2006) suggest for large values of p to set p to a value of 2 and recalculate the calculations again. On the other hand, Eca and Hoekstra (2006) and Ali et al. (2009) state different types of convergence conditions, where:

- for $0 < R < 1$ there is monotonic convergence,
- for $-1 < R < 0$ there is oscillatory convergence,
- for $R > 1$ there is divergence and
- for $R < -1$ there is oscillatory divergence.

APPENDIX E NUMERICAL RESULTS OF FLOW BEHAVIOUR INSIDE GALLERIES FOR ALL CASES

The following presented images are aimed to allow a better and extended overview of the results obtained from all investigated gallery shapes, crank speeds and flow rates. Within the main text reference (Chapter) was made to specific sections of the galleries and Figure E.1 highlights these again for better understanding. While the images portraying the air content and distribution in the galleries (Figures E.2 to E.9 and Figures E.18 to E.27) are superimposed from 10 consecutive cycles, the vector images (Figures E.10 to E.17 and (Figures E.28 to E.37) show *one* representative flow condition from *one* of the 10 consecutive cycles. There are some differences in the flow within the 10 consecutive cycles, but the shown cycle encapsulates the best represented conditions of the flow. The red-coloured arrows ($\longrightarrow$) indicate the flow direction of the oil and the blue-coloured arrows ($\longrightarrow$) represent the flow direction of air. All arrows are of identical length and do not represent the velocity magnitude, only the direction.

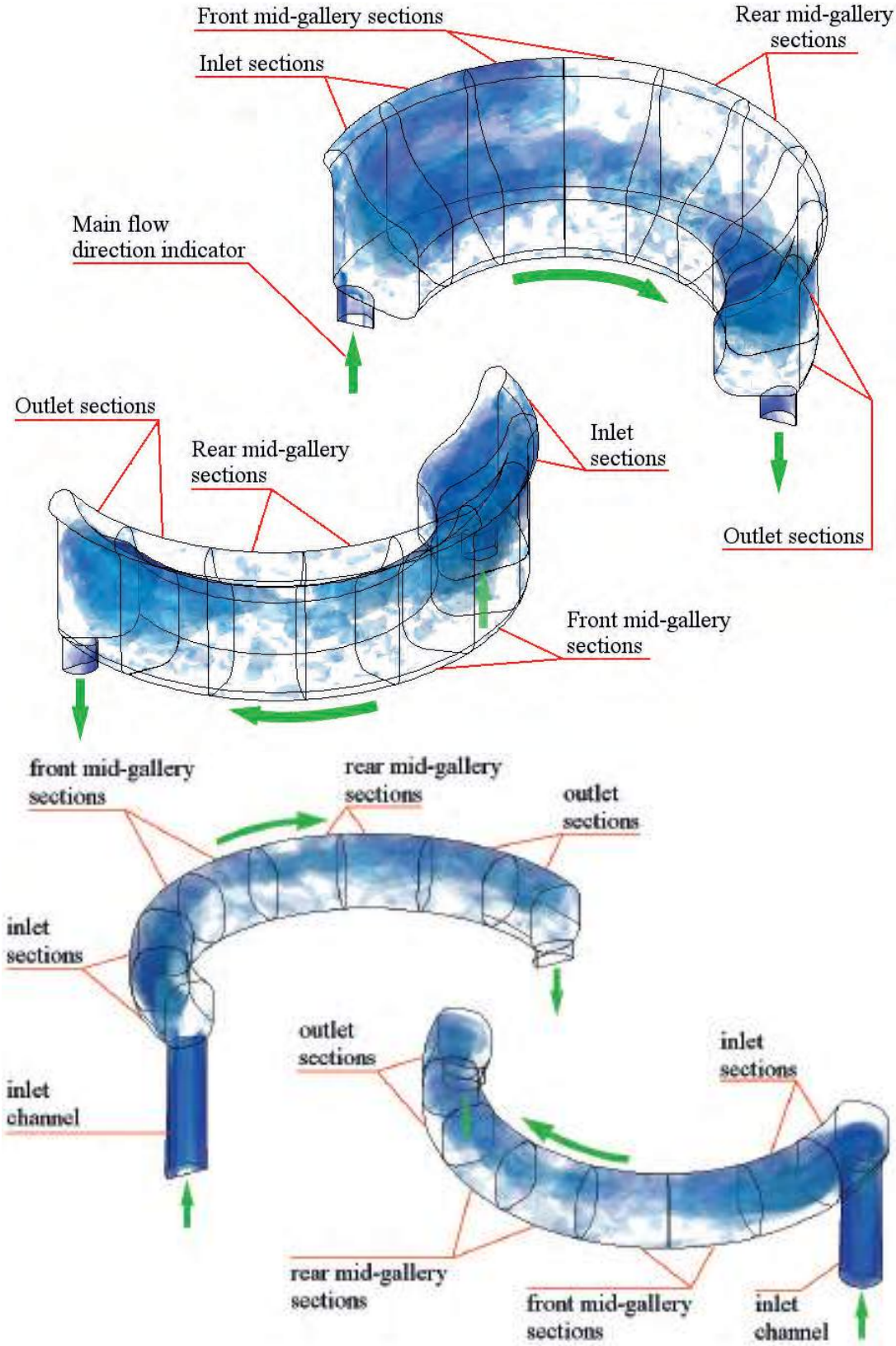

Fig. E.1 Definition of gallery sections for *LGM* (top) and *SGM*(bottom)

E.1 Air content and distribution for *LGM* at *BDC*

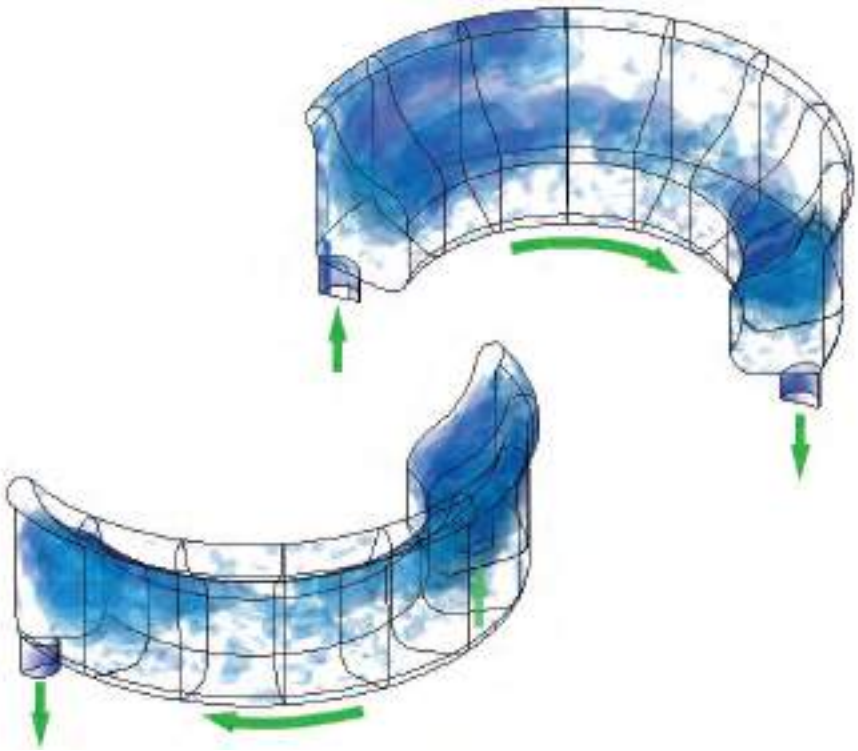

Fig. E.2 *LGM* air content and distribution at *BDC*, *600 rpm* and *4.0 l/min*

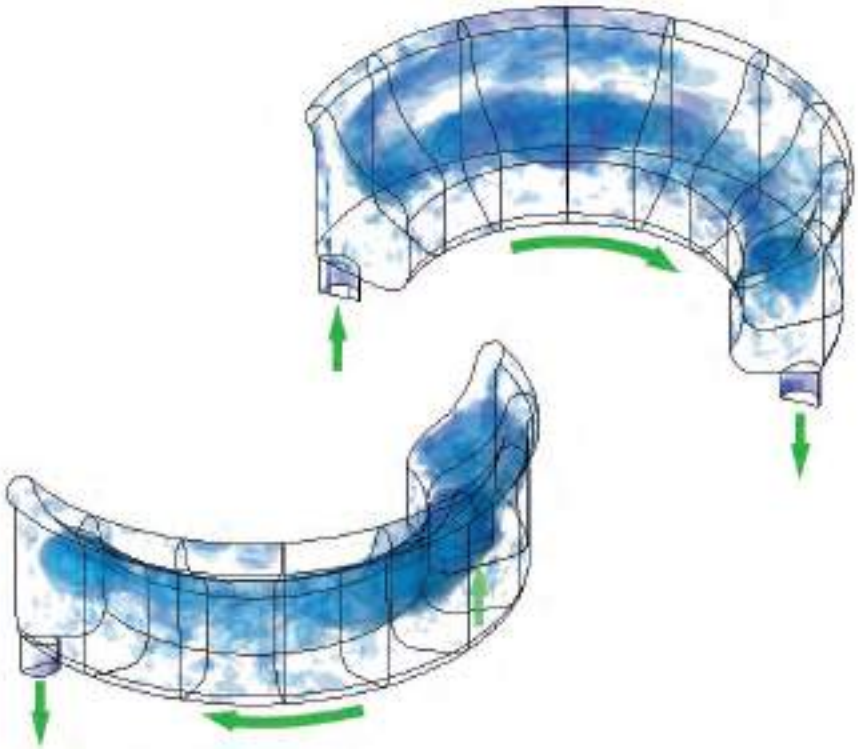

Fig. E.3 *LGM* air content and distribution at *BDC*, *600 rpm* and *6.0 l/min*

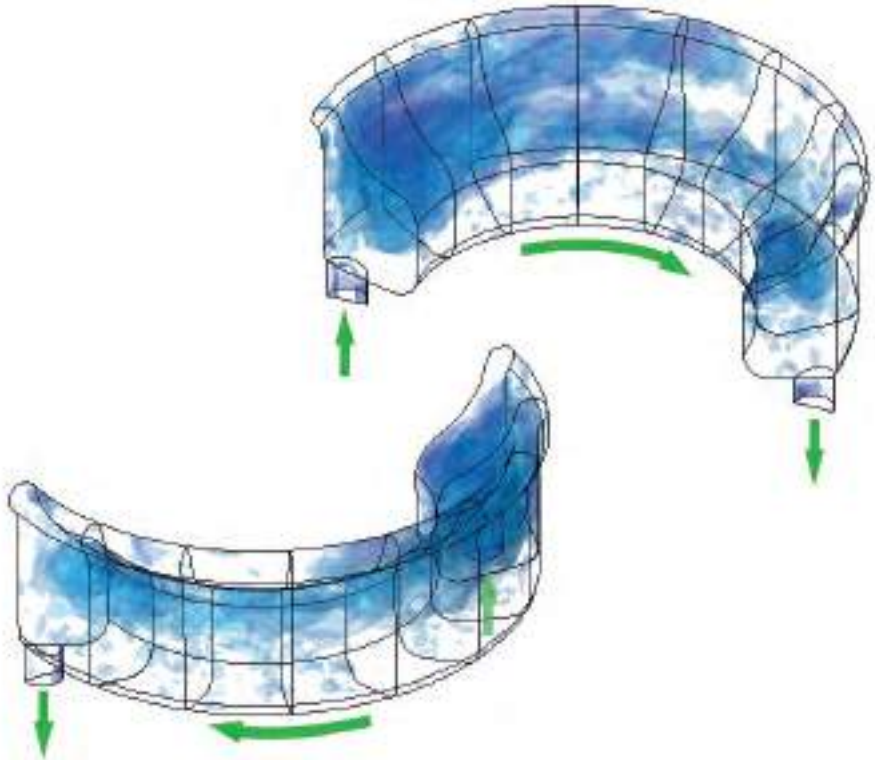

Fig. E.4 *LGM* air content and distribution at *BDC*, *300 rpm* and *4.0 l/min*

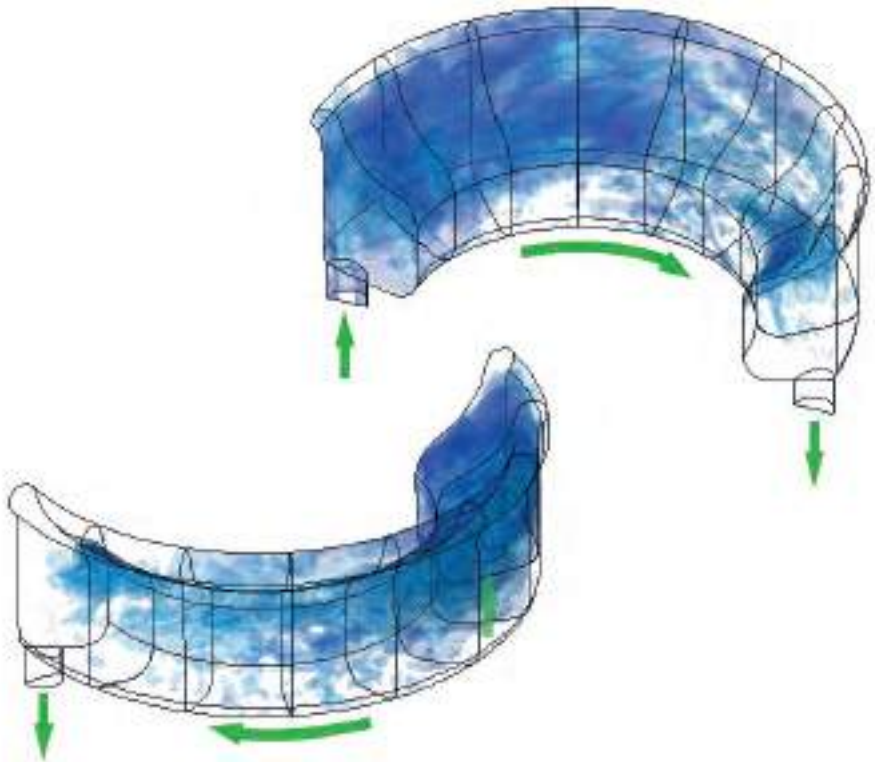

Fig. E.5 *LGM* air content and distribution at *BDC*, *300 rpm* and *6.0 l/min*

E.2 Air content and distribution for *LGM* at *TDC*

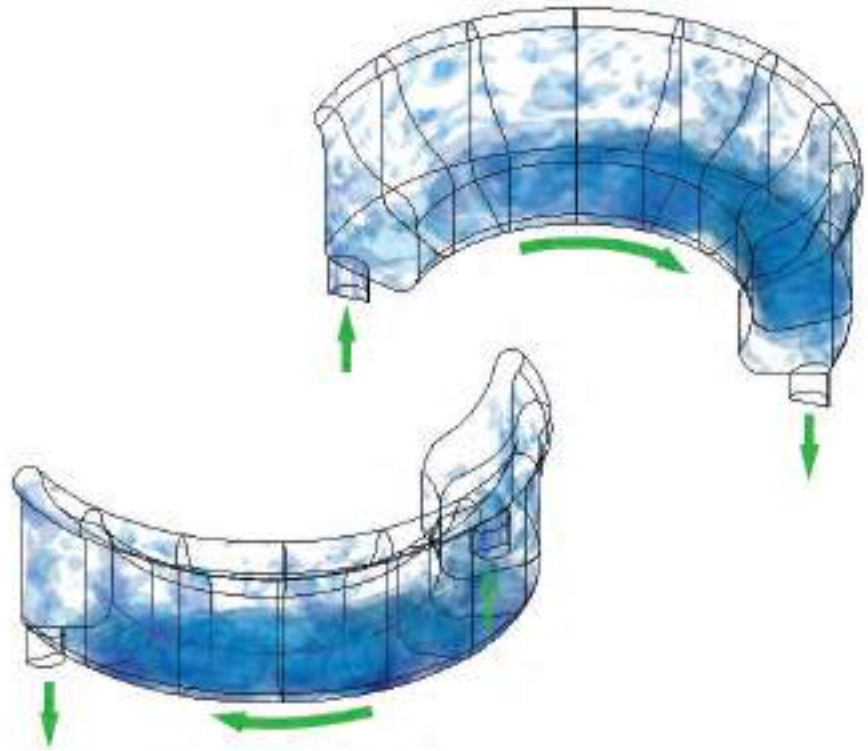

Fig. E.6 *LGM* air content and distribution at *TDC*, *600 rpm* and *4.0 l/min*

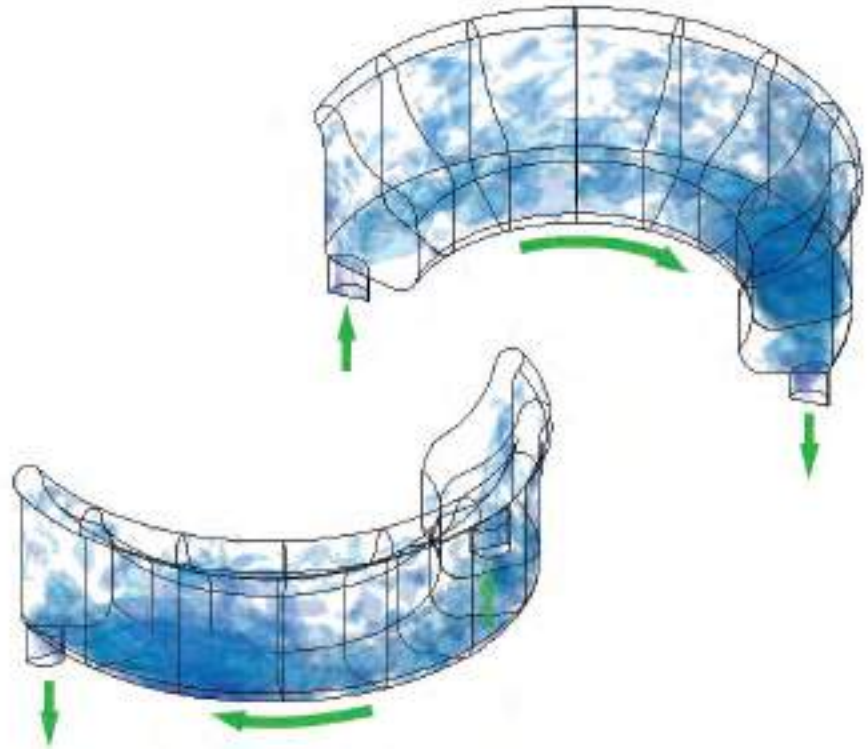

Fig. E.7 *LGM* air content and distribution at *TDC*, *600 rpm* and *6.0 l/min*

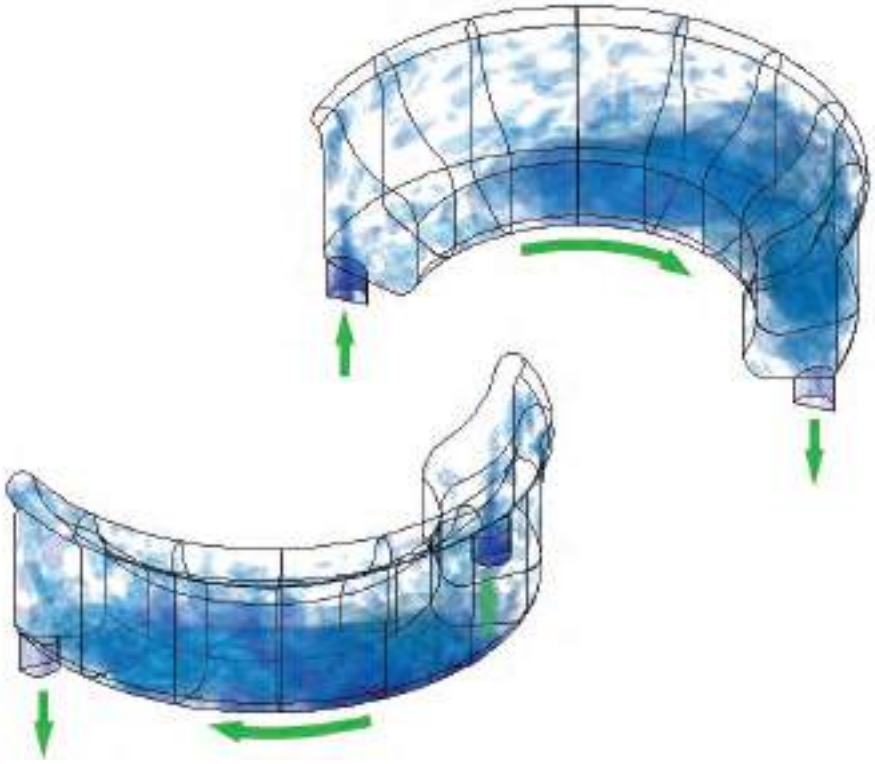

Fig. E.8 *LGM* air content and distribution at *BDC*, *300 rpm* and *4.0 l/min*

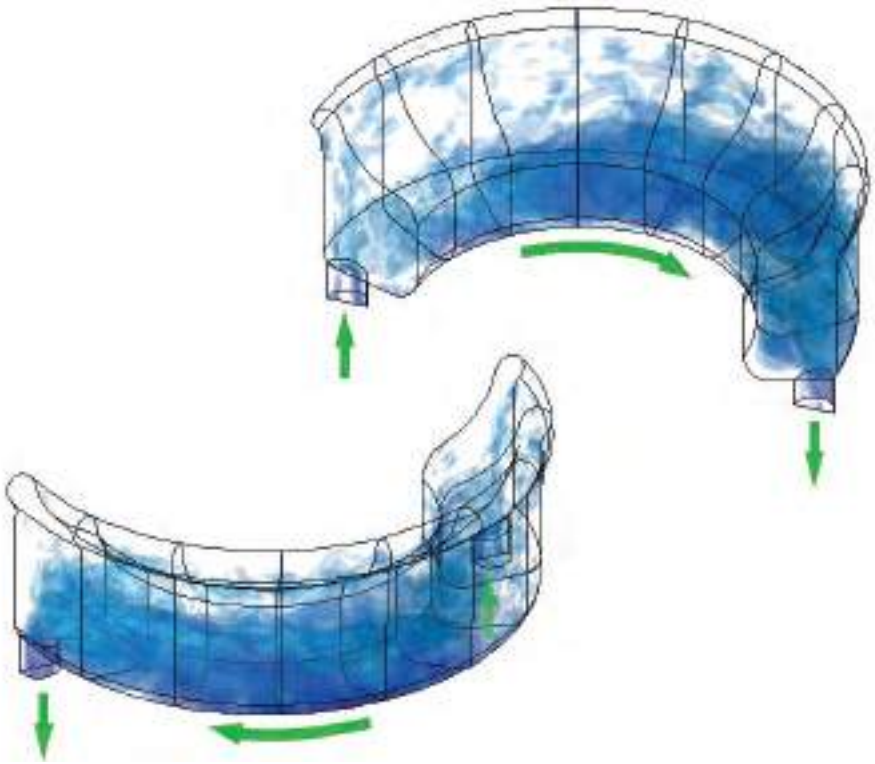

Fig. E.9 *LGM* air content and distribution at *TDC*, *300 rpm* and *6.0 l/min*

E.3 Air and oil flow direction vectors for *LGM* at *BDC*

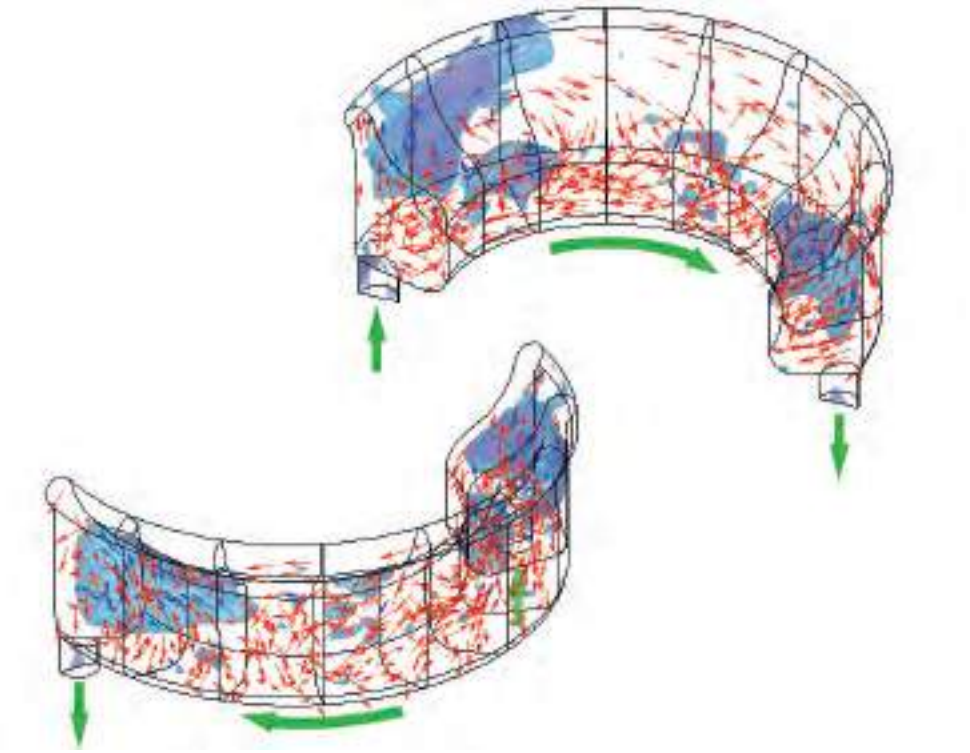

Fig. E.10 *LGM* air and oil flow direction at *BDC*, *600 rpm* and *4.0 l/min*

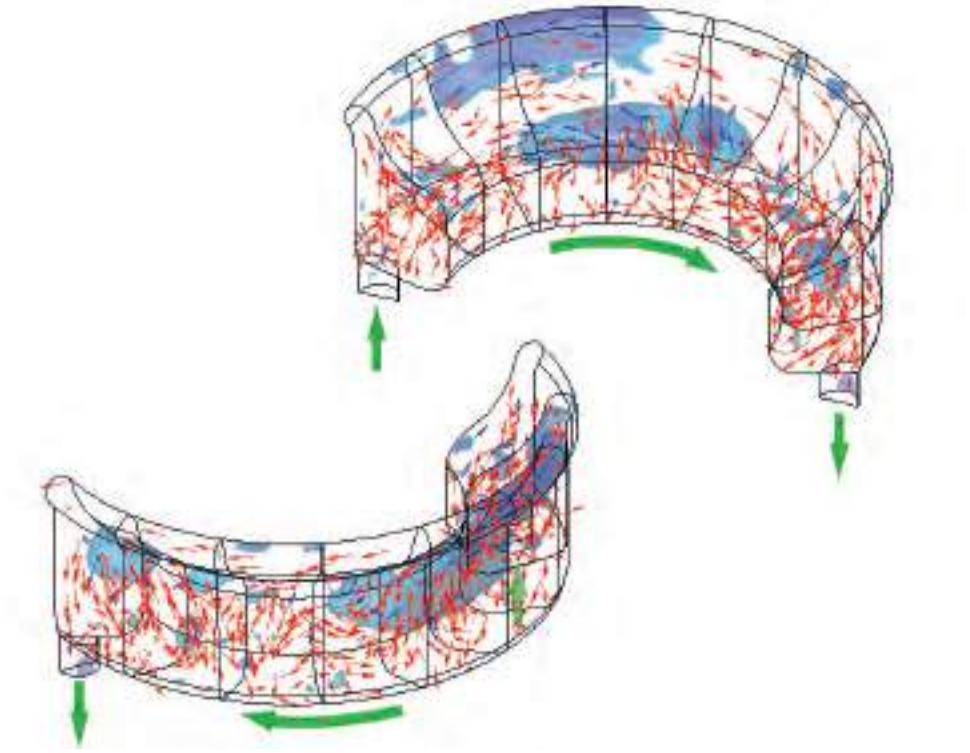

Fig. E.11 *LGM* air and oil flow direction at *BDC*, *600 rpm* and *6.0 l/min*

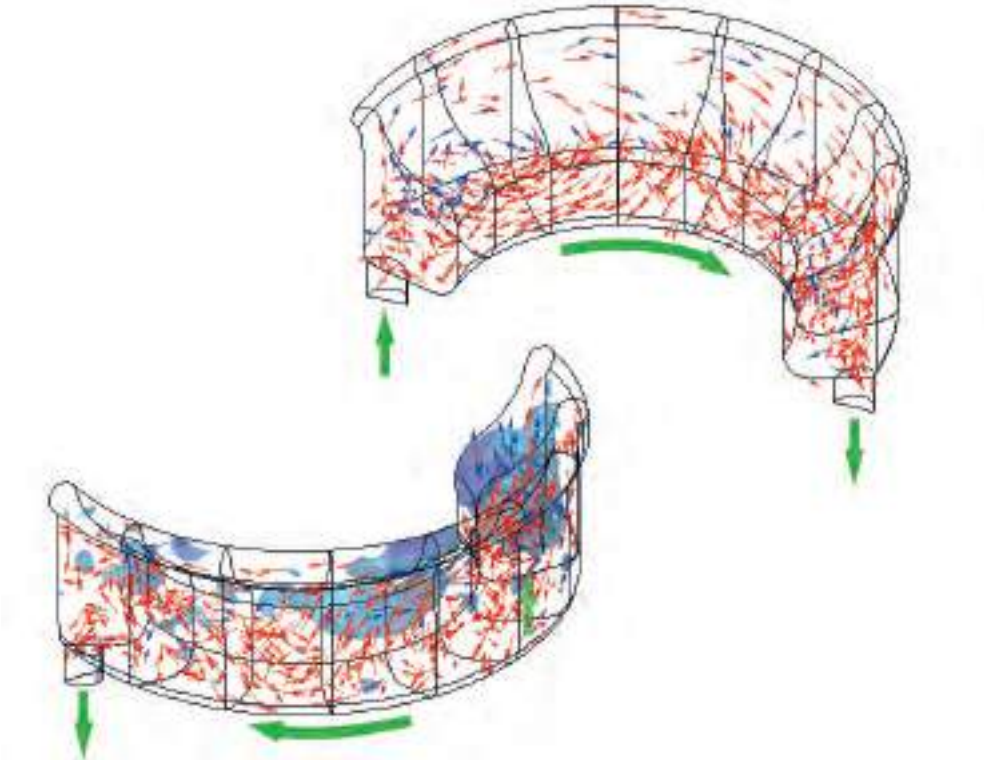

Fig. E.12 *LGM* air and oil flow direction at *BDC*, *300 rpm* and *4.0 l/min*

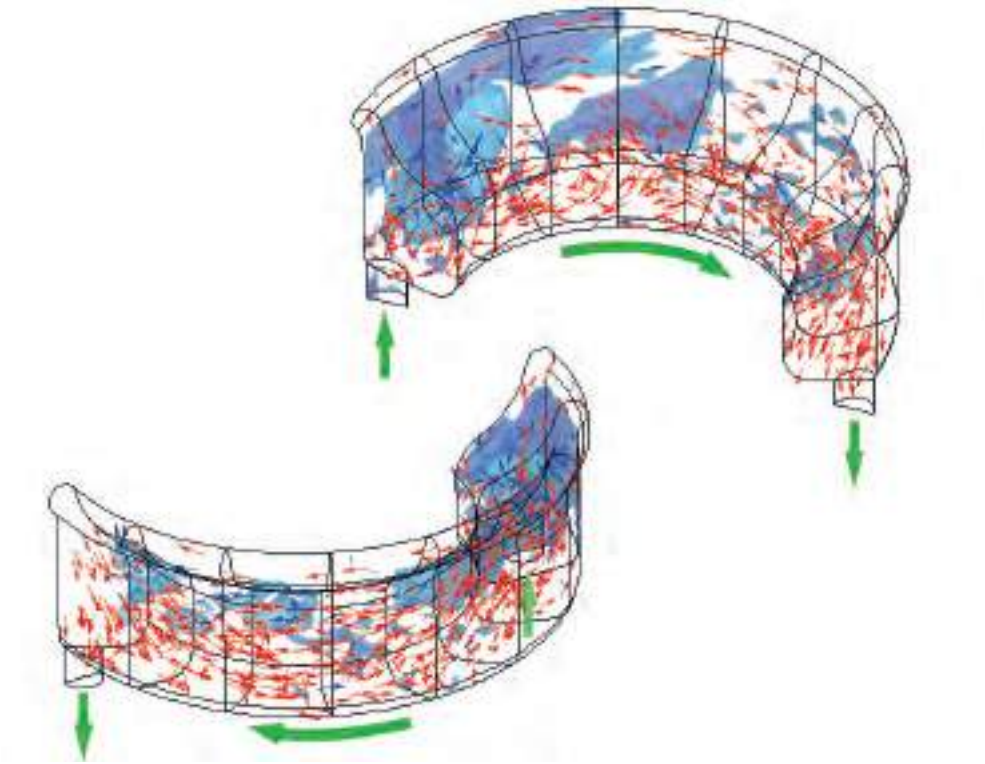

Fig. E.13 *LGM* air and oil flow direction at *BDC*, *300 rpm* and *6.0 l/min*

E.4 Air and oil flow direction vectors for *LGM* at *TDC*

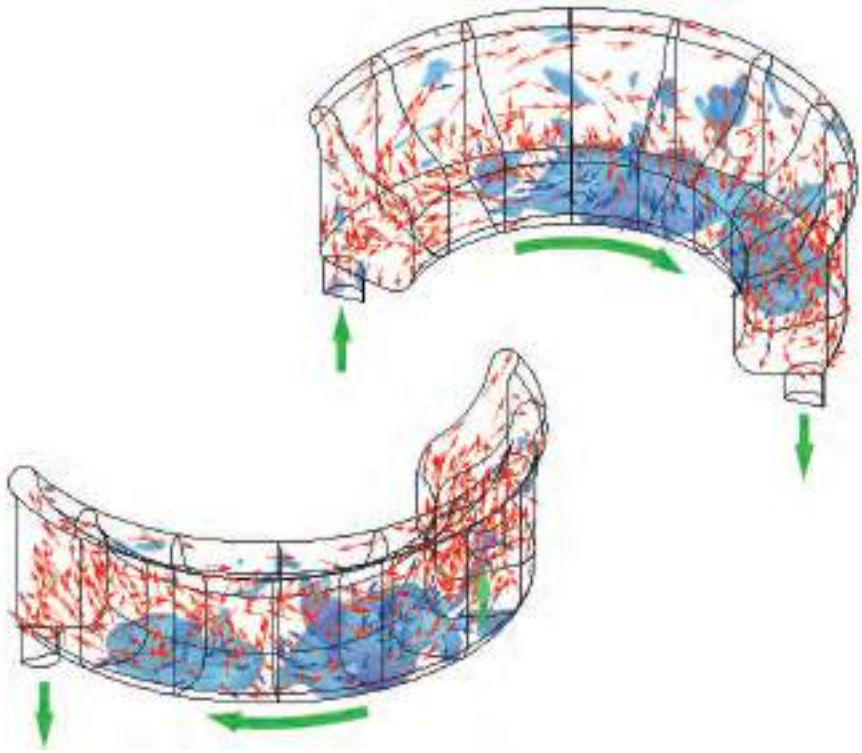

Fig. E.14 *LGM* air and oil flow direction at *TDC*, *600 rpm* and *4.0 l/min*

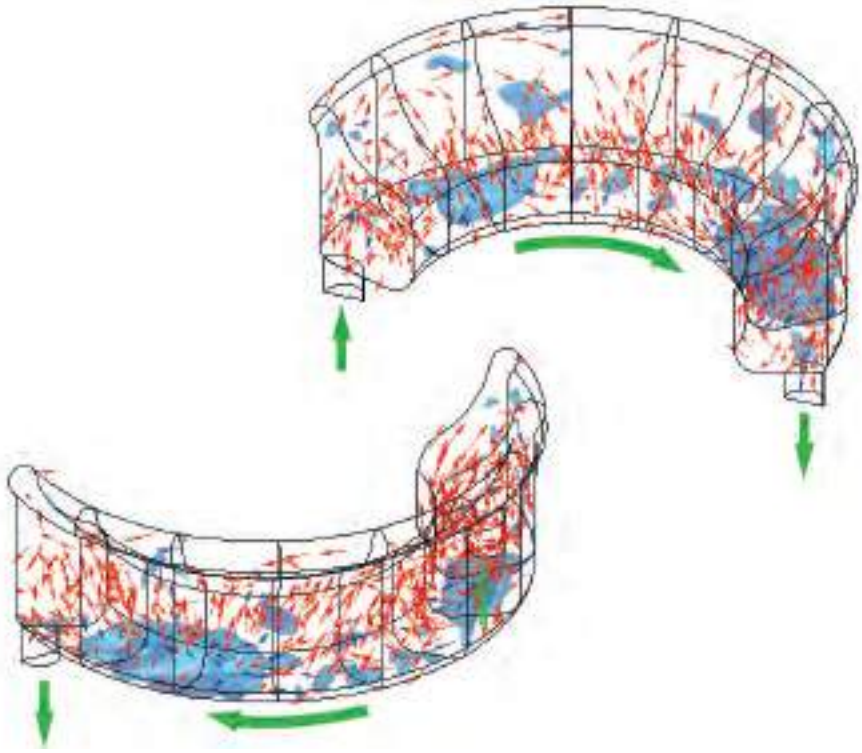

Fig. E.15 *LGM* air and oil flow direction at *TDC*, *600 rpm* and *6.0 l/min*

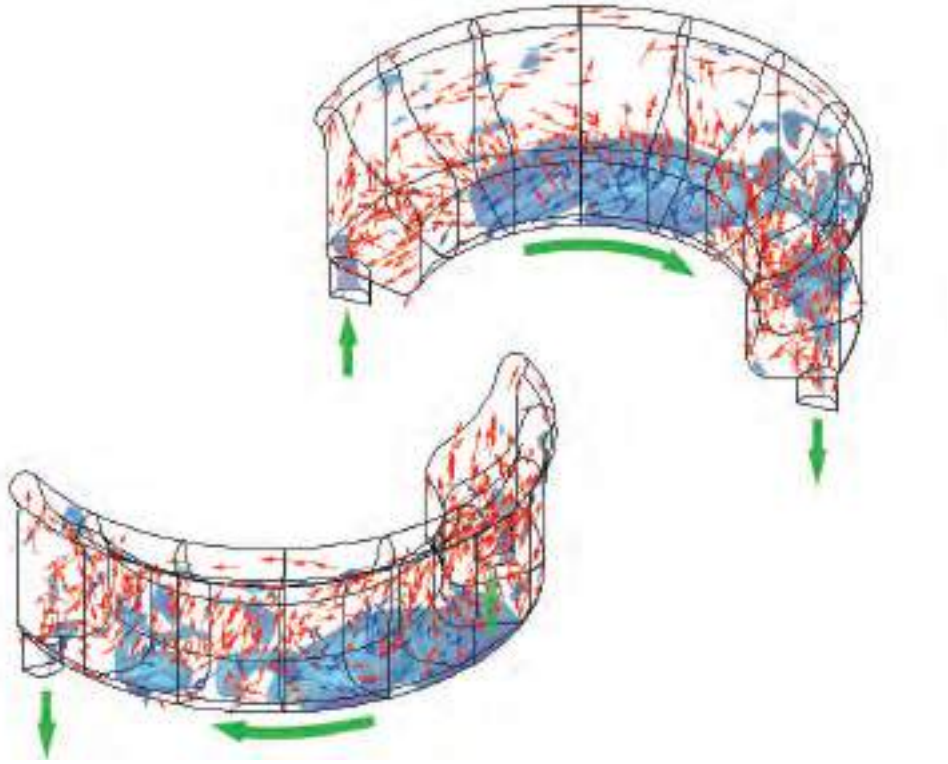

Fig. E.16 *LGM* air and oil flow direction at *TDC*, *300 rpm* and *4.0 l/min*

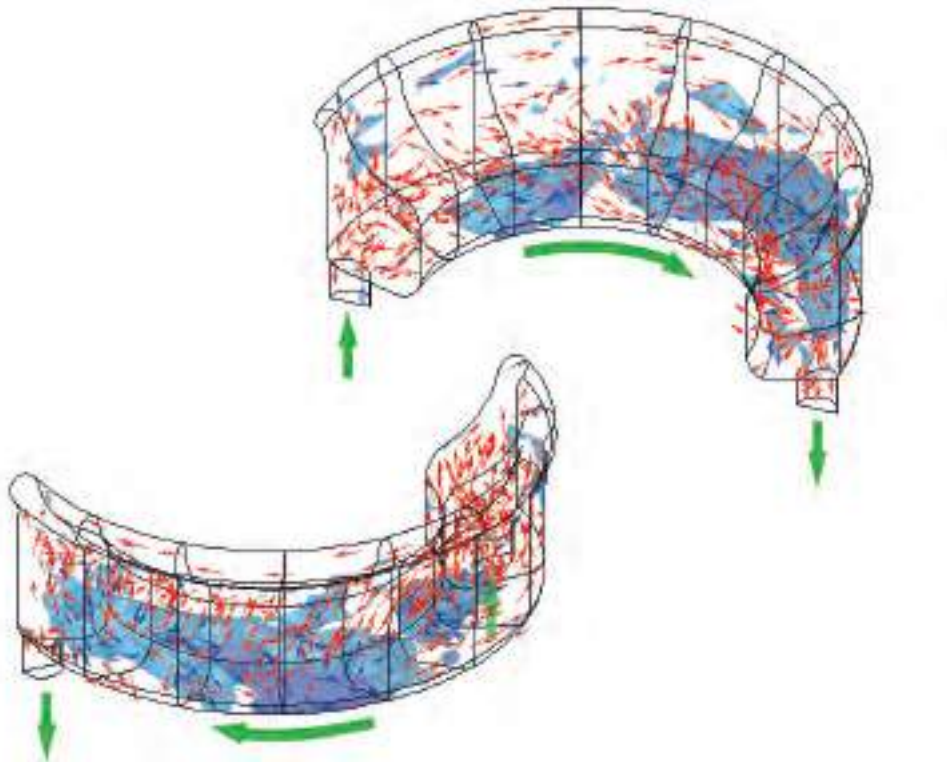

Fig. E.17 *LGM* air and oil flow direction at *TDC*, *300 rpm* and *6.0 l/min*

E.5 Air content and distribution for *SGM* at *BDC*

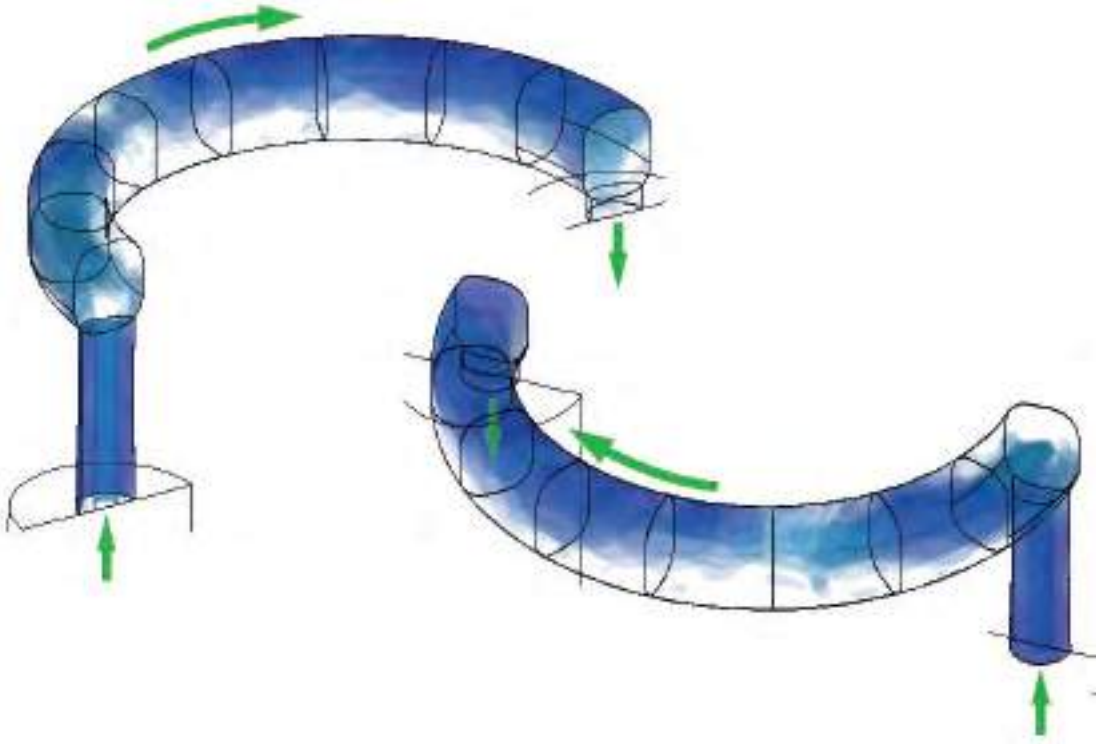

Fig. E.18 *SGM* air content and distribution at *BDC*, *500 rpm* and *1.105 l/min*

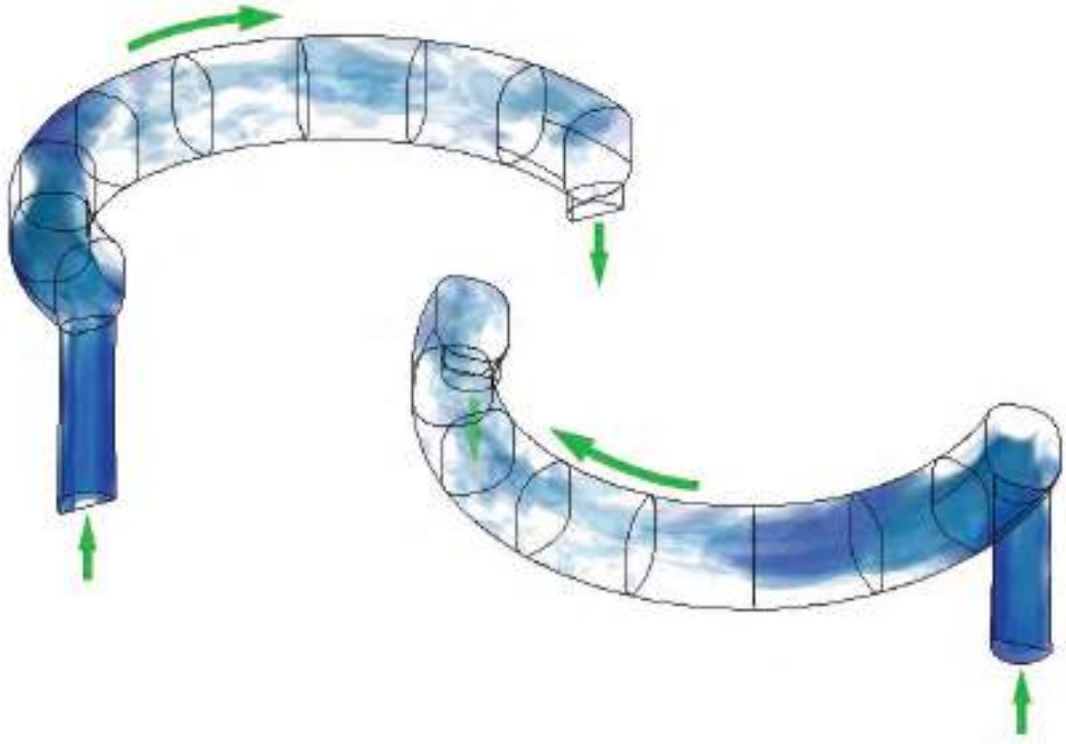

Fig. E.19 *SGM* air content and distribution at *BDC*, *500 rpm* and *2.121 l/min*

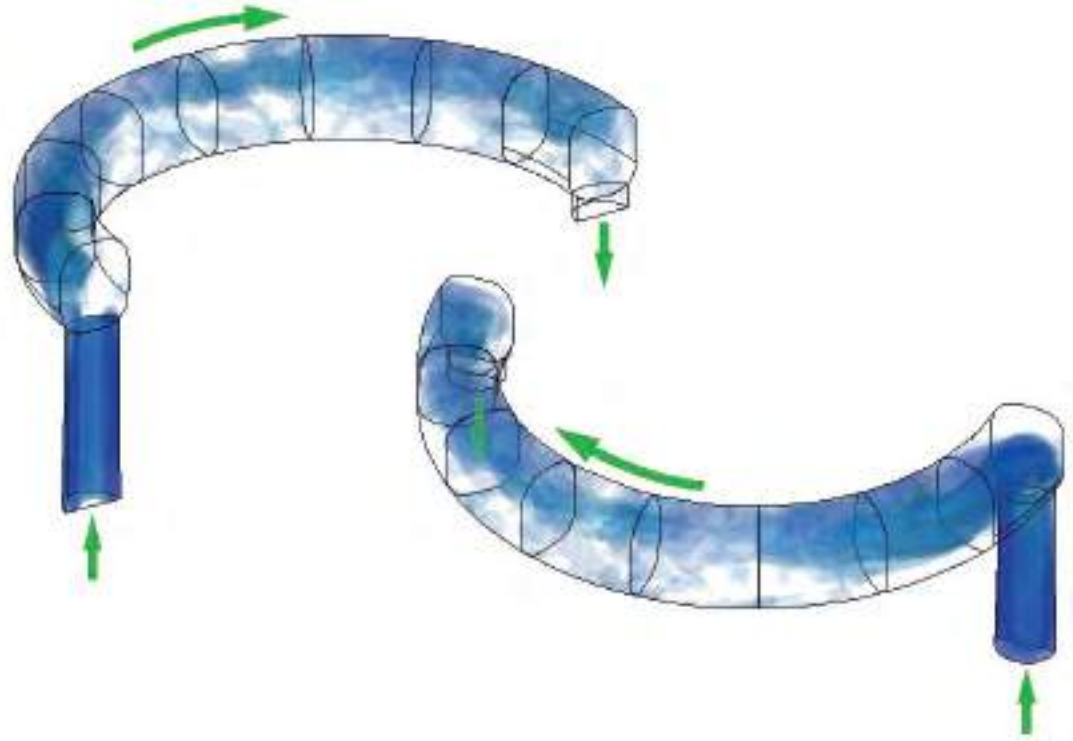

Fig. E.20 *SGM* air content and distribution at *BDC*, *750 rpm* and *1.651 l/min*

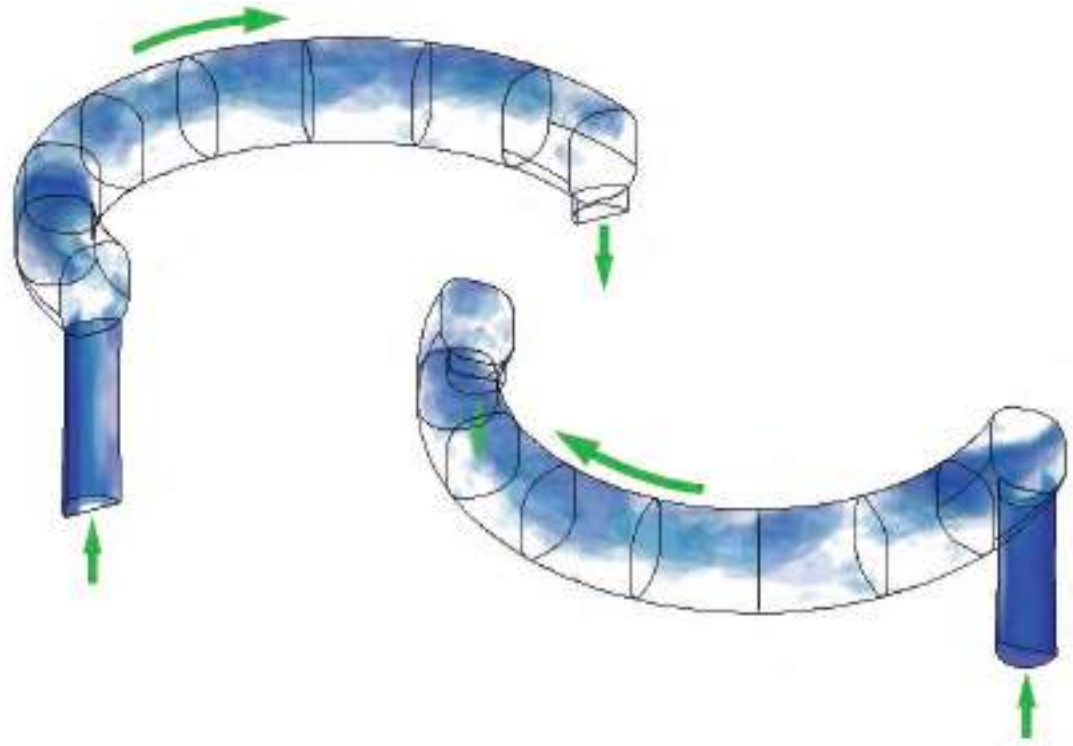

Fig. E.21 *SGM* air content and distribution at *BDC*, *1000 rpm* and *1.105 l/min*

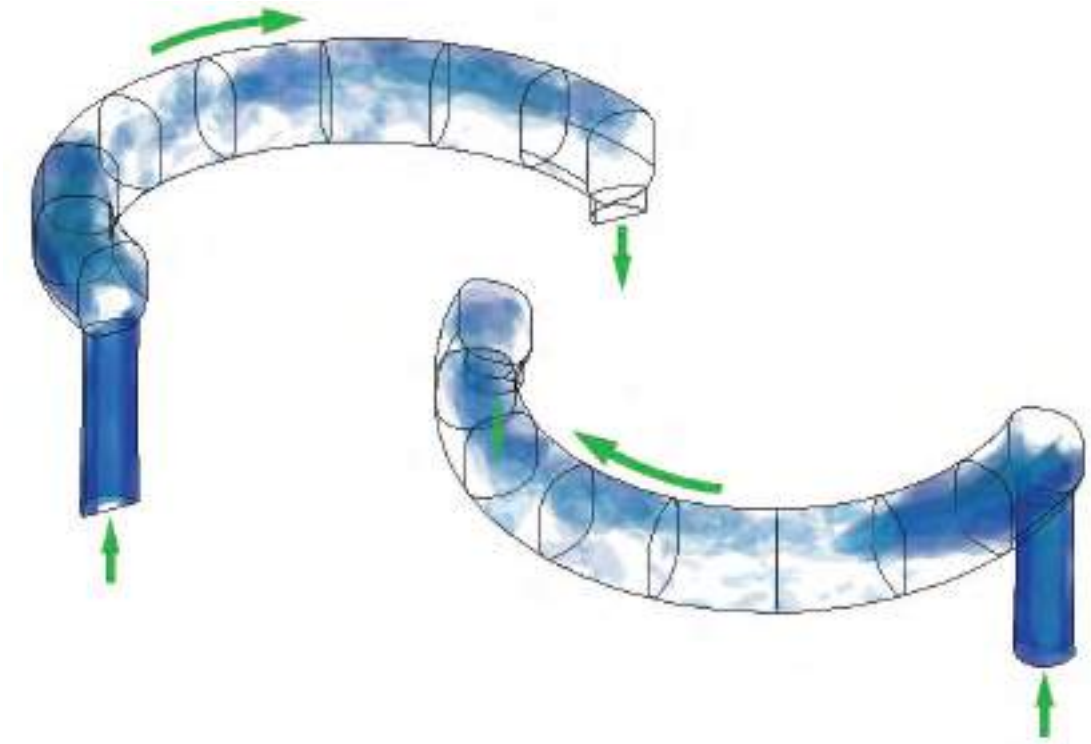

Fig. E.22 *SGM* air content and distribution at *BDC*, *1000 rpm* and *2.121 l/min*

E.6 Air content and distribution for *SGM* at *TDC*

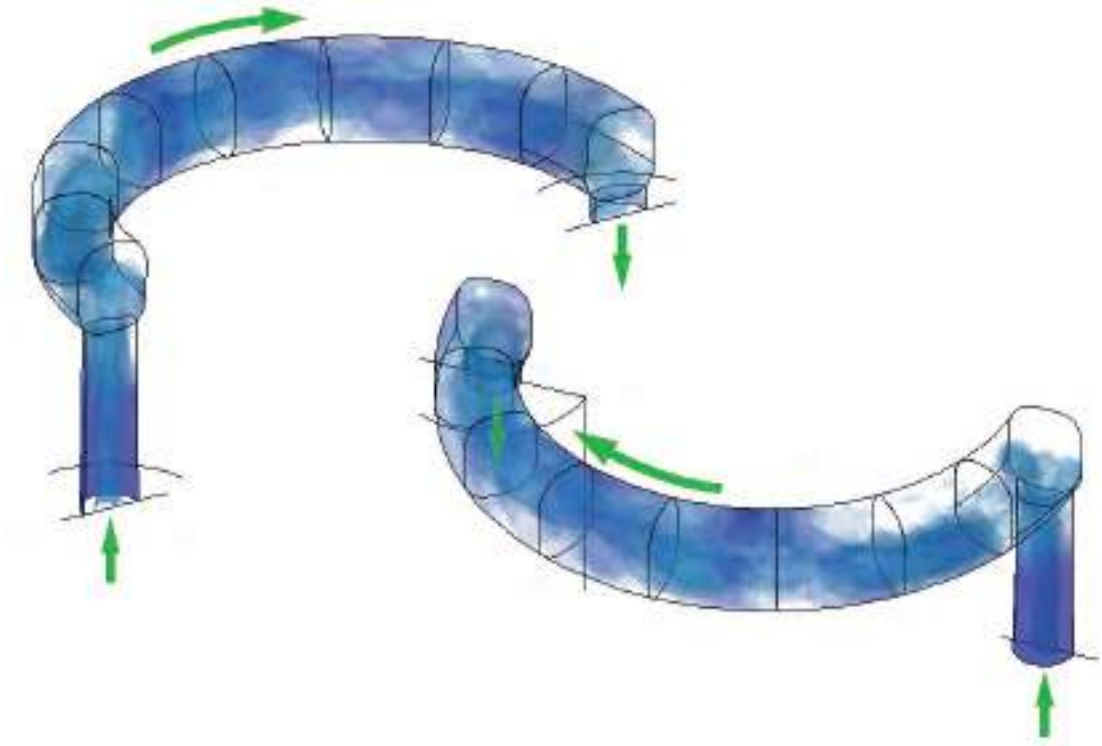

Fig. E.23 *SGM* air content and distribution at *TDC*, *500 rpm* and *4.0 l/min*

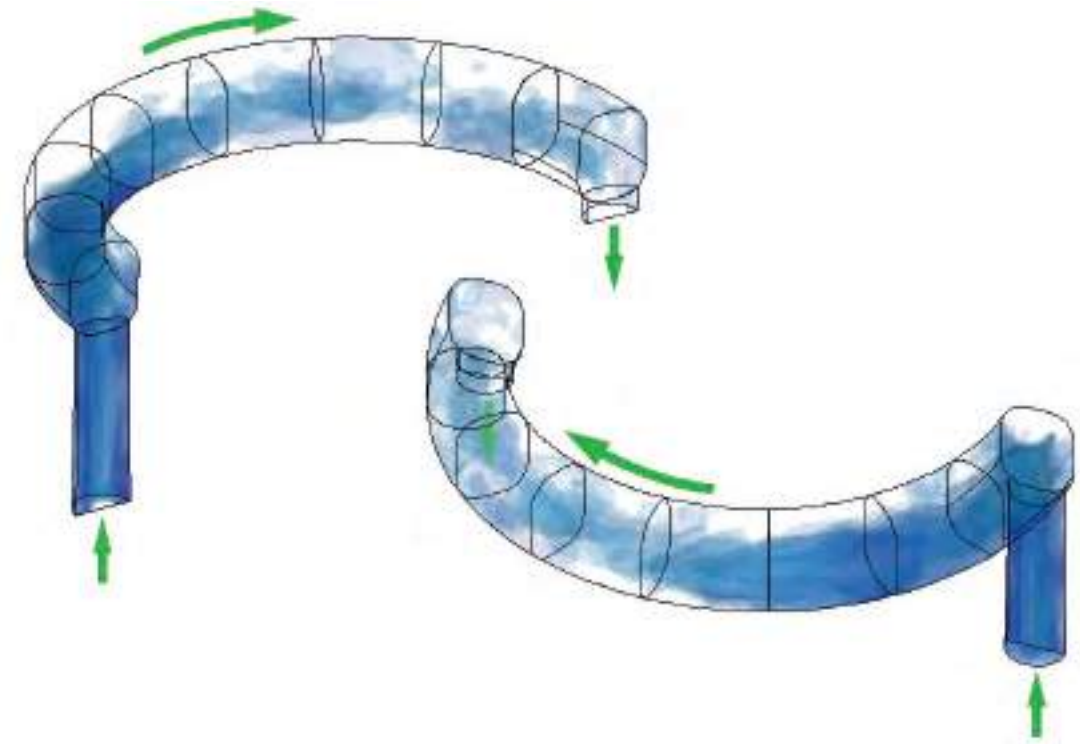

Fig. E.24 *SGM* air content and distribution at *TDC*, *500 rpm* and *2.121 l/min*

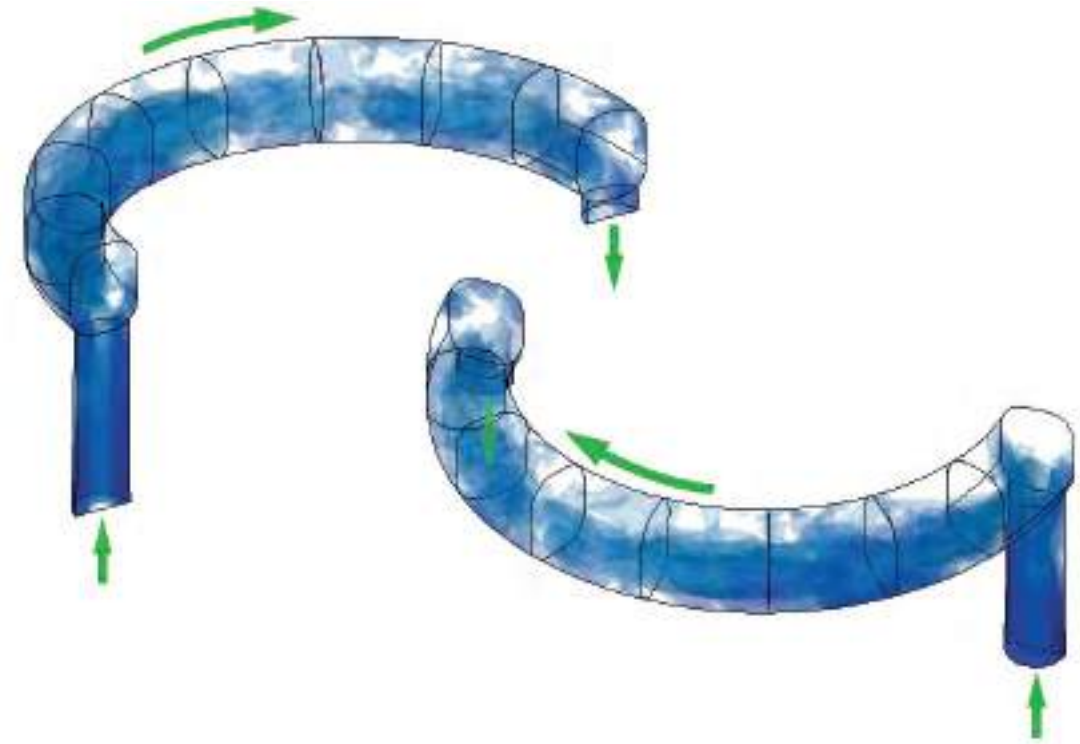

Fig. E.25 *SGM* air content and distribution at *TDC*, *750 rpm* and *1.651 l/min*

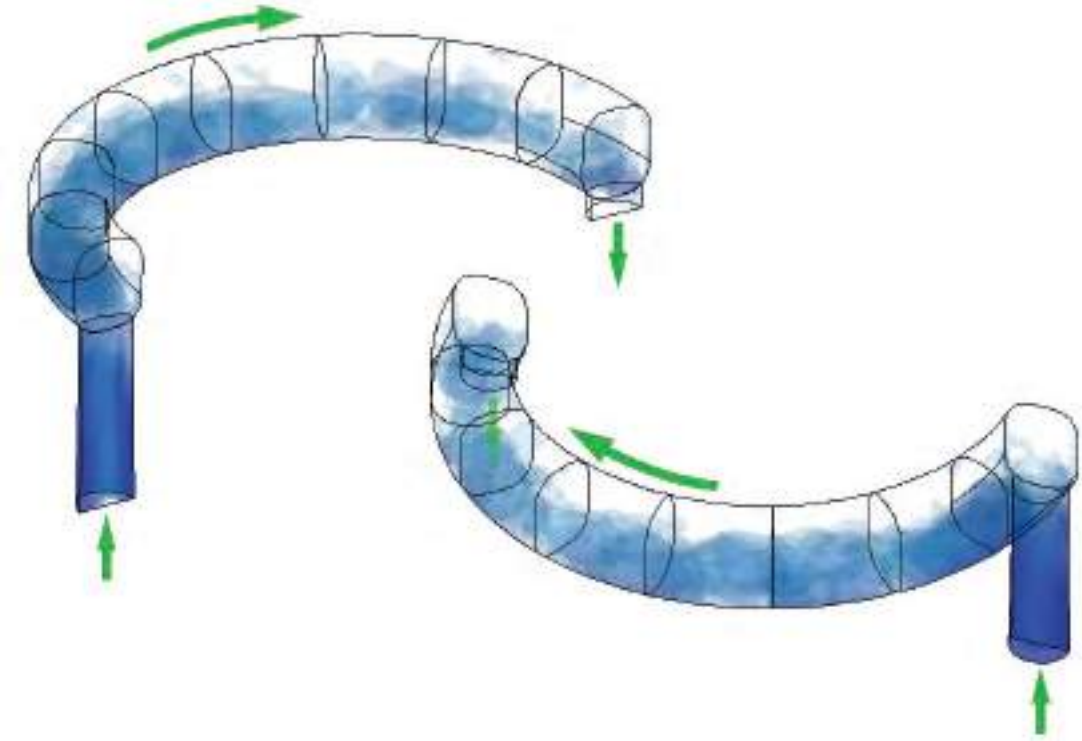

Fig. E.26 *SGM* air content and distribution at *TDC*, *1000 rpm* and *1.1050 l/min*

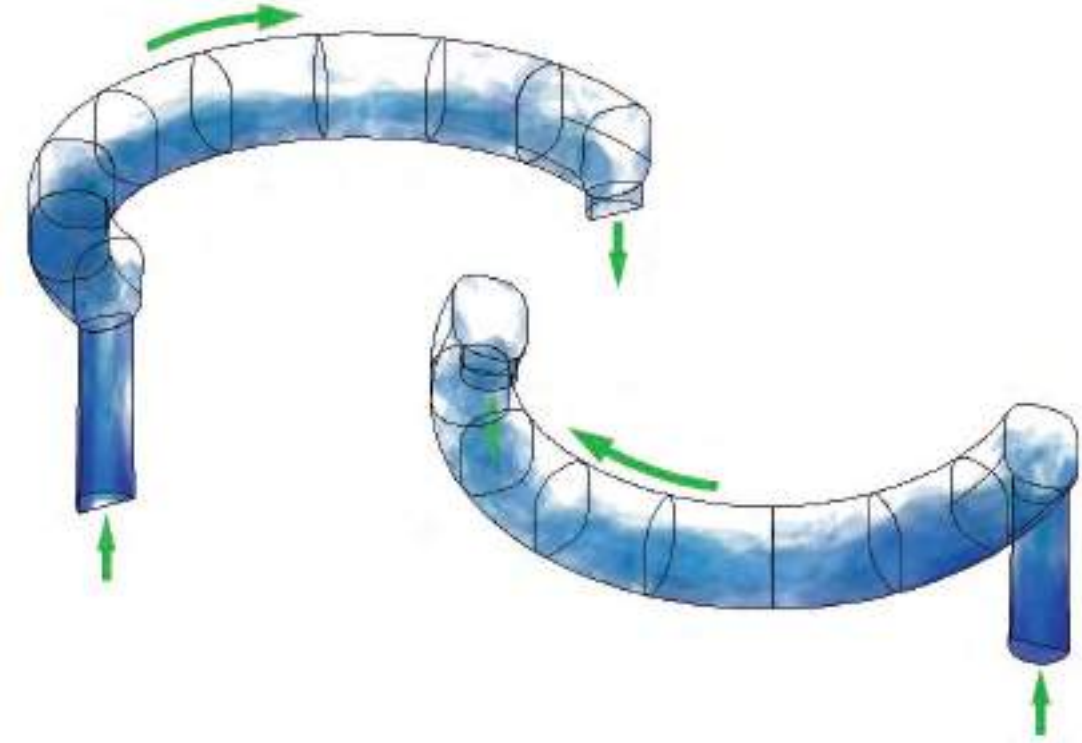

Fig. E.27 *SGM* air content and distribution at *TDC*, *1000 rpm* and *2.121 l/min*

E.7 Air and oil flow direction vectors for *SGM* at *BDC*

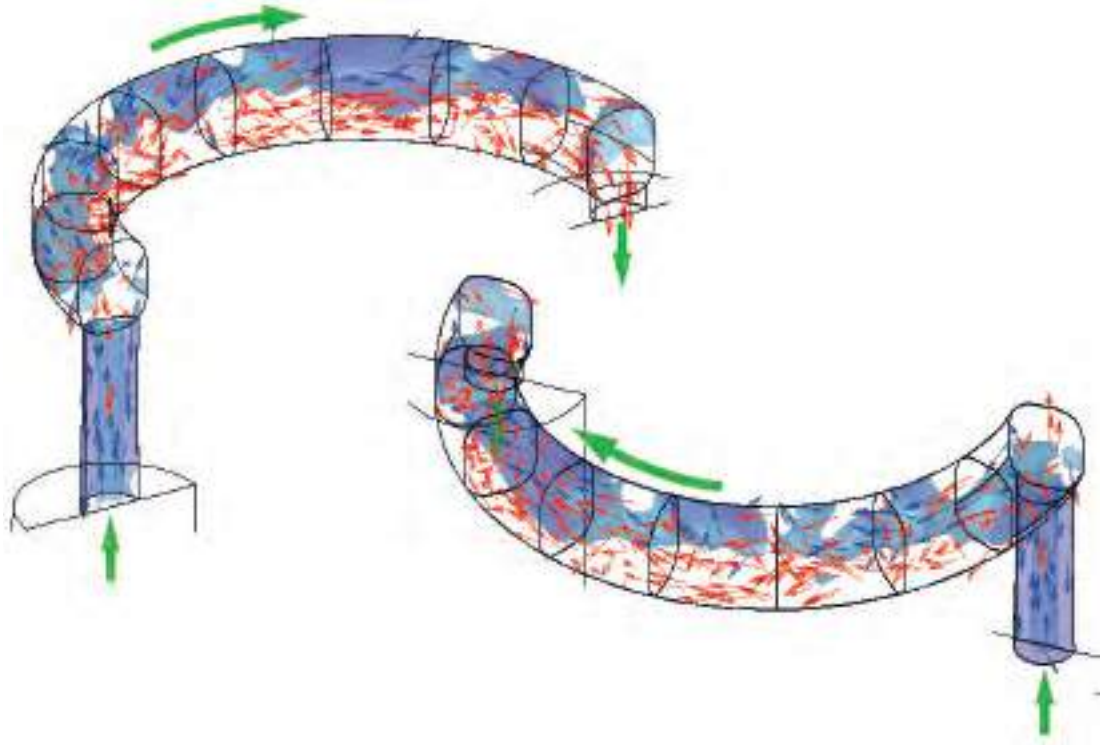

Fig. E.28 *SGM* air and oil flow direction at *BDC*, *500 rpm* and *1.105 l/min*

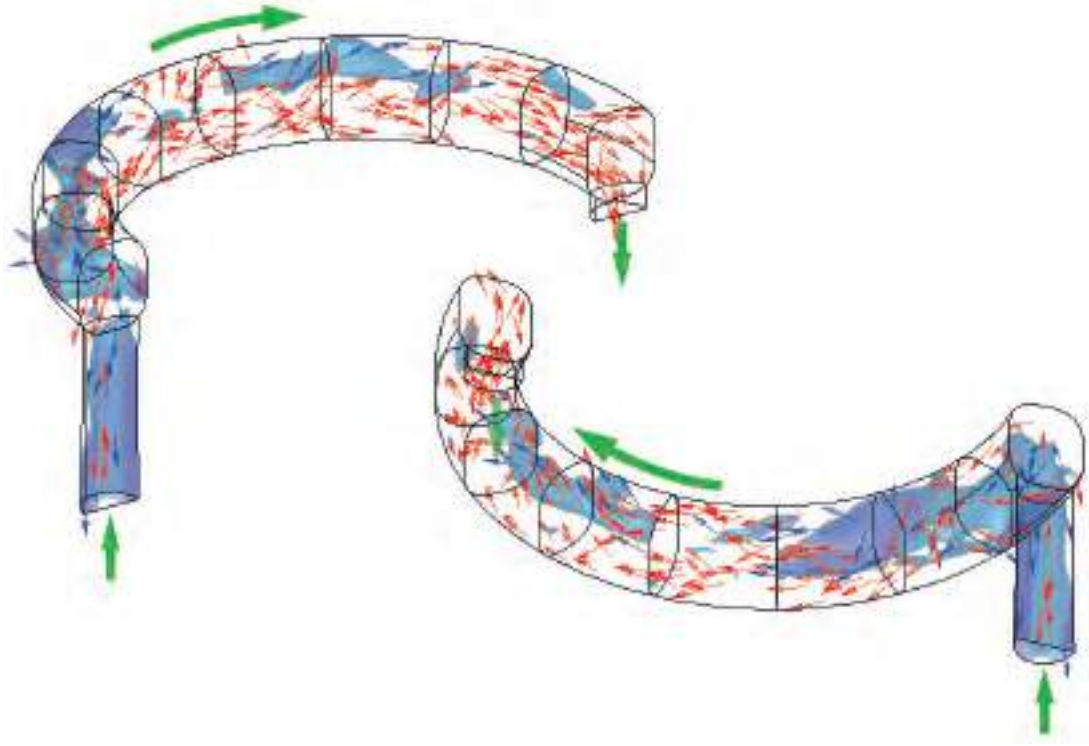

Fig. E.29 *SGM* air and oil flow direction at *BDC*, *500 rpm* and *2.121 l/min*

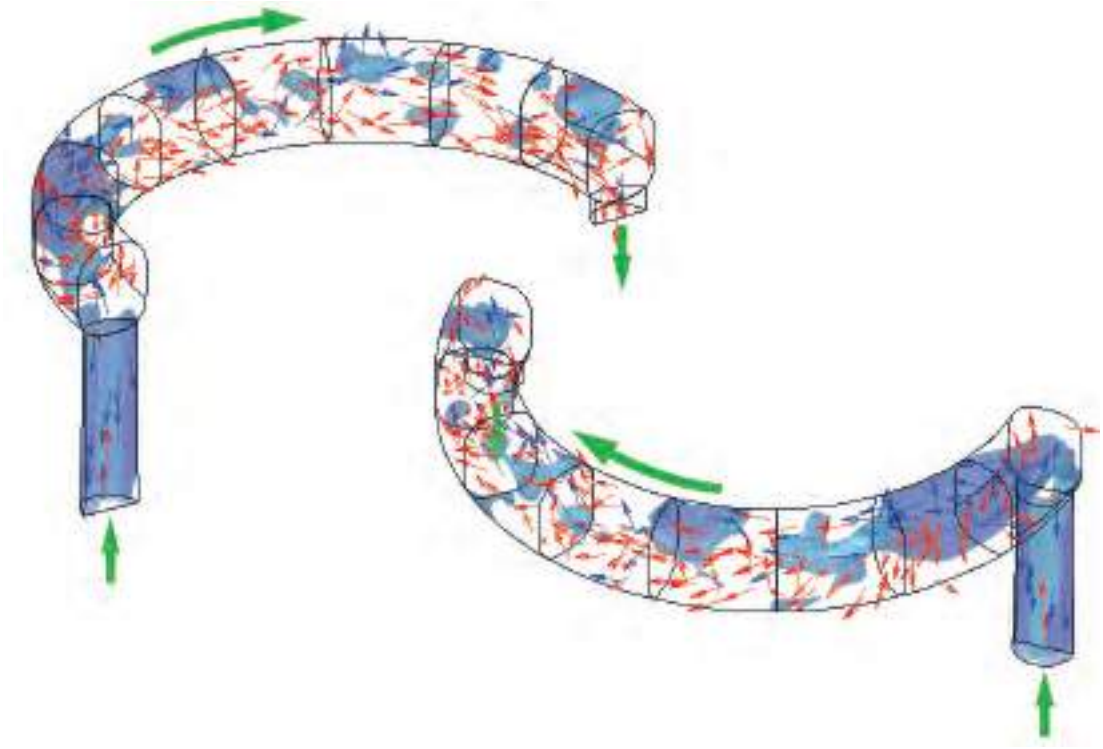

Fig. E.30 *SGM* air and oil flow direction at *BDC*, *750 rpm* and *1.651 l/min*

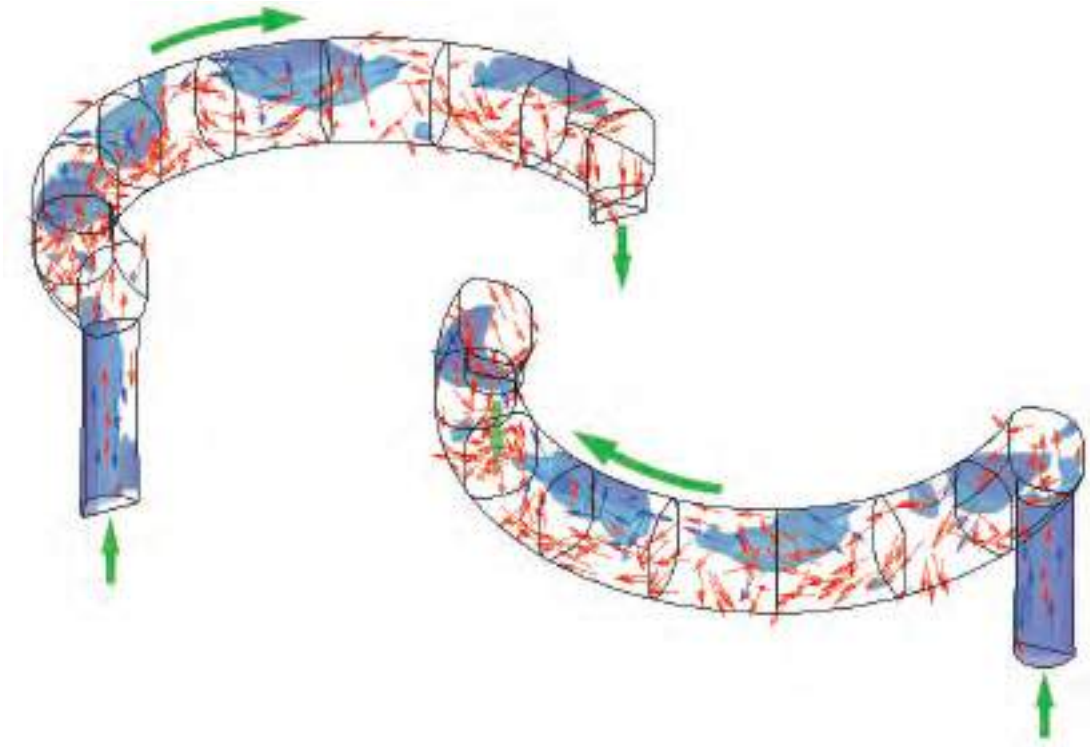

Fig. E.31 *SGM* air and oil flow direction at *BDC*, *1000 rpm* and *1.105 l/min*

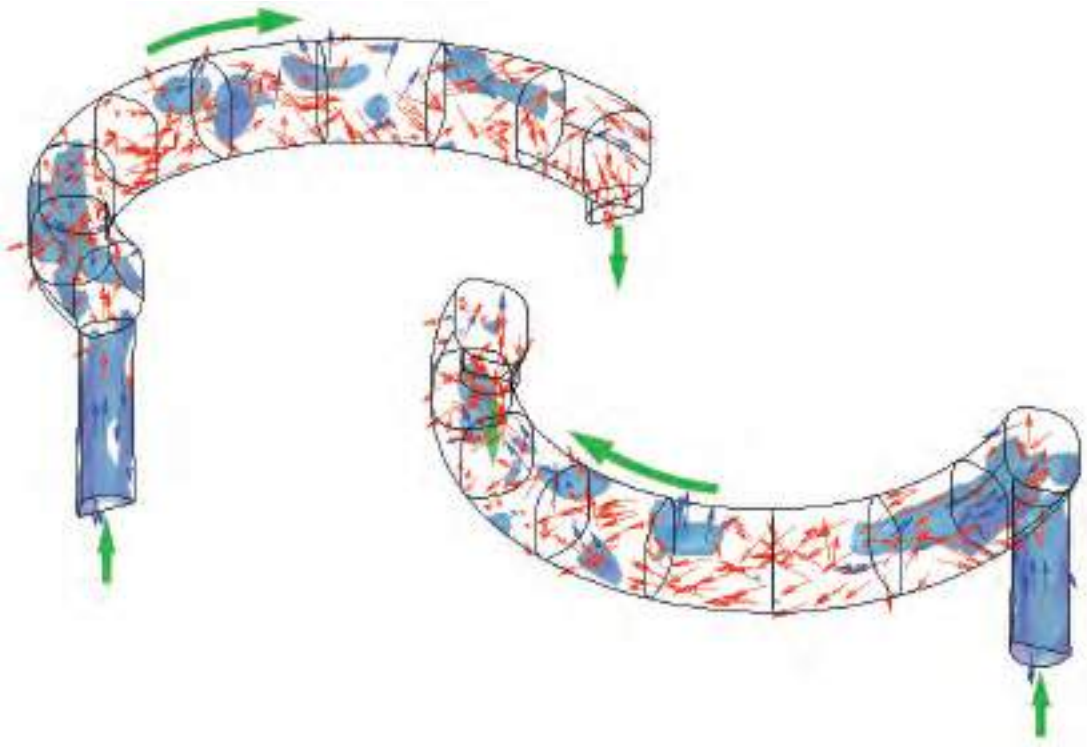

Fig. E.32 *SGM* air and oil flow direction at *BDC*, *1000 rpm* and *2.121 l/min*

E.8 Air and oil flow direction vectors for *SGM* at *TDC*

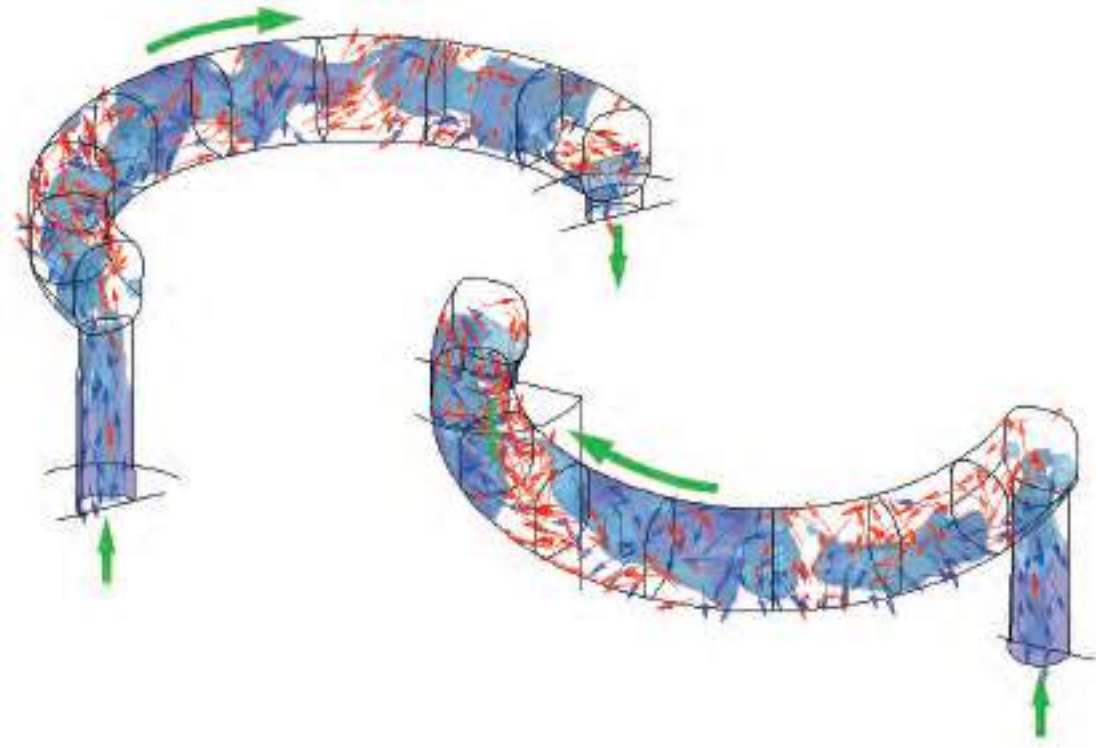

Fig. E.33 *SGM* air and oil flow direction at *TDC*, *500 rpm* and *1.105 l/min*

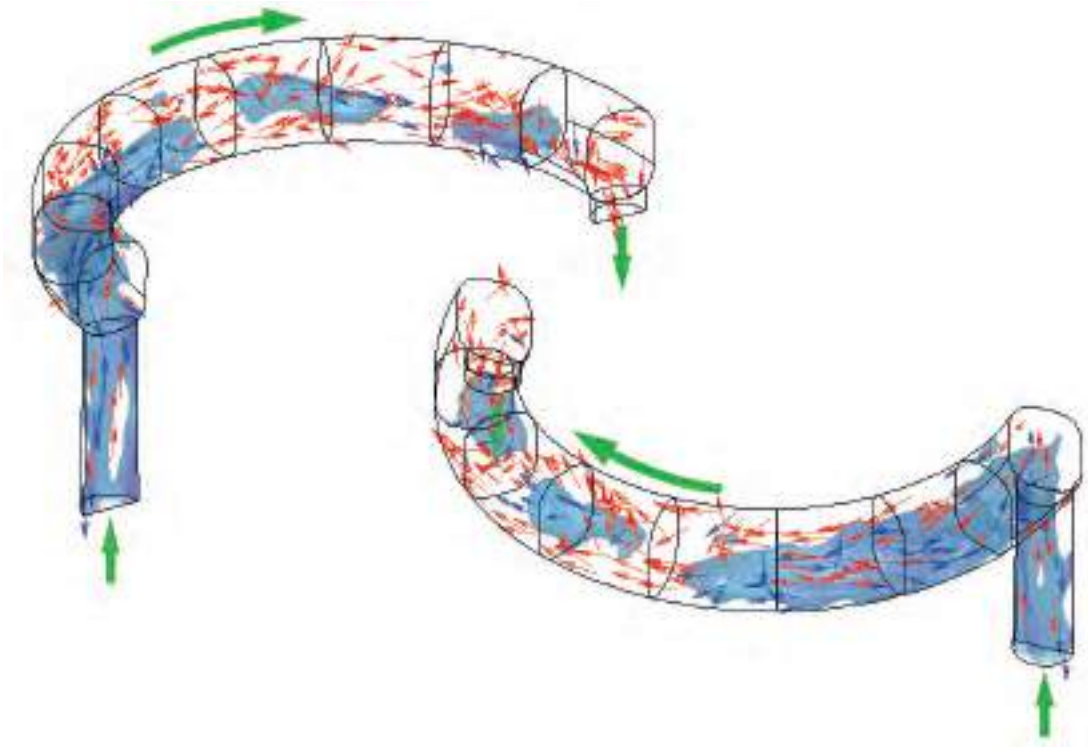

Fig. E.34 *SGM* air and oil flow direction at *TDC*, *500 rpm* and *2.121 l/min*

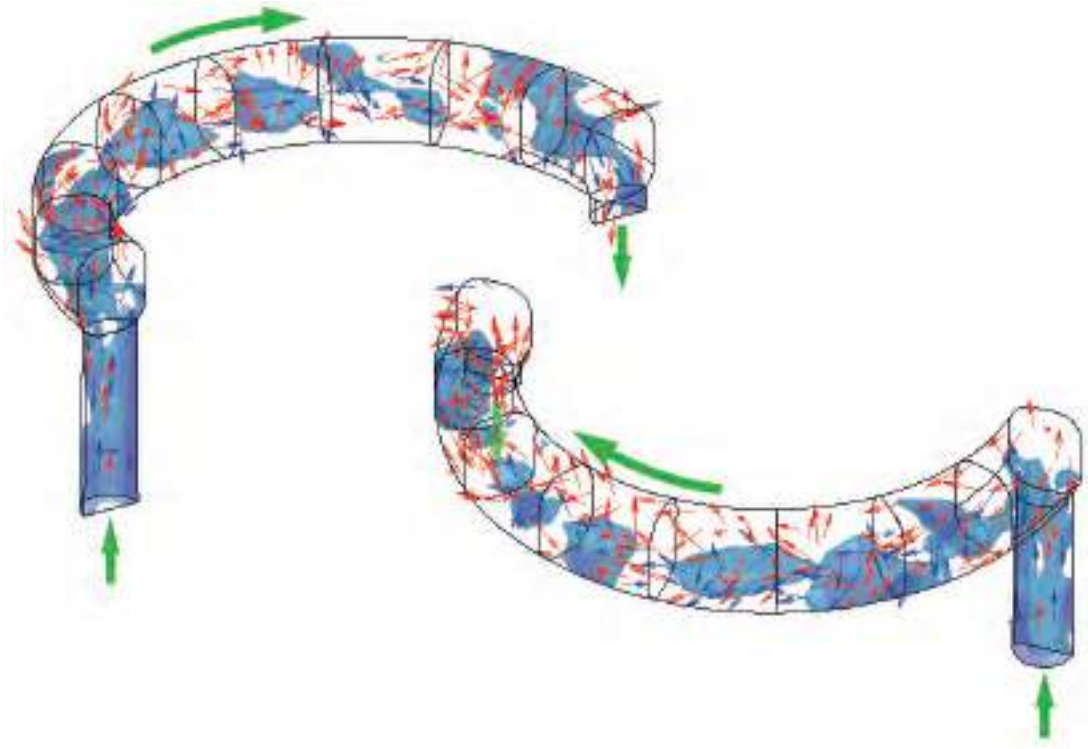

Fig. E.35 *SGM* air and oil flow direction at *TDC*, *750 rpm* and *1.651 l/min*

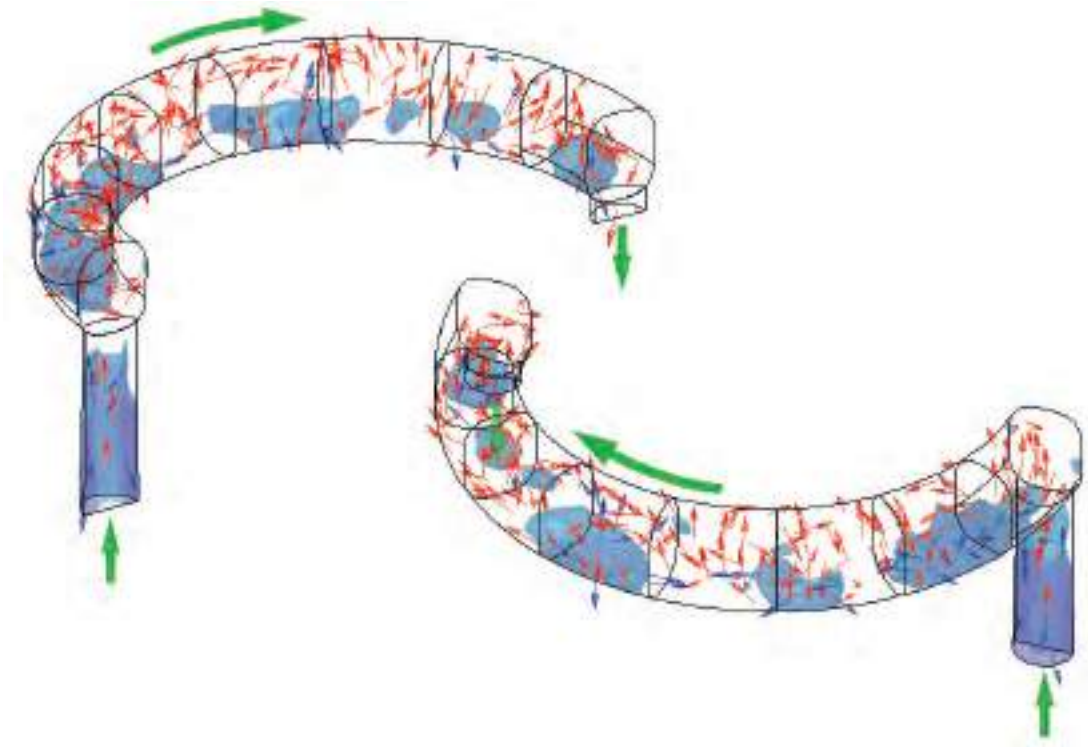

Fig. E.36 *SGM* air and oil flow direction at *TDC*, *1000 rpm* and *1.105 l/min*

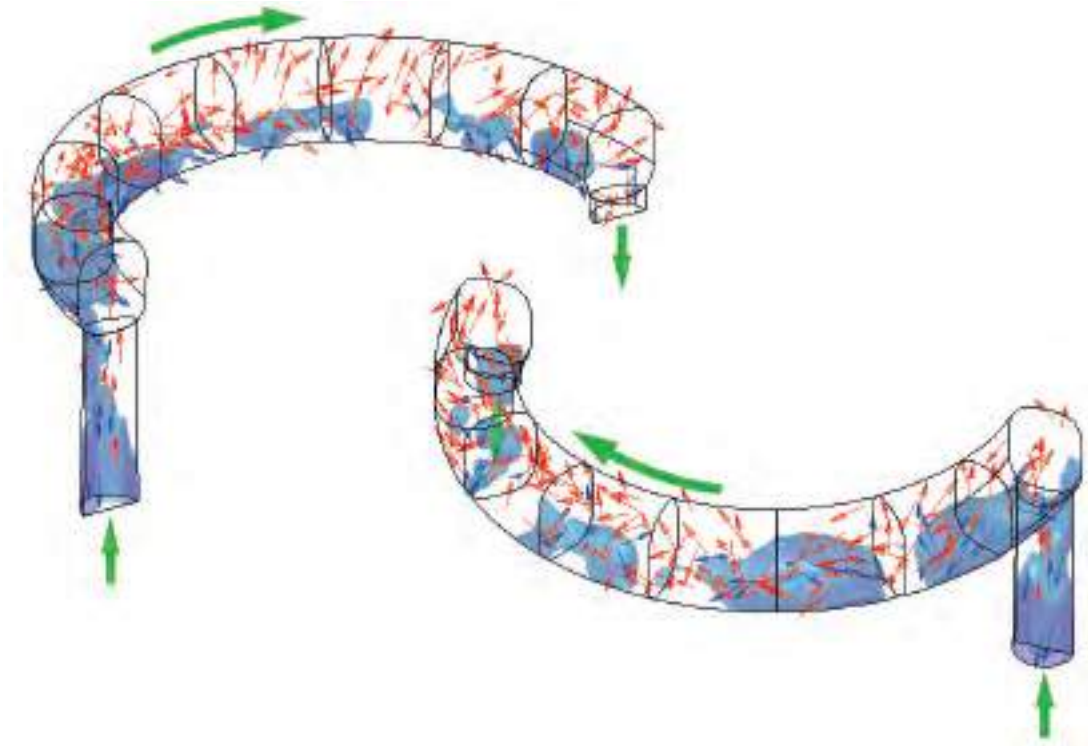

Fig. E.37 *SGM* air and oil flow direction at *TDC*, *1000 rpm* and *2.121 l/min*